Crystal Engineering of Room Temperature Phosphorescence in Organic Solids

Ehsan Hamzehpoor

Department of Chemistry

McGill University, Montreal

December 2022

A thesis submitted to McGill University in partial fulfillment of the requirements of the degree of Doctor of Philosophy

Dedicated to

The glow beneath my thoughts,

my "Delbar" and wife Yeganeh

and our son Masih

Abstract

Phosphorescence, a spin-forbidden emission of light from an excited triplet state, has a wide range of applications, but it generally relies on the presence of heavy elements, such as rare metals, in the material. Until recently, it was believed that organic materials composed of light atoms (C, H, N, O only) were incapable of phosphorescence at room temperature. However, this paradigm has shifted in the last decade, opening the quest for room-temperature organic phosphors. In this thesis, we study design strategies to achieve crystalline organic phosphorescent materials.

Chapters 2 and 3 focus on carbonyl-containing organic phosphors based on acridone moiety and the established relationships between their crystal packing of these molecules and the observed phosphorescent properties. In chapter 2, we found that varying the rotational alignment of the trioxoazatriangulene (TANGO) molecules within their columnar π-stacks, through varying the steric size of substituents, channels the emission pathway from pure fluorescence to pure phosphorescence, achieving a record high phosphorescence quantum yield (Φ_{Phos} = 42%). A detailed photophysical analysis of N-substituted acridones in chapter 3 revealed the dependence of triplet-triplet annihilation (TTA), a critical quenching pathway for phosphorescence, on the π-stacking distances in the crystal packing. These two chapters highlight the fundamental challenge in the design of phosphorescence in crystalline organic materials: *i.e.,* its critical dependence on molecular packing, which is not readily amenable to molecular design. In this context, the precise molecular engineering of the Covalent Organic Framework (COF) structure via principles of reticular chemistry brings new opportunities for organic phosphorescent materials.

En route to exploring these opportunities, we first addressed a long-standing challenge in synthesizing optically-pure boroxine and dioxaborole COFs, developing direct polymerization of arylpinacolate esters via transesterification (or metathesis) with methylboronic acid (or its esters). We have shown the generality of this approach, synthesizing nine different COFs, and demonstrated its advantages in avoiding hydrolytic and oxidative defects in the products.

In chapter 5, we used the COF platform for designing highly phosphorescent ($\Phi_{\text{Phos.}} \leq 29\%$) porous polyboroxine materials via copolymerization of halogenated (Cl, Br) and unsubstituted

benzenediboronic monomers. We showed that the phosphorescent properties of the resulting COFs can be tuned by controlling the type of the halogen dopant and the doping ratio. We further demonstrate the unique advantages of phosphorescent COFs by realizing a luminescent oxygen sensor with an ultra-wide dynamic detection range (8 orders of magnitude) and fast response time (<200 ms).

In chapter 6, we explored π-conjugated (cyanovinylene-linked) COF based on trioxaazatriangulene (TANG) building blocks as near-infrared (NIR) emitters. We studied the impact of acceptor strength, rotational degree of freedom of the linker, temperature, and humidity on the NIR emission of these materials.

Résumé

La phosphorescence, une émission de lumière interdite par le spin à partir d'un état triplet excité, a un large éventail d'applications mais elle dépend généralement de la présence d'éléments lourds tels que des métaux rares dans le matériau. Jusqu'à récemment, on pensait que les matériaux organiques composés d'atomes légers (C, H, N, O uniquement) étaient incapables de phosphorescence à température ambiante. Cependant, ce paradigme a changé au cours de la dernière décennie, ouvrant la voie à la recherche de phosphores organiques à température ambiante. Dans cette thèse, nous étudions les stratégies de conception pour obtenir des matériaux phosphorescents organiques cristallins.

Les chapitres 2 et 3 se concentrent sur les phosphores organiques contenant des carbonyles et basés sur la fraction acridone et sur les relations établies entre l'emballage cristallin de ces molécules et les propriétés phosphorescentes observées. Dans le chapitre 2, nous avons découvert que la variation de l'alignement rotationnel des molécules de trioxoazatriangulène (TANGO) dans leurs empilements π-colonnaires, en faisant varier la taille stérique des substituants, canalise la voie d'émission de la fluorescence pure à la phosphorescence pure, atteignant un rendement quantique de phosphorescence record (Φ_{Phos} = 42 %). Une analyse photophysique détaillée des acridones N-substituées dans le chapitre 3 a révélé la dépendance de l'annihilation triplet-triplet (TTA), une voie d'extinction critique pour la phosphorescence, sur les distances d'empilement cristallin. Ces deux chapitres mettent en évidence le défi fondamental de la conception de la phosphorescence dans les matériaux organiques cristallins, à savoir sa dépendance critique de l'empilement moléculaire, qui n'est pas facilement accessible à la conception moléculaire. Dans ce contexte, l'ingénierie moléculaire précise de la structure du cadre organique covalent (COF) via les principes de la chimie réticulaire offre de nouvelles possibilités pour les matériaux organiques phosphorescents.

En route pour explorer ces opportunités, nous avons tout d'abord relevé un défi de longue date dans la synthèse de COFs de boroxine et de dioxaborole optiquement purs en développant la polymérisation directe d'esters d'arylpinacolate par transestérification (ou métathèse) avec l'acide méthylboronique (ou ses esters). Nous avons montré la généralité de cette approche en

synthétisant neuf COFs différents, et démontré son avantage à éviter les défauts hydrolytiques et oxydatifs dans les produits.

Dans le chapitre 5, nous avons utilisé la plateforme COF pour concevoir des matériaux polyboroxine poreux hautement phosphorescents ($\Phi_{Phos} \leq 29\%$) via la copolymérisation de monomères benzènediboroniques halogénés (Cl, Br) et non substitués. Nous avons montré que les propriétés phosphorescentes des COFs résultants peuvent être accordées en contrôlant le type de dopant halogène et le ratio de dopage. Nous avons également démontré les avantages uniques des COFs phosphorescents en réalisant un capteur d'oxygène luminescent avec une gamme de détection dynamique ultra large (8 ordres de grandeur) et un temps de réponse rapide (<200 ms).

Dans le chapitre 6, nous avons exploré les COF π-conjugués (liés au cyanovinylène) basés sur des blocs de construction trioxaazatriangulène (TANG) comme émetteurs dans le proche infrarouge (NIR). Nous avons étudié l'impact de la force de l'accepteur, du degré de liberté de rotation du lieur, de la température et de l'humidité sur l'émission NIR de ces matériaux.

Acknowledgments

First and foremost, I would like to sincerely thank the most impactful person in my life, my academic supervisor, Prof. Dmytro F. Perepichka, for believing in me when I applied to McGill as my last hope for graduate studies in Canada. I appreciate his advice, patience, availability, and the freedom he gave me to explore my interests and my “crazy Friday night ideas.” I am also grateful for his valuable lessons in research ethics, critical thinking, physical chemistry, organic chemistry, experiment design, and scientific writing. I want to thank him for being an excellent mentor both in my academic journey and personal life. The last five years I spent in his laboratory at McGill have been life-changing for me, and I will forever be grateful to him for allowing me to be a part of his group.

I would also like to thank all the professors on my academic Ph.D. committee for their guidance, challenging questions, and support: Prof. Janine Mauzeroll, Prof. Tomislav Friščić, and Prof. Jean-Philip Lumb. I am genuinely grateful to Prof. Gonzalo Cosa for the valuable comments and discussions on photophysics, especially the invaluable Friday meetings.

To all my past and present mentors and teachers, from Mr. Halvayee, my 3rd-grade elementary teacher, who urged my parents to send me to the town for a better school, to my undergraduate supervisors who provoked my curiosity and passion for science, Prof. Farnoosh Faridbod, Prof. Farnaz Jafarpour, and Prof. Alireza Shayesteh.

I am incredibly grateful to two of my dearest friends and colleagues, Cory Ruchlin and Allen Tao, without whom the research underlying my thesis would not have been feasible. Thank you to my comrade Cory for adding the joy of explorations to my study years, his contribution to this thesis, his support and the discussions we had on our scientific and philosophical thoughts, his wonderful scientific-artistic spirit, the memory of long nights of data acquisition and the excitement we shared discovering emissive crystals and after-glow materials. Thank you to Allen for being such a passionate researcher, for his help and contributions to this thesis, and for being a great support over these years.

To all my colleagues in the Perepichka group, past and present, for all the advice, support, and wonderful memories that we have shared in OM341: Yoko Sakai-Otsuka, Muhammad Rizwan

Niazi, Ying-Hsuan Liu, Afshin Dadvand, Nathan Yee, Lakshmi Vellanki, Kiran Saghar Unikela, and Thaksen Jadhav and many more, I also want to thank all the amazing undergraduate students I had the chance to work with: Lisa Vlosva, Vincent Vermeulen, Sydney Mikulin, and Aleksander Mikov.

I would like to express my deep gratitude to all my fellow researchers and collaborators at McGill, Concordia, UdeM, and INRS, from whom I have learned a lot: Chenghao Liu, Gianluca Galeotti, Jorge Eduardo Ramos-Sanchez, Durbis Castillo-Pazos, Farshid Effati, Muhammad Ghufran Rafique, Mahdi Salehi.

I sincerely thank the departmental and administrative staff. A special thanks to Chantal Marotte, Linda Del Paggio, Nikoo Taghavi, and Chelsea Briand-Pitts for their constant and unconditional help during these years. Thank you to Dr. Alexander Wahba and Dr. Nadim Saade for helping with HRMS data, Petr Fiurasek for all the training and help with CQMF facilities and instruments, Hatem M. Titi for being a great friend, collaborator, and facility manager and for all his help with PXRD, crystallography, and surface area measurements and to Dr. Robin Stein for all her help with NMR and EPR.

I am grateful to all my friends in Montreal who made Montreal a home for me. To Nick and Sylvie, with whom I learned French (language, culture, and cuisine), and Gabriele Cappelli, who showed me that light exists even in the darkest corners of our lives if only we decide to look for it.

I would like to express my deepest appreciation and love to my dear parents Najmeh Dehyadegari, Mohammadreza Hamzehpoor, for their support throughout my life and for helping me reach my dreams.

Also, I express my appreciation to my parents-in-law, Soudabeh Moradi and Gholamreza Habibi for their support and help and all the inspirations in the last few years.

Last but by no means least, I would like to thank the love of my life, Yeganeh Habibi, for the last four years of immense support, the moments she stood by my side and brought me back to the right track, and all the obstacles we surmounted together. Thank you for being an amazing wife, friend, and inspiring scientist.

Table of contents

1. An Introduction to Organic Room Temperature Phosphorescence

2. Crystal Engineering of Room Temperature Phosphorescence in Organic Solids

3. Room Temperature Phosphorescence vs. Triplet-Triplet Annihilation in N-Substituted Acridone Solids

4. Synthesis of Boroxine and Dioxaborole Covalent Organic Frameworks via Transesterification and Metathesis of Pinacol Boronates

5.Efficient Room-Temperature Phosphorescence of Covalent Organic Frameworks through Covalent Halogen Doping

6. Azatriangulene-based Near Infrared Emissive Covalent Organic Framework

7. Discussion and Future Remarks

Appendix

List of Abbreviations

Å	Ångström
Aq.	Aqueous
a.u.	Arbitrary Unit
atm.	Atmosphere
P_0	Atmospheric Pressure
APCI	Atmospheric Pressure Chemical Ionization
Z	Atomic Number
ATR	Attenuated Total Reflection
τ_{avg}	Average Lifetime
E_{BG}	Bandgap Energy
BET	Brunauer–Emmett–Teller
CCDC	Cambridge Crystallographic Data Centre
^{13}C-NMR	Carbon-13 Nuclear Magnetic Resonance
CAT	Catechol
CT	Charge Transfer
COF	Covalent Organic Framework
CP-MAS	Cross-Polarization Magic Angle Spinning
CSP	Crystal Structure Predictability
T_{dec}	Decomposition Temperature
°C	Degrees Celsius
DF	Delayed Fluorescence
τ_{DF}	Delayed Fluorescence Lifetime
t_d	Delayed Time
DFT	Density Functional Theory
DET	Dexter Energy Transfer
DCM	Dichloromethane
DSC	Differential Scanning Colorimetry
D.R.	Diffuse Reflectance

DMSO	Dimethylsulfoxide
DMF	Dimethylformamide
ddd	Doublet of Doublets of Doublets
dd	Doublet of Doublets
dt	Doublet of Triplets
DZP	Double-Zeta Potential
DVS	Dynamic Vapor Sorption
Z_{eff}	Effective Atomic Nuclear Charge
EPR	Electron Paramagnetic Resonance
Φ_{ET}	Electron Transfer Yield
eV	Electronvolt
EW	Electron-Withdrawing
ESI	Electrospray Ionization
λ_{em}	Emission Wavelength
EDX	Energy-Dispersive X-Ray Spectroscopy
$K_{eq.}$	Equilibrium Constant
eq.	Equivalent
λ_{ex}	Excitation Wavelength
x_e	Extent of Reaction Progress at the Equilibrium
FFT	Fast Fourier Transform
Fl	Fluorescence
τ^F	Fluorescence Lifetime
$\lambda^F{}_{max}$	Fluorescence Maximum Wavelength
Φ_{Fl}	Fluorescence Quantum Yield
k_F	Fluorescence Rate Constant
FTIR	Fourier-Transform Infrared Spectroscopy
FWHM	Full Width at Half Maximum
S_0	Ground Singlet State
σ^p	Hammett Constant

HAADF-STEM	High Angle Annular Dark-Field Mapping in Scanning Transmission Electron Microscope
HDR	High Dynamic Range
HOMO	Highest Occupied Molecular Orbital
HRMS	High-Resolution Mass Spectrometry
HR-TEM	High-Resolution Transmission Electron Microscopy
HFS	Hirshfeld Surface
^{1}H-NMR	Hydrogen-1 Nuclear Magnetic Resonance
ICP-OES	Inductively Coupled Plasma Optical Emission Spectroscopy
I_{TTA}	Intensity of Triplet-Triplet Annihilation
IC	Internal Conversion
k_{IC}	Internal Conversion Rate Constant
ISC	Intersystem Crossing
Φ_{ISC}	Intersystem Crossing Yield
kcal	Kilocalories
LED	Light-Emitting Diode
Liq.	Liquid
LUMO	Lowest Unoccupied Molecular Orbital
MS	Mass Spectrometry
λ^{abs}_{max}	Maximum Absorption Wavelength
λ_{max}	Maximum Wavelength
MHz	Megahertz
m_p	Melting Point
T_m	Melting Temperature
MOFs	Metal Organic Frameworks
MBA	Methylboronic Acid
μM	Micromolar
μs	Microsecond
mbar	Millibar
mJ	Milliejoule

meV	Millielectronvolt
Mg	Milligram
ml	Millilitre
mmol	Millimole
ms	Millisecond
min	Minute
M	Molar
MRE	Multi-Resonance Effect
Nm	Nanometer
ns	Nanosecond
NTO	Natural Transition Orbital
NCS	N-Chlorosuccinimide
NIR	Near-Infrared
Nd: YAG	Neodymium-Doped Yttrium Aluminum Garnet
NDF	Neutral Density Filter
NLDFT	Non-Linear Density Functional Theory
k_{nr}	Non-Radiative Rate Constant
τ_n	Nth Component of Lifetime
S_n	N^{th} Singlet Excited State
T_n	N^{th} Triplet Excited State
NMR	Nuclear Magnetic Resonance
OD	Optical Density
OLED	Organic Light-Emitting Diode
ORTP	Organic Room Temperature Phosphorescence
DOS	Partial Density of States
ppm	Parts Per Million
PBA	Phenyldiboronic Acid
Ph.	Phosphorescence
τ_P , τ_{Phos}	Phosphorescence Lifetime

λ^{P}_{max}	Phosphorescence Maximum Emission
$I_{phos.}$	Phosphorescence Peak Intensity
Φ_{phos} ,Φ_{p}	Phosphorescence Quantum Yield
λ_{Phos}	Phosphorescence Wavelength
PL	Photoluminescence
PLQY	Photoluminescent Quantum Yield
Φ_{air}	Photoluminescent Quantum Yield in Air
Φ_{vac}	Photoluminescent Quantum Yield in Vacuum
PMT	Photomultiplier Tube
ArBpin	Pinacol Aryl Boronates
pH	Potential of Hydrogen or Power of Hydrogen
PXRD	Powder X-Ray Diffraction
Φ	Quantum Yield
QSDFT	Quenched Solid Density Function Theory
k_q	Quenching Constant
QA	Quinacridone
$^{3}k_{r}$	Radiative Transition Rate of the Triplet State
k	Rate Constant
k_f	Rate Constants of the Forward Reaction
k_r	Rate Constants of the Reverse Reaction
cm^{-1}	Reciprocal Centimetre
RT	Room Temperature
RTP	Room Temperature Phosphorescence
SEM	Scanning Electron Microscopy
s	Second
SAED	Selected Area Electron Diffraction
sh	Shoulder Peak
SCXRD	Single Crystal X-Ray Diffraction
ΔE_{S-T}	Singlet-Triplet Energy Gap

SAXS	Small Angle X-Ray Scattering
SOC	Spin Orbit Coupling
STP	Standard Temperature and Pressure
S_A	Surface Area
T	Temperature
THF	Tetrahydrofuran
TMS	Tetramethylsilane
TADF	Thermally Activated Delayed Fluorescence
TGA	Thermogravimetric Analysis
t	Time
TCSPC	Time Correlated Single Photon Counting
TD-DFT	Time Dependent Density Functional Theory
TD-SCF	Time-Dependent Self-Consistent Field
TA	Transient Absorption
TEM	Transmission Electron Microscopy
TFA	Trifluoroacetic Acid
$^3\tau$	Triplet Emission Lifetime
V_{TET}	Triplet Exciton Transfer Electronic Coupling
TTA	Triplet-Triplet Annihilation
2D/3D	Two/Three-Dimensional
UV	Ultraviolet
UV-Vis	Ultraviolet and Visible Light
vdW	van der Waals
VT	Variable Temperature
Vol., v	Volume
wt%	Weight Percent
XPS	X-Ray Photoelectron Spectroscopy

Chapter 1

An Introduction to Organic Room Temperature Phosphorescence

1.1. History of phosphorescence

Light emission phenomena have fascinated mankind since the earliest times. Phosphorus was the name given by the ancient Greeks, meaning “light bearer”: Φωσ = light; φόρος = to bear, for any phenomenon of glowing in the dark. For example, the light from the morning star (Venus), aurora borealis, the milky seas effect, fireflies, luminescent wood, rotten fish and meat, and glowing gems and stones were all accounted as phosphorescent phenomena.[1] The same name, phosphor, was later assigned to the element phosphorus isolated by Hennig Brand in 1669 for its glowing vapors upon burning when exposed to the air.[2, 3]

In 1888, German physicist and historian of science, Eildhardt Wiedemann, established a taxonomy of light-emitting phenomena, which brought a more consolidated definition of phosphorescence. He coined the term "*Luminescenz*" to refer to *"all those phenomena of light which are not solely conditioned by the rise in temperature (incandescence)",* and classified luminescence into six kinds according to the method of excitation, which remains the dominant classification in photophysics. [a] He recognized thermoluminescence, electroluminescence, crystaloluminescence, triboluminescence, chemiluminescence, and photoluminescence as the result of excitation by warming, electric field, crystallization, crushing/breaking crystals, chemical reaction, and light, respectively.[1, 4]

Photoluminescence was later subdivided into *fluorescence* and *phosphorescence*, based on the light emission duration after the excitation source is turned off. Fluorescence was considered an emission of light that disappears instantaneously upon cessation of the excitation. In contrast, phosphorescence persists (on the time scale of seconds, perceivable by the naked eye) after the excitation radiation is ceased.[4] Materials that exhibit phosphorescence are often called phosphors, one of the most famous examples being calcinated Bolognian stone (impure barium sulfide), discovered in 1602 by a cobbler from Bologna, Vincenzo Cascariolo. [1]

In 1929 Francis Perrin defined the distinction between fluorescence and phosphorescence based on their mechanism, suggesting that unlike the instantaneous emission of fluorescence, in

---

[a] Almost all the newly discovered light-emitting mechanisms such as radioluminescence, mechanoluminescence, sonoluminescence, etc. fit into these categories.

phosphorescence, the excited species pass through a metastable intermediate state before emission.[5] The nature of this metastable intermediate was not known until after the quantum mechanics revolution in the early 20th century. In 1944, G. N. Lewis and M. Kasha, pioneers of modern molecular photophysics, stated for the first time, "*We are now in a position to distinguish sharply between fluorescence and phosphorescence. Fluorescence is the light emitted in falling from an S level to an S level or from a T level to a T level. Phosphorescence is the light emitted when the molecule falls from a level of one class to a level of the other class.*" [6, b] One year later, G. N. Lewis and M. Calvin further confirmed the triplet state nature (a biradical with spin quantum number S=1) of phosphors by illustrating the paramagnetic behavior of phosphorescent compounds upon photoexcitation.[7]

1.2. Basic photophysics of phosphorescence

In modern molecular photophysics, we use the term fluorescence for the photoluminescence phenomena in which the spin multiplicity[c] is retained upon excitation-emission. In contrast, phosphorescence involves a change in multiplicity, typically from singlet to triplet or vice versa. As depicted in the simplified Jablonski diagram (Figure 1.1), upon photoexcitation, a closed-shell molecule in the singlet ground state (S_0) is promoted to an excited singlet state (S_n, $n \geq 1$). According to Kasha's rule,[8] the singlet excited state molecule will subsequently undergo radiationless internal conversion (IC) to the lowest singlet excited state (S_1).

The S_1 excited state will then undergo deactivation via one of the following competitive processes: (1) radiative decay to S_0 (fluorescence); (2) non-radiative decay to S_0 through IC or energy transfer; or (3) intersystem crossing (ISC; red arrow in Figure 1.1a) to a triplet state (T_n, $n \geq 1$). [d]

---

[b] In their article, S refers to singlet excited state and T refers to the triplet state.

[c] (number of probable spin angular momentum corresponding to a given total spin quantum number <s>.

[d] IC and ISC are radiationless de-excitation into a lower excited state. In IC the molecular spin multiplicity remains the same during, whereas it changes during ISC.

ISC is a spin-forbidden process that is accelerated by spin-orbit coupling, which is greater in magnitude in large atomic number elements (see section 1.4.1). Following the ISC, the triplet exciton will decay to the lowest triplet state (T_1) through IC. Eventually, the T_1 excitons deactivate to S_0 via a radiative emission (phosphorescence) or non-radiatively by vibrational relaxation or energy transfer to quenchers such as triplet diatomic oxygen molecules ($^3O_2$). The long lifetimes (due to the spin-forbidden ISC processes) of phosphors, coupled with their sensitivity to the molecular environment, have attracted increasing attention to phosphors' applications in sensing,[9-11] anti-counterfeiting, and data encryption.[12-14] Additionally, the extended phosphorescence lifetime is beneficial for bioimaging as it allows the elimination of the autofluorescence background of cells and tissues.[15, 16] The peculiar electronic configuration of the triplet state in the phosphors also enables applications in amplified photon up-conversion,[17] light-emitting[18-22] and photovoltaic diodes,[23] lasers,[24] and 3D displays.[25]

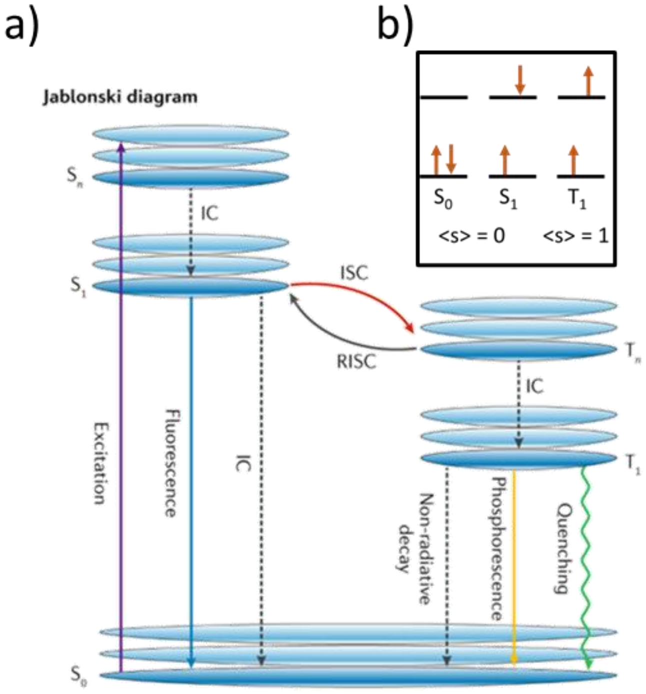

Figure 1.1. a) The simplified Jablonski diagram showing the different pathways that molecules could undergo upon excitation b) Inset showing a schematic representation of electronic levels of the ground state (S_0), singlet excited state (S_1), and triplet state (T_1) and their corresponding spin state(<s>). The figure is adapted with permission from ref. [26] Copyright (2020) Springer Nature limited.

1.3. Organic room temperature phosphorescence (ORTP)

Nearly all the efficient phosphors reported to date contain heavy metals (for example, Pt and Ir complexes in phosphorescent organic light-emitting diodes (OLEDs)[27, 28]). Conversely, purely organic luminophores (made from the top three rows of elements) have been widely explored for their fluorescence behavior but are generally considered non-phosphorescent at room temperature. This is due to the inefficient spin-orbit coupling (SOC) for low atomic number elements. SOC accelerates the ISC process, thus the small SOC in organic compounds does not allow the rates of ISC to compete with those of IC and the fluorescence deactivation of S_1. Even in the scenario where T_1 is formed in an organic molecules, it is easily deactivated by thermal vibrations (or other non-radiative pathways) at room temperature, faster than the spin-forbidden radiative $T_1 \rightarrow S_0$ transition (phosphorescence) could take place. Therefore, few organic molecules are phosphorescent, and until recently, their phosphorescence was only observed in glassy matrices such as polymeric matrices and frozen solvents at cryogenic temperatures.[29-31]

Nonetheless, organic phosphors have many potential advantages over metal-containing materials, including reduced toxicity and environmental footprint, longer emission lifetimes, lower cost, and wide tunability of photophysical properties, which has attracted scientists to this field. The first report of organic phosphors capable of emitting at room temperature (organic room temperature phosphorescence, ORTP) dates back to the 1930s when the crystals of tetraphenylmethane and its derivatives were shown to emit blue-green phosphorescence persisting for seconds after the excitation source was turned off.[32] A few other crystalline organic phosphors were reported during the next 3-4 decades.[33-37] However, the development of thorough purification and characterization techniques later suggested that the observed ORTP emission might have resulted from impurities[33] and the field of ORTP remained dormant until the early 2000s.

The pioneering work of B. Z. Tang and co-workers in 2010 on the ORTP of substituted benzophenone crystals[38] and J. Kim and co-workers in 2011 on the ORTP in halogen-bonded benzaldehyde doped crystals[39] rejuvenated the field by illustrating how crystal engineering of inter-molecular interactions in the solid-state can induce ORTP emission. Soon after, other organic molecules which exhibit efficient ORTP under ambient conditions were developed, drawing rapidly growing attention from materials scientists and photophysicists.[26, 40] Over the last decade, significant advances have been made in the rational design and formulation of pure organic luminophores with high ORTP efficiency, which has brought about the realization of various applications (Figure 1.2).

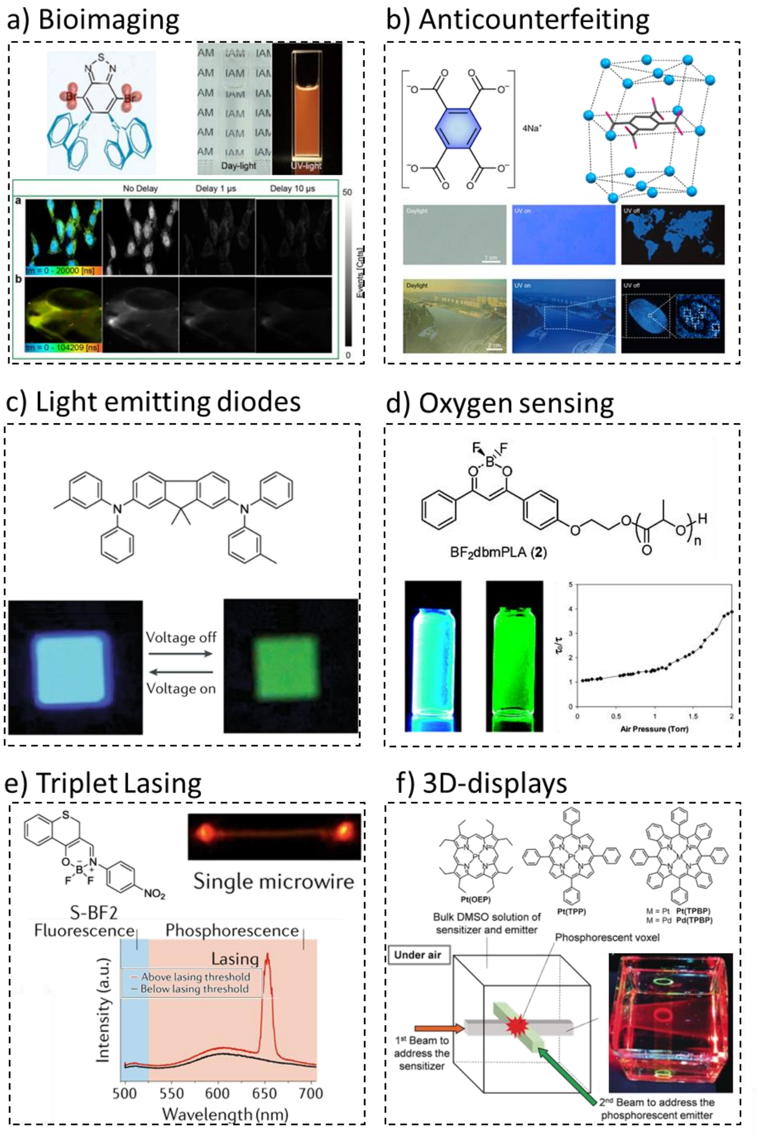

Figure 1.1. Applications of ORTP materials. a) Suppressing the autofluorescence background in cell imaging with benzothiadiazole-based ORTP nanocrystals. b) Printable anti-counterfeiting ink based on phosphorescent sodium pyromellitate. c) An OLED with ORTP emitting layer showing afterglow when the voltage is off. d) Phosphorescent difluoroboron dibenzoylmethane-tagged poly(lactic acid) used for O_2 sensing. e) Lasing from the crystal of S-BF_2 complex. f) 3D displays based on phosphorescent emission enhancement through local oxygen consumption in the solution of phosphorescent Pt porphyrin dyes in DMSO in air. Panel *a* adapted with permission from ref.[41], Copyright (2019) American chemical society. Panel *b* is adapted with permission from ref.[14] Copyright (2022) Springer Nature limited. Panel *c* is adapted with permission from ref. [42] Copyright (2015) John Wiley and Sons. Panel *d* is adapted with permission from ref.[43] Copyright (2007) American Chemical Society, Panel *e* is adapted with permission from ref.[24] Copyright (2017) American Chemical Society and Panel *f* is adapted with permission from ref.[44] Copyright (2020) John Wiley and Sons.

1.4. Design of ORTPs

The phosphorescence quantum efficiency (Φ_p) of a material depends on several photophysical properties: (1) the yield of ISC (Φ_{ISC} for $S_1 \rightarrow T_n$) generating the triplet excited state, (2) the rate of phosphorescence (k_p for $T_1 \rightarrow S_0$), and (3) the competing non-radiative triplet deactivation pathways (vibrational relaxation, k_{nr}, and energy transfer quenching pathways, k_q) as illustrated in equation 1.1. To achieve efficient phosphorescence, ISC rate (k_{ISC}) should be comparable to, or ideally higher than, the S_1 radiative (k_F 10^8-10^{10} s^{-1}) and internal conversions rates (k_{IC}, ~10^7–10^{10} s^{-1}) of S_1 (equation 1.2). Additionally, the k_p should surpass the k_{nr} and k_q of T_1.

$$\Phi_p = \Phi_{ISC} k_p \tau_p = \Phi_{ISC} k_p \left(\frac{1}{k_p + k_q + k_{nr}}\right) \qquad \text{(Equation 1.1)}$$

$$\Phi_{ISC} = \frac{k_{ISC}}{k_F + k_{IC} + k_{ISC}} \qquad \text{(Equation 1.2)}$$

where τ_p is the phosphorescence lifetime, and k_{ISC}, k_F, and k_{IC} are the rate constants for intersystem crossing, fluorescence, and internal conversion, respectively.

k_{ISC} is determined by the electronic configuration and energy levels of the molecule (see section 1.4.1 for discussion) but also depends on intermolecular interactions and molecular environments.[26, 45] Thus, solvent polarity has been shown to affect the ISC rates, and consequently, the Φ_p and τ_p, of aromatic ketones due to the change of T_1 orbital transitions from (n-π^*) to (π,π^*) in high polarity media.[46, 47] Furthermore, temperature dependence of ISC has been demonstrated in anthracene derivatives where the thermally activated $S_1 \rightarrow T_2$ ISC ($\Delta E_{S1\text{-}T2}$ ~+0.45 kcal mol^{-1}) is significantly suppressed by cooling of the solution.[48]

Apart from achieving efficient ISC, the other key factor for enhancing Φ_p is the acceleration of k_P or deceleration of $k_{nr} + k_q$ so phosphorescence can compete with the non-radiative decay of the triplet excited state. As will be discussed in the following section 1.4.1., enhancing spin-orbit coupling (SOC) through the heavy atom effect and El-Sayed's rule can accelerate both the k_{ISC} and k_p. Nevertheless, enhancement of one individually (k_{ISC} or k_p) cannot yield efficient phosphorescence. For instance, naphthalene in solution has a large Φ_{ISC} (~70%) but a small k_P (~10^{-1} s^{-1}) and consequently shows a $\Phi_p < 5\%$ at 77 K (<0.01% at room temperature).[49, 50]

1.4.1. Strategies to obtain k_{ISC} and k_p

The most critical parameter that determines the efficiency of ISC and the k_p is SOC.[e] Two main molecular design strategies to enhance the SOC are (1) the heavy atom effect and (2) the coupling of molecular orbital transitions with different angular momenta (El Sayed's rule).

1.4.1.1. Heavy-atom effect

SOC is directly proportional to Z_{eff}^4, where the Z_{eff} is the effective atomic nuclear charge. Conventionally, in the context of SOC, elements from Z = 1 (hydrogen) to Z = 10 (neon) are considered to be "light" (very small SOC), and elements with Z > 10 are considered "heavy."[50] For example, light atoms present in purely organic materials show SOC energies of <0.1, 0.1, 0.2, 0.4 kcal mol^{-1} for hydrogen, carbon, nitrogen, and oxygen, whereas heavier halogens possess 2.0, 7.0, and 14.0 kcal mol^{-1} for Cl, Br, I, respectively.[50] Thus, incorporating heavier elements with larger SOC energies into organic molecules increases the k_{ISC} .

The increasing heavy atom effect in a series of metal-organic complexes of dibenzoylmethane with Al^{3+}, Sc^{3+}, Y^{3+}, La^{3+}, Gd^{3+}, and Lu^{3+} ions reveals that while the fluorescence and phosphorescence energies were nearly unaffected by the type of ion, the phosphorescence to fluorescence ratio and triplet lifetimes vary markedly, with the heavier ions showing the most efficient and faster phosphorescence (Table 1.1).[51]

Apart from the incorporation of metals such as Ir and Pt, the heavy atom effect can be introduced by other, non-metallic heavy atoms such as chlorine,[52, 53] bromine,[10, 39, 54] iodine,[55-57] sulfur,[58-60] selenium[61] and tellurium (Figure 1.3).[61, 62] For example, in halogenated benzene and naphthalene, the phosphorescence-to-fluorescence ratio increases approximately with the square of the SOC energy of substituent atoms.[63]

---

[e] If SOC is small, ISC can proceed via spin-spin coupling (SSC) or hyperfine interaction (HFI) (see ref. 45).

Table 1.1. The spectroscopic data of the metal-organic complexes of dibenzoylmethane, obtained from ref. [51].

Metal ion	Z_{eff}	τ_p (seconds)	Fl./Phos. ratio
Al	13	0.70	NA.
Sc	21	0.39	5.2
Y	39	0.24	0.98
Lu	71	0.10	0.48
La	57	0.06	0.36
Gd	64	0.002	0.00 (no observable fluorescence)

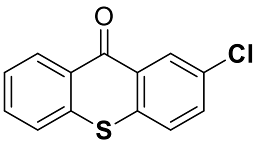

crystalline powder
$\Phi_{phos.}$ 75%
$\tau_{phos.}$ 1.33 ms

1.1.

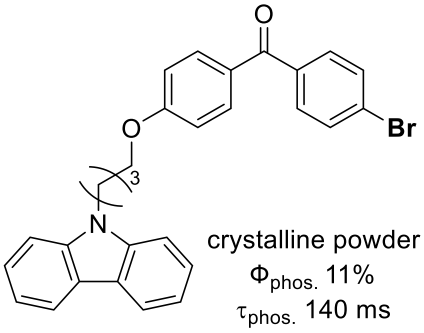

crystalline powder
$\Phi_{phos.}$ 11%
$\tau_{phos.}$ 140 ms

1.2.

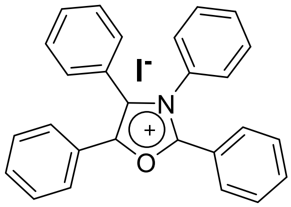

crystalline powder
$\Phi_{phos.}$ 35%
$\tau_{phos.}$ 0.48 ms

1.3.

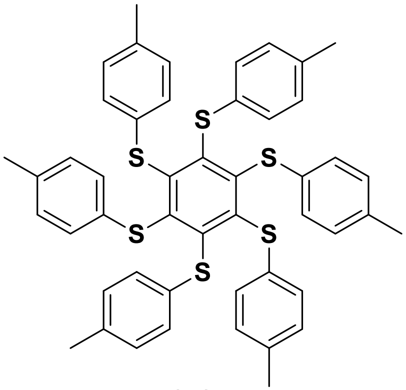

solution
$\Phi_{phos.}$ quant.
$\tau_{phos.}$ 3 μs

1.4.

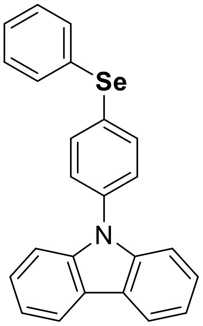

crystalline powder
$\Phi_{phos.}$ 7%
$\tau_{phos.}$ 380 ms

1.5.

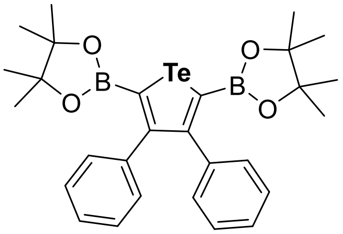

crystalline powder
$\Phi_{phos.}$ 4.5%
$\tau_{phos.}$ 52μs

1.6.

Figure 1.3. Examples of ORTP molecules with SOC enhanced by non-metallic heavy atoms. 1.1 ref.[52]; 1.2 ref.[10]; 1.3. ref.[56]; 1.4. ref[58]; 1.5. ref.[61] and 1.6. ref.[62]

The heavy atom effect can also be implemented through intermolecular interactions (external heavy atom effect) to enhance the SOC of organic molecules. In 1952, Kasha reported that dissolving α-chloronaphthalene in ethyl iodide results in a yellow-emissive solution, in which the singlet $\rightarrow$ triplet absorption has significantly increased. He rationalized this observation by a model based on "collisional perturbation of spin-orbital coupling in the π-electron orbitals of naphthalene".[64]

This external heavy atom effect is explored in organic salts by designing heavy atom-containing counterions, for example, in quinolinium salts,[65] and molecularly doped ionic polymers.[66] In 2018, Wang et al. reported a series of emissive 1,2,3,4-tetraphenyloxazolium salts with different counterions.[56] Only bromide and iodide salts exhibited ORTP emission, while fluoride, chloride, and hexafluorophosphate showed only fluorescent emission (Figure 1.4). The internal heavy atom effect is described by the participation of heavy atom orbitals in the excitation where the spin transition occurs.[50] On the other hand, the external heavy-atom effect on SOC of molecules has been suggested to occur by mixing of electronic states,[45] [67, 68] charge transfer interaction[69] and exciplex formations[70] between the perturber and the luminophore.

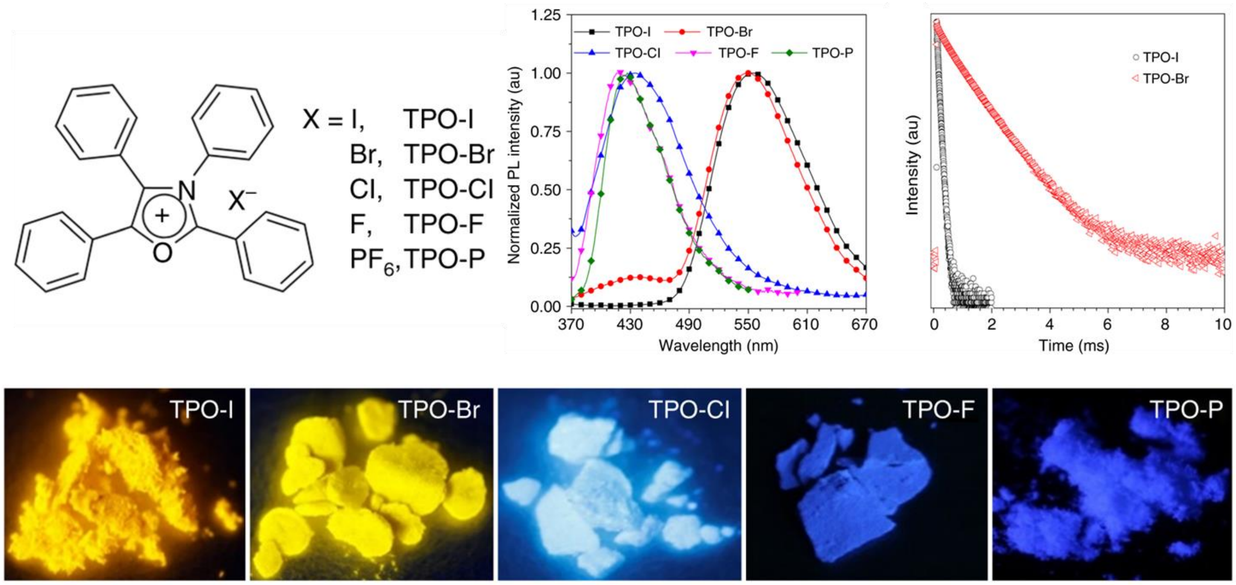

Figure 1.4. Chemical structures and luminescent emission spectra and photographs of 1,2,3,4-tetraphenyloxazolium salts with different counterions. Adapted with permission from ref. [56], Copyright (2018) Springer Nature limited.

1.4.1.2. El-Sayed's rule

Most aromatic compounds have weak SOC (~3x10^{-4} kcal mol^{-1}) and slow k_{ISC} (<10^8 s^{-1}), which would result in low phosphorescent efficiency.[71] In 1963, M. El-Sayed theoretically investigated the reason behind the unexpected efficient phosphorescence of some heterocycles, such as pyrazine, as compared to their hydrocarbon counterparts.[72] He concluded that the k_{ISC} is enhanced when the transition involves a change of orbital angular momentum, which became known as El-Sayed's rule.[72-74] According to El-Sayed's rule, for purely organic molecules, effective SOC only occurs in transitions from $^1(n,\pi^*) \rightarrow {}^3(\pi,\pi^*)$ and $^1(\pi,\pi^*) \rightarrow {}^3(n,\pi^*)$, in which the molecular transition orbitals p_x and p_y overlap, allowing the spin-transitions to occur (Figure 1.5). By contrast, the ISC from $^1(\pi,\pi^*) \rightarrow {}^3(\pi,\pi^*)$ or from $^1(n,\pi^*) \rightarrow {}^3(n,\pi^*)$ is not favored because there is no change of orbital angular momentum with which the flipping of electron spin can couple (inefficient SOC). For example, k_{ISC} of naphthalene with a $^1(\pi,\pi^*) \rightarrow {}^3(\pi,\pi^*)$ transition is ~10^6 s^{-1} whereas that of benzophenone with $^1(n,\pi^*) \rightarrow {}^3(\pi,\pi^*)$ is ~10^{11} s^{-1}.[50]

Similarly, T_1 with a $^3(n,\pi^*)$ configuration can relax to S_0 with a high k_P, owing to the spin-flip-allowed transition from $^1(n,\pi^*)$ to $^1n^2$, whereas T_1 with a $^3(\pi,\pi^*)$ configuration exhibits an extremely slow decay rate owing to the spin-flip-forbidden transition from $^3(\pi,\pi^*)$ to $^1\pi^2$.

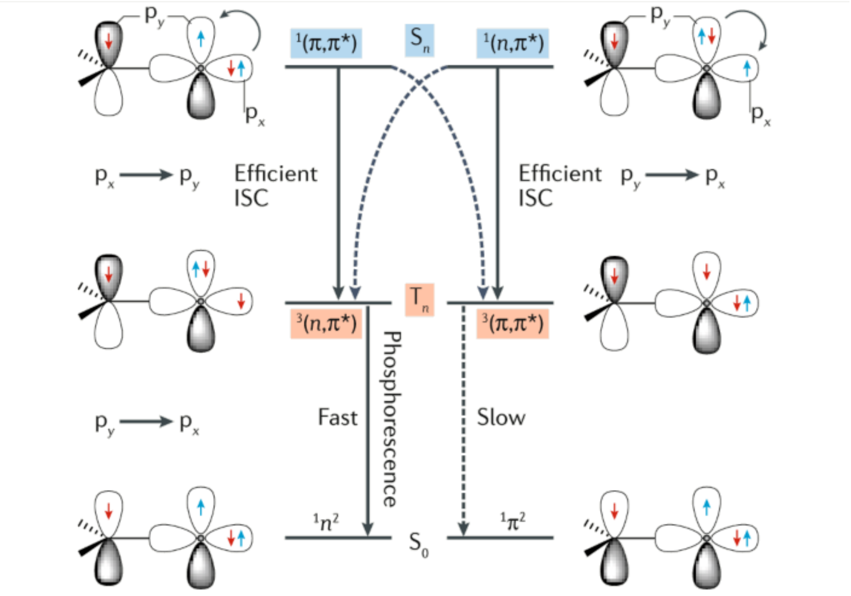

Figure 1.5. Schematic illustration of the El-Sayed's rule for ISC. Adapted with permission from ref. [75]. Copyright (2020) Springer Nature limited.

El-Sayed's rule has become the second common strategy to enhance the k_{ISC} of organic molecules (in addition to the heavy-atom effect discussed above). Incorporation of functional groups containing heteroatoms (O,[42, 53, 76, 77,] N,[78, 79] S, [61, 80-82] P[78]) into the molecular scaffolds enhances the phosphorescence efficiency of organic materials (Figure 1.6), as their lone-pair electrons endow the (n,π*) characteristic to the S_1 state, while a mostly (π,π*) characteristic is retained for the triplet states. Other molecular orbital transitions, such as (π,p) of boron in boronic acid and esters[83-87] and (σ,π^*) transitions in twisted hydrocarbons[88] have also been suggested to enhance the ISC and phosphorescence.

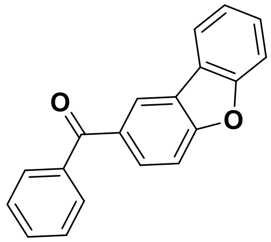

Crystalline powder
$\Phi_{phos.}$ 34.5%
$\tau_{phos.}$ 232 ms
1.7.

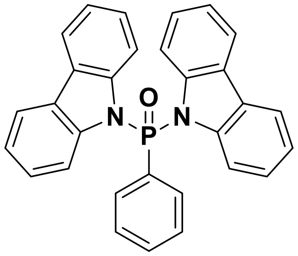

Crystalline powder
$\Phi_{phos.}$ 2.81%
$\tau_{phos.}$ 670 ms
1.8.

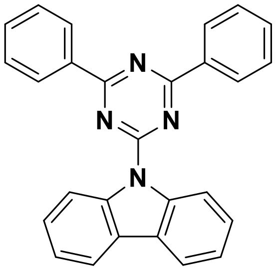

Crystalline powder
$\Phi_{phos.}$ 1.25%
$\tau_{phos.}$ 1060 ms
1.9.

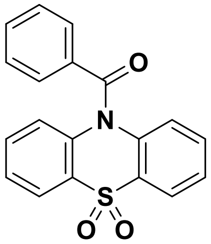

Crystalline powder
$\Phi_{phos.}$ 3.6%
$\tau_{phos.}$ 455 ms
1.10.

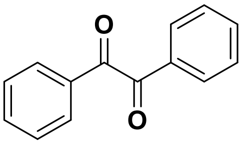

Crystalline powder
$\Phi_{phos.}$ 12.7%
$\tau_{phos.}$ 0.18 ms
1.11.

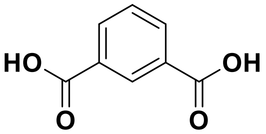

Crystalline powder
$\tau_{phos.}$ 970 ms

1.12.

Figure 1.6. ORTP molecules with SOC enhanced by heteroatoms with lone pairs. 1.7. ref.[53]; 1.8. ref.[78]; 1.9. ref.[79]; 1.10. ref[42]; 1.11. ref.[53] and 1.12. ref. [76]

1.4.2. Suppression of the non-radiative decay and quenching processes of T_1

Organic materials typically have small k_p of ~10^0-10^2 s^{-1} (for example, 1.9 s^{-1} for 1-chloronaphthalene and 150 s^{-1} for benzophenone in frozen solutions),[50] which is comparable to k_{nr} ~10^0-10^4 (depending on the rigidity of the matrix and temperature). Furthermore, depopulating and quenching the triplet excitons via $^3O_2$ or triplet-triplet annihilation (TTA) is detrimental to the ORTP effciency.[36, 89-93] Therefore, suppression of k_q and k_{nr} is critical for phosphorescence.

1.4.2.1. Embedding phosphors in a rigid matrix

A common method to suppress the non-radiative deactivations in ORTP emitters is to embed them into rigid host matrices, which also minimizes collisional quenching of triplet states with $^3O_2$. Examples of the most common rigid hosts utilized to increase ORTP are (1) polymers such as poly(vinyl alcohol)[94-97] and poly(methyl methacrylate) (PMMA),[98-101] (2) micelles,[102] (3) amorphous molecular solids such as steroids[103, 104] and cyclodextrins,[105, 106] (4) inorganic crystals[107] and (5) molecular crystals.[38, 103-106, 108-111]

Increasing the local motion in a PMMA host matrix by raising the temperature (especially, above the glass transition) has been shown to significantly reduce the T_1 lifetimes of benzophenone, suggesting that the host's molecular motions induce intramolecular vibrations in the guest, promoting k_{nr} and resulting in low phosphorescent emission.[31] Hydrogen and halogen bonds in polymers[90, 96, 112, 113] have been exploited to reduce the vibrational relaxation of the phosphor.[114] Covalent grafting of phosphors on the side chain,[115-118] the main chain,[119, 120] or the terminal position[43, 121] of the polymers has also been explored to enhance the ORTP efficiency over the physically mixed guest@polymer systems.

Strengthening the intermolecular interactions between the host and the guest by cross-linking [13, 122] has also been shown to dramatically enhance the RTP behavior. Jinsang and co-workers demonstrated this effect by doping a dienophile-modified derivative of a bromobenzaldehyde phosphor into furan-contained polymer capable of Diels–Alder click chemistry (Figure 1.7). They observed an increase in Φ_p of thin films made by crosslinked polymers (26%) that were nearly two times higher than that of phosphor-doped polymer systems having no such covalent linkage (15%).[122]

Molecular crystals have long been studied as (alternatives to polymer) hosts to realize ORTPs.[33, 123-125] In fact, the observed phosphorescence in derivatives of tetraphenylmethane as the first discovered crystalline ORTP was suggested to originate from a small amount of triphenylmethane dopants, as noted in 1939 by D. B. Clapp.[32] The complexity of molecular interactions in crystals and the phase separation of most guests when incorporated in organic crystals hampered their wide application as ORTP hosts. However, in 2011, Kim and co-workers showed efficient solid-state phosphorescence (Φ_p up to 55%) in a series of aryldibromide halogen-bonded crystals doped with structurally similar bromobenzaldehydes,[39] sparking the renewed interest in ORTP materials.

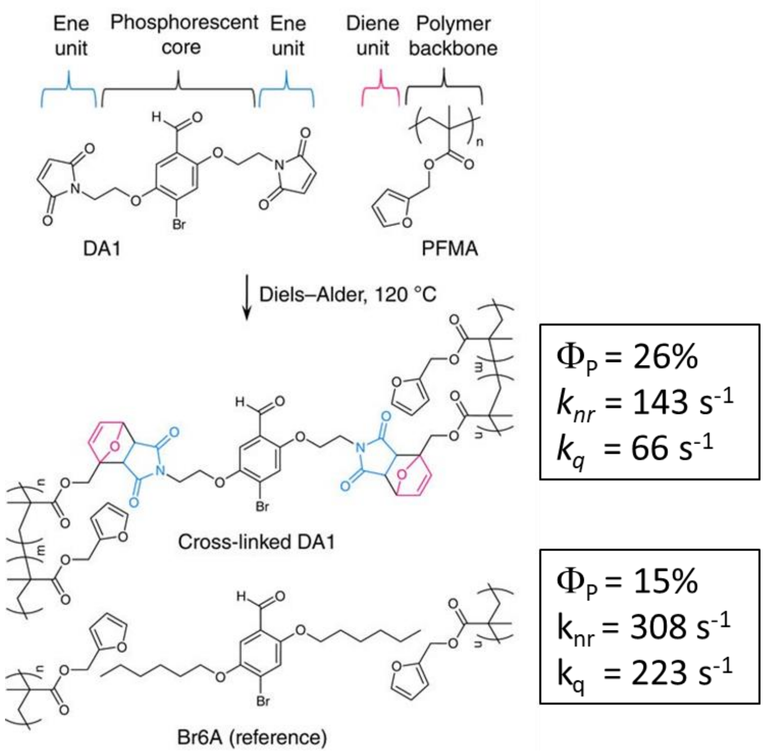

Figure 1.7. Chemical structures of Diels-Alder cross-linked DA1-doped PFMA polymer and Br6A-doped PFMA blend and their photophysical characteristics. Adapted with permission from ref.[122], copyright (2015) Springer Nature limited.

Although embedding more phosphors in the host can be expected to result in higher brightness of the ORTP, the increased concentration also enhances the incidence of triplet-triplet annihilation (TTA) and lowers the Φ_p.[126, 127] As such, organic phosphors are typically highly diluted in rigid matrices to isolate the phosphors and minimize encounters of their triplet excited states.[128] Alternatively, W. Huang and co-workers achieved the isolation of phosphors using salts of aryl carboxylates [14, 129] with a variety of cations. They found that the formation of high-density ionic bonds around carboxylic acid groups of the chromophores leads to a segregated molecular arrangement with negligible inter-chromophore interactions. This structural confinement allowed the realization of record-high blue phosphorescence with Φ_p up to 96.5% (Figure 1.2b).[14]

1.5. ORTP emission in pure molecular crystals

Generally, achieving ORTP emission in pure crystals of phosphors poses a particular challenge due to the enhanced TTA as well as other aggregation-caused quenching processes.[130] The TTA mechanism was originally proposed to explain the delayed fluorescence of π-conjugated materials, during which two T_1 states encounter one another and annihilate, producing S_0 and S_1 states.[131] TTA is particularly efficient in conjugated phosphors with a planar structure, such as anthracene, owing to the high π-overlap of the individual molecules.[132, 133]

In their seminal work in 2010, B. Z. Tang and co-workers showed that benzophenone derivatives are non-emissive at room temperature in solution and in an amorphous condensed phase (absorbed on a TLC plate or doped into a polymer), whereas in the crystalline state, the confined intramolecular motions resulted in a decrease of k_{nr} and bright RTP under ultraviolet (UV) irradiation is observed at room temperature (Figure 1.8).[38] The authors concluded that the carbonyl group, halogen atom, and nonplanar conformation are the key elements of designing the ORTP solids.

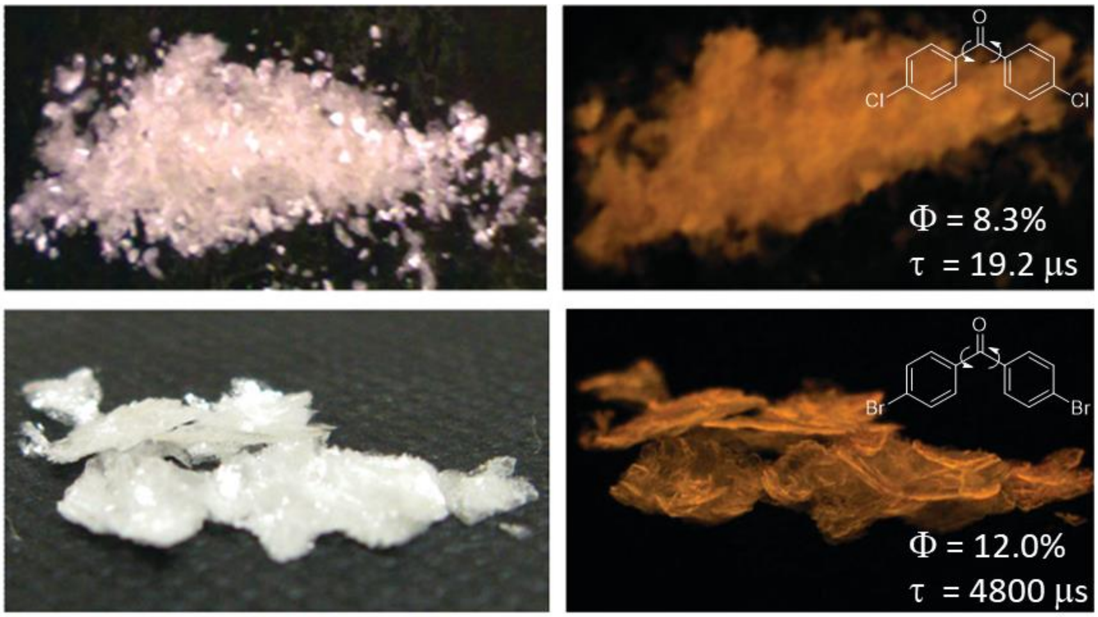

Figure 1.8. Photograph of dibromo and dichlorobenzophenone crystals at room light and under UV excitation. The figure is adapted with permission from ref.[38], Copyright (2010) from American Chemical Society.

Since then, several pure ORTP solids have been reported (Figures 1.3, 1.4, 1.6)[10, 39, 42, 52-62, 76-82] and with few exceptions, their molecular designs are based on non-planar flexible structures that limit π–π interactions in the solid state (reducing the TTA) and show aggregation-induced emission.[130] The role of molecular interaction and solid-state packing has been widely acknowledged in these ORTPs. However, the mechanism behind the behavior is not well-understood and no unified structure-luminescent property has been suggested for ORTPs**.** As such, despite all the progress in understanding the mechanisms underlying ORTPs, the realization of these materials is still an empirical exercise, and precise design of ORTP crystals with desired properties (emission wavelength, lifetime, etc.) is not possible.

The main reason behind this formidable challenge is that when molecules aggregate and crystallize, their electronic levels are significantly perturbed, changing their photophysical behavior.[134, 135] Depending on the specific crystal packing, different intermolecular interactions will lead to different electronic couplings between the adjacent molecules. Already by 1958, E. G. McRae and M. Kasha had predicted that the way molecules are packed in solids could dramatically change their fluorescence/phosphorescence properties.[136] Their calculations suggest that parallel stacking of co-aligned molecules will result in higher phosphorescence efficiency compared to tilted molecular stacks.

The seminal work of Huang and co-workers in 2015 showed the effect of strong coupling in H-aggregated molecules (analogous to parallel stacking described by Kasha[136]) that results in the stabilization of excited triplet states.[79] The H-aggregation was manifested as an aggregation-induced blue shifted in the absorption spectra and validated by the single crystal structure analysis (SCXRD). Time-dependent density functional theory (TD-DFT) calculations of individual molecules and H-aggregated dimers suggested that ISC is probably enhanced upon aggregation due to more transition channels from $S_1 \rightarrow T_n$ (Figure 1.9). The newly formed triplet states were also stabilized by H-aggregation, which acted as an energy trap for the locally excited molecules, that resulted in a long-lived excited state and ORTP with lifetime of >1 s.

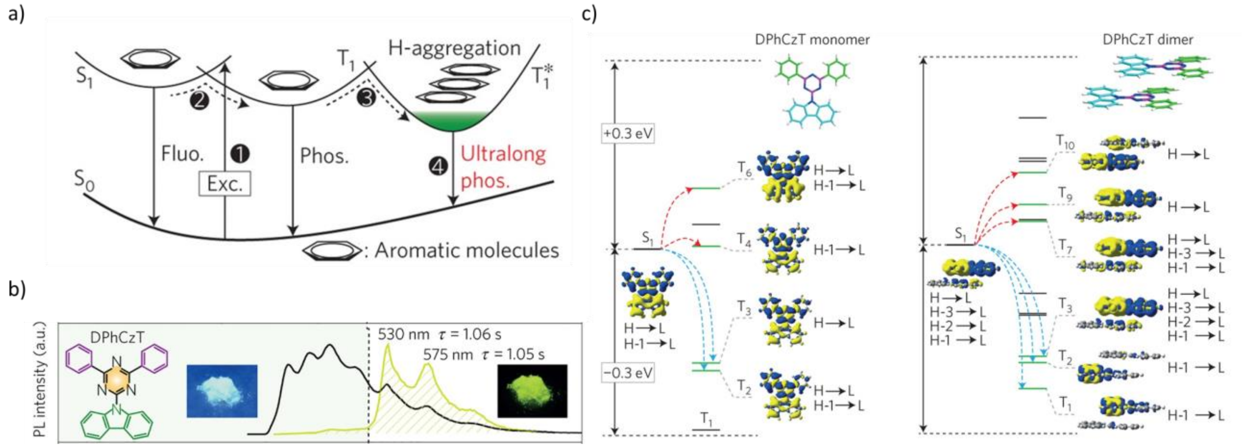

Figure 1.9. a) Proposed mechanism of ultralong ORPT by stabilizing the lowest triplet excited state (T1). b) Luminescence of DPhCzT and c) its energy diagram calculated by TD-DFT. Adapted with permission from ref. [79]. Copyright (2015) Springer Nature limited.

Bryce and co-workers suggested another mechanism for enhancing phosphorescence in molecular crystals. Using TD-DFT and the single crystal X-ray crystallography (SC-XRD) of 4-(9H-carbazol-9-yl)benzophenone(Cz-BP), they showed that close intermolecular contact of moieties capable of different excited-state configurations, for example, carbonyl (n-π*) and carbazole (π-π*) results in significant interactions between their orbitals (Figure 1.10).[54] Similar to Huang's report, the multiplication of accessible ISC channels in the aggregated state (dimer cluster corresponding to the observed crystal packing) compared to the isolated molecule in the gas phase, was suggested to be a contributing factor of the ORTP.

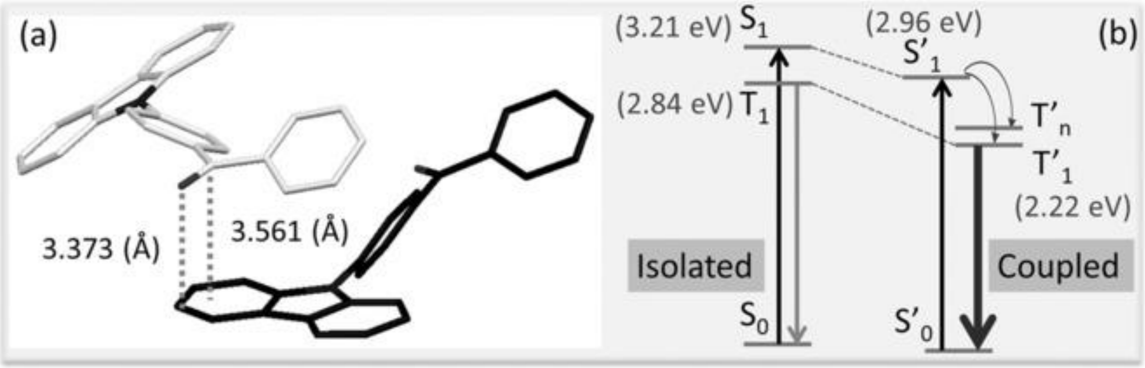

Figure 1.10. a) Intermolecular electronic coupling of the carbonyl and carbazole groups in two Cz-BP molecules that are in close proximity in the single crystal. b) Energy level diagram of the isolated and coupled Cz-BP molecule(s). Adapted with permission from ref.[54] Copyright (2020) John Wiley and Sons.

Furthermore, by studying 7 different derivatives of 10-phenyl-10H-phenothiazine-5,5-dioxide, Z. Li and co-workers found that stronger π-π interactions in the crystalline solids with electron-withdrawing substituents dramatically enhance their phosphorescence lifetime from 88 ms for the methoxybenzene-substituted phosphor (π-π of ~4.25 Å) up to 410 ms in fluorophenyl-substituted compound (π-π of ~4.25 Å).[9]

Studying polymorphs of the same molecule can be particularly helpful in elucidating the effects of crystal packing on the photophysical behavior of ORTP solids.[12, 137, 138] Investigating the three polymorphs of N-(4-cyanophenyl)phenothiazine, Zhen and co-workers showed different phosphorescence lifetimes of 226 ms, 41 ms, and 36 ms and quantum yields of 23%, 18%, and 7% (Figure 1.11 a).[137] Z. Li and co-workers reported two polymorphs (A and B) of ortho-substituted triphenylamine, one of which showed ORTP emission with a 33 ms lifetime. In comparison, polymorph B showed very weak emission with a 1 ms lifetime but upon grinding, exhibited mechanoluminescence. [138] Using a combination of SCXRD and solid-state NMR, they suggested that the latter polymorph includes inhomogeneous interactions, having regions of strong interactions and regions of free volume around molecules in the crystal structure, which enhances the k_{nr} and facilitates the crystal fracture resulting in the mechanoluminescent property.

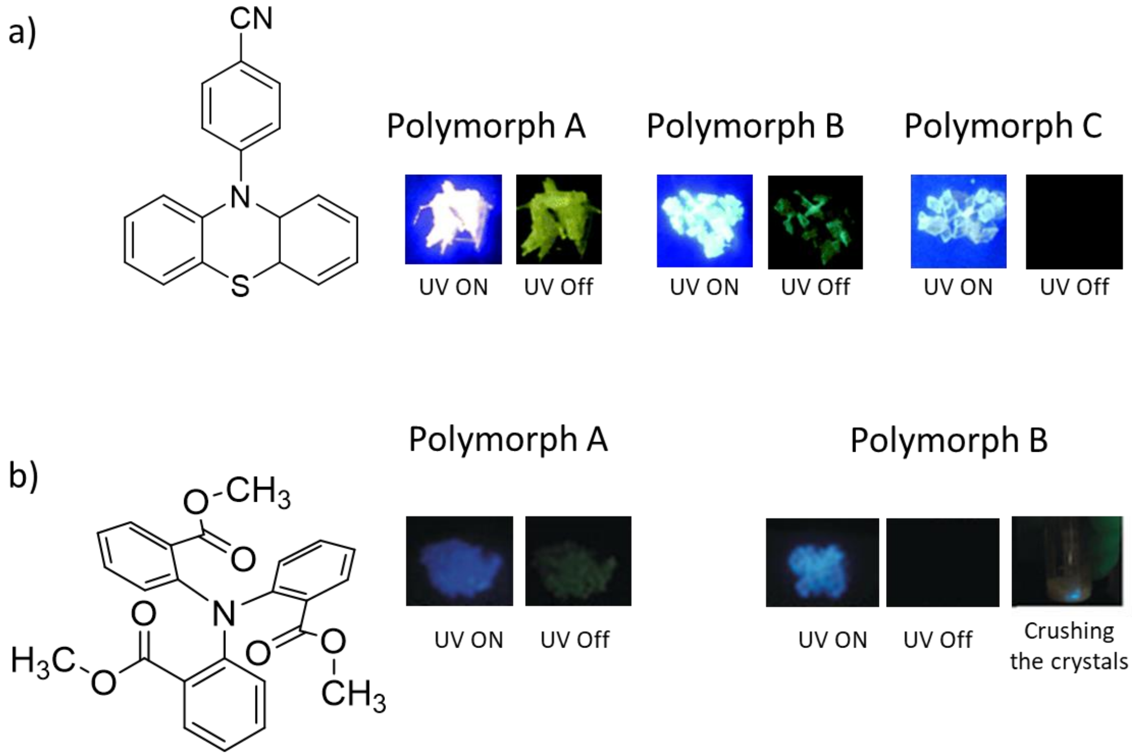

Figure 1.11. ORTP polymorph crystals of a) N-(4-cyanophenyl)phenothiazine b) trimethyl 2,2',2''-nitrilotribenzoate and their emission under UV light and upon ceasing the UV excitation. Adapted with permission from a) ref. [137] copyright (2017) Royal Society of Chemistry and b) ref. [138] copyright (2019) John Wiley and Sons.

Grinding the crystals (amorphization) also has shown to significantly alter the emission of several other ORTP solids and is attributed to defects introduced in the crystal packing.[57, 139] Cumulatively, recent literature clearly illustrates the importance of intermolecular interactions in the solid on the photophysical behavior of ORTP materials.

1.6. Conclusion

To date, several molecular design ideas to enhance the intersystem crossing rate of organic materials have been reported, such as a change of transition orbitals according to El Sayed's rule and the heavy atom effect. The role of molecular packing in defining the singlet/triplet exciton behavior of pure ORTPs has been widely acknowledged but still poorly understood. Consequently, developing efficient ORTP materials is still an empirical exercise, and these materials remain scarce. The formidable (larger) problem of crystal structure prediction and the complexity of emerging properties in molecular solids have hindered the engineering of ORTP materials. In this thesis, we sought to explore novel ORTP materials, both expanding the scope of phosphorescent molecular motifs and gaining new insights in their design principles by probing the relation between their supramolecular structure and photoluminescence.

1.7. Thesis Outline

In **Chapter 2,** we report our serendipitous finding of highly emissive trioxoazatriangulene derivatives ($\Phi_p \leq 42\%$). We demonstrated that all derivatives have identical photophysical behavior in solution; however, in crystalline solids, they can show either fluorescent or phosphorescent behavior depending on the alignment of transition dipoles in molecular π-stacks.

In **Chapter 3**, we report a series of emissive N-aryl/N-alkylacridone derivatives in which different crystal packing significantly alters the phosphorescence energy and the triplet-triplet annihilation pathways in their solids. We found that TTA appears strongly in N-arylacridones with small substituents that pack as antiparallel π-stacks, and measurably weaker in MetAc with coparallel π-stacks and nonexistant in derivatives with isolated π-dimers.

In **Chapter 4,** we report a novel method to synthesize boroxine and dioxaborole-linked covalent organic frameworks (COFs) with high optical purity. This work formed a foundation for our future development of phosphorescent COF, as a tunable platform with structure (and properites) engineered via reticular chemistry approach.

In **Chapter 5**, we introduce a covalent-doping strategy toward achieving the first highly phosphorescent boroxine-linked COF ($\Phi_P \leq 29\%$) by copolymerization of halogenated and unsubstituted phenyldiboronic acids. This doping approach allows for tuning the phosphorescence-to-fluorescence ratio by changing the dopant type and concentration. We also demonstrate a highly efficient COF-based oxygen sensor with an ultra-wide dynamic detection range (~10^3-10^{-5} torr of partial oxygen pressure).

In **Chapter 6**, we report the first near-infrared (NIR) emissive COFs based on the trioxaazatriangulene (TANG) building block. We show that the donor-acceptor interactions in these COFs result in small band gaps (as low as 1.54 eV) which is responsible for NIR emission extending up to 1100 nm.

In **Chapter 7**, we provide a general discussion of the work and summarize it with conclusions and outlook for future studies.

1.8. References

1. Harvey, E. N., A history of luminescence from the earliest times until 1900. *Am. Philos. Soc.* **1957**.

2. Weeks, M. E., The discovery of the elements. II. Elements known to the alchemists. *J. Chem. Educ.* **1932,** *9*, 11.

3. Weeks, M. E., The discovery of the elements. XXI. Supplementary note on the discovery of phosphorus. *J. Chem. Educ.* **1933,** *10*, 302.

4. Wiedemann, E., Ueber Fluorescenz und Phosphorescenz I. Abhandlung. *Ann. Phys.* **1888,** *270*, 446-463.

5. Perrin, F., *La fluorescence des solutions-Induction moléculaire.–Polarisation et durée d'émission.–Photochimie*, Annales de physique, *EDP Sci.*, **1929**; 169-275.

6. Lewis, G. N.; Kasha, M., Phosphorescence and the triplet state. *J. Am. Chem. Soc.* **1944,** *66*, 2100-2116.

7. Lewis, G. N.; Calvin, M., Paramagnetism of the phosphorescent state. *J. Am. Chem. Soc.* **1945,** *67*, 1232-1233.

8. Kasha, M., Characterization of electronic transitions in complex molecules. *Discuss. Faraday Soc.* **1950,** *9*, 14-19.

9. Yang, J.; Zhen, X.; Wang, B.; Gao, X.; Ren, Z.; Wang, J.; Xie, Y.; Li, J.; Peng, Q.; Pu, K.; Li, Z., The influence of the molecular packing on the room temperature phosphorescence of purely organic luminogens. *Nat. Commun.* **2018,** *9*, 840.

10. Fateminia, S. M. A.; Mao, Z.; Xu, S.; Yang, Z.; Chi, Z.; Liu, B., Organic nanocrystals with bright red persistent room-temperature phosphorescence for biological applications. *Angew. Chem. Int. Ed.* **2017,** *56*, 12160-12164.

11. Shi, H.; Zou, L.; Huang, K.; Wang, H.; Sun, C.; Wang, S.; Ma, H.; He, Y.; Wang, J.; Yu, H., A highly efficient red metal-free organic phosphor for time-resolved luminescence imaging and photodynamic therapy. *ACS Appl. Mater. Interfaces* **2019,** *11*, 18103-18110.

12. Gu, M.; Shi, H.; Ling, K.; Lv, A.; Huang, K.; Singh, M.; Wang, H.; Gu, L.; Yao, W.; An, Z.; Ma, H.; Huang, W., Polymorphism-dependent dynamic ultralong organic phosphorescence. *Research* **2020,** *2020*, 8183450.

13. Su, Y.; Phua, S. Z. F.; Li, Y.; Zhou, X.; Jana, D.; Liu, G.; Lim, W. Q.; Ong, W. K.; Yang, C.; Zhao, Y., Ultralong room temperature phosphorescence from amorphous organic materials toward confidential information encryption and decryption. *Sci. Adv.* **2018,** *4*, eaas9732.

14. Ye, W.; Ma, H.; Shi, H.; Wang, H.; Lv, A.; Bian, L.; Zhang, M.; Ma, C.; Ling, K.; Gu, M.; Mao, Y.; Yao, X.; Gao, C.; Shen, K.; Jia, W.; Zhi, J.; Cai, S.; Song, Z.; Li, J.; Zhang, Y.; Lu, S.; Liu, K.; Dong, C.; Wang, Q.; Zhou, Y.; Yao, W.; Zhang, Y.; Zhang, H.; Zhang, Z.; Hang, X.; An, Z.; Liu, X.; Huang, W., Confining isolated chromophores for highly efficient blue phosphorescence. *Nat. Mater.* **2021,** *20*, 1539-1544.

15. Zhao, Q.; Huang, C.; Li, F., Phosphorescent heavy-metal complexes for bioimaging. *Chem. Soc. Rev.* **2011,** *40*, 2508-2524.

16. Zhen, X.; Qu, R.; Chen, W.; Wu, W.; Jiang, X., The development of phosphorescent probes for in vitro and in vivo bioimaging. *Biomater. Sci.* **2021,** *9*, 285-300.

17. Ieuji, R.; Goushi, K.; Adachi, C., Triplet–triplet upconversion enhanced by spin–orbit coupling in organic light-emitting diodes. *Nat. Commun.* **2019,** *10*, 5283.

18. Zhan, G.; Liu, Z.; Bian, Z.; Huang, C., Recent advances in organic light-emitting diodes based on pure organic room temperature phosphorescence materials. *Front. Chem.* **2019,** *7*, 305.

19. Kang, S. W.; Baek, D.-H.; Ju, B.-K.; Park, Y. W., Green phosphorescent organic light-emitting diode exhibiting highest external quantum efficiency with ultra-thin undoped emission layer. *Sci. Rep.* **2021,** *11*, 1-8.

20. Sun, J.; Ahn, H.; Kang, S.; Ko, S.-B.; Song, D.; Um, H. A.; Kim, S.; Lee, Y.; Jeon, P.; Hwang, S.-H., Exceptionally stable blue phosphorescent organic light-emitting diodes. *Nat. Photon.* **2022,** *16*, 212-218.

21. Lee, J.; Chen, H.-F.; Batagoda, T.; Coburn, C.; Djurovich, P. I.; Thompson, M. E.; Forrest, S. R., Deep blue phosphorescent organic light-emitting diodes with very high brightness and efficiency. *Nat. Mater.* **2016,** *15*, 92-98.

22. Zhan, G.; Liu, Z.; Bian, Z.; Huang, C., Recent advances in organic light-emitting diodes based on pure organic room temperature phosphorescence materials. *Front. Chem.* **2019,** *7*, 305.

23. Yum, J.-H.; Baranoff, E.; Hardin, B. E.; Hoke, E. T.; McGehee, M. D.; Nüesch, F.; Grätzel, M.; Nazeeruddin, M. K., Phosphorescent energy relay dye for improved light harvesting response in liquid dye-sensitized solar cells. *Energy Environ. Sci* **2010,** *3*, 434-437.

24. Yu, Z.; Wu, Y.; Xiao, L.; Chen, J.; Liao, Q.; Yao, J.; Fu, H., Organic Phosphorescence Nanowire Lasers. *J. Am. Chem. Soc.* **2017,** *139*, 6376-6381.

25. Wan, S.; Zhou, H.; Lin, J.; Lu, W., A prototype of a volumetric three-dimensional display based on programmable photo-activated phosphorescence. *Angew. Chem. Int. Ed.* **2020,** *59*, 8416-8420.

26. Zhao, W.; He, Z.; Tang, B. Z., Room-temperature phosphorescence from organic aggregates. *Nat. Rev. Mater.* **2020,** *5*, 869-885.

27. Baldo, M. A.; O'Brien, D. F.; You, Y.; Shoustikov, A.; Sibley, S.; Thompson, M. E.; Forrest, S. R., Highly efficient phosphorescent emission from organic electroluminescent devices. *Nature* **1998,** *395*, 151-154.

28. Kappaun, S.; Slugovc, C.; List, E. J., Phosphorescent organic light-emitting devices: working principle and iridium based emitter materials. *Int. J. Mol. Sci.* **2008,** *9*, 1527-1547.

29. Nichols, E. L.; Merritt, E., Studies in luminescence i. the phosphorescence and fluorescence of organic substances at low temperatures. *Phys. Rev.* **1904,** *18*, 355.

30. Olness, D.; Sponer, H., Phosphorescence lifetime studies in some organic crystals at low temperatures. *J. Chem. Phys.* **1963,** *38*, 1779-1782.

31. Horie, K.; Mita, I., Photochemistry in polymer solids. Decay of benzophenone phosphorescence in poly (methyl methacrylate). *Chem. Phys. Lett.* **1982,** *93*, 61-65.

32. Clapp, D. B., The phosphorescence of tetraphenylmethane and certain related substances. *J. Am. Chem. Soc.* **1939,** *61*, 523-524.

33. Bilen, C.; Harrison, N.; Morantz, D., Unusual room temperature afterglow in some crystalline organic compounds. *Nature* **1978,** *271*, 235-237.

34. Kropp, J. L.; Dawson, W. R., Radiationless deactivation of triplet coronene in plastics. *J. Phys. Chem.* **1967,** *71*, 4499-4506.

35. Schulman, E. M.; Walling, C., Triplet-state phosphorescence of adsorbed ionic organic molecules at room temperature. *J. Phys. Chem.* **1973,** *77*, 902-905.

36. Schulman, E.; Parker, R., Room temperature phosphorescence of organic compounds. The effects of moisture, oxygen, and the nature of the support-phosphor interaction. *J. Phys. Chem.* **1977,** *81*, 1932-1939.

37. Kallmann, H.; Kramer, B.; Sucov, E., Long time phosphorescence of organic crystals. *J. Chem. Phys.* **1955,** *23*, 1043-1047.

38. Yuan, W. Z.; Shen, X. Y.; Zhao, H.; Lam, J. W. Y.; Tang, L.; Lu, P.; Wang, C. L.; Liu, Y.; Wang, Z. M.; Zheng, Q.; Sun, J. Z.; Ma, Y. G.; Tang, B. Z., Crystallization-induced phosphorescence of pure organic luminogens at room temperature. *J. Phys. Chem. C* **2010,** *114*, 6090-6099.

39. Bolton, O.; Lee, K.; Kim, H. J.; Lin, K. Y.; Kim, J., Activating efficient phosphorescence from purely organic materials by crystal design. *Nat. Chem.* **2011,** *3*, 205-210.

40. Chen, C.; Liu, B., Enhancing the performance of pure organic room-temperature phosphorescent luminophores. *Nat. Commun.* **2019,** *10*, 1-15.

41. Shi, H.; Zou, L.; Huang, K.; Wang, H.; Sun, C.; Wang, S.; Ma, H.; He, Y.; Wang, J.; Yu, H.; Yao, W.; An, Z.; Zhao, Q.; Huang, W., A Highly Efficient Red Metal-free Organic Phosphor for Time-Resolved Luminescence Imaging and Photodynamic Therapy. *ACS Appl. Mater. Interfaces* **2019,** *11*, 18103-18110.

42. Kabe, R.; Notsuka, N.; Yoshida, K.; Adachi, C., Afterglow organic light-emitting diode. *Adv. Mater.* **2016,** *28*, 655-660.

43. Zhang, G.; Chen, J.; Payne, S. J.; Kooi, S. E.; Demas, J.; Fraser, C. L., Multi-emissive difluoroboron dibenzoylmethane polylactide exhibiting intense fluorescence and oxygen-sensitive room-temperature phosphorescence. *J. Am. Chem. Soc.* **2007,** *129*, 8942-8943.

44. Wan, S.; Zhou, H.; Lin, J.; Lu, W., A prototype of a volumetric three-dimensional display based on programmable photo-activated phosphorescence. *Angew. Chem. Int. Ed.* **2020,** *59*, 8416-8420.

45. Marian, C. M., Understanding and controlling intersystem crossing in molecules. *Annu. Rev. Phys. Chem.* **2021,** *72*, 617-640.

46. Kellmann, A., Intersystem crossing and internal conversion quantum yields of acridine in polar and nonpolar solvents. *J. Phys. Chem.* **1977,** *81*, 1195-1198.

47. Rauh, R. D.; Leermakers, P. A., Solvent effects upon the phosphorescence lifetimes and photoreactivity of butyrophenone. *J. Am. Chem. Soc.* **1968,** *90*, 2246-2249.

48. Hamanoue, K.; Nakayama, T.; Ikenaga, K.; Ibuki, K., Temperature effect on the formation of the lowest excited triplet states of 9-bromoanthracene and 9,10-dibromoanthracene. *J. Photochem. Photobiol. A: Chem.* **1993,** *74*, 147-152.

49. Behlen, F. M.; Rice, S., Intersystem crossing in cold isolated molecules of naphthalene. *J. Chem. Phys.* **1981,** *75*, 5672-5684.

50. Turro, N. J.; Ramamurthy, V.; Scaiano, J. C., *Modern molecular photochemistry of organic molecules*. University Science Books Sausalito, CA: 2010; Vol. 188.

51. Yuster, P.; Weissman, S., Effects of perturbations on phosphorescence: luminescence of metal organic complexes. *J. Chem. Phys.* **1949,** *17*, 1182-1188.

52. Wen, Y.; Liu, H.; Zhang, S.; Gao, Y.; Yan, Y.; Yang, B., One-dimensional π–π stacking induces highly efficient pure organic room-temperature phosphorescence and ternary-emission single-molecule white light. *J. Mater. Chem. C* **2019,** *7*, 12502-12508.

53. Zhao, W.; He, Z.; Lam, J. W.; Peng, Q.; Ma, H.; Shuai, Z.; Bai, G.; Hao, J.; Tang, B. Z., Rational molecular design for achieving persistent and efficient pure organic room-temperature phosphorescence. *Chem* **2016,** *1*, 592-602.

54. Yang, Z.; Mao, Z.; Zhang, X.; Ou, D.; Mu, Y.; Zhang, Y.; Zhao, C.; Liu, S.; Chi, Z.; Xu, J.; Wu, Y.-C.; Lu, P.-Y.; Lien, A.; Bryce, M. R., Intermolecular electronic coupling of organic units for efficient persistent room-temperature phosphorescence. *Angew. Chem. Int. Ed.* **2016,** *55*, 2181-2185.

55. Xiao, L.; Wu, Y.; Chen, J.; Yu, Z.; Liu, Y.; Yao, J.; Fu, H., Highly efficient room-temperature phosphorescence from halogen-bonding-assisted doped organic crystals. *J. Phys. Chem. A* **2017,** *121*, 8652-8658.

56. Wang, J.; Gu, X.; Ma, H.; Peng, Q.; Huang, X.; Zheng, X.; Sung, S. H. P.; Shan, G.; Lam, J. W. Y.; Shuai, Z.; Tang, B. Z., A facile strategy for realizing room temperature phosphorescence and single molecule white light emission. *Nat. Commun.* **2018,** *9*, 2963.

57. Mao, Z.; Yang, Z.; Mu, Y.; Zhang, Y.; Wang, Y. F.; Chi, Z.; Lo, C. C.; Liu, S.; Lien, A.; Xu, J., Linearly tunable emission colors obtained from a fluorescent‐phosphorescent dual-emission compound by mechanical stimuli. *Angew. Chem.Int. Ed.* **2015,** *54*, 6270-6273.

58. Fermi, A.; Bergamini, G.; Roy, M.; Gingras, M.; Ceroni, P., Turn-on phosphorescence by metal coordination to a multivalent terpyridine ligand: a new paradigm for luminescent sensors. *J. Am. Chem. Soc.* **2014,** *136*, 6395-6400.

59. Tao, Y.; Chen, R.; Li, H.; Yuan, J.; Wan, Y.; Jiang, H.; Chen, C.; Si, Y.; Zheng, C.; Yang, B., Resonance-activated spin-flipping for efficient organic ultralong room-temperature phosphorescence. *Adv. Mater.* **2018,** *30*, 1803856.

60. Yu, Z.; Wu, Y.; Xiao, L.; Chen, J.; Liao, Q.; Yao, J.; Fu, H., Organic phosphorescence nanowire lasers. *J. Am. Chem. Soc.* **2017,** *139*, 6376-6381.

61. Xu, L.; Li, G.; Xu, T.; Zhang, W.; Zhang, S.; Yin, S.; An, Z.; He, G., Chalcogen atom modulated persistent room-temperature phosphorescence through intramolecular electronic coupling. *Chem. Commun.* **2018,** *54*, 9226-9229.

62. He, G.; Wiltshire, B. D.; Choi, P.; Savin, A.; Sun, S.; Mohammadpour, A.; Ferguson, M. J.; McDonald, R.; Farsinezhad, S.; Brown, A., Phosphorescence within benzotellurophenes and color tunable tellurophenes under ambient conditions. *Chem. Commun.* **2015,** *51*, 5444-5447.

63. McClure, D. S., Triplet‐singlet transitions in organic molecules. lifetime measurements of the triplet state. *J. Chem. Phys.* **1949,** *17*, 905-913.

64. Kasha, M., Collisional perturbation of spin-orbital coupling and the mechanism of fluorescence quenching. A visual demonstration of the perturbation. *J. Chem. Phys.* **1952,** *20*, 71-74.

65. Sun, X.; Zhang, B.; Li, X.; Trindle, C. O.; Zhang, G., External heavy-atom effect via orbital interactions revealed by single-crystal X-ray diffraction. *J. Phys. Chem. A* **2016,** *120*, 5791-5797.

66. Yan, Z. A.; Lin, X.; Sun, S.; Ma, X.; Tian, H., Activating room-temperature phosphorescence of organic luminophores via external heavy ‐ atom effect and rigidity of ionic polymer matrix. *Angew. Chem. Ind. Ed.* **2021,** *60*, 19735-19739.

67. McGlynn, S.; Sunseri, R.; Christodouleas, N., External heavy atom spin-orbital coupling effect. i. the nature of the interaction. *J. Chem. Phys.* **1962,** *37*, 1818-1824.

68. Komada, Y.; Yamauchi, S.; Hirota, N., Mechanisms of external heavy atom effects on the lowest excited triplet states: Naphthalene and biphenyl X traps. *J. Chem. Phys.* **1985,** *82*, 1651-1660.

69. Minaev, B. F.; Knuts, S.; Ågren, H., On the interpretation of the external heavy atom effect on singlet-triplet transitions. *Chem. Phys.* **1994,** *181*, 15-28.

70. Shimizu, Y.; Azumi, T., Mechanism of external heavy atom effect on intersystem crossing in fluid solutions. Analysis based on fluorescence decay data. *J. Phys. Chem.* **1982,** *86*, 22-26.

71. Henry, B. R.; Siebrand, W., Spin–orbit coupling in aromatic hydrocarbons. Analysis of nonradiative transitions between singlet and triplet states in benzene and naphthalene. *J. Chem. Phys.* **1971,** *54*, 1072-1085.

72. El ‐ Sayed, M., Spin – orbit coupling and the radiationless processes in nitrogen heterocyclics. *J. Chem. Phys.* **1963,** *38*, 2834-2838.

73. Lower, S.; El-Sayed, M., The triplet state and molecular electronic processes in organic molecules. *Chem. Rev.* **1966,** *66*, 199-241.

74. Baba, M., Intersystem Crossing in the $^1n\pi^*$ and $^1\pi\pi^*$ States. *J. Phys. Chem. A* **2011,** *115*, 9514-9519.

75. Zhao, W. J.; He, Z. K.; Tang, B. Z., Room-temperature phosphorescence from organic aggregates. *Nat. Rev. Mater.* **2020,** *5*, 869-885.

76. Kuno, S.; Akeno, H.; Ohtani, H.; Yuasa, H., Visible room-temperature phosphorescence of pure organic crystals via a radical-ion-pair mechanism. *Phys. Chem. Chem. Phys.* **2015,** *17*, 15989-15995.

77. Wei, P.; Zhang, X.; Liu, J.; Shan, G. G.; Zhang, H.; Qi, J.; Zhao, W.; Sung, H. H.; Williams, I. D.; Lam, J. W. Y.; Tang, B. Z., New wine in old bottles: prolonging room-temperature phosphorescence of crown ethers by supramolecular interactions. *Angew. Chem. Int. Ed.* **2020,** *59*, 9293-9298.

78. Tao, Y.; Chen, R.; Li, H.; Yuan, J.; Wan, Y.; Jiang, H.; Chen, C.; Si, Y.; Zheng, C.; Yang, B.; Xing, G.; Huang, W., Resonance-activated spin-flipping for efficient organic ultralong room-temperature phosphorescence. *Adv. Mater.* **2018,** *30*, 1803856.

79. An, Z.; Zheng, C.; Tao, Y.; Chen, R.; Shi, H.; Chen, T.; Wang, Z.; Li, H.; Deng, R.; Liu, X., Stabilizing triplet excited states for ultralong organic phosphorescence. *Nat. Mater.* **2015,** *14*, 685-690.

80. Xu, B.; Wu, H.; Chen, J.; Yang, Z.; Yang, Z.; Wu, Y.-C.; Zhang, Y.; Jin, C.; Lu, P.-Y.; Chi, Z., White-light emission from a single heavy atom-free molecule with room temperature phosphorescence, mechanochromism and thermochromism. *Chem. Sci.* **2017,** *8*, 1909-1914.

81. Hayduk, M.; Riebe, S.; Voskuhl, J., Phosphorescence through hindered motion of pure organic emitters. *Chem. Eur. J.* **2018,** *24*, 12221-12230.

82. Tian, S.; Ma, H.; Wang, X.; Lv, A.; Shi, H.; Geng, Y.; Li, J.; Liang, F.; Su, Z. M.; An, Z., Utilizing d–π bonds for ultralong organic phosphorescence. *Angew. Chem. Int. Ed.* **2019,** *58*, 6645-6649.

83. Shoji, Y.; Ikabata, Y.; Wang, Q.; Nemoto, D.; Sakamoto, A.; Tanaka, N.; Seino, J.; Nakai, H.; Fukushima, T., Unveiling a new aspect of simple arylboronic esters: long-lived room-temperature phosphorescence from heavy-atom-free molecules. *J. Am. Chem. Soc.* **2017,** *139*, 2728-2733.

84. Li, M.; Cai, X.; Qiao, Z.; Liu, K.; Xie, W.; Wang, L.; Zheng, N.; Su, S.-J., Achieving high-efficiency purely organic room-temperature phosphorescence materials by boronic ester substitution of phenoxathiine. *Chem. Commun.* **2019,** *55*, 7215-7218.

85. Zhou, Y.; Qin, W.; Du, C.; Gao, H.; Zhu, F.; Liang, G., Long-lived room-temperature phosphorescence for visual and quantitative detection of oxygen. *Angew. Chem. Int. Ed.* **2019,** *58*, 12102-12106.

86. Li, M.; Ling, K.; Shi, H.; Gan, N.; Song, L.; Cai, S.; Cheng, Z.; Gu, L.; Wang, X.; Ma, C., Prolonging ultralong organic phosphorescence lifetime to 2.5 s through confining rotation in molecular rotor. *Adv. Opt. Mater.* **2019,** *7*, 1800820.

87. Hackney, H. E.; Perepichka, D. F., Recent advances in room temperature phosphorescence of crystalline boron containing organic compounds: Nanoscience: Special Issue Dedicated to Professor Paul S. Weiss. *Aggregate* **2022,** *3*, e123.

88. Salla, C. A.; Farias, G.; Rouzières, M.; Dechambenoit, P.; Durola, F.; Bock, H.; de Souza, B.; Bechtold, I. H., Persistent solidstate phosphorescence and delayed fluorescence at room temperature by a twisted hydrocarbon. *Angew. Chem. Int. Ed.* **2019,** *58*, 6982-6986.

89. Kwon, M. S.; Yu, Y.; Coburn, C.; Phillips, A. W.; Chung, K.; Shanker, A.; Jung, J.; Kim, G.; Pipe, K.; Forrest, S. R., Suppressing molecular motions for enhanced room-temperature phosphorescence of metal-free organic materials. *Nat. Commun.* **2015,** *6*, 1-9.

90. Gan, N.; Shi, H.; An, Z.; Huang, W., Recent advances in polymer-based metal-free room - temperature phosphorescent materials. *Adv. Funct. Mater.* **2018,** *28*, 1802657.

91. Cai, S.; Shi, H.; Zhang, Z.; Wang, X.; Ma, H.; Gan, N.; Wu, Q.; Cheng, Z.; Ling, K.; Gu, M.; Ma, C.; Gu, L.; An, Z.; Huang, W., Hydrogen-bonded organic aromatic frameworks for ultralong phosphorescence by intralayer π–π interactions. *Angew. Chem. Int. Ed.* **2018,** *57*, 4005-4009.

92. Easley, C. J.; Mettry, M.; Moses, E. M.; Hooley, R. J.; Bardeen, C. J., Boosting the Heavy Atom Effect by Cavitand Encapsulation: Room Temperature Phosphorescence of Pyrene in the Presence of Oxygen. *J. Phys. Chem. A* **2018,** *122*, 6578-6584.

93. Lehner, P.; Staudinger, C.; Borisov, S. M.; Klimant, I., Ultra-sensitive optical oxygen sensors for characterization of nearly anoxic systems. *Nat. Commun.* **2014,** *5*, 1-6.

94. Kwon, M. S.; Lee, D.; Seo, S.; Jung, J.; Kim, J., Tailoring Intermolecular Interactions for Efficient Room-Temperature Phosphorescence from Purely Organic Materials in Amorphous Polymer Matrices. *Angew. Chem. Int. Ed.* **2014,** *53*, 11177-11181.

95. Schulman, E. M.; Parker, R. T., Room temperature phosphorescence of organic compounds. The effects of moisture, oxygen, and the nature of the support-phosphor interaction. *J. Phys. Chem.* **1977,** *81*, 1932-1939.

96. Al-Attar, H. A.; Monkman, A. P., Room-temperature phosphorescence from films of isolated water-soluble conjugated polymers in hydrogen-bonded matrices. *Adv. Funct. Mater.* **2012,** *22*, 3824-3832.

97. Gao, R.; Fang, X.; Yan, D., Direct white-light emitting room-temperature-phosphorescence thin films with tunable two-color polarized emission through orientational hydrogen-bonding layer-by-layer assembly. *J. Mater. Chem. C* **2018,** *6*, 4444-4449.

98. Lee, D.; Bolton, O.; Kim, B. C.; Youk, J. H.; Takayama, S.; Kim, J., Room temperature phosphorescence of metal-free organic materials in amorphous polymer matrices. *J. Am. Chem. Soc.* **2013,** *135*, 6325-6329.

99. Horie, K.; Morishita, K.; Mita, I., Photochemistry in polymer solids. 3. Kinetics for nonexponential decay of benzophenone phosphorescence in acrylic and methacrylic polymers. *Macromolecules* **1984,** *17*, 1746-1750.

100. Reineke, S.; Baldo, M. A., Room temperature triplet state spectroscopy of organic semiconductors. *Sci. Rep.* **2014,** *4*, 3797.

101. Bergamini, G.; Fermi, A.; Botta, C.; Giovanella, U.; Di Motta, S.; Negri, F.; Peresutti, R.; Gingras, M.; Ceroni, P., A persulfurated benzene molecule exhibits outstanding phosphorescence in rigid environments: from computational study to organic nanocrystals and OLED applications. *J. Mater. Chem. C* **2013,** *1*, 2717-2724.

102. Kalyanasundaram, K.; Grieser, F.; Thomas, J., Room temperature phosphorescence of aromatic hydrocarbons in aqueous micellar solutions. *Chem. Phys. Lett.* **1977,** *51*, 501-505.

103. Hirata, S.; Totani, K.; Yamashita, T.; Adachi, C.; Vacha, M., Large reverse saturable absorption under weak continuous incoherent light. *Nat. Mater.* **2014,** *13*, 938-946.

104. Totani, K.; Okada, Y.; Hirata, S.; Vacha, M.; Watanabe, T., Thermoresponsive persistent phosphorescent color change using efficient thermally activated reverse energy transfer with a large energy difference. *Adv. Opt. Mater.* **2013,** *1*, 283-288.

105. Scypinski, S.; Love, L. C., Cyclodextrin-induced room-temperature phosphorescence of nitrogen heterocycles and bridged biphenyls. *Anal. Chem.* **1984,** *56*, 331-336.

106. Li, D.; Lu, F.; Wang, J.; Hu, W.; Cao, X. M.; Ma, X.; Tian, H., Amorphous metal-free roomerature phosphorescent small molecules with multicolor photoluminescence via a host-guest and dual-emission strategy. *J. Am. Chem. Soc.* **2018,** *140*, 1916-1923.

107. Gunshefski, M.; Santana, J. J.; Stephenson, J.; Winefordnert, J. D., Solid-surface room temperature phosphorescence. *Appl. Spectrosc. Rev.* **1992,** *27*, 143-192.

108. Chen, C.; Chi, Z.; Chong, K. C.; Batsanov, A. S.; Yang, Z.; Mao, Z.; Yang, Z.; Liu, B., Carbazole isomers induce ultralong organic phosphorescence. *Nat. Mater.* **2021,** *20*, 175-180.

109. Notsuka, N.; Kabe, R.; Goushi, K.; Adachi, C., Confinement of long‐lived triplet excitons in organic semiconducting host‐guest systems. *Adv. Funct. Mater.* **2017,** *27*, 1703902.

110. Yan, X.; Peng, H.; Xiang, Y.; Wang, J.; Yu, L.; Tao, Y.; Li, H.; Huang, W.; Chen, R., Recent advances on host–guest material systems toward organic room temperature phosphorescence. *Small* **2022,** *18*, 2104073.

111. Li, L.; Wu, W. X.; Liu, Z. F.; Jin, W. J., Effect of geometry factors on the priority of σ-hole⋯π and π-hole⋯π bond in phosphorescent cocrystals formed by pyrene or phenanthrene and trihaloperfluorobenzenes. *New J. Chem.* **2018,** *42*, 10633-10641.

112. Fang, M.-M.; Yang, J.; Li, Z., Recent advances in purely organic room temperature phosphorescence polymer. *Chin. J. Polym. Sci.* **2019,** *37*, 383-393.

113. Kwon, M. S.; Lee, D.; Seo, S.; Jung, J.; Kim, J., Tailoring intermolecular interactions for efficient room‐temperature phosphorescence from purely organic materials in amorphous polymer matrices. *Angew. Chem. Int. Ed.* **2014,** *53*, 11177-11181.

114. Forni, A.; Lucenti, E.; Botta, C.; Cariati, E., Metal free room temperature phosphorescence from molecular self-interactions in the solid state. *J. Mater. Chem. C* **2018,** *6*, 4603-4626.

115. Fang, M.; Yang, J.; Xiang, X.; Xie, Y.; Dong, Y.; Peng, Q.; Li, Q.; Li, Z., Unexpected room-temperature phosphorescence from a non-aromatic, low molecular weight, pure organic molecule through the intermolecular hydrogen bond. *Mater. Chem. Front.* **2018,** *2*, 2124-2129.

116. Chen, H.; Yao, X.; Ma, X.; Tian, H., Amorphous, efficient, room-temperature phosphorescent metal-free polymers and their applications as encryption ink. *Adv. Opt. Mater.* **2016,** *4*, 1397-1401.

117. Ogoshi, T.; Tsuchida, H.; Kakuta, T.; Yamagishi, T. a.; Taema, A.; Ono, T.; Sugimoto, M.; Mizuno, M., Ultralong room-temperature phosphorescence from amorphous polymer poly (styrene sulfonic acid) in air in the dry solid state. *Adv. Funct. Mater.* **2018,** *28*, 1707369.

118. Zhang, Y.-F.; Wang, Y.-C.; Yu, X.-S.; Zhao, Y.; Ren, X.-K.; Zhao, J.-F.; Wang, J.; Jiang, X.-Q.; Chang, W.-Y.; Zheng, J.-F., Isophthalate-based room temperature phosphorescence: from small molecule to side-chain jacketed liquid crystalline polymer. *Macromolecules* **2019,** *52*, 2495-2503.

119. Chen, X.; He, Z.; Kausar, F.; Chen, G.; Zhang, Y.; Yuan, W. Z., Aggregation-induced dual emission and unusual luminescence beyond excimer emission of poly (ethylene terephthalate). *Macromolecules* **2018,** *51*, 9035-9042.

120. Kanosue, K.; Hirata, S.; Vacha, M.; Augulis, R.; Gulbinas, V.; Ishige, R.; Ando, S., A colorless semi-aromatic polyimide derived from a sterically hindered bromine-substituted dianhydride exhibiting dual fluorescence and phosphorescence emission. *Mater. Chem. Front.* **2019,** *3*, 39-49.

121. Chen, X.; Xu, C.; Wang, T.; Zhou, C.; Du, J.; Wang, Z.; Xu, H.; Xie, T.; Bi, G.; Jiang, J., Versatile room‐temperature‐phosphorescent materials prepared from N-substituted naphthalimides: emission enhancement and chemical conjugation. *Angew. Chem. Int. Ed.* **2016,** *55*, 9872-9876.

122. Kwon, M. S.; Yu, Y.; Coburn, C.; Phillips, A. W.; Chung, K.; Shanker, A.; Jung, J.; Kim, G.; Pipe, K.; Forrest, S. R.; Youk, J. H.; Gierschner, J.; Kim, J., Suppressing molecular motions for enhanced room-temperature phosphorescence of metal-free organic materials. *Nat. Commun.* **2015,** *6*, 8947.

123. Bolton, O.; Lee, K.; Kim, H.-J.; Lin, K. Y.; Kim, J., Activating efficient phosphorescence from purely organic materials by crystal design. *Nat. Chem.* **2011,** *3*, 205-210.

124. Ding, B.; Ma, L.; Huang, Z.; Ma, X.; Tian, H., Engendering persistent organic room temperature phosphorescence by trace ingredient incorporation. *Sci. Adv.* **2021,** *7*, eabf9668.

125. Hochstrasser, R. M., The luminescence of organic molecular crystals. *Rev. Mod. Phys.* **1962,** *34*, 531.

126. Hirata, S., Recent advances in materials with room-temperature phosphorescence: photophysics for triplet exciton stabilization. *Adv. Opt. Mater.* **2017,** *5*, 1700116.

127. Ma, X.; Xu, C.; Wang, J.; Tian, H., Amorphous pure organic polymers for heavy-atom-free efficient room-temperature phosphorescence emission. *Angew. Chem. Int. Ed.* **2018,** *57*, 10854-10858.

128. Hirata, S.; Vacha, M., White afterglow room-temperature emission from an isolated single aromatic unit under ambient condition. *Adv. Opt. Mater.* **2017,** *5*, 1600996.

129. Cheng, Z.; Shi, H.; Ma, H.; Bian, L.; Wu, Q.; Gu, L.; Cai, S.; Wang, X.; Xiong, W. w.; An, Z., Ultralong phosphorescence from organic ionic crystals under ambient conditions. *Angew. Chem. Int. Ed.* **2018,** *57*, 678-682.

130. Mei, J.; Leung, N. L.; Kwok, R. T.; Lam, J. W.; Tang, B. Z., Aggregation-induced emission: together we shine, united we soar! *Chem. Rev.* **2015,** *115*, 11718-11940.

131. Saltiel, J.; March, G. R.; Smothers, W. K.; Stout, S. A.; Charlton, J. L., Spin-statistical factor in the triplet-triplet annihilation of anthracene triplets. *J. Am. Chem. Soc.* **1981,** *103*, 7159-7164.

132. Liu, D. K.; Faulkner, L. R., Delayed fluorescence efficiencies of anthracene and phenanthrene. *J. Am. Chem. Soc.* **1978,** *100*, 2635-2639.

133. Sternlicht, H.; Nieman, G.; Robinson, G., Triplet-triplet annihilation and delayed fluorescence in molecular aggregates. *J. Chem. Phys.* **1963,** *38*, 1326-1335.

134. Gong, Y.; Zhao, L.; Peng, Q.; Fan, D.; Yuan, W. Z.; Zhang, Y.; Tang, B. Z., Crystallization-induced dual emission from metal-and heavy atom-free aromatic acids and esters. *Chem. Sci.* **2015,** *6*, 4438-4444.

135. Ma, H.; Shi, W.; Ren, J.; Li, W.; Peng, Q.; Shuai, Z., Electrostatic interaction-induced room-temperature phosphorescence in pure organic molecules from QM/MM calculations. *J. Phys. Chem. Lett* **2016,** *7*, 2893-2898.

136. McRae, E. G.; Kasha, M., Enhancement of phosphorescence ability upon aggregation of dye molecules. *J. Chem. Phys.* **1958,** *28*, 721-722.

137. Yang, J.; Ren, Z.; Chen, B.; Fang, M.; Zhao, Z.; Tang, B. Z.; Peng, Q.; Li, Z., Three polymorphs of one luminogen: how the molecular packing affects the RTP and AIE properties? *J. Mater. Chem. C* **2017,** *5*, 9242-9246.

138. Wang, J.; Chai, Z.; Wang, J.; Wang, C.; Han, M.; Liao, Q.; Huang, A.; Lin, P.; Li, C.; Li, Q., Mechanoluminescence or room‐temperature phosphorescence: molecular packing-dependent emission response. *Angew. Chem. Int. Ed.* **2019,** *58*, 17297-17302.

139. Gong, Y.; Chen, G.; Peng, Q.; Yuan, W. Z.; Xie, Y.; Li, S.; Zhang, Y.; Tang, B. Z., Achieving persistent room temperature phosphorescence and remarkable mechanochromism from pure organic luminogens. *Adv. Mater.* **2015,** *27*, 6195-6201.

Chapter 2

Crystal Engineering of Room Temperature Phosphorescence in Organic Solids

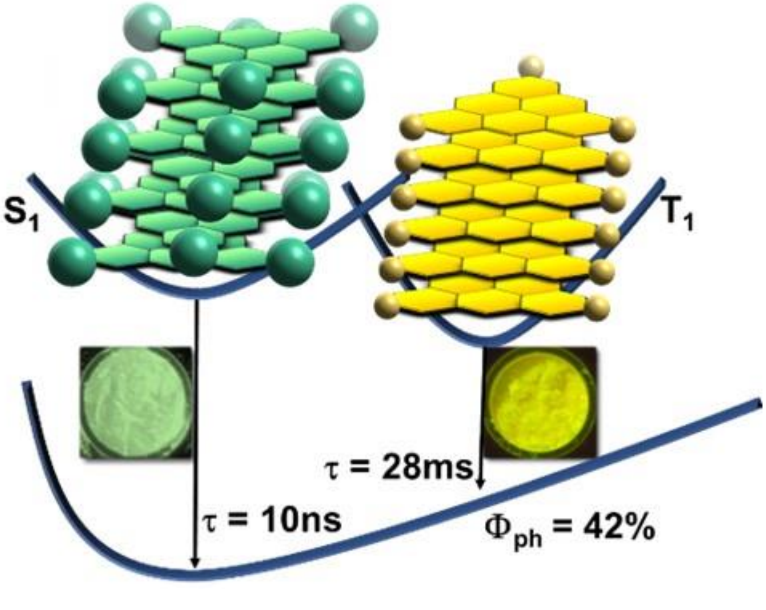

Preface

In this chapter, we show how the molecular packing in the crystal affects the phosphorescent behavior of a series of azatriangulenetrione (TANGO). Unsubstituted HTANGO, halogen-substituted TXTANG (X = Cl, Br, I), and t-butyl-substituted *t*BuTANGO derivatives were synthesized, and their photophysical properties were investigated in solution (at room temperature and frozen at 77 K) and crystalline solids. We found that all TANGO derivatives showed similar photophysical properties in solution. In the solid state, however, unsubstituted HTANGO and the halogenated permutations showed efficient room temperature phosphorescence (Φ_p up to 42% for HTANGO), whereas the *t*BuTANGO emits only pure fluorescence. X-ray crystallography revealed that all derivatives have crystal packings made of 1D-columnar π-stacks, with only *t*BuTANGO molecules exhibiting a rotation of 60° within π-columns due to the steric bulkiness of the side groups. Using the density functional theory calculation, we then rationalized that the alignment of transition dipoles within the π-stacks upon rotation could indeed control the efficiencies of the singlet and triplet emission channels.

This chapter is reprinted with permission from E. Hamzehpoor, and D. F. Perepichka, "Crystal Engineering of Room Temperature Phosphorescence in Organic Solids" *Angew. Chem. Int. Ed. Engl.* **2020**, *59*, 9977-9981. HRMS and NMR spectra of all TANGOs and their corresponding precursors (**2-5**) are reported in Appendix 1 of the thesis.

Author contribution

I have synthesized, purified, and performed structural characterization, photophysical characterization (steady-state, lifetime analysis, and quantum yields), and density functional theory calculations. The manuscript was written by me and revised and edited by Dmytro F. Perepichka.

2.1. Abstract

We report a series of highly emissive azatriangulenetrione (TANGO) solids in which the luminescent properties are controlled by engineering the molecular packing by adjusting the steric size of substituents. The co-alignment of “phosphorogenic” carbonyl groups within the π-stacks results in an almost pure triplet emission in HTANGO, TCTANGO, TBTANGO and TITANGO, while their rotation by ≈60° in the sterically hindered *t*BuTANGO leads to an almost pure singlet emission. Despite strong π-interactions, aggregation-induced quenching and triplet–triplet annihilation are avoided in HTANGO and TCTANGO which display efficient phosphorescence in the solid state. To our knowledge, HTANGO with the solid-state phosphorescence quantum yield of 42% at room temperature is the most efficient phosphor composed of the 1st /2nd row elements only.

2.2. Introduction:

There is a rapidly growing interest in organic room temperature phosphorescent (ORTP) dyes as alternatives to traditional inorganic/metal-organic phosphors.[1, 2] Their potential applications include time-gated biological imaging/sensing,[3, 4] anticounterfeiting and data encryption,[5, 6] high-efficiency light-emitting diodes,[7-10] improving charge generation in photovoltaic devices,[11] phosphorescence lasing[12] and amplified upconversion emission.[13] ORTP emitters carry several potential advantages over their heavy metal containing counterparts such as lower toxicity, and environmental footprint, longer lifetimes, low-cost processing, and vast opportunities for tuning their photophysical properties.[6, 14, 15]

Phosphorescence is a spin-forbidden radiative decay of the lowest-energy triplet state T_1 which can be formed from a singlet excited state (S_1) via intersystem crossing (ISC). However, in most organic materials the ISC is very slow and generally cannot compete with fluorescence and non-radiative decays. A common approach to design phosphorescence in organic compounds is the incorporation of heavy atoms such as Br, I, S, Te which enhance the spin orbit coupling (SOC).[16-20] Another strategy to enhance the SOC is coupling n-π^* and π-π^* transitions with different angular momentum, that can be realized in carbonyl (C=O) containing derivatives.[4, 6, 15, 17, 21-24] Apart from efficient ISC, achieving ORTP also requires suppressing the competing nonradiative decay, usually realized through embedding phosphorescent molecules in a rigid (polymer[24, 25] or crystal[17]) matrix. A dilute concentration of the phosphor in such solid solutions is generally required to avoid their deactivation via triplet-triplet annihilation.

In the last few years, several pure ORTP solids have been reported.[15, 16, 21, 23] With very few exceptions,[26] their molecular design is based on non-planar flexible structures that limit π-π interactions in the solid state resulting in ‘aggregation-induced emission’. The pioneering B.Z Tang’s work explicitly cites “carbonyl group, halogen atom and nonplanar conformation” as the key for the design of ORTP solids.[23, 27] Several other groups have found ORTP in the crystals of similar nonplanar molecules, although in most cases the overall emission is still dominated by fluorescence.[6, 15, 21, 28, 29]

The role of molecular packing in defining the singlet/triplet exciton dynamics in the solids is widely acknowledged but still poorly understood. W. Huang, X. Lui and co-workers proposed H-aggregation as a design principle for stabilization of triplet excitons. The authors have indeed achieved an ultralong (>1 s) phosphorescence in various carbazole derivatives, although in all cases the fluorescence channel still dominated the emission.[28] Bryce *et al.* proposed that the ISC is enhanced by intermolecular electronic coupling of the "π" (carbazole) and "n" (carbonyl or sulfonyl) moieties, and demonstrated that pure (fluorescence-free) ORTP (PLQY ~5%) can be achieved in such organic solids when substituted with bromine.[30] Several groups have further studied the effect of solid state structure on phosphorescent properties through permutation of substituents in the molecule.[3, 15, 29, 31, 32] However, predictability of the induced changes and the generality of the deduced structure-properties relationships are limited by the complexity of the crystal packing of these low-symmetry molecules. The rational control of the solid-state packing and crystal engineering of ORTPs to design efficient organic phosphors is still missing in the field.

To address this problem, we synthesized a family of planar carbonyl-bridged D_{3h} symmetric triphenylamine derivatives (azatriangulenetriones; TANGOs, Scheme 2.1) that display efficient luminescence in the solid state.[a](**a**) By adjusting the size of substituents, we can control the molecular orientation within the π-stacks and switch from an almost pure fluorescence to pure phosphorescence. The parent non-substituted TANGO (HTANGO) shows phosphorescence quantum yields of 42 ± 2% (in air) and lifetime of 28.6 ms. To the best of our knowledge, this is the highest efficiency of ORTP in organic solids without a heavy atom effect. We investigated the effects of the molecular structure and crystal packing on the luminescence of different TANGO derivatives and carried out time dependent density functional theory calculations (TD-DFT) to shed light on the observed relationships.

---

a) HTANGO was reported previously.[37] However, only solution fluorescence in trifluoroacetic acid was reported. Supramolecular assemblies of some TANGO derivatives are also known.[38, 39] No solid emission or phosphorescent properties have been described for any of these derivatives.

2.3. Result and Discussion

The TANGO derivatives were synthesized from triphenylamine derivatives **1-5** (Scheme 2.1.) and purified by Soxhlet extraction followed by multiple vacuum sublimations (performed until the solid-state emission spectra remain unchanged). TGA analysis of all TANGO derivatives shows a remarkable thermal stability ($T_{dec} > 400$ °C in air, Figure 2.4 in Supporting Information).

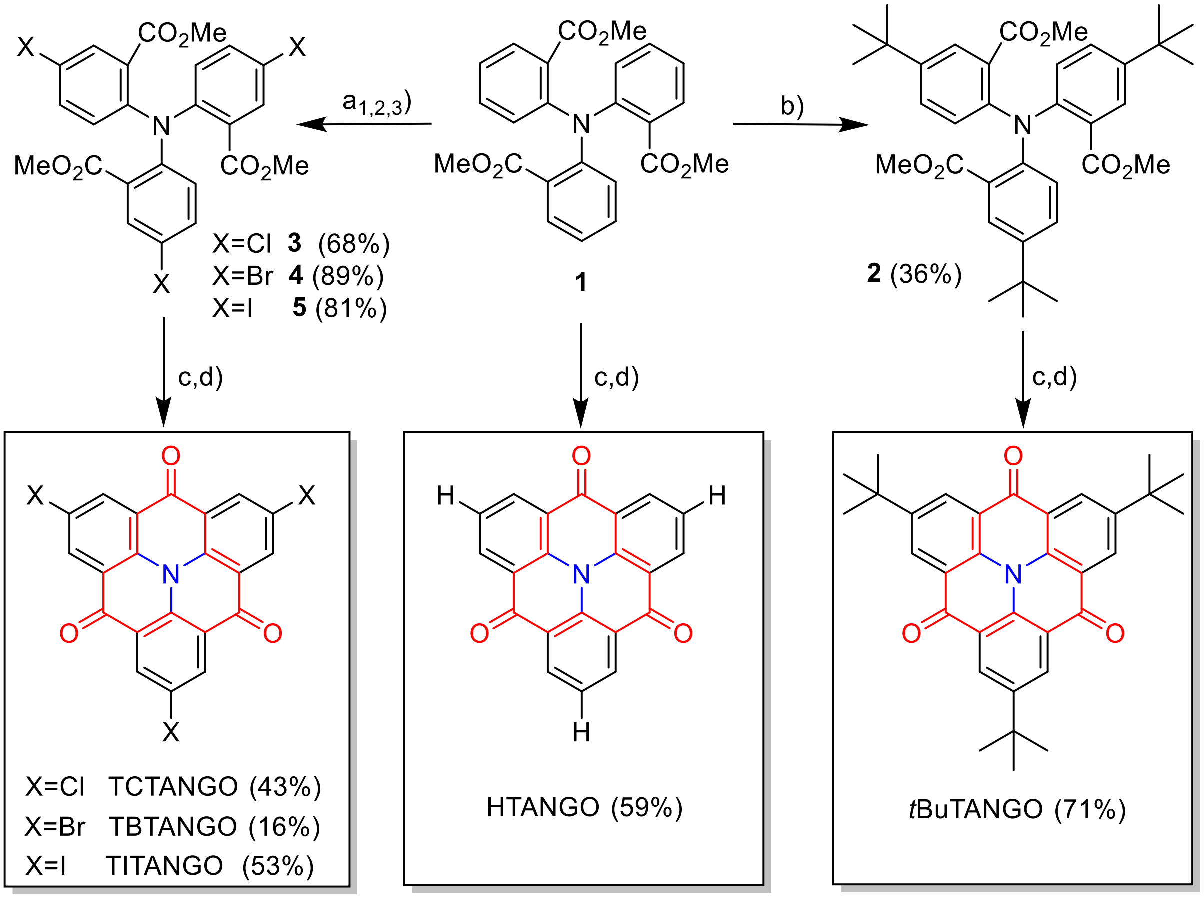

Scheme 2.1. Synthesis of TANGO derivatives: a$_1$) NCS, ACN; a$_2$) PyH$^+$Br$_3^-$, EtOH/Benzene; a$_3$) I$_2$, Ag$_2$SO$_4$, EtOH; b) FeCl$_3$, *t*-BuCl; c) KOH, MeOH/H$_2$O; d) SOCl$_2$/DMF, SnCl$_4$, DCM.

With exception of *t*BuTANGO, TANGO derivatives are scarcely soluble in organic solvents. Solutions with μM concentrations can be also prepared in chloroform for HTANGO and TCTANGO (but not TBTANGO and TITANGO). Solution UV-Vis absorption of HTANGO shows a strong vibronically structured π-π* absorption band at λ^{abs}_{max} = 408 nm which slightly red-shifts in TCTANGO (429 nm) and *t*BuTANGO (422 nm) (Figure 2.1 a-c). Upon UV excitation all three solutions reveal a deep blue emission with relatively low photoluminescence quantum yields (PLQY) of 1%, 5% and 13% for HTANGO, TCTANGO and *t*BuTANGO, respectively. The emission maxima (λ^{F}_{max} = 422, 445 and 440 nm for HTANGO, TCTANGO and *t*BuTANGO, respectively) follow the same trend as the absorption, with similar Stokes shift of ~0.13 eV. Their emission shows a monoexponential decay with the lifetime τ^F = 3.5 ns (HTANGO), 3.9 ns (TCTANGO) and 0.9 ns (*t*BuTANGO) indicating the fluorescence nature of the emission (Figure 2.7). No detectable delayed (>0.1 ms) emission was observed in these solutions at room temperature and their emission spectra were not affected by the presence of air.

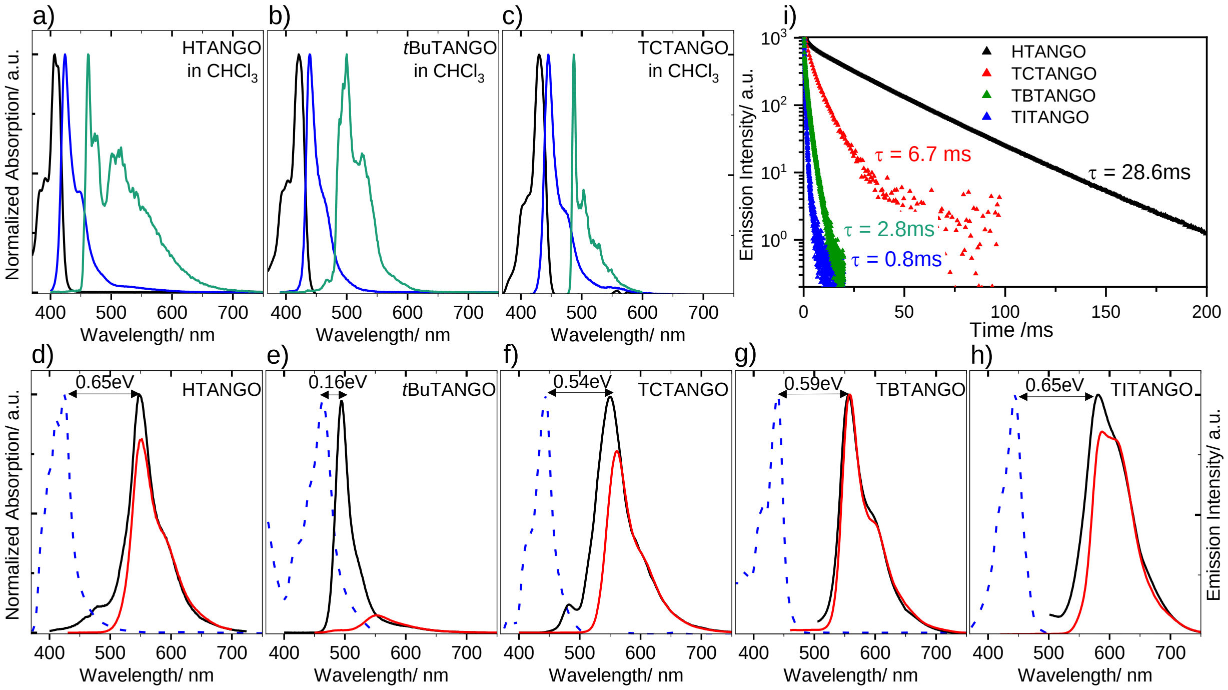

Figure 2.1. a-c) Absorption (black) and emission (steady state at room temperature, blue; 0.2 ms delayed at 77 K, green) of HTANGO, *t*BuTANGO and TCTANGO in chloroform solutions. d-h) Solid state absorption (blue), steady state (black) and delayed (red) emission of TANGO solids at room temperature and i) corresponding phosphorescence lifetime. The arrows in (d-h) show Stokes shifts.

Nevertheless, the ISC does take place in all three derivatives, as expected in aromatic ketones.[33] In frozen solution at 77 K, the delayed emission can be detected by a naked eye (Figure 2.8) and the emission spectra show vibronically structured phosphorescence bands at λ^{P}_{max}= 461 nm (τ^{P} = 145 ms), λ^{P}_{max} = 487 nm (τ^{P} = 91 ms) and λ^{P}_{max} = 498 nm (τ^{P} = 464 ms) for HTANGO, TCTANGO and *t*BuTANGO, respectively. A broad shoulder in the HTANGO spectrum at ~550–600 nm (not observed for TCTANGO and *t*BuTANGO) might be due to partial aggregation upon freezing (Figure 2.1a).

In the solid state HTANGO shows a significantly red-shifted emission with λ^{P}_{max} = 538 nm and lifetime of τ^{P} = 28.6 ms (Figure 2.1d, i). Its total emission (t_d = 0 ms) and delayed emission (t_d = 0.2 ms) spectra are nearly superimposable, showing the dominance of the phosphorescence pathway (Figure 2.1d). The PLQY was found to be 42 ± 2% for the single crystals of HTANGO (25 ± 3% for vapor deposited films). TCTANGO solid displays a similar photoluminescence behavior: a red-shifted emission with λ^{P}_{max} = 560 nm and τ^{P} = 6.7 ms (PLQY of 26%). The shorter phosphorescence lifetime of TCTANGO comparing to HTANGO is likely attributed to the heavy atom effect. Indeed, the lifetime further decreases for the heavier TBTANGO (τ^{P} = 2.8 ms; λ^{P}_{max} = 570 nm) and TITANGO (τ^{P} = 0.8 ms; λ^{P}_{max} = 589 nm), albeit with low PLQY (~1.5% for TBTANGO, ~1% for TITANGO).

A completely different behavior, however, was observed in the solid state of *t*BuTANGO which displays a less pronounced red-shift vs solution (λ^{F}_{max} = 495 nm) and fast radiative decay (τ^{F} = 10.0 ns) revealing an almost pure fluorescence with PLQY = 11% (Figure 2.1e and Figure 2.7d). The striking difference between the luminescence lifetimes of the TANGOs was visualized with a high-speed camera (supporting information of the manuscript[34]) which reveals a progressively diminishing afterglow in the order $\tau_{HTANGO} >> \tau_{TCTANGO} > \tau_{TBTANGO} > \tau_{TITANGO}$. Such behavior of TANGO derivatives coupled with their remarkable environmental stability could find applications in pigments for advanced encrypted codes (which use specific delay time and wavelength for decryption).[5] The observed differences in the solid-state emission of the TANGO derivatives cannot be fully attributed to molecular effects. All three soluble TANGO derivatives showed similar photoluminescence properties in solution, with mild red-shifts of λ^{F}_{max} due to Cl and *t*Bu substituents and comparable lifetimes (~1-4 ns). We have performed TD-DFT calculations (B3LYP/6-31G(d)) for optimized molecules in gas phase in both singlet and triplet states and carried out natural transition orbital (NTO) and spin-orbit coupling (SOC) analysis (Figure 2.9, 2.10). According to El-Sayed's rules, the ISC is favored for transitions between ^{1}n-π* and ^{3}π-π*.[33] NTO analysis indeed predicts that only HTANGO and TITANGO show n-π* S_1 and π-π* T_1 transition orbitals. In all other TANGOs both S_1 and T_1 transition states show pure π-π* behavior. The resulting high $SOC_{S1\rightarrow T1}$ for HTANGO (45 cm^{-1}) and TITANGO (88 cm^{-1}) can indeed contribute to efficient ISC of these two compounds but leaves unexplained the observed trend of the phosphorescence efficiency: HTANGO > TCTANGO >> TBTANGO > TITNAGO and almost complete lack of phosphorescence in *t*BuTANGO solid state.

In order to understand the effects of molecular packing on the photoluminescence of TANGOs, their single crystals were grown via physical vapor deposition. X-ray crystallographic analysis reveals that all TANGO derivatives are nearly planar (out of plane deviation <0.33 Å) and pack in one-dimensional slipped π-stacks with interplanar distances of 3.40–3.46 Å (Figure 2.2). According to crystal structures of TANGOs, the major difference in their packing relates to the alignment of the transition dipoles ($N\cdots C{=}O \leftrightarrow N^{+}\cdots C{-}O^{-}$) within the stack. These dipoles are co-parallel in all TANGO derivatives except for *t*BuTANGO, where the steric hindrance of *t*-butyl group forces the adjacent molecules to rotate 60° versus each other to maintain the π-π interactions. Accordingly, the absorption (i.e. $S_0 \rightarrow S_1$ transition) of *t*BuTANGO in the solid state shows a large bathochromic shift (0.27 eV) vs that in solution, while only a small ~0.1 eV shift was observed for HTANGO and TCTANGO (Figure 2.5). This difference is reminiscent of J-/H-aggregation in dipolar fluorescent dyes, where the J-aggregation results in large red-shift of the absorption/ emission wavelength (versus those of the individual dye molecules in solution) enhancing the oscillator strength of the $S_0 \leftrightarrow S_1$ transition and H-aggregation causes the opposite effect resulting in optically inactive "dark" singlet excited state.[19]

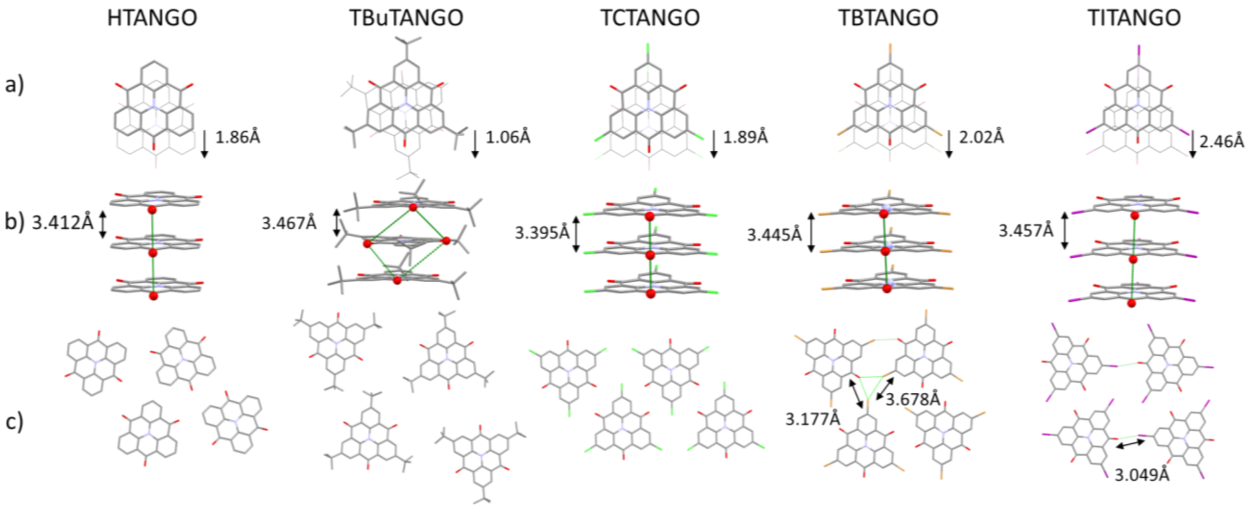

Figure 2.2. Crystal structure of TANGOs showing molecular orientation within π-stacks, in the top (a) and side view (b), and in the adjacent stacks (c). The arrows in (a) show molecular displacement in the stacks, along the O=C···N axis. The red balls in (b) represent the oxygens highlighting the eclipsed (HTANGO, TCTANGO, TBTANGO, TITANGO) and staggered (TBuTANGO) packing; the arrows show interplanar distances. The arrows in (c) show Br···O and I···O halogen bonds.

To shed further light on the role of crystal packing on the excited state properties, TD-DFT calculations were performed for the π-stacked TANGO dimers with varied dihedral angle α between their N···C=O dipoles representing the different rotation of the molecules within π-stacks (Figure 2.3). The $S_1 \rightarrow S_0$ oscillator strength is zero for $\alpha = 0°$ (corresponding to HTANGO packing) but it increases to 0.063 for $\alpha = 60°$ (corresponding to *t*BuTANGO packing). As a result, the singlet excited state of *t*BuTANGO undergoes a fast (fluorescence) decay ($\tau^F = 10$ ns), while the optically inactive singlet excitons in HTANGO (and TCTANGO/TBTANGO/TITANGO) persist for sufficiently long times for ISC.

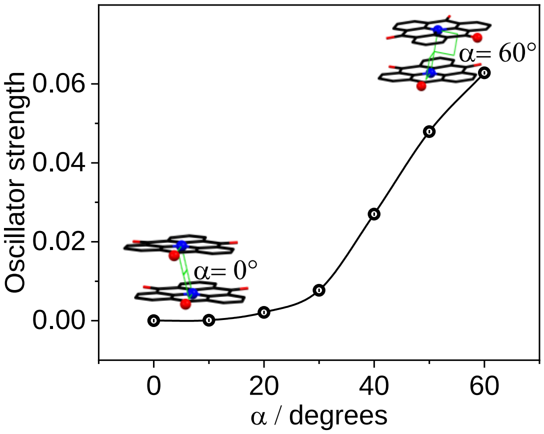

Figure 2.3. TD-DFT calculated oscillator strength of TANGO π-dimers as a function of their rotational alignment (α = 0° and 60° correspond to crystal packing of HTANGO and *t*BuTANGO, respectively).

The reason for the lower phosphorescence quantum yield of TBTANGO and TITANGO comparing to HTANGO and TCTANGO is less obvious. The larger halogen atoms lead to more slipped π-stacks: the displacement along the O=C···N axis increases from 1.86 Å for HTANGO and 1.89 Å for TCTANGO, to 2.02 Å for TBTANGO and 2.46 Å for TITANGO (Figure 2.2a). These changes can affect the coupling of triplet excitons in terms of transition from a phosphorescence-promoting H-aggregation to J-aggregation.[14a] The previous work has attributed solid state phosphorescence in bromobenzaldehyde derivatives to halogen bonding between the bromine and carbonyl groups.[9e] In our case, the halogen bonding interactions have been observed in TBTANGO (O···Br = 3.18 Å) and TITANGO (O···I = 3.05 Å) (Figure 2.2c) but their phosphorescence is much weaker than that of HTANGO and TCTANGO which lack such interactions. The inconsequential role of the halogen bonds is probably explained by the weak exciton coupling between the stacks (N···N distances 9.40-14.20 Å), comparing to that within the stacks (N···N distances 3.52-4.15 Å). However, we cannot completely exclude the possible role of defects, particularly for TITANGO with weak C-I bonds.

2.4. Conclusion

In summary, we introduced a new class of emissive azatriangulenetrione pigments whose crystal packing can be designed by tuning the bulkiness of substituent. Using X-ray crystallography we showed that all derivatives pack in columnar π-stacks with the relative molecular orientation controlled by the size of the substituent: the *t*-butyl group causes 60° rotation resulting in almost pure fluorescence (*t*BuTANGO, PLQY = 11%) while smaller side groups (H, Cl, Br, I) lead to co-aligned π-stacks and these derivatives display pure phosphorescence emission at room temperature with PLQY of up to 42% (for HTANGO). The latter sets a new record of efficiency of room temperature phosphorescence in pure organic solids in the absence of the heavy atom effect. Achieving efficient phosphorescence in densely packed solids with strong π-π interactions is particularly impressive as triplet-triplet annihilation and extended exciton diffusion is generally thought to lead to exciton quenching. These results may open new opportunities for design of solid state phosphorescent lasers,[12] electroluminescent devices,[35] upconverting materials for light harvesting and related applications.[36]

2.5. Acknowledgments

We thank Francine Bélanger-Gariepy and Thierry Maris for performing X-ray crystallographic analysis, Dr. Kishan Prithipaul of High-Speed Imaging Inc. for providing a high-speed camera, and Lisa Vlasova for the help in the synthesis of precursor 1. We thank Robin S. Stein for NMR spectroscopy, and Alexander Wahba and Nadim Saade for mass spectrometry.

2.6. References

1. Kenry; Chen, C.; Liu, B., Enhancing the performance of pure organic room-temperature phosphorescent luminophores. *Nat. Commun.* **2019,** *10*, 2111.

2. Forni, A.; Lucenti, E.; Botta, C.; Cariati, E., Metal free room temperature phosphorescence from molecular self-interactions in the solid state. *J. Mater. Chem. C* **2018,** *6*, 4603-4626.

3. Yang, J.; Zhen, X.; Wang, B.; Gao, X.; Ren, Z.; Wang, J.; Xie, Y.; Li, J.; Peng, Q.; Pu, K.; Li, Z., The influence of the molecular packing on the room temperature phosphorescence of purely organic luminogens. *Nat. Commun.* **2018,** *9*, 840.

4. Fateminia, S. M. A.; Mao, Z.; Xu, S.; Yang, Z.; Chi, Z.; Liu, B., Organic nanocrystals with bright red persistent room-temperature phosphorescence for biological applications. *Angew. Chem. Int. Ed.* **2017,** *56*, 12160-12164.

5. Su, Y.; Phua, S. Z. F.; Li, Y.; Zhou, X.; Jana, D.; Liu, G.; Lim, W. Q.; Ong, W. K.; Yang, C.; Zhao, Y., Ultralong room temperature phosphorescence from amorphous organic materials toward confidential information encryption and decryption. *Sci. Adv.* **2018,** *4*, eaas9732.

6. Tao, Y.; Chen, R.; Li, H.; Yuan, J.; Wan, Y.; Jiang, H.; Chen, C.; Si, Y.; Zheng, C.; Yang, B.; Xing, G.; Huang, W., Resonance-activated spin-flipping for efficient organic ultralong room-temperature phosphorescence. *Adv. Mater.* **2018,** *30*, 1803856.

7. Lee, J.; Chen, H.-F.; Batagoda, T.; Coburn, C.; Djurovich, P. I.; Thompson, M. E.; Forrest, S. R., Deep blue phosphorescent organic light-emitting diodes with very high brightness and efficiency. *Nat. Mater.* **2016,** *15*, 92-98.

8. Zhang, Y.; Lee, J.; Forrest, S. R., Tenfold increase in the lifetime of blue phosphorescent organic light-emitting diodes. *Nat. Commun.* **2014,** *5*, 5008.

9. Shao, S.; Ding, J.; Wang, L.; Jing, X.; Wang, F., White electroluminescence from all-phosphorescent single polymers on a fluorinated poly (arylene ether phosphine oxide) backbone simultaneously grafted with blue and yellow phosphors. *J. Am. Chem. Soc.* **2012,** *134*, 20290-20293.

10. Kwon, T.-H.; Kim, M. K.; Kwon, J.; Shin, D.-Y.; Park, S. J.; Lee, C.-L.; Kim, J.-J.; Hong, J.-I., Highly efficient light-harvesting system based on a phosphorescent acceptor coupled with dendrimer donors via Singlet−Singlet and Triplet−Triplet energy transfer. *Chem. Mater.* **2007,** *19*, 3673-3680.

11. Yum, J.-H.; Baranoff, E.; Hardin, B. E.; Hoke, E. T.; McGehee, M. D.; Nüesch, F.; Grätzel, M.; Nazeeruddin, M. K., Phosphorescent energy relay dye for improved light harvesting response in liquid dye-sensitized solar cells. *Energy Environ. Sci.* **2010,** *3*, 434-437.

12. Yu, Z.; Wu, Y.; Xiao, L.; Chen, J.; Liao, Q.; Yao, J.; Fu, H., Organic phosphorescence nanowire lasers. *J. Am. Chem. Soc.* **2017,** *139*, 6376-6381.

13. Garfield, D. J.; Borys, N. J.; Hamed, S. M.; Torquato, N. A.; Tajon, C. A.; Tian, B.; Shevitski, B.; Barnard, E. S.; Suh, Y. D.; Aloni, S., Enrichment of molecular antenna triplets amplifies upconverting nanoparticle emission. *Nat. Photon.* **2018,** *12*, 402-407.

14. Xu, J.; Feng, H.; Teng, H.; Chen, G.; Pan, S.; Chen, J.; Qian, Z., Reversible switching between phosphorescence and fluorescence in a unimolecular system controlled by external stimuli. *Chem. Eur. J.* **2018,** *24*, 12773-12778.

15. Xiong, Y.; Zhao, Z.; Zhao, W.; Ma, H.; Peng, Q.; He, Z.; Zhang, X.; Chen, Y.; He, X.; Lam, J. W. Y.; Tang, B. Z., Designing efficient and ultralong pure organic room-temperature phosphorescent materials by structural isomerism. *Angew. Chem. Int. Ed.* **2018,** *57*, 7997-8001.

16. Wang, J.; Gu, X.; Ma, H.; Peng, Q.; Huang, X.; Zheng, X.; Sung, S. H. P.; Shan, G.; Lam, J. W. Y.; Shuai, Z.; Tang, B. Z., A facile strategy for realizing room temperature phosphorescence and single molecule white light emission. *Nat. Commun.* **2018,** *9*, 2963.

17. Bolton, O.; Lee, K.; Kim, H. J.; Lin, K. Y.; Kim, J., Activating efficient phosphorescence from purely organic materials by crystal design. *Nat. Chem.* **2011,** *3*, 205-210.

18. Fermi, A.; Bergamini, G.; Roy, M.; Gingras, M.; Ceroni, P., Turn-on phosphorescence by metal coordination to a multivalent terpyridine ligand: a new paradigm for luminescent sensors. *J. Am. Chem. Soc.* **2014,** *136*, 6395-6400.

19. He, G.; Wiltshire, B. D.; Choi, P.; Savin, A.; Sun, S.; Mohammadpour, A.; Ferguson, M. J.; McDonald, R.; Farsinezhad, S.; Brown, A., Phosphorescence within benzotellurophenes and color tunable tellurophenes under ambient conditions. *Chem. Commun.* **2015,** *51*, 5444-5447.

20. He, G.; Torres Delgado, W.; Schatz, D. J.; Merten, C.; Mohammadpour, A.; Mayr, L.; Ferguson, M. J.; McDonald, R.; Brown, A.; Shankar, K.; Rivard, E., Coaxing solid-state phosphorescence from tellurophenes. *Angew. Chem. Int. Ed.* **2014,** *53*, 4587-4591.

21. Xu, L.; Li, G.; Xu, T.; Zhang, W.; Zhang, S.; Yin, S.; An, Z.; He, G., Chalcogen atom modulated persistent room-temperature phosphorescence through intramolecular electronic coupling. *Chem. Commun.* **2018,** *54*, 9226-9229.

22. He, Z. K.; Zhao, W. J.; Lam, J. W. Y.; Peng, Q.; Ma, H. L.; Liang, G. D.; Shuai, Z. G.; Tang, B., White light emission from a single organic molecule with dual phosphorescence at room temperature. *Nat. Commun.* **2017,** *8*, 1-8.

23. Yuan, W. Z.; Shen, X. Y.; Zhao, H.; Lam, J. W.; Tang, L.; Lu, P.; Wang, C.; Liu, Y.; Wang, Z.; Zheng, Q., Crystallization-induced phosphorescence of pure organic luminogens at room temperature. *J. Phys. Chem. C* **2010,** *114*, 6090-6099.

24. Lee, D.; Bolton, O.; Kim, B. C.; Youk, J. H.; Takayama, S.; Kim, J., Room temperature phosphorescence of metal-free organic materials in amorphous polymer matrices. *J. Am. Chem. Soc.* **2013,** *135*, 6325-6329.

25. Ma, X.; Xu, C.; Wang, J.; Tian, H., Amorphous pure organic polymers for heavy-atom-free efficient room-temperature phosphorescence emission. *Angew. Chem. Int. Ed.* **2018,** *57*, 10854-10858.

26. Zhou, C.; Zhang, S.; Gao, Y.; Liu, H.; Shan, T.; Liang, X.; Yang, B.; Ma, Y., Ternary emission of fluorescence and dual phosphorescence at room temperature: A single-molecule white light emitter based on pure organic aza-aromatic material. *Adv. Funct. Mater.* **2018,** *28*, 1802407.

27. Zhao, W.; He, Z.; Lam, Jacky W. Y.; Peng, Q.; Ma, H.; Shuai, Z.; Bai, G.; Hao, J.; Tang, Ben Z., Rational molecular design for achieving persistent and efficient pure organic room-temperature phosphorescence. *Chem* **2016,** *1*, 592-602.

28. An, Z.; Zheng, C.; Tao, Y.; Chen, R.; Shi, H.; Chen, T.; Wang, Z.; Li, H.; Deng, R.; Liu, X.; Huang, W., Stabilizing triplet excited states for ultralong organic phosphorescence. *Nat. Mater.* **2015,** *14*, 685-690.

29. Zhang, T.; Wang, X.; An, Z.; Fang, Z.; Zhang, Y.; Yuan, W. Z., Pure organic persistent room-temperature phosphorescence at both crystalline and amorphous states. *ChemPhysChem* **2018,** *19*, 2389-2396.

30. Yang, Z.; Mao, Z.; Zhang, X.; Ou, D.; Mu, Y.; Zhang, Y.; Zhao, C.; Liu, S.; Chi, Z.; Xu, J.; Wu, Y. C.; Lu, P. Y.; Lien, A.; Bryce, M. R., Intermolecular electronic coupling of organic units for efficient persistent room-temperature phosphorescence. *Angew. Chem. Int. Ed.* **2016,** *55*, 2181-2185.

31. Cai, S.; Shi, H.; Tian, D.; Ma, H.; Cheng, Z.; Wu, Q.; Gu, M.; Huang, L.; An, Z.; Peng, Q.; Huang, W., Enhancing ultralong organic phosphorescence by effective π-type halogen bonding. *Adv. Funct. Mater.* **2018,** *28*, 1705045.

32. Zhang, K.; Sun, Q.; Tang, L.; Wang, Y.; Fan, X.; Liu, L.; Xue, S.; Yang, W., Cyclic boron esterification: screening organic room temperature phosphorescent and mechanoluminescent materials. *J. Mater. Chem. C* **2018,** *6*, 8733-8737.

33. Baba, M., Intersystem Crossing in the $^1n\pi^*$ and $^1\pi\pi^*$ States. *J. Phys. Chem. A* **2011,** *115*, 9514-9519.

34. The video is in the supporting information of the manuscript.

35. Wong, M. Y.; Zysman-Colman, E., Purely organic thermally activated delayed fluorescence materials for organic light-emitting diodes. *Adv. Mater.* **2017,** *29*, 1605444.

36. Pun, A. B.; Campos, L. M.; Congreve, D. N., Tunable emission from triplet fusion upconversion in diketopyrrolopyrroles. *J. Am. Chem. Soc.* **2019,** *141*, 3777-3781.

37. Field, J. E.; Venkataraman, D., Heterotriangulenes-structure and properties. *Chem. Mater.* **2002,** *14*, 962-964.

38. Haedler, A. T.; Kreger, K.; Issac, A.; Wittmann, B.; Kivala, M.; Hammer, N.; Kohler, J.; Schmidt, H. W.; Hildner, R., Long-range energy transport in single supramolecular nanofibres at room temperature. *Nature* **2015,** *523*, 196-199.

39. Valera, J. S.; Sánchez-Naya, R.; Ramírez, F. J.; Zafra, J. L.; Gómez, R.; Casado, J.; Sanchez, L., Solvent-directed helical stereomutation discloses pathway complexity on n-heterotriangulene-based organogelators. *Chem. Eur. J.* **2017,** *23*, 11141-11146.

2.7. Supplementary Information

2.7.1. Synthesis

Methyl 2-aminobenzoate, $SnCl_4$ (98%) and $SOCl_2$ were purchased from Sigma Aldrich. KOH, HCl, EtOAC, hexane, MeOH, EtOH, MeCN and CH_2Cl_2 were purchased from Fisher. Trimethyl 2,2',2''-nitrilotribenzoate (1) was synthesized according to literature.[1] All TANGO derivatives were synthesized as described below. HTANGO, TCTANGO, TBTANGO and TITANGO used in photoluminescence studies were additionally purified by Soxhlet extraction (i-PrOH, THF and $CHCl_3$) and subject to fractional vacuum sublimation (at least twice or until their emission spectra and photoluminescence quantum yield remain unchanged).

4H-Benzo[9,1]quinolizino[3,4,5,6,7-d,e,f,g]acridine-4,8,12-trione (HTANGO):[2] **1** (1.50 g, 3.60 mmol) and KOH (2.02 g, 36 mmol) were dissolved in MeOH (40 ml) and H_2O (10 ml). After stirring at 60 °C for 24 h, the solution was diluted with H_2O (100 ml) and acidified (pH~3) with aq. HCl (1M). The resulting precipitate was filtered off, excessively washed with H_2O and dried under vacuum to give the triacid as a pale-yellow powder (0.98 g, 73 %) which was used without further purification and characterization for the next step. The resulting triacid (0.98 g, 2.6 mmol), SOCl2 (10 ml), and DMF (0.5 ml) were stirred in dry CH_2Cl_2 (30 mL) at 40°C for 3 h. $SnCl_4$ (0.30 ml, 2.6 mmol) was then added and the solution was stirred at 40°C for further 20 h. The yellow precipitate was filtered off and stirred in aq. NaOH (1 M, 50 mL) for 30 min. After filtration the residue was excessively washed with H_2O and acetone and dried to yield HTANGO (499 mg, 59%). The residue was then transferred to a sublimation chamber and sublimed under vacuum to give pure crystalline powder of HTANGO. APCI-MS calcd. for $C_{21}H_{10}NO_3$ $[MH]^+$ 324.0655, found 324.0661; extremely low solubility of the product in organic solvents precluded NMR characterization.

Trimethyl 6,6',6''-nitrilotris(3-(*tert*-butyl)benzoate) (2): To a solution of **1** (1.50 g, 3.60 mmol) in 100 ml t-butyl chloride anhydrous $FeCl_3$(0.25 g,1.54 mmol) was added and the reaction mixture brought up to reflux. After 4 hours the solvent was evaporated, and the crude product was dissolved in ethyl acetate, washed with brine and dried under vacuum and the residue was purified by column chromatography (SiO_2, hexanes/EtOAc 20:1) to provide **2** as a pale-yellow solid (0.77 g, 36%). ESI-MS (MeOH) calcd. for $C_{36}H_{45}NO_6Na^+$ $[M]^+$ 610.3144, found 610.3162; ^{1}H

NMR (500 MHz, $CDCl_3$) δ 7.57 (d, *J* = 2.5 Hz, 3H), 7.39 (dd, *J* = 8.6, 2.5 Hz, 3H), 7.01 (d, *J* = 8.6 Hz, 3H), 3.36 (s, 9H), 1.32 (s, 27H); ^{13}C NMR (126 MHz, $CDCl_3$) δ 168.33, 146.05, 144.65, 129.25, 127.33, 126.82, 125.38, 51.55, 34.37, 31.23.

2,6,10-Tri-*tert*-butyl-4H-benzo[9,1]quinolizino[3,4,5,6,7-defg]acridine-4,8,12-trione (*t*BuTANGO): 2 (0.70 g, 1.2 mmol) and KOH (0.67 g, 12 mmol) were dissolved in MeOH (40 mL) and H_2O (10 mL). After being stirred at 60 °C for 24 h, the solution was diluted with H_2O (100 mL) and acidified (pH~3) with aq. HCl (1 M). The resulting precipitate was filtered off, excessively washed with H_2O, and dried under vacuum to give the triacid as a pale-yellow powder (0.62 g, 95%) which was used without further purification and characterization for the next step. The resulting triacid (0.60 g, 1.10 mmol), $SOCl_2$ (10 ml), and DMF (0.1 ml) were stirred in dry CH_2Cl_2 (30 mL) at 40 °C for 3 h. $SnCl_4$ (0.14 mL, 1.20 mmol) was then added and the solution was stirred at 40 °C for further 20 h. The mixture cooled down in ice bath and aq. NaOH was added dropwise (1 M, 50 mL) for 30 min. The yellow precipitate was filtered off and dried under vacuum. The residue was purified by column chromatography (SiO_2, hexanes/EtOAc 1:7) to provide *t*BuTANGO as a yellow solid (0.39 g, 72%). APCI-MS calcd. for $C_{33}H_{34}NO_3$ $[M]^+$ 492.2538, found 492.2533; ^{1}H NMR (500 MHz, $CDCl_3$) δ 9.08 (s, 6H), 1.57 (s, 27H); ^{13}C NMR (126 MHz, $CDCl_3$) δ 176.57, 148.96, 135.41, 131.54, 122.97, 35.20, 31.25.

Trimethyl 6,6',6''-nitrilotris(3-chlorobenzoate) (3): **1** (2.00 g, 4.77 mmol) in 75 ml acetonitrile was brought to reflux and NCS (2.23 g, 16.70 mmol) was added portionwise in 3 hours. Reaction stirred overnight under reflux conditions. The solvent was evaporated, and the crude product was washed with brine and dried under vacuum. The residue was purified by column chromatography (SiO_2, hexanes/EtOAc 9:1) to provide **3** as a pale-yellow solid (1.69 g, 68%). ESI-MS (toluene) calcd. for $C_{24}H_{18}O_6NCl_3Na$ $[M]^+$ 544.0097, found 544.0110; ^{1}H NMR (500 MHz, $CDCl_3$) δ 7.59 (d, *J* = 2.5 Hz, 3H), 7.33 (dt, *J* = 8.7, 2.2 Hz, 3H), 6.98 (d, *J* = 8.7 Hz, 3H), 3.45 (s, 9H). ^{13}C NMR (126 MHz, $CDCl_3$) δ 165.92, 144.88, 132.42, 130.80, 129.35, 128.83, 127.16, 52.16.

2,6,10-Trichloro-4H-benzo[9,1]quinolizino[3,4,5,6,7-defg]acridine-4,8,12-trione (TCTANGO): 2 (1.64 g, 3.15 mmol) and KOH (1.76 g, 31.5 mmol) were dissolved in MeOH (40 mL) and H_2O (10 mL). After stirring at 60°C for 24 h, the solution was diluted with H_2O (100 mL) and acidified (pH~3) with aq. HCl (1 M). The resulting precipitate was filtered off, excessively washed with H_2O, and dried under vacuum to give the triacid as a pale-yellow powder (1.35 g, 89%) which was used without further purification and characterization for the next step. The triacid (1.35 g, 2.81 mmol), $SOCl_2$ (10ml), and DMF (0.1 ml) were stirred in dry CH_2Cl_2 (30 mL) at 40 °C for 3h. $SnCl_4$ (0.33 mL, 2.81 mmol) was then added and the solution was stirred at 40 °C for further 20 h. The yellow precipitate was filtered off and stirred in aq. NaOH (1 M, 50 mL) for 30 min. After filtration the residue was excessively washed with H_2O and acetone and dried to yield a yellow powder (0.51 g, 43%). The residue was then transferred to a sublimation chamber and sublimed under vacuum to give pure TCTANGO. APCI-MS calcd. for $C_{21}H_7Cl_3NO_3$ $[MH]^+$ 425.9486, found 425.9478; extremely low solubility of the product in organic solvents precluded NMR characterization.

Trimethyl 6,6',6''-nitrilotris(3-bromobenzoate) (4): To a solution of **1** (1.50g, 3.6 mmol) in 100 ml EtOH/Benzene (v/v 1:1) was added pyridinium tribromide (17.10 g, 53.6 mmol) and stirred under reflux for 6 hours. The solvent was evaporated, and the crude product was dissolved in ethyl acetate, washed with brine and dried under vacuum residue was purified by column chromatography (SiO_2, hexanes/EtOAc 4:1) to provide **4** as a pale-yellow solid (2.10 g, 89%). APCI-MS calcd. for $C_{24}H_{19}Br_3NO_6$ $[M]^+$ 653.8757, found 653.8751; ^1H NMR (400 MHz, $CDCl_3$) δ 7.69 (d, J = 2.5 Hz, 3H), 7.42 (dd, J = 8.7, 2.5 Hz, 3H), 6.87 (d, J = 8.7 Hz, 3H), 3.40 (s, 9H).; ^{13}C NMR (101 MHz, $CDCl_3$) δ 165.74, 145.25, 135.34, 133.71, 129.13, 127.48, 116.81, 52.15.

2,6,10-Tribromo-4H-benzo[9,1]quinolizino[3,4,5,6,7-defg]acridine-4,8,12-trione (TBTANGO): 4 (1.5g, 2.3 mmol) and KOH (1.29g, 23mmol) were dissolved in MeOH (40 mL) and H_2O (10 mL). After stirring at 60°C for 24 h, the solution was diluted with H_2O (100 mL) and acidified (pH~3) with aq. HCl (1 M). The resulting precipitate was filtered off, excessively washed with H_2O, and dried under vacuum to give the triacid as a pale-yellow powder (1.05, 75%) which was used without further purification and characterization for the next step. The triacid (1.00 g, 1.63 mmol), $SOCl_2$ (10ml), and DMF (0.5ml) were stirred in dry CH_2Cl_2 (30 mL) at 40°C for 3 h. $SnCl_4$ (497 mg, 0.22 mL, 1.91 mmol) was then added and the solution was stirred at 40 °C for further

20 h. The yellow precipitate was filtered off and stirred in aq. NaOH (1 M, 50 mL) for 30 min. After filtration the residue was excessively washed with H_2O and acetone and dried to yield TBTANGO as a yellow powder (148 mg, 16%). The residue was then transferred to a sublimation chamber and sublimed under vacuum to give pure TBTANGO. APCI-MS calcd. for $C_{21}H_7Br_3NO_3$ $[MH]^+$ 557.7971, found 557.7966; extremely low solubility of the product in organic solvents precluded NMR characterization.

Trimethyl 6,6',6''-nitrilotris(3-iodobenzoate) (5): To a solution of **1** (2.00 g, 4.77 mmol) in 100 ml EtOH was added iodine (4.12 g, 16.2 mmol) and silver sulfate (4.45 g, 14.2 mmol) and stirred in room temperature for 4 hours. The reaction mixture was washed with sodium thiosulfate (0.1M) and the dried under vacuum and the residue was purified by column chromatography (SiO_2, hexanes/EtOAc 5:1) to provide **5** as a pale-yellow solid (3.10 g, 81%). APCI-MS: calcd. for $C_{24}H_{19}I_3NO_6$ $[MH]^+$ 797.8341, found 797.8315; ^{1}H NMR (500 MHz, $CDCl_3$) δ 7.92 (d, *J* = 2.2 Hz, 3H), 7.66 (dd, *J* = 8.7, 2.2 Hz, 3H), 6.78 (d, *J* = 8.6 Hz, 3H), 3.44 (s, 9H); ^{13}C NMR (126 MHz, $CDCl_3$) δ 165.64, 145.79, 141.22, 139.59, 129.32, 127.66, 87.08, 52.16.

2,6,10-Triiodo-4H-benzo[9,1]quinolizino[3,4,5,6,7-defg]acridine-4,8,12-trione (TITANGO): 5 (3.00 g, 3.76 mmol) and KOH (2.11 g, 36.7 mmol) were dissolved in MeOH (40 mL) and H_2O (10 mL). After stirring at 60°C for 24 h, the solution was diluted with H_2O (100 mL) and acidified (pH~3) with aq. HCl (1 M). The resulting precipitate was filtered off, excessively washed with H_2O, and dried under vacuum to give the triacid as a pale-yellow powder (2.32, 82%) which was used without further purification and characterization for the next step. The resulting triacid (2.32 g, 3.07 mmol), $SOCl_2$ (10 ml), and DMF (0.1 ml) were stirred in dry CH_2Cl_2 (30 mL) at 40 °C for 3 h. $SnCl_4$ (0.36 mL, 1.62 mmol) was then added and the solution was stirred at 40 °C for further 20 h. The yellow precipitate was filtered off and stirred in aq. NaOH (1 M, 50 mL) for 30 min. After filtration the residue was washed with copious amount of H_2O and acetone and dried to give TITANGO as a yellow powder (1.14 g, 53%). The residue was then transferred to a sublimation chamber and sublimed under vacuum to give pure TITANGO. APCI-MS calcd. for $C_{21}H_6I_3NO_3$ $[M]^+$ 701.7555, found 701.7533; extremely low solubility of the product in organic solvents precluded NMR characterization.

2.7.2. Thermogravimetric Analysis (TGA)

Thermogravimetric analysis (TGA) was conducted on a TA Instruments Q500 Thermogravimetric System with a Pt pan under dynamic atmosphere of N_2. Samples were heated up to 550 °C at a rate of 20 °C/min under N_2 and 15 °C/min under air. The balance and purge flow were 10 ml/min and 90 ml/min, respectively.

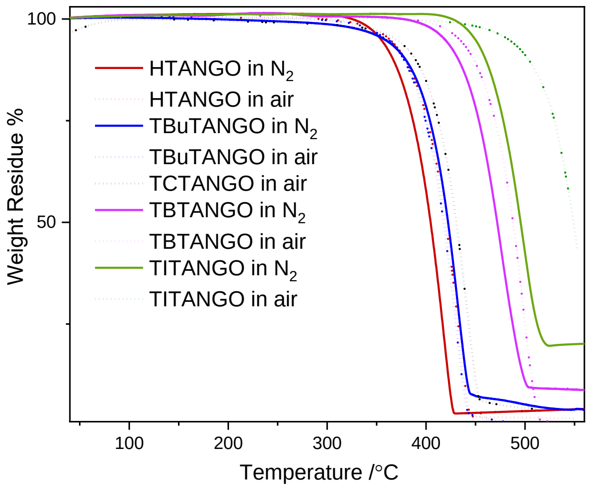

Figure 2.4. TGA analysis of the TANGO derivatives.

2.7.3. UV-Vis Absorption Spectroscopy and Steady state fluorescence/phosphorescence

The solution and thin film UV-Vis absorption spectra of TANGOs were collected on a JASCO V-670 spectrophotometer. Films were made on quartz using vapor deposition under vacuum. Room temperature total emission and delayed emission of TANGOs were measured on a Varian Cary Eclipse fluorescence spectrophotometer from Agilent, using a solid sample holder also from Agilent. Low temperature measurements were conducted on the same instrument using a liquid nitrogen dewar assembly from Horiba Scientific.

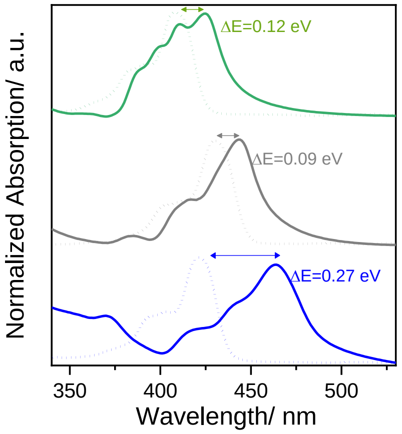

Figure 2.5. UV-Vis spectra of TANGO derivatives in solid state (solid lines) and solution (dashed line) of HTANGO (green), TCTANGO (gray) and *t*BuTANGO (blue).

2.7.4. Absolute Photoluminescence Quantum Yields (PLQYs)

Fluorescence quantum yield measurements were conducted in a Quanta-ϕ integrated sphere setup from Horiba Scientific, connected to and operated from a Fluorolog fluorometer also from Horiba Scientific. Samples were placed on disposable powder cups (Spectralon material) and covered with a quartz lid. Excitation was performed at 400 nm. Using a 'four spectra method', data acquisition was performed with 3 nm slits for both excitation and emission with integration times of 1 s/nm. Reflectance of the excitation wavelength was collected using a ND filter with optical density of 2. The data analysis was executed with the software included with the Quanta-ϕ integrated sphere.

2.7.5. Lifetime measurement and time resolved emission spectra

Phosphorescence lifetimes were measured on a Varian Cary Eclipse spectrophotometer from Agilent. The delay time and gate times used to measure lifetimes were chosen according to lifetimes, all in millisecond time scale. Low temperature measurements were conducted on the same instrument using a liquid nitrogen dewar assembly from Horiba Scientific. The emission lifetime of the samples was determined by the Time Correlated Single Photon Counting (TCSPC) technique using an Edinburgh Instruments mini-tau lifetime spectrophotometer equipped with an EPL 405 pulsed diode laser. The emission was filtered through a bandpass filter of 500 ± 50 nm.

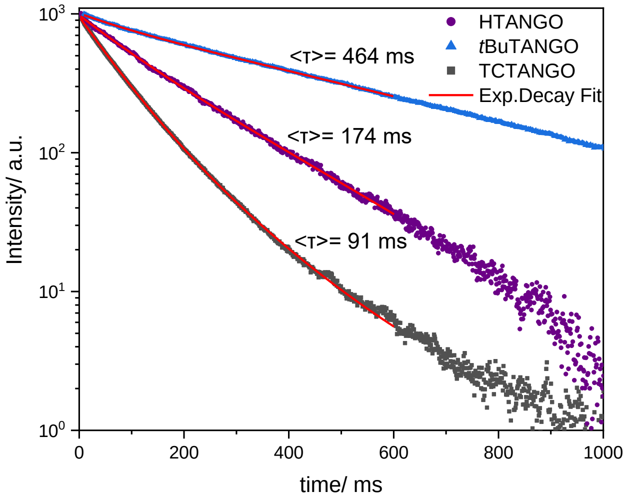

Figure 2.6. Frozen chloroform solution phosphorescence decay at 77 K λ_{ex}=410 nm for all derivatives, λ_{em}= 460 nm, 490 nm and 480 nm for HTANGO, *t*BuTANGO and TCTANGO, respectively.

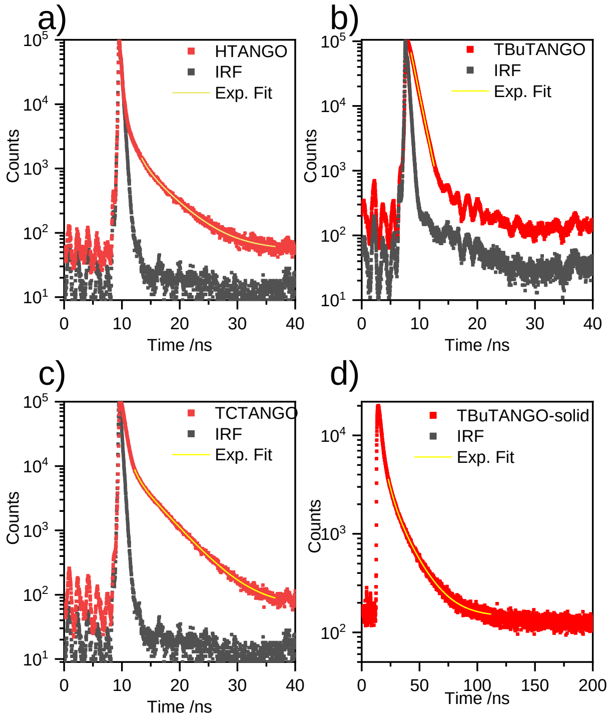

Figure 2.7. a,b,c) Fluorescence decay of TANGO derivatives in chloroform solutions at room temperature; d) *t*BuTANGO solid fluorescence decay at room temperature.

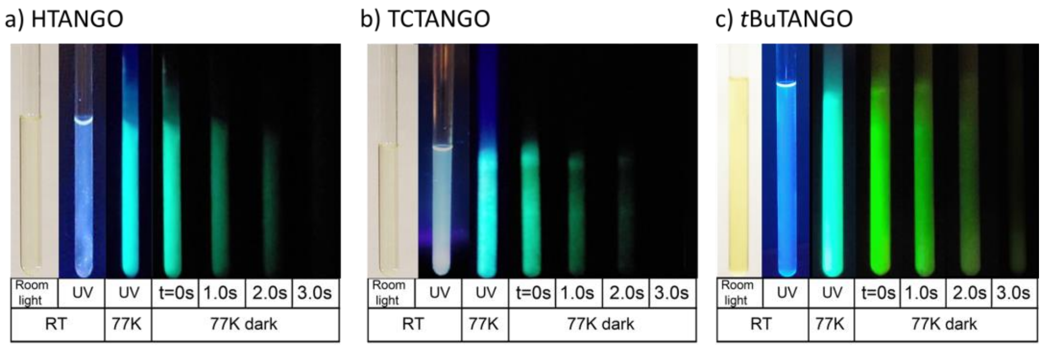
a) HTANGO
b) TCTANGO
c) *t*BuTANGO

Figure 2.8. Photographs of TANGO derivatives in chloroform solutions.

Table 2.1. Room temperature biexponential fit of TANGO derivatives in room temperature solutions.

	$\tau_{1\text{ , ns}}$	a_1	$\tau_{2\text{, ns}}$	a_2	$\tau_{\text{avg, ns}}$
HTANGO	1.2	33%	4.7	67%	3.5
TCTANGO	0.8	12%	4.3	88%	3.9
*t*BuTANGO	0.8	66%	1.25	33%	0.9
*t*BuTANGO$_{\text{solid}}$	2.9	77%	14.6	23%	9.9

The average fluorescence lifetime is calculated using the following equation: $\tau_{av} = (\sum\alpha_i\tau_i/\sum\alpha_i)$

2.7.6. DFT calculations

Geometry optimization, singlet and triplet excited state energies, transition orbital components and natural transition orbitals (NTOs) of all TANGO derivatives were obtained by TD-DFT calculations using B3LYP/6-31G(d) (lanl2dz in case of TITANGO) in Gaussian 16 software. TD-DFT calculations of TANGO dimers (Figure 2.3) were carried out on non-optimized geometries found by X-ray crystallography, using B3LYP/6-31G(d) with the D3 dispersion correction.

The SOC matrix elements were calculated with SOC-TD-DFT with ZORA Hamiltonian[3] using ADF package.[4, 5] B3LYP hybrid exchange–correlation functional was used with double-zeta + polarization (DZP) (TPZ in case of TITANGO). Spin-orbit couplings were calculated as root mean squares $<S|H_{so}|T>^2$ in cm^{-1}.

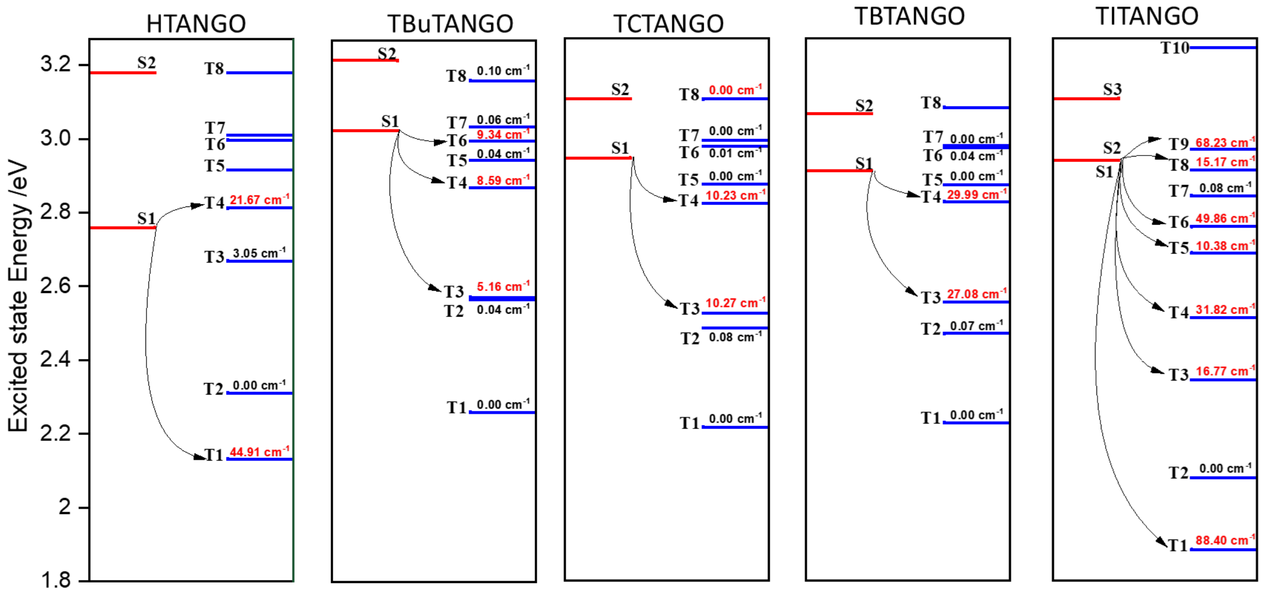

Figure 2.9. The Calculated energy level diagrams of TANGO derivatives, spin orbit coupling values (the inset numbers) and possible ISC pathways.

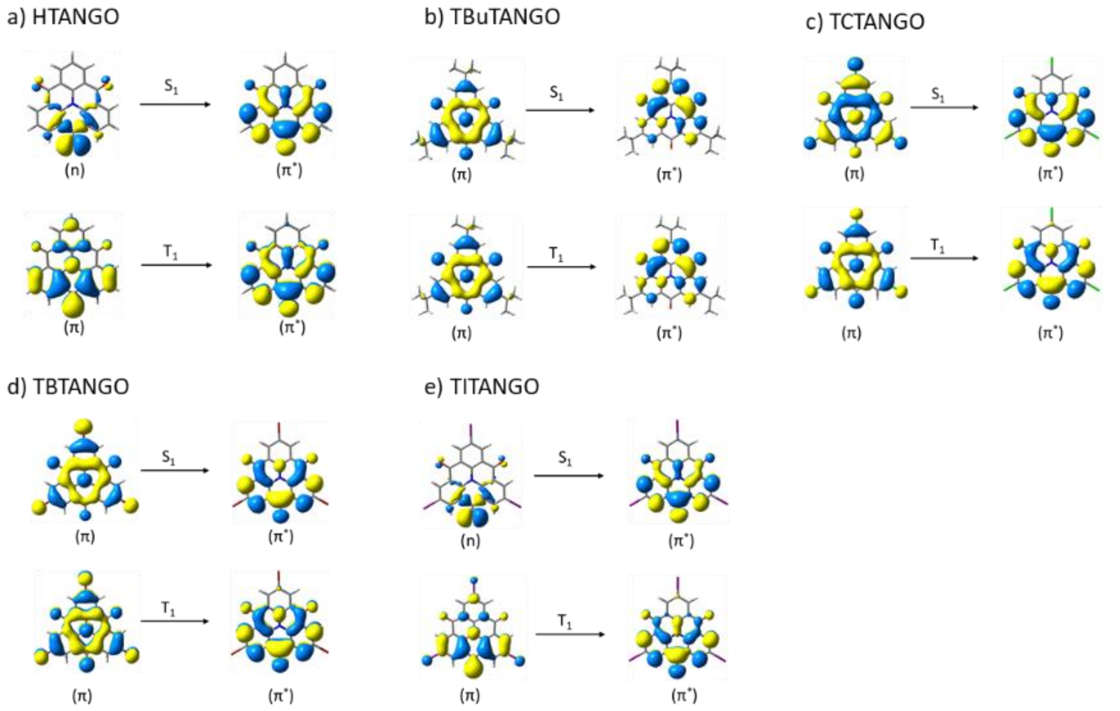

Figure 2.10. Natural transition orbitals (NTOs) of TANGO derivatives for S_1 and T_1 and their n-π*/ π -π*characteristic.

Table 2.2. HTANGO transition orbital components and corresponding normalized coefficients

Ex. State Multiplicity	E(eV)	composition			Normalized Coefficient
S_1	2.76	*HOMO-2*	→	*LUMO*	0.03
		HOMO-1	→	*LUMO*	0.93
		HOMO-1	→	*LUMO+4*	0.02
T_1	2.22	*HOMO-3*	→	*LUMO*	0.22
		HOMO	→	*LUMO*	0.70

Table 2.3. HTANGO SOC matrix of S_1-T_n.

$\langle S\vert Hso\vert T\rangle$	**T_1**	**T_2**	**T_3**	**T_4**	**T_5**	**T_6**	**T_7**
S_1	44.91	0	3.05	21.67	2.13	0	1.84

Table 2.4. *t*BuTANGO transition orbital components and corresponding normalized coefficients

Ex. State Multiplicity	E(eV)	Composition			Normalized Coefficient
S_1	3.02	HOMO	→	LUMO	0.97
T_1	2.46	HOMO-8	→	LUMO	0.03
		HOMO-7	→	LUMO+1	0.03
		HOMO	→	LUMO	0.90

Table 2.5. *t*BuTANGO SOC matrix for S_1-T_n.

$\langle S\vert Hso\vert T\rangle$	**T_1**	**T_2**	**T_3**	**T_4**	**T_5**	**T_6**	**T_7**	**T_8**
S_1	0	0.04	5.16	8.59	0.04	9.34	0.06	0.1

Table 2.6. TCTANGO transition orbital components and corresponding normalized coefficients.

Ex. State Multiplicity	E(eV)	Composition	Normalized Coefficient
S_1	2.95	HOMO → LUMO	0.97
T_1	2.37	HOMO- → LUMO	0.05
		HOMO → LUMO	0.89

Table 2.7. TCTANGO SOC matrix for matrix for S_1-T_n.

<S|Hso|T>	**T_1**	**T_2**	**T_3**	**T_4**	**T_5**	**T_6**	**T_7**	**T_8**
S_1	0	0.08	10.27	10.23	0	0.01	0	27.26

Table 2.8. TBTANGO transition orbital components and corresponding normalized coefficients.

Ex. State Multiplicity	E(eV)	composition	Normalized Coefficient
S_1	2.91	*HOMO → LUMO*	0.98
T_1	2.36	*HOMO-7 → LUMO*	0.04
		HOMO → LUMO	0.89

Table 2.9. TBTANGO SOC matrix for different S-T and T-T pathways.

<S|Hso|T>	**T_1**	**T_2**	**T_3**	**T_4**	**T_5**	**T_6**	**T_7**	**T_8**
S_1	0	0.07	27.08	29.99	0	0.04	0	0.01

Table 2.10. TITANGO transition orbital components and corresponding normalized coefficients.

Ex. State Multiplicity	*E(eV)*	*composition*	*Normalized Coefficient*
S_1	2.93	*HOMO-5 → LUMO*	0.06
		HOMO-5 → LUMO+1	0.07
		HOMO-4 → LUMO	0.07
		HOMO-4 → LUMO+1	0.06
		HOMO-1 → LUMO	0.38

		HOMO-1 → *LUMO+1*	0.30
T_1	1.88	*HOMO-7* → *LUMO*	0.31
		HOMO-7 → *LUMO+4*	0.02
		HOMO → *LUMO*	0.62

Table 2.11. TITANGO SOC matrix for different S-T and T-T pathways

<S|Hso|T>	**T_1**	**T_2**	**T_3**	**T_4**	**T_5**	**T_6**	**T_7**	**T_8**	**T_9**	**T_{10}**
S_1	88.4	0.0	16.8	31.8	10.4	49.9	0.1	15.2	68.2	5.4

2.7.7. References of Supplementary Information

1. Fang, Z.; Teo, T.-L.; Cai, L.; Lai, Y.-H.; Samoc, A.; Samoc, M., Bridged triphenylamine-based dendrimers: tuning enhanced two-photon absorption performance with locked molecular planarity. *Org. Lett.* **2009,** *11*, 1-4.

2. Field, J. E.; Venkataraman, D., Heterotriangulenes Structure and Properties. *Chem. Mater.* **2002,** *14*, 962-964.

3. van Lenthe, E.; Ehlers, A.; Baerends, E.-J., Geometry optimizations in the zero order regular approximation for relativistic effects. *J. Chem. Phys.* **1999,** *110*, 8943-8953.

4. Fonseca Guerra, C.; Snijders, J. G.; te Velde, G.; Baerends, E. J., Towards an order-N DFT method. *Theor. Chem. Acc.* **1998,** *99*, 391-403.

5. te Velde, G.; Bickelhaupt, F. M.; Baerends, E. J.; Fonseca Guerra, C.; van Gisbergen, S. J. A.; Snijders, J. G.; Ziegler, T., Chemistry with ADF. *J. Comput. Chem.* **2001,** *22*, 931-967.

Chapter 3

Room Temperature Phosphorescence
vs.
Triplet-Triplet Annihilation
in N-Substituted Acridone Solids

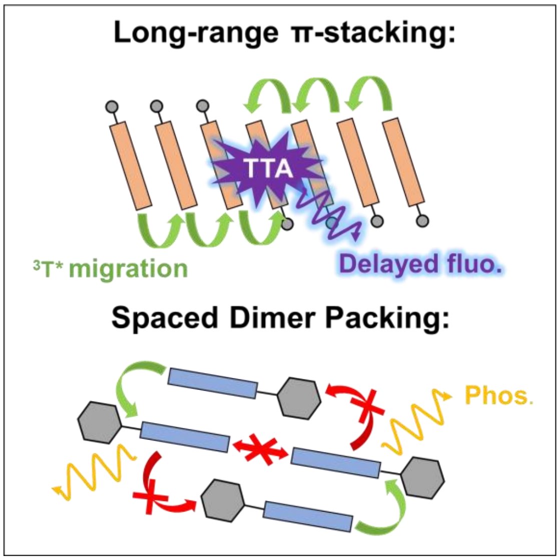

Preface

In the previous chapter, we showed that the luminescence properties of highly emissive TANGO derivatives are controlled by their molecular packing, whereby carbonyl groups co-aligned in sterically unencumbered TANGO derivatives lead to room-temperature phosphorescence. In contrast, the ~60° rotation induced by bulky tert-butyl groups results in an almost pure fluorescence.

In this chapter, we explore the structure-luminescent properties relationships in acridone derivatives, another structurally related class of compounds to TANGOs. Six acridone derivatives with N-alkyl and N-aryl substituents of varying electronic (electron-withdrawing and -donating) and steric effects, including methyl, phenyl (Ph), 4-CNPh, 4-OMePh, 4-*t*BuPh, and 4-SF5Ph, were synthesized and characterized. Similar to TANGOs, these substituents did not significantly perturb the electronic level of the acridone and all derivatives showed similar photophysics in solution. In the crystalline state, however, they showed varied room temperature phosphorescent behavior and, in some cases, triplet-triplet annihilation (TTA)-induced delayed fluorescence. Using X-ray crystallography combined with the solid-state spectroscopy, we found that the molecules' orientation has a pronounced effect on the phosphorescence energy and TTA efficiency. TTA appears strong in N-aryl acridones with small substituents, i.e., Ph, OMePh, and CNPh Acridones with antiparallel π-stacks, measurably weaker in MetAc with co-parallel π-stacks (despite shorter π-distances) and non-existent in the other derivatives with isolated π-dimers. This work provided further insight into the effect of crystal structure on triplet dynamics and TTA, which is one of the most critical quenching mechanisms of triplets in pure ORTP materials, making another step toward rational control of triplet excitons and their dynamics in molecular solids.

Author contribution

Allen Tao and I have synthesized, purified, and performed structural characterization of all materials reported in this chapter. Cory Ruchlin and I performed photophysical characterization (steady-state, lifetime analysis, and quantum yields) and density functional theory calculations. Jorge Ramos-Sanchez and Gonzalo Cosa performed the laser flash photolysis measurements. Hatem M. Titi performed the X-ray crystallography and thermogravimetric analysis. The manuscript was written by Cory Ruchlin and by me and edited by Dmytro F. Perepichka. Cory Ruchlin and I contributed equally to this work.

It is reprinted with permission from E. Hamzehpoor, C. Ruchlin, Y. Tao, J. E. Ramos-Sanchez, H. M. Titi, G. Cosa, D. F. Perepichka, "Room Temperature Phosphorescence vs Triplet–Triplet Annihilation in N-Substituted Acridone Solids" *J. Phys. Chem. Lett* **2021**, 12, 6431-6438.

3.1. Abstract

Organic room temperature phosphorescent (ORTP) compounds have recently emerged as a promising class of emissive materials with a multitude of potential applications. However, the number of building blocks that give rise to efficient ORTP materials is still limited, and the rules for engineering phosphorescent properties in organic solids are not well understood. Here, we report ORTP in a series of N-substituted acridone derivatives with electron-donating, electron-withdrawing, and sterically bulky substituents. X-ray crystallography shows that the solid-state packing varies progressively between coparallel and antiparallel π-stacking and separated π-dimers, depending on the size of the substituent. The detailed photophysical studies supported by DFT calculations reveal complex dynamics of singlet and triplet excited states, depending on the electronic effects of substituents and solid-state packing. The programmable molecular packing provides a lever to control the triplet–triplet annihilation that is manifested as delayed fluorescence in acridone derivatives with continuous (both parallel and antiparallel) π-stacking.

3.2. Introduction

Organic room temperature phosphorescent (ORTP) materials are of great interest for various applications, such as time-gated biological imaging/sensing,[1, 2] anti-counterfeiting, data encryption,[3, 4] light-emitting,[5, 6] and photovoltaic diodes,[7] nanowire lasing,[8] amplified photon up-conversion[9] and 3D displays.[10] ORTP emitters present potential advantages over heavy metal-containing phosphors[11, 12] including reduced toxicity and environmental footprint, longer emission lifetimes, lower cost, and greater tunability of photophysical properties.

Both phosphorescence (transition from T_1 to S_0) and the generation of T_1 from an excited singlet state (e.g. S_1) via intersystem crossing (ISC) are spin-forbidden processes. These processes are generally much slower than the spin allowed radiative relaxation of S_1 (fluorescence). Accordingly, most organic materials exhibit insignificant phosphorescence as they mostly fail to populate the excited triplet state, and, even if T_1 is formed, phosphorescence is most frequently outcompeted by non-radiative pathways. One strategy to enhance the ISC and phosphorescence is the incorporation of heavy atoms which increase spin-orbit coupling (SOC).[13] Additionally, the SOC (and therefore the ISC) can be promoted by coupling n-π* and π-π* transitions with different angular momenta. Such transitions are typically exhibited by carbonyl or triazine derivatives, and most ORTP materials incorporate such moieties (Scheme 3.1). [1, 11, 14-17] In turn, to inhibit competitive non-radiative deactivation pathways, including vibrational relaxation and oxygen quenching, organic phosphors have to be embedded in rigid matrices such as polymers[4, 18] and molecular solids.[16, 19]

Notably, dilute concentrations in such matrices are typically required in preparing ORTP materials to reduce aggregation-caused quenching, particularly via triplet-triplet annihilation (TTA).[19] The TTA mechanism was originally proposed to explain the delayed fluorescence of π-conjugated materials,[20] and explored extensively as a means to increase the efficiency of organic light-emitting diodes (OLEDs)[21, 22] and to realize photon up-conversion.[23, 24] However, there has been little discussion of TTA in ORTP solids and its implication in achieving high phosphorescence efficiency in crystalline materials is not well understood.[25, 26] Nevertheless, several pure ORTP solids have also been reported in the last decade (Scheme 3.1).

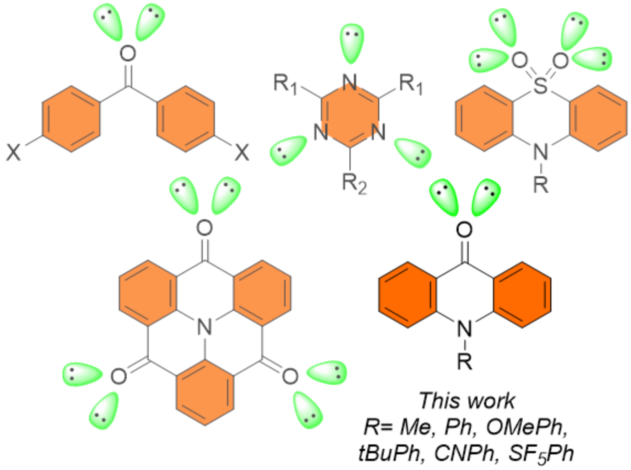

Scheme 3.1. Reported ORTP scaffolds and acridone (this work) with n-π* transitions, represented by green (n) and orange (π*).

The pioneering work of Tang and co-workers illustrates the design principles of carbonyl-containing, halogenated compounds to achieve efficient RTP.[16, 27] The non-planar structure of the explored molecules prevents strong π-overlap and minimizes the exciton delocalization and quenching. In 2015, Huang and co-workers showed that H-aggregation in molecular solids can result in ultralong phosphorescence (emission lifetimes >1 s).[17] It is noteworthy that although the phosphorescence quantum yield (Φ_p) and the triplet emission lifetime (${}^3\tau$) relate to each other (equation 3.1), different strategies are required to enhance the phosphorescence efficiency and to achieve the ultra-long phosphorescence. Increasing the radiative transition rate of the triplet state (${}^3k_r$) leads to higher Φ_p (equation 3.1), but it also shortens its lifetime (equation 3.2).

$$\Phi_P = {}^3k_r \cdot {}^3\tau \qquad \text{(Equation 3.1)}$$

$${}^3\tau = 1/({}^3k_r + {}^3k_{nr}) \qquad \text{(Equation 3.2)}$$

Several groups have studied the effect of solid-state structure on phosphorescent properties through the permutation of substituents in the molecular scaffolds[1, 25, 28-30] or by examining different polymorphs of a compound.[3, 31, 32] Different interactions such as halogen bonding,[19, 33, 34] intermolecular electronic coupling of "π" and "n" moieties[15] and efficient π-π stacking[1] have been proposed to promote ISC and lead to efficient RTP. However, due to the molecular complexity of the used materials and the large variety of adopted crystal structures, no unified, predictive structure-property relationship has yet been developed for the design of ORTP solids.

Recently, we have reported a series of planar azatriangulenetriones (TANGOs) phosphors and showed that TANGO derivatives with small substituents stack with aligned transition dipoles leading to efficient ORTP whereas those bulky substituents in tBuTANGO stack with misalignment of their dipoles and display only fluorescent emission.[14] Acridone, the basic structural fragment of TANGO, is an important building block present in a number of naturally occurring compounds known for their bioactive properties.[35, 36] Different derivatives of acridone have been utilized as hosts for OLEDs[37-39] and Thermally Activated Delayed Fluorescence (TADF) emitters.[37, 40-45] To our knowledge, no ORTP derivatives of acridone have been reported. However, their high symmetry/structural simplicity is a great asset in uncovering the complex structure-property relationships in the excited-state dynamics of organic crystals.

In this study, we synthesized a series of acridone derivatives with substituents of varied steric size and electronic effects, that crystallize in distinctly different packing motifs: co-parallel (i), antiparallel (ii), and dimerized (iii) π-stacking and isolated π-dimers (iv). All acridone derivatives show ORTP at 500-600 nm and have triplet lifetimes varying between ~5 and ~80 ms in the solid-state, depending on the structure. Importantly, the TTA-induced delayed fluorescence, one of the phosphorescence deactivation pathways, can be controlled by tuning the crystal packing through varying the size of substituents.

A series of acridone derivatives with N-alkyl (MetAc) and N-aryl groups including non-substituted (PhenAc), electron-withdrawing (CNAc, Hammet constant $\sigma^{p}_{CN} = 0.66$), electron-donating (OMeAc, $\sigma^{p}_{OMe} = -0.27$), bulky electron-donating (*t*BuAc, $\sigma^{p}_{tBu} = -0.20$), and bulky electron-withdrawing (SF5Ac, $\sigma^{p}_{SF5} = 0.68$) phenyl substituents were synthesized by the direct alkylation or arylation of acridone (Scheme 3.2.). The products were purified using column chromatography and characterized using NMR spectroscopy, mass spectrometry, and X-ray crystallography. To eliminate the possible role of impurities in the solid-state luminescence,[46] the chromatographically purified derivatives were subject to additional repeated vacuum sublimation and recrystallization.

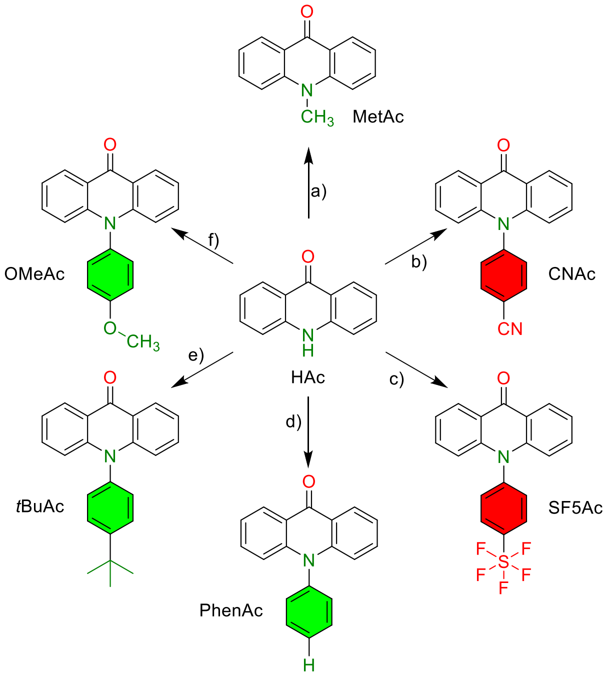

Scheme 3.1. Synthesis of a) MetAc: NaH, DMF, CH_3I, and b-f) N-Aryl Acridone: Ar-X (X = Br, I), Cu, CuI, phenanthroline, K_2CO_3, DMF, 130 °C, 48h.

3.3. Solution photophysics

In solution (~10 µM in chloroform), all the substituted acridones show similar longest-wavelength absorption (λ^{abs}_{max} of ~390-400 nm) and emission (λ^{em}_{max} = 403-409 nm) bands (Figure 3.1a, Table 3.1). The characteristic vibronic splitting of these bands and relatively small Stokes shifts (~15 nm) suggest the local π-π* excitation of the acridone as their origin. Time-dependent density functional theory calculations (TD-DFT) in gas-phase, on contrary, predict a forbidden n-π* as the lowest singlet excited state (S_1) for all derivatives (except for CNAc in which the S_1 is predicted to be a charge transfer (CT) transition, acridone → CNPh) (Figure 3.2 and Figures 3.22, 3.23 in Supporting Information). However, the relative stability of the n-π*, π-π* and CT states is sensitive to the environment as well as the used functional (see the comparison of B3LYP, cam-B3LYP, and wB97xd in Figure 3.27). The same calculations performed in a continuum solvent model ($CHCl_3$) correctly predicts π-π* S_1 state for most derivatives (Figure 3.22).

Table 3.1. Photophysical properties of acridone derivative in $CHCl_3$ solution.

	abs λ_{max} (nm)	Fl λ_{max} (nm)	Fl τ_{RT}[a] (ns)	$^3\tau^*_{RT}$[b] (μs)	PLQY[c]	Ph λ_{max} (nm)	Ph τ_{77K}[e] (ms)	Fl k_R (ns^{-1})	Fl k_{NR} (ns^{-1})
HAc	389	401	14.9 [d]	0.66	0.81d	490	440	0.054	0.013
MetAc	389	408	4.6 ± 0.3	2.10	0.64	496	1610	0.14	0.078
PhenAc	396	407	3.8 ± 0.5	5.54	0.63	486	1400	0.17	0.097
OMeAc	396	409	3.8 ± 1.0	3.81	0.44	463	440	0.12	0.15
CNAc	390	403	2.3 ± 0.5	3.88	0.38	456sh[f], 495	860	0.17	0.27
tBuAc	397	409	5.2 ± 0.3	5.06	0.79	488	1470	0.15	0.040
SF5Ac	390	403	4.3 ± 0.5	5.99	0.23	453sh[f], 484	810	0.05	0.18

[a] Determined using λ_{ex} = 405 nm, calculated from single-exponential fits. [b] Determined from laser flash photolysis in CH_2Cl_2, monitoring at 630 nm. [c] Determined relative to coumarin 153 standard in ethanol. [d] In aqueous solutions; obtained from ref.[47] [e] Monitoring at 500 nm. [f] Stands for shoulder peak.

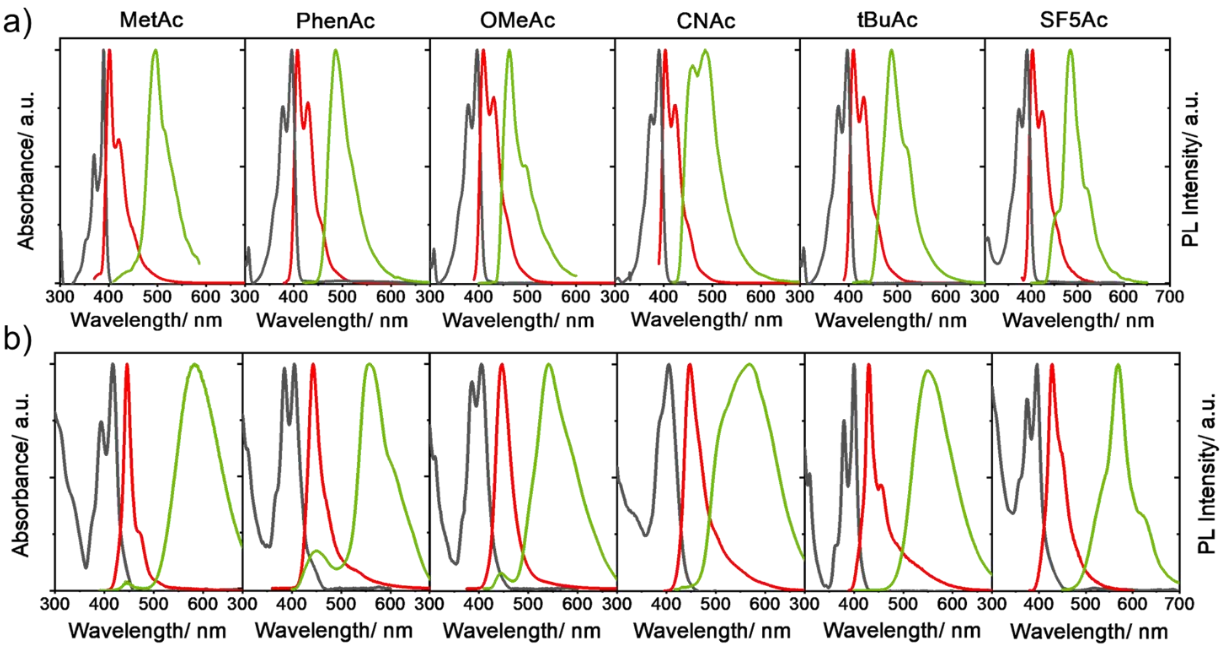

Figure 3.1. a) Absorption (grey) and emission (steady-state at RT, red; 1.0 ms delayed at 77 K, green) of MetAc, PhenAc, OMeAc, CNAc, tBuAc, and SF5Ac in $CHCl_3$ solutions. b) Solid-state absorption of thin films on quartz (grey), steady-state (red), and delayed (green) emission of acridone solids (microcrystalline powders) at RT. HAc absorption/emission in the solution is shown in Figure 3.8.

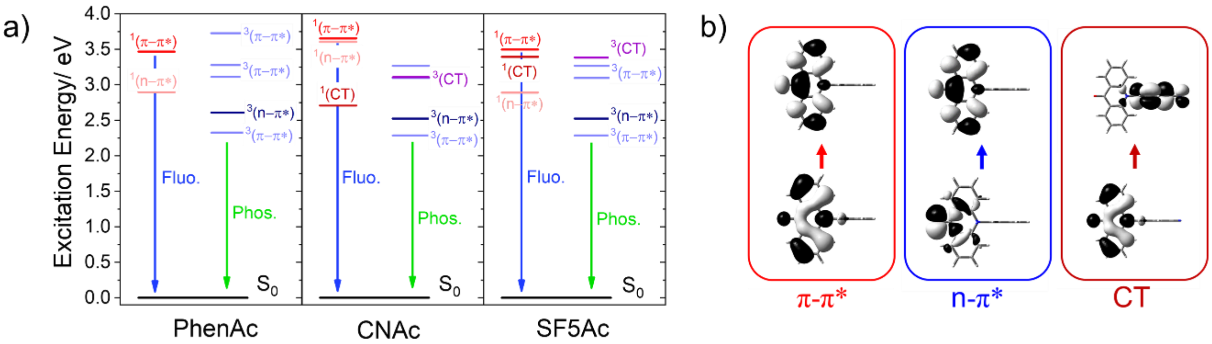

Figure 3.2. a) Energy diagram of low-lying singlet and triplet states of PhenAc, CNAc, and SF5Ac in the gas phase. b) π-π*, n-π*, and CT topologies of excited states of acridone derivatives, obtained from the natural transition orbitals using TD-DFT of optimized geometry for the lowest singlet and triplet states in the gas phase. All derivatives show similar topologies for same transitions (Figures 3.22, 3.23).

The photoluminescence quantum yield (PLQY) of less than unity (23-79%) suggests the possibility of ISC which is also dominant in related ketones (e.g., xanthone[48] and thioxanthone[49]), yet no detectable delayed emission was observed in solutions at room temperature. We also note that lower PLQYs and shorter fluorescence lifetimes are observed for the derivatives with electron-withdrawing (CNAc, SF5Ac) and electron-donating (OMeAc) substituents in comparison to PhenAc, tBuAc, and MetAc (Table 3.1). This might be a result of faster ISC in the former derivatives, due to mixing with the above-mentioned CT states (Figure 3.2).[50]

To explore the dynamics of excited triplet states, laser flash photolysis studies were carried out in chloroform solutions (Figures 3.3, 3.19). Following laser excitation, bleaching of the acridone ground-state absorption at ~400 nm and the appearance of new transient absorption bands at ~330 nm and ~630 nm were recorded in the photoinduced absorption spectra for all compounds. These bands decay with lifetimes of ~1-6 μs under an inert atmosphere (Table 3.1) but in air the lifetimes shorten to ~0.7 μs. Given the resemblance of these transient absorption spectra with those of xanthone and the quenching by oxygen, they were attributed to the T-T absorption.[51] The substituents in the N-phenyl ring show little effect on the T-T absorption maxima (621-640 nm) or the lifetimes (~4-6 μs) indicating localization of T_1 exciton on the acridone ring.

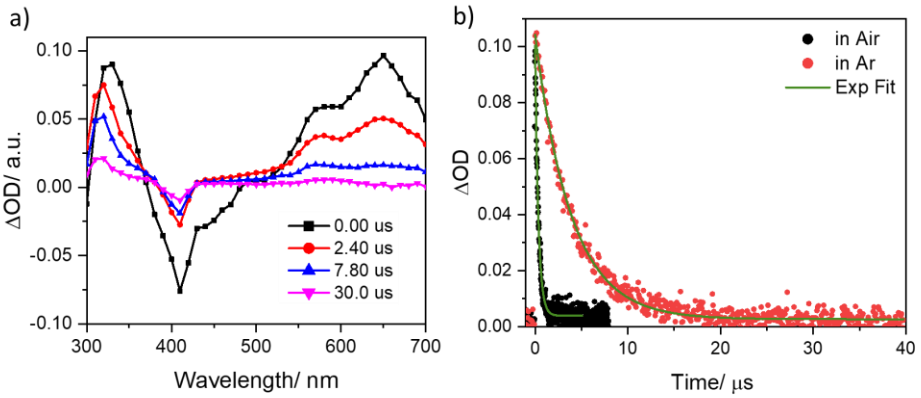

Figure 3.3. (a) Transient absorption spectra (λ_{ex} = 405 nm) and (b) temporal evolution of ΔOD (monitored at 630 nm) for deoxygenated (red) and oxygenated (black) CNAc solution in CH_2Cl_2 (for other transient absorption spectra, see Figure 3.19).

To suppress the non-radiative relaxation of T_1 and probe the phosphorescence of the isolated molecules, we studied the emission of acridone derivatives in glass matrices prepared from dilute solutions rapidly cooled to 77 K. Compared to room temperature, the steady-state luminescence of these glasses is slightly redshifted (4–23 nm, Figure 3.11), likely due to increasing of the solvent polarity at low temperature.[52, 53] For these glass matrices, phosphorescence could be observed by the naked eye (Figure 3.21a). Time-gated emission measurements disentangle the phosphorescence from the fluorescence, revealing phosphorescent decay lifetimes in the range of 0.44 - 1.47 s (Table 3.1). Interestingly, shorter phosphorescence lifetimes and lower fluorescence quantum yields were observed for acridone derivatives with electron-withdrawing (CNAc, SF5Ac) and electron-donating substituents (OMeAc), possibly suggesting more efficient intersystem-crossing. A moderate positive solvatochromism (~20–25 nm red shift from cyclohexane to acetonitrile) suggests a π-π* nature of T_1 (Figure 3.13), in agreement with TD-DFT (Figure 3.2). However, the n-π* triplet (T_2) is only slightly higher in energy (in the gas phase) and may also contribute to the observed phosphorescence. Indeed, an apparent 'dual' phosphorescence, with a blue-shifted (~460 nm) shorter-lived and red-shifted (~490 nm) longer-lived emission bands were observed in frozen $CHCl_3$ glass of OMeAc, CNAc, and SF5Ac (Figure 3.14).

3.4. Solid-state photophysics

The absorption of crystalline acridone solids is bathochromically shifted compared to that of the solution as a result of strong π-stacking in the solid-state (see the discussion of crystal packing below), with MetAc having the most pronounced shift (214 meV). As the size of the substituents increases (resulting in weaker intermolecular coupling), the crystallization-induced shift decreases, with only minute shifts in absorption in tBuAc and SF5Ac (20 meV, Figure 3.9).

While the parent HAc is non-emissive in the solid-state due to an excited-state proton transfer [54] (Figure 3.28), all other derivatives display strong fluorescence (red-shifted from their solutions by ~200–400 meV) as well as pronounced ORTP with lifetimes in the range of ~5–80 ms (Figure 3.1 b, Table 3.2). The phosphorescence bands are bathochromically shifted compared to those of the frozen solutions as a result of intermolecular interactions and exciton delocalization (Figure 3.4). Upon cooling to 77 K, all acridone solids show an expected increase of the phosphorescence lifetimes (0.13–0.44 s) and, more interestingly, also reveal a pronounced hypsochromic shift (140–209 meV) with respect to the ORTP spectra. A smaller (44-110 meV) hypsochromic shift upon the cooling was also observed in the fluorescence maxima (Figure 3.12). A close inspection of the phosphorescence spectra (most apparent for CNAc) suggests a presence of co-existing higher-energy (~500 nm) and lower-energy (~570 nm) emissive states. Their ratio varies based on substituents, which also affects the width of the ORTP band. The emission of the lower-energy state in all derivatives at 77 K is suppressed in favor of the higher-energy state, explaining the observed blue shift of the delayed emission. Also, the room-temperature phosphorescence spectra show a (smaller) redshift upon increasing excitation delay (i.e., for longer-lived triplet states, Figure 3.14). While the nature of these two states is not presently clear, their temperature behavior and the spectral shift suggest that delocalization and diffusion of triplet excitons play a role in the observed photophysical behavior.

Table 3.2. Photophysical properties of acridone derivative in solid-state.

	Abs λ_{max} (nm)	Fl λ_{max} (nm)	Fl τ_{RT}[a] (ns)	Ph$_{RT}$ λ_{max} (nm)	Ph τ_{RT} (ms)	Ph$_{77K}$ λ_{max} (nm)	Ph τ_{77K} (ms)
HAc	420	--	--	--	--	--	--
MetAc	416	446	4.4 ± 0.3	582	15.7	530	191
PhenAc	405	443	2.0 ± 0.7	557	15.1	517	344
OMeAc	405	447	2.8 ± 0.1	541	48.0	510	262
CNAc	405	448	1.5 ± 0.4	568	46.1	519	420
tBuAc	399	430	4.1 ± 0.3	549	81.5	516	442
SF5Ac	396	428	3.7 ± 0.5	569	5.2	521	135

[a] Determined from TCSPC diode laser λ_{ex} = 405 nm, calculated from the average of double-exponential fit.

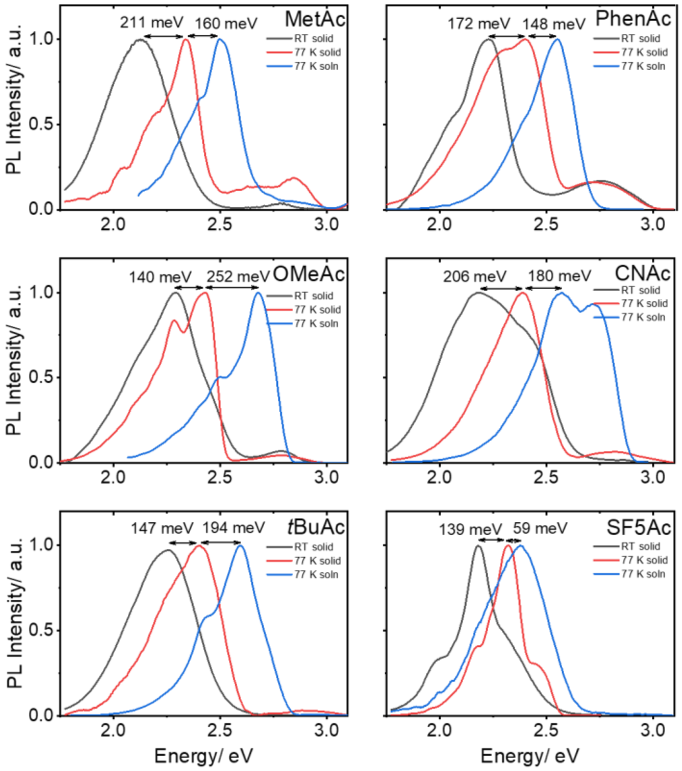

Figure 3.4. Delayed (1 ms) emission spectra of acridone derivatives in CHCl$_3$ glass matrices at 77 K (blue), in microcrystalline powders at room temperature (grey) and solid-state at 77K (red).

3.5. Delayed fluorescence

Another important feature of the delayed spectra of MetAc, PhenAc, OMeAc, and CNAc is an additional emission peak at ~445 nm, which closely matches the solid-state fluorescence. This feature persists and is even more pronounced at low temperatures (Figure 3.20 in Supporting Information), and thus cannot be due to thermally-activated delayed fluorescence, observed in other acridone derivatives.[37, 40-45] Furthermore, intensity-dependent studies of this peak show an approximately quadratic relation to the triplet populations of the system, monitored by the peak intensity of the phosphorescence (Figure 3.5). We attribute this phenomenon to TTA, where two T_1 states encounter one another and annihilate, producing S_0 and S_1 states, and resulting in delayed fluorescence.[55] MetAc and PhenAc show the highest TTA-induced fluorescence (relative to the phosphorescence maxima) which diminishes in OMeAc, is low but detectable in CNAc, and is completely absent in tBuAc and SF5Ac. Given similar PLQYs and triplet lifetimes in all acridone derivatives, the observed differences in TTA-induced fluorescence are most likely due to different diffusion of triplet excitons (see below).[56, 57]

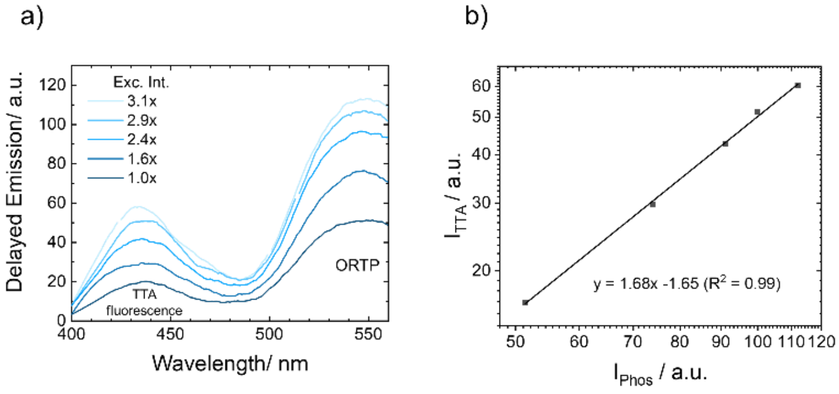

Figure 3.5. a) Delayed emission spectra of PhenAc microcrystalline powder upon illumination attenuated by neutral density filters. b) Corresponding intensity dependence of TTA-induced delayed fluorescence, plotted on double-logarithmic scale versus phosphorescence peak intensity.

To understand the role of molecular packing in the vastly different photophysics of the acridone solids, we performed X-ray crystallographic analysis of single crystals (SCXRD) of the studied acridone derivatives and recorded powder X-ray diffraction of the samples used in the above photophysical measurements to prove their high crystallinity and presence of the same polymorphs as in SCXRD (Figure 3.26 in Supporting Information).

All acridone derivatives have a nearly planar acridone core (average out-of-plane deviation of ~0.035 Å) with nearly perpendicular aryl substituents (dihedral angle of ~78-89°). However, the packing varies markedly with substituents (Figure 3.6). MetAc packs in one-dimensional slipped π-stacks (3.41 Å) with co-parallel alignment of transition dipoles ($N\cdots C{=}O \rightarrow N^{+}\cdots C{-}O^{-}$). PhenAc, OMeAc, and CNAc pack in antiparallel stacks of π-dimers. The degree of dimerization varies with the size of substituent, from small for PhenAc (π-π distances 3.58/3.64 Å) to very large for OMeAc (3.56/4.83 Å). The lower dimerization and shorter average π-π distance of PhenAc are expected to lead to faster migration of triplets, corroborating the higher TTA-induced delayed fluorescence of PhenAc comparing to OMeAc and CNAc. tBuAc and SF5Ac with even larger substituents pack with isolated dimers (no continuous stacks). The only electronic communication between the dimers is through the weak $C{=}O\cdots H{-}C$ hydrogen bonding (Figure 3.6b).

These packing arrangements offer insights into a mechanism for controlling the TTA in organic crystals. Bulky substituents interrupt the long-range π-stacking, hindering the migration of triplets and the phosphorescence-quenching TTA. The triplet migration takes place via the Dexter Energy Transfer (DET) mechanism involving a simultaneous hole and electron transfer.[58] Thus, we calculated triplet energy transfer electronic coupling (V_{TET}), based on diabatic model of CT-mediated superexchange pathways.[59, 60] for the weakly-coupled intermolecular pairs for each of the three crystal types (Figure 3.25a). V_{TET} is greatest in the closely packed MetAc, and weaker in the greater spaced PhenAc and SF5Ac, with the isolated dimers of SF5Ac being the most weekly coupled. These results demonstrate that TTA, or for that matter any charge-mobility mediated properties in ORTP materials, are enabled (as in MetAc and PhenAc) or disabled (as in SF5Ac) by the electronic coupling of the “weakest links” in the migration path. We also note that no TTA has been observed in structurally related N-arylphenothiaziane-S,S-dioxides (Scheme 3.1) ORTP dyes which, like tBuAc and SF5Ac, also pack in isolated π-dimers.[1] These observations show a possibility of controlling the TTA through crystal engineering, by adjusting the size of substituents.

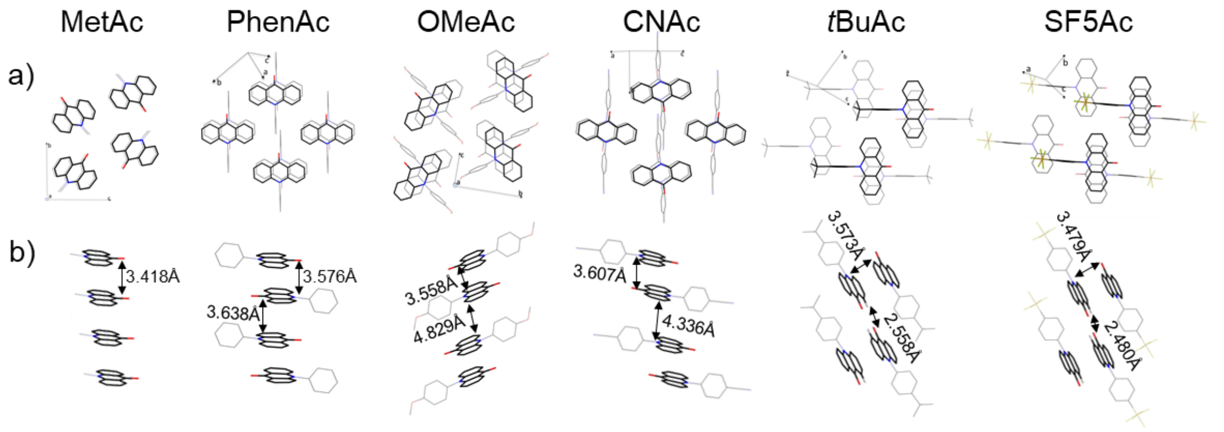

Figure 3.6. Crystal structure of acridone derivatives showing molecular packing within π-stacks, in the a) top and b) side view for MetAc (CCDC: 1453140) PhenAc (CCDC: 1232243), OMeAc (CCDC: 1998381, this work), CNAc (CCDC: 1534549), tBuAc (CCDC: 1998383, this work), SF5Ac (CCDC: 199838, this work).

3.6. Conclusion

In summary, we have developed acridone-based ORTP dyes with substituents of varying electronic and steric effects. All derivatives except the parent HAc showed room-temperature phosphorescence at ~500-650 nm in the solid-state and, in some cases, TTA-induced delayed fluorescence at ~450 nm. Although the substituents in the N-phenyl ring are almost fully decoupled from the acridone chromophore due to large inter-ring twist, the CT states (between acridone and substituted phenyl) are energetically accessible and appear to affect the dynamics of triplet states. The X-ray crystallographic analysis suggests that the orientation of the molecules has a great effect on phosphorescence energy and TTA-efficiency. The latter appears strongly in PhenAc, OMeAc with antiparallel π-stacks, measurably weaker in MetAc with co-parallel π -stacks (despite shorter π-distances) and non-existing in other derivatives that showed isolated π-dimers. This work opens an opportunity of controlling the TTA in organic crystals, either suppressing it to avoid quenching triplet excitons and to achieve more efficient ORTP; or enhancing it for applications in OLED devices[21, 22] or photon up-conversion.[23, 24] The results shed further light on the phosphorescence behavior of molecular crystals, as a complex phenomenon composed of both intrinsic (molecular and supramolecular) and extrinsic (temperature, traps[46], etc.) factors. While several supramolecular concepts (H-aggregation[12d], halogen bonding[19], and strong π-π stacking[1]) have been proposed, no universal structure-property relationships exist for the design of ORTP crystals. This work makes another step towards rational control of the dynamics of triplet excitons in molecular solids and may open further opportunities for the design of bioactive phosphorescent nanoparticles,[2] optoelectronic devices,[6] and upconverting materials.[9, 61]

3.7. Acknowledgments

We thank Dr. Kishan Prithipaul of High-Speed Imaging Inc. for providing a high-speed camera, Robin Stein for the help with NMR spectroscopy, and Alexander Wahba and Nadim Saade for mass spectrometry.

3.8. References

1. Yang, J.; Zhen, X.; Wang, B.; Gao, X.; Ren, Z.; Wang, J.; Xie, Y.; Li, J.; Peng, Q.; Pu, K.; Li, Z., The influence of the molecular packing on the room temperature phosphorescence of purely organic luminogens. *Nat. Commun.* **2018,** *9*, 840.

2. Fateminia, S. M. A.; Mao, Z.; Xu, S.; Yang, Z.; Chi, Z.; Liu, B., Organic Nanocrystals with Bright Red Persistent Room-Temperature Phosphorescence for Biological Applications. *Angew. Chem. Int. Ed.* **2017,** *56*, 12160-12164.

3. Gu, M.; Shi, H.; Ling, K.; Lv, A.; Huang, K.; Singh, M.; Wang, H.; Gu, L.; Yao, W.; An, Z.; Ma, H.; Huang, W., Polymorphism-Dependent Dynamic Ultralong Organic Phosphorescence. *Research* **2020,** *2020*, 8183450.

4. Su, Y.; Phua, S. Z. F.; Li, Y.; Zhou, X.; Jana, D.; Liu, G.; Lim, W. Q.; Ong, W. K.; Yang, C.; Zhao, Y., Ultralong room temperature phosphorescence from amorphous organic materials toward confidential information encryption and decryption. *Sci. Adv.* **2018,** *4*, eaas9732.

5. Lee, J.; Chen, H.-F.; Batagoda, T.; Coburn, C.; Djurovich, P. I.; Thompson, M. E.; Forrest, S. R., Deep blue phosphorescent organic light-emitting diodes with very high brightness and efficiency. *Nat. Mater.* **2016,** *15*, 92-98.

6. Zhan, G.; Liu, Z.; Bian, Z.; Huang, C., Recent Advances in Organic Light-Emitting Diodes Based on Pure Organic Room Temperature Phosphorescence Materials. *Front. Chem.* **2019,** *7*, 305.

7. Yum, J.-H.; Baranoff, E.; Hardin, B. E.; Hoke, E. T.; McGehee, M. D.; Nüesch, F.; Grätzel, M.; Nazeeruddin, M. K., Phosphorescent energy relay dye for improved light harvesting response in liquid dye-sensitized solar cells. *Energy Environ. Sci* **2010,** *3*, 434-437.

8. Yu, Z.; Wu, Y.; Xiao, L.; Chen, J.; Liao, Q.; Yao, J.; Fu, H., Organic Phosphorescence Nanowire Lasers. *J. Am. Chem. Soc.* **2017,** *139*, 6376-6381.

9. Ieuji, R.; Goushi, K.; Adachi, C., Triplet–triplet upconversion enhanced by spin–orbit coupling in organic light-emitting diodes. *Nat. Commun* **2019,** *10*, 5283.

10. Wan, S.; Zhou, H.; Lin, J.; Lu, W., A Prototype of a Volumetric Three-Dimensional Display Based on Programmable Photo-Activated Phosphorescence. *Angew. Chem. Int. Ed.* **2020,** *59*, 8416-8420.

11. Kenry; Chen, C.; Liu, B., Enhancing the performance of pure organic room-temperature phosphorescent luminophores. *Nat. Commun.* **2019,** *10*, 2111.

12. Forni, A.; Lucenti, E.; Botta, C.; Cariati, E., Metal free room temperature phosphorescence from molecular self-interactions in the solid state. *J. Mater. Chem. C* **2018,** *6*, 4603-4626.

13. Wang, J.; Gu, X.; Ma, H.; Peng, Q.; Huang, X.; Zheng, X.; Sung, S. H. P.; Shan, G.; Lam, J. W. Y.; Shuai, Z.; Tang, B. Z., A facile strategy for realizing room temperature phosphorescence and single molecule white light emission. *Nat. Commun.* **2018,** *9*, 2963.

14. Hamzehpoor, E.; Perepichka, D. F., Crystal Engineering of Room Temperature Phosphorescence in Organic Solids. *Angew. Chem. Int. Ed.* **2020,** *59*, 9977-9981.

15. Yang, Z.; Mao, Z.; Zhang, X.; Ou, D.; Mu, Y.; Zhang, Y.; Zhao, C.; Liu, S.; Chi, Z.; Xu, J.; Wu, Y.-C.; Lu, P.-Y.; Lien, A.; Bryce, M. R., Intermolecular Electronic Coupling of Organic Units for Efficient Persistent Room-Temperature Phosphorescence. *Angew. Chem. Int. Ed.* **2016,** *55*, 2181-2185.

16. Yuan, W. Z.; Shen, X. Y.; Zhao, H.; Lam, J. W. Y.; Tang, L.; Lu, P.; Wang, C. L.; Liu, Y.; Wang, Z. M.; Zheng, Q.; Sun, J. Z.; Ma, Y. G.; Tang, B. Z., Crystallization-Induced Phosphorescence of Pure Organic Luminogens at Room Temperature. *J. Phys. Chem. C* **2010,** *114*, 6090-6099.

17. An, Z.; Zheng, C.; Tao, Y.; Chen, R.; Shi, H.; Chen, T.; Wang, Z.; Li, H.; Deng, R.; Liu, X.; Huang, W., Stabilizing triplet excited states for ultralong organic phosphorescence. *Nat. Mater.* **2015,** *14*, 685-690.

18. Lee, D.; Bolton, O.; Kim, B. C.; Youk, J. H.; Takayama, S.; Kim, J., Room temperature phosphorescence of metal-free organic materials in amorphous polymer matrices. *J. Am. Chem. Soc.* **2013,** *135*, 6325-6329.

19. Bolton, O.; Lee, K.; Kim, H. J.; Lin, K. Y.; Kim, J., Activating efficient phosphorescence from purely organic materials by crystal design. *Nat. Chem.* **2011,** *3*, 205-210.

20. Kepler, R.; Caris, J.; Avakian, P.; Abramson, E., Triplet excitons and delayed fluorescence in anthracene crystals. *Phys. Rev. Lett.* **1963,** *10*, 400.

21. Sinha, S.; Monkman, A., Delayed electroluminescence via triplet–triplet annihilation in light emitting diodes based on poly [2-methoxy-5-(2′-ethyl-hexyloxy)-1, 4-phenylene vinylene]. *Appl. Phys. Lett.* **2003,** *82*, 4651-4653.

22. Kondakov, D. Y., Triplet–triplet annihilation in highly efficient fluorescent organic light-emitting diodes: current state and future outlook. *Philos. Trans. R. Soc. Ser. A* **2015,** *373*, 20140321.

23. Singh-Rachford, T. N.; Castellano, F. N., Photon upconversion based on sensitized triplet–triplet annihilation. *Coord. Chem. Rev.* **2010,** *254*, 2560-2573.

24. Bharmoria, P.; Bildirir, H.; Moth-Poulsen, K., Triplet–triplet annihilation based near infrared to visible molecular photon upconversion. *Chem. Soc. Rev.* **2020,** *49*, 6529-6554.

25. Zhang, T.; Wang, X.; An, Z.; Fang, Z.; Zhang, Y.; Yuan, W. Z., Pure Organic Persistent Room-Temperature Phosphorescence at both Crystalline and Amorphous States. *ChemPhysChem* **2018,** *19*, 2389-2396.

26. Wu, X.; Huang, C.-Y.; Chen, D.-G.; Liu, D.; Wu, C.; Chou, K.-J.; Zhang, B.; Wang, Y.; Liu, Y.; Li, E. Y., Exploiting racemism enhanced organic room-temperature phosphorescence to demonstrate Wallach's rule in the lighting chiral chromophores. *Nat. Commun* **2020,** *11*, 1-10.

27. Zhao, W.; He, Z.; Lam, Jacky W. Y.; Peng, Q.; Ma, H.; Shuai, Z.; Bai, G.; Hao, J.; Tang, Ben Z., Rational Molecular Design for Achieving Persistent and Efficient Pure Organic Room-Temperature Phosphorescence. *Chem* **2016,** *1*, 592-602.

28. Xiong, Y.; Zhao, Z.; Zhao, W.; Ma, H.; Peng, Q.; He, Z.; Zhang, X.; Chen, Y.; He, X.; Lam, J. W. Y.; Tang, B. Z., Designing Efficient and Ultralong Pure Organic Room-Temperature Phosphorescent Materials by Structural Isomerism. *Angew. Chem. Int. Ed.* **2018,** *57*, 7997-8001.

29. Mao, Z.; Yang, Z.; Fan, Z.; Ubba, E.; Li, W.; Li, Y.; Zhao, J.; Yang, Z.; Aldred, M. P.; Chi, Z., The methylation effect in prolonging the pure organic room temperature phosphorescence lifetime. *Chem. Sci.* **2019,** *10*, 179-184.

30. Wang, Y.; Zhang, Z.; Liu, L.; Yuan, S.; Ma, J.; Liu, D.; Xue, S.; Sun, Q.; Yang, W., Cyanophenylcarbazole isomers exhibiting different UV and visible light excitable room temperature phosphorescence. *J. Mater. Chem. C* **2019,** *7*, 9671-9677.

31. Wang, J.; Chai, Z.; Wang, J.; Wang, C.; Han, M.; Liao, Q.; Huang, A.; Lin, P.; Li, C.; Li, Q.; Li, Z., Mechanoluminescence or Room-Temperature Phosphorescence: Molecular Packing-Dependent Emission Response. *Angew. Chem. Int. Ed.* **2019,** *58*, 17297-17302.

32. Yang, J.; Ren, Z.; Chen, B.; Fang, M.; Zhao, Z.; Tang, B. Z.; Peng, Q.; Li, Z., Three polymorphs of one luminogen: how the molecular packing affects the RTP and AIE properties? *J. Mater. Chem. C* **2017,** *5*, 9242-9246.

33. Cai, S.; Shi, H.; Tian, D.; Ma, H.; Cheng, Z.; Wu, Q.; Gu, M.; Huang, L.; An, Z.; Peng, Q.; Huang, W., Enhancing Ultralong Organic Phosphorescence by Effective π-Type Halogen Bonding. *Adv. Funct. Mater.* **2018,** *28*, 1705045.

34. Wang, Y.; Yang, J.; Tian, Y.; Fang, M.; Liao, Q.; Wang, L.; Hu, W.; Tang, B. Z.; Li, Z., Persistent organic room temperature phosphorescence: what is the role of molecular dimers? *Chem. Sci.* **2020,** *11*, 833-838.

35. Kelly, J. X.; Smilkstein, M. J.; Brun, R.; Wittlin, S.; Cooper, R. A.; Lane, K. D.; Janowsky, A.; Johnson, R. A.; Dodean, R. A.; Winter, R.; Hinrichs, D. J.; Riscoe, M. K., Discovery of dual function acridones as a new antimalarial chemotype. *Nature* **2009,** *459*, 270-273.

36. Gensicka-Kowalewska, M.; Cholewiński, G.; Dzierzbicka, K., Recent developments in the synthesis and biological activity of acridine/acridone analogues. *RSC Adv.* **2017,** *7*, 15776-15804.

37. Pander, P.; Swist, A.; Motyka, R.; Soloducho, J.; Dias, F. B.; Data, P., Thermally activated delayed fluorescence with a narrow emission spectrum and organic room temperature phosphorescence by controlling spin–orbit coupling and phosphorescence lifetime of metal-free organic molecules. *J. Mater. Chem. C* **2018,** *6*, 5434-5443.

38. Vezzu, D. A. K.; Deaton, J. C.; Shayeghi, M.; Li, Y.; Huo, S., Acridinone/Amine(carbazole)-Based Bipolar Molecules: Efficient Hosts for Fluorescent and Phosphorescent Emitters. *Org. Lett.* **2009,** *11*, 4310-4313.

39. Sharma, B. K.; Shaikh, A. M.; Agarwal, N.; Kamble, R. M., Synthesis, photophysical and electrochemical studies of acridone-amine based donor–acceptors for hole transport materials. *RSC Adv.* **2016,** *6*, 17129-17137.

40. Kulszewicz-Bajer, I.; Zagorska, M.; Banasiewicz, M.; Gunka, P. A.; Toman, P.; Kozankiewicz, B.; Wiosna-Salyga, G.; Pron, A., Effect of the substituent position on the electrochemical, optical and structural properties of donor-acceptor type acridone derivatives. *Phys. Chem. Chem. Phys.* **2020,** *22*, 8522-8534.

41. Awasthi, A. A.; Gupta, N.; Siddiqui, Q. T.; Parab, P.; Palit, D. K.; Bose, S.; Agarwal, N., Synthesis of acridone-naphthylamine derivative and its thermally-activated delayed fluorescence studies for application in OLEDs. *J. Chem. Sci.* **2019,** *131*, 94.

42. Liu, R.; Gao, H.; Zhou, L.; Ji, Y.; Zhang, G., Effects of N-Substitution on the Property of Acridone. *ChemistrySelect* **2019,** *4*, 7797-7804.

43. Mamada, M.; Inada, K.; Komino, T.; Potscavage, W. J.; Nakanotani, H.; Adachi, C., Highly Efficient Thermally Activated Delayed Fluorescence from an Excited-State Intramolecular Proton Transfer System. *ACS Cent. Sci.* **2017,** *3*, 769-777.

44. Siddiqui, Q. T.; Awasthi, A. A.; Bhui, P.; Muneer, M.; Chandrakumar, K. R.; Bose, S.; Agarwal, N., Thermally Activated Delayed Fluorescence (Green) in Undoped Film and Exciplex Emission (Blue) in Acridone–Carbazole Derivatives for OLEDs. *J. Phys. Chem. C* **2018,** *123*, 1003-1014.

45. Wan, Q.; Zhang, B.; Tong, J.; Li, Y.; Wu, H.; Zhang, H.; Wang, Z.; Pan, Y.; Tang, B. Z., Feasible structure-modification strategy for inhibiting aggregation-caused quenching effect and constructing exciton conversion channels in acridone-based emitters. *Phys. Chem. Chem. Phys.* **2019,** *21*, 9837-9844.

46. Chen, C.; Chi, Z.; Chong, K. C.; Batsanov, A. S.; Yang, Z.; Mao, Z.; Yang, Z.; Liu, B., Carbazole isomers induce ultralong organic phosphorescence. *Nat. Mater.* **2021,** *20*, 175-180.

47. González-Blanco, C.; Velázquez, M. M.; Costa, S. M. B.; Barreleiro, P., Fluorescence study of acridone in w/o microemulsions perturbed by the addition of water-soluble polymers. *J. Colloid Interface Sci.* **1997,** *189*, 43-50.

48. Scaiano, J., Solvent effects in the photochemistry of xanthone. *J. Am. Chem. Soc.* **1980,** *102*, 7747-7753.

49. Mundt, R.; Villnow, T.; Ziegenbein, C. T.; Gilch, P.; Marian, C.; Rai-Constapel, V., Thioxanthone in apolar solvents: ultrafast internal conversion precedes fast intersystem crossing. *Phys. Chem. Chem. Phys.* **2016,** *18*, 6637-6647.

50. Etherington, M. K.; Gibson, J.; Higginbotham, H. F.; Penfold, T. J.; Monkman, A. P., Revealing the spin–vibronic coupling mechanism of thermally activated delayed fluorescence. *Nat. Commun* **2016,** *7*, 13680.

51. Abdullah, K. A.; Kemp, T. J., Solvatochromic effects in the fluorescence and triplet—triplet absorption spectra of xanthone, thioxanthone and N-methylacridone. *J. Photochem.* **1986,** *32*, 49-57.

52. Kiefer, P. M.; Hynes, J. T., Temperature-Dependent Solvent Polarity Effects on Adiabatic Proton Transfer Rate Constants and Kinetic Isotope Effects. *Isr. J. Chem.* **2004,** *44*, 171-184.

53. An additional strongly red-shifted band due to aggregation was also observed in frozen hexane matrixes, Figure 3.13.

54. Fushimi, K.; Kikuchi, K.; Kokubun, H., The hydrogen bonding effect of pyridine on the deactivation of the excited states of acridone. *J. Photochem.* **1976,** *5*, 457-468.

55. Saltiel, J.; March, G. R.; Smothers, W. K.; Stout, S. A.; Charlton, J. L., Spin-statistical factor in the triplet-triplet annihilation of anthracene triplets. *J. Am. Chem. Soc.* **1981,** *103*, 7159-7164.

56. Serevičius, T.; Komskis, R.; Adomėnas, P.; Adomėnienė, O.; Kreiza, G.; Jankauskas, V.; Kazlauskas, K.; Miasojedovas, A. n.; Jankus, V.; Monkman, A.; Juršėnas, S., Triplet–Triplet Annihilation in 9,10-Diphenylanthracene Derivatives: The Role of Intersystem Crossing and Exciton Diffusion. *J. Phys. Chem. C* **2017,** *121*, 8515-8524.

57. Mikhnenko, O. V.; Blom, P. W.; Nguyen, T.-Q., Exciton diffusion in organic semiconductors. *Energy Environ. Sci* **2015,** *8*, 1867-1888.

58. Closs, G. L.; Johnson, M. D.; Miller, J. R.; Piotrowiak, P., A connection between intramolecular long-range electron, hole, and triplet energy transfers. *J. Am. Chem. Soc.* **1989,** *111*, 3751-3753.

59. Tamura, H., Diabatization for Time-Dependent Density Functional Theory: Exciton Transfers and Related Conical Intersections. *J. Phys. Chem. A* **2016,** *120*, 9341-9347.

60. Tamura, H., Triplet Exciton Transfers and Triplet–Triplet Annihilation in Anthracene Derivatives via Direct versus Superexchange Pathways Governed by Molecular Packing. *J. Phys. Chem. A* **2020,** *124*, 7943-7949.

61. Garfield, D. J.; Borys, N. J.; Hamed, S. M.; Torquato, N. A.; Tajon, C. A.; Tian, B.; Shevitski, B.; Barnard, E. S.; Suh, Y. D.; Aloni, S., Enrichment of molecular antenna triplets amplifies upconverting nanoparticle emission. *Nat. Photon.* **2018,** *12*, 402-407.

3.9. Supplementary Information

3.9.1. Synthesis

10H-Acridin-9-one, aryl halides, and all the other chemicals were bought from commercial sources and used with no further modifications unless otherwise noted. All solvents were of at least reagent grade. DMF was dried over activated molecular sieves (4 Å) before use. ^{1}H/^{13}C-NMR spectra were recorded on 500 MHz Bruker AVIII NMR spectrometer, referenced vs solvent ($CDCl_3$; ^{13}C: δ = 77.0 ppm; ^{1}H: δ = 7.25 ppm) and ^{19}F-NMR was recorded on Varian Mercury 400 MHz NMR Spectrometer. MetAc was synthesized according to the literature method[1] and all N-arylacridones were synthesized using modified Ullmann coupling similar to previous reports.[2]

10-Methyl-9(10H)-acridone (MetAc). To a solution of 9(10H)-acridone (500 mg, 2.56 mmol) in dry DMF (15 mL) was added NaH (0.25 g, 60% oil dispersion, 6.4 mmol) at 0 °C. The reaction mixture was slowly brought up to 60 °C for 30 min, then iodomethane (800 µl, 12.8 mmol) was added, and stirring was continued at 60 °C overnight. Then the reaction mixture was cooled to room temperature and quenched with distilled water. The resulting solids were collected by filtration and thoroughly washed with cold ethanol and water to yield fluffy crystals with quantitative yield (530 mg, 99%). The compound was recrystallized twice (from ethanol) and sublimed in vacuum prior to the spectroscopic studies. DSC: T_m = 201.8 °C (onset), 203.9 °C (peak). ^{1}H NMR (500 MHz, $CDCl_3$) δ 8.60 (dd, J = 8.0, 1.7Hz, 2H), 7.76 (ddd, J = 8.7, 7.0, 1.7 Hz, 2H), 7.56 (dd, J = 8.7, 0.9 Hz, 2H), 7.32 (ddd, J = 8.0, 7.0, 0.9 Hz, 2H), 3.93 (s, 3H). ^{13}C NMR (126 MHz, $CDCl_3$) δ 178.17, 142.63, 133.82, 127.84, 122.58, 121.28, 114.74, 33.65. The obtained spectroscopic data were in agreement with the literature data.[1]

General procedure for N-Arylacridones: (500 mg, 2.56 mmol), aryl halide (2.82 mmol), Cu powder (32.5 mg, 0.5 mmol), phenanthroline (97.6 mg, 0.5 mmol), and K_2CO_3 (1.77 g, 12.8 mmol) were added to a Schlenck tube followed by anhydrous DMF (20 mL). The reaction mixture was degassed using the freeze-thaw-pump cycle and refilled with N_2. Then the reaction mixture was brought to reflux (150-160°C, under argon 1 atm). After 48h the reaction mixture was cooled down to room temperature, acidified with HCl (2M), and extracted with chloroform. The organic phase was dried over $MgSO_4$ and the solvent was removed under reduced pressure. The crude product was purified on a SiO_2 column using gradient (0-25%) ethyl acetate/hexane to afford the desired N-arylacridone.

10-Phenyl-9(10H)-acridone (PhenAc) was synthesized from acridone and iodobenzene according to the general procedure, with an isolated yield of 58%. DSC: T_m = 274.8°C (onset) and 276.3°C (peak). ^{1}H NMR (500 MHz, $CDCl_3$) δ 8.62 (dd, J = 8.0, 1.7, 2H), 7.78 – 7.71 (m, 2H), 7.74 – 7.64 (m, 1H), 7.53 (ddd, J = 8.7, 7.0, 1.7 Hz, 2H), 7.43 – 7.37 (m, 2H), 7.31 (ddd, J = 8.0, 7.0, 1.0 Hz, 2H), 6.78 (d, J = 8.5, 2H). ^{13}C NMR (126 MHz, $CDCl_3$) δ 178.22, 143.17, 139.01, 133.29, 131.12, 130.09, 129.62, 127.34, 121.84, 121.56, 116.81. The spectroscopic data was in agreement with the literature.[3]

10-(4-Methoxyphenyl)-9(10H)-acridone (OMeAc) was synthesized from acridone and 4-bromoanisole according to the general procedure, with an isolated yield of 40%. DSC: T_m= 229.1 °C (onset) and 231.7 °C (peak). ^{1}H NMR (500 MHz, $CDCl_3$) δ 8.61 (ddd, J = 8.1, 1.7, 0.6 Hz, 2H), 7.53 (ddd, J = 8.6, 7.0, 1.7 Hz, 2H), 7.34 – 7.27 (m, 4H), 7.18 (m, 2H), 6.85 (d, J = 8.5, 2H), 3.98 (s, 3H). ^{13}C NMR (126 MHz, $CDCl_3$) δ 178.24, 160.15, 143.53, 133.25, 131.41, 131.03, 127.30, 121.89, 121.49, 116.90, 116.18, 55.69. The spectroscopic data was in agreement with the literature.[2]

4-(9(10H)Acridone-yl)benzonitrile (CNAc) was synthesized from acridone and 4-bromobenzonitrile according to the general procedure, with an isolated yield of 32%. DSC: T_m= 309.2 °C (onset) and 312.8 °C (peak). ^{1}H NMR (500 MHz, $CDCl_3$) δ 8.62 (dd, J= 8.0, 1.7 Hz, 2H), 8.07 (m, 2H), 7.61 – 7.52 (m, 4H), 7.34 (ddd, J = 8.0, 7.0, 1.0 Hz, 2H), 6.66 (d, J= 8.6 Hz, 2H). ^{13}C NMR (126 MHz, $CDCl_3$) δ 177.97, 143.20, 142.48, 135.12, 133.66, 131.68, 127.72, 122.14, 121.93, 117.63, 116.09, 114.04. The spectroscopic data was in agreement with the literature.[4]

10-(4-(Tert-butyl)phenyl)9(10H)-acridone (tBuAc). tBuAc was synthesized from acridone and 1-bromo-4-tert-butylbenzene according to the general procedure, with an isolated yield of 44%. DSC: T_m= 299.3 °C (onset) and 301.4 °C (peak) .^{1}H NMR (500 MHz, $CDCl_3$) δ 8.61 (ddd, J = 8.0, 1.4, 0.4 Hz, 2H), 7.75 – 7.69 (m, 2H), 7.53 (ddd, J = 8.7, 7.0, 1.7 Hz, 2H), 7.34 – 7.27 (m, 4H), 6.82 (d, J = 8.6, 2H), 1.49 (s, 9H). ^{13}C NMR (126 MHz, $CDCl_3$) δ 178.24, 152.85, 143.32, 136.16, 133.21, 129.39, 127.97, 127.26, 121.84, 121.47, 116.96, 35.03, 31.44. The spectroscopic data were in agreement with the literature.[5]

10-(4-(Pentafluoro-l6-sulfaneyl)phenyl)acridin-9(10H)-one (SF5Ac) was synthesized from acridone and 1-iodo-4-(pentafluorosulfanyl)benzene according to the general procedure, with an isolated yield of 30%. HRMS calculated for $C_{19}H_{13}F_5NOS$: 398.0633; observed (APCI, [MH^+]) = 398.0622. ^{1}H NMR (500 MHz, $CDCl_3$) δ 8.62 (ddd, J = 8.0, 3.4, 1.6 Hz, 2H), 8.18 – 8.11 (m, 2H), 7.57 (ddd, J = 8.6, 6.9, 1.7 Hz, 4H), 7.34 (ddd, J = 8.0, 7.0, 1.0 Hz, 2H), 6.70 (d, J = 8.5 Hz, 2H). ^{13}C NMR (126 MHz, $CDCl_3$) δ 177.98, (154.52, 154.37, 154.22),* 142.59, 141.95, 133.64, 131.02, (129.19, 129.15, 129.11, 129.08),* 127.65, 122.07, 121.92, 116.21.*split by the fluorine. ^{19}F NMR (376 MHz, $CDCl_3$) δ 82.77 (qn, J = 150.5 Hz, 1F), 63.09 (d, J = 150.5 Hz, 4F). See Appendix 2 for NMR spectra and HRMS of SF5Ac

3.9.2. Thermogravimetric Analysis (TGA)

Thermogravimetric analysis (TGA) and differential scanning calorimetry were conducted on TGA 1 Mettler Toledo. The samples were measured in Al-pans under a dynamic atmosphere of air and heated up to 600 °C at a rate of 10 °C/min.

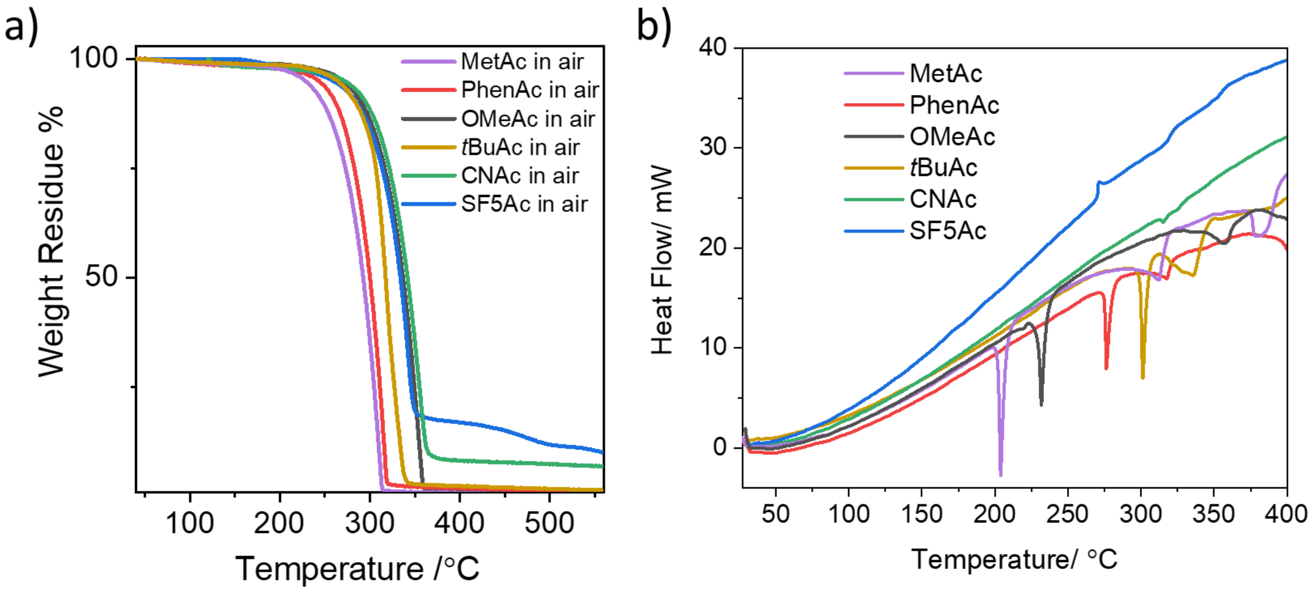

Figure 3.7. a) TGA and b) DSC analysis of the acridone derivatives.

3.9.3. UV-Vis Absorption Spectroscopy and Steady-State Fluorescence/Phosphorescence spectroscopy

The solution and thin film UV-Vis absorption spectra of acridones were collected on the JASCO V-670 spectrophotometer. Films were vacuum-deposited on quartz. Room temperature total emission and delayed emission of acridones were measured on Varian Cary Eclipse fluorescence spectrophotometer from Agilent, using a solid sample holder also from Agilent. Low-temperature measurements were conducted on the same instrument using a liquid nitrogen Dewar assembly from Horiba Scientific.

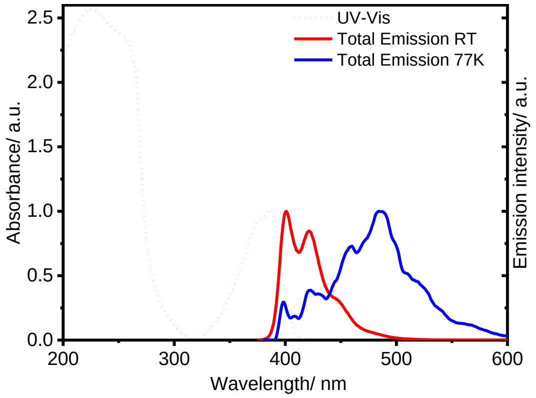

Figure 3.8. The absorption (dotted line) and emission (steady state at room temperature, red; steady-state in 77 K, blue) of HAc in chloroform solution.

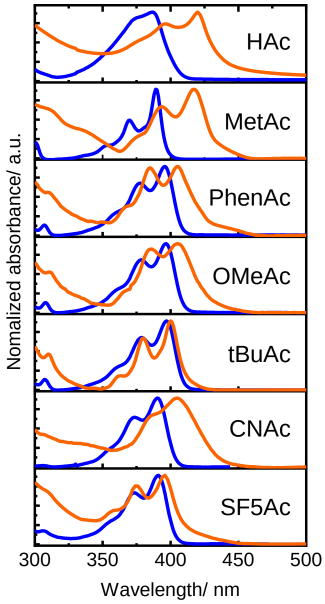

Figure 3.9. Crystallization-induced shift of absorbance in acridone derivatives (blue: $CHCl_3$ solution, orange: vacuum-deposited films).

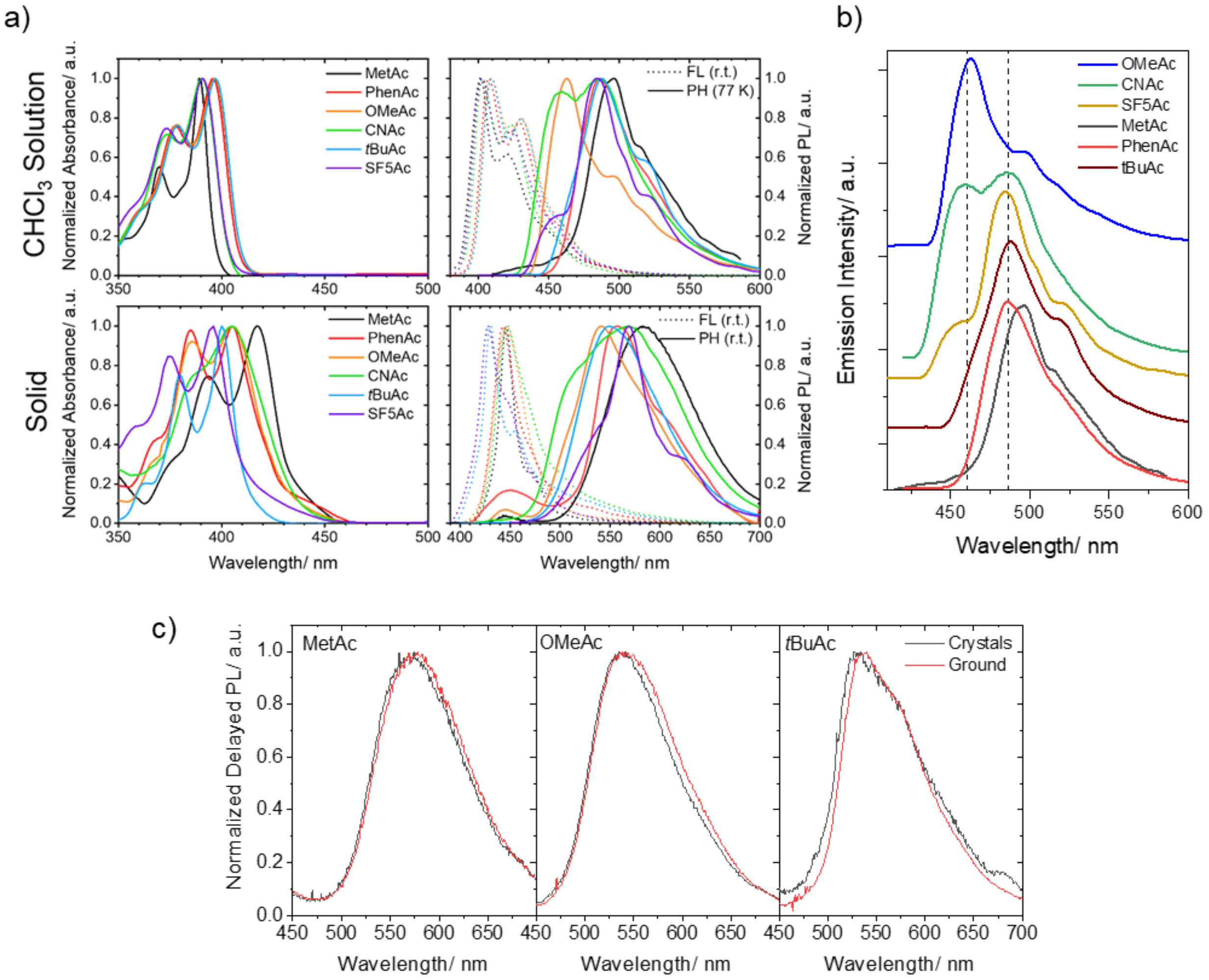

Figure 3.10. a) Overlaid absorption (left) and photoluminescence spectra (right; steady state, dashed; delayed, solid) of acridone derivatives in CHCl$_3$ solution (top), and vacuum-deposited films (bottom). b) Delayed spectra for CHCl$_3$ solutions captured with 1.0 ms acquisition delay in liquid N$_2$ (77 K). Delayed spectra for crystalline solid samples captured with 0.2 ms acquisition delay at room temperature , λ_{ex} = 370 nm. c) Comparison of delayed emission in the solid-state of macroscopic (mm) single crystals before and after grinding.

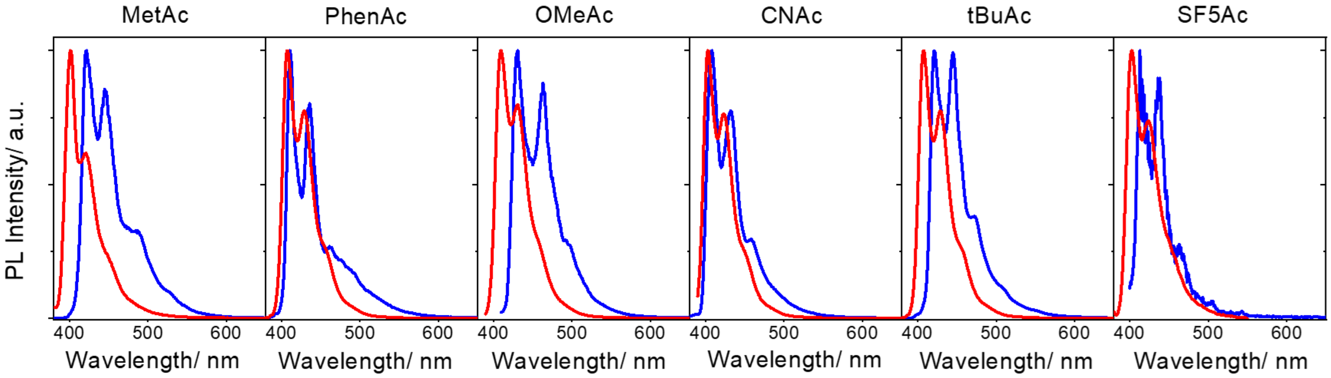

Figure 3.11. Steady-state luminescence spectra $CHCl_3$ solutions of acridone derivatives, at room temperature (red) and frozen in liquid N_2 (blue).

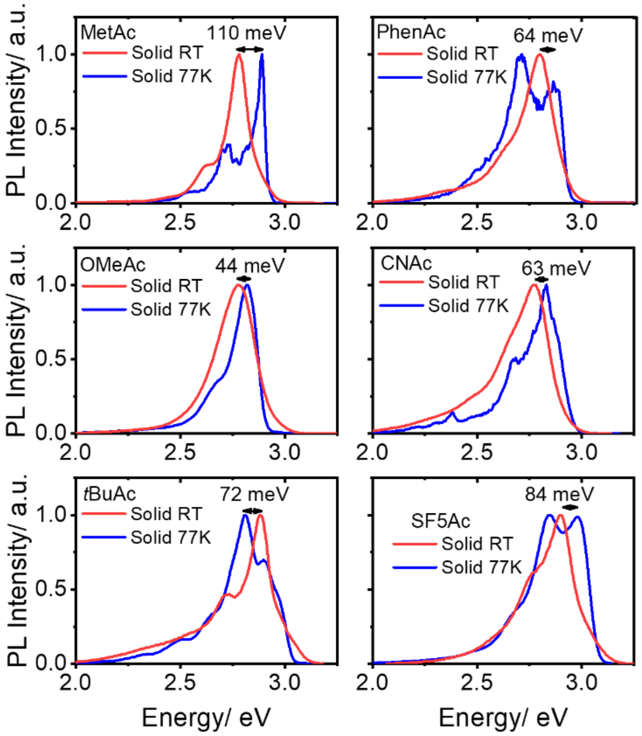

Figure 3.12. Comparison of acridones steady-state emission (fluorescence) spectra in crystalline powders at room temperature (red) and 77 K (blue)**.**

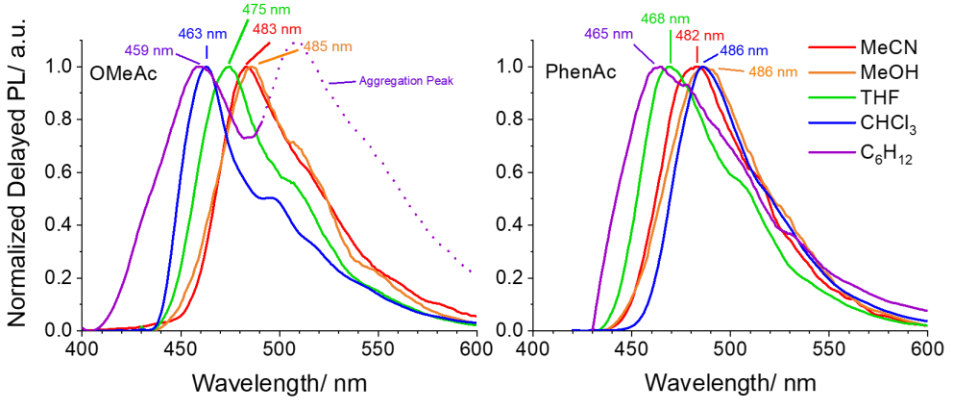

Figure 3.13. Phosphorescence spectra of OMeAc (left) and PhenAc (right) in frozen glasses (liq. N$_2$) of solvents of various polarities.

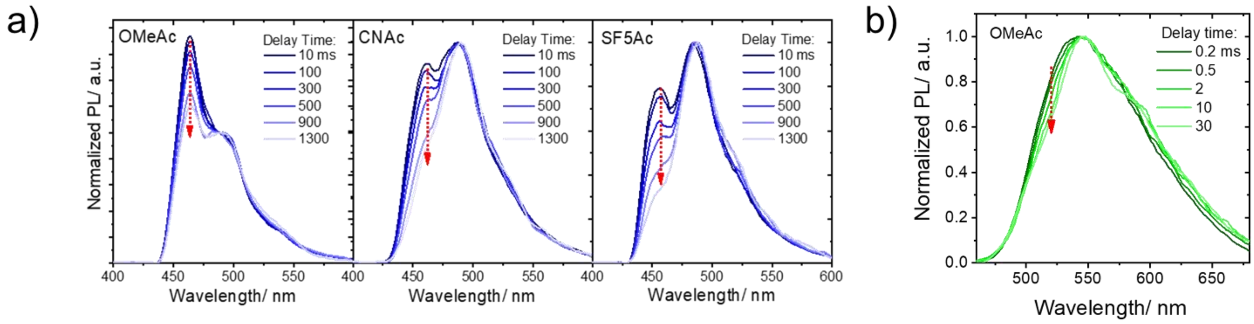

Figure 3.14. Phosphorescence spectra showing fast decay of the higher energy emission band in a) frozen CHCl$_3$ solutions at 77 K and b) solid-state at room temperature.

3.9.4. Lifetime Measurement and Time-Resolved Emission Spectra

Phosphorescence lifetimes were measured on the Varian Cary Eclipse spectrophotometer from Agilent. The delay time and gate times used to measure lifetimes were adjusted according to lifetimes, all in millisecond time scale. Low-temperature measurements were conducted on the same instrument using a liquid nitrogen Dewar assembly from Horiba Scientific. The emission lifetime of the samples was determined by the Time-Correlated Single Photon Counting (TCSPC) technique using an Edinburgh Instruments mini-tau lifetime spectrophotometer equipped with an EPL 405 pulsed diode laser. The emission was filtered through a bandpass filter of 450± 50 nm. The solutions and solids were prepared using the same procedure as explained in the UV-Vis and spectroscopy section (vide supra). The data were fitted (single exponential for solution lifetimes and biexponential for solids' emission) using OriginPro 8.5 to obtain the fluorescent lifetimes.

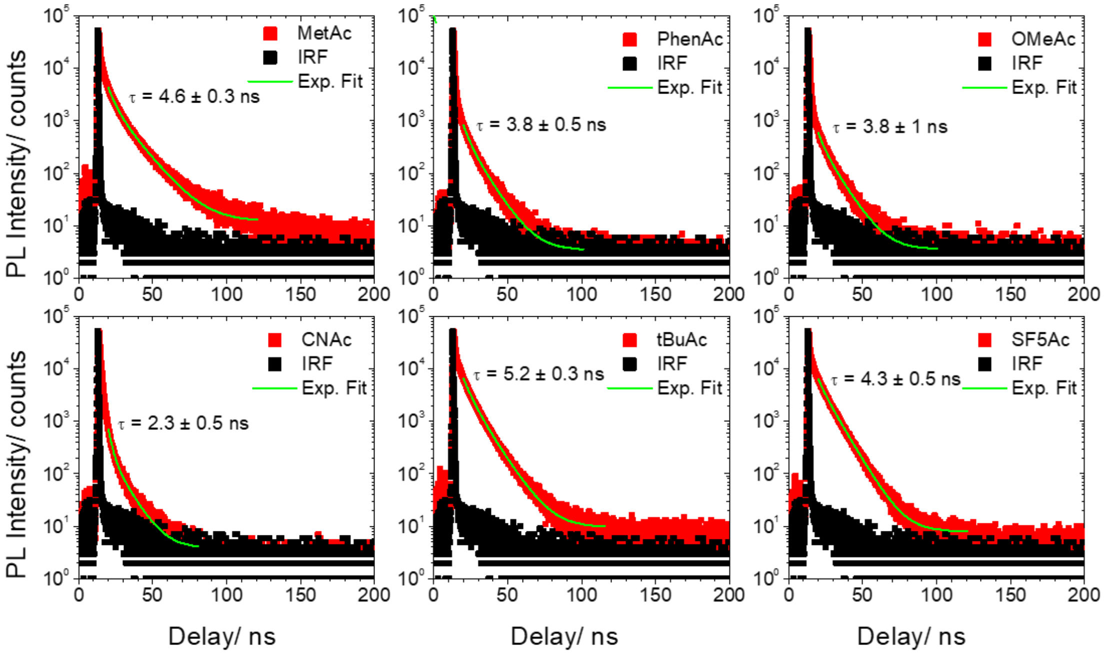

Figure 3.15. Fluorescent decays of dilute chloroform solutions for acridone derivatives at room temperature, acquired *via* TCSPC, λ_{ex} = 405 nm.

Table 3.3. Decay fitting parameters of room temperature fluorescence in $CHCl_3$ solutions λ_{ex} = 405 nm.

	$\tau_{1\ (ns)}$	a_1	$\tau_{2\ (ns)}$	a_2	$\tau_{avg\ (ns)}$	$\sigma_{\langle\tau\rangle}$
MetAc	4.3	96%	12.8	4%	4.6	0.2_5
PhenAc	3.6	97%	9.8	3%	3.8	0.5
OMeAc	3.6	96%	9.8	4%	3.8	1.1
CNAc	2.3	~100%	--	--	2.3	0.4_5
*t*BuAc	4.6	90%	10.2	10%	5.2	0.3
SF5Ac	3.7	89%	9.2	11%	4.3	0.5

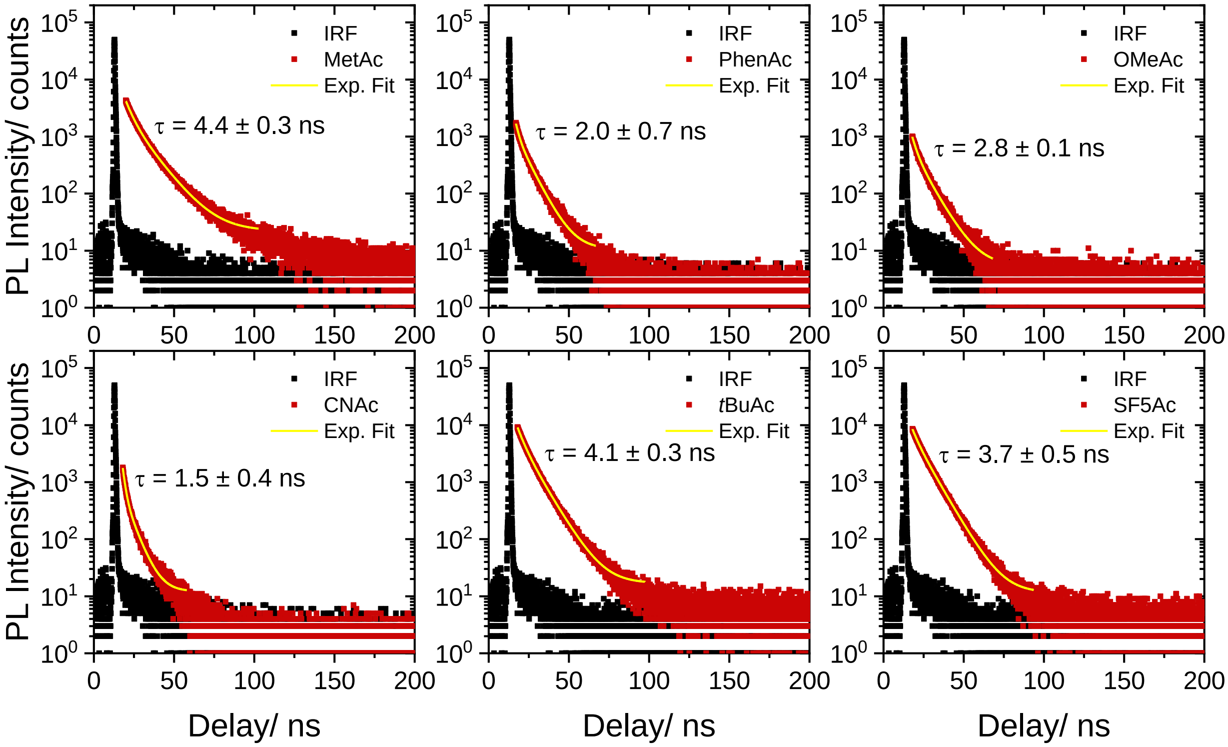

Figure 3.16. Fluorescent lifetimes of crystalline powders of acridone derivatives at room temperature, acquired *via* TCSPC, λ_{ex} = 405 nm.

Table 3.4. Decay fitting parameters of solid-state fluorescence λ_{ex} = 405 nm.

	$\tau_{1\,(ns)}$	a_1	$\tau_{2,(ns)}$	a_2	$\tau_{avg,}$ (ns)	$\sigma_{\langle\tau\rangle}$
MetAc	4.1	96%	11.9	4%	4.4	0.3
PhenAc	1.9	99.7%	7.7	0.2%	2.0	0.7
OMeAc	2.7	99%	8.8	1%	2.7_5	0.1
CNAc	1.4_5	~100%	5.8	~0%	1.4_5	0.4
*t*BuAc	3.7	92%	9.2	8%	4.1	0.3
SF5Ac	3.2_5	92%	8.9	8%	3.7	0.5

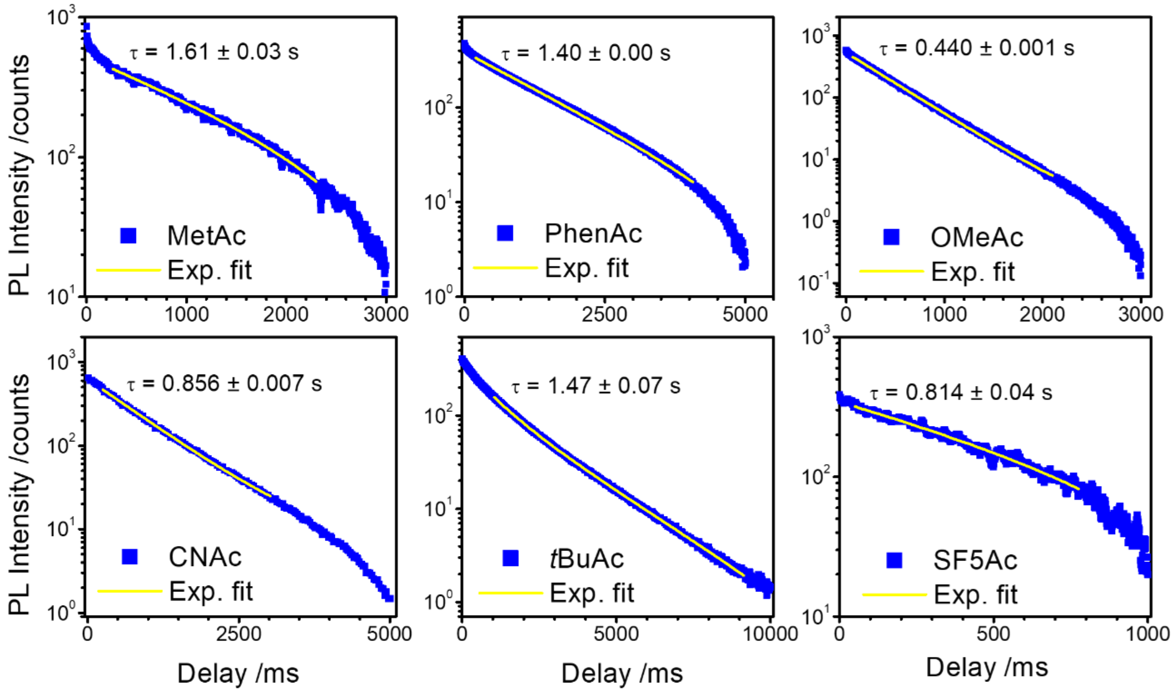

Figure 3.17. Phosphorescent decays of acridone derivatives in 77 K-frozen solutions, with exponential fits. λ_{ex} = 370 nm.

Table 3.5. Decay fitting parameters of 77 K-frozen solutions' phosphorescence. λ_{ex} = 370 nm

	$\tau_{1(s)}$	a_1	$\tau_{2(s)}$	a_2	$\tau_{avg,\ (ms)}$
MetAc	1.610	100%	--	--	1.610
PhenAc	1.402	100%	--	--	1.402
OMeAc	0.440	100%	--	--	0.440
CNAc	0.857	100%	--	--	0.857
*t*BuAc	2.120	47%	0.902	53%	1.470
SF5Ac	0.814	100%	--	--	0.814

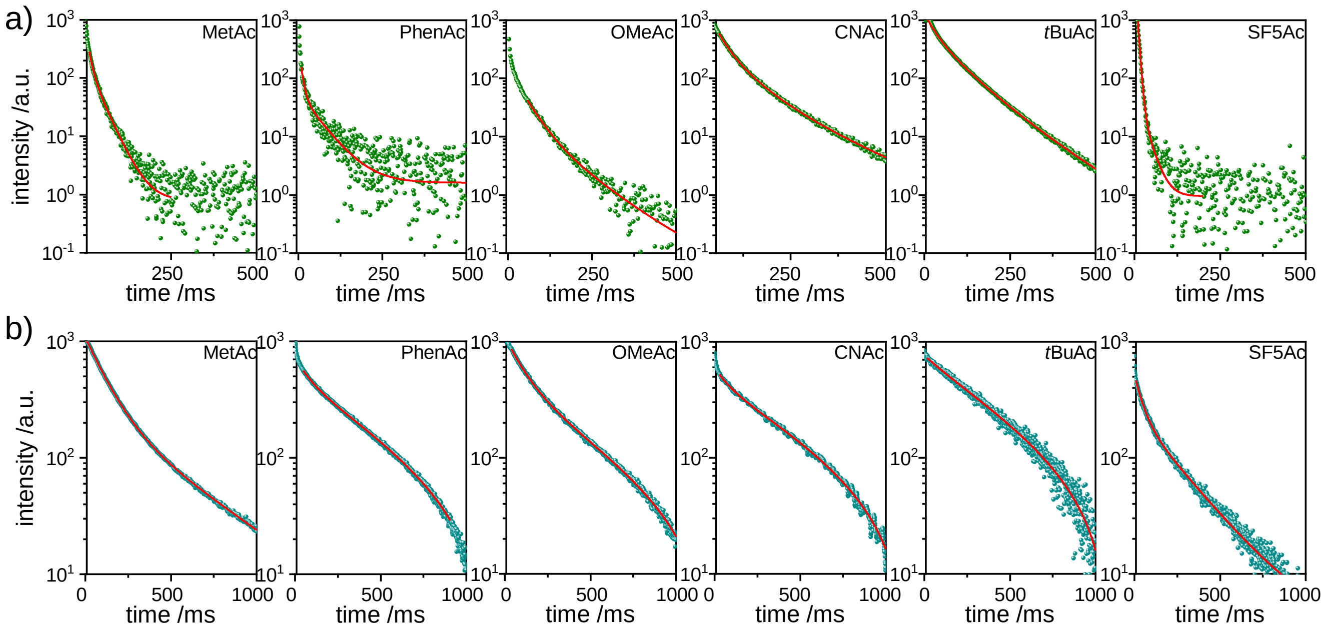

Figure 3.18. Phosphorescent decays of acridone derivatives in a) room temperature solid b) 77 K-cooled solids of acridones, with bi-exponential fits(red). λ_{ex} = 370 nm.

Table 3.6. Decay fitting parameters of solid-state phosphorescence at room temperature and 77 K. λ_{ex} = 370 nm.

		τ_1 (ms)	a_1	τ_2 (ms)	a_2	τ_{avg} (ms)
Room-Temperature solids	MetAc	9.5	74%	33.5	26%	15.7
	PhenAc	8.00	85%	55.0	15%	15.05
	OMeAc	38.7	86%	105.2	14%	48.0
	CNAc	26.7	50%	65.5	50%	46.1
	*t*BuAc	45.6	34%	100.0	66%	81.5
	SF5Ac	5.2	100%	--	--	5.2
77 K-cooled solids	MetAc	113.5	68%	354.8	32%	190.7
	PhenAc	75.9	32%	470.8	68%	344.4
	OMeAc	101.3	57%	474.7	43%	261.9
	CNAc	76.5	24%	527.8	76%	419.5
	*t*BuAc	106.8	10%	478.8	90%	441.6
	SF5Ac	45.3	55%	243.9	45%	134.7

3.9.5. Laser Flash Photolysis

Experiments were conducted using a laser flash photolysis setup (Luzchem). An Nd: YAG (Continuum Surelite CLII-10, 10 Hz, 450 mJ at 1064 nm) laser was used for excitation at a wavelength of 355 nm. 8 mJ laser pulses were used with a pulse width of 6 ns. A 150 W Xe lamp was used as the monitoring light source. The detector consisted of a photomultiplier tube (PMT) connected to a digital oscilloscope (Tektronix TDS2012). All data were collected via the commercially available LFP 7.0 software (Luzchem). All samples were prepared freshly in 10 x 10 mm quartz cells before and after degassing with argon gas for 10 min. Samples were irradiated with at least 10 laser shots to acquire ΔOD temporal evolution traces. The time per division recorded by the detector was varied from 500 nm to 5 μs on a sample-to-sample basis to optimize signal clarity and resolution. Kinetic traces of ΔOD were fitted using OriginPro 8.5 to obtain transient lifetimes.

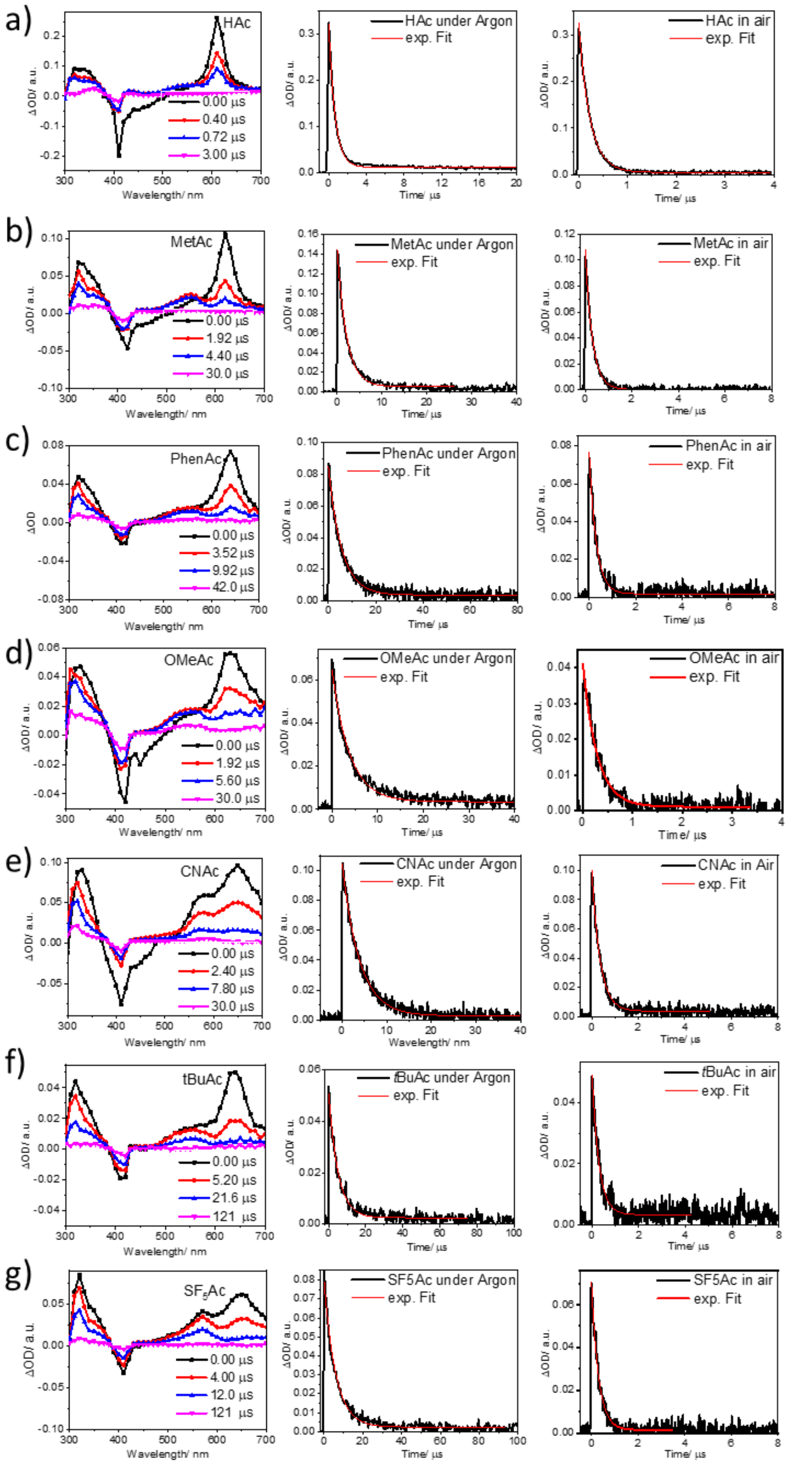

Figure 3.19. The change in transient absorption of the triplet states generated after laser flash (left), the ΔOD temporal evolution (at 630 nm) for deoxygenated solutions (middle) and oxygenated solutions (right) of a) HAc, b) MetAc, c) PhenAc, d) OMeAc, e) *t*BuAc, f) CNAc and g) SF5Ac at room temperature, in DCM.

3.9.6. TTA-Induced Delayed Fluorescence

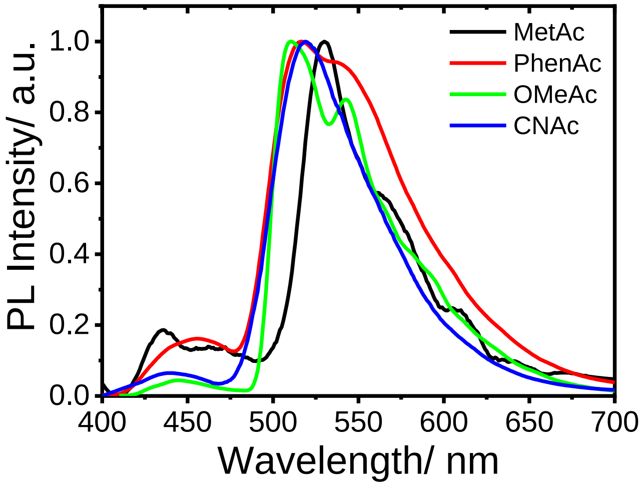

Figure 3.20. Delayed emission spectra of acridone derivative solids at 77 K, showing persistence of delayed fluorescence feature at low temperature.

3.9.7. Photographs of the Phosphorescence

The phosphorescence of acridone crystalline solids and dilute solutions in 77 K were observable by the naked eye due to their ultralong phosphorescent lifetimes. The images in figure 3.21 were captured with a smartphone camera. To capture the fast-phosphorescent decay of solids at room temperature (<100 μs) we used high-speed camera Imaging (supporting video). Acridone crystalline powders were placed on glass and were excited by a UV lamp (360-390 nm) and the phosphorescence decay was detectable even after the light was turned off. The emission of the samples was captured using a Photron Fastcam NOVA S16 (Photron USA, CA, USA). A 50 mm Navitar c-mount lens was used together with a 5 mm lens extender to allow for greater magnification and smaller working distance. The emission of the sample was captured at a speed of 9000 fps with an exposure time of 100 μs and a lens aperture of 2 for all samples. The High Dynamic Range (HDR) function of the control software, Photron Fastcam Viewer 4 (PFV4, Photron USA, CA, USA), was used to enhance the darker section of the image to allow for better image quality. The same level of HDR enhancement was used for all samples to allow for proper visual evaluation.

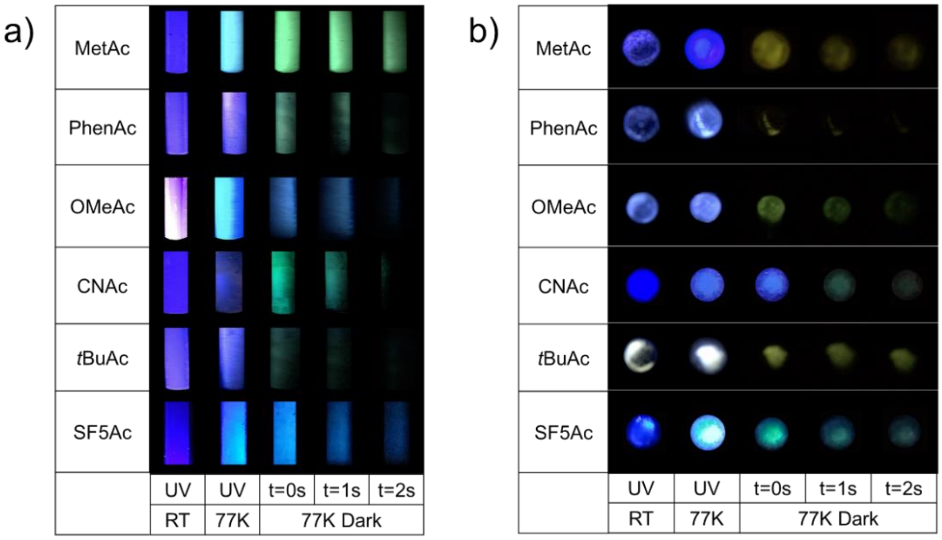

Figure 3.21. Photoluminescence photos of the a) frozen solutions b) crystalline powders in liquid nitrogen with the UV light on and after the UV light is off.

3.9.8. DFT Calculations

Optimized ground state (S_0) geometries of all acridone derivatives were obtained by density function theory (DFT) calculations using B3LYP/6-31G(d) in Gaussian 16 software.[6] Optimized excited state (S_1/T_1) geometries were obtained using time-dependent self-consistent field (TD-SCF) calculations, also using B3LYP/6-31G(d) in Gaussian 16.[7-13] Natural transition orbitals (NTO)[14] were then extracted and visualized also using Gaussian 16 and Gaussview 6.0.

For summary of orbital transitions of the studied acridone obtained via TD-DFT see Appendix 3.

Table 3.7. Molecular orbital levels of the acridones, obtained from optimized structures in the gas-phase using B3LYP 6-31G(d). All the energies are in eV.

	HAc	MetAc	PhenAc	OMeAc	CNAc	*t*BuAc	SF5Ac
LUMO+2	-0.06	-0.03	-0.71	-0.31	-1.30	-0.56	-1.67
LUMO+1	-0.45	-0.41	-0.71	-0.67	-1.68	-0.65	-1.67
LUMO	**-1.51**	**-1.51**	**-1.41**	**-1.36**	**-2.00**	**-1.37**	**-1.78**
HOMO	**-5.62**	**-5.57**	**-5.52**	**-5.46**	**-5.82**	**-5.47**	**-5.81**
HOMO-1	-6.40	-6.36	-6.30	-6.00	-6.60	-6.26	-6.56
HOMO-2	-6.94	-6.87	-6.80	-6.48	-7.05	-6.75	-7.05

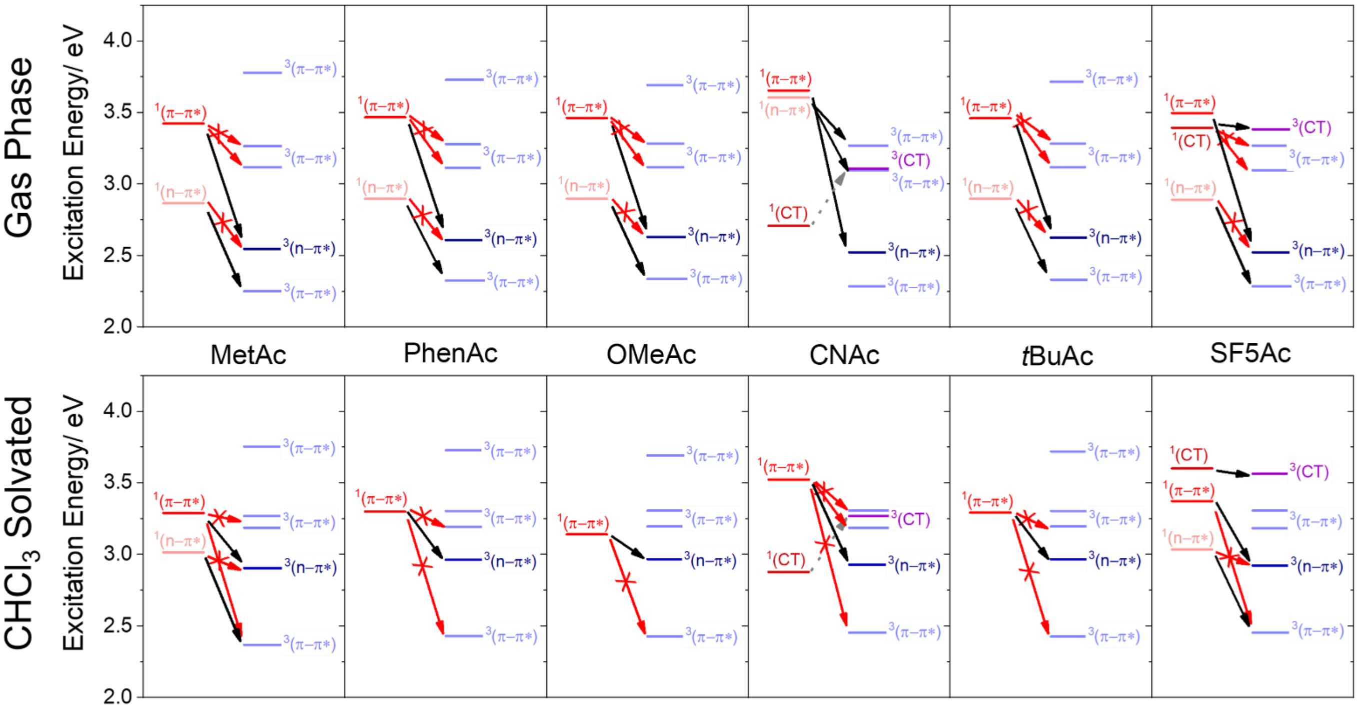

Figure 3.22. Low-lying singlet and triplet states in acridone derivatives, showing allowed and forbidden ISC pathways. TD-DFT, B3LYP/6-31G(d) level of theory in the gas-phase and with CHCl$_3$ solvation.

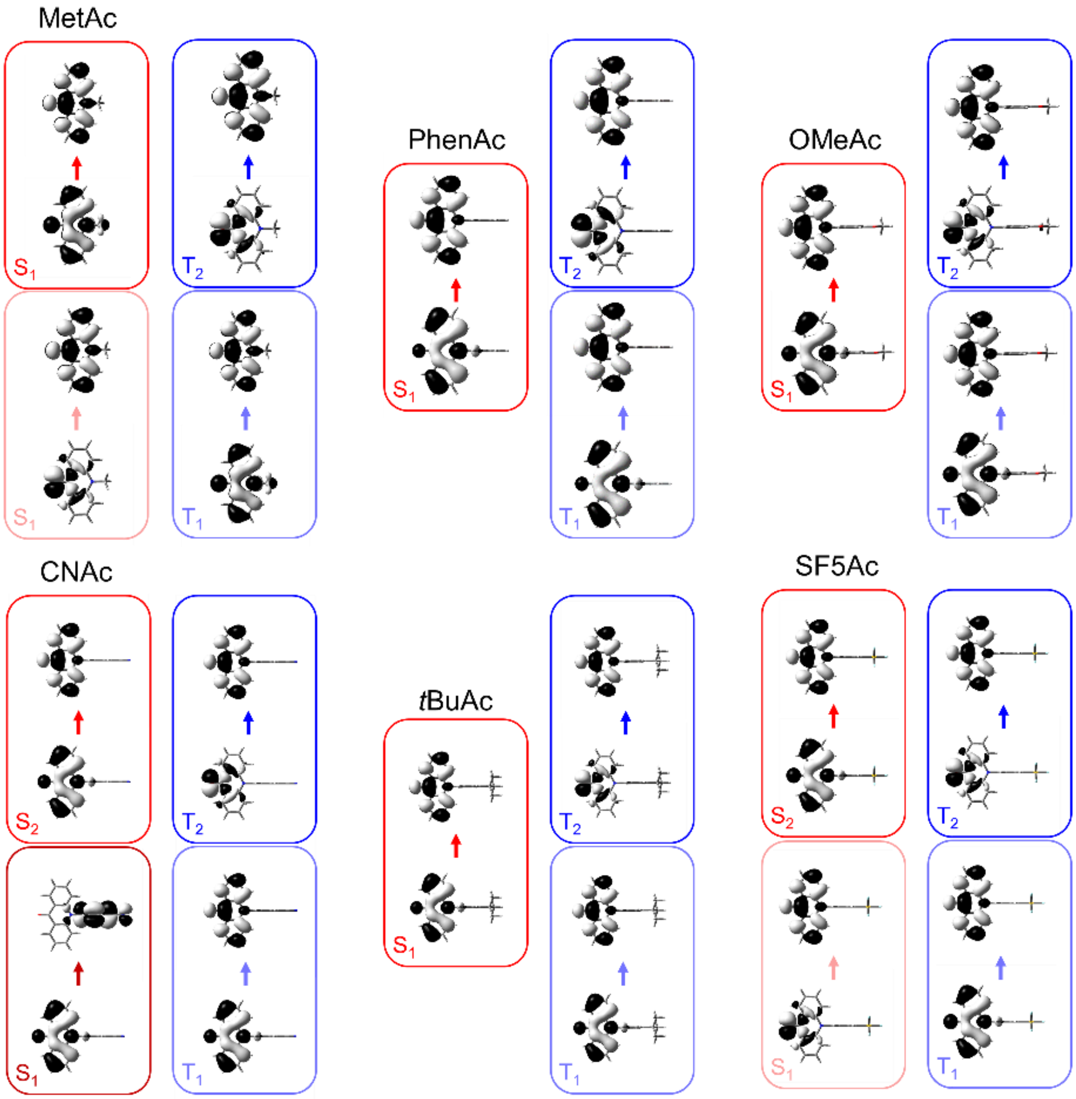

Figure 3.23. The natural transition orbital representation of acridone derivatives for the optimized geometry of the lowest singlet and triplet states. TDDFT, B3LYP/6-31G(d) level of theory with $CHCl_3$ solvation. [a] Low-lying (S_1, S_2, T_1, T_2) excited states of π-π* and n-π* character, in both gas-phase and with $CHCl_3$ solvation.

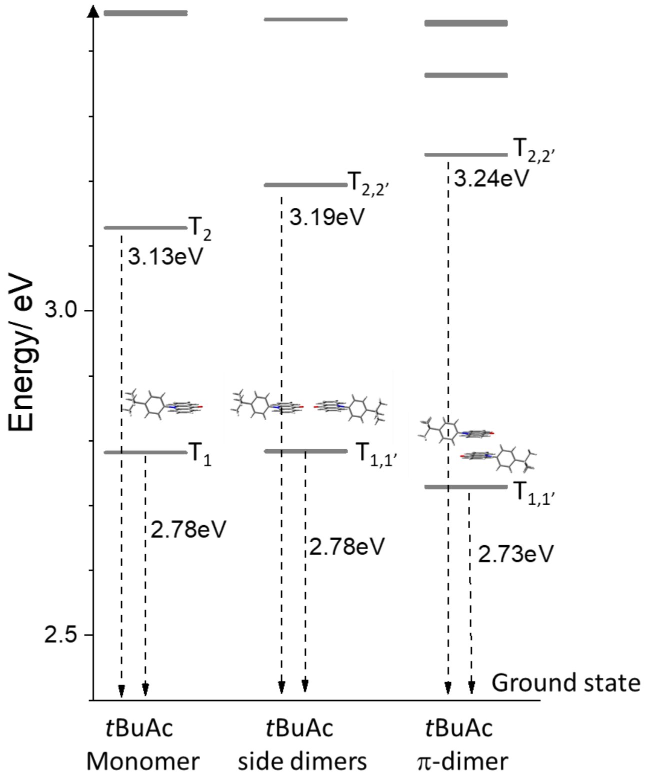

Figure 3.24. Energetic diagram of *t*BuAc triplet state of a) monomer, b) side dimers, and c) π-dimer, calculated using TD-DFT B3LYP(6-31g(d)); geometries were obtained from the crystal structure with no further optimizations. The calculations show a significant transition dipole interaction and T_1 stabilization in the π-dimer but not in the side dimer.

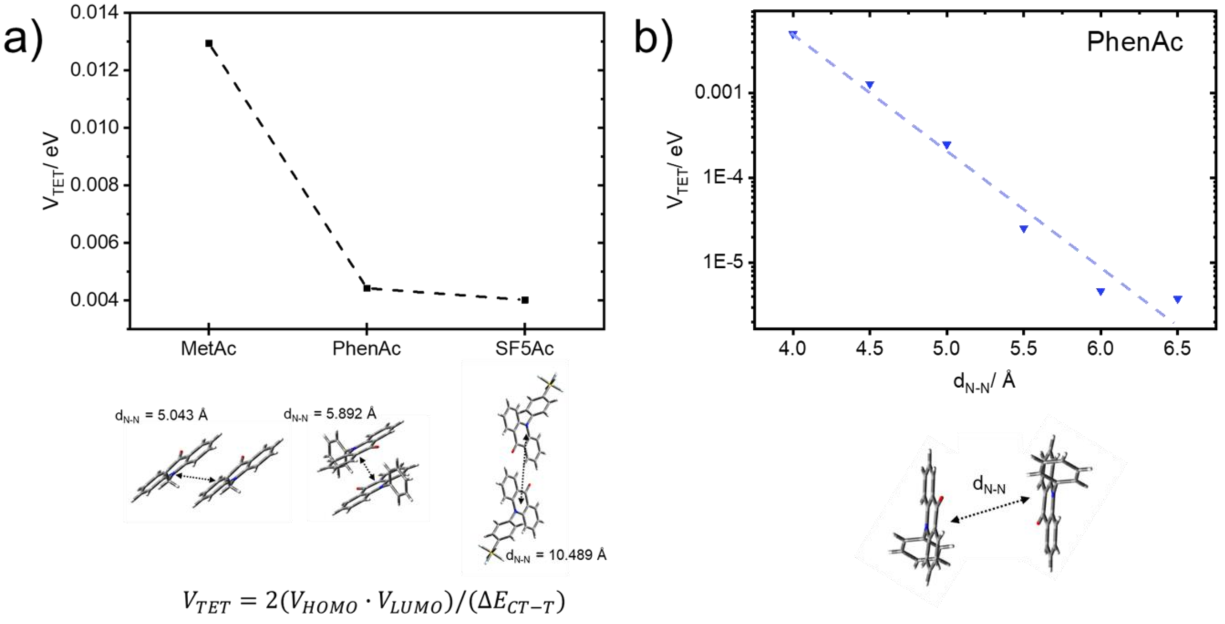

$$V_{TET} = 2(V_{HOMO} \cdot V_{LUMO})/(\Delta E_{CT-T})$$

Figure 3.25. a) Triplet energy transfer electronic coupling across weakly coupled crystal dimers of MetAc, PhenAc, and SF5Ac. b) Logarithmic plot of electronic coupling in PhenAc dimer vs the arbitrarily varied intermolecular distance (d_{N-N}). Calculated using B3LYP/TZP in Amsterdam Density Functional package.[15]

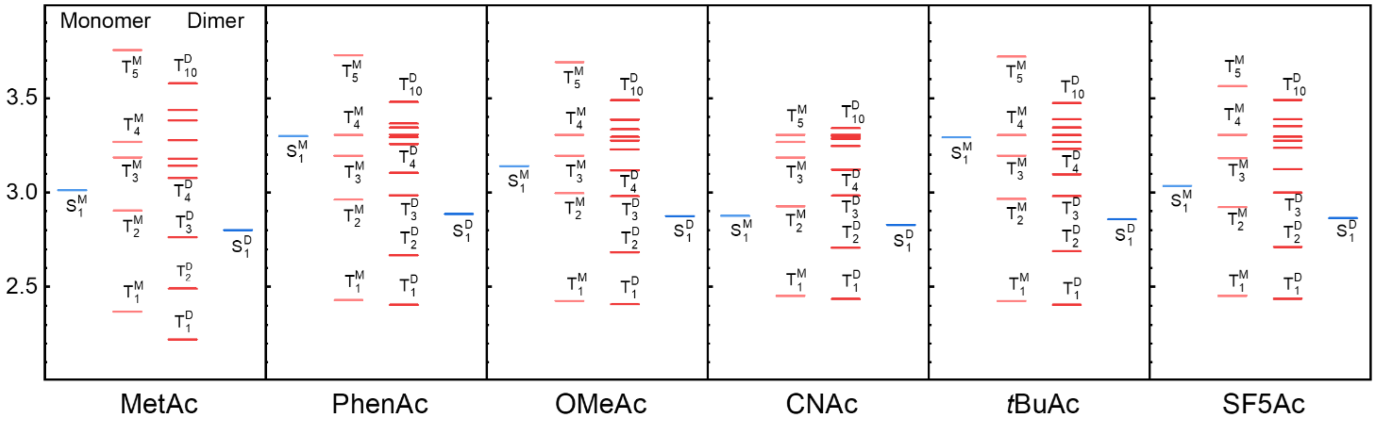

Figure 3.26. Energy level diagram of acridone derivative monomers versus those of the dimers obtained from crystal structures. All calculations are done with TD-DFT, B3LYP/6-31G(d) level of theory.

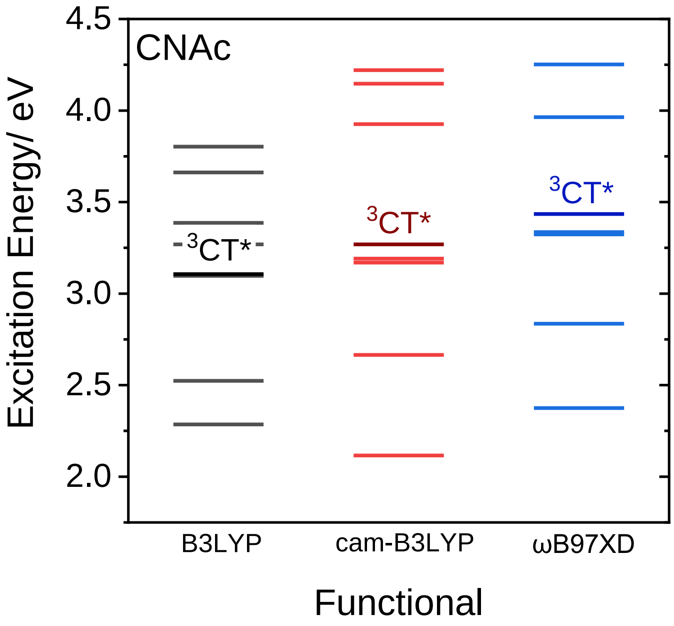

Figure 3.27. Triplet excited states of CNAc, evaluated by TD-DFT using different functionals, all with 6-31G(d) basis set. In B3LYP, the ^{3}CT* excited state appears as T_4 (3.10 eV), and in cam-B3LYP and ωB97XD the CT states appear as T_5 (3.27 eV and 3.44 eV, respectively).

3.9.9. X-ray crystallography

Crystal structures were obtained for OMeAc (CCDC: 1998381), *t*BuAc(CCDC: 1998383), and SF5Ac (CCDC: 199838) using recrystallization from ethanol (OMeAc, SF5Ac) and physical vapour deposition (*t*BuAc). Single crystal X-ray diffraction (SCXRD) data were measured on a Bruker D8 Venture diffractometer equipped with a Photon 200 CMOS area detector, and *IμS* microfocus X-ray source (Bruker AXS, Cu*Kα* source). All measurements were carried out at room temperature on crystals coated with a thin layer of amorphous oil to decrease crystal deterioration, structural disorder, or any related thermal motion effects and to improve the accuracy of the structural results. Structure solution was carried out using the SHELXTL package from Bruker.[16] The parameters were refined for all data by full-matrix-least-squares or F2 using SHELXL.[17] All of the nonhydrogen atoms were refined with anisotropic thermal parameters. Hydrogen atoms were placed in calculated positions and allowed to ride on the carrier atoms. All hydrogen atom thermal parameters were constrained to ride on the carrier atom. Powder X-ray diffraction (PXRD) patterns were collected on a Bruker D2 Phaser powder diffractometer equipped with a

CuKα source and Lynxeye detector. The patterns were collected in the angle region between 3-40° (2θ) with a step size of 0.05°.

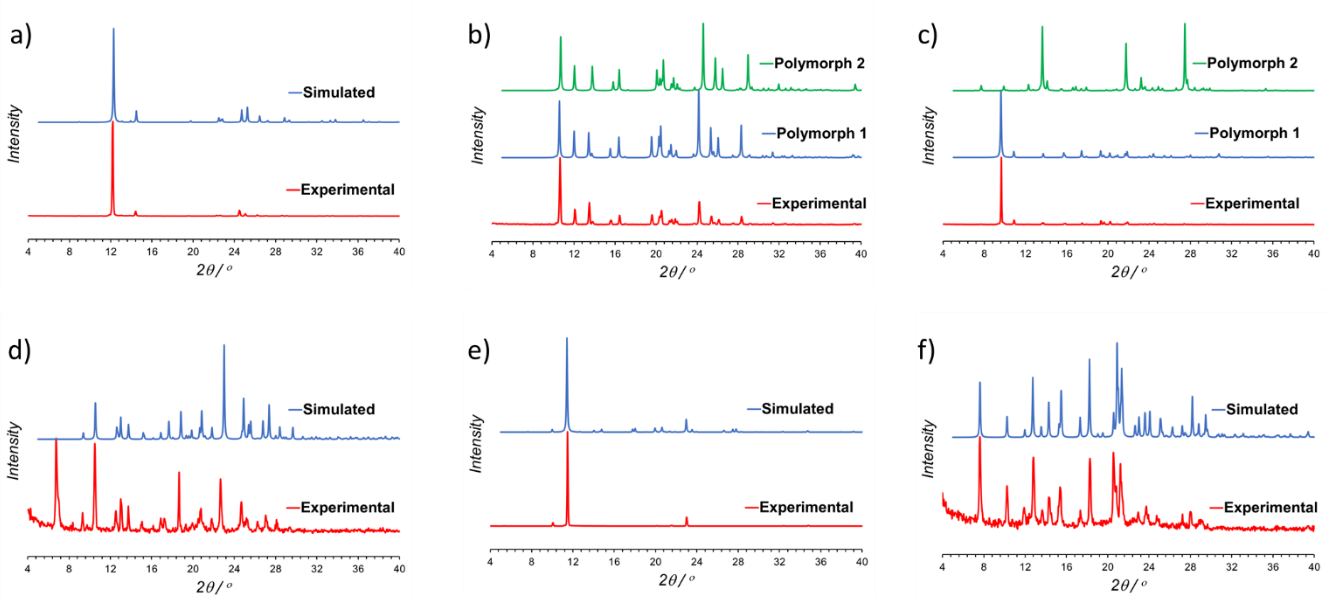

Figure 3.28. The powder X-ray diffraction patterns (PXRD) of the obtained crystalline powders which were used for spectroscopy, versus that of the simulated PXRD patterns for a) MetAc (CCDC 1453140) b) PhenAc (Polymorph1 with CCDC:1232243 and Polymorph2 with CCDC: 1883546) c) OMeAc (Polymorph1-*this work*- CCDC: 199838 and Polymorph2 with CCDC: 1972073) d) CNAc (CCDC: 1534549) e) *t*BuAc (CCDC: 1998383, *this work*), SF5Ac (CCDC: 199838, *this work*).

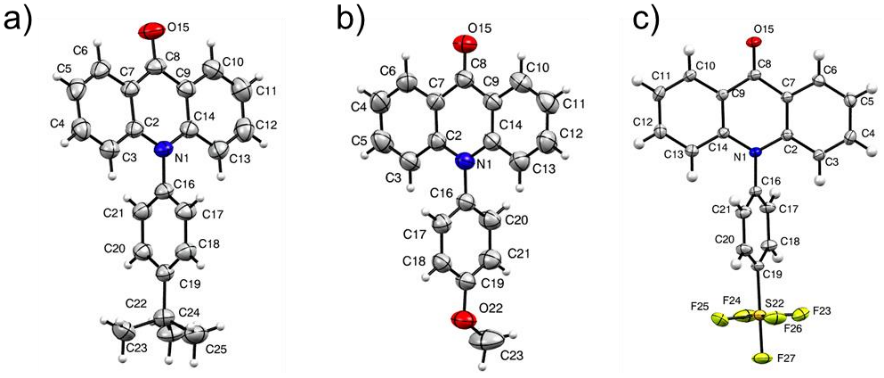

Figure 3.29. ORTEP diagrams of a) *t*BuAc b) OMeAc and c) SF5Ac crystal structures.

Table 3.8. Crystal data and structure refinement for *t*BuAc

Identification code	10-(4-(tert-butyl) phenyl)9(10H)-acridone
Empirical formula	C23H21NO
Formula weight	327.41
Temperature/K	298(2)
Crystal system	triclinic
Space group	P-1
a/Å	8.3941(2)
b/Å	9.5535(2)
c/Å	11.7695(2)
α/°	94.7930(10)
β/°	97.1200(10)
γ/°	110.7850(10)
Volume/Å3	867.29(3)
Z	2
ρcalcg/cm3	1.254
μ/mm-1	0.565
F(000)	348.0
Crystal size/mm3	0.550 × 0.150 × 0.080
Radiation	CuKα (λ = 1.54178)
2Θ range for data collection/°	7.642 to 144.866
Index ranges	-10 ≤ h ≤ 10, -11 ≤ k ≤ 11, -12 ≤ l ≤ 14
Reflections collected	24821
Independent reflections	3386 [Rint = 0.0693, Rsigma = 0.0418]
Data/restraints/parameters	3386/0/229
Goodness-of-fit on F2	1.031
Final R indexes [I>=2σ (I)]	R1 = 0.0537, wR2 = 0.1387
Final R indexes [all data]	R1 = 0.0674, wR2 = 0.1592
Largest diff. peak/hole / e Å-3	0.19/-0.17

Table 3.9. Crystal data and structure refinement for OMeAc

Identification code	10-(4-Methoxyphenyl)-9(10H)-acridone
Empirical formula	C20H15NO2
Formula weight	301.33

Temperature/K	298(2)
Crystal system	monoclinic
Space group	P21/c
a/Å	9.23340(10)
b/Å	18.3930(2)
c/Å	9.25630(10)
α/°	90
β/°	101.0870(10)
γ/°	90
Volume/Å3	1542.66(3)
Z	4
ρcalcg/cm3	1.297
μ/mm-1	0.671
F(000)	632.0
Crystal size/mm3	0.250 × 0.200 × 0.120
Radiation	CuKα (λ = 1.54178)
2Θ range for data collection/°	9.76 to 144.914
Index ranges	-11 ≤ h ≤ 11, -22 ≤ k ≤ 22, -9 ≤ l ≤ 11
Reflections collected	28877
Independent reflections	3035 [Rint = 0.0538, Rsigma = 0.0269]
Data/restraints/parameters	3035/0/209
Goodness-of-fit on F2	1.051
Final R indexes [I>=2σ (I)]	R1 = 0.0449, wR2 = 0.1120
Final R indexes [all data]	R1 = 0.0591, wR2 = 0.1289
Largest diff. peak/hole / e Å-3	0.17/-0.12

Table 3.10. Crystal data and structure refinement for SF5Ac

Identification code	10-(4-(pentafluoro-l6-sulfaneyl) phenyl)acridin-9(10H)-one
Empirical formula	C19H12F5NOS

Formula weight	397.36
Temperature/K	150(2)
Crystal system	triclinic
Space group	P-1
a/Å	8.0213(10)
b/Å	9.1999(11)
c/Å	11.8714(15)
α/°	93.525(5)
β/°	100.287(5)
γ/°	108.942(5)
Volume/Å3	808.55(18)
Z	2
ρcalcg/cm3	1.632
μ/mm-1	2.388
F(000)	404.0
Crystal size/mm3	0.400 × 0.200 × 0.200
Radiation	CuKα (λ = 1.54178)
2Θ range for data collection/°	7.632 to 145.294
Index ranges	-9 ≤ h ≤ 9, -11 ≤ k ≤ 11, -13 ≤ l ≤ 14
Reflections collected	28038
Independent reflections	3168 [Rint = 0.0458, Rsigma = 0.0236]
Data/restraints/parameters	3168/0/244
Goodness-of-fit on F2	1.069
Final R indexes [I>=2σ (I)]	R1 = 0.0402, wR2 = 0.1194
Final R indexes [all data]	R1 = 0.0432, wR2 = 0.1239
Largest diff. peak/hole / e Å-3	0.42/-0.51

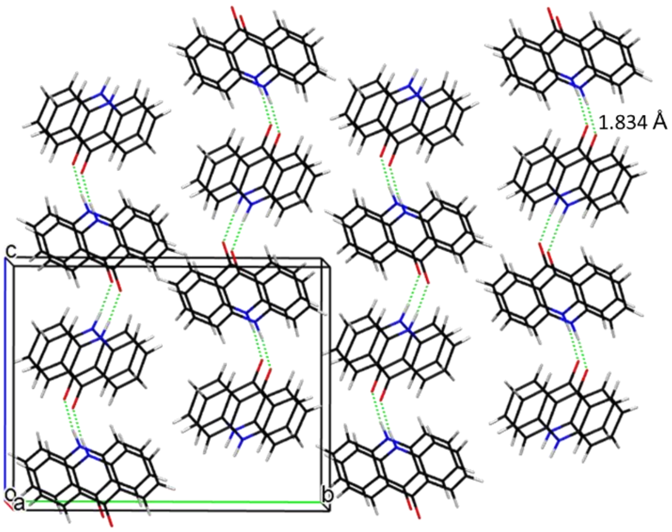

Figure 3.30. The hydrogen-bonded network of HAc in the solid-state; obtained from CCDC: 1175940. The green dashed lines show the C=O…H-N contacts.

3.9.10. References of Supplementary information

1. Maegawa, Y.; Mizoshita, N.; Tani, T.; Inagaki, S., Transparent and visible-light harvesting acridone-bridged mesostructured organosilica film. *J. Mater. Chem.* **2010,** *20*, 4399-4403.

2. Matsuo, Y.; Wang, Y.; Ueno, H.; Nakagawa, T.; Okada, H., Mechanochromism, Twisted/Folded Structure Determination, and Derivatization of (N-Phenylfluorenylidene)acridane. *Angew. Chem. Int. Ed.* **2019,** *58*, 8762-8767.

3. Huang, P.-C.; Parthasarathy, K.; Cheng, C.-H., Copper-catalyzed intramolecular oxidative C-H functionalization and C-N formation of 2-aminobenzophenones: unusual pseudo-1,2-shift of the substituent on the aryl ring. *Chem. Eur. J.* **2013,** *19*, 460-464.

4. Zhou, W.; Liu, Y.; Yang, Y.; Deng, G.-J., Copper-catalyzed intramolecular direct amination of sp2 C–H bonds for the synthesis of N-aryl acridones. *Chem. Commun.* **2012,** *48*, 10678-10680.

5. Janke, J.; Villinger, A.; Ehlers, P.; Langer, P., Synthesis of Acridones by Palladium-Catalyzed Buchwald–Hartwig Amination. *Synlett* **2019,** *30*, 817-820.

6. Frisch, M. J.; Trucks, G. W.; Schlegel, H. B.; Scuseria, G. E.; Robb, M. A.; Cheeseman, J. R.; Scalmani, G.; Barone, V.; Petersson, G. A.; Nakatsuji, H.; Li, X.; Caricato, M.; Marenich, A. V.; Bloino, J.; Janesko, B. G.; Gomperts, R.; Mennucci, B.; Hratchian, H. P.; Ortiz, J. V.; Izmaylov, A. F.; Sonnenberg, J. L.; Williams; Ding, F.; Lipparini, F.; Egidi, F.; Goings, J.; Peng, B.; Petrone, A.; Henderson, T.; Ranasinghe, D.; Zakrzewski, V. G.; Gao, J.; Rega, N.; Zheng, G.; Liang, W.; Hada,

M.; Ehara, M.; Toyota, K.; Fukuda, R.; Hasegawa, J.; Ishida, M.; Nakajima, T.; Honda, Y.; Kitao, O.; Nakai, H.; Vreven, T.; Throssell, K.; Montgomery Jr., J. A.; Peralta, J. E.; Ogliaro, F.; Bearpark, M. J.; Heyd, J. J.; Brothers, E. N.; Kudin, K. N.; Staroverov, V. N.; Keith, T. A.; Kobayashi, R.; Normand, J.; Raghavachari, K.; Rendell, A. P.; Burant, J. C.; Iyengar, S. S.; Tomasi, J.; Cossi, M.; Millam, J. M.; Klene, M.; Adamo, C.; Cammi, R.; Ochterski, J. W.; Martin, R. L.; Morokuma, K.; Farkas, O.; Foresman, J. B.; Fox, D. J. *Gaussian 16 Rev. C.01*, Wallingford, CT, 2016.

7. Bauernschmitt, R.; Ahlrichs, R., Treatment of electronic excitations within the adiabatic approximation of time dependent density functional theory. *Chem. Phys. Lett.* **1996,** *256*, 454-464.

8. Casida, M. E.; Jamorski, C.; Casida, K. C.; Salahub, D. R., Molecular excitation energies to high-lying bound states from time-dependent density-functional response theory: Characterization and correction of the time-dependent local density approximation ionization threshold. *J. Chem. Phys.* **1998,** *108*, 4439-4449.

9. Furche, F.; Ahlrichs, R., Adiabatic time-dependent density functional methods for excited state properties. *J. Chem. Phys.* **2002,** *117*, 7433-7447.

10. Scalmani, G.; Frisch, M. J.; Mennucci, B.; Tomasi, J.; Cammi, R.; Barone, V., Geometries and properties of excited states in the gas phase and in solution: Theory and application of a time-dependent density functional theory polarizable continuum model. *J. Chem. Phys.* **2006,** *124*, 094107.

11. Stratmann, R. E.; Scuseria, G. E.; Frisch, M. J., An efficient implementation of time-dependent density-functional theory for the calculation of excitation energies of large molecules. *J. Chem. Phys.* **1998,** *109*, 8218-8224.

12. Van Caillie, C.; Amos, R. D., Geometric derivatives of excitation energies using SCF and DFT. *Chem. Phys. Lett.* **1999,** *308*, 249-255.

13. Van Caillie, C.; Amos, R. D., Geometric derivatives of density functional theory excitation energies using gradient-corrected functionals. *Chem. Phys. Lett.* **2000,** *317*, 159-164.

14. Martin, R. L., Natural transition orbitals. *J. Chem. Phys.* **2003,** *118*, 4775-4777.

15. te Velde, G.; Bickelhaupt, F. M.; Baerends, E. J.; Fonseca Guerra, C.; van Gisbergen, S. J. A.; Snijders, J. G.; Ziegler, T., Chemistry with ADF. *J. Comput. Chem.* **2001,** *22*, 931-967.

16. Sheldrick, G. M., SHELXT–Integrated space-group and crystal-structure determination. *Acta Crystallogr. A* **2015,** *71*, 3-8.

17. Sheldrick, G. M., Crystal structure refinement with SHELXL. *Acta Crystallogr. C* **2015,** *71*, 3-8.

Chapter 4

Synthesis of Boroxine and Dioxaborole Covalent Organic Frameworks via Transesterification and Metathesis of Pinacol Boronates

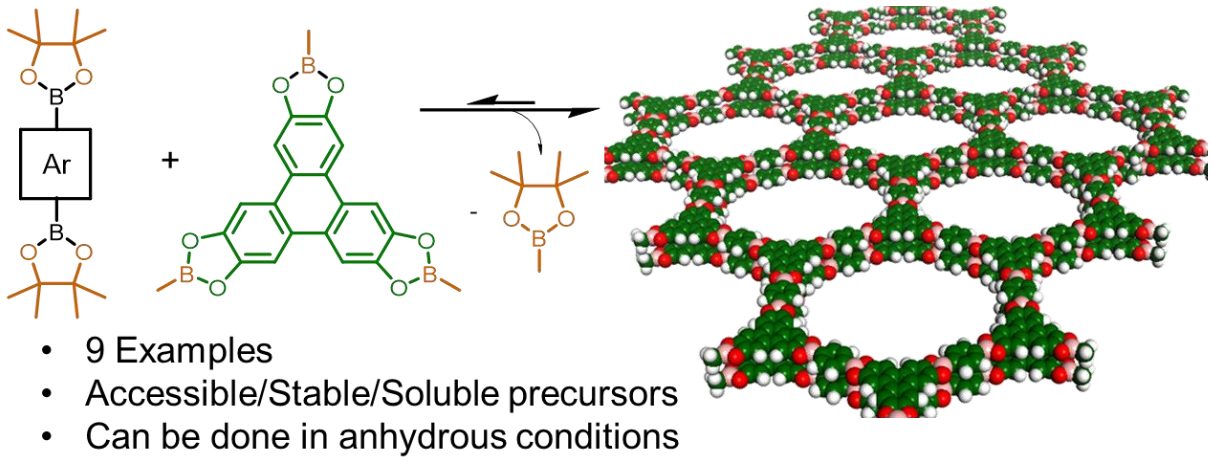

- 9 Examples
- Accessible/Stable/Soluble precursors
- Can be done in anhydrous conditions

Preface

In Chapters 2 and 3, we investigated the effect of intermolecular interactions on the luminescent properties of two classes of carbonyl-bridged triarylamines (TANGOs and acridones). In the course of the work, we realized that the alignment of molecules with respect to each other and their interactions with neighboring molecules critically determine the photophysical behavior of the ORTP. In the case of highly symmetric D_{3h} TANGO derivatives, the crystal structures had an overall resemblance with only slight differences (such as halogen bonds in TBTANGO), which allowed us to decipher the effect of packing on the luminescence characteristics. In acridone derivatives, however, the intermolecular interactions in the crystal varied significantly between substituents, and our six explored molecules showed three classes of crystal packing. The role of molecular interaction and solid-state packing has been widely acknowledged in the field of ORTP. Nevertheless, the challenge of crystal structure prediction hinders the possibility of crystal engineering phosphorescent materials in molecular crystals for desired applications. Consequently, optimizing luminescence in ORTP materials is still an empirical exercise.

A potential solution to this formidable problem of crystal structure prediction is to use the covalent organic frameworks (COFs) as a class of porous polymers in which organic building blocks are precisely integrated into extended structures. This level of molecularly precise control over the topology of assembly of the organic building block could be a convenient tool for engineering the structure and photophysical properties of ORTP materials.

Since the original report of COFs by O. M. Yaghi and co-workers in 2005 (ref 1 of this chapter), the field has significantly developed, with a large portion of COF research focused on developing methods to incorporate novel linkages and building blocks. Boroxine and dioxaborole are the first and most studied linkages for COFs formations, with some record-high crystallinity and porosities as compared to the other linkages of COFs, due to the highly reversible nature of their bond. However, our initial attempts to make boroxine and dioxaborole linked TANGO-based COFs proved challenging due to the insolubility of TANGO-triboronic acid and its protodeborylation in the presence of water (the byproduct of the polymerization reaction). Additionally, we noted that most reported dioxaborole-linked COFs suffer from optically-active impurities due to the partial oxidation of the catechol linkers, which drastically perturbs the luminescence of the resulting COF.

In this chapter, we address the above-mentioned challenges in synthesis of optically pure boroxine and dioxaborole-linked COFs. We developed a transesterification (and metathesis) methodology that enabled us to use pinacol arylboronates with methylboronic acid (MBA; or corresponding MBA-protected catechols) as highly soluble, easy to purify and bench-stable building blocks, unlike the conventional boronic COF synthesis which relies on less stable and often poorly soluble arylboronic acids and catechols. This metathesis polymerization does not form water as a byproduct, which eliminates the protodeborylation of certain boronic acids during polymerization and also opens possibilities to explore hydrolytically unstable precursors. The dioxaborole COFs synthesized using a metathesis polymerization benefit from the high optical purity and low density of defects *vs.* those synthesized by standard polycondensation. We confirmed the generality of this synthetic strategy by comparing it with seven known COFs, earlier prepared by the classical boronic acid/catechol condensation reaction. We then applied our metathesis polymerization to obtain two new COFs, Py4THB and B2HHTP, whose synthesis was previously precluded by the insolubility/instability of the boronic acid precursors. In addition to being a valuable new tool for the design/synthesis of new COFs, our approach also provided new opportunities for mechanistic studies of COF formation, as we demonstrated by applying liquid NMR for the first time for kinetic measurements of the COF polymerizations.

Author Contribution

I have synthesized, purified, and performed structural characterization of all materials reported in this chapter. Antranik Jonderian and Eric McCalla performed X-ray diffraction analysis of the COFs. The manuscript was written by me and edited by Dmytro F. Perepichka.

It is reprinted with permission from E. Hamzehpoor, A. Jonderian, E. McCalla, D. F. Perepichka, "Synthesis of Boroxine and Dioxaborole Covalent Organic Frameworks via Transesterification and Metathesis of Pinacol Boronates" *J. Am. Chem. Soc.* **2021**, *143*, 13274-13280.

4.1. Abstract

Boroxine and dioxaborole are the first and some of the most studied synthons of covalent organic frameworks (COFs). Despite their wide application in the design of functional COFs over the last 15 years, their synthesis still relies on the original Yaghi's condensation of boronic acids (with itself or with polyfunctional catechols), some of which are difficult to prepare, poorly soluble, or unstable in the presence of water. Here, we propose a new synthetic approach to boroxine COFs on the basis of the transesterification of pinacol aryl boronates (aryl-Bpins) with methyl boronic acid (MBA) and dioxaborole COFs (through the metathesis of pinacol boronates with MBA-protected catechols). The aryl-Bpin and MBA-protected catechols are easy to purify, highly soluble, and bench-stable. Furthermore, the kinetic analysis of the two model reactions reveals high reversibility (K_{eq} ~ 1) and facile control over the equilibrium. Unlike the conventional condensation, which forms water as a byproduct, the byproduct of the metathesis (MBA pinacolate) allows for easy kinetic measurements of the COF formation by conventional ^{1}H NMR. We show the generality of this approach by the synthesis of seven known boroxine/dioxaborole COFs whose crystallinity is better or equal to those reported by conventional condensation. We also apply metathesis polymerization to obtain two new COFs, Py4THB and B2HHTP, whose synthesis was previously precluded by the insolubility and hydrolytic instability, respectively, of the boronic acid precursors.

4.2. Introduction

Since the 2005 pioneering work of Yaghi and co-workers, crystalline two- and three-dimensional (2D/3D) porous covalent solids – Covalent Organic Frameworks (COFs) –have emerged as a unique class of organic materials with many attractive properties and applications, including gas storage and separation, catalysis, sensing, optoelectronics, energy storage, etc.[1-5] The wide design space of molecular building blocks provides an infinite spectrum of possible topologies, pore sizes, chemical, and physical properties in the obtained frameworks.[5] Achieving order in COFs relies on reversible (dynamic) covalent bonding between their constituent building blocks, which allows the system to self-assemble into a minimum-energy topology, *via* error-correction mechanisms. Boroxine and dioxaborole are the first explored synthons that endow such reversibility by condensation of di/tri-functional boronic acid with itself or with polyfunctional catechols, respectively.[1] Despite their hydrolytic instability, the highly dynamic nature of the boroxine and dioxaborole linkages makes them very attractive synthons in the design of COFs with excellent structural order (including COF single crystals[6]) and many optoelectronically functional COFs have been synthesized by condensation of areneboronic acids.[7-11] Notably, despite 15 years of extensive exploration of such COFs, only a few chemical modifications of the original synthetic approach[1] have been reported.[12, 13]

In both boroxine and dioxaborole synthesis water is produced upon condensation. Thus achieving anhydrous conditions during COF formation is impractical. This potentially limits the scope of the accessible boronic acids due to their protodeborylation in presence of water.[14] Many polycyclic aromatic di/tri-boronic acids are rather insoluble, which complicates their purification and limits their reactivity in the COF synthesis. On the contrary, most pinacol boronate esters are readily soluble, stable, and can be easily purified by chromatography, sublimation, or recrystallization (which is essential for producing high-quality COFs).[15] The synthetic access to most multifunctional arylboronic acids relies on the deprotection of the corresponding pinacol esters (Bpin).[16] However, the latter can be a surprisingly challenging task, both kinetically (due to steric bulkiness) and thermodynamically (due to the difunctional nature of pinacol).[17] The standard deprotection approaches include strong Lewis acids (BCl_3),[18] oxidants ($NaIO_4$),[19] and reductants ($LiAlH_4$)[20] which limit the scope of the building blocks that are stable in those conditions. In the case of dioxaborole COFs, a similar problem is presented for catechol building blocks which are often sparingly soluble, difficult to purify, and prone to oxidation by air.

To address this problem, Knochel, Bein, and co-workers used a two-step process where the pinacol ester of benzothiadiazolbisbenzeneboronic acid is first deprotected via HCl hydrolysis and then reacted in the same pot with 2,3,6,7,10,11-hexahydroxytriphenylene (HHTP) to afford a dioxaborole COF.[13] However, the harsh reaction conditions required for the deprotection (180 °C, microwave) limit the utility of this method. Dichtel and co-workers have used an acetal protecting group to mitigate the challenge of oxidative instability/insolubility of multifunctional catechols, which allowed them to introduce large phthalocyanine nodes in the COF.[12] Also, other protected building blocks (aldehydes and carboxylic acids) have been previously used to overcome the reversibility and crystallization challenges of imine- and ester-linked COFs.[21, 22]

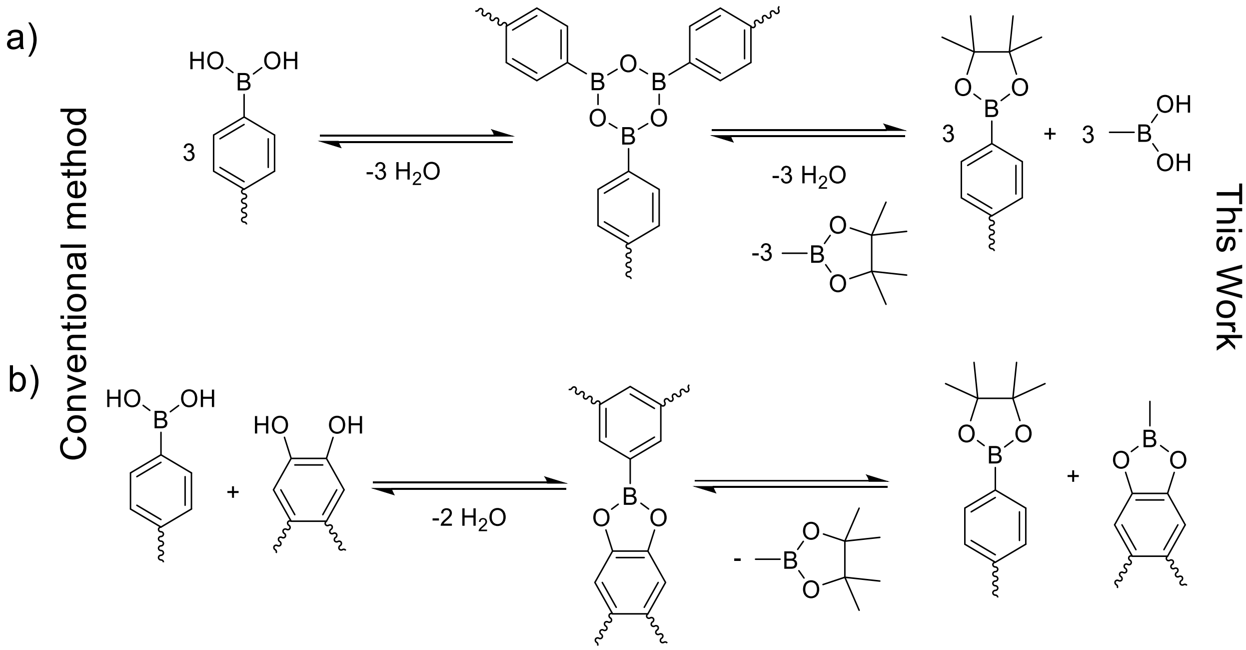

Scheme 4.1. Conventional *vs.* transesterification/metathesis synthesis of a) boroxine b) dioxaborole COFs.

Here, we propose a new approach for the synthesis of COFs directly from boronic esters, using transesterification with methaneboronic acid (**MBA**) and metathesis with **MBA**-protected catechols (Scheme 4.1.). Using this strategy, we synthesized nine different boroxine and dioxaborole COFs from polyfunctional aryl-Bpins and MBA-protected 2,3,6,7,10,11-hexahydroxytriphenylene (**MBA-HHTP**) and 1,2,4,5-tetrahydroxybenzene (**MBA-THB**). This method opens access to highly stable boroxine and dioxaborole COFs on the basis of chemically sensitive and poorly soluble building blocks.

4.3. Results and discussion

Recently Hinkes and Klien have reported a convenient deprotection of pinacol boronate esters via their transesterification with **MBA** catalyzed by trifluoroacetic acid (TFA) or by collidine base.[23] We hypothesized that applying this approach to multidentate aryl-Bpins may result in their in-situ polymerization directly resulting in the formation of COFs, avoiding the cumbersome deprotection step. As the reversibility/dynamic nature of the reaction is the key for COF crystallinity, we first studied the kinetics of the model pinacol boronate **PBpin** deprotection with **MBA** in the presence of 5 vol% TFA by NMR (Figure 4.1a). The reaction medium (toluene-d_8/dioxane) was chosen to approximate the conditions of the solvothermal COF synthesis.[1] At 90 °C and 1 M concentration of **MBA**, the transesterification reaches an equilibrium in <30 minutes. Examining the reaction kinetics at different starting concentrations, we show that the equilibrium constant is close to unity (K_{eq} = 1.08 ± 0.10), and thus the rate constants of the forward (k_f) and reverse (k_r) reactions are almost identical ($k_f \sim k_r = 5.2 \pm 0.5 \times 10^{-3}$ $M^{-1} s^{-1}$ at 90 °C and ~0.13×10^{-3} $M^{-1} s^{-1}$ at 25 °C, Figures 4.7, 4.9). The deprotection is accompanied by simultaneous condensation of the resulting phenylboronic acid into triphenylboroxine, with a comparable rate (Figure 4.1a).

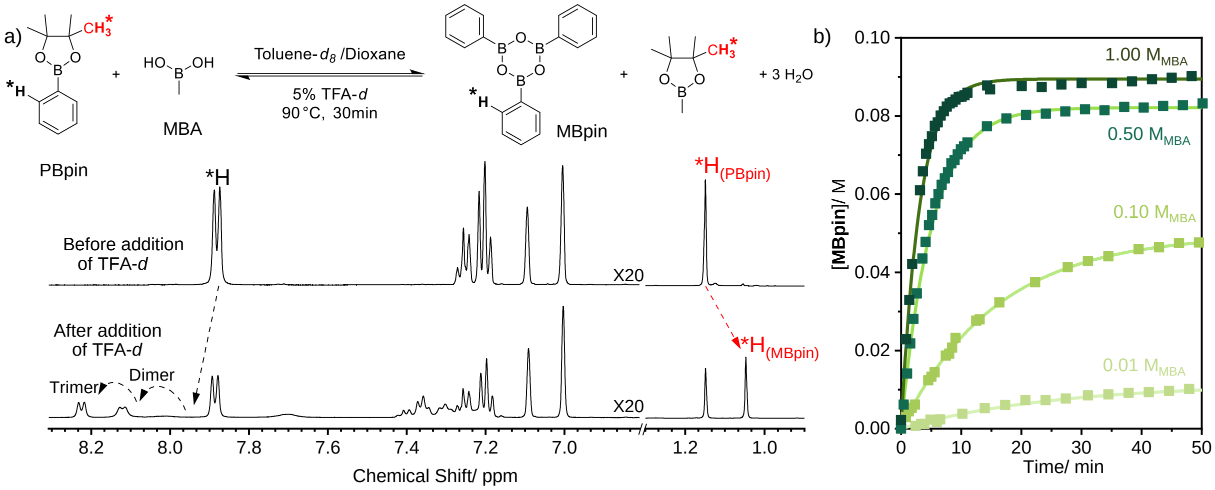

Figure 4.1. a) Reaction scheme and ^{1}H NMR spectra (toluene-d_8/dioxane 1:1, 90 °C) of PBpin (0.1 M) and MBA (0.1 M) before and 1 h after addition of TFA (5 vol%); b) Corresponding kinetic plots of transesterification at different initial concentrations of MBA (scatter plots, quantified using δ_{MBpin} = 1.04 ppm and δ_{PBpin} = 1.14 ppm signals) and fitting kinetics curves (solid lines).

Subjecting a mixture of 1,4-di(pinacolboryl)benzene (**PDBpin**) and **MBA** to standard solvothermal conditions (mesitylene/dioxane, 120 °C) in the presence of TFA results in boroxine-linked **COF-1$_T$** ($_T$ for transesterification) as a white powder (Figure 4.2). The yield of polymerization of PDBpin in a sealed ampule is controlled by equilibrium and varies from 68% with an equimolar amount of **MBA** to nearly quantitative (99%) with 20 eq. excess of **MBA** (Table 4.1). The equilibrium can also be shifted by performing the reaction in an open flask while distilling off the **MBpin** by-product, which was used to prepare crystalline **COF-1$_T$** on a larger scale using an equimolar amount of **MBA**.

The spectroscopic and diffraction data of as-prepared **COF-1$_T$** are identical to those of **COF-1** prepared from benzene-1,4-diboronic acid.[1] The Fourier transform infrared (FTIR) spectroscopy shows the absence of the CH$_{pinacol}$ and OH stretch (*ca.* 2980, 3275 cm^{-1}) and the emergence of a new strong peak at 696 cm^{-1} (B_3O_3 ring out of plane bending[24]) indicating the successful deprotection of the **PDBpin** and the complete condensation of the resulting boronic acid into boroxine (Figure 4.13).

The powder X-ray diffraction (PXRD) pattern of the activated (180 °C, 0.1 mbar, 12 h) **COF-1$_T$** displayed the characteristic[1] diffraction pattern with peaks at 2θ= 6.8°, 11.7°, 13.7°, 15.0°, 19.2°

and 27.1° (Figure 4.2). The Pawley refinement (Table 4.8) of the diffraction pattern of **COF-1$_T$** indicates the same unit cell and very similar crystallinity (FWHM= 0.4°) with the published **COF-1**.[1] The Brunauer–Emmett–Teller (BET) surface area of the activated **COF-1$_T$** (794 m^2g^{-1}, Figure 4.16) is close to the higher end of reported surface areas for **COF-1** (690-812 m^2 g^{-1}).[1, 25]

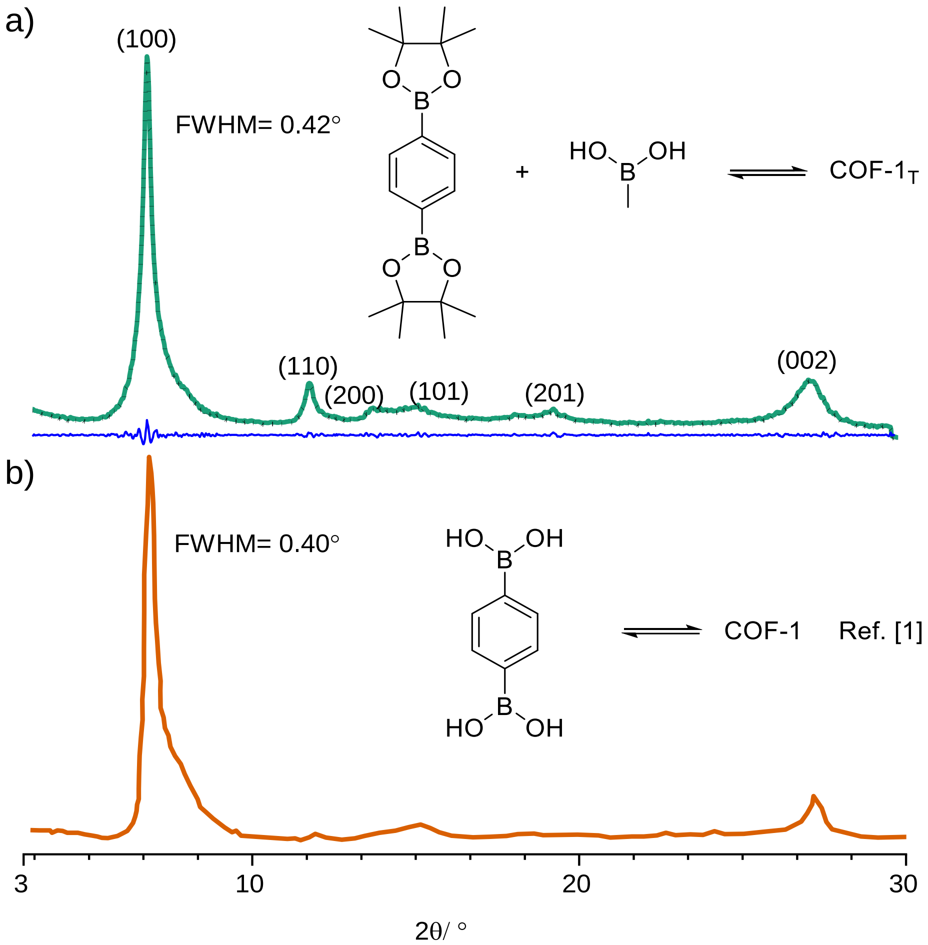

Figure 4.2. PXRD of activated **COF-1$_T$** (green) with Pawley refinement (dotted black, residual in blue) and of **COF-1** synthesized by the conventional method (orange; replotted from ref. [1]).

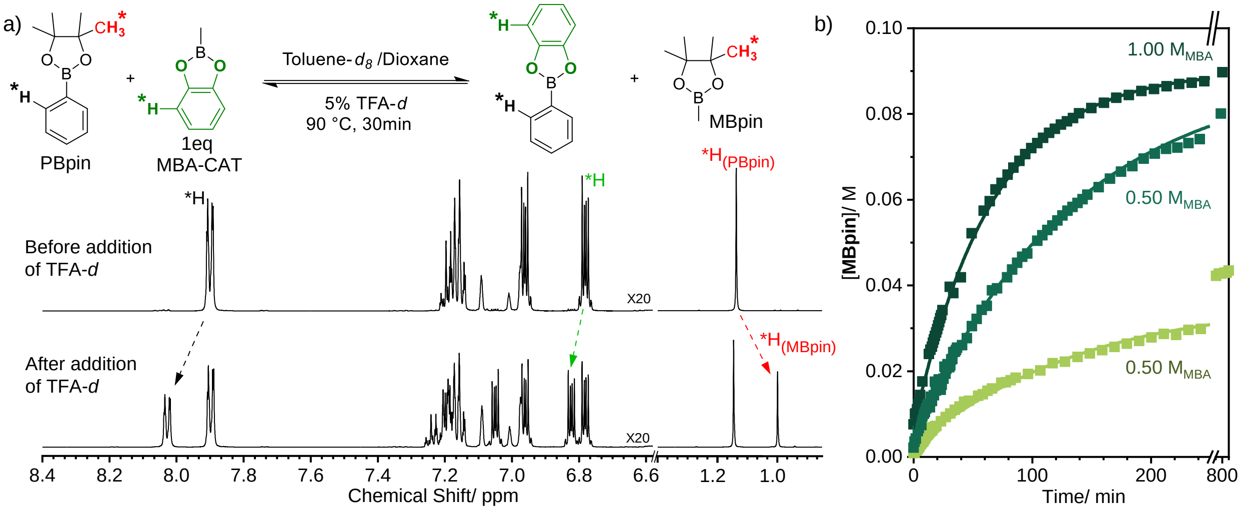

Figure 4.3. a) Reaction scheme and ^{1}H NMR spectra (toluene-d_8/dioxane 1:1, 90°C) of **PBpin** (0.1 M) and **MBA-CAT** (0.1 M) before and 5 h after addition of TFA (5 vol%); b) Corresponding kinetic plots of metathesis at different initial concentrations of **MBA-CAT** (scatter plots, quantified using δ_{MBpin} = 1.04 ppm and δ_{PBpin} = 1.14 ppm signals) and fitting kinetics curves (solid lines).

When the in-situ deprotection/polymerization is carried out in the presence of multifunctional catechols, the reaction directly produces dioxaborole-linked COFs. Thus, **PDBpin** in the presence of **HHTP** resulted in **COF-5$_T$** with diffraction and spectroscopic characteristics consistent with those previously reported for **COF-5** obtained from benzene-1,4-diboronic acid (Figure 4.20).[1] We note that oxidative instability and low solubility of **HHTP** and most other polyfunctional catechols are significant problems for the synthesis of high-quality dioxaborole COFs.[12] Using catechol monomers inevitably leads to oxidized (colored) impurities which are detrimental for optoelectronic applications. Even when the reaction is carried out in the strictest anaerobic condition, the trace amounts of catechols trapped in the COF pores will lead to noticeable colorization upon storage. To solve this problem of catechols instability and poor solubility, we decided to explore an exchange reaction (*metathesis*) of **MBA**-protected catechols with pinacol boronate esters to access dioxaborole COFs. Unlike their catechol precursors, **MBA-HHTP** and **MBA-THB** are highly stable in ambient conditions (Figure 4.38), soluble in common organic solvents, and can be easily sublimed under vacuum.

The kinetic measurements on the model reaction of PBpin with MBA-CAT show a ~20-fold decrease of the rate constants (0.26 ± 0.02 $\times 10^{-3}$ M^{-1} s^{-1} at 90 °C, 5% TFA, Figures 4.3b, 4.9b) comparing to transesterification (Figure 4.1b). The reaction reaches equilibrium within a few hours, with $K_{eq} = 0.71 \pm 0.12$. As expected, no boronic acid/boroxine intermediates are detected during the metathesis (Figures 4.3a, 4.8b) and, in contrast to all reported boronic COFs, water is neither produced during nor required for dynamic polymerization/crystallization of the COF. **COF-5$_M$** ($_M$ for metathesis) was synthesized from **MBA-HHTP** and **PDBpin** in 77% yield only in ~1 h. Surprisingly, the reaction occurred even in the absence of the TFA catalyst, over a longer time. The FTIR spectrum of **COF-5$_M$** is almost indistinguishable from that of **COF-5** prepared from corresponding boronic acid and catechol (Figure 4.19), but unlike the latter, it shows the complete absence of OH stretch due to $B(OH)_2$ defects and end-group (*ca.* 3250 cm^{-1}) in **COF-5$_M$**, indicative of a much lower density of $B(OH)_2$ defects compared to the standard **COF-5**.[1] PXRD of **COF-5$_M$** shows same sharp diffraction peaks at 3.4°, 6.0°, 6.4°, 9.1° as the reported **COF-5** (Figure 4.4a). Its BET surface area (1610 $m^2 g^{-1}$) and the pore size (26 Å, Figure 4.4b) are essentially identical to those reported for **COF-5** (1590 $m^2 g^{-1}$; 26 Å).[1] However, **COF-5$_M$** displays a significantly improved optical purity comparing to **COF-5** (Figure 4.4d). As expected from its large DFT-calculated bandgap (3.88 eV, Figure 4.35), **COF-5$_M$** is colorless, while the dark-grey tint of **COF-5** indicates the presence of catechol oxidation products (semiquinone radicals and quinones/hydroquinone charge-transfer complexes, Figure 4.39) which are also manifested in a strong EPR signal (Figure 4.4 c). The fluorescence lifetimes of the **COF-5$_M$** show longer decay times as compared to **COF-5** (Figure 4.4d, 4.34.; $\tau = 5.7 \pm 0.13$ ns for **COF-5$_M$**, 2.3 ± 0.19 ns **COF-5** prepared under N_2 and 3 ns for **COF-5** reported previously)[26] which can be attributed to the elimination of fluorescence-quenching impurities.

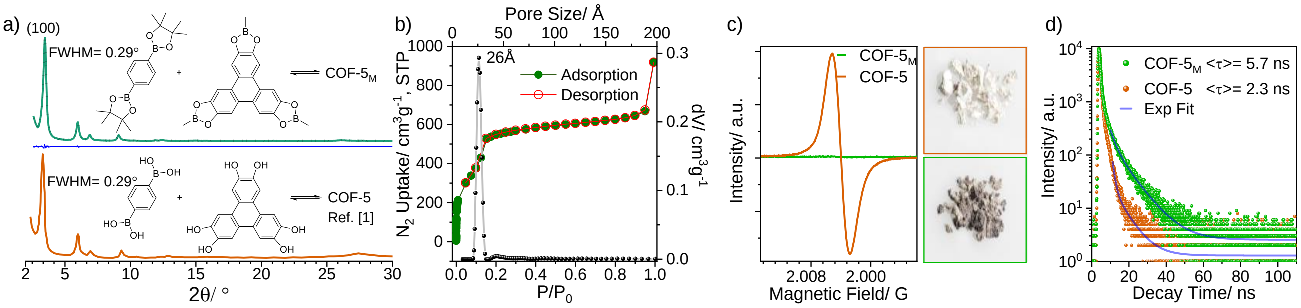

Figure 4.4. a) PXRD of activated **COF-5$_M$** (green) with Pawley refinement (dotted black, residual in blue, Table 4.8) and of **COF-5** synthesized by the conventional method (orange; data replotted from ref. [1]). b) N_2 adsorption isotherm for **COF-5$_M$** and corresponding pore size distribution (black). c) EPR spectra and photographs of **COF-5$_M$** (green) and **COF-5** (orange). d) Fluorescence decay curves, λ_{ex}= 373 nm and λ_{em}= 430 nm.

Kinetic analysis of COF formation is important for the understanding of the growth mechanism and reaction optimization towards improved COF crystallinity/order.[27-32] However, analyzing the kinetics of heterogeneous polymerization is a challenge, and only recently the experimental measurements of the kinetic of COF formation have been reported using X-ray scattering,[32, 33] turbidity,[34, 35], and PXRD/Raman spectroscopy.[36] Each of these techniques possesses its unique advantages and limitations, but none has the generality/resolution of liquid NMR, as commonly employed in measuring the rate of bond formation in molecular chemistry. Since both the reactants and the by-product (**MBpin**) are soluble and thus quantifiable by NMR, our metathesis polymerization allows for easy kinetic study of polymerization. Unlike turbidity which is based on monitoring the formation of micron-scale COF particles and is limited to the early stages of the reaction (<30% completion)[34], NMR screening allows the full range kinetic analysis (0-100%).

The initial rate kinetic measurements on the **COF-5$_M$** formation (0.1 M **PDBpin** with 0.066 M **MBA-HHTP**) in presence of TFA (5 vol%) at 90 °C showed the rate constant *ca.* 300 times faster than when the same reaction is performed in the absence of TFA as the catalyst (Figure 4.5, determined from the initial rate kinetics). It is noteworthy that the rate constant of the COF formation is ~70 times faster than that of **MBA-CAT** (the model compound). This is important because the kinetics of molecular model reactions has been used in theoretical modeling of COF formation, but the differences between them are believed to be the source of discrepancies with the experimental observations.[31]

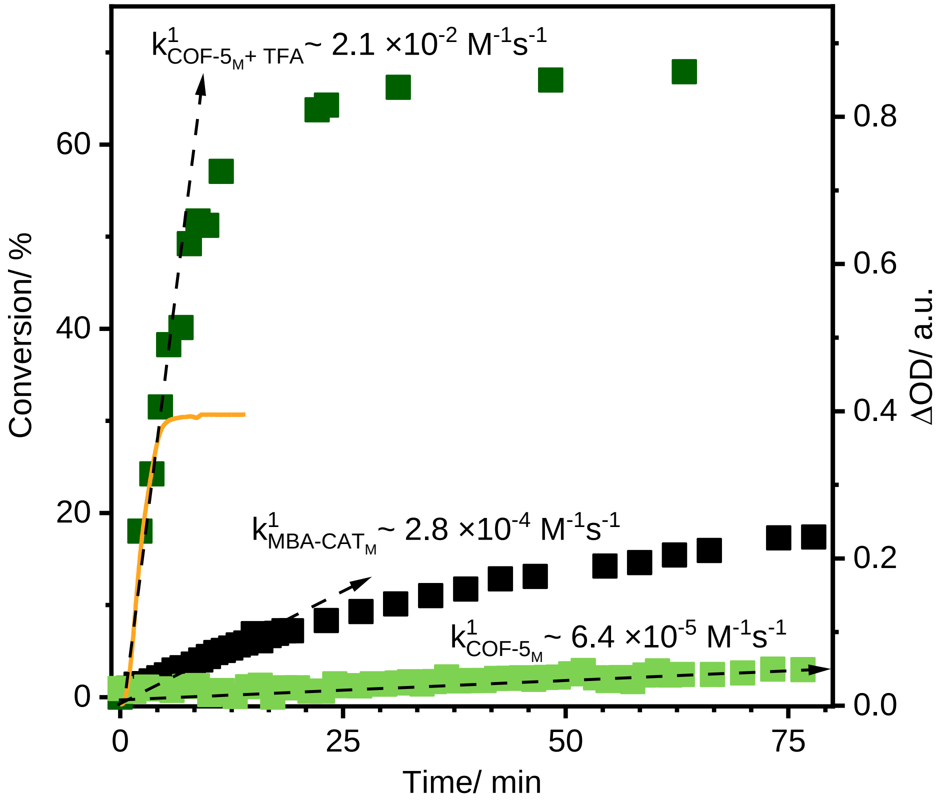

Figure 4.5. Kinetic plot of metathesis for **COF-5$_M$** formation (0.1 M PDBpin and 0.066 M **MBA-HHTP**, toluene-*d*$_8$/dioxane 1:1, 90°C) in the absence of TFA (light green), and in 5 vol% TFA (NMR: dark green, turbidity (ΔOD): orange) *vs.* metathesis of **PBpin** (0.1 M) + **MBA-CAT** (0.1 M) + 5 vol% TFA in the same conditions (black). Dashed arrows show the rate constant obtained from the initial rate kinetics.

Both the transesterification and the metathesis polymerization approaches are general as demonstrated by the successful synthesis of **PPyCOF**,[9] **COF-18Å**,[37] **COF-6**,[8] **COF-10**,[8, 38], and **TP-COF**[39] that have been previously made from deprotected boronic acid and catechol precursors (Scheme 4.2.). All COFs were obtained in high yields (66-79%) with crystallinity and porosities identical to the previous reports (see Figures 4.13-4.33 and Tables 4.1-4.7 for the synthetic details and characterization).

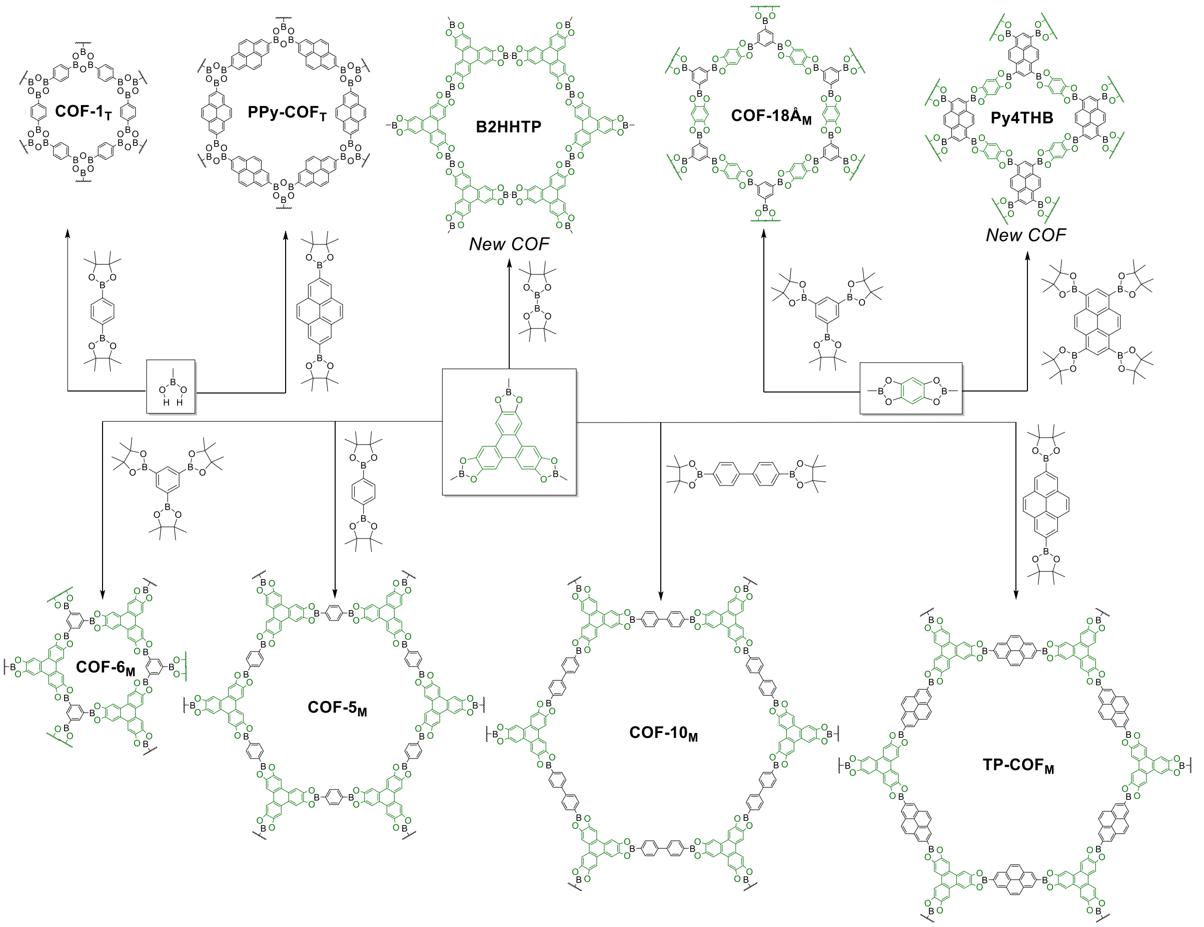

Scheme 4.2. Scope of the COF synthesis via transesterification and metathesis reactions.

Having demonstrated the general applicability of the aryl-Bpin metathesis polymerization in the synthesis of the known COFs, we decided to apply this reaction for new COFs which would be challenging to obtain by classical condensation of boronic acids (Figure 4.6). The oblique Liebe lattice of **Py4THB** is of potential interest for materials with exotic electronic and magnetic properties.[40-42] Although 1,3,6,8-pyrenetetraboronic acid is known,[43] no COFs have been reported with this building block. The extremely low solubility of this compound impedes its chemical reactivity and even spectroscopic characterization.[43] On the contrary, its pinacol ester, BpinPy4, is highly soluble in organic solvents and can be readily purified by chromatography and recrystallization. Metathesis of the BpinPy4 with **MBA-THB** produces **Py4THB** COF as a yellow powder in 87% yield (Figure 4.6a). The FTIR spectroscopy of the **Py4THB** shows the complete disappearance of $CH_{3(Bpin)}$ (*ca.* 2977cm^{-1}) stretching vibration bands (Figure 4.31). The PXRD measurement reveals characteristic diffraction peaks at 2θ = 6.16° (100), 12.35° (200), 26.6° (001)

as expected for the AA stacked oblique lattice model (Figures 4.6a, 4.36 and Table 4.8). The BET porosity measurement of the activated COFs reveal high surface area of 822 $m^2.g^{-1}$ (Figure 4.32; theoretical value of 1260 $m^2.g^{-1}$) and average pore size of 11 Å (theoretical pore size 11.4 Å).

The absence of water in the metathesis polymerization can open access to hydrolytically unstable building blocks for the synthesis of COFs. Previous attempts to synthesize the **B2HHTP** COF (Scheme 4.2.) by condensation of tetrahydroxydiboron with **HHTP** resulted in a low yield (30%) and poor crystallinity of the product.[44] We speculate that oxidative cleavage of the B-B bond by water[45] could be the reason for these discouraging results. However, metathesis polymerization of **B_2Pin_2** with **MBA-HHTP** affords highly crystalline **B2HHTP** COF in 90% yield. The FTIR is in line with the expected changes (Figure 4.33) and the PXRD shows diffraction peaks at 2θ = 4.67° (100), 8.07° (110), 9.22° (200), 12.25° (210), 16.71° (310), 27.0° (001) as predicted by the AA stacked hexagonal model (Figure 4.37 and Table 4.8).

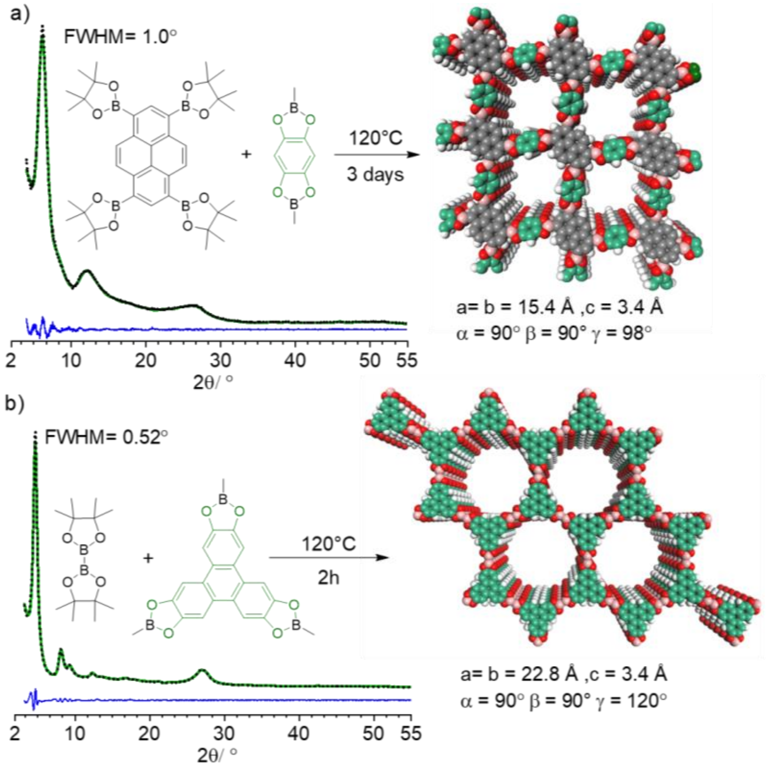

Figure 4.6. PXRD pattern(green) with Pawley refinement (dotted black, residual in blue, Table 4.8) of a) **Py4THB** and b) **B2HHTP**. DFT optimized (B3LYP/6-31G(d)) models with calculated unit cells shown on the right.

4.4. Conclusion

We reported a one-step synthesis of boroxine and dioxaborole COFs directly from pinacol-protected multidentate areneboronates using a transesterification with methylboronic acid and a new metathesis polymerization with catechol methylboronates. While preparation of such COFs from corresponding areneboronic acids is well established, our method presents noteworthy advantages for large aromatic or chemically sensitive building blocks, as it allows using highly soluble/easily characterizable and stable boronic esters instead of boronic acids and avoids the deprotection step. The dioxaborole COFs synthesized using metathesis polymerization benefit from high optical purity and low density of defects *vs.* those synthesized by standard polycondensation, due to elimination of unprotected chemically sensitive catechols. Also, water is neither formed in the metathesis reaction nor is required to achieve crystalline COFs which opens opportunities for precise control of dynamic polymerization and provides access to sensitive areneboronic acids (which can undergo protodeborylation in presence of water). We have shown the generality of these reactions by synthesizing seven popular COFs and also applied the metathesis polymerization to obtain two new COFs **(Py4THB and B2HHTP)** which could not be prepared using a standard polycondensation due to the extreme insolubility and instability of the corresponding boronic acid, respectively.

4.5. Acknowledgments

We thank Hatem M. Titi for assistance with N_2-isotherm analysis and X-ray diffraction, Robin S. Stein for the help with NMR spectroscopy, and Alexander Wahba and Nadim Saade for mass spectrometry.

4.6. References

1. Côté, A. P.; Benin, A. I.; Ockwig, N. W.; O'Keeffe, M.; Matzger, A. J.; Yaghi, O. M., Porous, Crystalline, Covalent Organic Frameworks. *Science* **2005,** *310*, 1166-1170.

2. Geng, K.; He, T.; Liu, R.; Dalapati, S.; Tan, K. T.; Li, Z.; Tao, S.; Gong, Y.; Jiang, Q.; Jiang, D., Covalent Organic Frameworks: Design, Synthesis, and Functions. *Chem. Rev.* **2020,** *120*, 8814-8933.

3. Liu, X.; Huang, D.; Lai, C.; Zeng, G.; Qin, L.; Wang, H.; Yi, H.; Li, B.; Liu, S.; Zhang, M., Recent advances in covalent organic frameworks (COFs) as a smart sensing material. *Chem. Soc. Rev.* **2019,** *48*, 5266-5302.

4. Kandambeth, S.; Dey, K.; Banerjee, R., Covalent Organic Frameworks: Chemistry beyond the Structure. *J. Am. Chem. Soc.* **2019,** *141*, 1807-1822.

5. Huang, N.; Wang, P.; Jiang, D., Covalent organic frameworks: a materials platform for structural and functional designs. *Nat. Rev. Mater.* **2016,** *1*, 16068.

6. Evans, A. M.; Parent, L. R.; Flanders, N. C.; Bisbey, R. P.; Vitaku, E.; Kirschner, M. S.; Schaller, R. D.; Chen, L. X.; Gianneschi, N. C.; Dichtel, W. R., Seeded growth of single-crystal two-dimensional covalent organic frameworks. *Science* **2018,** *361*, 52-57.

7. Bertrand, G. H.; Michaelis, V. K.; Ong, T. C.; Griffin, R. G.; Dinca, M., Thiophene-based covalent organic frameworks. *Proc. Natl. Acad. Sci. U. S. A.* **2013,** *110*, 4923-4928.

8. Cote, A. P.; El-Kaderi, H. M.; Furukawa, H.; Hunt, J. R.; Yaghi, O. M., Reticular synthesis of microporous and mesoporous 2D covalent organic frameworks. *J. Am. Chem. Soc.* **2007,** *129*, 12914-12915.

9. Wan, S.; Guo, J.; Kim, J.; Ihee, H.; Jiang, D., A photoconductive covalent organic framework: self-condensed arene cubes composed of eclipsed 2D polypyrene sheets for photocurrent generation. *Angew. Chem. Int. Ed.* **2009,** *48*, 5439-5442.

10. Evans, A. M.; Castano, I.; Brumberg, A.; Parent, L. R.; Corcos, A. R.; Li, R. L.; Flanders, N. C.; Gosztola, D. J.; Gianneschi, N. C.; Schaller, R. D.; Dichtel, W. R., Emissive Single-Crystalline Boroxine-Linked Colloidal Covalent Organic Frameworks. *J. Am. Chem. Soc.* **2019,** *141*, 19728-19735.

11. El-Kaderi, H. M.; Hunt, J. R.; Mendoza-Cortés, J. L.; Côté, A. P.; Taylor, R. E.; O'Keeffe, M.; Yaghi, O. M., Designed synthesis of 3D covalent organic frameworks. *Science* **2007,** *316*, 268-272.

12. Spitler, E. L.; Dichtel, W. R., Lewis acid-catalysed formation of two-dimensional phthalocyanine covalent organic frameworks. *Nat. Chem.* **2010,** *2*, 672-677.

13. Dogru, M.; Sonnauer, A.; Zimdars, S.; Döblinger, M.; Knochel, P.; Bein, T., Facile synthesis of a mesoporous benzothiadiazole-COF based on a transesterification process. *CrystEngComm* **2013,** *15*, 1500-1502.

14. Cox, P. A.; Leach, A. G.; Campbell, A. D.; Lloyd-Jones, G. C., Protodeboronation of Heteroaromatic, Vinyl, and Cyclopropyl Boronic Acids: pH-Rate Profiles, Autocatalysis, and Disproportionation. *J. Am. Chem. Soc.* **2016,** *138*, 9145-9157.

15. Lennox, A. J. J.; Lloyd-Jones, G. C., Selection of boron reagents for Suzuki–Miyaura coupling. *Chem. Soc. Rev.* **2014,** *43*, 412-443.

16. Hall, D. G., *Boronic acids: preparation, applications in organic synthesis and medicine*. John Wiley & Sons: 2006.

17. Roy, C. D.; Brown, H. C., Stability of boronic esters – Structural effects on the relative rates of transesterification of 2-(phenyl)-1,3,2-dioxaborolane. *J. Organomet. Chem.* **2007,** *692*, 784-790.

18. Matteson, D. S.; Michnick, T. J.; Willett, R. D.; Patterson, C. D., [(1R)-1-acetamido-3-(methylthio) propyl] boronic acid and the x-ray structure of its ethylene glycol ester. *Organometallics* **1989,** *8*, 726-729.

19. Coutts, S. J.; Adams, J.; Krolikowski, D.; Snow, R. J., Two efficient methods for the cleavage of pinanediol boronate esters yielding the free boronic acids. *Tetrahedron Lett.* **1994,** *35*, 5109-5112.

20. Diemer, V.; Chaumeil, H.; Defoin, A.; Carré, C., Syntheses of extreme sterically hindered 4-methoxyboronic acids. *Tetrahedron* **2010,** *66*, 918-929.

21. Vitaku, E.; Dichtel, W. R., Synthesis of 2D Imine-Linked Covalent Organic Frameworks through Formal Transimination Reactions. *J. Am. Chem. Soc.* **2017,** *139*, 12911-12914.

22. Zhao, C.; Lyu, H.; Ji, Z.; Zhu, C.; Yaghi, O. M., Ester-Linked Crystalline Covalent Organic Frameworks. *J. Am. Chem. Soc.* **2020,** *142*, 14450-14454.

23. Hinkes, S. P. A.; Klein, C. D. P., Virtues of Volatility: A Facile Transesterification Approach to Boronic Acids. *Org. Lett.* **2019,** *21*, 3048-3052.

24. Smith, M. K.; Northrop, B. H., Vibrational Properties of Boroxine Anhydride and Boronate Ester Materials: Model Systems for the Diagnostic Characterization of Covalent Organic Frameworks. *Chem. Mater.* **2014,** *26*, 3781-3795.

25. Dong, D.; Zhang, H.; Zhou, B.; Sun, Y.; Zhang, H.; Cao, M.; Li, J.; Zhou, H.; Qian, H.; Lin, Z.; Chen, H., Porous covalent organic frameworks for high transference number polymer-based electrolytes. *Chem. Commun.* **2019,** *55*, 1458-1461.

26. Flanders, N. C.; Kirschner, M. S.; Kim, P.; Fauvell, T. J.; Evans, A. M.; Helweh, W.; Spencer, A. P.; Schaller, R. D.; Dichtel, W. R.; Chen, L. X., Large Exciton Diffusion Coefficients in Two-Dimensional Covalent Organic Frameworks with Different Domain Sizes Revealed by Ultrafast Exciton Dynamics. *J. Am. Chem. Soc.* **2020,** *142*, 14957-14965.

27. Koo, B.; Heden, R.; Clancy, P., Nucleation and growth of 2D covalent organic frameworks: polymerization and crystallization of COF monomers. *Phys. Chem. Chem. Phys.* **2017,** *19*, 9745-9754.

28. Nguyen, V.; Grunwald, M., Microscopic Origins of Poor Crystallinity in the Synthesis of Covalent Organic Framework COF-5. *J. Am. Chem. Soc.* **2018,** *140*, 3306-3311.

29. Li, H.; Evans, A. M.; Castano, I.; Strauss, M. J.; Dichtel, W. R.; Bredas, J. L., Nucleation-Elongation Dynamics of Two-Dimensional Covalent Organic Frameworks. *J. Am. Chem. Soc.* **2020,** *142*, 1367-1374.

30. Li, H.; Chavez, A. D.; Li, H.; Li, H.; Dichtel, W. R.; Bredas, J. L., Nucleation and Growth of Covalent Organic Frameworks from Solution: The Example of COF-5. *J. Am. Chem. Soc.* **2017,** *139*, 16310-16318.

31. Li, H.; Evans, A. M.; Dichtel, W. R.; Bredas, J.-L., Quantitative Description of the Lateral Growth of Two-Dimensional Covalent Organic Frameworks Reveals Self-Templation Effects. *ACS Mater. Lett.* **2021,** *3*, 398-405.

32. Castano, I.; Evans, A. M.; Li, H.; Vitaku, E.; Strauss, M. J.; Bredas, J. L.; Gianneschi, N. C.; Dichtel, W. R., Chemical Control over Nucleation and Anisotropic Growth of Two-Dimensional Covalent Organic Frameworks. *ACS Cent. Sci.* **2019,** *5*, 1892-1899.

33. Li, R. L.; Flanders, N. C.; Evans, A. M.; Ji, W.; Castano, I.; Chen, L. X.; Gianneschi, N. C.; Dichtel, W. R., Controlled growth of imine-linked two-dimensional covalent organic framework nanoparticles. *Chem. Sci.* **2019,** *10*, 3796-3801.

34. Smith, B. J.; Dichtel, W. R., Mechanistic studies of two-dimensional covalent organic frameworks rapidly polymerized from initially homogenous conditions. *J. Am. Chem. Soc.* **2014,** *136*, 8783-8789.

35. Smith, B. J.; Hwang, N.; Chavez, A. D.; Novotney, J. L.; Dichtel, W. R., Growth rates and water stability of 2D boronate ester covalent organic frameworks. *Chem. Commun.* **2015,** *51*, 7532-7535.

36. Emmerling, S. T.; Germann, L. S.; Julien, P. A.; Moudrakovski, I.; Etter, M.; Friščić, T.; Dinnebier, R. E.; Lotsch, B. V., In situ monitoring of mechanochemical covalent organic framework formation reveals templating effect of liquid additive. *Chem* **2021,** *7*, 1639-1652.

37. Tilford, R. W.; Gemmill, W. R.; zur Loye, H.-C.; Lavigne, J. J., Facile Synthesis of a Highly Crystalline, Covalently Linked Porous Boronate Network. *Chem. Mater.* **2006,** *18*, 5296-5301.

38. Doonan, C. J.; Tranchemontagne, D. J.; Glover, T. G.; Hunt, J. R.; Yaghi, O. M., Exceptional ammonia uptake by a covalent organic framework. *Nat. Chem.* **2010,** *2*, 235-238.

39. Wan, S.; Guo, J.; Kim, J.; Ihee, H.; Jiang, D., A belt-shaped, blue luminescent, and semiconducting covalent organic framework. *Angew. Chem. Int. Ed.* **2008,** *47*, 8826-8830.

40. Jin, E.; Asada, M.; Xu, Q.; Dalapati, S.; Addicoat, M. A.; Brady, M. A.; Xu, H.; Nakamura, T.; Heine, T.; Chen, Q.; Jiang, D., Two-dimensional sp(2) carbon-conjugated covalent organic frameworks. *Science* **2017,** *357*, 673-676.

41. Cui, B.; Zheng, X.; Wang, J.; Liu, D.; Xie, S.; Huang, B., Realization of Lieb lattice in covalent-organic frameworks with tunable topology and magnetism. *Nat. Commun.* **2020,** *11*, 66.

42. Jiang, W.; Huang, H.; Liu, F., A Lieb-like lattice in a covalent-organic framework and its Stoner ferromagnetism. *Nat. Commun.* **2019,** *10*, 2207.

43. Wakchaure, V. C.; Ranjeesh, K. C.; Goudappagouda; Das, T.; Vanka, K.; Gonnade, R.; Babu, S. S., Mechano-responsive room temperature luminescence variations of boron conjugated pyrene in air. *Chem. Commun.* **2018,** *54*, 6028-6031.

44. PP, R.; Mondal, P. K.; Chopra, D., Synthesis and characterization of a 2D covalent organic framework (COF) of hexagonal topology using boronate linkages. *J. Chem. Sci.* **2018,** *130*, 51.

45. Wiberg, E.; Ruschmann, W., Über eine neue Borsäure (‚Unterborsäure') der Formel $H_4B_2O_4$ und ihre Ester. *Ber. Dtsch. Chem. Ges.* **1937,** *70*, 1393-1402.

4.7. Supplementary information

4.7.1. Materials and General Methods:

All boronic acids and pinacolate esters were purchased from CombiBlocks and used without further purification. Dried solvents (DCM, $CHCl_3$, THF, acetone) were purified on a MBraun solvent purification system and kept under activated 4 Å molecular sieves at least 48 h before use. Other solvents were purchased from commercial sources and used without further purification. Column chromatography was performed using silica gel on an Isolera One Flash instrument from Biotage.

FTIR spectra of powders were obtained on a Nicolet 6700 FT-IR instrument in the 600–4,000 cm^{-1} region using a Diamond ATR (SmartOrbit). ^{1}H and ^{13}C NMR spectra and VT-kinetic measurements were recorded on a Varian 500 (^{1}H, 500 MHz; ^{13}C, 126 MHz) and ^{11}B NMRs were recorded on a Bruker 400 (^{11}B, 128 MHz). ^{1}H NMR chemical shifts are reported relative to TMS and were referenced via residual proton resonances of the corresponding deuterated solvent (e.g. $CDCl_3$: 7.26 ppm); ^{13}C NMR spectra are reported relative to TMS via the carbon signals of the deuterated solvent (e.g. $CDCl_3$: 77.16 ppm). Signals for the carbons attached to boron, C(aryl)-B, are usually too broad to observe in the ^{13}C NMR spectra. ^{11}B NMR chemical shifts are quoted relative to $BF_3 \cdot Et_2O$ as the external standard. The NMR signals of anhydrides of benzeneboronic acid in Figure 4.1 were assigned according to the reported values.[1, 2] The NMR spectra of the synthesized precursors are reported in Appendix 4.

Electron paramagnetic resonance (EPR) measurements were obtained with a Bruker Elexsys 680 X-band EPR spectrometer.

Powder XRD measurements were performed in the transmission mode of the samples held between two thin mylar sheets using a Panalytical Empyrean diffractometer equipped with Mo anode (60 kV, 40 mA) and PIXcel3D detector. This gives a strong splitting of the $K\alpha_1$ and $K\alpha_2$ such that $K\alpha_2$ stripping was performed effectively. For ease of comparison with the rest of the literature, the scattering angles for all XRD patterns in this manuscript have been converted to match those obtained with Cu $K\alpha_1$ radiation. Surface area measurements were conducted on an Autosorb iQ (Quantachrome) analyzer by sorption of nitrogen (99.999%) at 77 K with activated

COFs (*ca.* 20 mg) degassed at 180 °C for 12 hours. Surface parameters were determined using multi-point BET (pressure range of 0.05-0.3) and Quenched Solid DFT(QSDFT) adsorption models included in the instrument software.

Density functional theory (DFT) calculations of the optimized COF geometries were performed on single layer COF (2D model), using B3LYP functional and 6-31G (d) basis set, under periodic boundary conditions as implemented in Gaussian 16.[3] Then different stacking modes (3D models) were assembled and the simulated PXRD was compared with the experimental PXRD.

PXRD refinements were performed using the Reflex module in Materials Studio. Background of the PXRD spectrum was removed, as well as by further refinements, in which the Thompson-Cox-Hastings pseudo-Voigt profile function was used for the profile fitting where all FWHM parameters (U, V, X, Y) were allowed to vary, and in addition, the zero-shift was corrected. Peak asymmetry was corrected using the Rietveld correction. Crystallite size and lattice strain broadenings were also refined. It should be noted that the instrument broadening is approximately 0.10° (FWHM) using a roughly ground silicon single crystal. This instrument FWHM is considerably smaller than all peak widths reported here and accounts for at most a 15% broadening of the sample peaks given the peaks are near Gaussian in shape and the smallest measured FWHM reported here is 0.19°. No correction for instrument broadening is therefore applied in the calculations of crystallite size.

The theoretical surface area was simulated using the 3D COF models, by Accessible solvent surface(@1.4Å) and volumes in the Material studio with a gridline of 0.15 Å.

4.7.2. Kinetic measurements.

Transesterification and metathesis were studied using ^{1}H NMR spectroscopy. To a 1 mL solution of 0.1 M (pinacolboryl)benzene (PBpin) in 1:1 toluene-d_8:Dioxane was added methaneboronic acid (**MBA**; for transesterification) or **MBA**-protected 1,2-dihydroxy benzene (**MBA-CAT**; for metathesis). TFA-*d* was then added to the mixture and the ^{1}H NMR spectra were recorded over time. The reaction progress was traced using integration of $H_{b(PBpin)}/H'_{b(MBpin)}$ (δ_{MBpin} ~ 1.04 ppm and δ_{MBpin} ~ 1.14 ppm).

The rate constants were obtained using the following rate-law approximation. For a reaction of a+b ⇌ c+d where K_{eq} = k_f/k_r = 1 (k_f = k_r where k_f and k_r are the rates of forward and backward reaction of the Equilibrium), if $[c]_0 = [d]_0 = 0$ and x_t is the extent of the reaction progress in each measured time and x_e is the extent of reaction at the equilibrium, the rate law can be written as:[4]

$$-[\ln(x_e - x_t) - \ln(x_e)]/([a]_0 + [b]_0) = kt$$

Equation 4.1

where k ($M^{-1}s^{-1}$) is the rate constant of the second-order reaction and k = k_f = k_b.

The reaction kinetics were fitted using the ReactLab KinSim free software developed by JPlus Consulting.[5]

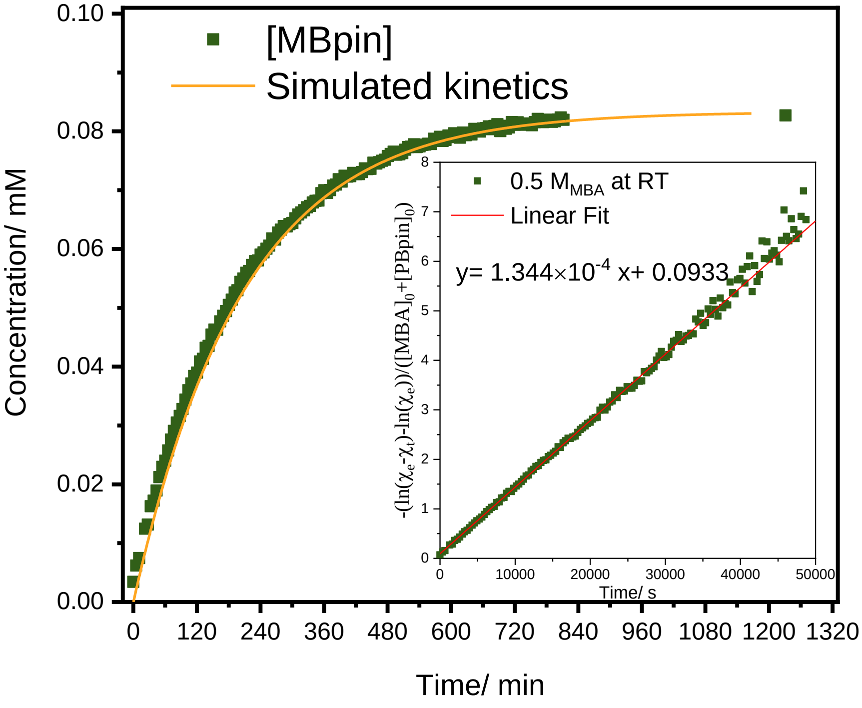

Figure 4.7. The kinetic plot of the transesterification reaction obtained from the ^{1}H NMR spectra (toluene-*d*$_8$/dioxane 1:1, 25°C) of PBpin (0.1 M) and MBA (0.5 M) with the addition of TFA (5 vol%). The inset is the plot of approximated rate-law according to equation 4.1. Scatter plots were quantified using δ_{MBpin} ~ 1.04 ppm and δ_{MBpin} ~ 1.14 ppm signals) and fitting kinetics curves (solid lines).

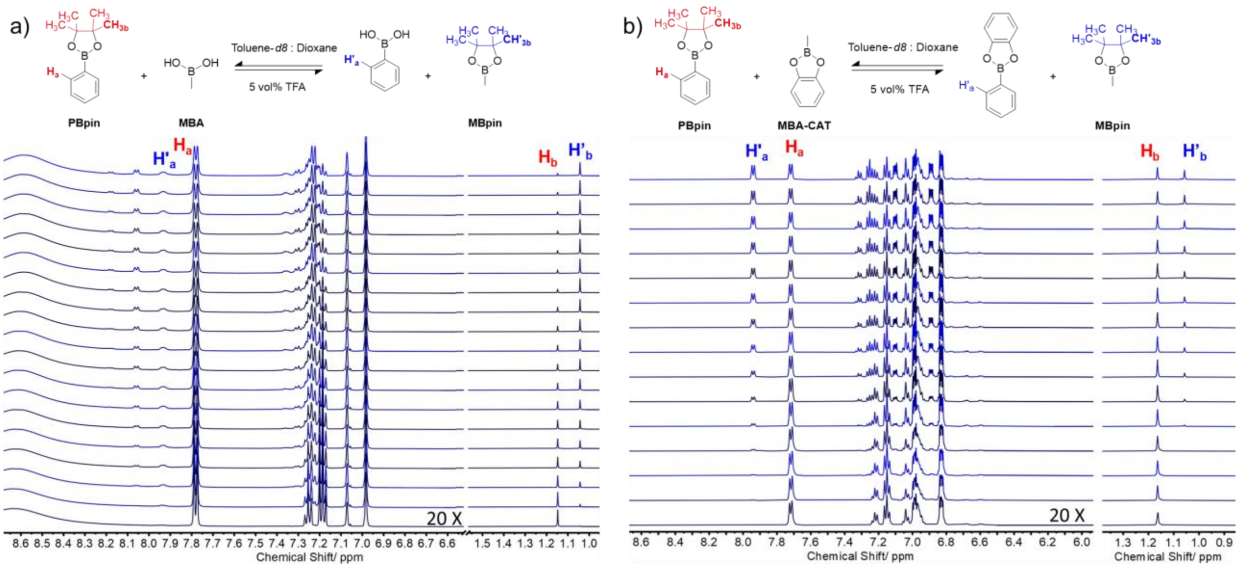

Figure 4.8. Reaction scheme and time evolution of ^{1}H NMR spectra (toluene-d_8/dioxane 1:1) for a) transesterification of PBpin (0.1 M) and MBA (0.5 M) after addition of TFA (5 vol%) at 25°C and b) transesterification of PBpin (0.1 M) and MBA-CAT (0.1 M) after addition of TFA (5 vol%) at 90°C.

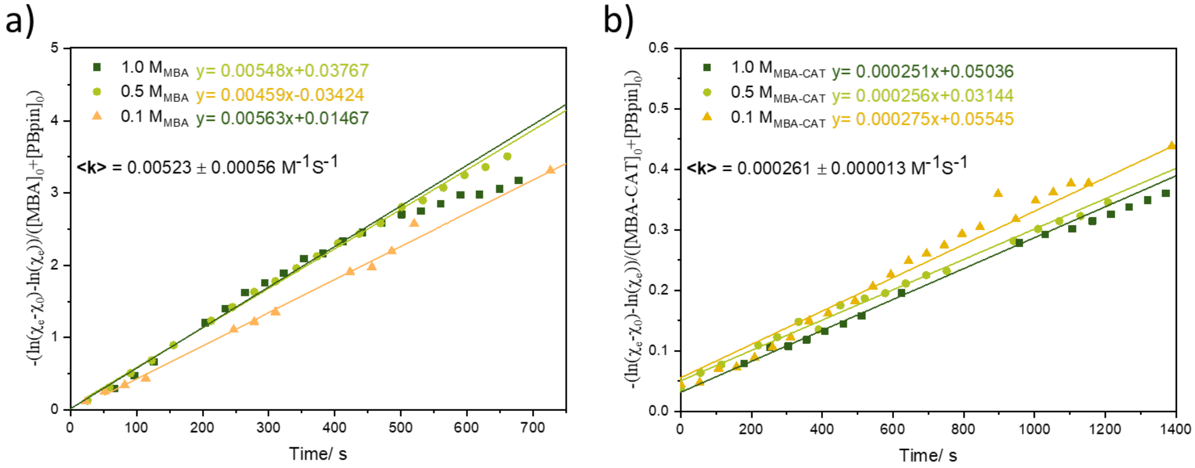

Figure 4.9. The plot of the reaction kinetics of a) transesterification (Figure 4.1) and b) metathesis (Figure 4.3) of 0.1 M **PBpin** and different initial concentrations of **MBA** or **MBA-CAT** (scatter plots) at 90 °C and the extracted the rate constants according to equation 4.1.

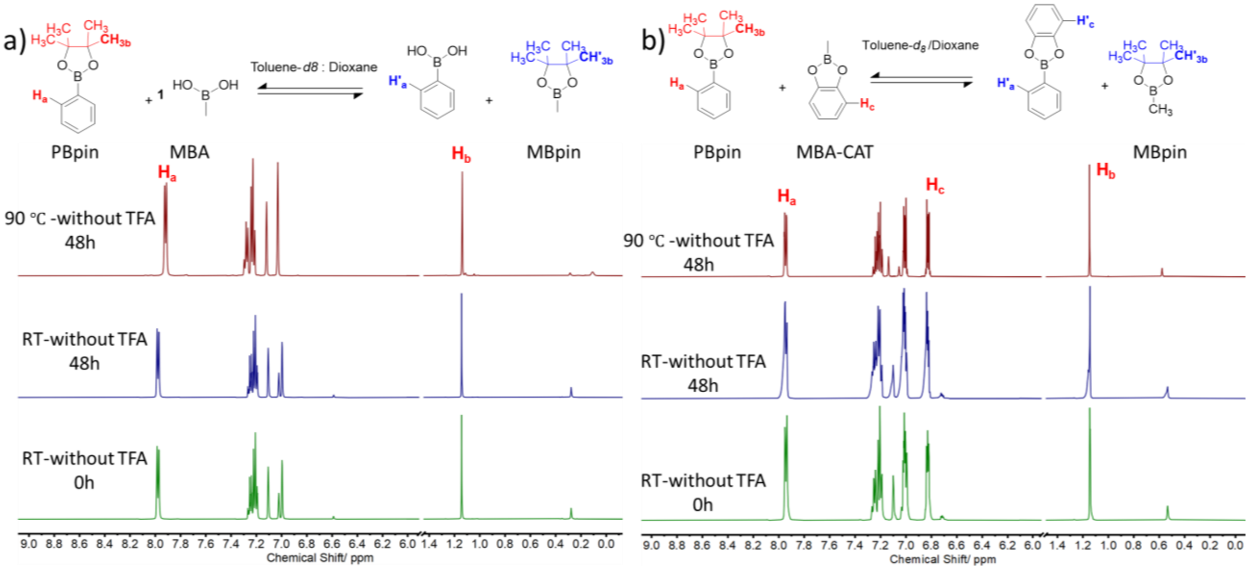

Figure 4.10. ^{1}H NMR of the (a) transesterification and (b) metathesis reaction at room temperature and 90 °C showing that no noticeable reaction occurs in the monomers without the catalyst.

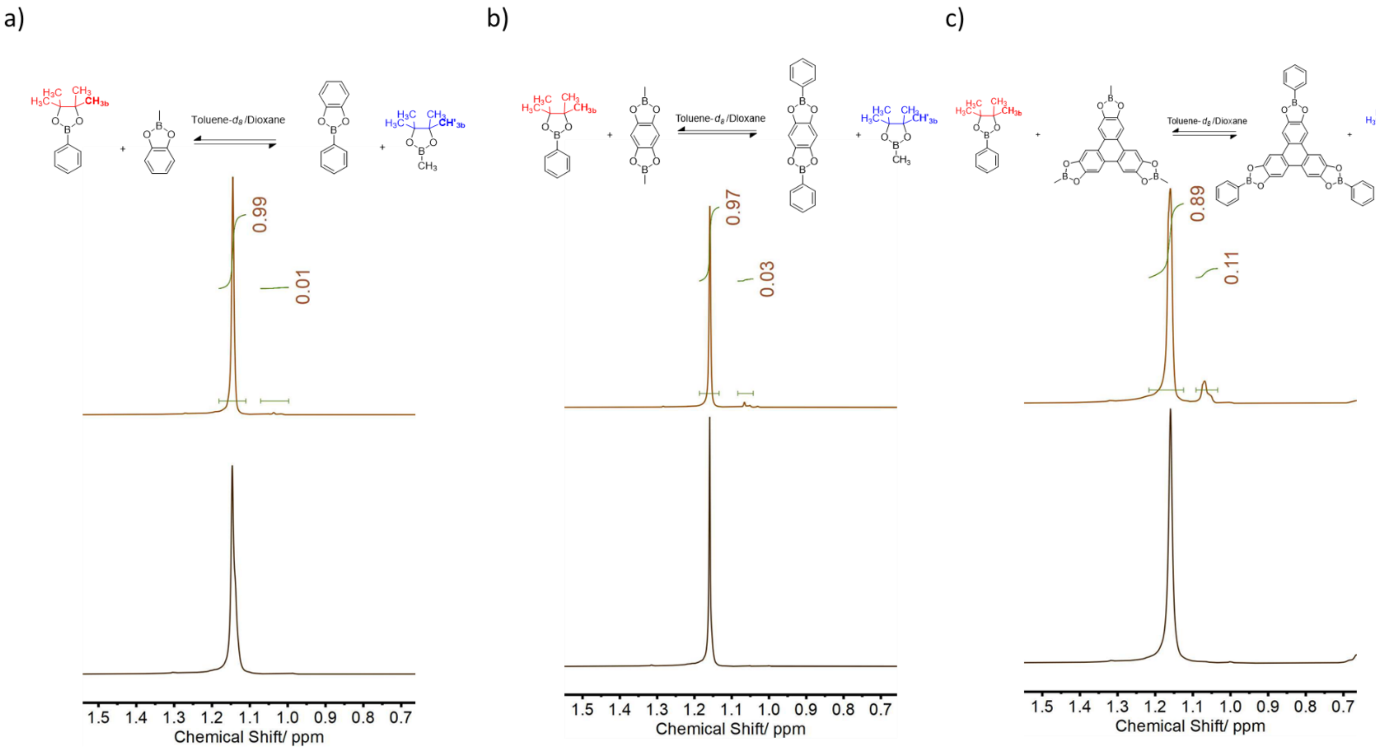

Figure 4.11. ^{1}H NMR ($H_{b(PBpin)}$ / $H'_{b(MBpin)}$ region) of **PBpin** metathesis with a) **MBA-CAT** b) **MBA-THB** and c) **MBA-HHTP** before (bottom) and after (top) heating at 90 °C for 12 h *without* catalyst. The comparison shows an acceleration of the non-catalytic reaction for larger/more electron-rich catechols.

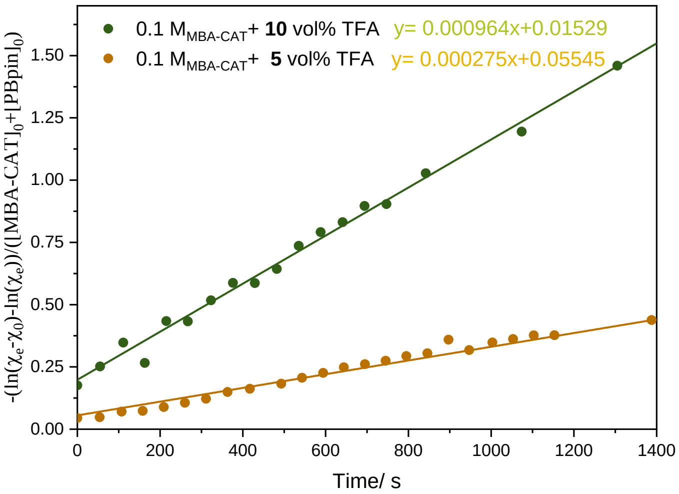

Figure 4.12. The plot of the reaction kinetics of metathesis of **PBpin** (0.1 M) with **MBA-CAT** (0.1 M) at different concentrations of TFA at 90 °C with the linear fitting and the corresponding rate constants according to equation 4.1. The results suggest second-order kinetics for the [TFA] in the reaction.

4.7.3. Synthesis of COFs

Method A (boroxine COFs from pinacol boronates). A 5 mL glass ampule was charged with corresponding pinacol boronate ester, **MBA**, and solvent mixture (see Tables 4.1-4.7). The resulting suspension was purged and sealed under argon and heated. After cooling <100 °C the ampule was opened and the resulting white precipitate was immediately filtered off, washed with dry chloroform, dried, and activated at 180 °C under vacuum (0.1 torr). It is noteworthy that extended storage of the reaction mixture at room temperature results in potential hydrolysis of the COF by reaction by-products.

Method B (dioxaborole COFs from pinacol boronates and catechols). A 5 mL glass ampule was charged with corresponding pinacol boronate, **MBA**, the catechol, and solvent mixture (see the Tables). The resulting suspension was purged and sealed under argon and heated. After cooling <100 ^{o}C the ampule was opened and the resulting white precipitate was immediately filtered off, washed with dry chloroform, dried, and activated at 180 °C under vacuum (0.1 torr).

Method C (dioxaborole-linked COF from pinacol boronates and **MBA**-protected catechols). A 5 mL glass ampule was charged with corresponding pinacol boronate ester, **MBA**-protected polyfunctional catechol, and solvent mixture. The resulting suspension was purged and sealed under argon and heated. After cooling <100 °C the ampule was opened and the resulting white precipitate was immediately filtered off, washed with dry chloroform, dried, and activated at 180 °C under vacuum (0.1 torr).

4.7.3.1. COF-1:

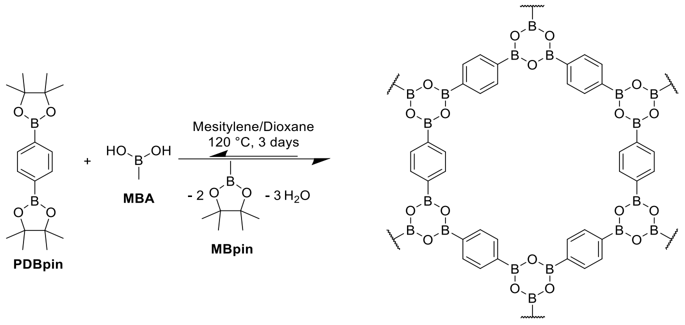

Table 4.1. Optimization of reaction conditions for boroxine **COF1**$_T$.

Entry	[MBA]	Catalyst	Condition	Yield	FWHM (110)	Correlation length (nm)^a
1	--	--	120 °C, 3 d	0%	--	--
2	--	5 v% TFA	120 °C, 3 d	0%	--	--
3	2eq	5 v% TFA	120 °C, 3 d	68%	0.42°	19
4	10eq	5 v% TFA	120 °C, 3 d	77%	0.23°	35
5	20eq	5 v% TFA	120 °C, 3 d	**99%**	0.48°	17
6	20eq	5 v% TFA	120 °C, 1 d	**55%**	0.19°	42
7	20eq	5 v% TFA	120 °C, 10 d	**62%**	0.19°	42
8	20eq	5 v% TFA	160 °C, 3 d	**57%**	0.33°	24
9	20eq	--	120 °C, 3 d	15%	0.61°	13
10	20eq	5 v% Collidine	120 °C, 3 d	**74%**	0.25°	32
11	20eq	5 v% Pyridine	120 °C, 3 d	0%	--	--
12	20eq	5 v% AcOH	120 °C, 3 d	3%	--	--
13	20eq	5 v% NH_3 (1M aq.)	120 °C, 3 d	3%	--	--
14	20eq	5 v% HCl (1M aq.)	120 °C, 3 d	0%	--	--
15	20eq	5 v% Pr_2EtN	120 °C, 3 d	**0%**	--	--
16	20eq	5 v% TMPP 5%	120 °C, 3 d	**0%**	--	--
17	20eq	5 v% TEA	120 °C, 3 d	**0%**	--	--
18	20eq	5 v% NH_3(conc.)	120 °C, 3 d	**0%**	--	--

a. The correlation length was calculated for the 110 peak according to the Scherrer equation: $\tau = \frac{0.9\,\lambda_{(Cu\,K_{\alpha})}}{\beta_{FWHM}.\cos(\theta)}$

Using Method A: PDBpin (33 mg, 0.10 mmol), **MBA** (120 mg, 2.00 mmol) and 1 mL of a 1:10:10 v:v:v solution of TFA:mesitylene:dioxane were added to a 5 mL glass ampule, purged (5 min) and sealed under argon atmosphere (1 atm). The sealed ampule was heated to 120 °C for 3 days (3d) to afford 16.0 mg of **COF1$_T$** (99%) as a white precipitate (the powder forms mainly on the walls of the glass ampule). Reaction screening was done using the same method with different parameters according to Table 4.1.

Scale-up synthesis of COF-1$_T$: PDBpin (330 mg, 1.00 mmol), **MBA** (120 mg, 2.00 mmol) and 10 mL 1:10:10 v:v:v solution of TFA:mesitylene:dioxane were added to a 25 mL round bottom flask equipped with a condenser, and the reaction was refluxed for 48 h during which time a white precipitate was formed. The reaction mixture was filtered hot and washed with dry chloroform and dry acetone to afford pure **COF-1$_T$** (115 mg, 89 %).

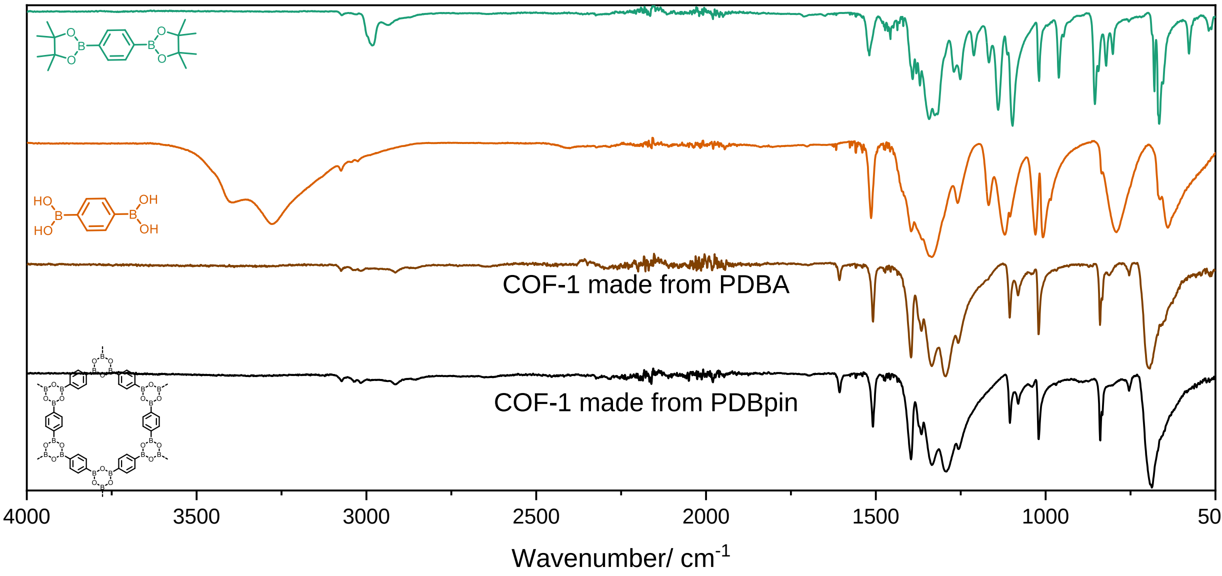

Figure 4.13. FTIR spectra of **PDBpin** (green), **PDBA** (orange) and **COF-1** (brown) and **COF-1$_T$** (black).

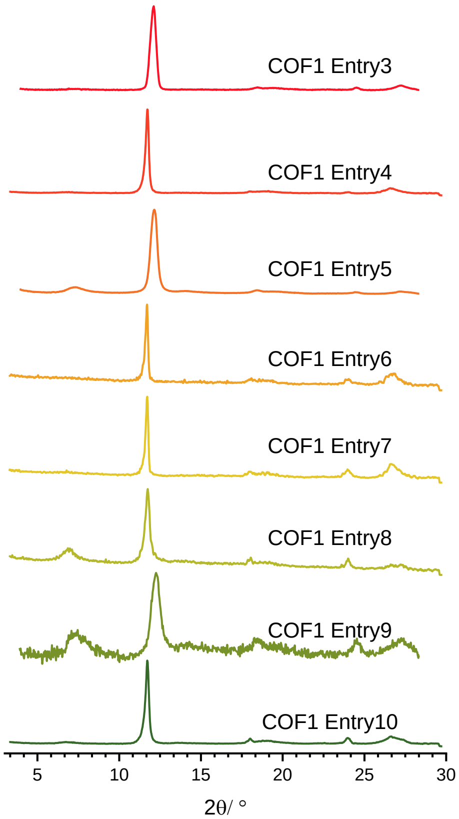

Figure 4.14. PXRD of the as-synthesized (not activated) **COF-1$_T$** according to Table 4.1. The as-synthesized **COF-1$_T$** is dominated by 11.7° (110) peak in the PXRD pattern corresponding to the AB-stacked layers, with mesitylene (solvent) occupying the pores.[6] After activation, the COF adopts an AA-stacking where the 6.8°(100) peak becomes dominant (main text, Figure 4.2).

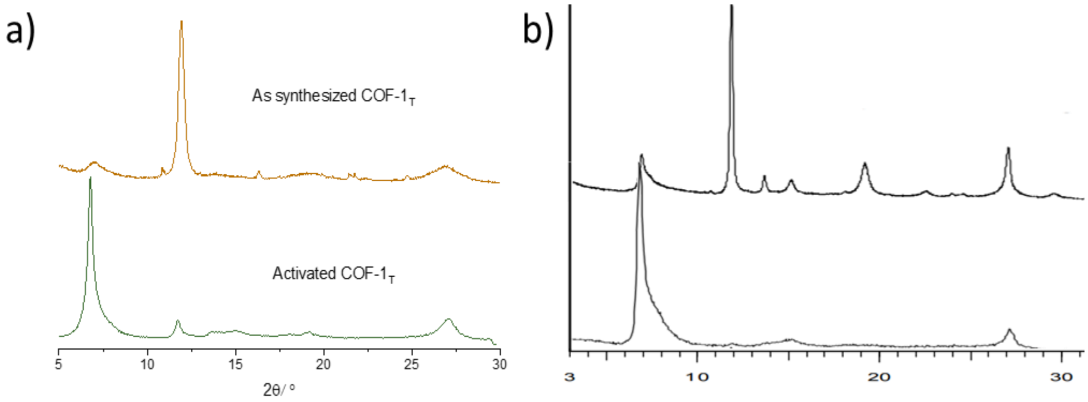

Figure 4.15. Phase change of **COF-1$_T$** a) and **COF-1** as reported in Ref[6] (copyright AAAS 2005) and b) after activation (180 °C, 0.1 mbar).

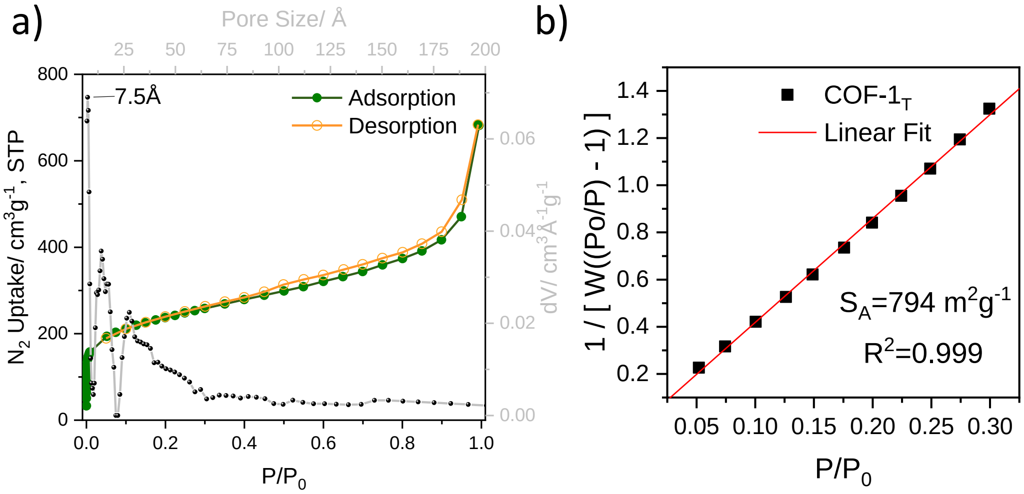

Figure 4.16. a) Nitrogen gas adsorption-desorption isotherm for **COF-1$_T$** and its corresponding QSDFT-pore size distribution model (black). b) BET plot for **COF-1$_T$** calculated from nitrogen adsorption data.

4.7.3.2. PPy-COF:

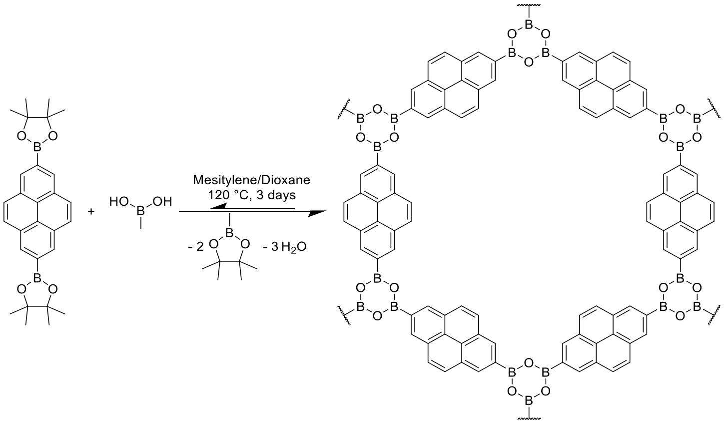

Using Method A: 2,7-Pyrenediboronic pinacolate ester (PyDBpin, 15 mg, 0.033 mmol), **MBA** (40 mg, 0.66 mmol), and 1 mL of a 10:100:100 v:v:v solution of TFA:mesitylene:dioxane was added to a 5ml glass ampule, purged 5 min and sealed under an argon atmosphere (1 atm). The sealed ampule was heated to 120 °C for 3 d to afford 7.5 mg of **PPy-COF** (79%) as a white precipitate (mainly formed on the walls of the ampule). Reaction screening was done using the same method with different parameters according to Table 4.2.

Table 4.2. Optimization of reaction conditions for boroxine **PPy-COF** using Method A.

Entry	[MBA]	Catalyst	condition	Yield	FWHM (100)	Correlation length (nm)[b]
1	20eq	5 v% TFA	120 °C, 3 d	79%	1.6°	5
2	20eq	5 v% TFA	160 °C, 3 d	74%	1.1°	4
3	20eq	5 v% Collidine	120 °C, 3 d	68%	1.8°	7
4	20eq	5 v% Collidine	120 °C, 3 d	59%	1.2°	7

a. Higher concentrations than 33 mM of PyDBpin lead to the formation of an amorphous gel.

b. The correlation length was calculated for the 100 peak according to the Scherrer equation: $\tau = \frac{0.9\, \lambda_{(Cu\, K_\alpha)}}{\beta_{FWHM} . \cos{(\theta)}}$

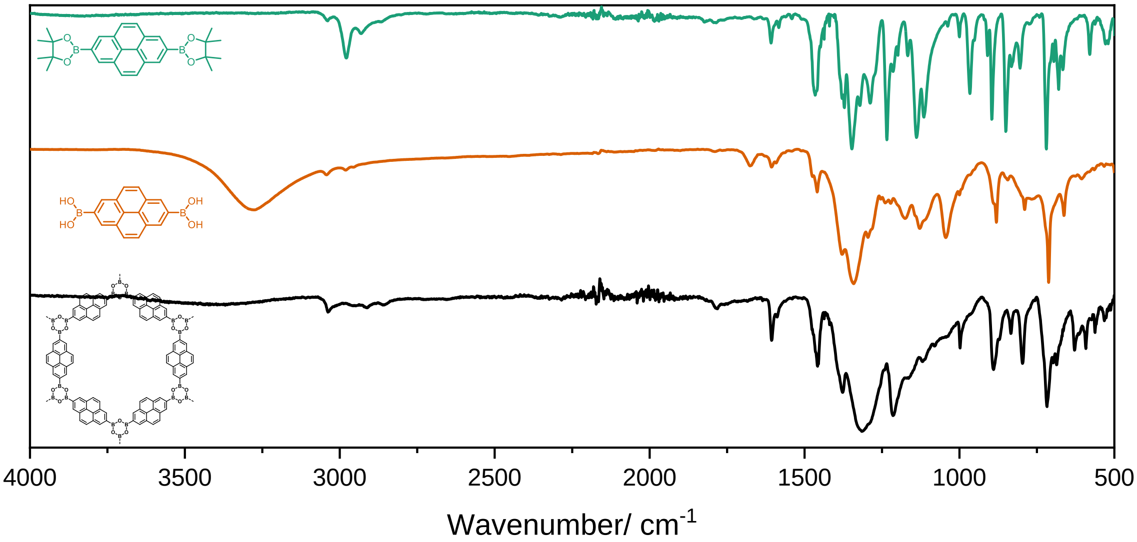

Figure 4.17. FTIR spectra of **PyDBpin** (green), **PyDBA** (orange), and **PPy-COF** (black, Entry 2 in Table 4.2).

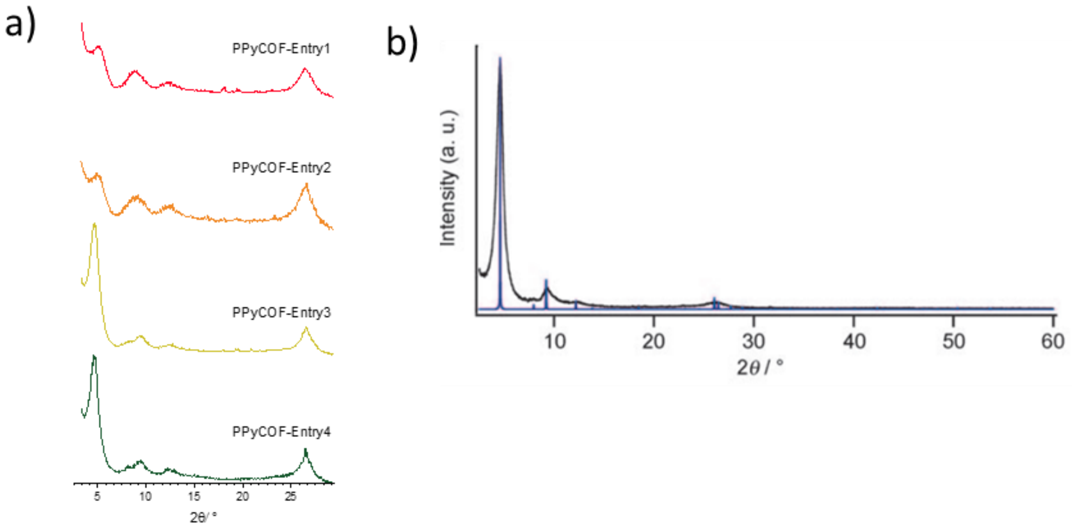

Figure 4.18. a) PXRD of the as-synthesized **PPy-COF** according to Table 4.2. b) Reported PXRD pattern of **PPy-COF** synthesized by condensation of pyrene-2,7-diboronic acid (graph adapted with permission from ref. [7] Copyright Wiley 2009).

4.7.3.3. COF-5:

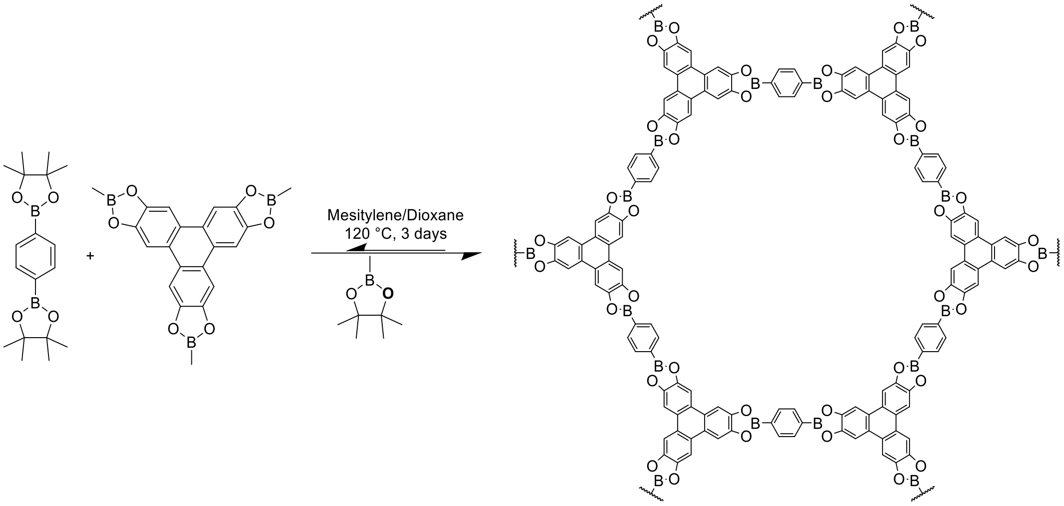

Using Method B (Entries 1-3): PDBpin (33.0 mg, 0.100 mmol), **MBA** (120 mg, 2.00 mmol), **HHTP** (21.6 mg, 0.066 mmol) and 1 mL of a 10:100:100 v:v:v solution of TFA:mesitylene:dioxane were added to a 5 mL glass ampule, purged 5 min and sealed under argon atmosphere (1 atm). The sealed ampule was heated to 120 °C for 3 days to afford 10.4 mg of **COF5**$_{\mathbf{T}}$ (67%) as a white precipitate. Reaction screening was done similar to the provided example with differed parameters according to Table 4.3.

Using Method C (Entries 4, 5): PDBpin (33.0 mg, 0.100 mmol), and **MBA-HHTP** (26.5 mg, 0.066 mmol) and 1 mL of a 10:100:100 v:v:v solution of TFA:mesitylene:dioxane were added to a 5 mL glass ampule, purged 5 min and sealed under argon atmosphere (1 atm). The sealed ampule was heated to 120 °C for 3 days to afford 28.5 mg of **COF5**$_{\mathbf{M}}$ (94%) as a white precipitate.

Reaction screening was done similar to the provided example with differed parameters according to Table 4.3.

Table 4.3. Optimization of reaction conditions for dioxaborole-linked **COF-5$_T$** and **COF-5$_M$**.

Entry COF-5T	MBA	Catalyst	Conditions	Yield	FWHM (100) peak	Correlation length (nm)[a]
1	20 eq	5 v% TFA	120 °C, 3 d	67%	0.22°	36
2	20 eq	--	120 °C, 3 d	60%	0.17°	47
3	--	5 v% TFA	120 °C, 3 d	36%	0.27°	30
Entry COF-5M	MBA-HHTP					
4	0.66 eq	5 v% TFA	120 °C, 1 h	77%	0.32°	25
5	0.66 eq	--	120 °C, 3 d	94%	0.19°	42

a. The correlation length was calculated for the 100 peak according to the Scherrer equation: $\tau = \frac{0.9\,\lambda_{(Cu\,K_\alpha)}}{\beta_{FWHM}.\cos(\theta)}$

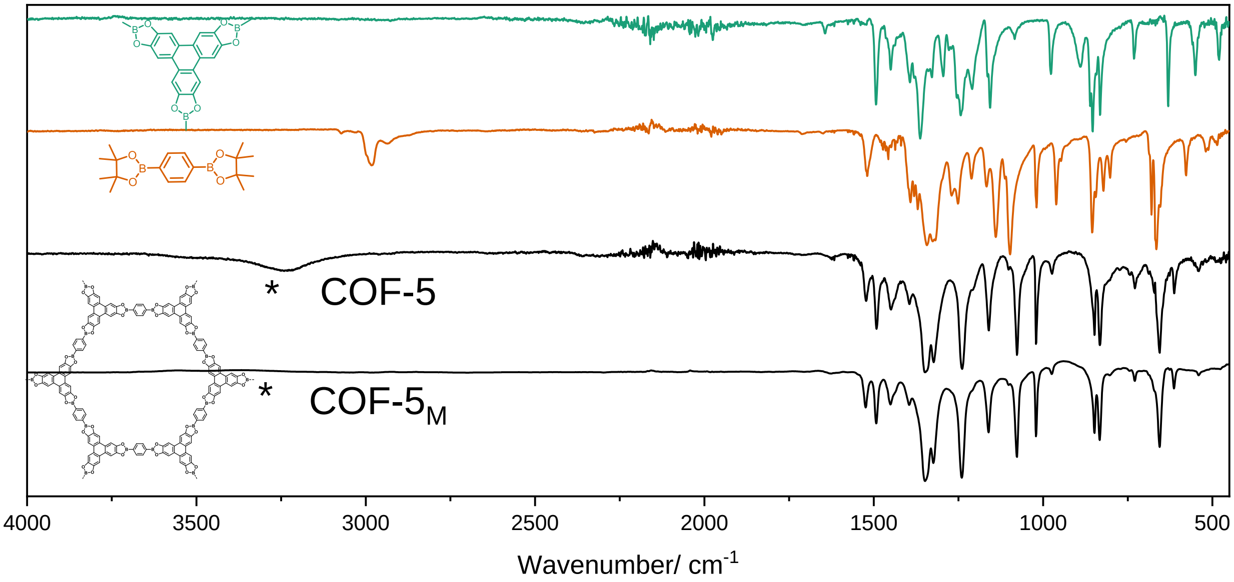

Figure 4.19. FTIR spectra of **MBA-HHTP** (green), **PDBpin**(orange), and **COF-5** and **COF-5$_M$**.

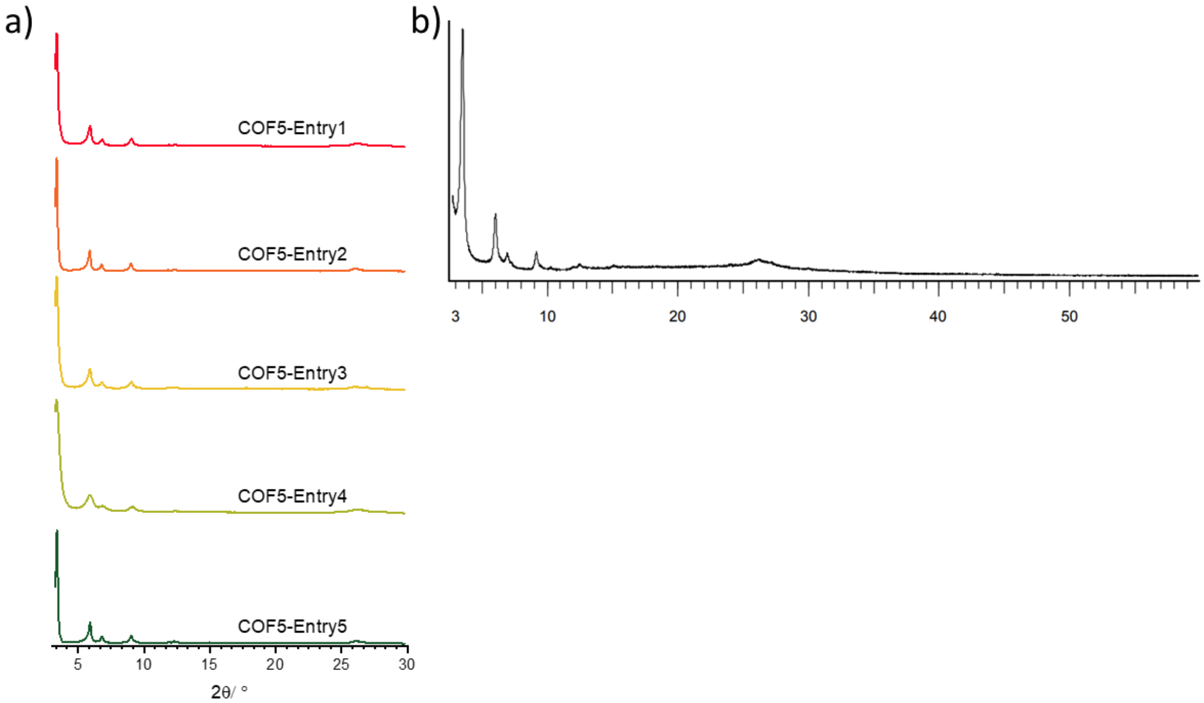

Figure 4.20. a) PXRD of the as-synthesized **COF-5$_T$** (Entry 1-3) and **COF-5$_M$** (Entry 4,5). b) reported PXRD pattern of **COF-5** synthesized by condensation of **PDBA** and **HHTP** (graph inserted from Ref. [6]. Copyright AAAS 2005).

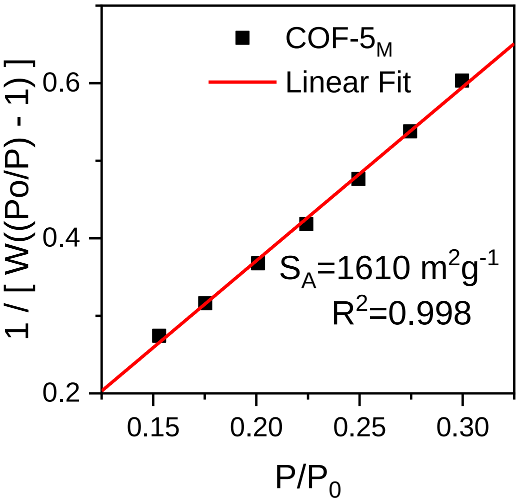

Figure 4.21. BET plot for **COF-5$_M$** calculated from nitrogen adsorption data.

4.7.3.4. COF-18Å:

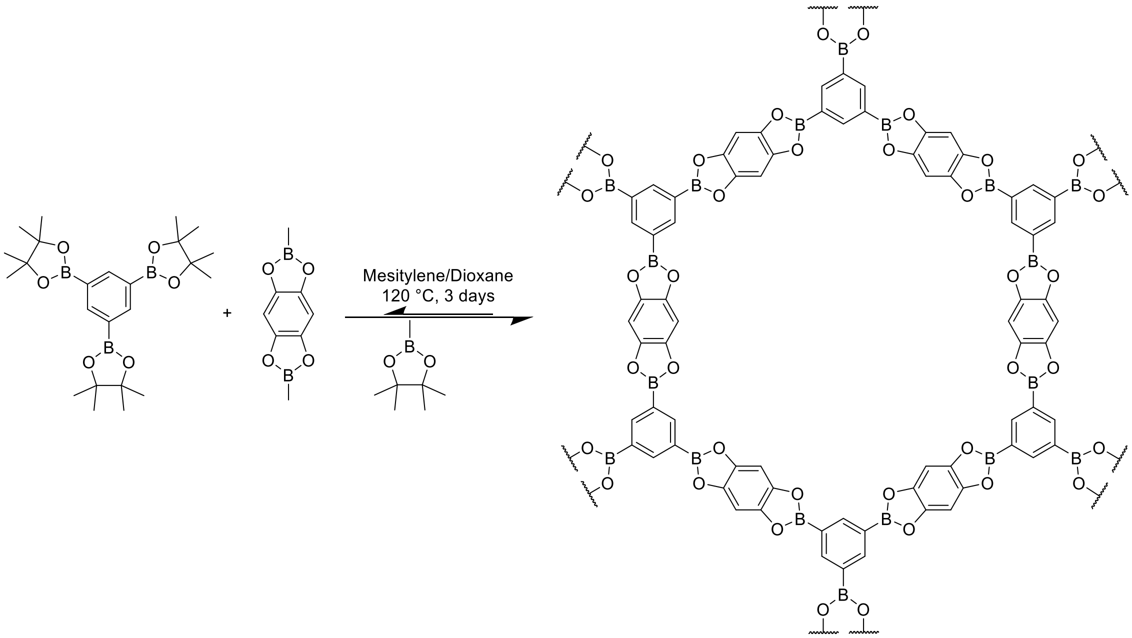

Using Method B (Entries 1-9): 1,3,5-Phenyltriboronic pinacolate ester (20 mg, 0.044 mmol), **MBA** (78.8 mg, 1.32 mmol), **THB** (9.4 mg, 0.066 mmol) and 1 ml 5:98:2 v:v:v solution of TFA:THF:MeOH were added to a 5 mL glass ampule, purged 5 min and sealed under argon atmosphere (1 atm). The sealed ampule was heated to 120 °C for 3 days to afford **COF-18Å$_T$** as a white precipitate (10.4 mg, 79%). Reaction screening was done similar to the provided examples with differed parameters according to Table 4.4.

Using Method C (Entries 10,11): 1,3,5-Phenyltriboronic pinacolate ester (20 mg, 0.044 mmol), **MBA-THB** (12.5 mg, 0.066 mmol), and 1ml 5:98:2 v:v:v solution of TFA:THF:MeOH were added to a 5 mL glass ampule, purged 5 min and sealed under argon atmosphere (1 atm). The sealed ampule was heated to 120 °C for 3 days to afford **COF-18Å$_M$** as a white precipitate (9.0 mg, 65%).

The obtained **COF-18Å** has a superior BET surface area of 1567 m^2g^{-1} as compared to the reported BET surface area (ca. 1260 $m^2.g^{-1}$).[8]

Table 4.4. Optimization of reaction conditions for Dioxaborole-linked **COF-18Å$_T$** (Entries1-9) and **COF-18Å$_M$** (Entries 10,11)

Entry	MBA	Catalyst	Solvent	Conditions	Yield	FWHM (100) plane	Correlation length(nm)[b]
1	30 eq	5 v% TFA	1:1 Diox/Mes	120 °C, 3 d	59%	Amorphous	--
2	30 eq	5 v% TFA	1:1 Diox/Mes	160 °C, 3 d	67%	Amorphous	--
3	30 eq	5 v% Collid.	1:1 Diox/Mes	120 °C, 3d	86%	Amorphous	--
4	30 eq	5 v% Collid.	1:1 Diox/Mes	160 °C, 3 d	70%	Amorphous	--
5	----	5 v% TFA	1:1 Diox/Mes	120 °C, 3 d	0%	Amorphous	--
6	30 eq	----	1:1 Diox/Mes	120 °C, 3 d	5%	Amorphous	--
7[a]	30 eq	5 v% TFA	1:49 MeOH/THF	120 °C, 3 d	67%	0.39°	20
8	30 eq	5 v% Collid.	1:49 MeOH/THF	120 °C, 3 d	75%	0.43°	18
9	30 eq	----	1:49 MeOH/THF	120 °C, 3 d	14%	0.41°	19
	MBA-THB	Catalyst	Solvent	Conditions	Yield	FWHM (100) plane	Correlation length (nm)[b]
10	1.5 eq	5 v% TFA	1:49 MeOH/THF	120 °C, 3 d	65%	0.62	13
11	1.5 eq	----	1:49 MeOH/THF	120 °C, 3 d	44%	0.73	11

a. The presence of MeOH is necessary to achieve crystalline **COF-18Å**. In the absence of MeOH in the 1:1 Diox/Mes, an amorphous gel is formed, possibly due to the competing formation of the boroxine polymers.

b. The correlation length was calculated for the 100 peak according to the Scherrer equation: $\tau = \frac{0.9\,\lambda_{(Cu\,K_\alpha)}}{\beta_{FWHM}.\cos{(\theta)}}$

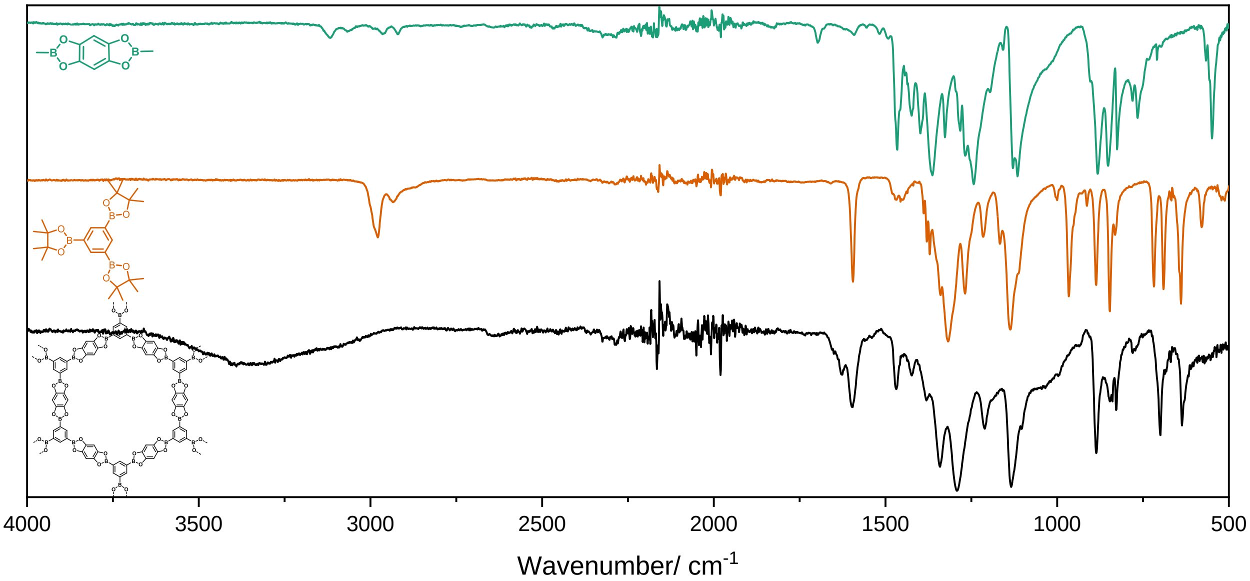

Figure 4.22. FTIR spectra of **MBA-THB** (green), 1,3,5-benzenetriboronic pinacolate ester (orange), and **COF-18Å$_M$** (black).

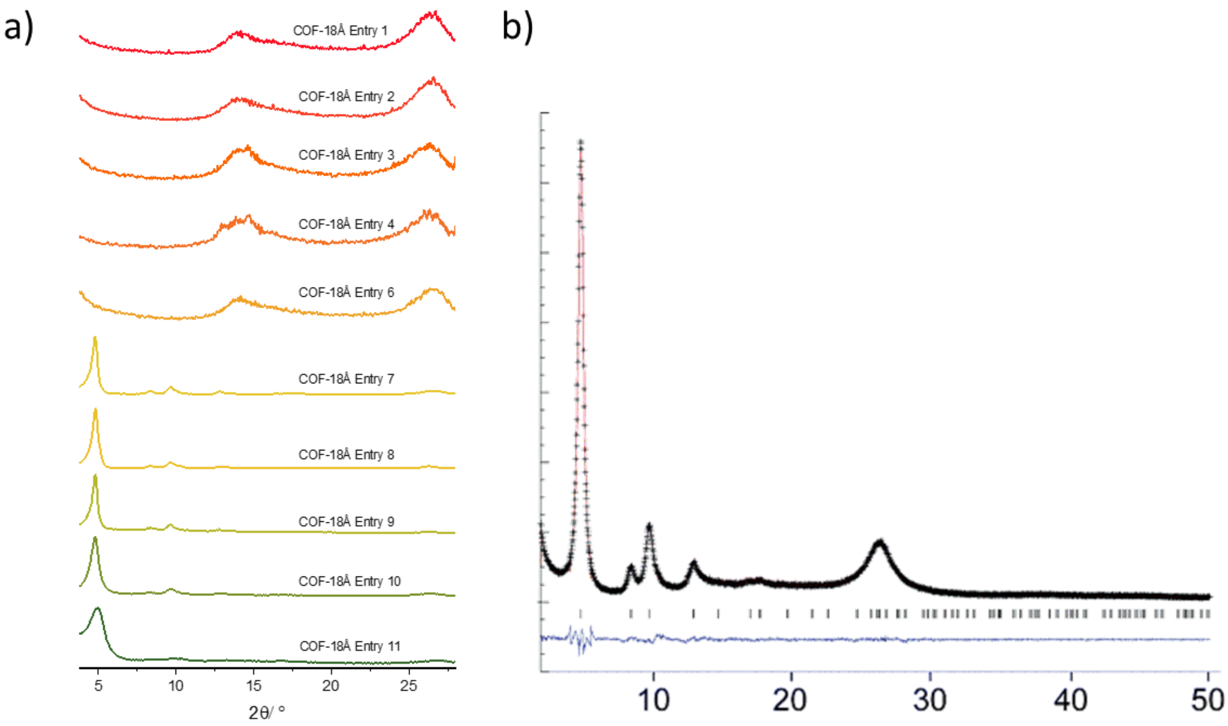

Figure 4.23. (a) PXRD of the as-synthesized **COF-18Å$_T$** (Entry1-9) and **COF-18$_M$** (Entry 10, 11). (b) Reported PXRD pattern of **COF-18Å** synthesized by condensation of 1,3,5-benzenetriboronic acid and **THB** (graph reprinted with permission from Ref. [8], copyright American Chemical Society 2006).

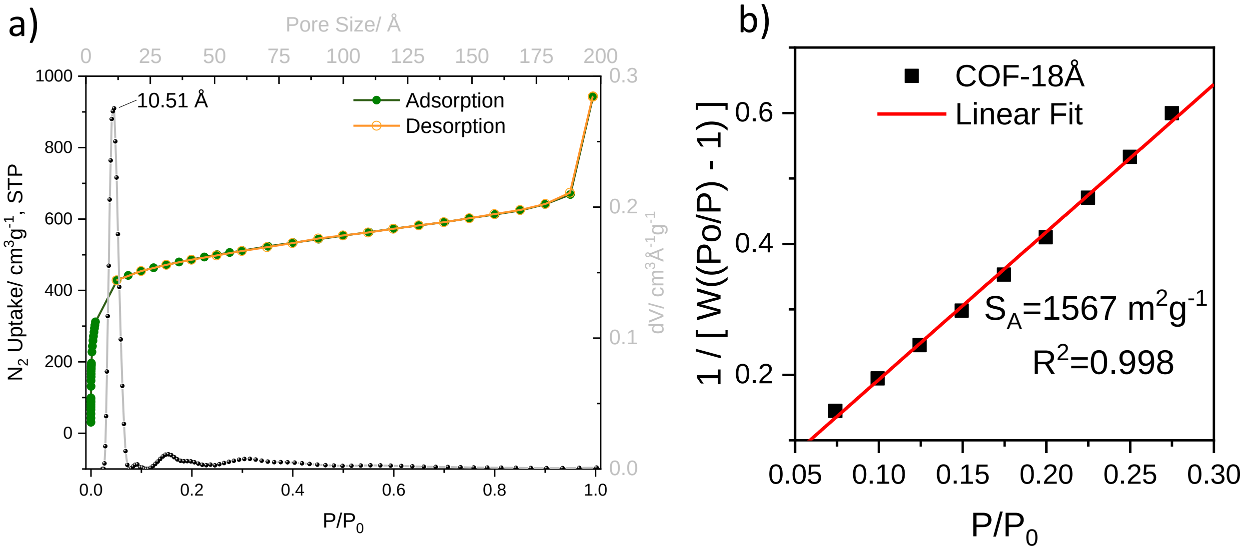

Figure 4.24. a) Nitrogen gas adsorption-desorption isotherm for **COF-18Å$_M$** and its corresponding QSDFT-pore size distribution model(black). b) BET plot for **COF-18Å$_M$** calculated from nitrogen adsorption data.

4.7.3.5. COF10:

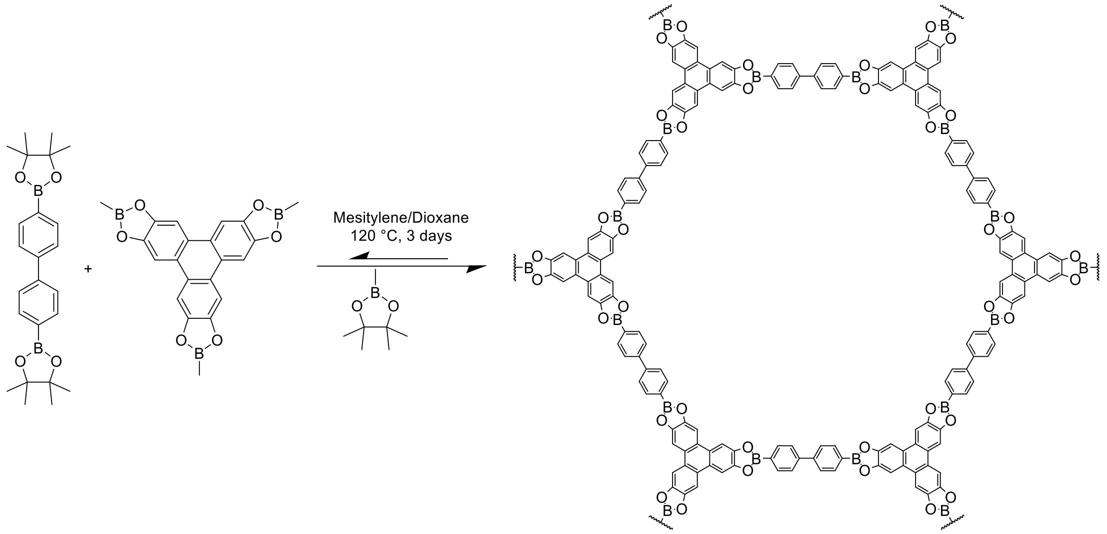

Using Method C. 1,4-Biphenyldiboronic pinacolate ester (41.0 mg, 0.100 mmol), **MBA-HHTP** (26.7 mg, 0.66 mmol) and 1 mL of a 10:100:100 v:v:v solution of TFA:mesitylene:dioxane were added to a 5 ml glass ampule, purged 5 min and sealed under argon atmosphere (1 atm). The sealed ampule was then heated to 120 °C for 3 days to afford **COF-10$_{\mathbf{M}}$** as a white precipitate (29.0 mg, 74%).

Table 4.5. Reaction conditions for Dioxaborole-linked **COF-10$_{\mathbf{M}}$**.

Entry	MBA-HHTP	Catalyst	Solvent	Conditions	Yield	FWHM (100) plane	Correlation length(nm)[a]
10	0.66 eq.	5 v% TFA	1:1 Mes/Diox	120 °C, 3 d	74%	0.79	10.1

a. The correlation length was calculated for the 100 peak according to the Scherrer equation: $\tau = \frac{0.9\,\lambda_{(Cu\,K_\alpha)}}{\beta_{FWHM}.\cos(\theta)}$

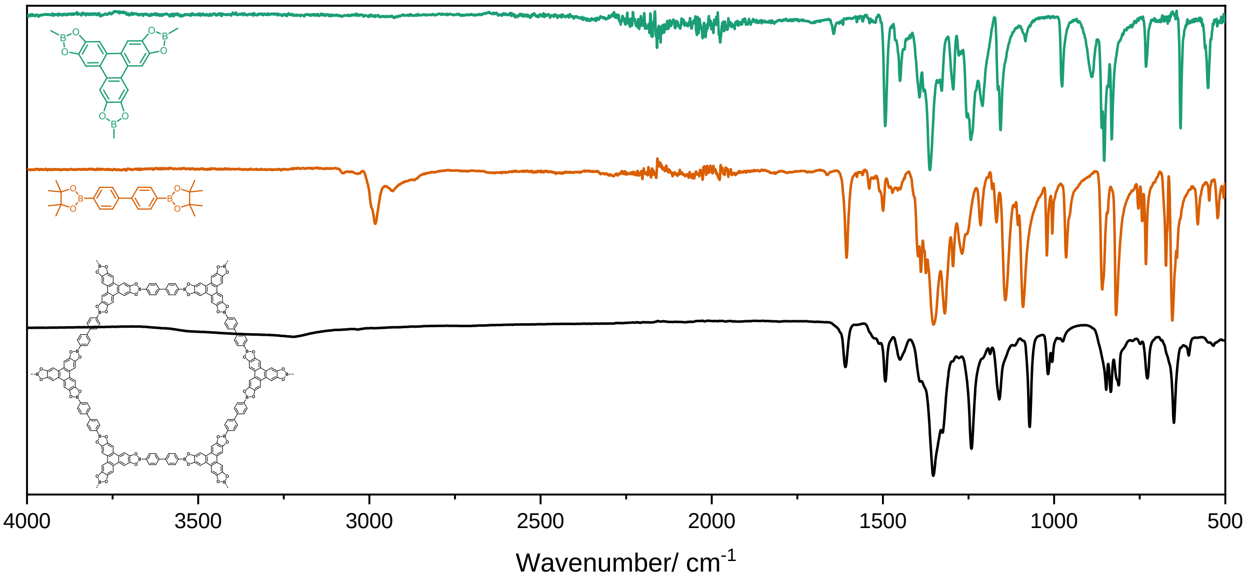

Figure 4.25. FTIR spectra of **MBA-HHTP** (green), 1,1′-biphenyl diboronic pinacolate ester (orange) and **COF-10$_M$** (black).

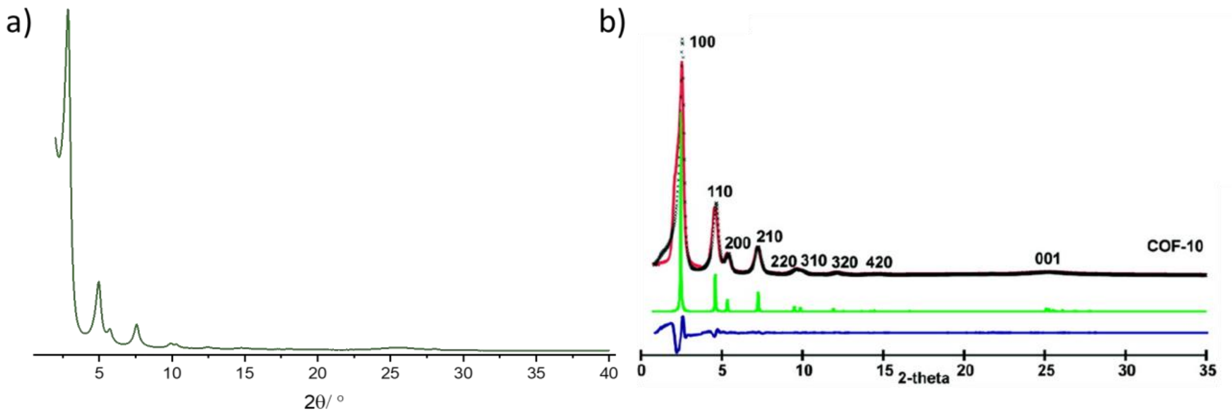

Figure 4.26. (a) PXRD of the as-synthesized **COF-10$_M$**, (b) reported PXRD pattern of **COF-10** synthesized by condensation of biphenyl diboronic acid and **HHTP** (graph inserted from ref. [9]).

4.7.3.6. TP-COF:

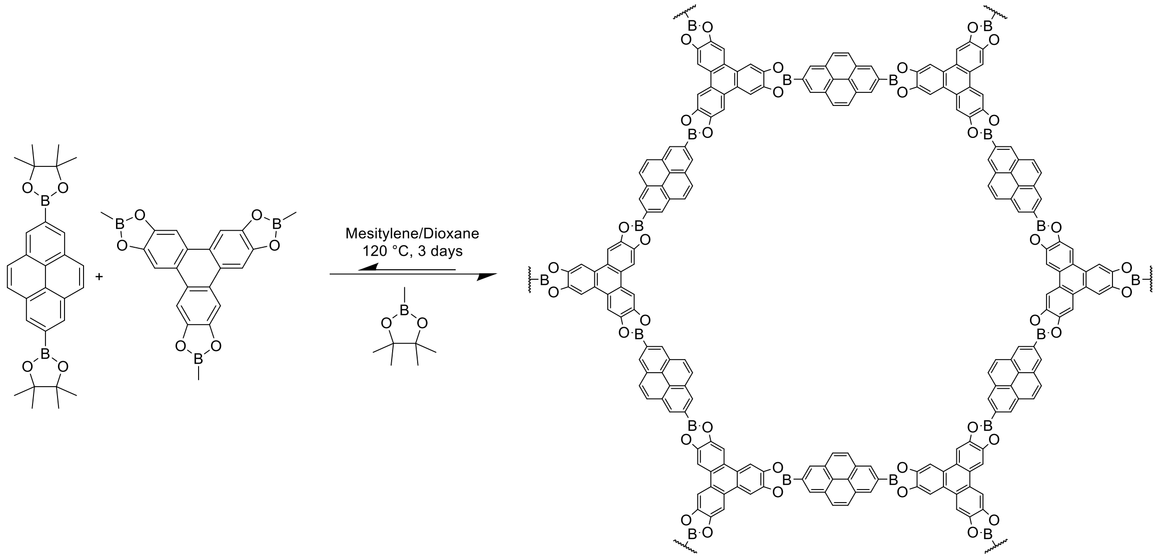

Using Method C: 1,4-Pyrenediboronic pinacol ester (45.4 mg, 0.100 mmol), **MBA-HHTP** (26.7 mg, 0.066 mmol) and 1 ml of a 10:100:100 v:v:v solution of TFA:mesitylene:dioxane were added to a 5 mL glass ampule, purged 5 min and sealed under argon atmosphere (1 atm). The sealed ampule was heated to 120 °C for 3 days to afford **TP-COF$_{\mathbf{M}}$** as a pale-yellow precipitate (29.0 mg, 66%).

Table 4.6. Reaction condition for Dioxaborole-linked **TP-COF$_{\mathbf{M}}$** .

Entry	MBA-HHTP	Catalyst	Solvent	Conditions	Yield	FWHM (100) plane	Correlation length(nm)^{b}
10	0.66 eq.	5 v% TFA	1:1 Mes/Diox	120 °C, 3 d	66%	0.79	10.1

a. The correlation length was calculated for the 100 peak according to the Scherrer equation:

$$\tau = \frac{0.9\,\lambda_{(Cu\,K_{\alpha})}}{\beta_{FWHM}.\cos(\theta)}$$

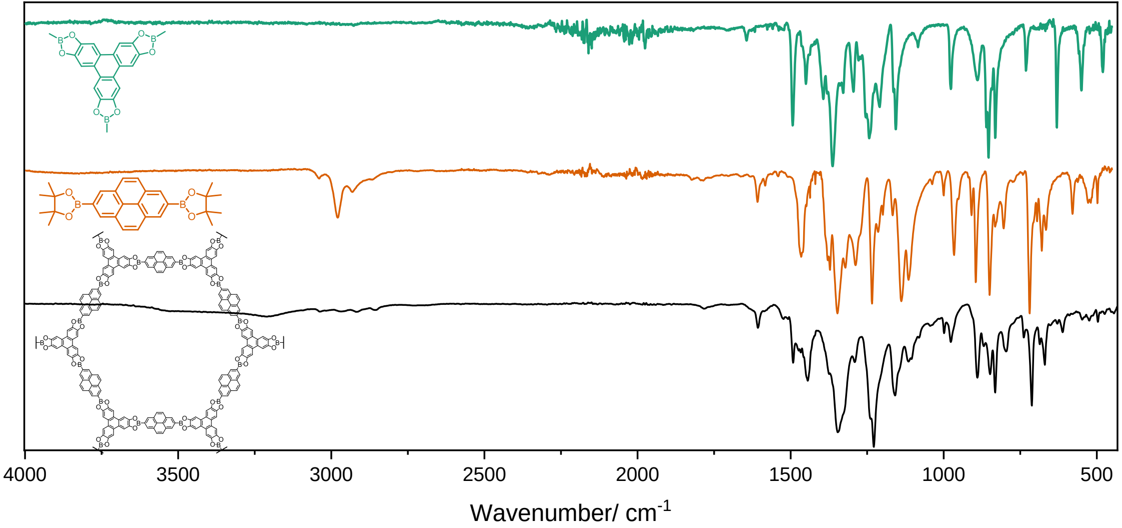

Figure 4.27. FTIR spectra of **MBA-HHTP** (green), 2,7-pyrenediboronic pinacol ester(orange) and **TP-COF$_M$** (black).

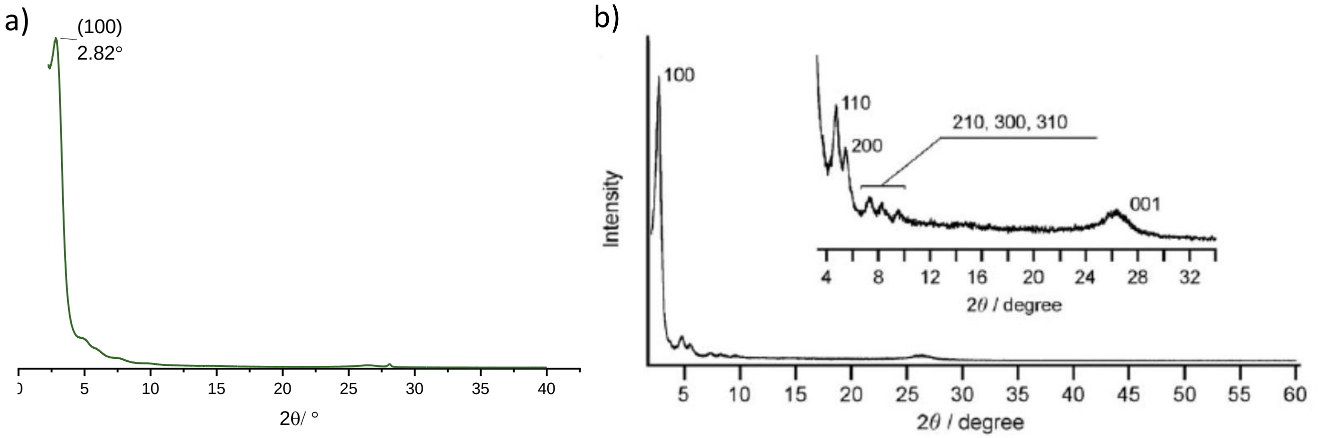

Figure 4.28. (a) PXRD of the as-synthesized **TP-COF$_M$**, (b) reported PXRD pattern of **TP-COF** synthesized by condensation of 2,7-pyrenediboronic acid and **HHTP** (graph reprinted with permission from ref. [10], Copyright Wiley 2008).

4.8.3.7. COF-6:

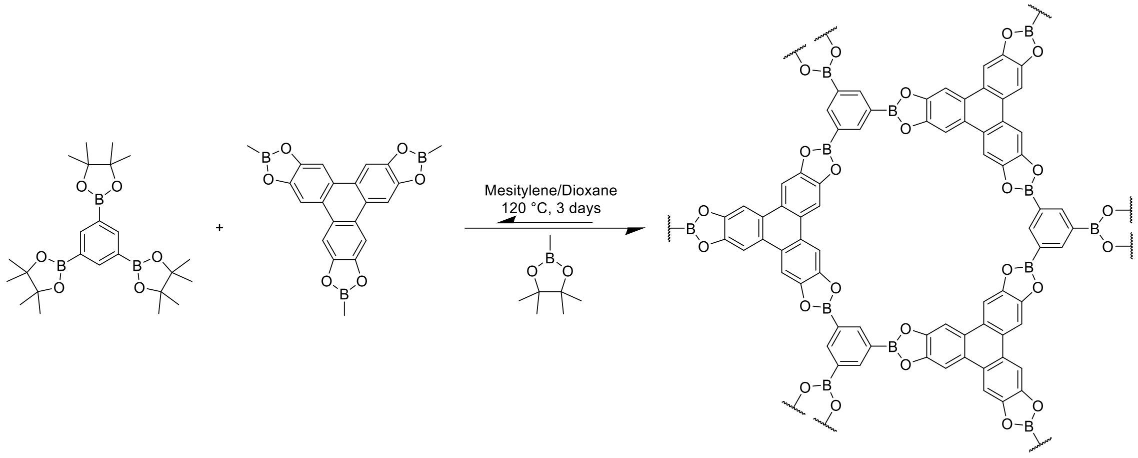

Using Method C: 1,3,5-Benzenetriboronic pinacolate ester (45.4 mg, 0.100 mmol), **MBA-HHTP** (39.4 mg, 0.100 mmol) and 1 mL of a 10:100:100 v:v:v solution of TFA:mesitylene:dioxane were added to a 5 mL glass ampule, purged 5 min and sealed under argon atmosphere (1 atm). The sealed ampule was heated to 120 °C for 3 days to afford **COF-6$_M$** as a white precipitate (31mg, 73%).

Table 4.7. Optimization of reaction conditions for Dioxaborole-linked **COF-6$_M$**.

Entry	MBA-HHTP	Catalyst	Solvent	Condition	Yield	FWHM (100) plane	Correlation length (nm)^b
1	1eq	5 v%TFA	1:1Diox/Mes	120 °C, 3 d	70%	Amorphous	--
2	1eq	5 v% TFA	48:48:4 Diox/Mes/MeOH	120 °C, 3 d	73%	0.82°	10

The presence of MeOH is necessary to achieve crystalline **COF-6$_M$**. In the absence of MeOH, an amorphous gel is formed, possibly due to the competing formation of the boroxine polymers.

The correlation length was calculated for the 100 peak according to the Scherrer equation: $\tau = \frac{0.9\,\lambda_{(Cu\,K_\alpha)}}{\beta_{FWHM}.\cos(\theta)}$

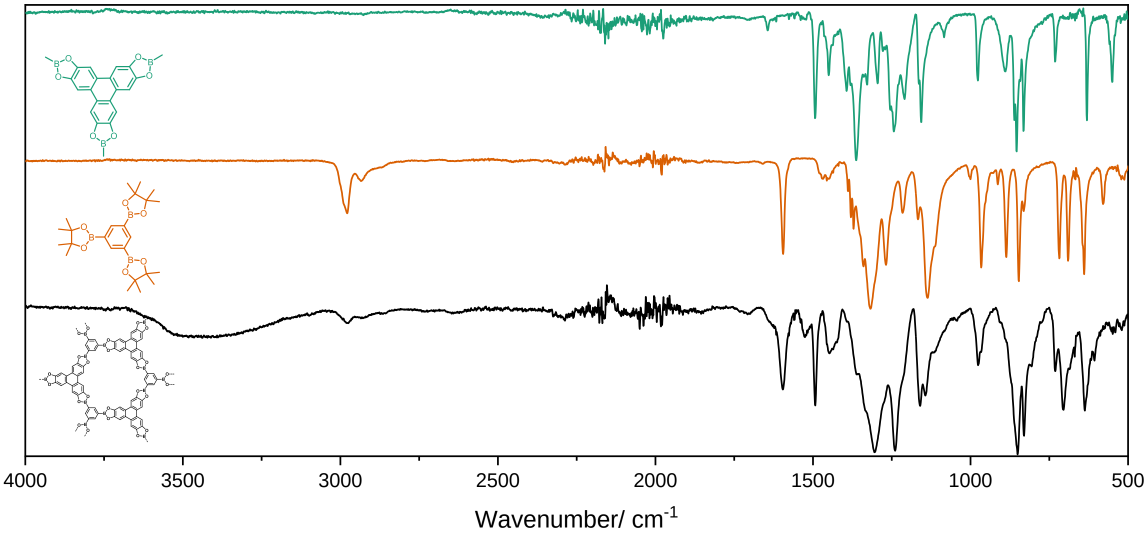

Figure 4.29. FTIR spectra of **MBA-HHTP** (green), 1,3,5-benzenetriboronic pinacolate ester(orange) and **COF-6$_M$** (black).

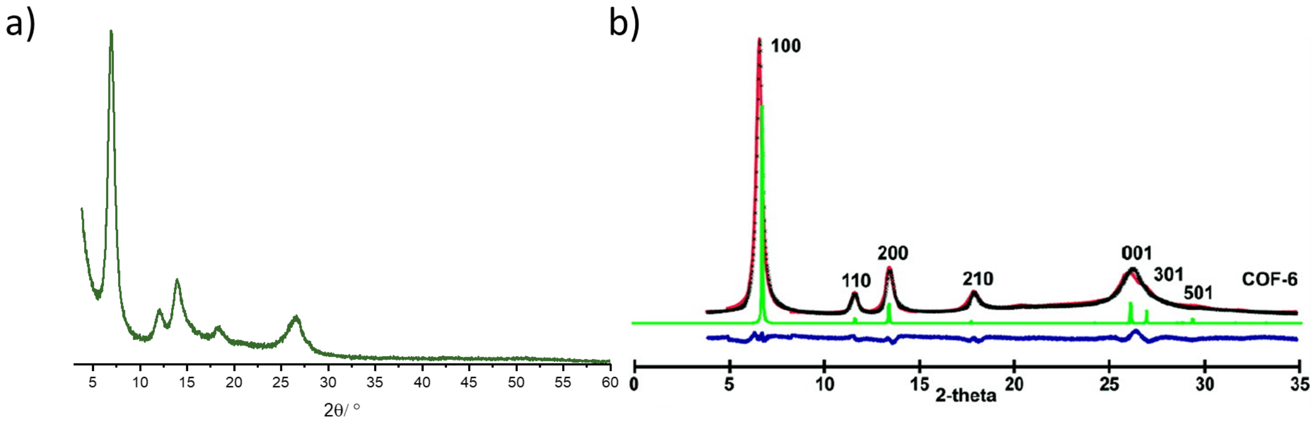

Figure 4.30. a) PXRD of the as-synthesized **COF-6$_M$**, b) PXRD pattern of **COF-6** synthesized by condensation of 1,3,5-benzenetriboronic acid and **HHTP** (graph inserted from ref. [9], Copyright ACS 2007).

4.7.3.8. Py4THB

Using Method C: 1,3,6,8-pyrenetetraboronic pinacol ester (35.5 mg, 0.050 mmol), **MBA-THB** (19.1 mg, 0.100 mmol) and 1 mL of a 10:100:100 v:v:v solution of collidine:mesitylene:dioxane were added to a 5 mL glass ampule, purged 5 min and sealed under argon atmosphere (1 atm). The sealed ampule was heated to 120 °C for 3 d to afford **Py4THB** as a dark yellow precipitate (22.5 mg, 87%).

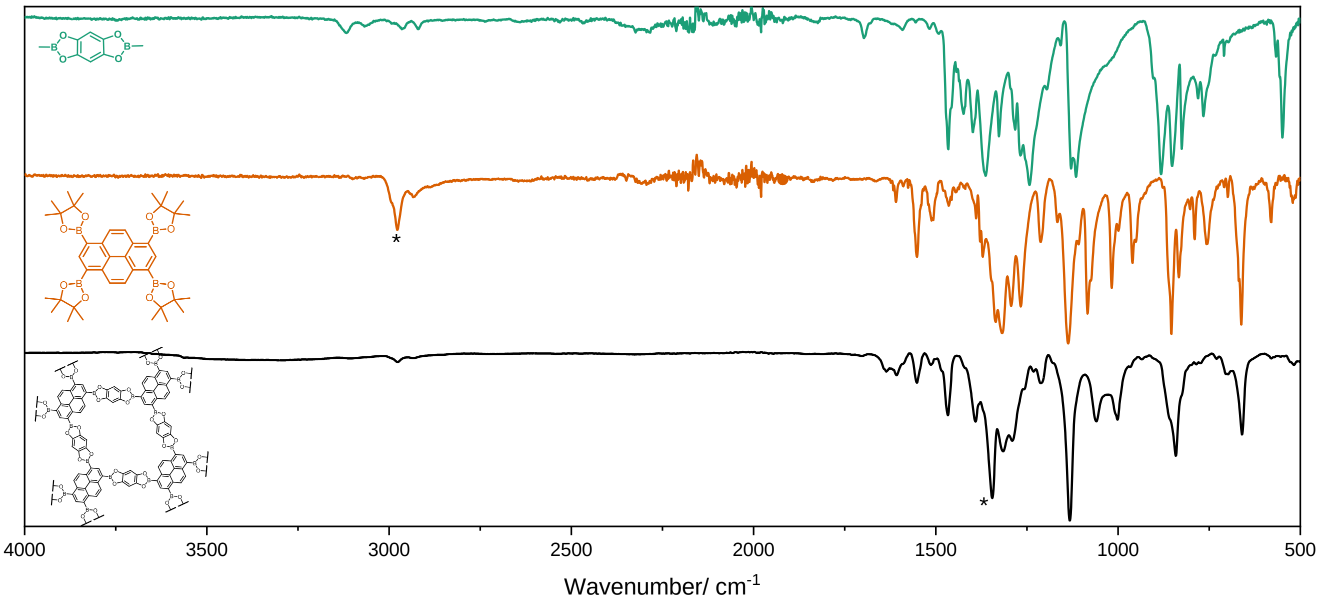

Figure 4.31. FTIR spectra of **MBA-THB** (green), 1,3,6,8-pyrenetetraboronic pinacol ester (orange), and **Py4THB** (black).

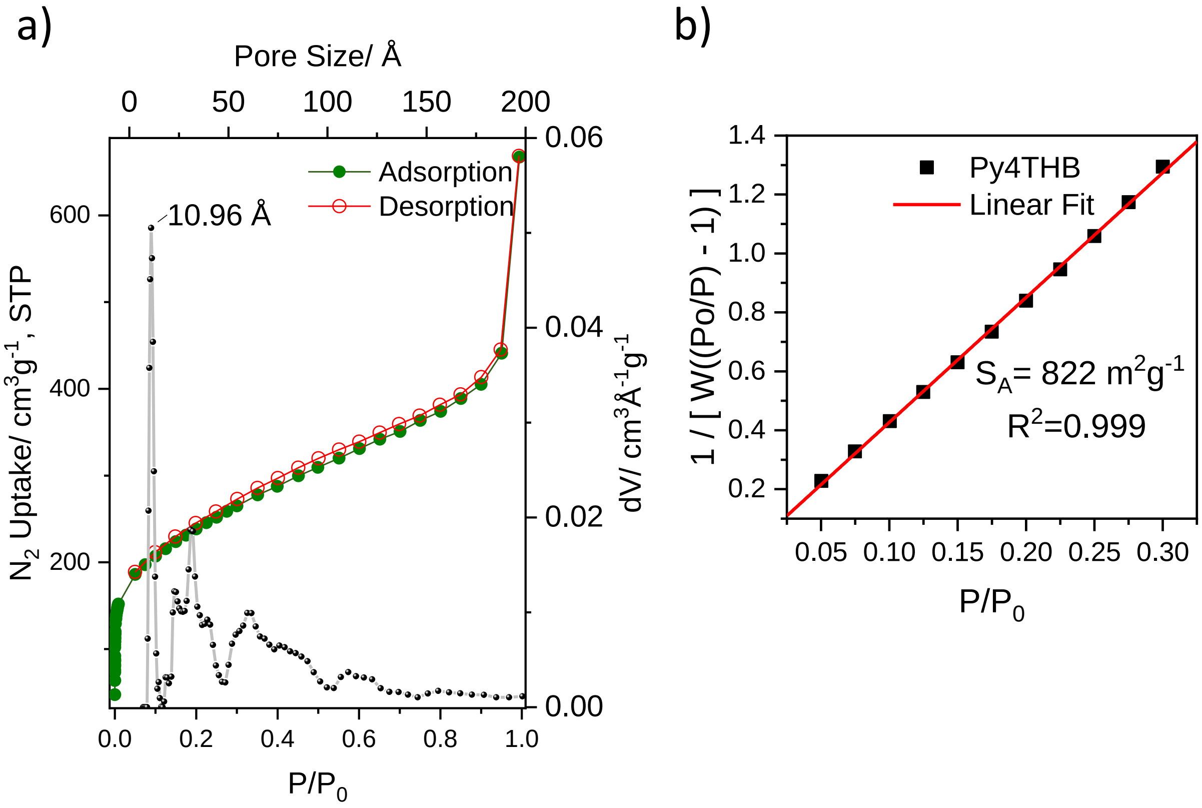

Figure 4.32. a) Nitrogen gas adsorption-desorption isotherm for **Py4THB** and its corresponding QSDFT-pore size distribution model (black). b) BET plot for **Py4THB** calculated from nitrogen adsorption data.

4.7.3.9. B2HHTP

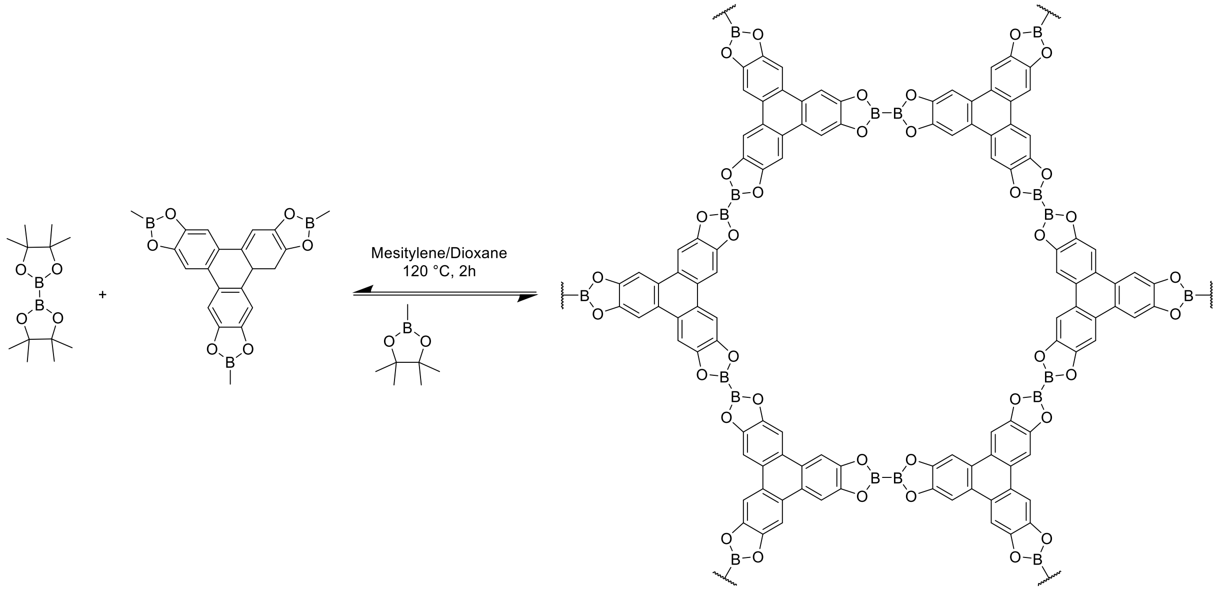

Using Method C: Bis(pinacolato)diboron (25.0 mg, 0.100 mmol), **MBA-HHTP** (26.0 mg, 0.06 mmol) and 1 mL of a 10:100:100 v:v:v solution of TFA:mesitylene:dioxane were added to a 5 mL glass ampule, purged 5 min and sealed under argon atmosphere (1 atm). The sealed ampule was heated to 120 °C for 2 h to afford **B2HHTP** as a white precipitate (20.5 mg, 90%).

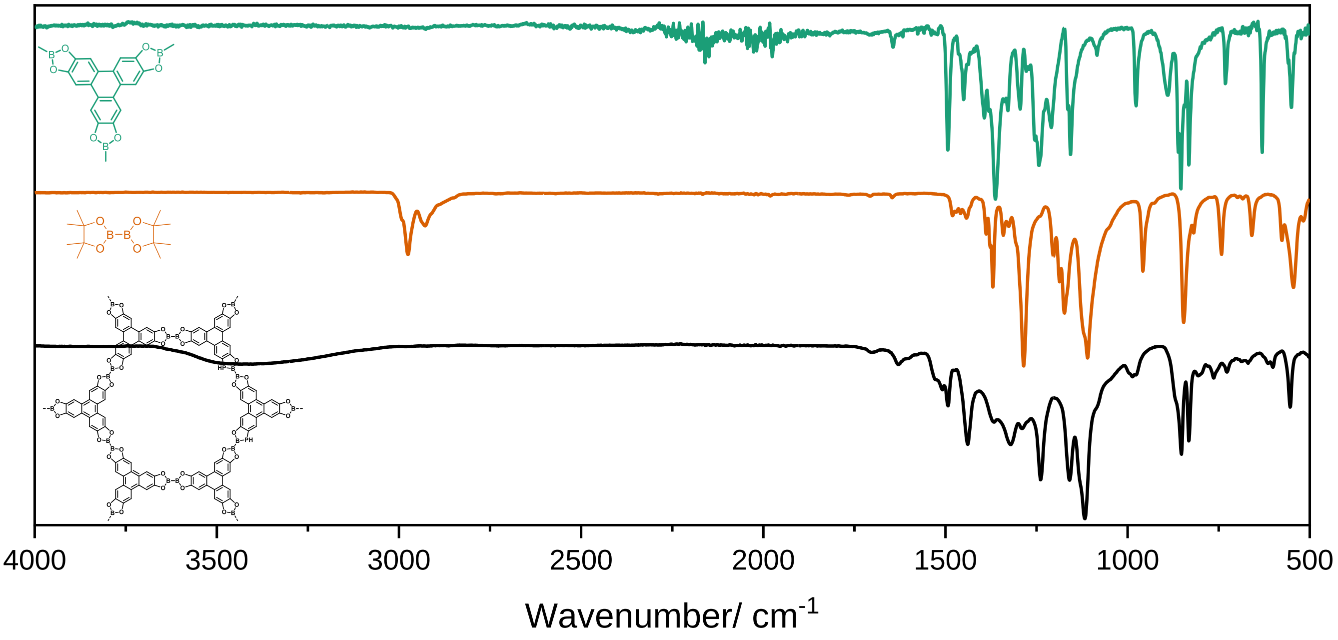

Figure 4.33. FTIR spectra of **MBA-HHTP** (green), bis(pinacolato)diboron (orange) and **B2HHTP** (black).

4.7.4. Lifetime Analysis of COF-5M

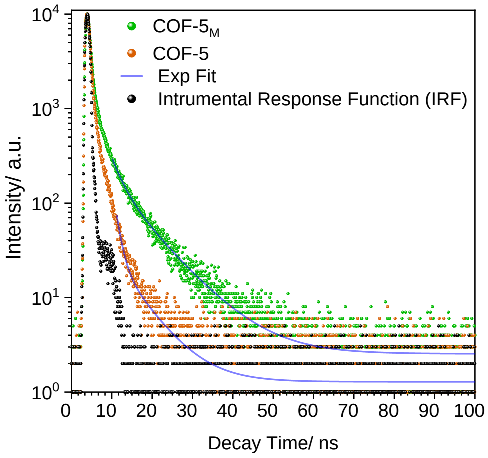

	τ_1 (ns)	a_1	τ_2 (ns)	a_2	τ_{avg} (ns)	$\sigma\langle\tau\rangle$
COF-5_M	2.5	54%	9.4	46%	5.7	0.13_5
COF-5	1.2	71%	6.8	21%	2.3	0.19

Figure 4.34. Fluorescence lifetimes of **COF-5_M** and **COF-5** powders (excitation at 373 nm, monitoring at 430 nm) and corresponding biexponential decay fitting parameters.

4.7.5. Computational Modeling

Table 4.8. The refined unit cell and the obtained Pawley refinement parameters.

COF	Unit Cell	Pawley refinement
COF-1_T (activated)	a= 15.0Å b= 15.20 Å c= 3.70Å α= 90° β= 90° γ= 60°	R_{wp} = 2.75%, R_p = 1.99%
COF-5_M (activated)	a= b=30.17 Å c= 3.46Å α= 90° β= 90° γ= 120°	R_{wp} = 3.68%, R_p = 1.95%
Py4THB	a= b= 15.4 Å c= 3.42Å α= 90° β= 90° γ= 98°	R_{wp} = 2.40%, R_p = 1.81%
B2HHTP	a= b= 22.8 Å c= 3.42Å α= 90° β= 90° γ= 120°	R_{wp} =3.0%, R_p = 2.33%

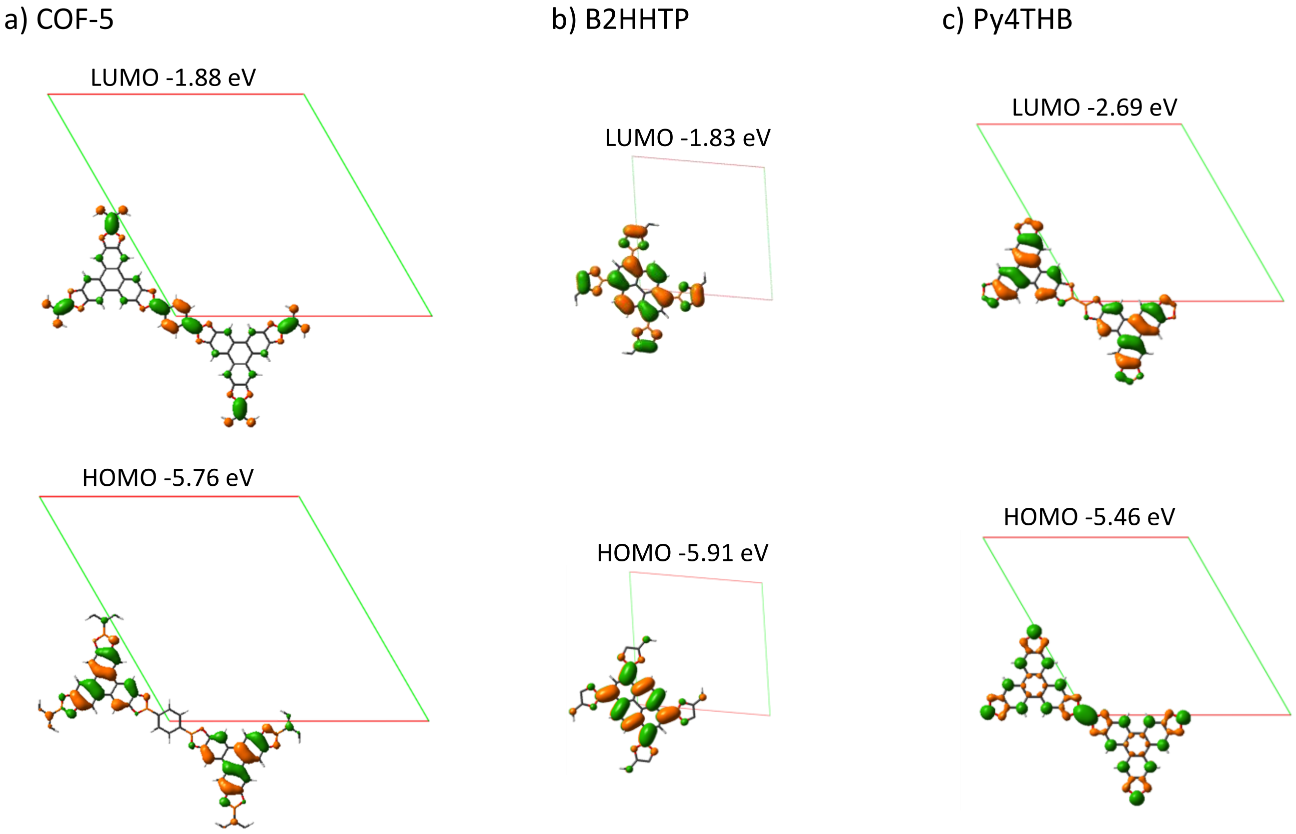

Figure 4.35. The HOMO/LUMO orbital topologies and energies of the COFs were obtained from optimized (B3LYP/6-31G(d)) monolayer calculations.

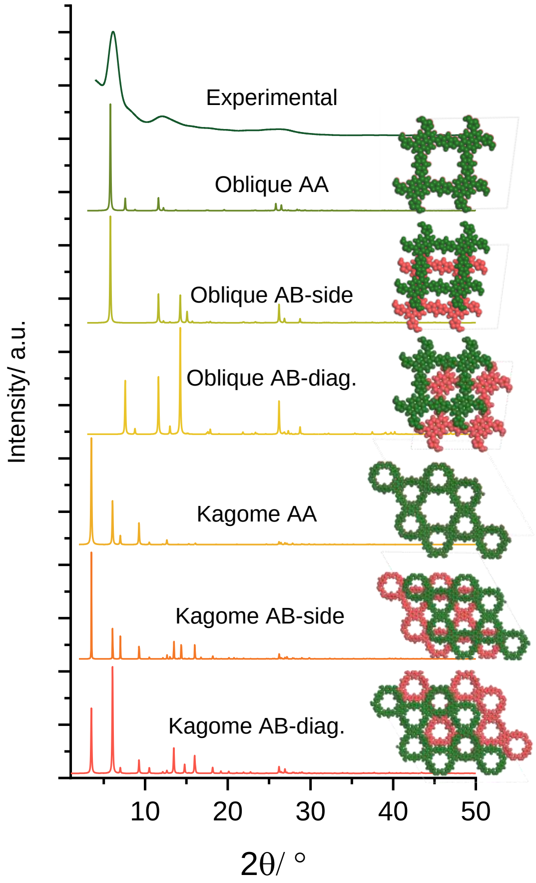

Figure 4.36. Experimental and simulated PXRD pattern of possible models of **Py4THB**.

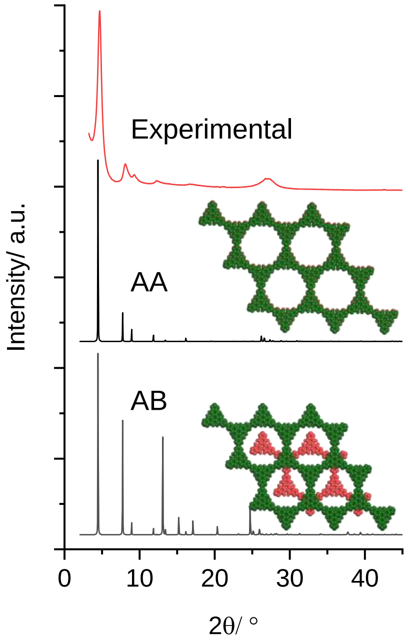

Figure 4.37. Experimental and simulated PXRD pattern of possible models of **B2HHTP**.

4.7.6. Oxidation of HHTP (photographs and products)

HHTP is readily oxidized in the air which leads to several radical and quinone intermediates.[11] These products can further complex with each other to make more stable charge transfer complexes also known as quinhydrones (Figure 4.39). The colored impurities and the EPR observation arise from the presence of the aforementioned impurities (Figure 4.38).

Figure 4.38. Effect of storage on **MBA-HHTP** and **HHTP** solids. The powders were left on the bench in the open air for the stability test.

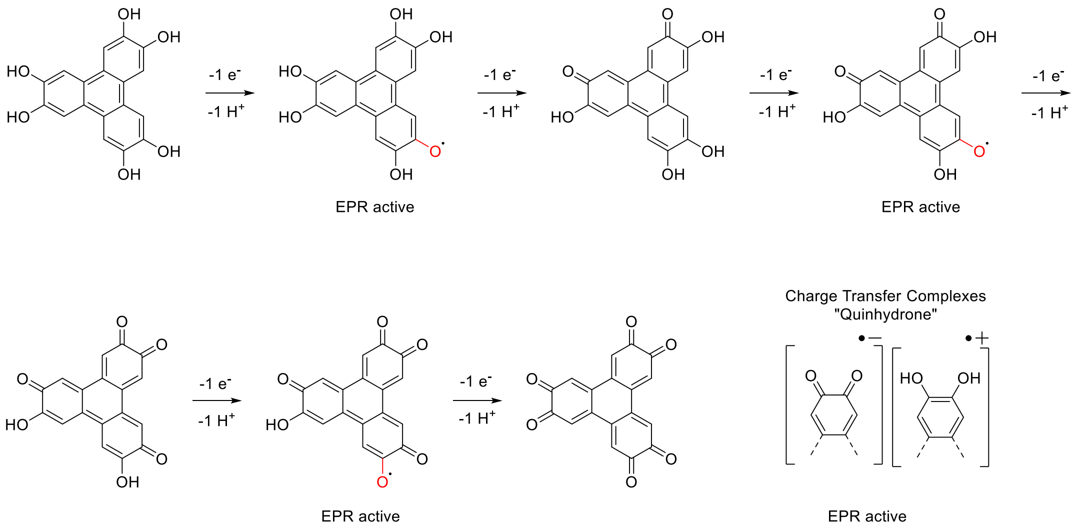

Figure 4.39. Semiquinone radicals, quinone intermediates, and the resulting quinone/hydroquinone charge-transfer complex (‘quinhydrone’) are expected from oxidation of 2,3,6,7,10,11-hexahydroxytriphenylene (HHTP). Both the radical intermediates as well as the quinhydrone complex are EPR active.[11]

4.7.7. Synthesis of monomers/precursors.

B-Methylcatecholborane (MBA-Cat):

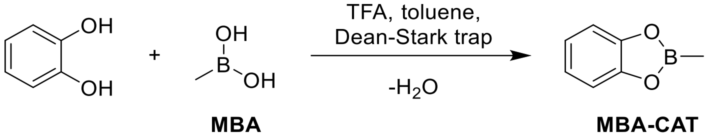

A mixture of catechol (1.00 g, 9.08 mmol) and **MBA** (0.598 g, 9.99 mmol) was added to a 5 vol% solution of TFA in toluene (50 mL). The reaction mixture was equipped with a Dean-Stark trap and refluxed for 2 h until all catechol solid was dissolved and no further accumulation of water in the Dean-Stark collector was observed. The produced solution was then concentrated on a rotavapor to afford a viscous brown liquid (1.10 g, 90%) which was distilled (under 0.1 torr) prior to use. The corresponding NMR spectral data matched that previously reported.[12] ^{1}H NMR (500 MHz, $CDCl_3$) δ 7.23 (m, 2H), 7.09 (m, 2H), 0.82 (s, 3H). ^{13}C NMR (126 MHz, $CDCl_3$) δ 148.29, 122.49, 112.17 (H_3C-B was not observed). ^{11}B NMR (128 MHz, $CDCl_3$) δ 35.43.

Tetrahydroxybenzene (THB):

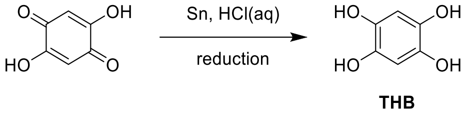

THB was synthesized according to the literature.[13] Granular tin metal (6.36 g, 53.5 mmol) was slowly added to a mixture of 2,5-dihydroxybenzoquinone (5.00 g, 35.7 mmol) in 50 mL of 36% aq. HCl, while stirring. This mixture was slowly heated to reflux while stirring for 3 h during which time a vigorous gas evolution was observed and the reaction mixture changed from an orange slurry to a pale yellow solution. The solution was filtered hot through a filter paper and allowed to cool slowly to 0 °C. The resulting white crystals of tetrahydroxybenzene were collected by filtration, washed with water, and dried in a vacuum (3.35 g. 66%). The compound was recrystallized twice from degassed (Ar purged) tetrahydrofuran with 1% acetic acid to afford pure **THB** (2.53 g, 50%) with the NMR spectra matching that reported before.[14] ^{1}H NMR (500 MHz, DMSO-d_6) δ 7.94 (s, 2H), 6.21 (s, 1H). ^{13}C NMR (126 MHz, DMSO-d_6) δ 137.48, 105.16.

2,6-Dimethylbenzo[1,2-d:4,5-d']bis([1,3,2]dioxaborole) (MBA-THB):

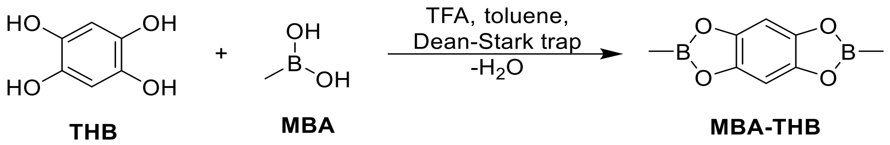

A mixture of **THB** (0.515 g, 3.62 mmol) and **MBA** (0.455 g, 7.61 mmol) was added to a 5 vol% solution of TFA in toluene (50 ml). The reaction mixture was equipped with a Dean-Stark trap and refluxed for 2 h until all solids were dissolved and there was no indication of water trapping in the Dean-Stark collector. The produced solution was filtered hot through a filter paper and concentrated on a rotavapor to afford **MBA-THB** (550 mg, 80%) as pure white crystals, which was used in COF synthesis without further purification. HRMS calculated for $C_8H_8B_2O_4$: 190.0603; observed (APCI, [M^+]) =190.0603 . ^{1}H NMR (500 MHz, $CDCl_3$) δ 7.11 (s, 2H), 0.79 (s, 6H); ^{13}C NMR (126 MHz, $CDCl_3$) δ 143.31, 97.58, (H_3B-C not observed); ^{11}B NMR (128 MHz, $CDCl_3$) δ 35.62.

2,3,6,7,10,11-Hexamethoxytriphenylene (HMTP):

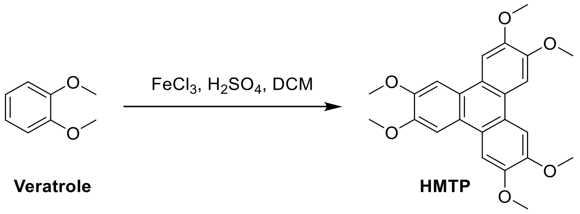

HMTP was synthesized according to the literature.[15] $FeCl_3$ (19.02 g, 117.3 mmol) was slowly added to a mixture of conc. H_2SO_4 (0.25 mL) and dry DCM (50 mL) and the resulting suspension was cooled with an ice bath to <5 °C. A solution of veratrole (5.00 mL, 36.2 mmol) in dry DCM (25 ml) was then added dropwise over 20 min. The reaction mixture was slowly warmed up to room temperature over 3 h while stirring. The resulting slurry was then quenched with 50 mL of methanol in small portions (5 ml per portion), during which the reaction mixture changed color from dark blue into pale yellow suspension. After stirring at room temperature for another 30 min, the precipitate was filtered, washed thoroughly with methanol (0.5 L) and water (5 × 10 mL), and dried under vacuum to afford **HMTP** (4.16 g, 78%) as a pale-yellow crystalline powder which was used for the next step without purification. The corresponding ^{1}H NMR spectral data matched those reported previously in the literature.[15] ^{1}H NMR (500 MHz, $CDCl_3$) δ 7.80 (s, 1H), 4.15 (s, 3H); ^{13}C NMR (126 MHz, $CDCl_3$) δ 148.82, 123.24, 104.34, 56.10.

2,3,6,7,10,11-Hexahydroxytriphenylene (HHTP):

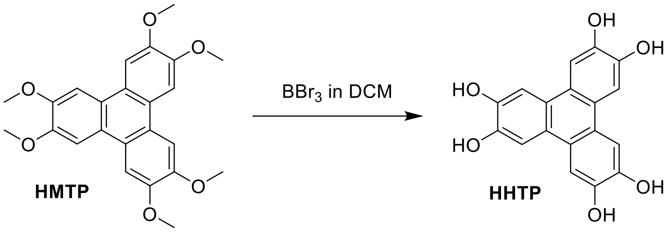

HHTP was synthesized according to the literature.[15] **HMTP** (1.00 g, 2.45 mmol) was dissolved in dry DCM (15 ml), purged with argon for 10 min, and cooled to -70 °C in an acetone-dry ice bath. BBr_3 (16 ml of 1M solution in DCM, 16 mmol) was then added dropwise. The reaction mixture was stirred under argon for 3 h and brought up to room temperature overnight. The reaction mixture was quenched by slow addition of deionized water (the DCM started to boil off). Saturated NaCl solution (15 ml) was then added and the mixture was extracted with 1% acetic acid solution in ethyl acetate (5 × 80 ml); this step should be performed quickly because of the oxidation of the HHTP observed as dark-purple colorization. The organic layer was dried by $MgSO_4$ and the solvent was evaporated under reduced pressure to afford 0.78 g (98%) of light green solid. The spectral data was identical to that reported.[15] ^{1}H NMR (500 MHz, DMSO-*d$_6$*) δ 7.62 (s, 1H); ^{13}C NMR (126 MHz, DMSO-*d$_6$*) δ 145.47, 122.32, 108.19.

2,7,12-Trimethyltriphenyleno[2,3-d:6,7-d':10,11-d'']tris([1,3,2]dioxaborole) (MBA-HHTP):

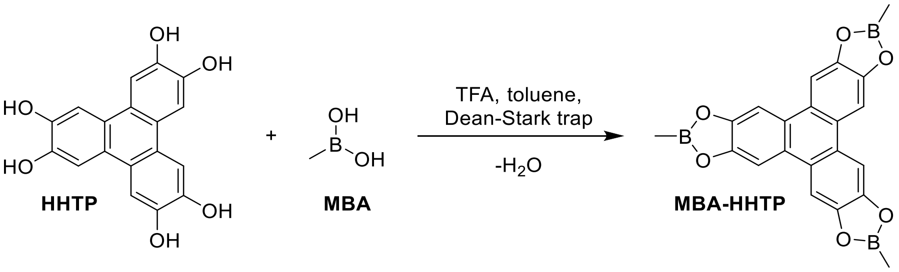

A mixture of **HHTP** (0.500 g, 1.54 mmol) and **MBA** (0.304 g, 5.09 mmol) was added to a 5 vol% TFA/toluene (50 mL). The reaction mixture was equipped with a Dean-Stark trap and was purged with Ar for 10 min and refluxed for 2 h until all solids were dissolved and there was no indication of water trapping in the Dean-Stark collector. The mixture was cooled to room temperature over 1 h and then kept in an ice bath for 30 min during which fluffy white crystals were formed. The crystals were filtered and dried under vacuum to afford **MBA-HHTP** (0.49 g, 80%) which was of sufficient purity (< 98% by NMR), and used in COF synthesis as is. HRMS calculated for $[MH^+]C_{21}H_{16}B_3O_6$: 397.1221; observed (APCI, $[MH^+]$) = 397.1240. ^{1}H NMR (500 MHz, $CDCl_3$) δ 8.16 (s, 1H), 0.93 (s, 3H); ^{13}C NMR (126 MHz, $CDCl_3$) δ 148.24, 125.56, 105.51, (the H_3B-C was not observed); ^{11}B NMR (128 MHz, $CDCl_3$) δ 36.06 (broad).

1,3,6,8-Pyrenetetraboronic pinacol ester

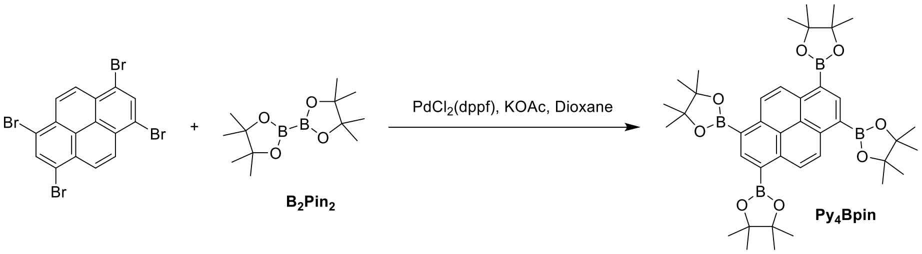

Py4Bpin was synthesized according to the literature.[16] 1,3,6,8-Tetrabromopyrene (0.500 g, 0.96 mmol) and B_2Pin_2 (1.47 g, 5.79 mmol) and KOAc (0.948 mg, 9.66 mmol) were dispersed in 1,4-dioxane (10 ml) in a 25 ml round bottom and degassed by purging with argon for 10 min. $PdCl_2$(dppf) (0.035 g, 0.048 mmol, 5 mol%) was added and the reaction mixture was purged for another 10 min and then refluxed for 72 h under argon. Then the mixture was cooled to room temperature and saturated NaCl solution (20 ml) and ethyl acetate (25 ml) were added. Organic phase was decanted and washed with saturated NaCl solution (2 × 20 ml), dried over $MgSO_4$, and concentrated under reduced pressure. The crude product was purified by column chromatography using hexane/DCM 2:8 as eluent, to give a light-yellow powder of the desired product (450 mg, 66%). The NMR spectral data matched that reported.[16] ^{1}H NMR (500 MHz, $CDCl_3$) δ 9.18 (s, 4H), 9.01 (s, 2H), 1.52 (s, 48H); ^{13}C NMR (126 MHz, $CDCl_3$) δ 141.30, 137.97, 129.41, 123.97, 83.81, 25.08, (the C-B was not observed); ^{11}B NMR (128 MHz, $CDCl_3$) δ 30.36.

4.7.8. References of Supplementary information

1. Chaudhari, S. R., Screening and assignment of phenylboronic acid and its anhydride formation by NMR spectroscopy. *Chem. Phys. Lett.* **2015,** *634*, 95-97.

2. Spitler, E. L.; Dichtel, W. R., Lewis acid-catalysed formation of two-dimensional phthalocyanine covalent organic frameworks. *Nat. Chem.* **2010,** *2*, 672-677.

3. Frisch, M. J.; Trucks, G. W.; Schlegel, H. B.; Scuseria, G. E.; Robb, M. A.; Cheeseman, J. R.; Scalmani, G.; Barone, V.; Petersson, G. A.; Nakatsuji, H.; Li, X.; Caricato, M.; Marenich, A. V.; Bloino, J.; Janesko, B. G.; Gomperts, R.; Mennucci, B.; Hratchian, H. P.; Ortiz, J. V.; Izmaylov, A. F.; Sonnenberg, J. L.; Williams; Ding, F.; Lipparini, F.; Egidi, F.; Goings, J.; Peng, B.; Petrone, A.; Henderson, T.; Ranasinghe, D.; Zakrzewski, V. G.; Gao, J.; Rega, N.; Zheng, G.; Liang, W.; Hada, M.; Ehara, M.; Toyota, K.; Fukuda, R.; Hasegawa, J.; Ishida, M.; Nakajima, T.; Honda, Y.; Kitao, O.; Nakai, H.; Vreven, T.; Throssell, K.; Montgomery Jr., J. A.; Peralta, J. E.; Ogliaro, F.; Bearpark, M. J.; Heyd, J. J.; Brothers, E. N.; Kudin, K. N.; Staroverov, V. N.; Keith, T. A.; Kobayashi, R.; Normand, J.; Raghavachari, K.; Rendell, A. P.; Burant, J. C.; Iyengar, S. S.; Tomasi, J.; Cossi, M.; Millam, J. M.; Klene, M.; Adamo, C.; Cammi, R.; Ochterski, J. W.; Martin, R. L.; Morokuma, K.; Farkas, O.; Foresman, J. B.; Fox, D. J. *Gaussian 16 Rev. C.01*, Wallingford, CT, 2016.

4. Callahan, R. W.; Keene, F. R.; Meyer, T. J.; Salmon, D. J., Intervalence transfer and electron transfer in the mixed-valence ion dichlorotetrakis (bipyridine) pyrazinediruthenium (3+). *J. Am. Chem. Soc.* **1977,** *99*, 1064-1073.

5. ReactLab™ KINSIM2. https://jplusconsulting.com/products/reactlab-kinsim-2/) (accessed on 14 Jan. 2021).

6. Côté, A. P.; Benin, A. I.; Ockwig, N. W.; O'Keeffe, M.; Matzger, A. J.; Yaghi, O. M., Porous, Crystalline, Covalent Organic Frameworks. *Science* **2005,** *310*, 1166-1170.

7. Wan, S.; Guo, J.; Kim, J.; Ihee, H.; Jiang, D., A photoconductive covalent organic framework: self-condensed arene cubes composed of eclipsed 2D polypyrene sheets for photocurrent generation. *Angew. Chem. Int. Ed.* **2009,** *48*, 5439-5442.

8. Tilford, R. W.; Gemmill, W. R.; zur Loye, H.-C.; Lavigne, J. J., Facile Synthesis of a Highly Crystalline, Covalently Linked Porous Boronate Network. *Chem. Mater.* **2006,** *18*, 5296-5301.

9. Cote, A. P.; El-Kaderi, H. M.; Furukawa, H.; Hunt, J. R.; Yaghi, O. M., Reticular synthesis of microporous and mesoporous 2D covalent organic frameworks. *J. Am. Chem. Soc.* **2007,** *129*, 12914-12915.

10. Wan, S.; Guo, J.; Kim, J.; Ihee, H.; Jiang, D., A belt-shaped, blue luminescent, and semiconducting covalent organic framework. *Angew. Chem. Int. Ed.* **2008,** *47*, 8826-8830.

11. Yang, J.; Cohen Stuart, M. A.; Kamperman, M., Jack of all trades: versatile catechol crosslinking mechanisms. *Chem. Soc. Rev.* **2014,** *43*, 8271-8298.

12. Ishida, K.; Yamazaki, H.; Hagiwara, C.; Abe, M.; Kusama, H., Efficient Generation and Synthetic Applications of Alkyl-Substituted Siloxycarbenes: Suppression of Norrish-Type Fragmentations of Alkanoylsilanes by Triplet Energy Transfer. *Chem. Eur. J.* **2020,** *26*, 1249-1253.

13. Weider, P. R.; Hegedus, L. S.; Asada, H., Oxidative cyclization of unsaturated aminoquinones. Synthesis of quinolinoquinones. Palladium-catalyzed synthesis of pyrroloindoloquinones. *J. Org. Chem.* **1985,** *50*, 4276-4281.

14. Park, S.; Liao, Z.; Ibarlucea, B.; Qi, H.; Lin, H.-H.; Becker, D.; Melidonie, J.; Zhang, T.; Sahabudeen, H.; Baraban, L.; Baek, C.-K.; Zheng, Z.; Zschech, E.; Fery, A.; Heine, T.; Kaiser, U.; Cuniberti, G.; Dong, R.; Feng, X., Two-Dimensional Boronate Ester Covalent Organic Framework Thin Films with Large Single Crystalline Domains for a Neuromorphic Memory Device. *Angew. Chem. Int. Ed.* **2020,** *59*, 8218-8224.

15. Yahiaoui, O.; Fitch, A. N.; Hoffmann, F.; Froba, M.; Thomas, A.; Roeser, J., 3D Anionic Silicate Covalent Organic Framework with srs Topology. *J. Am. Chem. Soc.* **2018,** *140*, 5330-5333.

16. Sprick, R. S.; Jiang, J. X.; Bonillo, B.; Ren, S.; Ratvijitvech, T.; Guiglion, P.; Zwijnenburg, M. A.; Adams, D. J.; Cooper, A. I., Tunable organic photocatalysts for visible-light-driven hydrogen evolution. *J. Am. Chem. Soc.* **2015,** *137*, 3265-3270.

Chapter 5

Efficient Room-Temperature Phosphorescence of Covalent Organic Frameworks through Covalent Halogen Doping

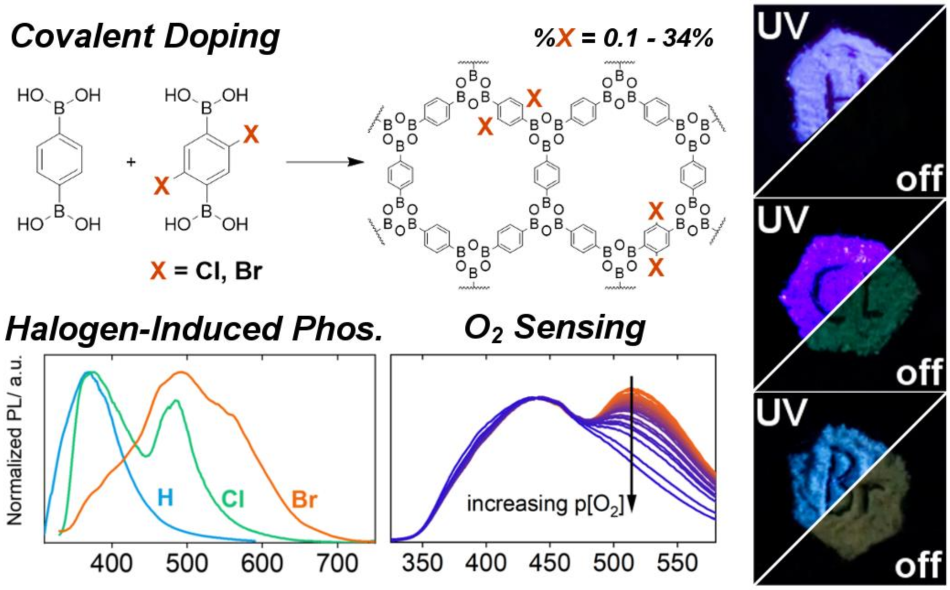

1.

Preface

In Chapters 2 and 3, we explored efficient ORTP emission in two series of organic molecules, TANGOs, and acridones. We showed that the type of molecular packing in crystalline solids plays a crucial role in their photophysical behaviour. For instance, in Chapter 2, we illustrated that efficient phosphorescence occurs in TANGO solids with parallel stacked molecules (bearing small permutations). In contrast, *t*BuTANGO with bulky substituents, ~60° rotation of the molecules in their π-stacks, results in only pure fluorescent emission. In Chapter 3, we manifested that triplet-triplet annihilation(TTA), as one of the key quenching mechanisms of phosphorescent emission, is highly dependent on the intermolecular interaction and orientation of neighboring molecules.

Even though these findings paved the way for our understanding of structure-photophysics relationships, their practical applications are hindered by the incapability of crystal structure prediction. As such, realizing new ORTPs is still based on empirical exercise rather than rational design.In this context, we aim to utilize covalent organic frameworks (COFs) as predictable organic solids toward the realization of tunable ORTPs. In Chapter 4, we designed a novel COF reaction toward boroxine and dioxaborole-linked COFs from soluble and stable precursors and in the absence of water (which is the byproduct of conventional reaction). Exploiting the developed reaction we synthesized seven known and two novel COFs. All obtained COFs possess high crystallinity and optical purity compared to those achieved from conventional condensation.

In this chapter, we report a covalent halogen doping strategy toward enhancing the phosphoresce efficiency in COFs. Such controlled halogen doping enhances the intersystem crossing while minimizing the TTA by diluting the phosphors. We synthesized 12 highly emissive covalently doped COFs ($\Phi_{phos} \leq 29\%$ at room temperature) with varying dopant type (Cl, Br) and doping ratio. XRD analysis of the COF powders suggested that all COFs have the same solid-state packing and topology; however, their phosphorescence properties significantly vary upon changing the doping ratio from almost pure fluorescence to pure phosphorescence emission. We found that in these COFs, enhancing the concentration of dopant initially increases the Φ_{phos}; however, at higher concentration, the emission quenches via TTA. The rigidity of the COF suppresses vibrational relaxation, and the presence of mesitylene solvent inside the pore blocks the oxygen permeation in the COFs, allowing for visible phosphorescence at room temperature in air. Furthermore, exploiting the porosity of the COFs and the simultaneous presence of the singlet and triplet emitting channels enables a highly efficient COF-based oxygen sensor with an ultra-wide dynamic detection range, ~ 10^3 -10^{-5} torr of partial oxygen pressure.

Author contributions

Dmytro F. Perepichka and I conceived the project and wrote the paper. Allen Tao and I have synthesized, purified, and performed structural characterization of all starting materials and COFs reported in this chapter. Cory Ruchlin and I performed photophysical characterization (steady-state, lifetime analysis and quantum yields) and density functional theory calculations. Cheng-hao Liu performed the TEM and HAADF mapping and Hatem M. Titi determined the BrPBA crystal structure and performed thermal analysis and Hirshfeld surface analysis. Manuscript was written by Cory Ruchlin and me and revised by Dmytro F. Perepichka. Cory Ruchlin and I contributed equally to this manuscript.

This chapter is reprinted with permission from Hamzehpoor, E.; Ruchlin, C.; Tao, Y. Z.; Liu, C. H.; Titi, H. M.; Perepichka, D. F., "Efficient room-temperature phosphorescence of covalent organic frameworks through covalent halogen doping". *Nat. Chem.* **2023**, 15, 83-90.

5.1. Abstract

Organic room-temperature phosphorescence, a spin-forbidden radiative process, has emerged as an interesting but rare phenomenon with multiple potential applications in optoelectronic devices, biosensing, and anticounterfeiting. Covalent organic frameworks (COFs) with accessible nanoscale porosity and precisely engineered topology can offer unique benefits in the design of phosphorescent materials, but these are presently unexplored. Here, we report an approach of covalent doping, whereby a COF is synthesized by copolymerization of halogenated and unsubstituted phenyldiboronic acids, allowing for random distribution of functionalized units at varying ratios, yielding highly phosphorescent COFs. Such controlled halogen doping enhances the intersystem crossing while minimizing the triplet-triplet annihilation by diluting the phosphors. The rigidity of the COF suppresses vibrational relaxation and allows high phosphorescence quantum yield ($\Phi_{phos} \leq 29\%$) at room temperature. The permanent porosity of the COFs and the combination of the singlet and triplet emitting channels enable a highly efficient COF-based oxygen sensor with an ultra-wide dynamic detection range, ~ 10^3 -10^{-5} torr of partial oxygen pressure.

5.2. Introduction

Since they were first reported in 2005,[1] covalent organic frameworks (COF) have seen an exponentially growing interest from materials scientists. Their ordered structure, precisely controlled *via* the choice of the building blocks, enables the design of topologies atypical for organic solids – from molecularly defined open porosity to layered 2D materials. The strong covalent bonds between the units provide remarkable structural and thermal stability and allow the electronic coupling between the molecular nodes to be tuned. In addition to many important applications already explored with other porous frameworks (for example, metal-organic frameworks (MOFs)) such as gas storage and separation, energy storage, water splitting, and catalysis,[2] the metal-free nature of COFs bears a number of advantages, namely low elemental toxicity, stability, and light-weight, while providing a unique platform to develop robust and sustainable functional materials. The programmable crystalline order and a plethora of configurable building blocks are highly desirable for applications such as light-emitting and photovoltaic materials, while the nanoscale porosity also opens access to sensing and other energy-transfer systems.[3] There has been substantial progress in the design and synthesis of fluorescent COFs,[3-7] but phosphorescent COFs remain essentially unexplored. The only reported example, based on benzil (a common triplet sensitizer) linkers, showed visible phosphorescence at 77 K but the phosphorescence efficiency at room temperature (~0.1%) was significantly lower than that of benzyl-based amorphous polymers and molecular crystals.[8]

Phosphorescence, a radiative relaxation of the triplet excited state (T_1; usually formed via a spin-forbidden intersystem crossing, ISC), is generally much slower than the spin-allowed radiative relaxation of S_1 (fluorescence). Most organic materials exhibit insignificant phosphorescence compared to fluorescence due to inefficient ISC. In recent years, organic room temperature phosphorescence (RTP) has become a ‘hot’ research topic, driven by both scientific curiosity (controlling spin-forbidden processes such as phosphorescence by molecular design) as well as promising practical applications[9-15] including biosensing/imaging,[13] anticounterfeiting/data encryption,[16] high-efficiency organic light-emitting diodes (breaking through the unfavorable 1:3 singlet: triplet spin-statistics),[17] and photovoltaics (overcoming Shockley-Queisser limit through up-conversion),[18, 19] 3D displays,[20] and light-controlled triplet qubits for quantum computing applications.[21] In most cases, the design of organic RTP materials relies on (1) heavy atoms or (2) functional groups that enable excitations with different orbital momenta for singlet and triplet states (e.g., n-π*→ π-π* for C=O), to increase the spin-orbit coupling and accelerate ISC. Recently, RTP has also been discovered in some crystalline organoboron derivatives, although the mechanism for its emergence is not yet well understood.[22, 23] Immobilization of chromophore molecules in the crystalline state[24,14, 15] or as a solid solution in rigid matrices[11, 25, 26] can suppress quenching of triplet state via vibrational relaxation and triplet-triplet annihilation and is generally required for efficient RTP.

One of the key challenges of RTP design in organic solids is its dependence on molecular packing,[13-15] the control of which (also known as 'crystal engineering') remains very difficult, despite several decades of efforts.[27] In this context, structural control of COFs based on principles of reticular chemistry seems to be a promising tool for the engineering of phosphorescent materials.

In this article, we report a strategy for the design of phosphorescent materials by incorporating a controlled amount of the functionalized co-monomers during COF synthesis (that is *in situ* doping). Such '*covalent doping*' allows us to integrate a precise amount of heteroatoms into a single-phase framework material. This doping is analogous to doping in inorganic semiconductors but fundamentally different from classical doping in organic materials where the dopant molecules or ions are incorporated through non-covalent interactions. A similar strategy has been used to control the composition and some properties of MOFs.[28-30] Also, synthesis of related 'solid solution' COFs by mixing different linkers has recently been reported.[31] Nevertheless, although molecular doping (by guest acceptors) has been used to improve electrical conductivity in COFs,[32-34] to the best of our knowledge it has not yet been used to tailor an optical property in organic framework materials.

Our approach combines three key factors necessary for achieving efficient phosphorescence: i) the heavy atom effect, ii) dilution of the phosphors to reduce triplet-triplet annihilation, and iii) a rigid, low phonon energy matrix to suppress the vibrational deactivation of the excited triplet state. We have synthesized halogenated derivatives of the prototypical boroxine-linked COF-1, exploring the effect of different halogens (Cl, Br) and doping concentrations on their photophysical properties (Figure 5.1). These COFs show high photoluminescence quantum yields (PLQY $\leq$40%) and a remarkably efficient RTP ($\Phi_{\text{phos.}} \leq$29%). The permanent porosity of these COFs enables the realization of a COF-based oxygen sensor with a wide dynamic range, from 762 Torr (pure oxygen at atmospheric pressure) to 10^{-5} Torr of partial oxygen pressure. Access to highly emissive phosphorescent COFs provides the means to rationally design solid-state organic RTPs and might unlock previously untapped technologies enabled by these materials.

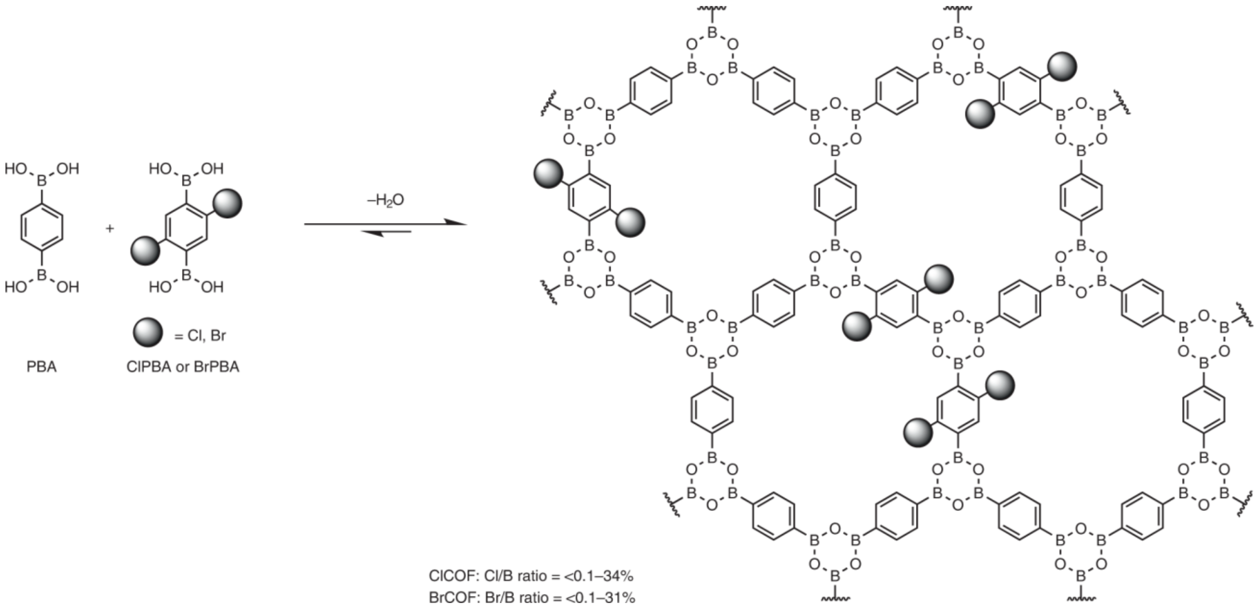

Figure 5.1. Schematic representation of the formation of doped COFs by copolymerization of PBA with ClPBA and BrPBA. The doping level can be tuned by changing the ratio of PBA and halogenated PBA.

5.3. Results and Discussion

5.3.1. Photophysical properties of boroxine COF-1

Boroxine is the first and one of the most studied COF synthons,[1] which has been used in the design of fluorescent COFs for over 10 years.[5, 6, 35] Surprisingly, no photophysical studies have been reported for the parent (the first reported[1]) COF-1. The precursor monomer of COF-1 (phenyldiboronic acid, PBA) is a highly fluorescent solid (PLQY = 66%, λ_{PL} = 329 nm) which shows a very weak RTP at $\lambda_{Phos.}$ = 494 nm with a long lifetime $\tau_{Phos.}$ = 0.92 s.[36] We expected that the incorporation of PBA moiety in a COF could restrict the vibrational relaxation of the T_1 state, and the co-facial arrangement of chromophores in an AA-stacked packing would result in H-aggregation type photophysical behavior, which is known to enhance RTP.[12] Following UV excitation (λ_{ex} = 300 nm), as-synthesized (non-activated) COF-1 shows intense deep-blue fluorescence (λ_{fl} = 390 nm, PLQY = 46%) which is red-shifted by ~0.77 eV compared to that of the crystalline PBA monomer (Figure 5.7). Delayed emission spectra of COF-1 in air show a delayed fluorescence (DF) at 390 nm and a broad phosphorescence band at 515 nm, with lifetimes τ_{DF} = 32.8 ± 1.0 ms and τ_{Phos} = 78.7 ± 1.4 ms, respectively (Figure 5.8). The large singlet-triplet gap (ΔE_{S-T}) of ~0.75 eV excludes the possibility of the thermally-activated reverse ISC. In addition, the twice shorter lifetime of the DF vs. the phosphorescence, along with its approximately quadratic relation to the triplet population of the system, suggests triplet-triplet annihilation (TTA) as an underlying mechanism for this DF (Figure 5.8 b,c).[37] TTA occurs when two T_1 states encounter one another and annihilate, generating S_0 and S_1 states responsible for the DF. Observation of this phenomenon implies efficient diffusion of T_1 excitons through the COF. We additionally note that the removal of oxygen (a known triplet quencher) from the COF pores under high vacuum results in a major enhancement of the DF intensity (×20) and phosphorescence intensity (×4; Figure 5.9). Furthermore, almost no phosphorescence has been observed in air after activation of the COF-1 (180 °C, 10^{-3} torr, 12 h) where removal of the solvent (mesitylene) guest molecules increases the pore accessibility. The phosphorescence of the activated COF can be restored by either evacuating the sample (Figure 5.9a) or by adding a drop of mesitylene (Figure 5.9 b, c) suggesting that the solvent guest molecules suppress the diffusion of oxygen and quenching of the triplet states. Nevertheless, the phosphorescence content of COF-1 is very low and the afterglow is not observable to the naked eye at room temperature (Figure 5.3c).

5.3.2. Synthesis and Structural Characterization of doped-COFs

To accelerate the ISC and enhance the phosphorescence, we decided to decorate the COF-1 backbone with halogen atoms (Figure 5.1). The chlorinated and brominated PBA monomers were synthesized on a multigram scale using iridium-catalyzed direct borylation of 1,4-dihalobenzenes with diboron pinacolate, followed by transesterification-deprotection with methylboronic acid to afford the corresponding boronic acids, ClPBA and BrPBA. Their molecular and crystal structure were fully characterized (see supporting information) and inductively coupled plasma optical emission spectroscopy (ICP-OES) showed no detectable amounts of heavy metals (Ir, Pd), ruling out inorganic phosphorescent impurities (<1 ppm, Figure 5.22 and Table 5.7).

Our initial efforts to polymerize ClPBA and BrPBA resulted in a low yield of boroxine-linked solids (Fourier-transform infrared (FTIR) spectroscopy) with very low porosity and no characteristic COF peaks in their X-ray diffraction patterns (Figure 5.10). This might be a result of the steric bulkiness of the halogens which destabilizes the planar triphenylboroxine node of the network; indeed, the Cl···O (3.11 Å) and Br···O (3.06 Å) contacts in the planar COF sheets are shorter than van der Waals distances (3.27 and 3.34 Å, respectively) and the condensation reaction is predicted to be more endothermic for the halogenated PBA (Figure 5.11). We thus decided to co-polymerize halogenated monomers with unsubstituted PBA to incorporate halogen atoms in covalently locked 2D sheets. A series of COFs with different halogen doping ratios were synthesized by co-condensation of PBA with ClPBA or BrPBA under standard solvothermal conditions (mesitylene/dioxane, 120 °C, 3 days) to afford ClCOF-N and BrCOF-N (where N represents the percentage of the doping measured as Cl/B or Br/B ratio by X-ray photoelectron spectroscopy (XPS)). The reaction yields gradually decrease from 96% for COF-1 (non-doped) to ~48% and 43% for ClCOF-34 and BrCOF-31, respectively, reflecting the steric hindrance of the halogen atoms (Figure 5.5). Since ClPBA, BrPBA, and PBA nodes have an identical length, no lattice strain is expected upon doping,[31] allowing for a homogenous distribution of dopants (no phase separation), as supported by high-angle annular dark-field mapping of samples in a scanning transmission electron microscope (HAADF-STEM, Figures 5.2 d,g). However, the lower equilibrium constant of boroxine formation for halogenated boronic acids[38] compared to non-substituted phenylboronic acid contributes to the lower yields of doped-COFs and explains why the halogen content of the COFs, assessed by XPS (Figures 5.2 a, c, f, and 5.14, 5.15) and ^{1}H NMR (Figures 5.2b and 5.16), is lower than the monomers' initial loading ratio. No appreciable amounts of other trace elements were found in the EDX, XPS, and ICP-MS results, further ruling out the presence of inorganic phosphorescent impurities.

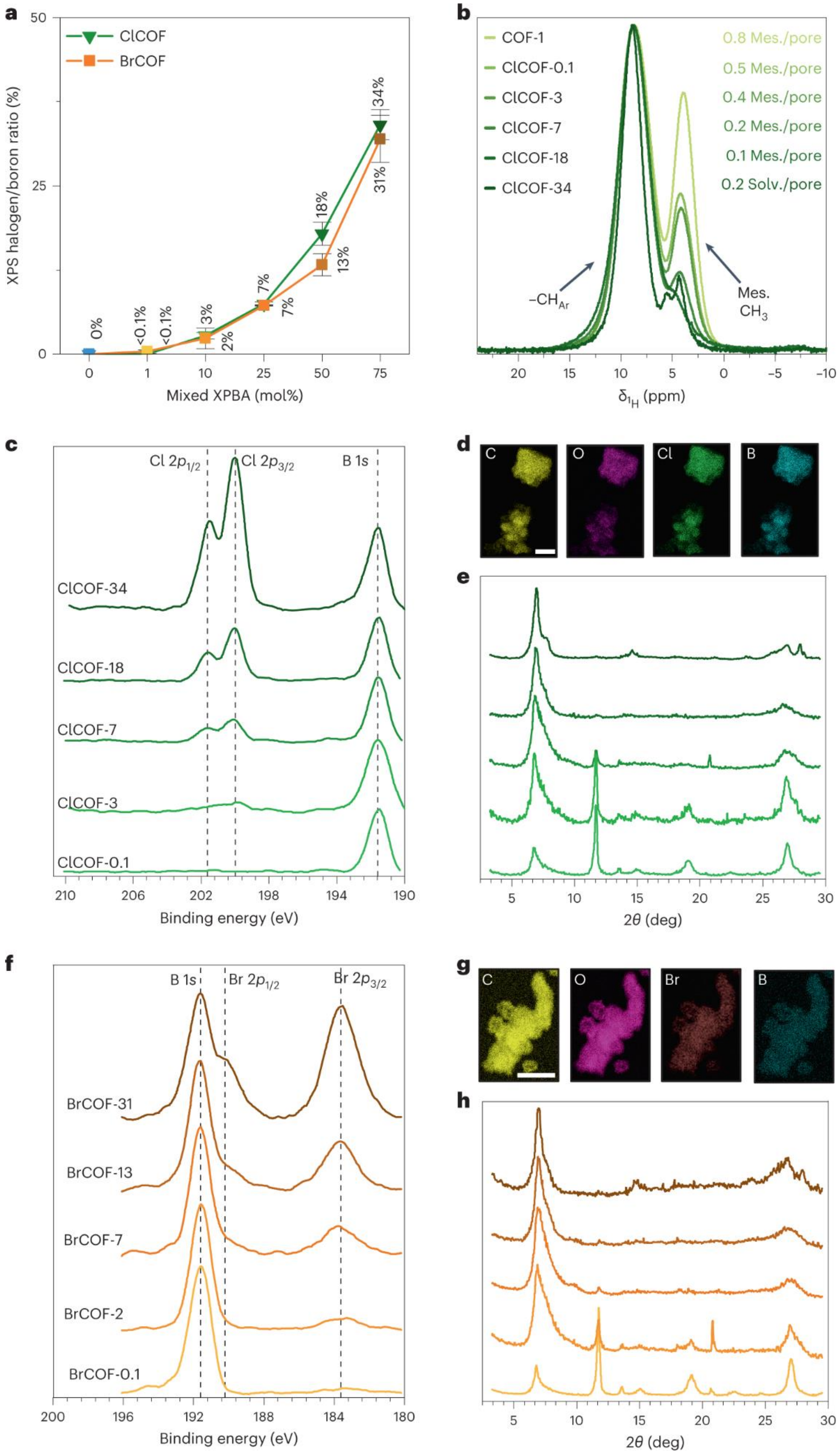
a
ClCOF
BrCOF
XPS halogen/boron ratio (%)
50
25
0
0%
<0.1%
<0.1%
3%
2%
7%
7%
18%
13%
34%
31%
0
1
10
25
50
75
Mixed XPBA (mol%)
b
COF-1
ClCOF-0.1
ClCOF-3
ClCOF-7
ClCOF-18
ClCOF-34
0.8 Mes./pore
0.5 Mes./pore
0.4 Mes./pore
0.2 Mes./pore
0.1 Mes./pore
0.2 Solv./pore
$-CH_{Ar}$
Mes. CH_3
20
15
10
5
0
−5
−10
$\delta_{^1H}$ (ppm)
c
Cl $2p_{1/2}$
Cl $2p_{3/2}$
B 1s
ClCOF-34
ClCOF-18
ClCOF-7
ClCOF-3
ClCOF-0.1
210
206
202
198
194
190
Binding energy (eV)
d
C
O
Cl
B
e
5
10
15
20
25
30
2θ (deg)
f
B 1s
Br $2p_{1/2}$
Br $2p_{3/2}$
BrCOF-31
BrCOF-13
BrCOF-7
BrCOF-2
BrCOF-0.1
200
196
192
188
184
180
Binding energy (eV)
g
C
O
Br
B
h
5
10
15
20
25
30
2θ (deg)

Figure 5.2. a) Doping level, as a percentage of total monomers containing halogen atoms, monitored by XPS versus the initial molar ratio of the ClPBA (green triangles) and BrPBA (orange squares) monomers, and without any halogenated monomers (blue squares, mean value of n = 3 sampling regions, error bars represent s.d.), showing incomplete incorporation of halogenated monomers**.** b–e), Characterization of Cl doping.b) Solid-state magic-angle spinning (23 kHz) ^{1}H NMR spectra showing the decrease of the mesitylene (Mes.) guest in (non-activated) ClCOF-Ns with increments in the doping level. c) High-resolution boron XPS, from which the actual halogen content is derived for ClCOF (green). d) Homogeneous elemental distribution of C (yellow), O (magenta), B (cyan) and Cl (green), confirmed by HAADF-STEM (200 kV) for ClCOF. Scale bar, 500 nm. e) Powder XRD spectra of the as-prepared (non-activated) ClCOFs. f-h) Characterization of Br doping. f), High-resolution boron XPS, from which the actual halogen content is derived for BrCOF (orange). g) Homogeneous elemental distribution of C (yellow), O (magenta), B (cyan) and Br (maroon), as confirmed by HAADF-STEM (200 kV) for BrCOF. Scale bar, 1 µm.h), Powder XRD of the as-prepared (non-activated) BrCOFs. For both ClCOFs (e) and BrCOFs (h), the PXRD spectra show high-angle anisotropic broadening and an increase of the (100)-to-(110) intensity ratio due to reduced inclusion of mesitylene guest molecules in doped COFs.

The FTIR spectra of the doped COFs show the disappearance of the OH stretching (ca. 3300 cm^{-1}) and the emergence of a new strong peak at 703-717 cm^{-1} for ClCOF-N and 694-707 cm^{-1} for BrCOF-N (B_2O_3 ring out of plane bending) indicative of complete condensation of the boronic acid groups into boroxine (Figures 5.17, 5.18). Also, the presence of distinct C=C aromatic stretches for the PBA (1508 cm^{-1}) and ClPBA (1473 cm^{-1}) or BrPBA (1471 cm^{-1}) shows the incorporation of both halogenated and non-halogenated monomers, with different ratios.

The X-ray diffraction (XRD) features of doped COFs are similar to those observed in COF-1 (Figures 5.2 e, h). The (*100*) plane diffraction intensity at 2θ = 6.8° increases at higher doping levels and the peaks reveal an anisotropic broadening toward the higher angles (smaller d-spacing), which has been previously observed upon similar 'filling' of the pores (with alkyl substituents).[39] The increasing halogen doping level also results in a progressive and substantial increase in the relative intensity of the (*100*) diffraction peak versus (*110*). A similar increase in the intensity of the (100) versus (110) peaks has been observed[1] previously upon activation of the parent boroxine COF-1 and was later explained[40] by the removal of the mesitylene guest molecules from the COF pores (see Supporting Information for further discussion). The Brunauer-Emmett-Teller (BET) analysis shows a moderate decrease of the surface area upon doping, from 740 m^2/g (COF-1) to 564 m^2/g (ClCOF-18) and 564 m^2/g (BrCOF-13) (Figure 5.21). The average pore diameter is not significantly affected by doping but the de Boer *t*-plot analysis of the pore size distribution suggests an increase of the mesoporosity content after doping, from 19% for COF-1 (17% reported in Ref. 1) to 41% for ClCOF-18 and 51% for BrCOF-13 (Table 5.6). The transmission electron microscopy (TEM, Figures 5.19, 5.20) shows rectangular 20-100 nm crystallites for the doped COFs. The overall data indicate that the 2D lattice of the boroxine COF is retained upon doping, although a random distribution of the halogen atoms leads to the expected decrease of the crystallinity and porosity. Our ‘covalent doping’ approach is general and could also be used with other substituents. To demonstrate this, mixed COFs with a similar degree of crystallinity/disorder to Cl/Br-doped COFs were prepared by co-polymerization of PBA with tetrafluoro-PBA (F4COF-50) and 2,5-dimethyl-PBA (MeCOF-50, Figures 5.36 a,b).

5.3.3. Photophysical Characterization of Doped COFs

The crystalline ClPBA and BrPBA monomers are significantly less emissive (PLQY < 0.5%) than the unsubstituted PBA, possibly due to deactivation of the S_1 exciton by enhanced ISC (heavy atom effect). However, they do not display any notable RTP, probably because weak intermolecular interactions (Figures 5.37-5.40) allow for a rapid vibrational deactivation of T_1.[41] This behavior changes profoundly once these monomers are covalently locked in the COF and further rigidified through strong π-π interactions (see the Hirshfeld analysis in Figures 5.40, 5.41). Although the emission of ClCOF-N with low doping level is still dominated by a fluorescence band (λ_{fl} = 365-390 nm), a phosphorescence peak is readily observed at ~450 nm in the steady-state spectra, and its contribution to overall luminescence increases, becoming the major emission channel at higher doping levels (Figure 5.3a). For the BrCOF-Ns, the steady-state emission is dominated by the phosphorescence band (480 nm) at 2% doping (Figure 5.3b), as expected due to strong spin-orbit coupling on the heavier Br atoms. A red-shifted feature at ~550 nm is observed in the steady-state emission of BrCOF-2/Br-COF-7 (Figure 5.3b) in vacuum, but it diminishes at higher doping levels. This red-shifted emission has an approximately ten times longer decay time compared to the main phosphorescence band at 480 nm (Figure 5.25) and might be due to the emission from the non-halogenated domains in the doped COFs. A similar blue shift of the phosphorescence band due to halogen substitution was observed in the frozen solution of PBA monomers (Figure 5.24c). The phosphorescence of both the ClCOFs and BrCOFs is observable to the naked eye as afterglow, and exhibits colors consistent with their delayed spectra (Figure 5.3c). Notably, neither F4COF-50 nor MeCOF-50 shows appreciable phosphorescence at room temperature (Figures 5.36 c,d), indicating that the enhancement observed in the halogenated COFs is the result of the heavy atom effect, and not the structural defects introduced by covalent doping.

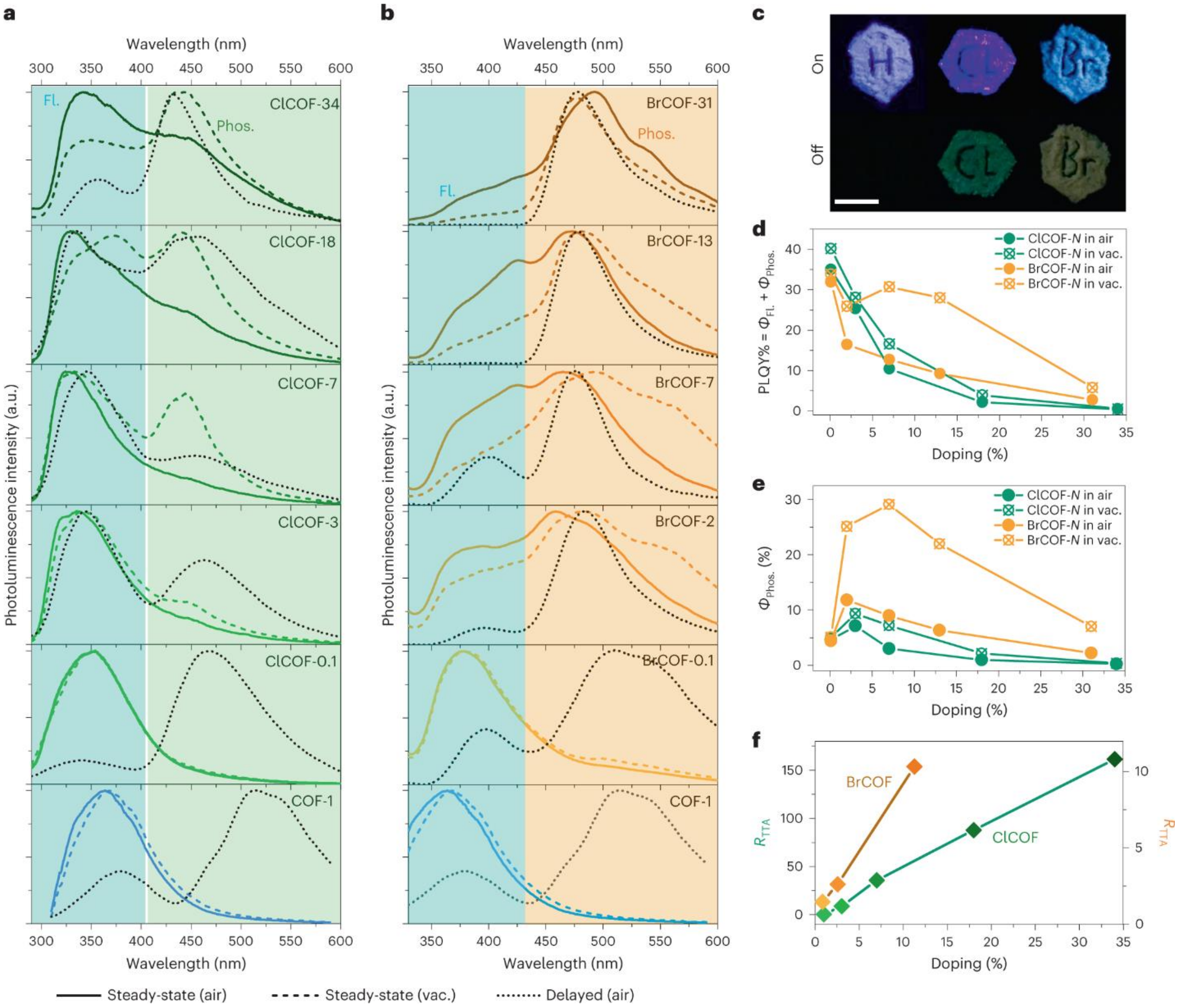

Figure 5.3. a,b) Steady-state photoluminescence spectra of as-prepared (non-activated) ClCOF-Ns (green traces, a) and BrCOF-Ns (orange traces, b) and COF-1 (blue traces), at room temperature (λ_{ex} = 300 nm) in air (solid lines) and vacuum (dashed lines), and their corresponding delayed spectra (black dotted lines); the approximate regions corresponding to fluorescence are highlighted in blue, and those of phosphorescence are highlighted in green for ClCOF and orange for BrCOF. c) Photographs of COF-1, ClCOF-18 and BrCOF-13 upon UV excitation (254 nm, 'On') and their afterglow, observed upon ceasing illumination ('Off'). Scale bar, 1 cm. d) Total PLQY

(=Φ_{Fl} + Φ_{Phos}) of ClCOF (green) and BrCOF (orange) in vacuum (10^{-5} torr, crossed circles) and in air (filled circles), showing a continuous drop of PLQY upon doping. e) Phosphorescence quantum yield of the ClCOF-Ns (green) and BrCOF-Ns (orange) in air (filled circles) and vacuum (10^{-5} torr, crossed circles), showing an initial increase then reduction with increments in halogen doping. f, TTA ratio (equation 5.1), monotonously increasing as a function of doping level in both ClCOF (green, left vertical axis) and BrCOF (orange, right vertical axis).

The phosphorescence lifetimes of BrCOF-N (τ_{phos} = 0.26 - 19.4 ms) are also much shorter than those of ClCOF-Ns (τ_{phos} = 144 – 259 ms), suggesting faster rates of phosphorescence (Figure 5.25, Table 5.8). Upon activation (180 °C, 10^{-3} torr, 12 h), the steady-state spectra of the doped COFs exhibit a substantial drop in phosphorescence intensity and its corresponding lifetime (for example, activated ClCOF-3 shows almost no detectable phosphorescence in air, Figure 5.31). Although the emission energies and fluorescence lifetime remain unchanged, activation mainly affects oxygen diffusion in the more accessible empty pores of activated COFs, devoid of the protecting mesitylene guest molecules (Figure 5.31).

The phosphorescence content of the steady-state photoluminescence can be tuned from 13% up to more than 65% for ClCOF-Ns (Figure 5.27) and up to 98% for BrCOF-Ns (Figure 5.28) by increasing the doping ratio. However, the total PLQY (PLQY = $\Phi_{Fl.}$ + $\Phi_{Phos.}$) decreases upon doping (Figure 5.3d) because the long-lived triplet states are more prone to quenching (by TTA, O_2, vibrational relaxation). The $\Phi_{Phos.}$ (obtained by the deconvolution of the steady-state spectra, Figures 5.27, 5.28) initially increases upon increasing the doping concentration, reaching a maximum of 9.3% (ClCOF-3) and 29.1% (BrCOF-7), but then decreases again at a higher doping level (Figure 5.3e). This behavior is most likely due to the self-quenching via TTA. Indeed, the time-delayed (t_{delay} = 0.2 ms) photoluminescence spectra (black dotted lines in Figures 3 a,b) show both the expected phosphorescence band and an additional DF emission due to TTA (as discussed above for non-doped COF-1). The ratio of their intensities (I_{DF}/I_{ph}) varies with the doping level. Because the intensity of the DF depends on both the efficiency of TTA process and the fluorescence quantum yield, we normalized the I_{DF}/I_{Phos} ratio by Φ_{Fl} (Figures 5.27, 5.28) to obtain the dimensionless TTA ratio ($R_{TTA,}$ Equation 1):

$$R_{TTA} = \frac{(I_{DF}/I_{Phos})}{\Phi_{Fl}} \qquad \text{(Equation 5.1)}$$

R_{TTA} increases monotonically with the increment of halogen doping, which can be expected due to smaller separation between the halogenated chromophores at higher doping levels (Figure 5.3f). This behavior highlights the necessary trade-off in the design of the doped phosphorescent materials: a higher doping level increases the population of triplet excitons but also amplifies their quenching via TTA.

5.3.4. Oxygen Sensing

Quenching of the triplet state by O_2 as a result of Dexter energy transfer is well-known in solutions of phosphorescent heavy metal complexes.[42] Heavy metal-containing porous solids such as porous silica[43, 44] and metal-organic frameworks[45-49] have been used in the design of phosphorescent oxygen sensors. However, using metal-free organic materials for O_2 sensing applications remains a challenge because the interaction with O_2 is suppressed by the dense crystalline matrix that is necessary for RTP in organic materials. In contrast to molecular solids[50, 51] (and even doped polymer matrices[52-55]), the microporous nature of COFs enables rapid permeation of O_2 through the channels of the COF crystal.

The ambient RTP of ClCOF-Ns and BrCOF-Ns is greatly enhanced under a high vacuum (<10^{-5} torr), whereas their fluorescence remains unchanged (Figures 5.4a, 5.27, 5.28, 5.35). This emission profile is retained upon refilling the evacuated sample with helium although a slight drop of phosphorescence was observed in other inert gasses (Ar, N_2), possibly due to residual O_2 impurities (Figure 5.29a). Exposing a sample of BrCOF-13 to different ranges of O_2 partial pressures, from 762 torr (pure O_2 at ambient pressure) down to high-vacuum (10^{-5} torr), reveals an ultra-wide dynamic range of O_2 detection, with a very fast (<100 ms) response time, limited by the evacuation and refill rates in our vacuum manifold (Figure 5.4c). Importantly, the unchanged fluorescence emission can be used as an internal reference for ratiometric O_2 sensing to compensate for fluctuations in the emission signal.[56] The plot of $r = I_{Phos.}/I_{Fl.}$ vs. p[O_2] deviates from the linear Stern-Volmer model based on diffusion-limited interaction (Figure 5.30), but it fits very well with the previously developed[44] model based on Freundlich adsorption isotherm using Equation 2:

$$\log\left(\frac{r_0}{r}-1\right)=\frac{1}{n}\log p[O_2]+\ \log K'_Q \qquad \text{(Equation 5.2)}$$

where r_0 and r are the ratio of phosphorescence to fluorescence intensities (I_{480nm}/I_{380nm}) in high vacuum (10^{-5} Torr) and at a different partial pressure of oxygen($p[O_2]$), respectively, n is an empirical constant and K_Q is a quenching constant.

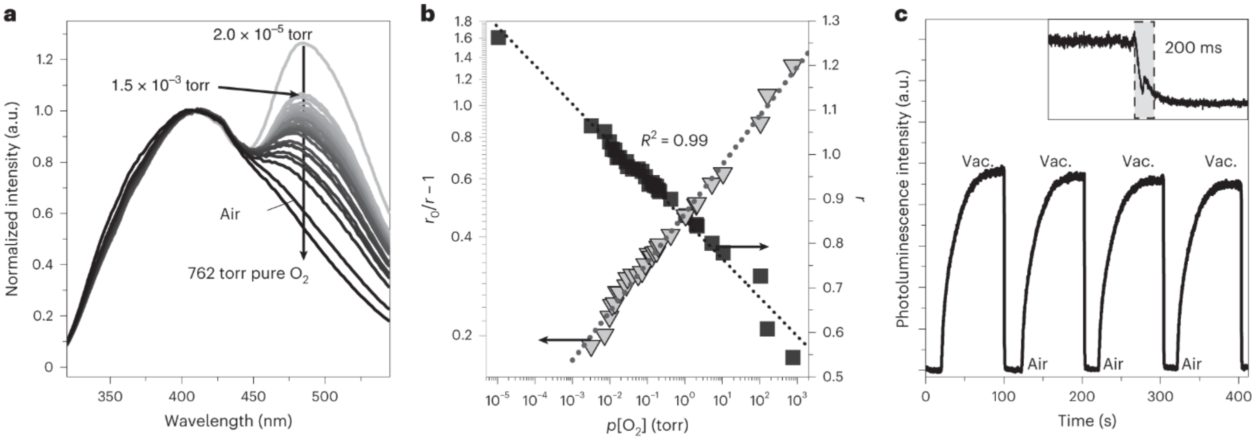

Figure 5.4. a) Steady-state photoluminescence spectra (λ_{ex} = 300 nm) of as-prepared (non-activated) BrCOF-13 at increasing partial O_2 pressures. The phosphorescence band at 490 nm diminishes with increasing O_2 pressure (grey to black). b) Phosphorescence/fluorescence ratio (r) for BrCOF-13 (black squares) and fit with the Freundlich adsorption isotherm ($r_0/r - 1$, grey inverted triangles) according to equation 5.2 versus the logarithm of $p[O_2]$, showing a very large dynamic response range. c) Reversible quenching and restoration of the phosphorescence of BrCOF-13 upon sequential exposure to air and vacuum (λ_{em} = 490 nm). Inset: high-resolution trace of phosphorescence quenching, showing the observed response to be nearly instantaneous (complete quenching in <200 ms), with the rate of change limited by the airflow/evacuation rate of the apparatus.

This model assumes that the phosphorescence quenching depends on the density of absorbed O_2 molecules on the surface rather than the O_2 concentration in the gas phase. Such logarithmic dependence of the phosphorescence on the partial pressure of O_2, emanating from the equilibrium absorption of the oxygen in the COF pores, allows for an ultra-wide detection range of up to 8 orders of magnitude (Figure 5.4b). This wide detection range and rapid response of the halogen-doped COFs (see the comparison with reported phosphorescent oxygen sensors in Table 5.9) highlights several potential applications for oxygen sensing, for example, in vacuum, in inert atmosphere gloveboxes, or encapsulation for an electronic device, although hydrolytic instability of boroxine COFs would be a problem for sensing in the presence of moisture.

5.4. Conclusion

In summary, we reported a strategy for tuning the optoelectronic properties of COFs via covalent doping. Controlled covalent halogen doping of the prototypical boroxine-linked COF-1 has allowed the realization of efficient RTP (phosphorescence quantum yields $\leq$ 29%, total photoluminescence quantum yields $\leq$ 40%) in such materials. The phosphorescence/ fluorescence ratio and the lifetime of the COFs can be engineered through the use of different dopants and doping concentrations which control the ISC (creating the triplet excitons) and TTA (quenching these triplets). We also note that the solvent (mesitylene) guest molecules partially suppress the oxygen permeation through the COF pores, allowing us to achieve RTP in air. The permanent porosity endows the COFs with highly dynamic O_2 sensing capabilities of more than eight orders of magnitude (from 762 to 10^{-5} Torr). We expect our covalent doping strategy to be broadly applicable for tuning a number of other properties and applications of COFs, such as charge/exciton mobility, photocatalysis, and so on.

5.5. Acknowledgments

We thank Robin S. Stein for assistance with solid-state NMR spectroscopy, Thierry Maris (University de Montreal) for X-ray crystallography and Antranik Jonderian and Eric McCalla for access to PXRD measurements and Alexander Wahba and Nadim Saade for mass spectrometry.

5.6. References

1. Côté, A. P.; Benin, A. I.; Ockwig, N. W.; O'Keeffe, M.; Matzger, A. J.; Yaghi, O. M., Porous, Crystalline, Covalent Organic Frameworks. *Science* **2005,** *310*, 1166-1170.

2. Huang, N.; Wang, P.; Jiang, D., Covalent organic frameworks: a materials platform for structural and functional designs. *Nat. Rev. Mater.* **2016,** *1*, 1-19.

3. Keller, N.; Bein, T., Optoelectronic processes in covalent organic frameworks. *Chem. Soc. Rev.* **2021,** *50*, 1813-1845.

4. Jadhav, T.; Fang, Y.; Patterson, W.; Liu, C. H.; Hamzehpoor, E.; Perepichka, D. F., 2D poly (arylene vinylene) covalent organic frameworks via aldol condensation of trimethyltriazine. *Angew. Chem. Int. Ed.* **2019,** *58*, 13753-13757.

5. Dalapati, S.; Jin, E.; Addicoat, M.; Heine, T.; Jiang, D., Highly emissive covalent organic frameworks. *J. Am. Chem. Soc.* **2016,** *138*, 5797-5800.

6. Evans, A. M.; Castano, I.; Brumberg, A.; Parent, L. R.; Corcos, A. R.; Li, R. L.; Flanders, N. C.; Gosztola, D. J.; Gianneschi, N. C.; Schaller, R. D.; Dichtel, W. R., Emissive Single-Crystalline Boroxine-Linked Colloidal Covalent Organic Frameworks. *J. Am. Chem. Soc.* **2019,** *141*, 19728-19735.

7. Ding, S.-Y.; Dong, M.; Wang, Y.-W.; Chen, Y.-T.; Wang, H.-Z.; Su, C.-Y.; Wang, W., Thioether-based fluorescent covalent organic framework for selective detection and facile removal of mercury (II). *J. Am. Chem. Soc.* **2016,** *138*, 3031-3037.

8. Wang, S.; Ma, L.; Wang, Q.; Shao, P.; Ma, D.; Yuan, S.; Lei, P.; Li, P.; Feng, X.; Wang, B., Covalent organic frameworks: a platform for the experimental establishment of the influence of intermolecular distance on phosphorescence. *J. Mater. Chem. C* **2018,** *6*, 5369-5374.

9. Zhao, W.; He, Z.; Tang, B. Z., Room-temperature phosphorescence from organic aggregates. *Nat. Rev. Mater.* **2020,** *5*, 869-885.

10. Chen, C.; Liu, B., Enhancing the performance of pure organic room-temperature phosphorescent luminophores. *Nat. Commun.* **2019,** *10*, 1-15.

11. Bolton, O.; Lee, K.; Kim, H. J.; Lin, K. Y.; Kim, J., Activating efficient phosphorescence from purely organic materials by crystal design. *Nat. Chem.* **2011,** *3*, 205-210.

12. An, Z.; Zheng, C.; Tao, Y.; Chen, R.; Shi, H.; Chen, T.; Wang, Z.; Li, H.; Deng, R.; Liu, X.; Huang, W., Stabilizing triplet excited states for ultralong organic phosphorescence. *Nat. Mater.* **2015,** *14*, 685-690.

13. Yang, J.; Zhen, X.; Wang, B.; Gao, X.; Ren, Z.; Wang, J.; Xie, Y.; Li, J.; Peng, Q.; Pu, K.; Li, Z., The influence of the molecular packing on the room temperature phosphorescence of purely organic luminogens. *Nat. Commun.* **2018,** *9*, 840.

14. Hamzehpoor, E.; Perepichka, D. F., Crystal Engineering of Room Temperature Phosphorescence in Organic Solids. *Angew. Chem. Int. Ed.* **2020,** *59*, 9977-9981.

15. Ye, W.; Ma, H.; Shi, H.; Wang, H.; Lv, A.; Bian, L.; Zhang, M.; Ma, C.; Ling, K.; Gu, M.; Mao, Y.; Yao, X.; Gao, C.; Shen, K.; Jia, W.; Zhi, J.; Cai, S.; Song, Z.; Li, J.; Zhang, Y.; Lu, S.; Liu, K.; Dong, C.; Wang, Q.; Zhou, Y.; Yao, W.; Zhang, Y.; Zhang, H.; Zhang, Z.; Hang, X.; An, Z.; Liu, X.; Huang, W., Confining isolated chromophores for highly efficient blue phosphorescence. *Nat. Mater.* **2021,** *20*, 1539-1544.

16. Gu, M.; Shi, H.; Ling, K.; Lv, A.; Huang, K.; Singh, M.; Wang, H.; Gu, L.; Yao, W.; An, Z.; Ma, H.; Huang, W., Polymorphism-Dependent Dynamic Ultralong Organic Phosphorescence. *Research* **2020,** *2020*, 8183450.

17. Lee, J.; Chen, H.-F.; Batagoda, T.; Coburn, C.; Djurovich, P. I.; Thompson, M. E.; Forrest, S. R., Deep blue phosphorescent organic light-emitting diodes with very high brightness and efficiency. *Nat. Mater.* **2016,** *15*, 92-98.

18. Yum, J.-H.; Baranoff, E.; Hardin, B. E.; Hoke, E. T.; McGehee, M. D.; Nüesch, F.; Grätzel, M.; Nazeeruddin, M. K., Phosphorescent energy relay dye for improved light harvesting response in liquid dye-sensitized solar cells. *Energy Environ. Sci* **2010,** *3*, 434-437.

19. Tabachnyk, M.; Ehrler, B.; Bayliss, S.; Friend, R. H.; Greenham, N. C., Triplet diffusion in singlet exciton fission sensitized pentacene solar cells. *Appl. Phys. Lett.* **2013,** *103*, 190_191.

20. Wan, S.; Zhou, H.; Lin, J.; Lu, W., A Prototype of a Volumetric Three-Dimensional Display Based on Programmable Photo-Activated Phosphorescence. *Angew. Chem. Int. Ed.* **2020,** *59*, 8416-8420.

21. Filidou, V.; Simmons, S.; Karlen, S. D.; Giustino, F.; Anderson, H. L.; Morton, J. J., Ultrafast entangling gates between nuclear spins using photoexcited triplet states. *Nat. Phys.* **2012,** *8*, 596-600.

22. Hackney, H. E.; Perepichka, D. F., Recent advances in room temperature phosphorescence of crystalline boron containing organic compounds. *Aggregate* **2021**, e123.

23. Wu, Z.; Nitsch, J.; Schuster, J.; Friedrich, A.; Edkins, K.; Loebnitz, M.; Dinkelbach, F.; Stepanenko, V.; Wurthner, F.; Marian, C. M.; Ji, L.; Marder, T. B., Persistent Room Temperature Phosphorescence from Triarylboranes: A Combined Experimental and Theoretical Study. *Angew. Chem. Int. Ed.* **2020,** *59*, 17137-17144.

24. Yuan, W. Z.; Shen, X. Y.; Zhao, H.; Lam, J. W. Y.; Tang, L.; Lu, P.; Wang, C.; Liu, Y.; Wang, Z.; Zheng, Q.; Sun, J. Z.; Ma, Y.; Tang, B. Z., Crystallization-Induced Phosphorescence of Pure Organic Luminogens at Room Temperature. *J. Phys. Chem. C* **2010,** *114*, 6090-6099.

25. Yan, X.; Peng, H.; Xiang, Y.; Wang, J.; Yu, L.; Tao, Y.; Li, H.; Huang, W.; Chen, R., Recent Advances on Host–Guest Material Systems toward Organic Room Temperature Phosphorescence. *Small* **2022,** *18*, 2104073.

26. Chen, C.; Chi, Z.; Chong, K. C.; Batsanov, A. S.; Yang, Z.; Mao, Z.; Yang, Z.; Liu, B., Carbazole isomers induce ultralong organic phosphorescence. *Nat. Mater.* **2021,** *20*, 175-180.

27. Nangia, A. K.; Desiraju, G. R., Crystal engineering: An outlook for the future. *Angew. Chem. Int. Ed.* **2019,** *58*, 4100-4107.

28. Deng, H.; Doonan, C. J.; Furukawa, H.; Ferreira, R. B.; Towne, J.; Knobler, C. B.; Wang, B.; Yaghi, O. M., Multiple functional groups of varying ratios in metal-organic frameworks. *Science* **2010,** *327*, 846-850.

29. Qin, J.-S.; Yuan, S.; Wang, Q.; Alsalme, A.; Zhou, H.-C., Mixed-linker strategy for the construction of multifunctional metal–organic frameworks. *J. Mater. Chem. A* **2017,** *5*, 4280-4291.

30. Yeung, H. H. M.; Li, W.; Saines, P. J.; Köster, T. K.; Grey, C. P.; Cheetham, A. K., Ligand-Directed Control over Crystal Structures of Inorganic–Organic Frameworks and Formation of Solid Solutions. *Angew. Chem. Int. Ed.* **2013,** *52*, 5544-5547.

31. Li, R. L.; Yang, A.; Flanders, N. C.; Yeung, M. T.; Sheppard, D. T.; Dichtel, W. R., Two-Dimensional Covalent Organic Framework Solid Solutions. *J. Am. Chem. Soc.* **2021,** *143*, 7081-7087.

32. Lakshmi, V.; Liu, C. H.; Rajeswara Rao, M.; Chen, Y.; Fang, Y.; Dadvand, A.; Hamzehpoor, E.; Sakai-Otsuka, Y.; Stein, R. S.; Perepichka, D. F., A Two-Dimensional Poly(azatriangulene) Covalent Organic Framework with Semiconducting and Paramagnetic States. *J. Am. Chem. Soc.* **2020,** *142*, 2155-2160.

33. Jin, E.; Asada, M.; Xu, Q.; Dalapati, S.; Addicoat, M. A.; Brady, M. A.; Xu, H.; Nakamura, T.; Heine, T.; Chen, Q., Two-dimensional sp2 carbon–conjugated covalent organic frameworks. *Science* **2017,** *357*, 673-676.

34. Rotter, J. M.; Guntermann, R.; Auth, M.; Mähringer, A.; Sperlich, A.; Dyakonov, V.; Medina, D. D.; Bein, T., Highly conducting Wurster-type twisted covalent organic frameworks. *Chem. Sci.* **2020,** *11*, 12843-12853.

35. Wan, S.; Guo, J.; Kim, J.; Ihee, H.; Jiang, D., A photoconductive covalent organic framework: self-condensed arene cubes composed of eclipsed 2D polypyrene sheets for photocurrent generation. *Angew. Chem. Int. Ed.* **2009,** *48*, 5439-5442.

36. Kuno, S.; Kanamori, T.; Yijing, Z.; Ohtani, H.; Yuasa, H., Long persistent phosphorescence of crystalline phenylboronic acid derivatives: photophysics and a mechanistic study. *ChemPhotoChem* **2017,** *1*, 102-106.

37. Hamzehpoor, E.; Ruchlin, C.; Tao, Y.; Ramos-Sanchez, J. E.; Titi, H. M.; Cosa, G.; Perepichka, D. F., Room Temperature Phosphorescence vs Triplet–Triplet Annihilation in N-Substituted Acridone Solids. *J. Phys. Chem. Lett* **2021,** *12*, 6431-6438.

38. Tokunaga, Y.; Ueno, H.; Shimomura, Y., Formation of boroxine: its stability and thermodynamic parameters in solution. *Heterocycles* **2002,** *57*, 787-790.

39. Tilford, R. W.; Mugavero III, S. J.; Pellechia, P. J.; Lavigne, J. J., Tailoring microporosity in covalent organic frameworks. *Adv. Mater.* **2008,** *20*, 2741-2746.

40. Gao, J.; Jiang, D., Covalent organic frameworks with spatially confined guest molecules in nanochannels and their impacts on crystalline structures. *Chem. Commun.* **2016,** *52*, 1498-1500.

41. Chai, Z.; Wang, C.; Wang, J.; Liu, F.; Xie, Y.; Zhang, Y. Z.; Li, J. R.; Li, Q.; Li, Z., Abnormal room temperature phosphorescence of purely organic boron-containing compounds: the relationship between the emissive behaviorand the molecular packing, and the potential related applications. *Chem. Sci.* **2017,** *8*, 8336-8344.

42. Wang, X.-d.; Wolfbeis, O. S., Optical methods for sensing and imaging oxygen: materials, spectroscopies and applications. *Chem. Soc. Rev.* **2014,** *43*, 3666-3761.

43. Han, B.-H.; Manners, I.; Winnik, M. A., Oxygen sensors based on mesoporous silica particles on layer-by-layer self-assembled films. *Chem. Mater.* **2005,** *17*, 3160-3171.

44. Carraway, E.; Demas, J.; DeGraff, B., Photophysics and oxygen quenching of transition-metal complexes on fumed silica. *Langmuir* **1991,** *7*, 2991-2998.

45. Barrett, S. M.; Wang, C.; Lin, W., Oxygen sensing via phosphorescence quenching of doped metal–organic frameworks. *J. Mater. Chem.* **2012,** *22*, 10329-10334.

46. Liu, S. Y.; Zhou, D. D.; He, C. T.; Liao, P. Q.; Cheng, X. N.; Xu, Y. T.; Ye, J. W.; Zhang, J. P.; Chen, X. M., Flexible, Luminescent Metal–Organic Frameworks Showing Synergistic Solid-Solution Effects on Porosity and Sensitivity. *Angew. Chem. Int. Ed.* **2016,** *55*, 16021-16025.

47. Ye, J.-W.; Lin, J.-M.; Mo, Z.-W.; He, C.-T.; Zhou, H.-L.; Zhang, J.-P.; Chen, X.-M., Mixed-Lanthanide Porous Coordination Polymers Showing Range-Tunable Ratiometric Luminescence for O2 Sensing. *lnorg. Chem.* **2017,** *56*, 4238-4243.

48. Qi, X.-L.; Liu, S.-Y.; Lin, R.-B.; Liao, P.-Q.; Ye, J.-W.; Lai, Z.; Guan, Y.; Cheng, X.-N.; Zhang, J.-P.; Chen, X.-M., Phosphorescence doping in a flexible ultramicroporous framework for high and tunable oxygen sensing efficiency. *Chem. Commun.* **2013,** *49*, 6864-6866.

49. Xie, Z.; Ma, L.; deKrafft, K. E.; Jin, A.; Lin, W., Porous phosphorescent coordination polymers for oxygen sensing. *J. Am. Chem. Soc.* **2010,** *132*, 922-923.

50. Cai, S.; Shi, H.; Zhang, Z.; Wang, X.; Ma, H.; Gan, N.; Wu, Q.; Cheng, Z.; Ling, K.; Gu, M., Hydrogen-Bonded Organic Aromatic Frameworks for Ultralong Phosphorescence by Intralayer π–π Interactions. *Angew. Chem. Int. Ed.* **2018,** *57*, 4005-4009.

51. Hirata, S.; Totani, K.; Zhang, J.; Yamashita, T.; Kaji, H.; Marder, S. R.; Watanabe, T.; Adachi, C., Efficient persistent room temperature phosphorescence in organic amorphous materials under ambient conditions. *Adv. Funct. Mater.* **2013,** *23*, 3386-3397.

52. Lehner, P.; Staudinger, C.; Borisov, S. M.; Klimant, I., Ultra-sensitive optical oxygen sensors for characterization of nearly anoxic systems. *Nat. Commun.* **2014,** *5*, 1-6.

53. Cai, S.; Ma, H.; Shi, H.; Wang, H.; Wang, X.; Xiao, L.; Ye, W.; Huang, K.; Cao, X.; Gan, N.; Ma, C.; Gu, M.; Song, L.; Xu, H.; Tao, Y.; Zhang, C.; Yao, W.; An, Z.; Huang, W., Enabling long-lived organic room temperature phosphorescence in polymers by subunit interlocking. *Nat. Commun.* **2019,** *10*, 1-8.

54. Yu, Y.; Kwon, M. S.; Jung, J.; Zeng, Y.; Kim, M.; Chung, K.; Gierschner, J.; Youk, J. H.; Borisov, S. M.; Kim, J., Room-Temperature-Phosphorescence-Based Dissolved Oxygen Detection by Core-Shell Polymer Nanoparticles Containing Metal-Free Organic Phosphors. *Angew. Chem. Int. Ed.* **2017,** *56*, 16207-16211.

55. Zhang, G.; Chen, J.; Payne, S. J.; Kooi, S. E.; Demas, J.; Fraser, C. L., Multi-emissive difluoroboron dibenzoylmethane polylactide exhibiting intense fluorescence and oxygen-sensitive room-temperature phosphorescence. *J. Am. Chem. Soc.* **2007,** *129*, 8942-8943.

56. Feng, Y.; Cheng, J.; Zhou, L.; Zhou, X.; Xiang, H., Ratiometric optical oxygen sensing: a review in respect of material design. *Analyst* **2012,** *137*, 4885-4901.

5.7. Supplementary information

5.7.1. Materials and Methods

1,4-Dichlorobenzene and 1,4-dibromobenzene were purchased from Sigma Aldrich; phenyldiboronic acid, diboron pinacolate ester, and methylboronic acid were purchased from CombiBlocks and used without further purification. Dried solvents (DCM, $CHCl_3$, THF, acetone) were purified on a MBraun solvent purification system and kept under activated 4 Å molecular sieves at least 48 h before use. Other solvents were purchased from commercial sources and used without further purification. Column chromatography was performed using silica gel on an Isolera One Flash instrument from Biotage.

FTIR spectra of powders were obtained on a Nicolet 6700 FT-IR instrument in the 500-4000 cm^{-1} region using a Diamond ATR (SmartOrbit).

NMR spectra (^1H and ^{13}C) were recorded on a Varian VNMRS spectrometer (^1H, 499.9 MHz; ^{13}C, 125.7 MHz). ^1H NMR chemical shifts are reported relative to TMS and were referenced via residual proton resonances of the corresponding deuterated solvent ($CDCl_3$: 7.26 ppm); ^{13}C NMR spectra are reported relative to TMS via the carbon signals of the deuterated solvent ($CDCl_3$: 77.16 ppm). All NMR spectra of precursors are provided as Appendix 5 of the thesis

SSNMR spectra (^1H) were recorded on a Varian VNMRS spectrometer operating at 499.9 MHz using a 3.2 mm Varian T3 probe under spinning at 23 kHz in 8 scans using a 3s recycle delay (sufficient for full relaxation). Spectra were referenced using powdered adamantane at 1.8 ppm relative to TMS.

Thermogravimetric analysis (TGA) was conducted on a TA Instruments Q500 Thermogravimetric system with a Pt pan under a dynamic atmosphere of N_2. Samples were heated up to 800°C at a rate of 10 °C/min under N_2. The balance and purge flows were 10 ml/min and 90 ml/min, respectively.

Differential scanning calorimetry (DSC) was performed on a TA instrument LTD DSC2500 under a stream of nitrogen (50 $cm^3\ min^{-1}$) gas, at a heating rate of 1 °C min^{-1}.

Powder X-ray diffraction (PXRD) patterns were collected on a Bruker D2 Phaser powder diffractometer equipped with a CuKα source and Lynxeye detector. The patterns were collected in the angle region between 3- 40° (2θ) with a step size of 0.05°.

X-ray photoelectron spectroscopy (XPS) spectra were obtained with a Thermo Scientific K-alpha spectrometer equipped with an Al K α (1486.6 eV) monochromatic source and flood gun for charge compensation at base pressures less than 10^{-8} Torr with a perpendicular take-off angle. Peak assignments and integrations were carried out by using the NIST XPS database and Avantage XPS software.

Transmission electron microscopy was conducted on a Talos F200X TEM (200kV). The sample was sonicated for 5 minutes in n-hexane before drop-casting onto a lacey carbon grid.

Surface area measurements were conducted on an Autosorb iQ (Quantachrome) analyzer by sorption of nitrogen (99.999%) at 77 K with activated COFs (*ca.* 20 mg, degassed at 180 °C, 10^{-3} Torr for 12 h). Surface parameters were determined using multi-point BET (pressure range of 0.05-0.3) and Quenched Solid DFT (QSDFT) adsorption models included in the instrument software.

The Inductively Coupled Plasma Optical Emission Spectroscopy (ICP-OES) was done using a Thermo Scientific iCAP 6500 spectrometer. COF samples were dissolved in concentrated nitric acid (5 ml; 68% wt/wt) at 95 °C. After 2 hours of acid digestion, the solutions (0.25 ml) were diluted into 4% nitric acid (25.00 ml) and submitted to ICP-OES. The operating software ITEVA (version 8) was used to control the instrument function and data handling and analysis.

Density functional theory (DFT) calculations of ClPBA and BrPBA were performed using B3LYP functional and 6-31G(d)/3-21G* basis sets, using geometry optimization and frequency options as implemented in Gaussian 16. Rev. B.01.[1] The vibration vectors and values were then extracted using GaussView 6.0 software. The calculated vibrational wavenumbers were scaled by the "vibrational scaling factors" suggested by the NIST (0.962 for B3LYP 6-31G*).[2] The vibration vectors are shown in Appendix 6 of the thesis.

Solution UV-vis absorption spectra were collected on a JASCO V-670 spectrophotometer in quartz cuvettes from Starna Cells Inc. The diffuse reflectance spectroscopy was done on ground samples diluted with KBr, using the Praying Mantis accessory by Agilent on Cary-5000 spectrometer also from Agilent.

Steady-state photoluminescence spectra were collected using a Fluorolog 3 fluorometer from Horiba Jobin-Yvon. For vacuum measurements, samples were placed in quartz EPR tubes attached with an SP Scienceware 4 mm tip-off manifold from Wilmad-LabGlass, hooked up to a Varian TPS-Compact high vacuum. **Quantum yield measurements** were performed with a Quanta-ϕ integrating sphere from Horiba Scientific. The phosphorescence quantum yields are calculated from the phosphorescence content obtained by deconvolution of steady-state spectra of the HaloCOFs (Figures 5.27, 5.28). The vacuum quantum yields are estimated by the enhancement factor obtained from the steady-state spectra in air vs vacuum. **The emission lifetimes** of the samples were determined by the Time-Correlated Single Photon Counting (TCSPC) technique using a DeltaDiode 373 nm pulsed laser diode controlled by a DeltaHub controller, both from Horiba Scientific.

Delayed emission spectra were measured on the Varian Cary Eclipse fluorescence spectrophotometer, with timing parameters set to accumulate the entire decay profiles and provide a sufficient signal-to-noise ratio (t_{delay} = 0.2 ms, t_{gate} = 10-200 ms, t_{decay} = 20 – 500 ms). For excitation intensity dependence measurements, the excitation power was attenuated using neutral density filters from CVI Laser Optics.

Quantum yield measurements. PLQY measurements were performed with a Quanta-ϕ integrating sphere from Horiba Scientific using Fluorolog-3 spectrometer. The phosphorescence quantum yields ($\Phi_{Phos.}$) were obtained from Gaussian deconvolution (Figures 5.27, 5.28) of the phosphorescence content in the steady-state spectra. The vacuum quantum yields are estimated by the enhancement factor obtained from the steady-state spectra in air vs. vacuum.

Photoluminescence measurements under vacuum and oxygen sensing. COF powders were placed in a quartz EPR tube attached to a multi-port vacuum glass manifold and attached to a Varian TPS-Compact high vacuum system. Different pressures were induced by adjusting the leak valve on the manifold and were measured by a Pirani pressure gauge at a port nearest to the sample.

COF photoluminescence photographs were taken by a Canon EOS 90D camera featuring an 18-135 IS USM lens (also from Canon). The afterglow images were obtained using an exposure time of 0.25 sec. For COF-1, the afterglow was not detectable at this camera setting, despite its long phosphorescence lifetime. We note that while a long lifetime is certainly crucial for afterglow, the apparent brightness of the afterglow also depends on the absorption cross-section and quantum yield. The weak spin-orbit coupling due to the absence of heavy atoms in COF-1 extends the lifetime of the T_1 state but also suppresses its formation (via ISC) and the radiative $T_1 – S_0$ transition. This results in very low phosphorescent quantum yields ($Φ_P$) and thus the afterglow is not bright enough to be captured by a conventional camera (or by eye).

5.7.2. Synthesis of precursors

2,2′-(2,5-Dichloro-1,4-phenylene)bis(4,4,5,5-tetramethyl-1,3,2-dioxaborolane) (**ClPBpin**). A mixture of (1,5-cyclooctadiene)(methoxy)iridium(I) dimer (0.113 g, 0.170 mmol), 4,4′-di-*tert*-butyl-2,2′-dipyridyl (0.365 g, 1.36 mmol), bis(pinacolato)diboron (21.590 g, 85.04 mmol) and 1,4-dichlorobenzene (5.000 g, 34.01 mmol) was added in 20 ml of dry cyclohexane. The mixture was then purged with N_2 for 10 min and heated up to 90 °C for 4 h in a pressurized Schlenk tube. After cooling to room temperature, the deep-red reaction mixture was added to 10 ml of hexane and stirred for 10 min. The white precipitate was vacuum filtered and washed with 2 × 5 ml of cold methanol and recrystallized twice from methanol (25 ml) to afford pure **ClBpin** (11.5 g, 85%). mp: 281–284 °C (DSC onset and peak, respectively), ^{1}H NMR (500 MHz, $CDCl_3$): δ 7.64 (s, 2H), 1.37 (s, 24H); ^{13}C NMR (126 MHz, $CDCl_3$): δ 137.16, 136.79, 132.95, 84.52, 24.78. The spectroscopic data were in agreement with the literature.[3]

2,2′-(2,5-Dibromo-1,4-phenylene)bis(4,4,5,5-tetramethyl-1,3,2-dioxaborolane) (**BrPBpin**). A mixture of (1,5-cyclooctadiene) (methoxy)iridium(I) dimer (84.3 mg, 0.127 mmol), 4,4′-di-*tert*-butyl-2,2′-dipyridyl (68.3 mg, 0.254 mmol), bis(pinacolato)diboron (4.04 g, 15.90 mmol) and 1,4-bromobenzene (1.500 g, 6.36 mmol) was added in 20 mL of dry cyclohexane. The mixture was purged with N_2 for 10min and heated up to 90 °C for 4 h in a pressurized Schlenk tube. After cooling to room temperature, the brown residue was added to 10 ml of hexane and stirred for 10 min. The white precipitate was vacuum filtered and washed with 2 × 5 ml cold methanol and dried under vacuum. The white solid was further purified by recrystallization in 2 × 15 ml of methanol to afford pure BrPBpin (2.36 g, 76%). mp: 308-310 °C (DSC onset and peak, respectively) ^{1}H NMR (500 MHz, $CDCl_3$): 7.76 (s, 2H), 1.39 (s, 24H); ^{13}C NMR (126 MHz, $CDCl_3$): 139.99, 136.15 (broad), 126.21, 84.67, 24.79. The spectroscopic data were in agreement with the literature.[4]

(2,5-Dichloro-1,4-phenylene)diboronic acid (**ClPBA**). **ClPBpin[1]** (1.00 g, 2.51 mmol) and methylboronic acid (MBA, 3.00 g, 50.14 mmol) were dissolved in 5 mL of dry chloroform with trifluoroacetic acid (5 vol%, 0.25 ml). The mixture was stirred for 2 h at room temperature during which a white precipitate formed. The solvent was evaporated and the resulting solids were kept under vacuum (~0.3 Torr) at room temperature to remove the excess MBA, affording white solid (450 mg, 77%) that was used without further purification. mp: >202 °C (dec.). ^{1}H NMR (500 MHz, DMSO-d_6 and a drop of D_2O) δ 7.33 (s, 2H). ^{13}C NMR (126 MHz DMSO-d_6 and a drop of D_2O) δ 139.35, 134.54, 133.83.

(2,5-dibromo-1,4-phenylene)diboronic acid (**BrPBA**). **BrPBpin**[2] (1.00 g, 2.05 mmol) and MBA (2.45 g, 41.00 mmol) were dissolved in 5 mL of dry chloroform with trifluoroacetic acid (5 vol%, 0.25 ml). The mixture was stirred for 2 h at room temperature during which a white precipitate formed. The solvent was evaporated and the resulting solids were kept under vacuum to remove the excess MBA. The afforded white solid (425 mg, 88%) was used without further purification. mp: >185 °C (dec.) ^{1}H NMR (500 MHz, DMSO-d_6 and a drop of D_2O) δ 7.39 (s, 2H). ^{13}C NMR (126 MHz DMSO-d_6 and a drop of D_2O) δ 142.66, 136.78, 124.26.

5.7.3. Synthesis of COF-1:

To a pyrex sealable ampule (5 ml) was added PBA (33 mg, 0.2 mmol) followed by 1 ml of a 1:1 v:v mixture of mesitylene: dioxane. The tube was subjected to freeze-pump-thaw cycles (3 times, flash-frozen in a liquid N_2 bath and evacuated to an internal pressure of 150 mTorr) and then flame-sealed under Ar (760 Torr). The reaction mixture was heated at 120 °C for 72 hours, yielding a white solid, which was isolated by filtration immediately after cooling and washed with dry chloroform (10 ml) and MeCN (10 ml) to afford COF-1 (25 mg, 96%).

5.7.4. General procedure for the synthesis of covalently-doped COFs.

Different ratios of PBA and halogenated monomer (ClPBA or BrPBA) were added to a sealable Pyrex ampule (5 ml) followed by 1 ml of a 1:1 v:v mixture of mesitylene: dioxane (Tables 5.1 and 5.2). The tube was subjected to freeze-pump-thaw cycles (3 times, flash-frozen in a liquid N_2 bath and evacuated to an internal pressure of 150 mTorr) and then flame-sealed under Ar (760 Torr). The reaction mixture was heated in a convection oven at 120 °C for 72 hours, yielding a white solid, which was isolated by filtration immediately after cooling to room temperautre and washed on filter with dry chloroform (10 ml) and MeCN (10 ml) and immediately placed under vacuum (0.3 mbar) for drying. The yields of the COF formation are reported in Figure 5.1 and Tables 5.1, 5.2 for ClCOF-N and BrCOF-N, respectively. The washing step (dry solvent and minimal contact with humid air during filtration) is critical to obtain spectroscopically pure COFs. A red-shifted emission, presumably due to hydrolytic defects in the 2D framework is observed if the protocol is not followed or after prolonged storage of COFs in air.

Table 5.1. Monomers loading and product yield in the syntheses of ClCOF-N

	PBA	ClPBA	COF formation Yield %
ClCOF-0.1	32.9 mg (198 μmol)	0.5 mg (2 μmol)	85 ± 5 % (22.1 mg)
ClCOF-3	29.9 mg (180 μmol)	4.7 mg (20 μmol)	75 ± 3 % (20.5 mg)
ClCOF-7	24.9 mg (150 μmol)	11.7 mg (50.0 μmol)	71± 2 % (20.8 mg)
ClCOF-18	16.6 mg (100 μmol)	23.5 mg (100 μmol)	53 ± 2 % (17.4 mg)
ClCOF-34	8.3 mg (50 μmol)	35.2 mg (150 μmol)	48 ± 5 % (17.4 mg)
Cl-100	----	46.9 mg (200 μmol)	35 ± 8 % (13.9 mg)

Table 5.2. Monomers loading and product yield in the syntheses of BrCOF-N.

	PBA	BrPBA	COF formation Yield %
BrCOF-0.1	32.9 mg (198 μmol)	0.6 mg (2 μmol)	74 ± 2 % (19.5 mg)
BrCOF-2	29.9 mg (180 μmol)	6.5 mg (20 μmol)	68 ± 2 % (20.5 mg)
BrCOF-7	24.9 mg (150 μmol)	16 mg (50 μmol)	62 ± 2 % (20.8 mg)
BrCOF-13	16.6 mg (100 μmol)	32.4 mg (100.0 μmol)	50 ± 2 % (17.4 mg)
BrCOF-31	8.3 mg (50 μmol)	48.5 mg (150 μmol)	43 ± 5 % (17.4 mg)
Br-100	----	64.7 mg (200 μmol)	14 ± 7 % (8.0 mg)

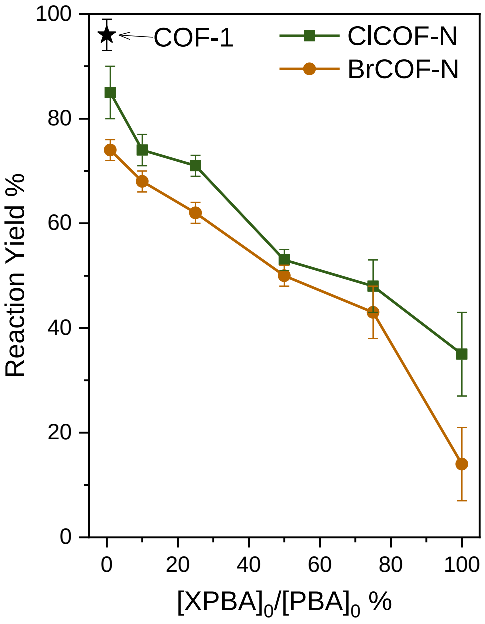

Figure 5.5. Synthesis of doped COFs by co-condensation of PBA with XPBA, showing a progressive drop of the isolated yield at higher doping concentrations. The data points are the mean value of n= 5 different synthetic batches. Error bars represent the standard deviations.

5.7.5. Characterization and photophysical properties of non-doped COF-1

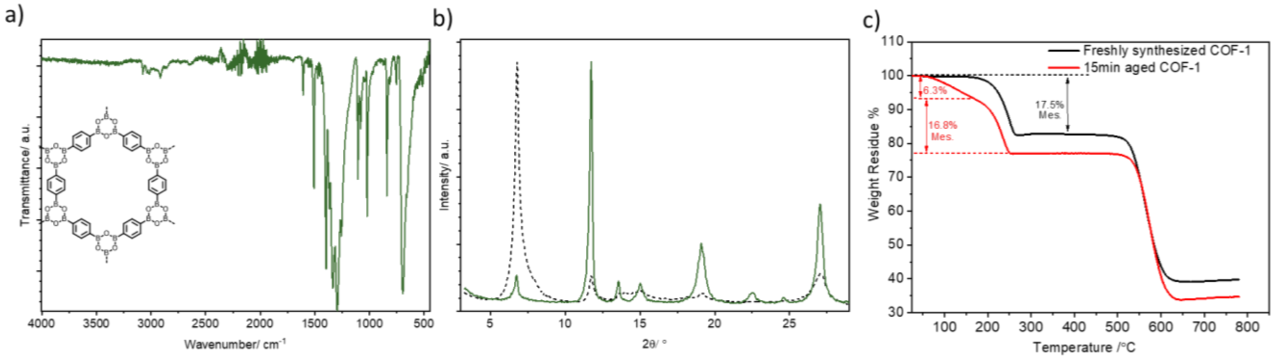

Figure 5.6. a) FTIR of non-doped COF-1 showing the absence of the OH stretch (~3250 cm^{-1}) and the emergence of the boroxine out-of-plane vibration at (699 cm^{-1}) are indicative of complete reaction. b) PXRD of non-activated COF-1 (solid) and activated (dashed) showing the difference in PXRD pattern upon pore evacuation. c) Thermogravimetric analysis of COF-1 (freshly synthesized, black) and aged 15 min in an open capped vial at ambient pressure, temperature, and humidity, showing the introduction of 6% of impurities from exposure to air.

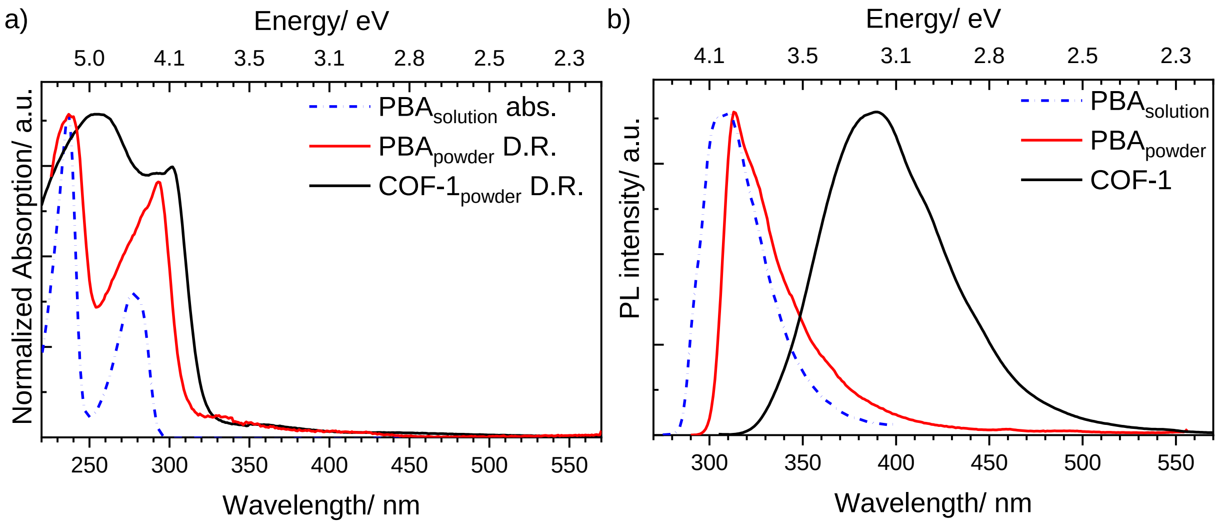

Figure 5.7. a) Absorption spectra of non-doped COF-1 powder and PBA as powder and in solution (~10^{-6} M in MeCN), obtained by diffuse reflectance (D.R.) and transmission mode, respectively. b) Steady-state emission of COF-1, PBA solution (~10^{-6} M in MeCN; λ_{ex} = 270 nm) and powder (λ_{ex} = 290 nm).

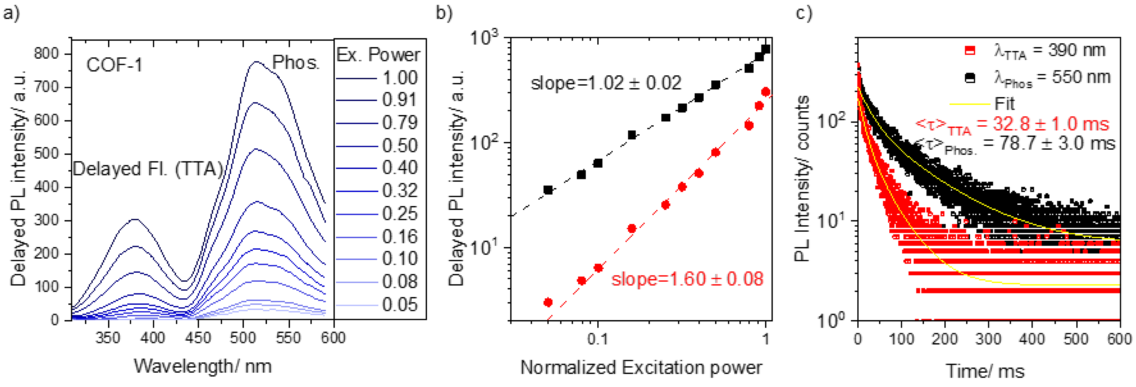

Figure 5.8. a) Delayed emission spectra of non-doped COF-1 (t_d = 0.1ms) microcrystalline powder with excitation intensity attenuated by neutral density filters. b) Corresponding intensity dependence of TTA-induced delayed fluorescence (DF) and phosphorescence, plotted on a double-logarithmic scale versus the excitation power, showing non-linear behavior of the DF feature c) lifetime analysis of the TTA-induced DF (λ_{em} = 390 nm) and phosphorescence (λ_{em} = 550 nm) showing the expected twice shorter lifetime for DF *vs*. phosphorescence.

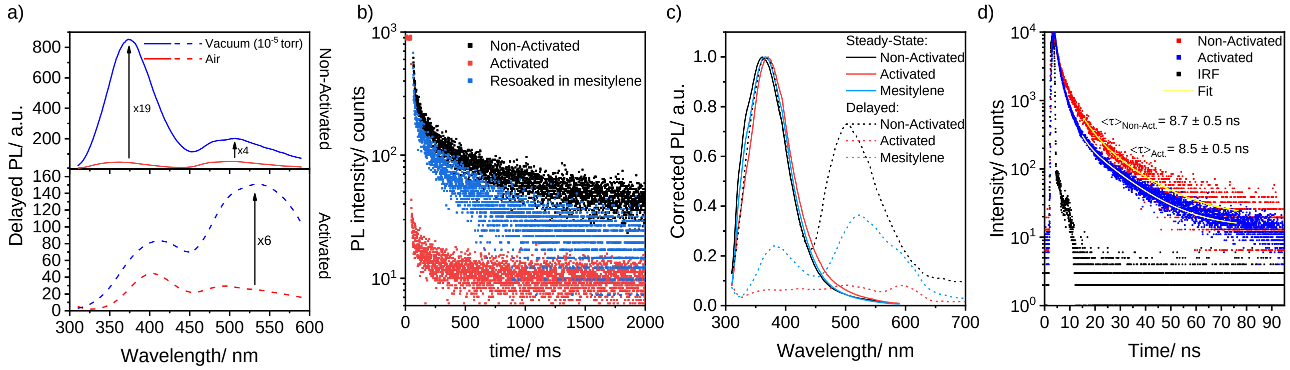

Figure 5.9. a) Delayed spectra of non-activated (top, solid lines) and activated (bottom, dashed lines) COF-1 (λ_{ex} = 300nm, t_d = 0.2 ms) in air (blue) vs. vacuum (ca. 10^{-5} torr, red), illustrating the enhancement of TTA-induced DF compared to phosphorescence under vacuum. (b) Phosphorescent life-time analysis of COF-1 samples non-activated (black), activated (red), and with mesitylene (blue). c) steady-state (solid) and time-gated (t_d = 0.2 ms, dashed) spectra of as-synthesized COF-1 (black), activated COF-1 (red) and activated COF-1 after addition of a drop of dried mesitylene (blue, all in air). d) TCSPC fluorescence lifetime analysis of COF-1 (λ_{ex} = 373 nm; λ_{em} = 440 nm), with bi-exponential fits (yellow).

5.7.6. Characterization of products of attempted synthesis of Cl-100 and Br-100

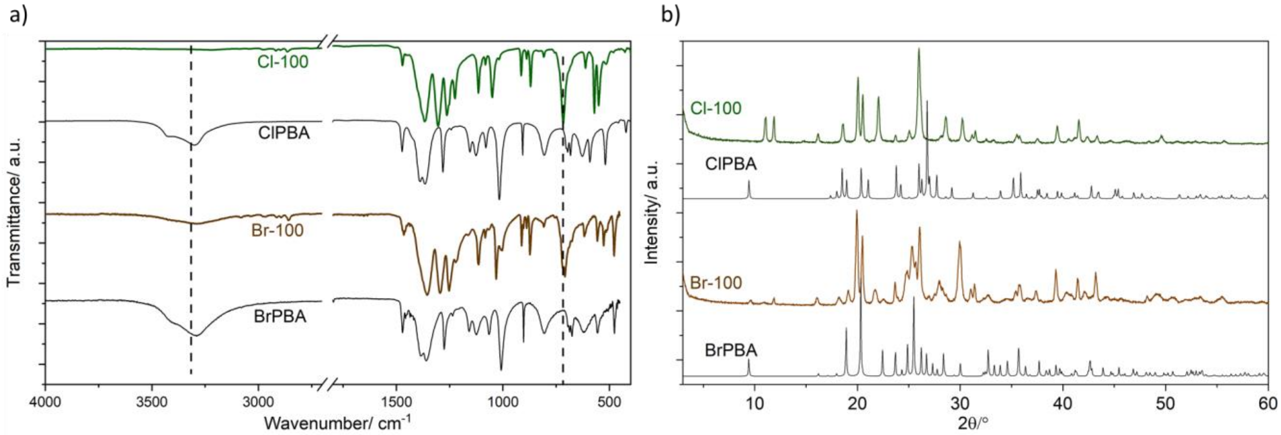

Figure 5.10. a) FTIR of ClPBA and BrPBA (black) and their condensation products Cl-100 (green) and Br-100 (brown) showing the absence of the OH stretch (~3250 cm^{-1}) and the emergence of the boroxine out-of-plane vibration at (716 cm^{-1} and 708 cm^{-1} for ClCOF100 and BrCOF100, respectively). b) PXRD of the Cl-100 (green) and Br-100 (brown) vs. that of simulated PXRD pattern of their precursors ClPBA and BrPBA (black), respectively. The PXRD patterns of the products do not match the expected pattern of a COF and multiple peaks match the monomer. This data suggests that the products are mainly composed of an amorphous phase and the observed pattern is due to a residual amount of the precursors. The several additional peaks

could be due to ClPBA and BrPBA cocrystals with dioxane, as was supported by the NMR of the samples (Figures 5.12, 5.13).

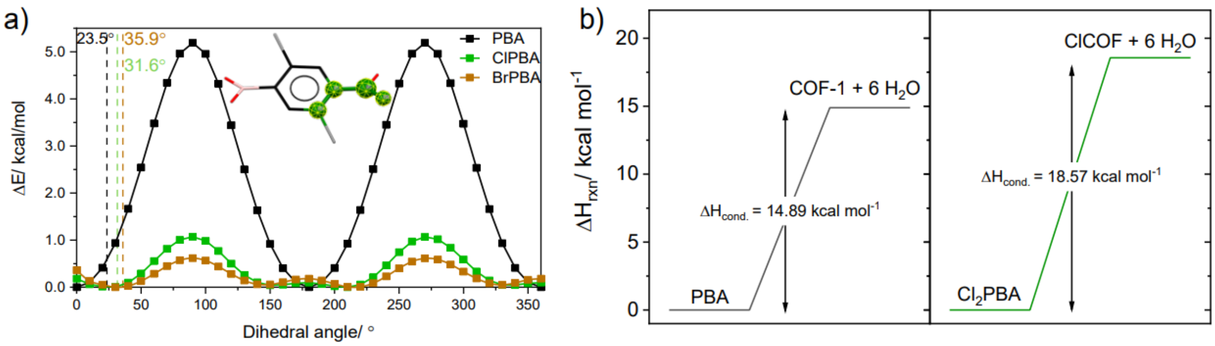

Figure 5.11. a) The energy scan (DFT B3LYP/6-31G(d)) of the dihedral angle between boronic acid and phenyl ring for PBA (black), ClPBA (green), and BrPBA (orange). The vertical dashed lines are the experimental dihedral angle obtained from the SC-XRD. The non-planar minimum energy conformation and lower rotation barriers for ClPBA and BrPBA are a result of the steric hindrance (Cl…O and Br…O). The steric origin of the lower rotational barrier is confirmed by the fact that in the planar configuration, the attractive $H_{Ar}\cdots O$ interaction is replaced with repulsive X…O interactions (3.06 Å and 3.11 Å for Br…O and Cl…O, in planar configuration vs. the vdW radius of Br…O =3.34 Å and Cl…O =3.27 Å, respectively). b) Calculated condensation enthalpies (DFT B3LYP/3-21G*) for PBA into COF-1 and ClPBA into ClCOF-100, showing greater endothermicity of the halogenated boronic acid's condensation.

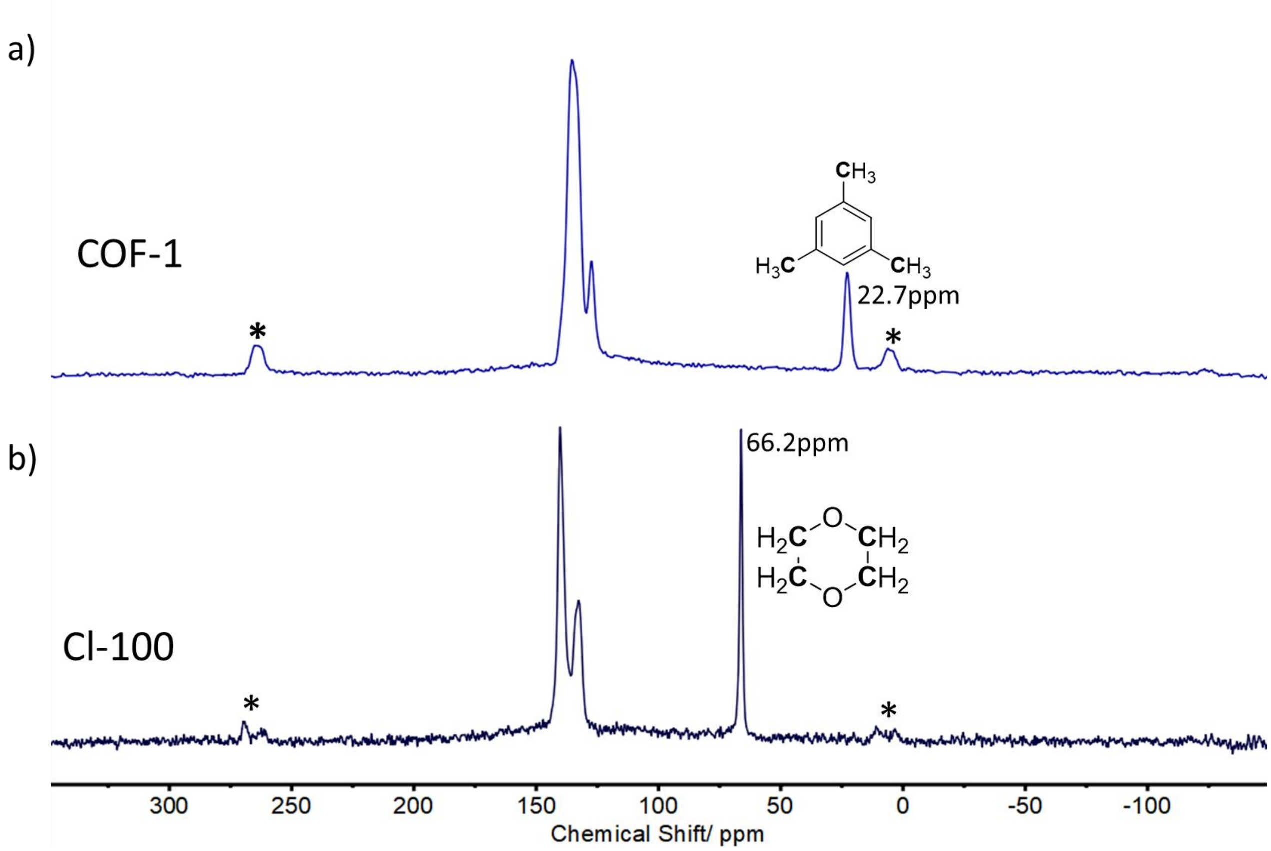

Figure 5.12. Solid-state CP/MAS ^{13}C-NMR spectra of a) COF-1 and b) product of ClPBA self-condensation Cl-100 showing mesitylene guests in COF-1 and dioxane guests in Cl-100.

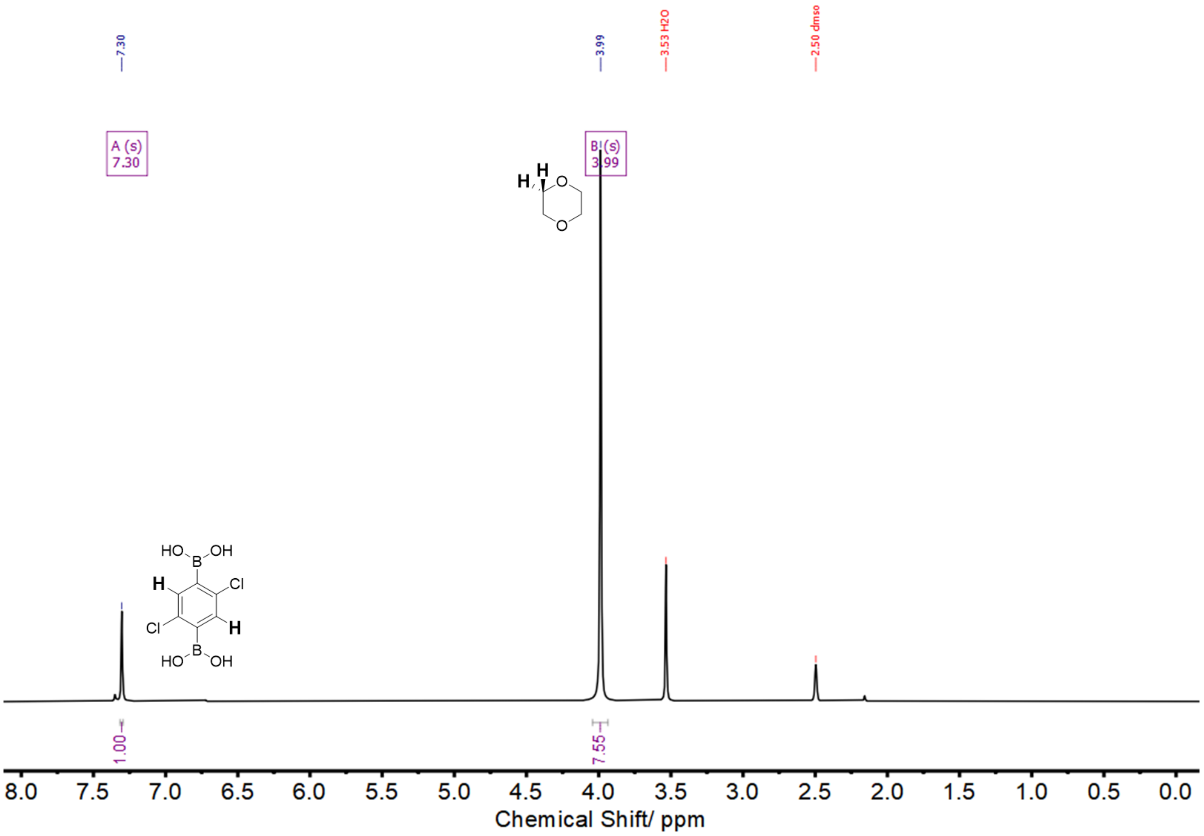

Figure 5.13. ^{1}H-NMR spectra of product of ClPBA self-condensation Cl-100 digested in DMSO-d_6 and a drop of D_2O, showing the inclusion of 2 molecules of dioxane per ClPBA building block in Cl-100. The small (~7%) signal at 7.36 ppm is most likely an oligomer of the ClPBA, due to spontaneous condensation of boronic acids into boroxine anhydrides.

5.7.7. X-ray Photoelectron Spectroscopy (XPS) and NMR of digested samples

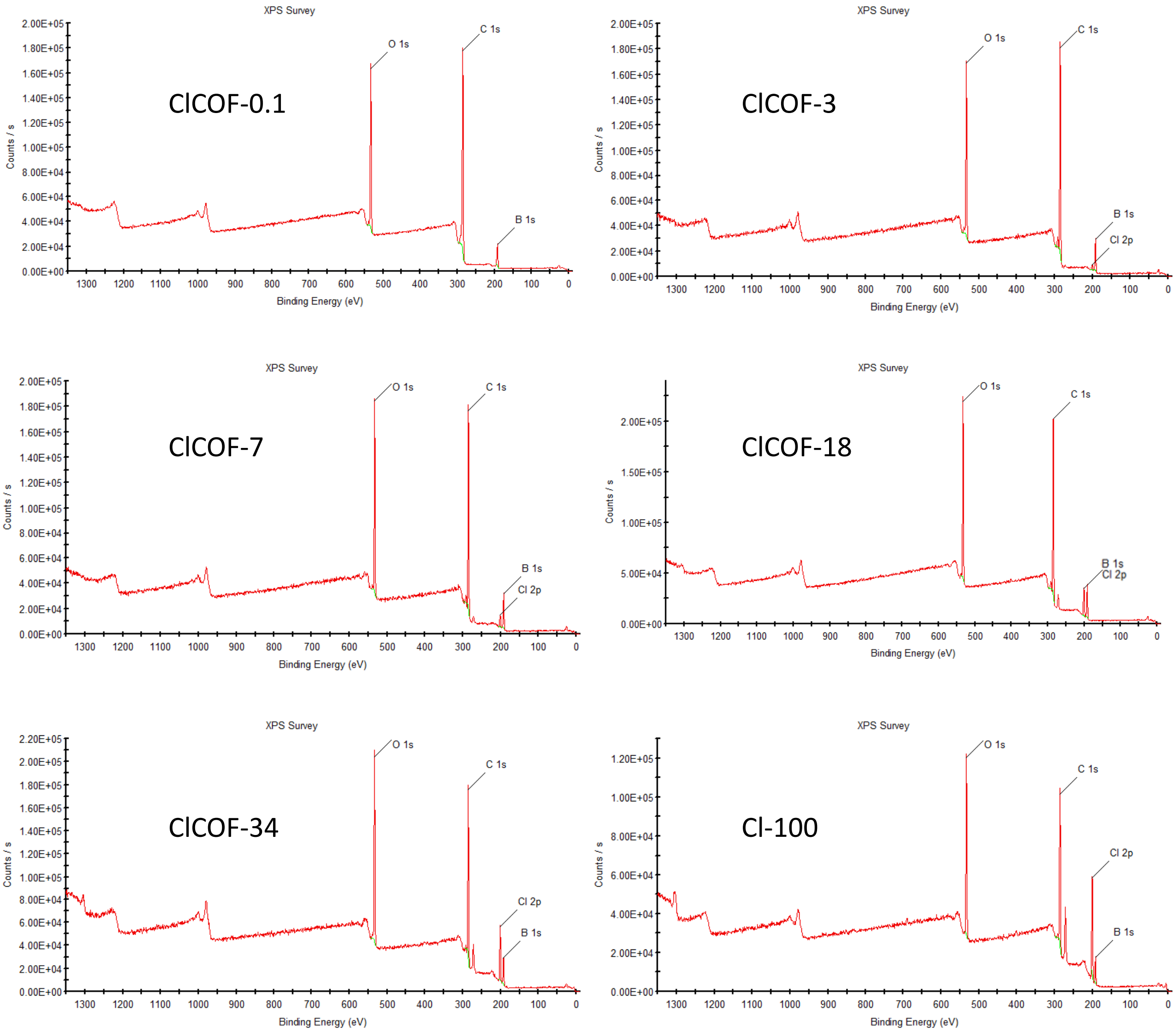

Figure 5.14. XPS survey spectra of ClCOF-N show the presence of O, C, Cl, and B and the absence of other elemental impurities. See the survey atomic ratios in Table 5.3.

Table 5.3. The atomic ratios of ClCOF-N was obtained from survey spectra (Figure 5.14) and the theoretically expected ratios for their corresponding doping percentage

.

	Theo. C%**	C%	σ*	Theo. O%**	O %	σ*	Theo. B%**	B %	σ*	Theo Cl%**	Cl %	σ*
ClCOF-0.1	60.0	61.4	± 2.6	20.0	19.3	± 1.2	20.0	19.2	± 2.3	0.0	0.02	---
ClCOF-3	59.6	59.5	± 1.1	19.9	19.6	± 1.2	19.9	20.3	± 0.2	0.6	0.5	± 0.1
ClCOF-7	59.2	60.1	± 4.6	19.7	21.0	± 1.3	19.7	17.7	± 3.4	1.4	1.2	± 0.2
ClCOF-18	57.9	56.6	± 4.3	19.3	22.2	± 1.7	19.3	18.3	± 4.2	3.5	3.0	± 0.5
ClCOF-34	56.2	49.1	± 1.1	18.7	25.3	± 1.4	18.7	19.6	± 2.2	6.4	6.1	± 0.4
Cl-100	50.0	52.2	± 0.9	16.7	21.4	± 1.5	16.7	13.8	± 0.4	16.7	12.6	± 0.7

* Standard deviation obtained from three measurements.

** The theoretical atomic% is calculated based on the ClPBA:PBA ratio (obtained from the experimental Cl/B).

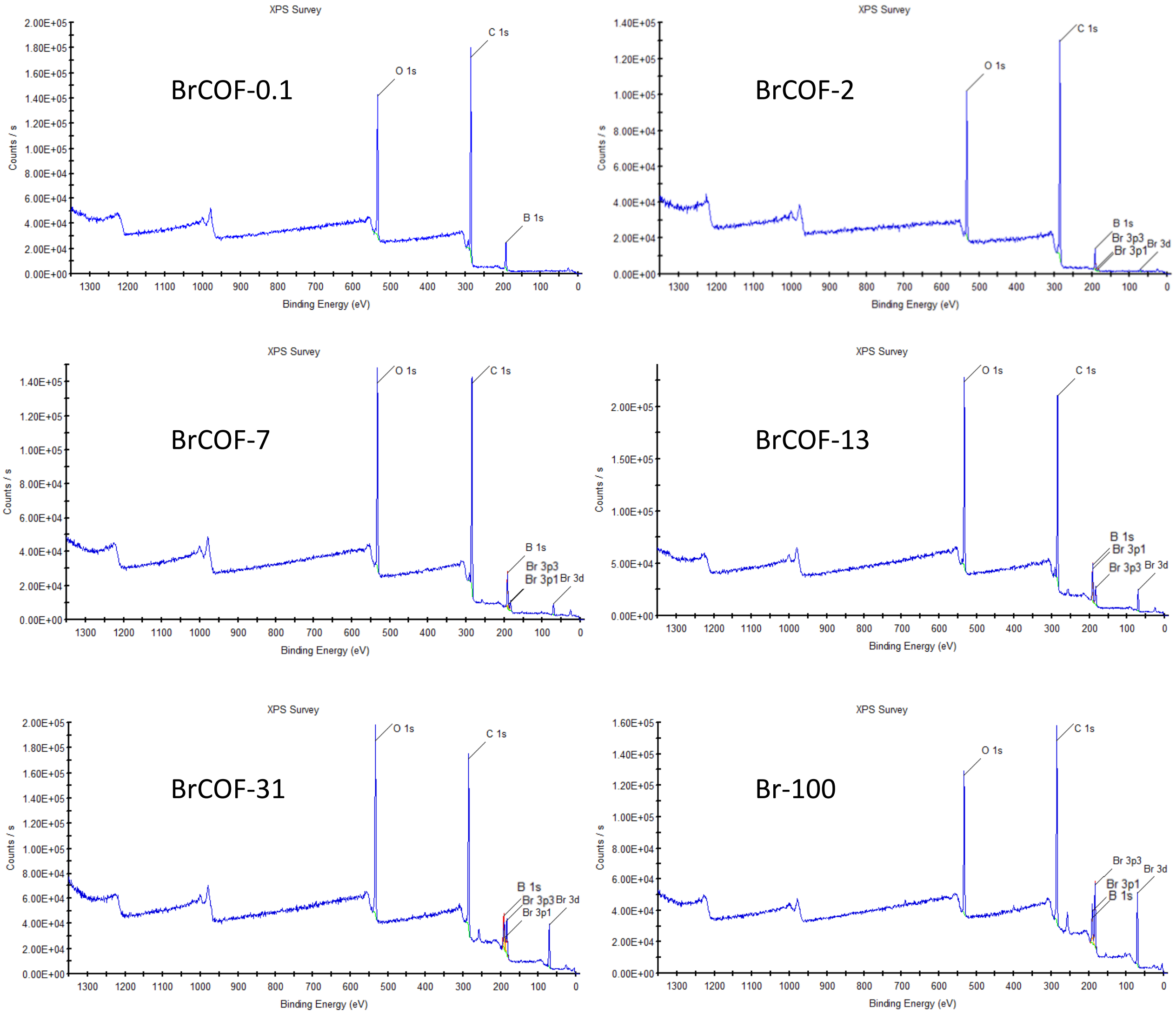

Figure 5.15. XPS survey spectra of BrCOF-N show the presence of O, C, Br, and B and the absence of other elemental impurities. See the survey atomic ratios in Table 5.4.

Table 5.4. The atomic ratio of BrCOF-N was obtained from survey spectra (Figure 5.15) and the theoretically expected ratios for their corresponding doping percentage.

	Theo. C%**	C%	σ*	Theo. O%**	O %	σ*	Theo. B%**	B %	σ*	Theo Br%**	Br %	σ*
BrCOF-0.1	60.0	58.9	± 1.6	20.0	23.0	± 3.1	20.0	18.1	± 1.6	0.0	0.0	---
BrCOF-2	59.8	60.5	± 5.3	19.9	21.9	± 2.8	19.9	17.2	± 2.6	0.4	0.3	± 0.2
BrCOF-7	59.2	58.1	± 0.4	19.7	21.8	± 1.4	19.7	19.1	± 1.7	1.4	1.0	± 0.1
BrCOF-13	58.5	53.6	± 3.1	19.5	26.0	± 5.8	19.5	18.6	± 2.5	2.5	1.8	± 0.2
BrCOF-31	56.5	53.6	± 2.1	18.8	25.1	± 0.7	18.8	17.3	± 2.3	5.8	4.0	± 0.2
Br-100	50.0	62.8	± 4.0	16.7	19.4	± 1.7	16.7	10.0	± 2.0	16.7	7.9	± 0.2

* Standard deviation obtained from three measurements.

** The theoretical atomic% is calculated based on the BrPBA: PBA ratio (obtained from the experimental Br/B).

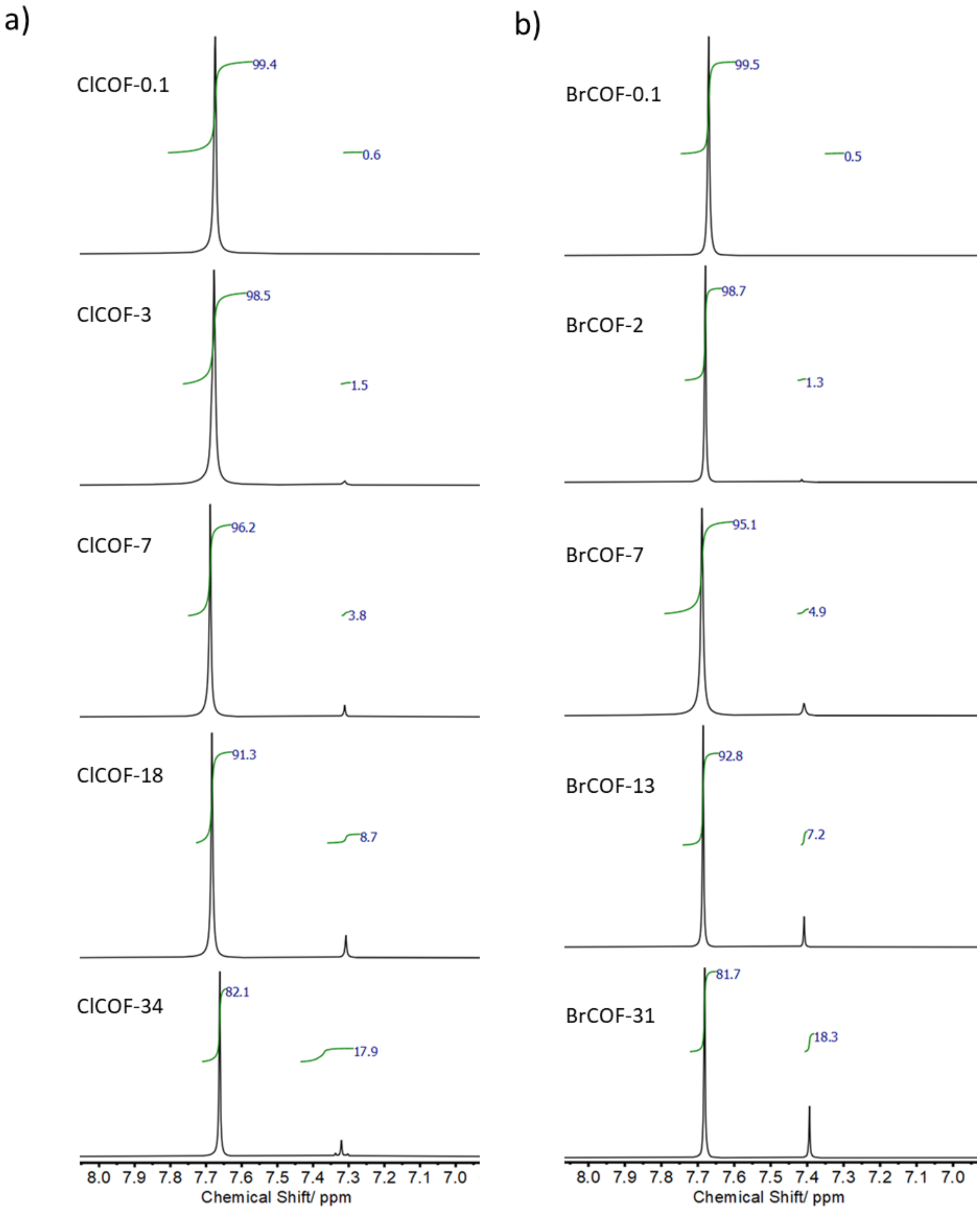

Figure 5.16. ^{1}H-NMR spectra of activated (180 °C, 10^{-3} torr, 12 h) a) ClCOF-Ns and b) BrCOF-Ns, digested in DMSO-d_6 and D_2O (1:1 vol%) and the corresponding integration of $4H_{PBA}$= 7.68 ppm and the $2H_{ClPBA}$=7.33 or $2H_{BrPBA}$= 7.39 ppm. See the obtained monomer ratios in Table 5.5.

Table 5.5. The PBA/XPBA ratio of ClCOF-Ns and BrCOF-Ns obtained from integration of $4H_{PBA}$= 7.68 ppm and the $2H_{ClPBA}$=7.33 or $2H_{BrPBA}$= 7.39 ppm in the NMR (Figure 5.16) spectra of digested ClCOF-Ns and BrCOF-Ns, as well as the theoretically expected ratios for their corresponding doping percentage. $\sigma_{(\%XPS-\%NMR)}$ represents the difference between the percentages obtained via XPS vs. NMR.

	Theo. H_{PBA}, %	Theo. H_{XPBA}, %	NMR H_{PBA}, %	H_{XPBA}, %	$\sigma_{XPS-NMR}$, %
ClCOF-0.1	99.9%	0.1%	99.4	0.6	1.1
ClCOF-3	98.5%	1.5%	98.5	1.5	0
ClCOF-7	96.4%	3.6%	96.2	3.8	0.3
ClCOF-18	90.1%	9.9%	90.9	9.1	1.3
ClCOF-34	79.5%	20.5%	82.1	17.8	3.7
BrCOF-0.1	99.9%	0.1%	99.5	0.5	-0.9
BrCOF-2	99.0%	1.0%	98.7	1.3	-0.6
BrCOF-7	96.4%	3.6%	95.1	4.9	-2.3
BrCOF-13	93.0%	7.0%	92.8	7.2	-0.4
BrCOF-31	81.7%	18.3%	81.7	18.3	0.1

5.7.8. FTIR spectroscopy

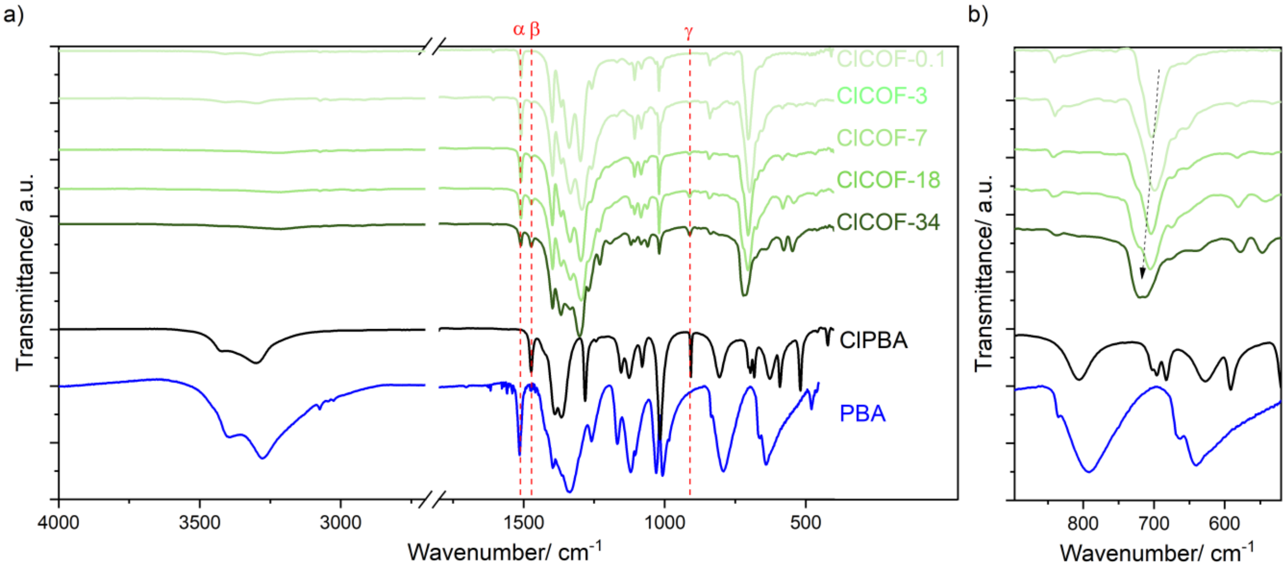

Figure 5.17. a) FTIR of ClCOF-Ns (green) and their parent boronic acids (ClPBA, black, and PBA, blue). The absence of the OH stretch (~3250 cm^{-1}) and the emergence of the boroxine out of plane vibration at (703-717 cm^{-1}) are indicative of complete reaction. The coexistence of the characteristic peaks of PBA at 1508 cm^{-1} (noted as α) and ClPBA at 1473 cm^{-1} (noted as β) along with progressive enhancement of the γ peaks corresponding to the ClPBA, shows the incorporation of both halogenated and non-halogenated monomers, with different ratios. b) Zoomed-in FTIR of ClCOF-N and their parent boronic acids (ClPBA and PBA) shows that the boroxine band is blue-shifted to higher energies with the increasing Cl doping level, due to the electron-withdrawing halogen substituents.

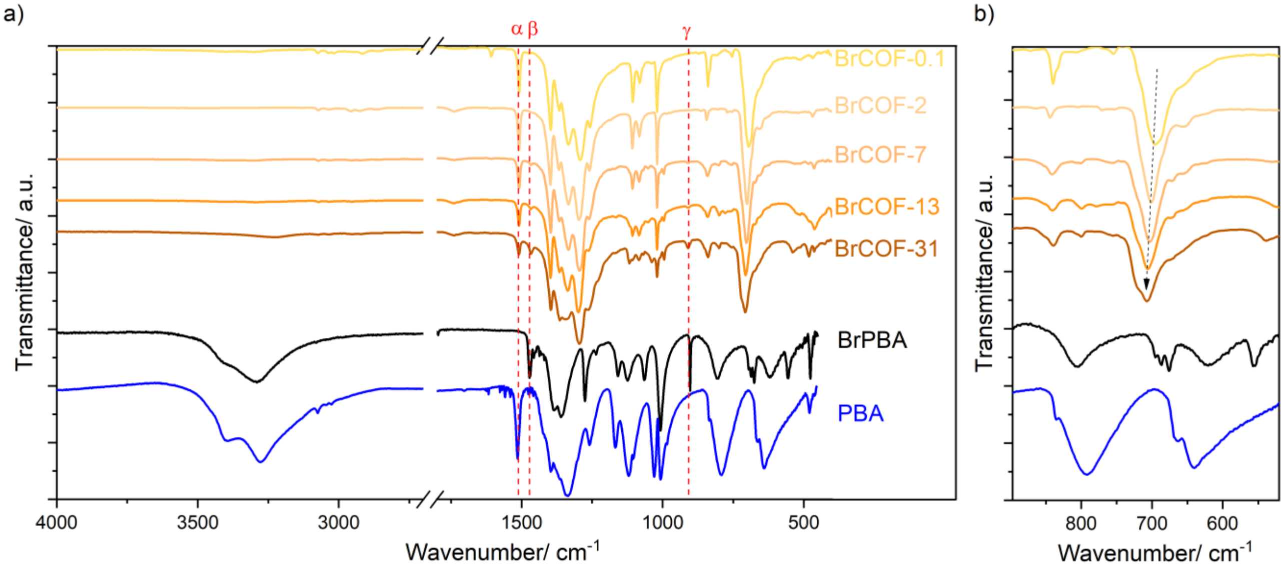

Figure 5.18. a) FTIR of BrCOF-Ns (orange) and their parent boronic acids (BrPBA, black, and PBA, blue). The absence of the OH stretch (~3250 cm^{-1}) and the emergence of the boroxine out of plane vibration at (694-707 cm^{-1}) are indicative of complete reaction. The coexistence of the characteristic peaks of PBA at 1508 cm^{-1} (noted as α, see) and BrPBA at 1471 cm^{-1} (noted as β) along with progressive enhancement of the γ-peak corresponding to the BrPBA vibrational features, shows the incorporation of both halogenated and non-halogenated monomers, with different ratios. b) Zoomed-in FTIR of BrCOF-N and their parent boronic acids (BrPBA and PBA) shows that the boroxine IR band is blue-shifted to higher energies with the increasing Br doping level, due to the electron-withdrawing halogen substituents.

5.7.9. Transmission Electron microscopy (TEM)

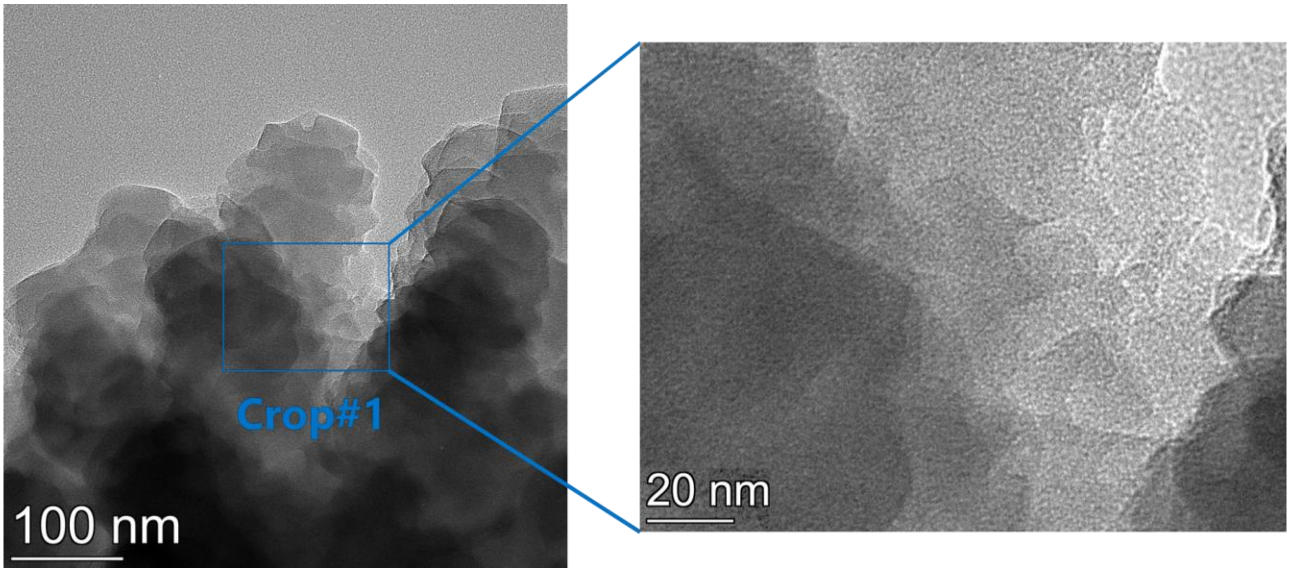

Figure 5.19. High-resolution transmission electron micrographs of the ClCOF-18 powder. No atomic resolution could be obtained due to rapid decomposition in the electron beam.

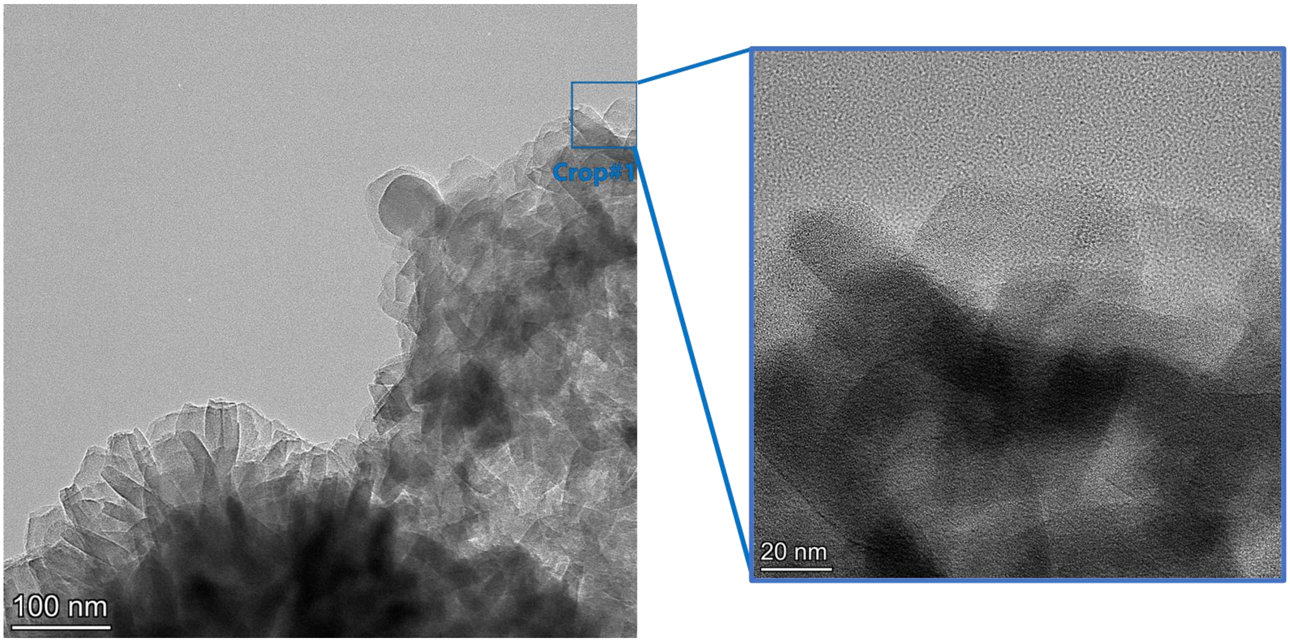

Figure 5.20. High-resolution transmission electron micrographs of the BrCOF-13 powder. No atomic resolution could be obtained due to rapid decomposition in the electron beam.

5.7.10. BET

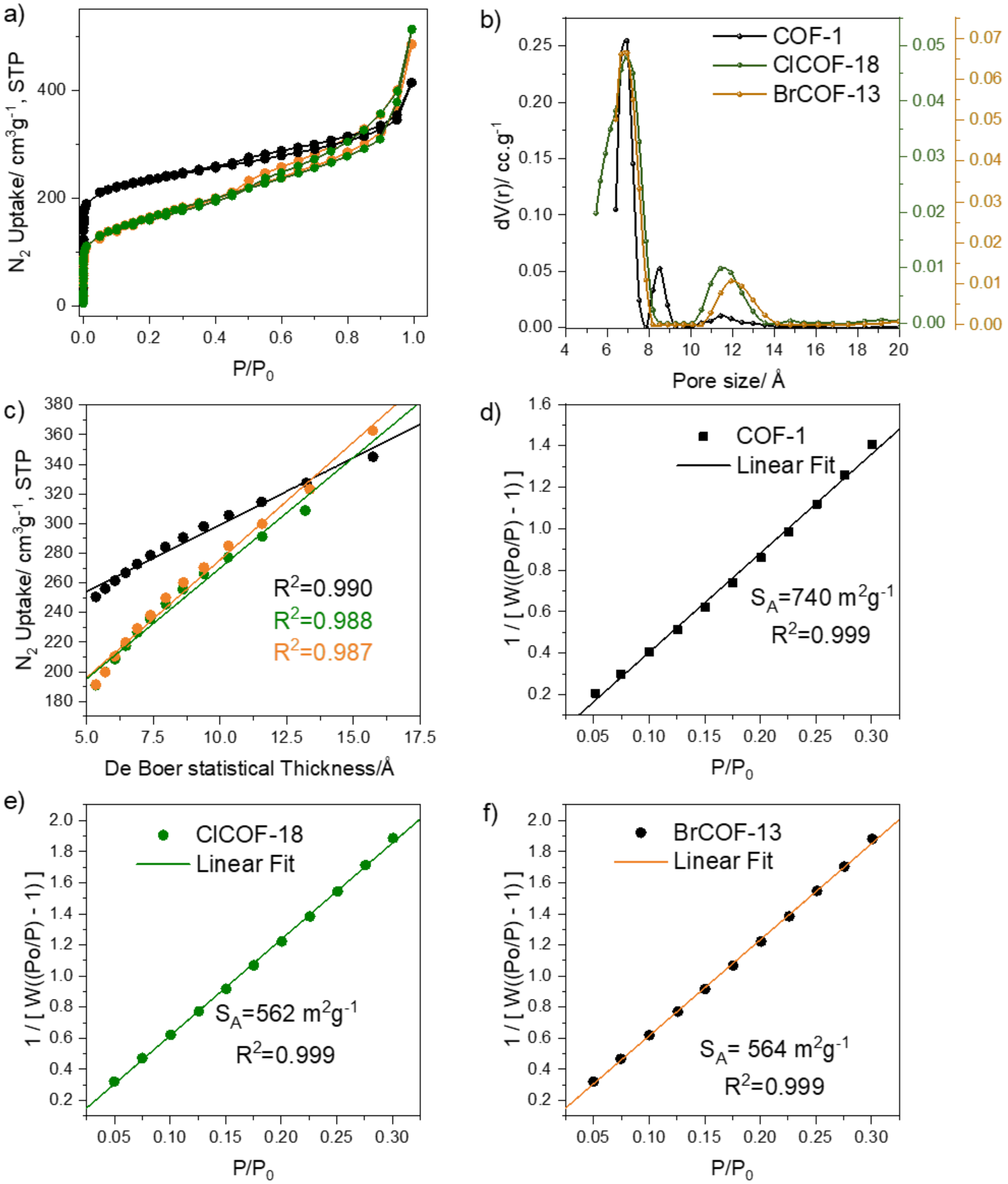

Figure 5.21. a) The N_2 adsorption isotherm at 77 K for COF-1 (black), ClCOF18 (green), and BrCOF-13 (orange). b) The QSDFT analysis of pore size distribution. c) De Boer statistical t-plots and d, e, f) multipoint BET plots and linear fitting calculated from nitrogen adsorption data.

Table 5.6. Summary of COF-1, ClCOF-18, and BrCOF-13 surface area and the porosity ratio obtained from de Boer *t*-plot analysis (Figure 5.21b).

Sample	BET surface area	Micropore surface area	Mesopore surface area (External SA)
Reported COF-1	711 m^2g^{-1}	83% (587 m^2g^{-1})	17% (124 m^2g^{-1})
COF-1	740 m^2g^{-1}	81% (600 m^2g^{-1})	19% (140 m^2g^{-1})
ClCOF-18	562 m^2g^{-1}	59% (331 m^2g^{-1})	41% (231 m^2g^{-1})
BrCOF-13	564 m^2g^{-1}	49% (279 m^2g^{-1})	51% (285 m^2g^{-1})

5.7.11. ICP-OES

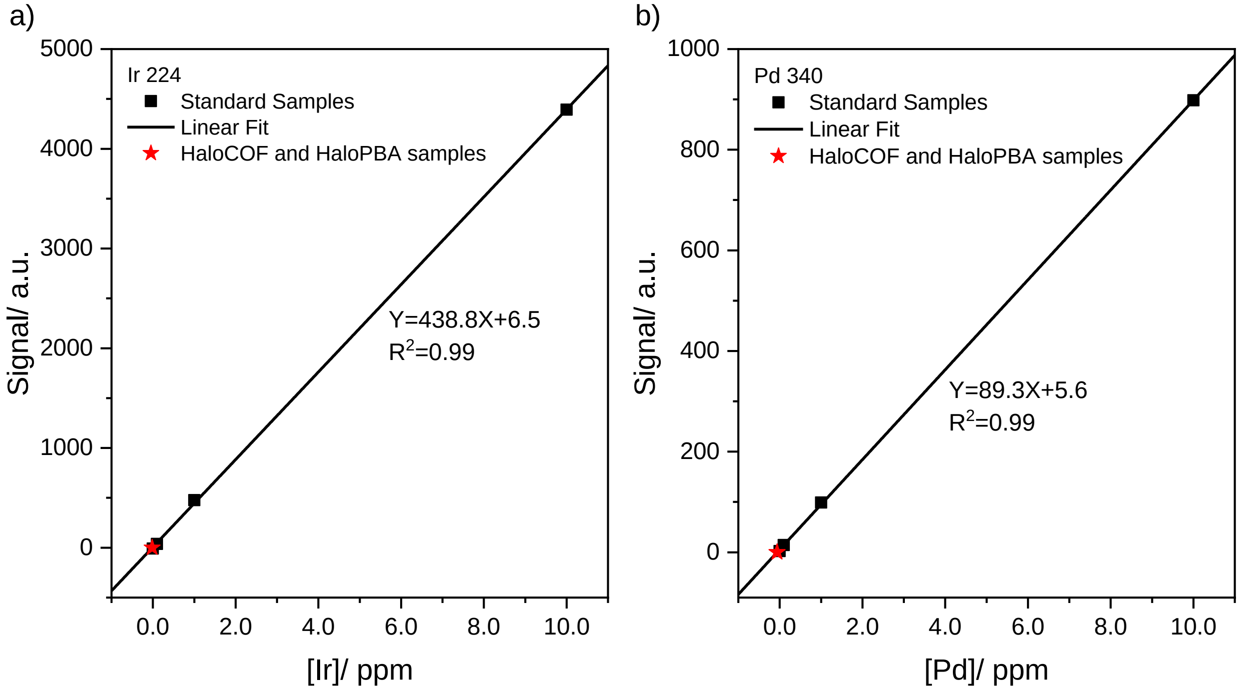

Figure 5.22. The ICP-OES calibration curve for a) iridium and b) palladium. All samples of ClPBA, ClCOF-18, and Cl-100, BrPBA, BrCOF-13, and Br-100 show Ir and Pd contents below the method detection limit.

Table 5.7. The ICP-OES determination of metal content in diboronic acid precursors and their condensation products.

Sample	Signal (Ir 224)	Calculated Conc. ppm	Signal (Pd 340)	Calculated Conc. ppm
Blank	-8.990	-0.035	2.270	-0.037
Standard_0.1 ppm	37.880	0.072	14.400	0.099
Standard _1 ppm	476.500	1.072	98.730	1.043
Standard _10 ppm	4392.000	9.999	898.100	9.994
ClPBA (1mg/ml)	0.002	-0.015	0.085	-0.062
ClCOF-18 (1mg/ml)	-0.013	-0.015	0.018	-0.063
Cl-100 (1mg/ml)	0.001	-0.015	-0.017	-0.063
BrPBA (1mg/ml)	-0.016	-0.015	-0.006	-0.063
BrCOF-13 (1mg/ml)	-0.004	-0.015	-0.016	-0.063
Br-100 (1mg/ml)	-0.012	-0.015	0.002	-0.063

5.7.12. PXRD and thermogravimetric analysis (TGA) of HaloCOFs

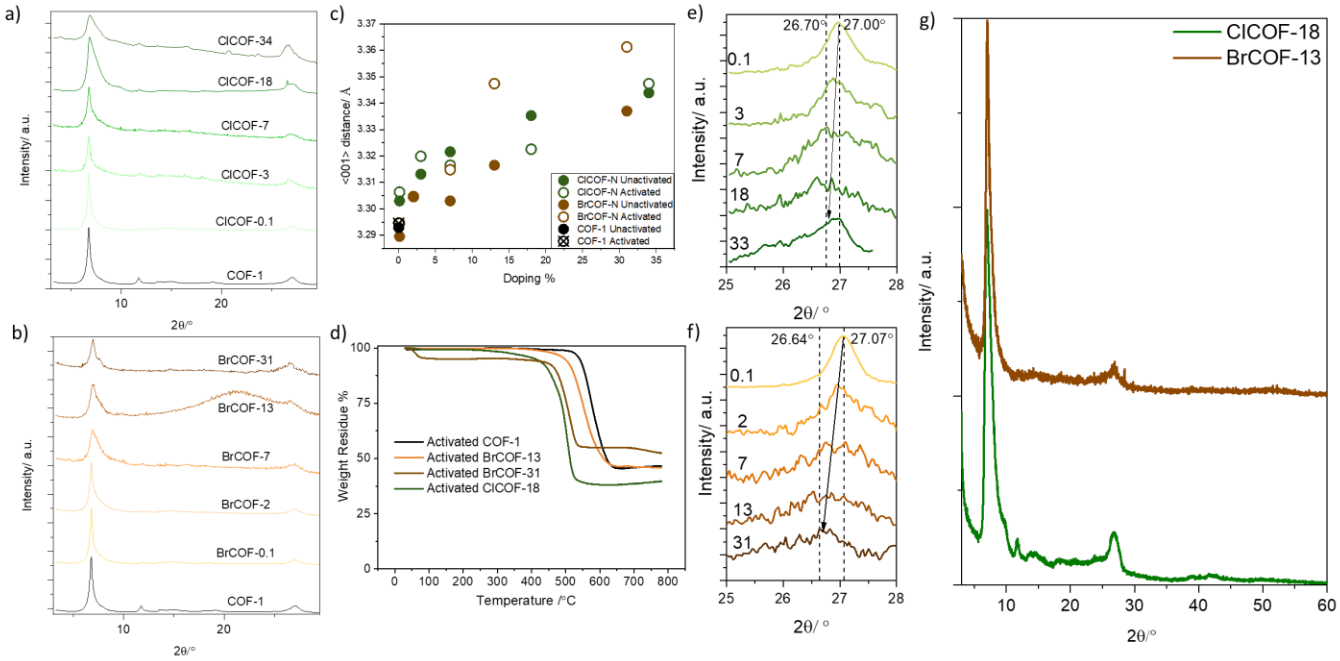

Figure 5.23. PXRD of the activated (180 °C, 10^{-3} torr, 12 h) a) ClCOF-N b) BrCOF-N series, showing that the <100> diffraction peak becomes dominant upon the evacuation of the solvent guest molecules. c) π-π interplanar distance calculated from the <001> diffraction of the PXRD for both non-activated and activated COFs. d) The thermogravimetric analysis (TGA) of activated COF-1 in comparison to ClCOF-18 and BrCOF-13 and BrCOF-34 showed high thermal stability of up to ca.

500°C. Enlarged PXRD of the non-activated ClCOF-N (e) BrCOF-N (f) series, showing the <001> diffraction peak slightly shift upon increasing doping level; g) The PXRD of the ClCOF-18 and BrCOF-13 from 3-60° showing the absence of any phase impurities in the resulting COFs.

A similar increase in the intensity of the <100> vs. <110> peaks upon activation of the parent boroxine COF-1 has been observed in the original work by Yaghi et al 2005, and was initially attributed to the transition from the AB to AA stacking modes. A more recent study, however, showed that this change of the PXRD pattern upon activation could be fully explained by the removal of the mesitylene guest molecules for the same AA stacking motif.[5] This latter hypothesis is in line with our observations, where the accommodation of halogen atoms inside the pores perturbs the inclusion of the mesitylene guests. Upon removal of the guest molecules by activation of the COFs (180 °C, 10^{-3} torr, 12 h), the <100> peak becomes dominant in their PXRD and all activated COFs show similar PXRD patterns (Figure 5.23). Analysis of the position of the <001> peak at ~27° (corresponding to π-π stacking) shows a slight increase of the interlayer distance at higher halogen concentration, from 0.329 nm for COF-1 to 0.335 nm and 0.336 nm for ClCOF-34 and BrCOF-31, respectively (Figure 5.23 c,e,f). The broadening of this peak at high doping levels can be due to a local variation of the π-π stacking distance in the vicinity of halogen atoms.

5.7.13. HaloCOFs Photophysics

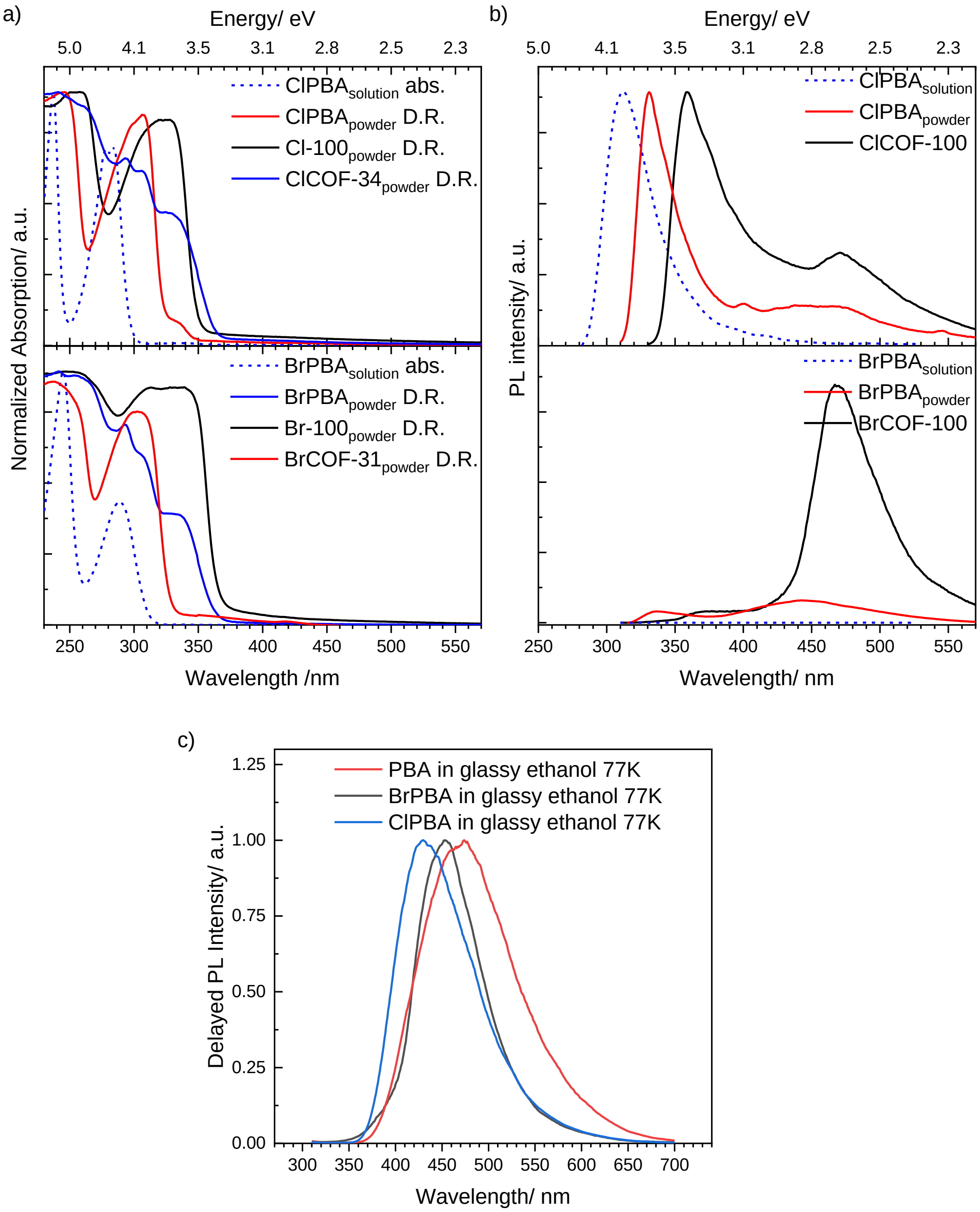

Figure 5.24. a) Absorption of Cl-100 (black), ClCOF-34 (blue solid line), Br-100 (black) and BrCOF-31 (red) and their corresponding ClPBA (red) and BrPBA (blue) monomer as powders (in diffuse reflectance mode, D.R.) and in solution (~10^{-6} M in MeCN). b) Steady-state emission of Cl-100, Br-100, ClPBA and BrPBA as powders and in solution (~10^{-6} M in MeCN; non-emissive) (λ_{ex} = 286 nm), c) Delayed spectra (t_d = 0.2ms, λ_{ex} = 286 nm) of the PBA, ClPBA and BrPBA monomers in glassy ethanolic solutions (~10^{-6} M). Cl-100 and Br-100 are the products of self-condensation of CPBA and BrPBA, respectively.

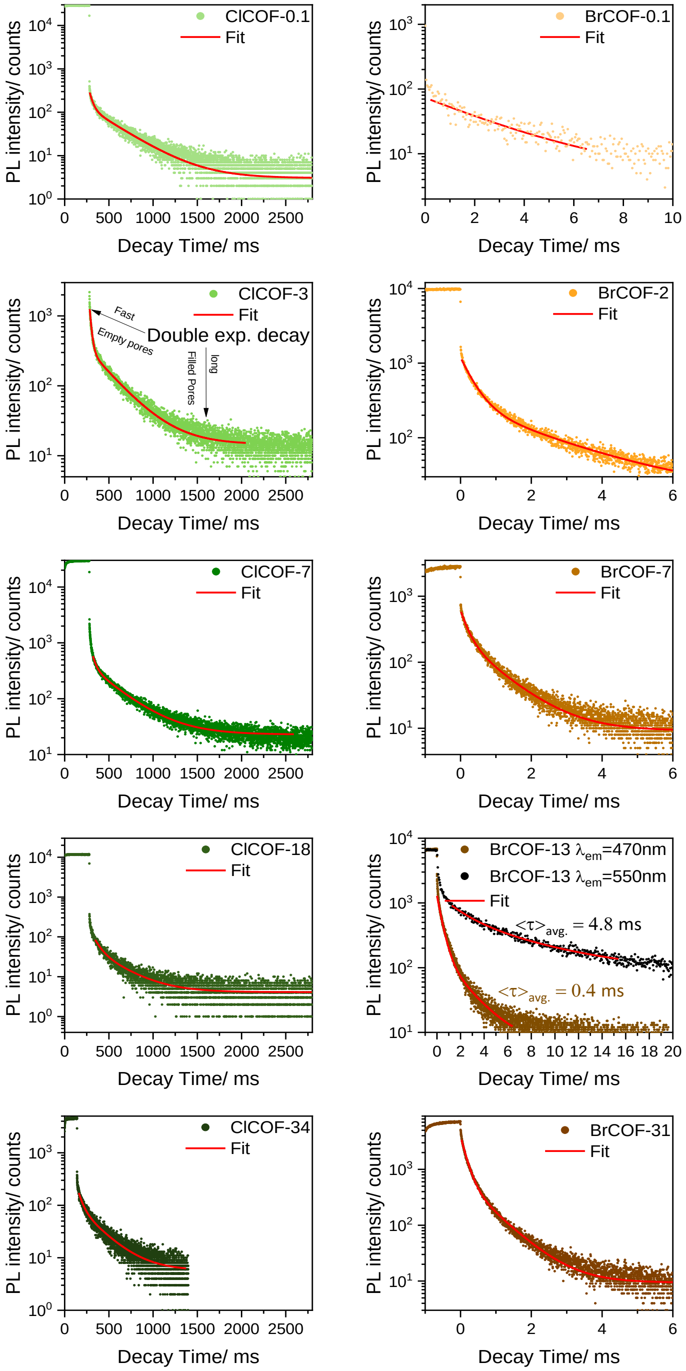

Figure 5.25. The TCSPC lifetime analysis of the ClCOF-N (green) and BrCOF-N (orange) in air with their corresponding biexponential fitting (red). The ClCOF-Ns show a noticeable biexponential phosphorescent decay with a short-lived (<20 ms) and a persistent phosphorescence (>250 ms) component. We attribute this behavior to partial blockage of the pores with mesitylene guest molecules. The TCSPC lifetime analysis of non-activated BrCOF-13 in air at two different emission wavelengths is shown in the figure, indicating a 10-fold enhancement of the stabilized (red-shifted) excitons.

Table 5.8. Decay fitting parameters of non-activated ClCOF-Ns’ and BrCOF-Ns’ phosphorescence in air. (λ_{ex} = 286 nm)

	τ_1 (ms)	a_1	τ_2,(ms)	a_2	τ_{avg}, (ms)	$\sigma(\tau)$
ClCOF-0.1	94.8	30%	329.3	70%	258.9	2.1
ClCOF-3	25.9	40%	292.5	60%	185.9	3.5
ClCOF-7	39.7	50%	320.4	50%	180.0	5.0
ClCOF-18	68.2	52%	268.7	48%	164.4	3.5
ClCOF-34	48.5	51%	243.4	49%	144.0	1.9
BrCOF-0.1	2.96	91%	180.00	9%	19.36	1.2
BrCOF-2	0.36	77%	2.29	23%	0.80	0.05
BrCOF-7	0.20	63%	0.93	37%	0.47	0.05
BrCOF-13	0.19	79%	1.17	21%	0.40	0.03
BrCOF-31	0.16	82%	0.72	18%	0.26	0.01

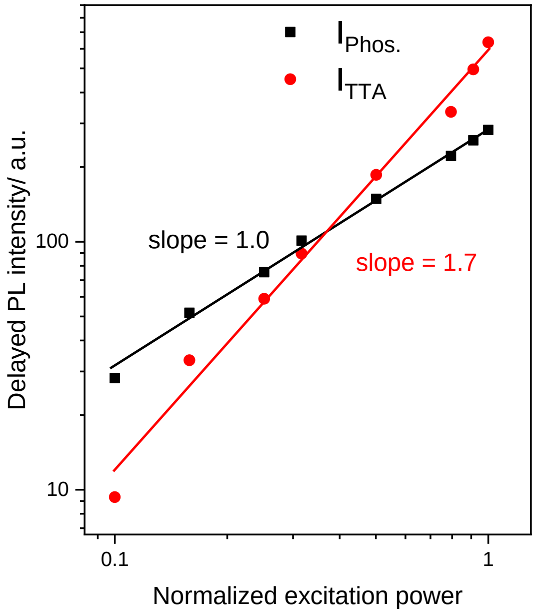

Figure 5.26. Intensity dependence of TTA-induced DF (red circles) and phosphorescence (black squares) of ClCOF-3, with linear fits (corresponding solid lines) vs excitation power in double-log plot, showing non-linear behavior of DF feature.

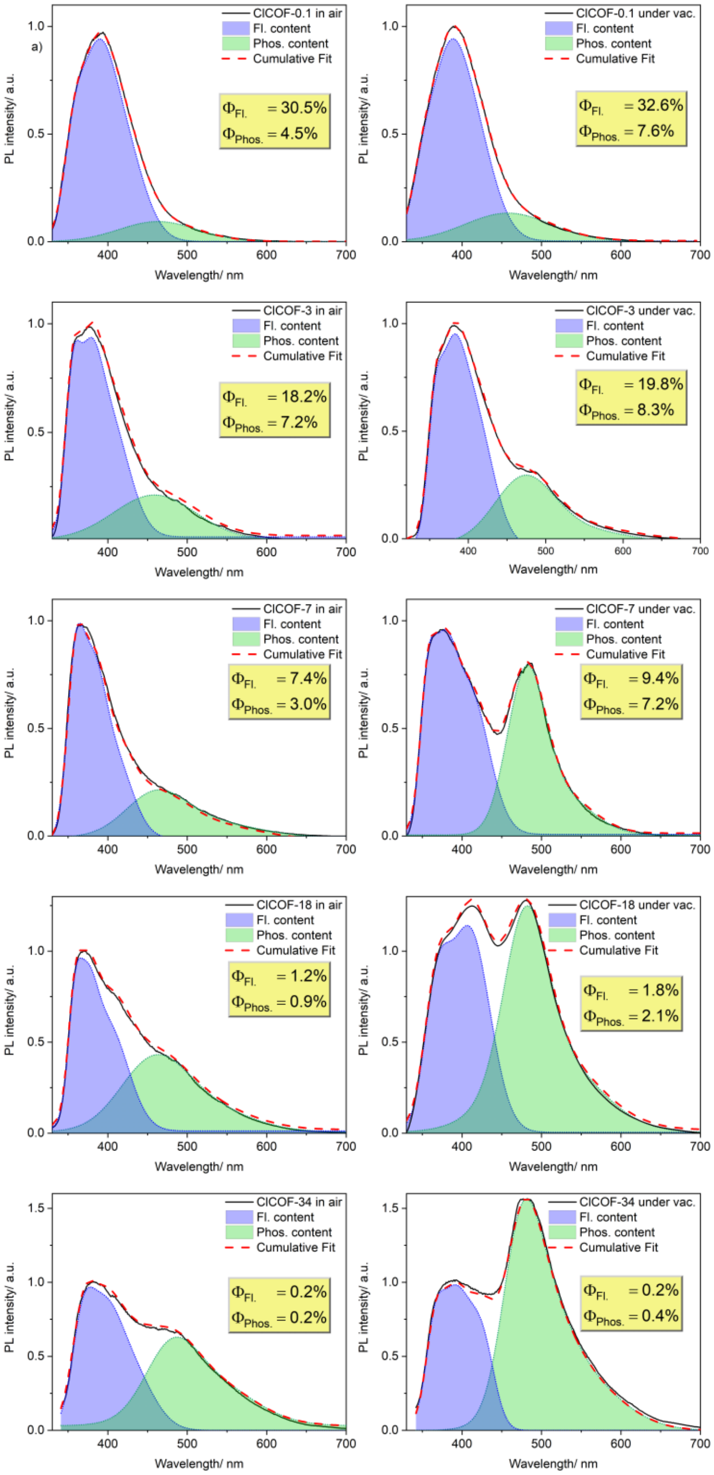

Figure 5.27. Deconvolution of the fluorescence (blue region) and phosphorescence (green region) components of the ClCOF-N steady-state emission. The spectra were fitted with four Gaussian functions (two Gaussian functions each for fluorescence and phosphorescence regime). The functions were fitted to produce the least residual value as the difference between the experimental data (black) and the cumulative fit graph (red dashed).

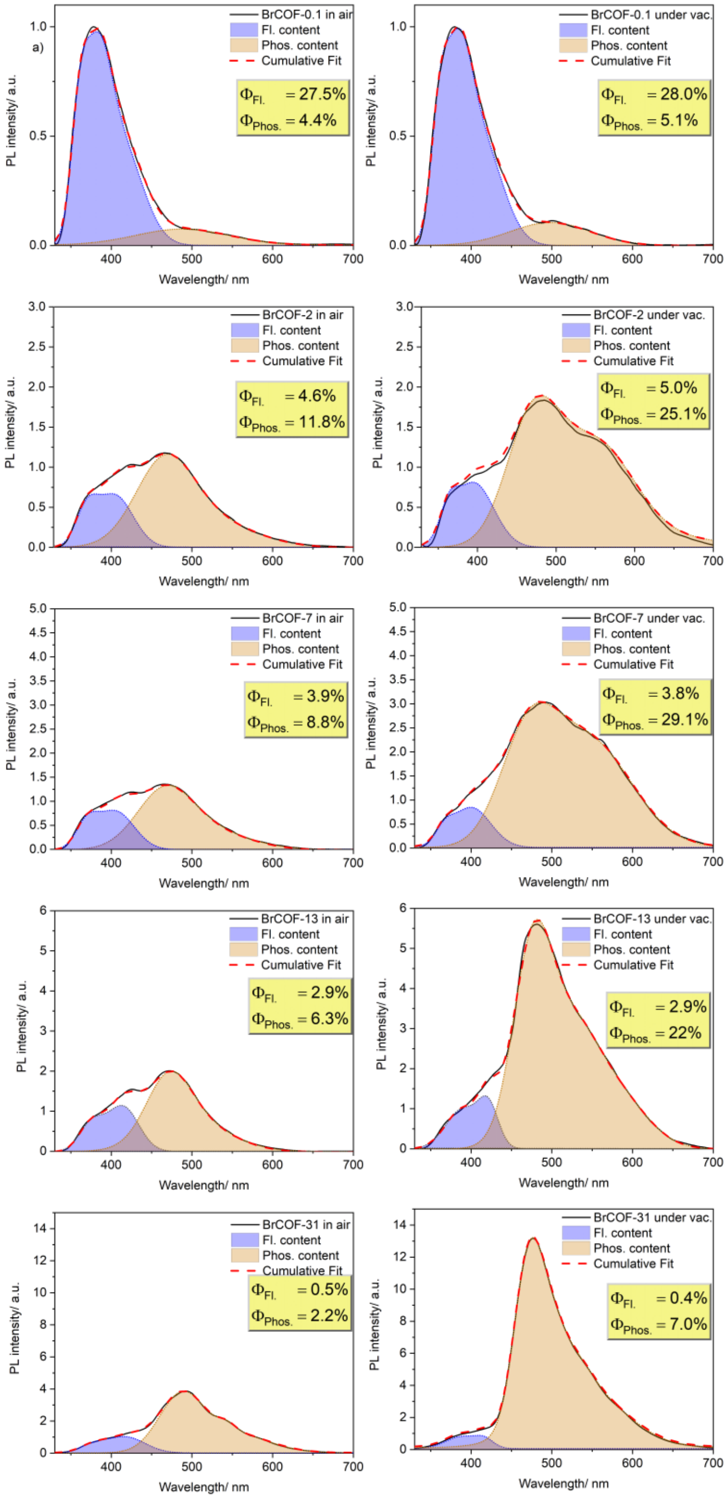

Figure 5.28. Deconvolution of the fluorescence (blue region) and phosphorescence (orange region) of the BrCOF-N steady-state emission. The spectra were fitted with four or five Gaussian functions (two Gaussian functions for fluorescence and two or three functions for phosphorescence regime). The functions were fitted to produce the least residual value as the difference between the experimental data (black) and the cumulative fit graph (red dashed).

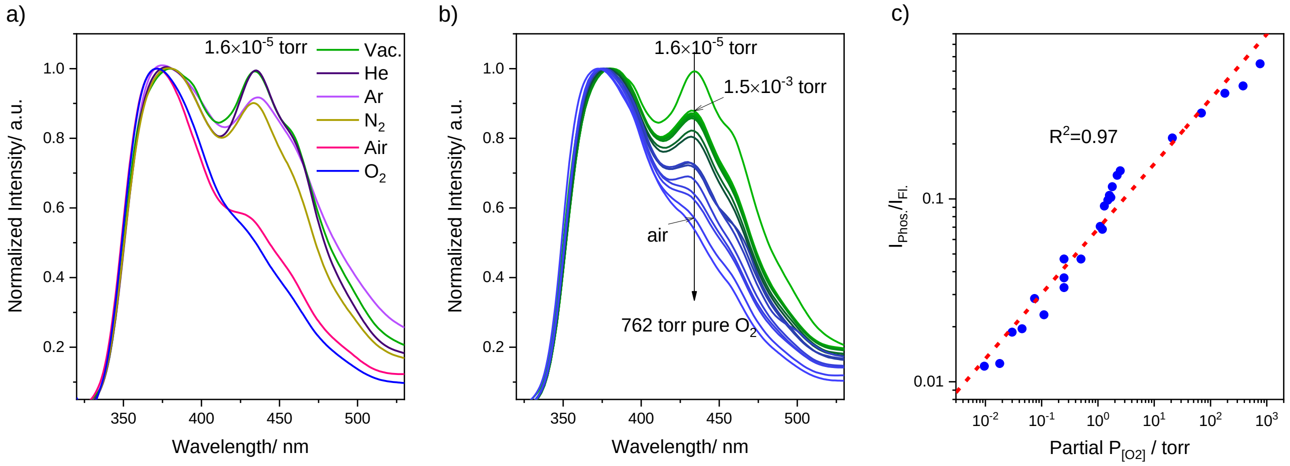

Figure 5.29. a) Effect of different gasses on the phosphorescent emission of as-prepared (non-activated) ClCOF-18 in vacuum (10^{-5} torr, green), He (black), Ar (purple), N_2 (gold), Air (red), and O_2 (blue); the slight decrease of phosphorescence vs. vacuum might be due to the residual O_2 impurities in commercial gases. b) Steady-state photoluminescence spectra (λ_{ex} = 300nm) of ClCOF-18 at different partial O_2 pressures. The phosphorescence band at 490 nm diminishes with increasing O_2 pressure (green-to-blue). e) The phosphorescence/fluorescence ratio (blue circles) for BrCOF-13, shows a very large dynamic range of response (red dashed line).

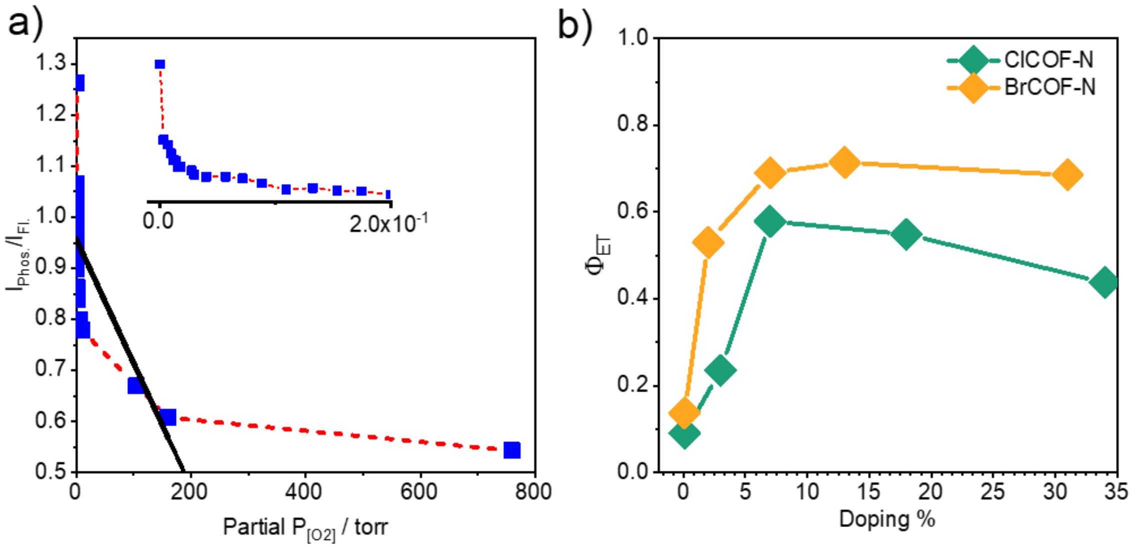

Figure 5.30. (a) Phosphorescence/fluorescence ratio (I_{480nm}/I_{380nm}) for as-prepared (non-activated) BrCOF-13, showing a large deviation from the Stern-Volmer linear fit (black). The inset is the zoomed area of the plot (0-0.2 torr). (b) The efficiency of the oxygen quenching ($\Phi_{ET} = 1 - \Phi_{air}/\Phi_{vac.}$) of as-prepared (non-activated) COFs reaches a maximum at ~10% halogen doping for both ClCOF (green) and BrCOF (orange). The slight decrease of Φ_{ET} at higher doping concentration may be due to a competition between TTA and O_2 quenching.

Table 5.9. Comparison of oxygen sensitivity by our COF with those reported for other organic (and some inorganic) phosphorescent materials reported in the literature

Phosphorescent material	Detection range (as reported)	Detection range (converted to partial O_2 pressure/ Torr)	Ref.
Organic			
Thianthrene derivatives doped in *Zeonex®*	0.02% - 2%	0.152 – 15.2	Leitonas et al., *Sensors Actuators B: Chem*. **2021**, 345, 130369. (SI Ref. [6])
4-Bpin(triphenylamine) doped polymer	0.2% – 20%	1.52 – 152	Zhou *et al., Angew. Chem. Int. Ed.* **2019**, 58, 12102. (SI Ref. [7])
Carbazole-based hydrogen-bonded organic frameworks	10% – 100%	76 – 760	Cai *et al., Angew. Chem. Int. Ed.* **2018**, 57, 4005. (MS Ref. 48)
BF_2 and Al complexes	2 – 6 ppm 20 – 100 ppm	$1.52\times10^{-3} – 4.56\times10^{-3}$ 0.0152 – 0.076	Lehner *et al., Nat. Commun.* **2014**, 5, 1. (MS Ref. 50)
Core-shell polymer nanoparticles	0.005 – 20 kPa	0.0375 – 150	Yu *et al., Angew. Chem. Int. Ed.* **2017,** 56, 16207. (MS Ref. 52)
BF_2 complex doped polymer	0.055 – 1 torr	0.055 – 1	Zhang *et al.,J. Am. Chem. Soc.* **2007**, 129, 8942. (MS Ref. 53)
C_{70} in organo-silica and ethyl cellulose	50 – 300 ppm	0.038 – 0.228	Nagl *et. al, Angew. Chem. Int. Ed.* **2007**, 46, 2317. (SI Ref. [8])
Halogen Doped COF-1	10^{-5}– 760 torr	10^{-5} – 760	***Our work***
Inorganic			
Ag-based MOF	10^{-3} – 2.4 Pa	7.5×10^{-6} – 0.018	Dong *et al., Nat. Commun.* **2020**, 11, 1. (SI Ref. [9])
Pt/Pd/Ru complexes doped SiO_2	0.06 – 100 torr	0.06 – 100	Han *et al., Chem. Mater,* **2005**, 17, 3160 (MS Ref. 41)
Ru complexes doped SiO_2	2 – 20 cm Hg	20 – 200	Carraway *et al., Langmuir* **1991**, 7, 2991 (MS Ref. 42)
MOF doped with Ir/Ru-complexes	0.05 – 0.80 atm	38 – 608	Barrett *et al., J. Mater. Chem.* **2012**, 22, 10329. (MS Ref. 43)
Cu-based MOF	0.1 – 5 ppm	$7.6\times10^{-5} – 3.8\times10^{-3}$	Liu *et al., Angew. Chem. Int. Ed.* **2016**, 55, 16021. (MS Ref. 44)
Tb/Eu doped microporous polymers	0.1 – 1 bar	76 – 760	Ye *et al., Inorg. Chem.* **2017**, 56, 4238. (MS Ref. 45)
Ru doped microporous polymers	0.001 – 1 bar	7.6 – 760	Qi *et al., Chem. Commun.* **2013**, 49, 6864. (MS Ref. 46)
Ir doped microporous polymers	0.05 – 1 atm	38 – 760	Xie, et al., *J. Am. Chem. Soc.* **2010**, 132, 922. (MS Ref. 47)

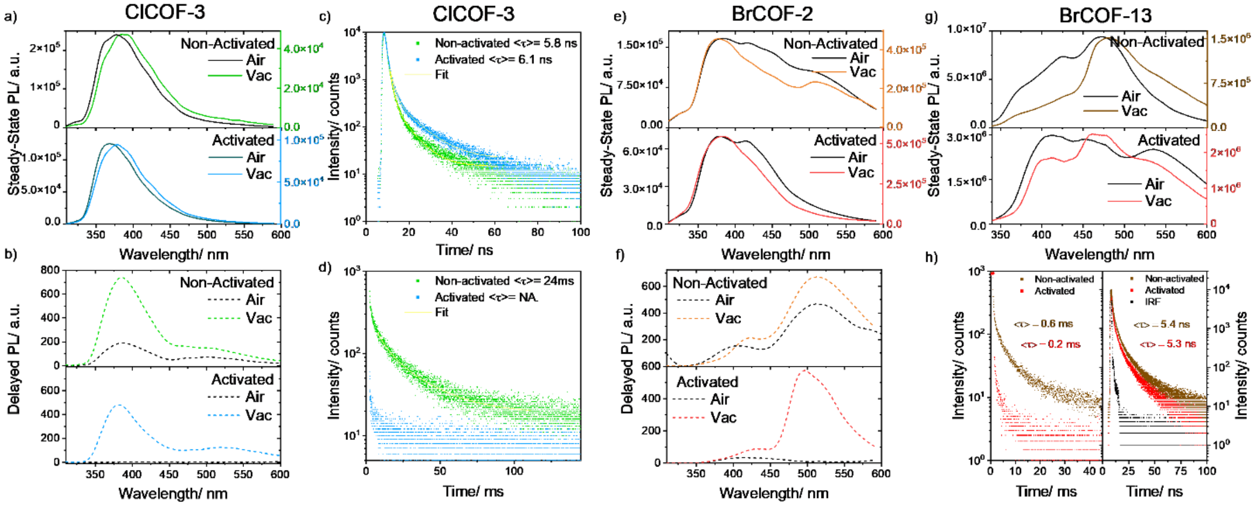

Figure 5.31. Steady-state (top) and delayed (bottom, t_d = 0.2 ms , t_{gate} = 20 ms) photoluminescence of a, b) ClCOF-3, e, f) BrCOF-2 and g) BrCOF-13 before (green, orange, brown, respectively) and after activation (blue, red, respectively) measured in air (black) and under vacuum. The TCSPC lifetime analysis of fluorescence and phosphorescence for c, d) ClCOF-3 and h) BrCOF-13 shows a significant decrease of phosphorescence after activation while the fluorescence signal only slightly changes. The phosphorescence of the activated BrCOF-3 is expectedly decreased after activation; however, fluorescent impurities (possibly from thermal decomposition) skewed the steady-state spectra which is also more prominent in steady-state spectra of g) BrCOF-13.

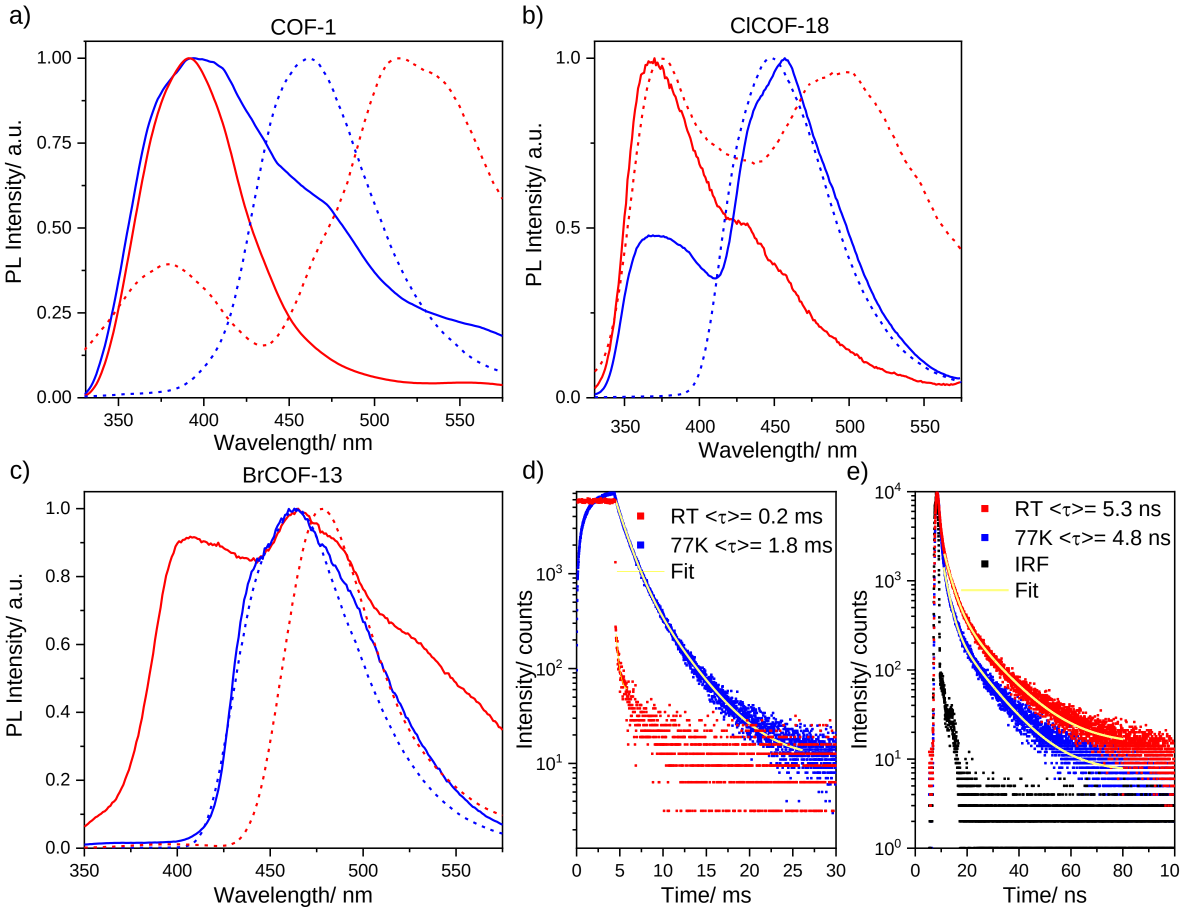

Figure 5.32. Steady-state (solid lines) and time-gated spectra (dotted lines, t_d = 0.2ms) a) COF-1, b) ClCOF-18, and c) BrCOF-13, at room temperature (red) and 77 K (blue), showing enhancement of phosphorescence emission upon cooling down the COFs to 77 K (all in the air). The TCSPC lifetime analysis of phosphorescence d) and fluorescence e) of BrCOF-13, shows a 9-fold enhancement of phosphorescence lifetime upon cooling, while fluorescence slightly decreased at 77 K.

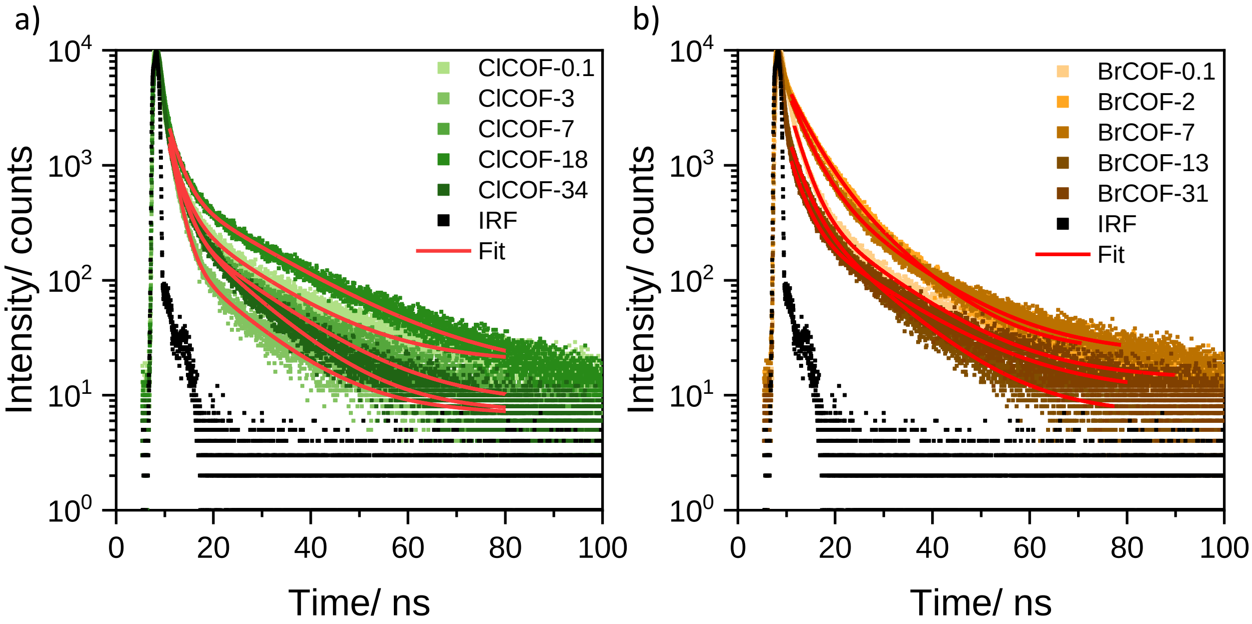

Figure 5.33. TCSPC lifetime analysis of fluorescence of activated a) ClCOF-Ns (green) and b) BrCOF-Ns (orange) in air (λ_{ex} = 373 nm, λ_{em} = 410-440 nm). Comparison of the fluorescence lifetime of COF-1 vs. the doped COFs shows a slight decrease of lifetime upon doping with the XPBA due to inactivation of S_1 excited state; however, no trend was observed upon increasing the doping ratio.

Table 5.10. Decay fitting parameters of TSCPC lifetime analysis (Figure 5.33) for activated ClCOF-Ns' and BrCOF-Ns' fluorescence in air. (λ_{ex} = 373 nm; λ_{em} = 410-440 nm)

	$\tau_{1\ (ns)}$	a_1	$\tau_{2,(ns)}$	a_2	$\tau_{avg,\ (ms)}$
ClCOF-0.1	2.3	76%	13.8	24%	5.1
ClCOF-3	2.6	70%	14.5	30%	6.1
ClCOF-7	2.3	77%	14.7	23%	3.9
ClCOF-18	2.3	74%	16.8	26%	6.2
ClCOF-34	2.2	77%	11.2	23%	4.3
BrCOF-0.1	2.6	81%	13.4	19%	4.6
BrCOF-2	4.1	70%	10.6	30%	6.0
BrCOF-7	3.6	80%	13.3	20%	5.5
BrCOF-13	2.8	73%	11.5	23%	5.1
BrCOF-31	2.6	74%	14.6	26%	5.7

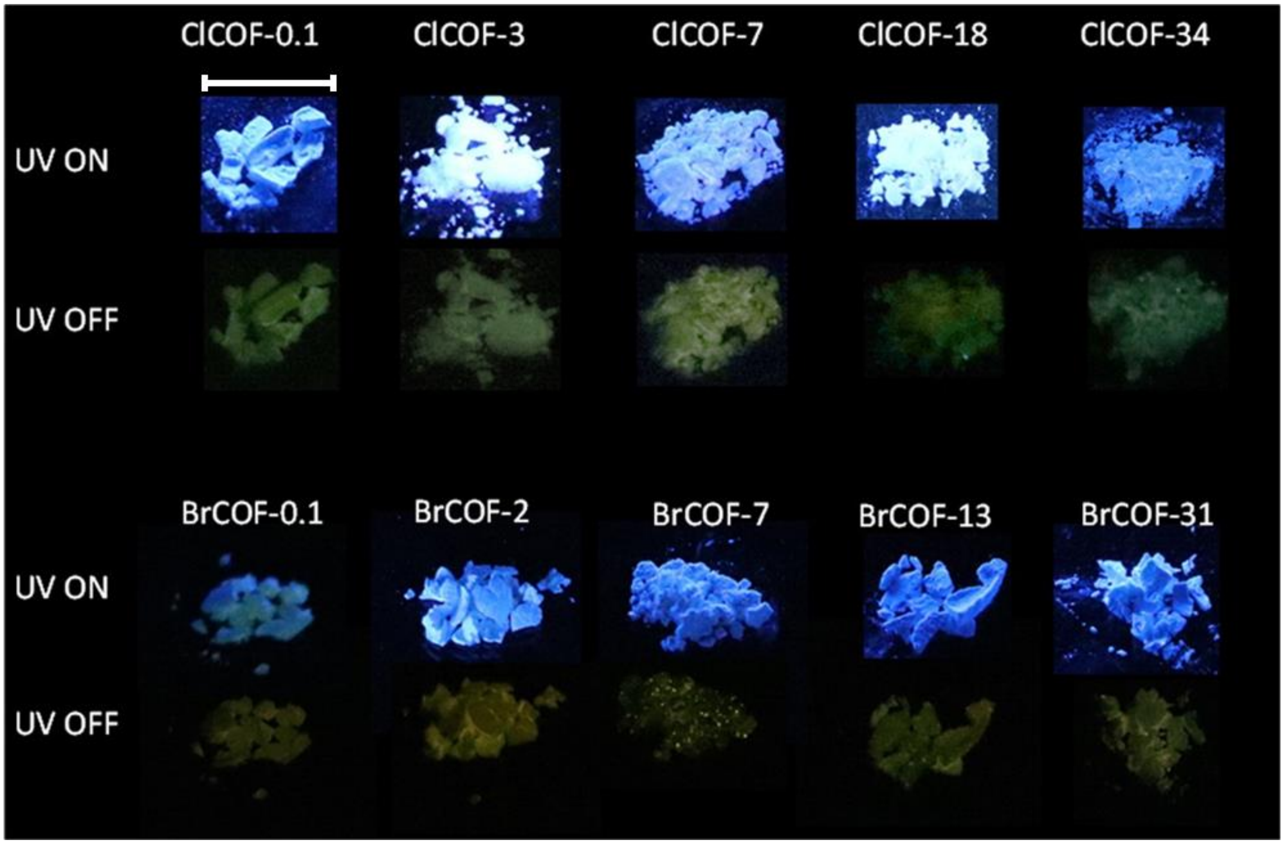

Figure 5.34. Photographs of non-activated COFs under continuous UV illumination (UV ON) and immediately after turning the UV lamp off, i.e. afterglow (UV OFF). Scale bar shows approximately 1 cm.

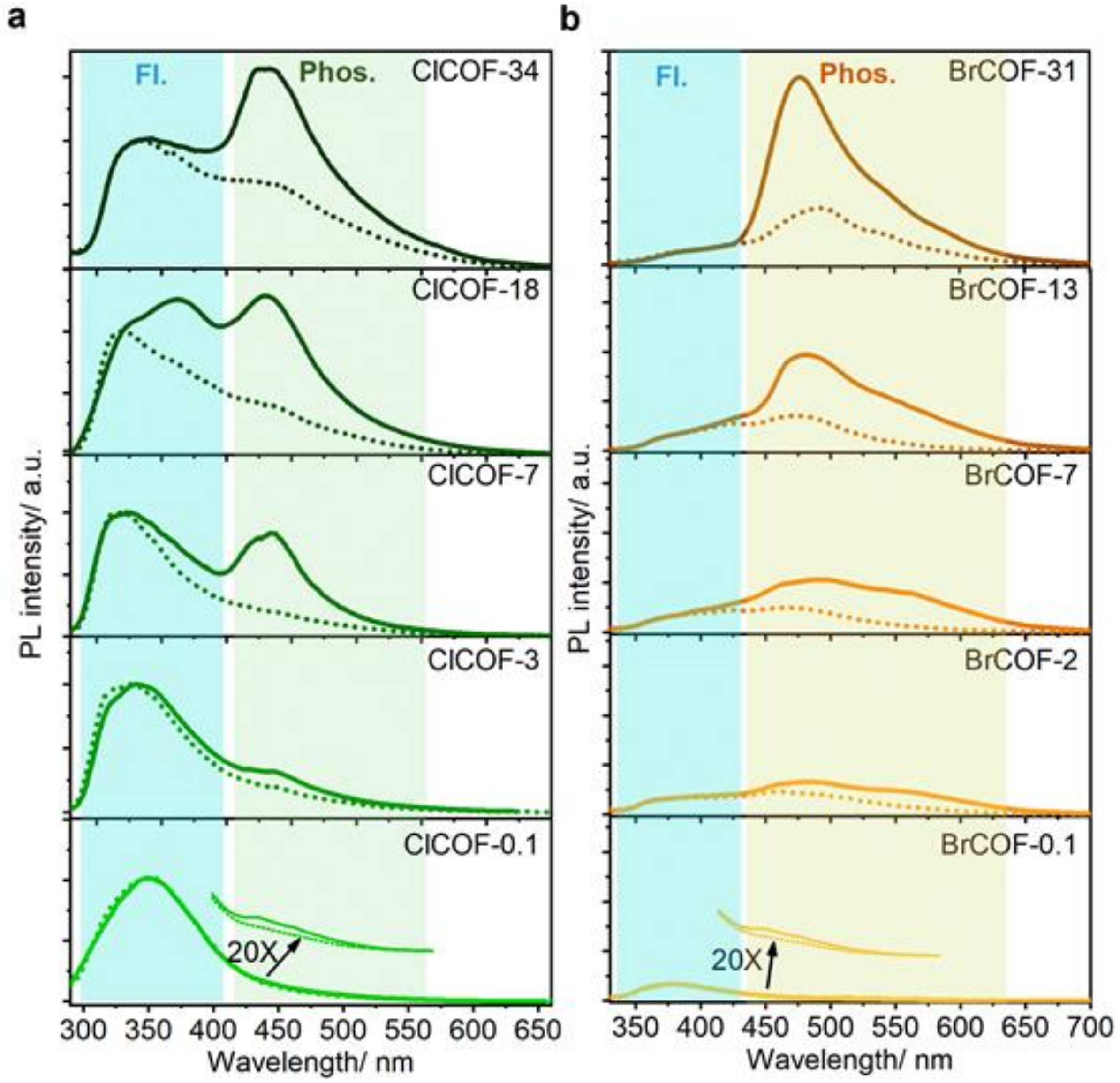

Figure 5.35. Steady-state photoluminescence spectra of a) as-prepared (non-activated) ClCOF-Ns (green) and b) BrCOF-Ns (orange) in air (dashed) and vacuum (solid lines) at room temperature (λ_{ex} = 300 nm) normalized by their fluorescence intensity illustrating the effect of O_2 quenching as well as higher doping level on the phosphorescence intensity.

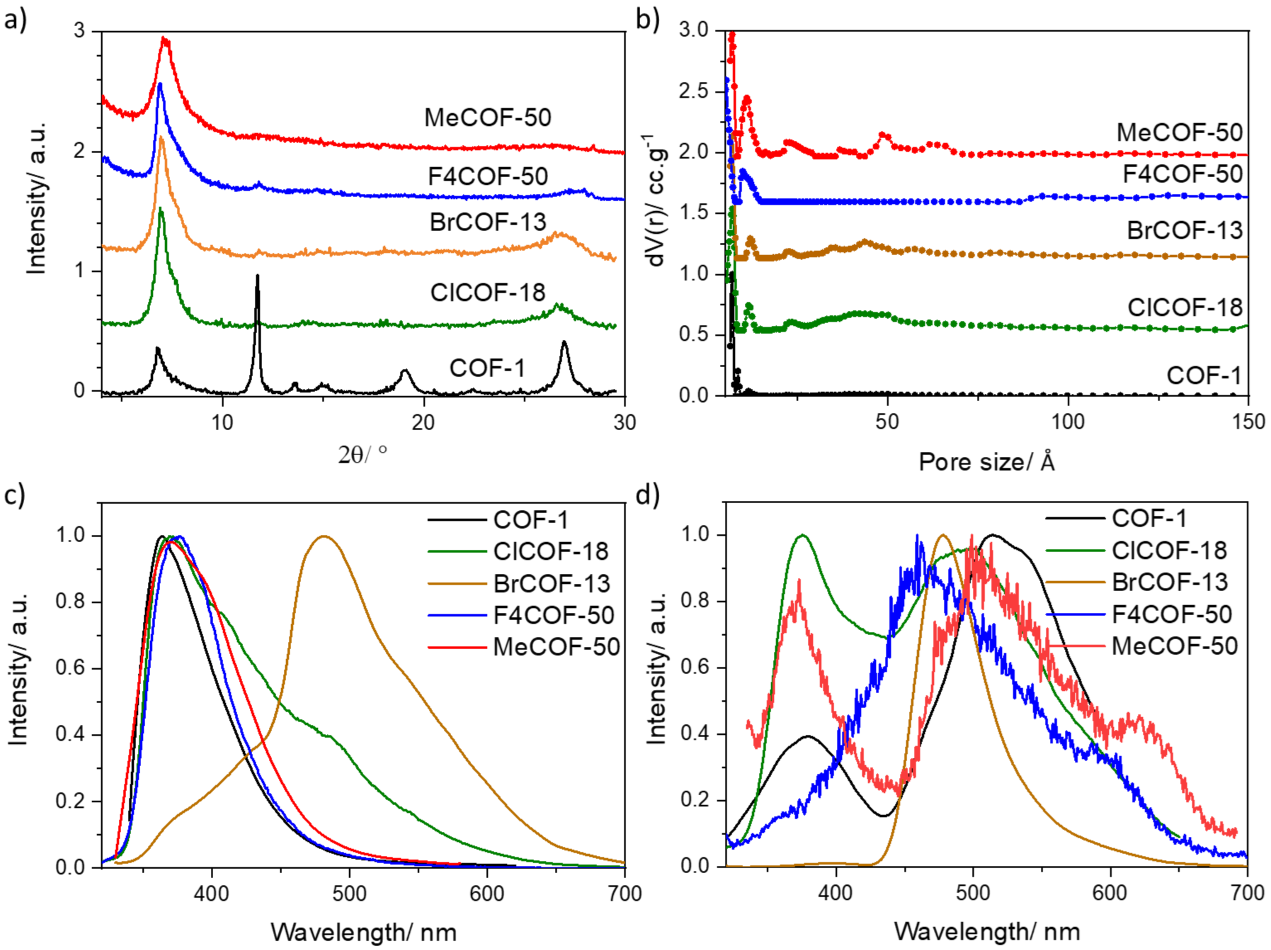

Figure 5.36. a) PXRD and b) QSDFT pore size distribution obtained from the N_2 isotherm, for COF-1 (black) as compared to doped COFs: ClCOF-18 (green), BrCOF-13 (orange), F4COF-50 (blue), and MeCOF-50 (red) showing a similar increase of disorder in all doped samples vs. the COF-1 (F4COF-50 prepared by copolymerization of PBA and tetrafluoro-PBA in 1:1 ratio; MeCOF-50 prepared by co-polymerization of PBA and 2,6-dimethyl-PBA in 1:1 ratio). c) Steady-state emission spectra showing the emergence of the phosphorescence at ~500 nm for the Cl- and Br-doped COFs but no detectable phosphorescence in F4COF-50 and MeCOF. d) Delayed (t_d = 0.2 ms) emission spectra of all five COFs. The phosphorescence emission for F4COF-50 and MeCOF-50 is extremely weak (thus low signal-to-noise ratio). These results suggest that the observed phosphorescence enhancement in halogen-doped COFs is due to heavy-atom effect of Cl/Br not due to doping-induced disorder/defects.

5.7.13. Crystal structure

The single-crystal X-ray diffraction (SCXRD) data for ClPBA (CCDC: 2119959) were collected from a shock-cooled single crystal at 150 K on a Bruker Venture Metaljet κ-geometry diffractometer with a Metal Jet using Helios MX Mirror Optics as monochromator and a Bruker CMOS Photon III detector. The diffractometer was equipped with an Oxford Cryostream 700 low-temperature device and used Ga K_α radiation (λ = 1.34139 Å). All data were integrated with *SAINT* and a multi-scan absorption correction using *SADABS* was applied.[10, 11] The structure was solved by dual methods using *XT* and refined by full-matrix least-squares methods against F^2 by *XL*.[12, 13] Structure solution and refinement cycles were performed within the graphical user interface of *OLEX2*.[14] All non-hydrogen atoms were refined with anisotropic displacement parameters. The hydrogen atoms were located from the Fourier difference map and fully refined isotropically. This report and the CIF file were generated using FinalCif.[15]

Table 5.11. Crystal data and structure refinement for ClPBA

Empirical formula	$C_6H_6B_2Cl_2O_4$
Formula weight	234.63
Temperature [K]	150
Crystal system	triclinic
Space group (number)	$P\bar{1}$ (2)
a [Å]	4.9381(1)
b [Å]	5.1689(2)
c [Å]	9.4693(2)
α [°]	81.335(1)
β [°]	89.280(1)
γ [°]	85.941(1)
Volume [Å^3]	238.341(12)
Z	1
ρ_{calc} [gcm^{-3}]	1.635
μ [mm^{-1}]	3.985
F(000)	118
Crystal size [mm^3]	0.09×0.07×0.04
Crystal color	clear light colorless
Crystal shape	Block
Radiation	Ga K_α (λ=1.34139 Å)
2Θ range [°]	8.22 to 121.22 (0.77 Å)

Index ranges	$-6 \le h \le 6$ $-6 \le k \le 6$ $-12 \le l \le 11$
Reflections collected	6468
Independent reflections	1079 R_{int} = 0.0415 R_{sigma} = 0.0336
Completeness to Θ = 53.594°	98.2 %
Data / Restraints / Parameters	1079/0/76
Goodness-of-fit on F^2	1.172
Final *R* indexes [$I \geq 2\sigma(I)$]	R_1 = 0.0318 wR_2 = 0.0886
Final *R* indexes [all data]	R_1 = 0.0322 wR_2 = 0.0889
Largest peak/hole [eÅ^{-3}]	0.43/-0.30

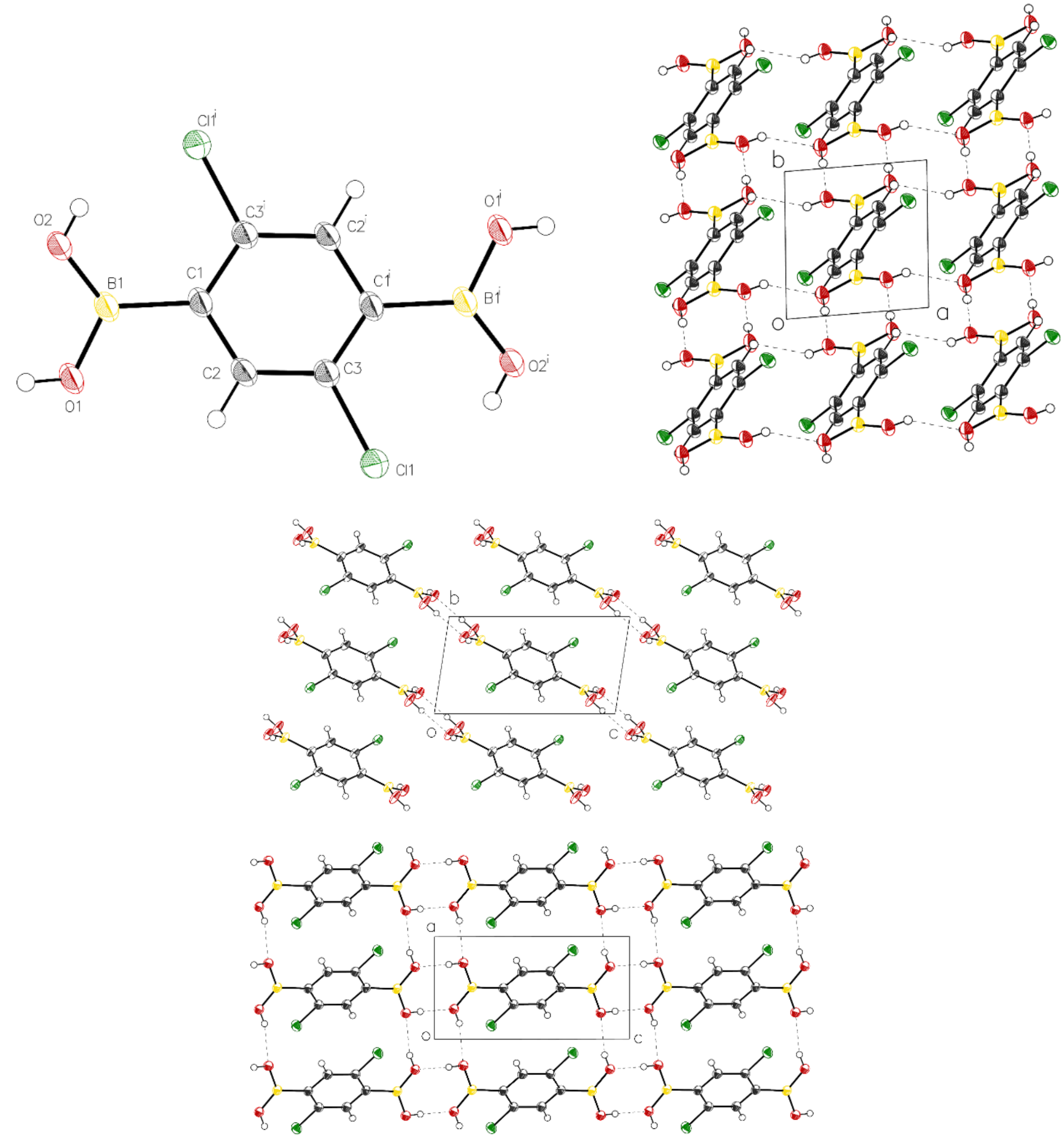

Figure 5.37. Thermal atomic displacement ellipsoid plot for ClPBA with the atomic numbering scheme (ellipsoids are drawn at the 50% probability level and hydrogen atoms are shown as the sphere of arbitrary size) and crystal packing showing projections along three crystallographic axes.

For BrPBA SCXRD data (CCDC: 2119960) were measured on a Bruker D8 Venture diffractometer equipped with a Photon 200 area detector, and IμS microfocus X-ray source (Bruker AXS, CuKα source). The measurement was carried out at room temperature in which the crystal was coated with a thin layer of amorphous oil to decrease crystal deterioration, structural disorder, or any related thermal motion effects and to improve the accuracy of the structural results. Structure solution was carried out using the SHELXTL package from Bruker.[12] The parameters were refined for all data by full-matrix-least-squares or F2 using SHELXL.[16] All of the nonhydrogen atoms were refined with anisotropic thermal parameters. All hydrogen atom thermal parameters were constrained to ride on the carrier atom.

Table 5.12. Crystal data and structure refinement for BrPBA

Identification code	BrPBA
Empirical formula	$C_6H_6B_2Br_2O_4$
Formula weight	323.55
Temperature/K	253(2)
Crystal system	triclinic
Space group	P-1
a/Å	4.9366(3)
b/Å	5.5791(3)
c/Å	9.5636(5)
α/°	78.819(4)
β/°	89.385(4)
γ/°	87.185(4)
Volume/Å^3	258.09(3)
Z	1
ρcalcg/cm^3	2.082
μ/mm^{-1}	9.858
F(000)	154.0
2Θ range for data collection/°	9.426 to 144.998
Index ranges	$-6 \le h \le 6$, $-6 \le k \le 6$, $-11 \le l \le 11$
Reflections collected	6358
Independent reflections	984 [R_{int} = 0.0474, R_{sigma} = 0.0298]
Data/restraints/parameters	984/0/67

Goodness-of-fit on F2	1.048
Final R indexes [I>=2σ (I)]	R1 = 0.0289, wR2 = 0.0763
Final R indexes [all data]	R1 = 0.0295, wR2 = 0.0769
Largest diff. peak /hole / e Å^{-3}	0.48/-0.52

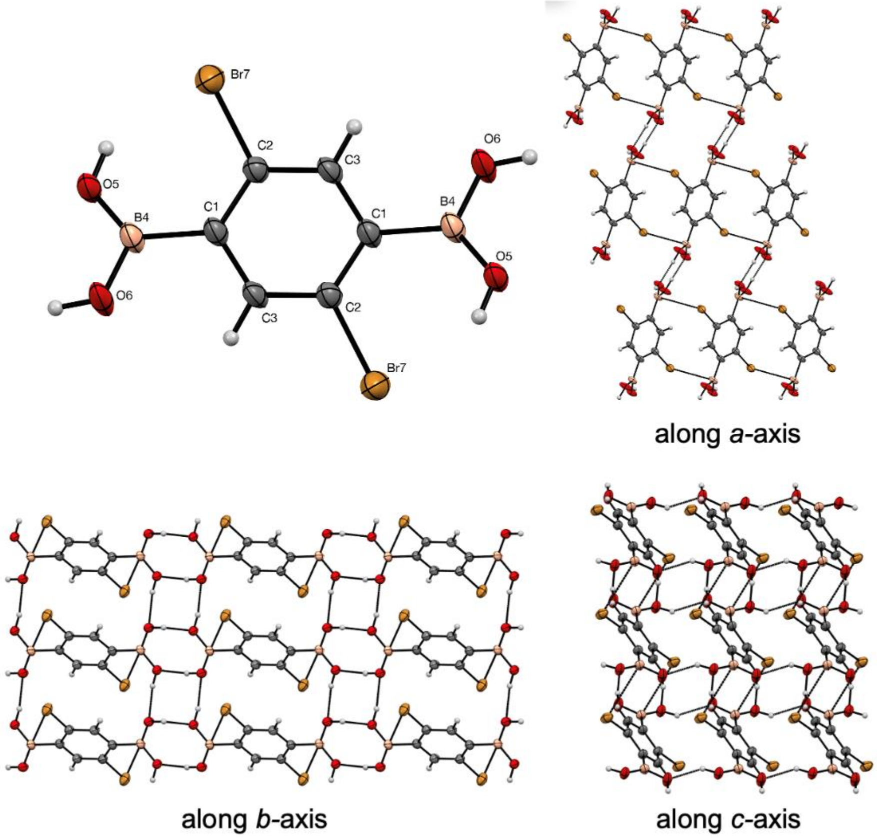

along *a*-axis

along *b*-axis

along *c*-axis

Figure 5.38. Thermal atomic displacement ellipsoid plot for BrPBA with the atomic numbering scheme (ellipsoids are drawn at the 50% probability level and hydrogen atoms are shown as the sphere of arbitrary size) and crystal packing showing projections along three crystallographic axes.

5.7.14. Hirshfeld Surface Analysis

The Hirshfeld surface (HFS) is a useful tool that uses a three-dimensional electron density illustration of a molecule in a crystal structure packing.[17-20] The molecule of interest is mapped through CrystalExplorer[21] (version 17.5, package5) to visualize the contribution of intermolecular interactions.

The PBA, ClPBA, and BrPBA intermolecular interactions in their crystal structure were analyzed by 2D fingerprint plots (Figure 5.39). In this illustration, the red spots on the HFSs indicate the presence of short intermolecular contacts, such as π-π stacking, hydrogen, and halogen bonding, while geometries without close interactions are depicted in blue. In the three cases, the double spikes in the fingerprint plot correspond to the H···O hydrogen interactions having approximate de + di values of 1.80, 1.80, and 1.90 Å, respectively, with significant contributions (> 25%) in the total supramolecular interactions. In addition, ClPBA and BrPBA compounds exhibit short X(Cl, Br)···H contacts, with intermolecular distances of 2.9 and 3.1 Å, respectively. The intermolecular attribution of these X···H interactions is 20.0% and 21.3%, respectively, out of the total cohesive interaction. The radar chart exhibits similar supramolecular attributions for ClPBA and BrPBA based on X···Donor (no X···X contacts were observed in these crystals) and H···O contacts, while PBA interactions are mainly dominated by van der Waals (vdW) and H···O bonds as shown in Figure 5.40. All linkers exhibit very low π···π stacking contributions, lower than < 2% for ClPBA and BrPBA and 9% for PBA.

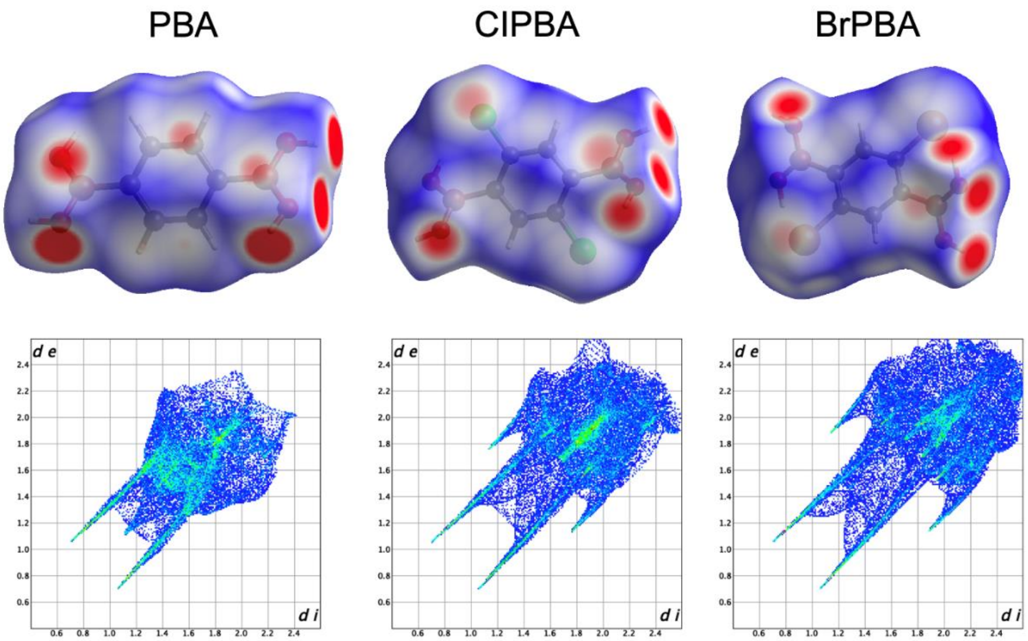

Figure 5.39. Calculated Hirshfeld surfaces and 2D fingerprint plots of all the intermolecular contacts are given for (from left to right) PBA, ClPBA, and BrPBA. The quantitative analysis of interactions in the crystals is summarized in Figure 5.40.

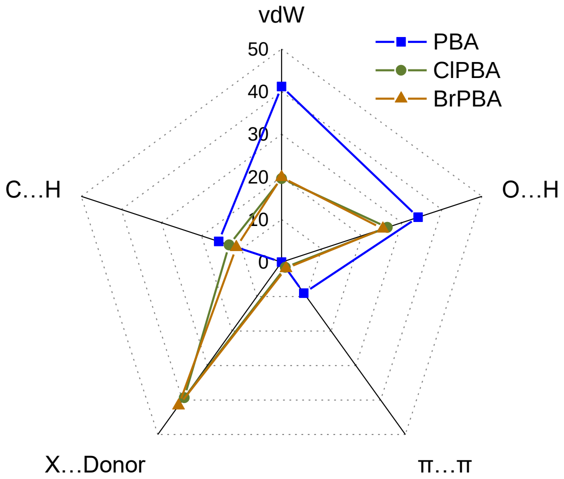

Figure 5.40. The radar chart of HFS analysis of PBA (blue), ClPBA (green), and BrPBA (brown) compounds showing the percentage of different intermolecular interactions.

The HFS analysis was also performed on the simulated and refined COF-1 structure based on the DFT and PXRD, respectively (Figure 5.41). We have placed mesitylene molecules in the cavity as dummy molecules to fill the pores (otherwise, the calculation of the HFS won't recognize the space in pores). Note that the HFS does not distinguish between intermolecular interactions and covalent bonds. Therefore, the strong sharp spikes in the 2D fingerprints are related to the B-O covalent bonds in the boroxine rings, as shown in Figure 5.11. The π···π contacts in COF-AA represent a contribution of 16.3% (depicted as the red area in the 2D fingerprint plots) from the total supramolecular interactions involved in this structure, and mainly from the COF layer above and below the Hirshfeld isosurface. On the other hand, COF-AB exhibits two different environments for the phenylboroxine building blocks. In one case the phenylboroxines in the backbones interact with another phenylboroxine from different layers, while in the other case phenylboroxine groups interact directly with mesitylene solvents occupying the cavities in the COFs. The π···π interactions caused by these two different environments are approximately similar, 14.6% and 13.4%, respectively. The radar chart of the COFs versus PBA exhibits that COF structures have dominated interactions of π-π stacking while PBA crystal mainly consists of hydrogen bonding (Figure 5.42). Higher vdW contribution is observed in the case of COF-AA in comparison to COF-AB due to directional weak interaction between the methyl groups of the mesitylene and the COF-layers. Despite the nature of the dominant vdW interactions, they mainly originate from the solvent interactions with the framework.

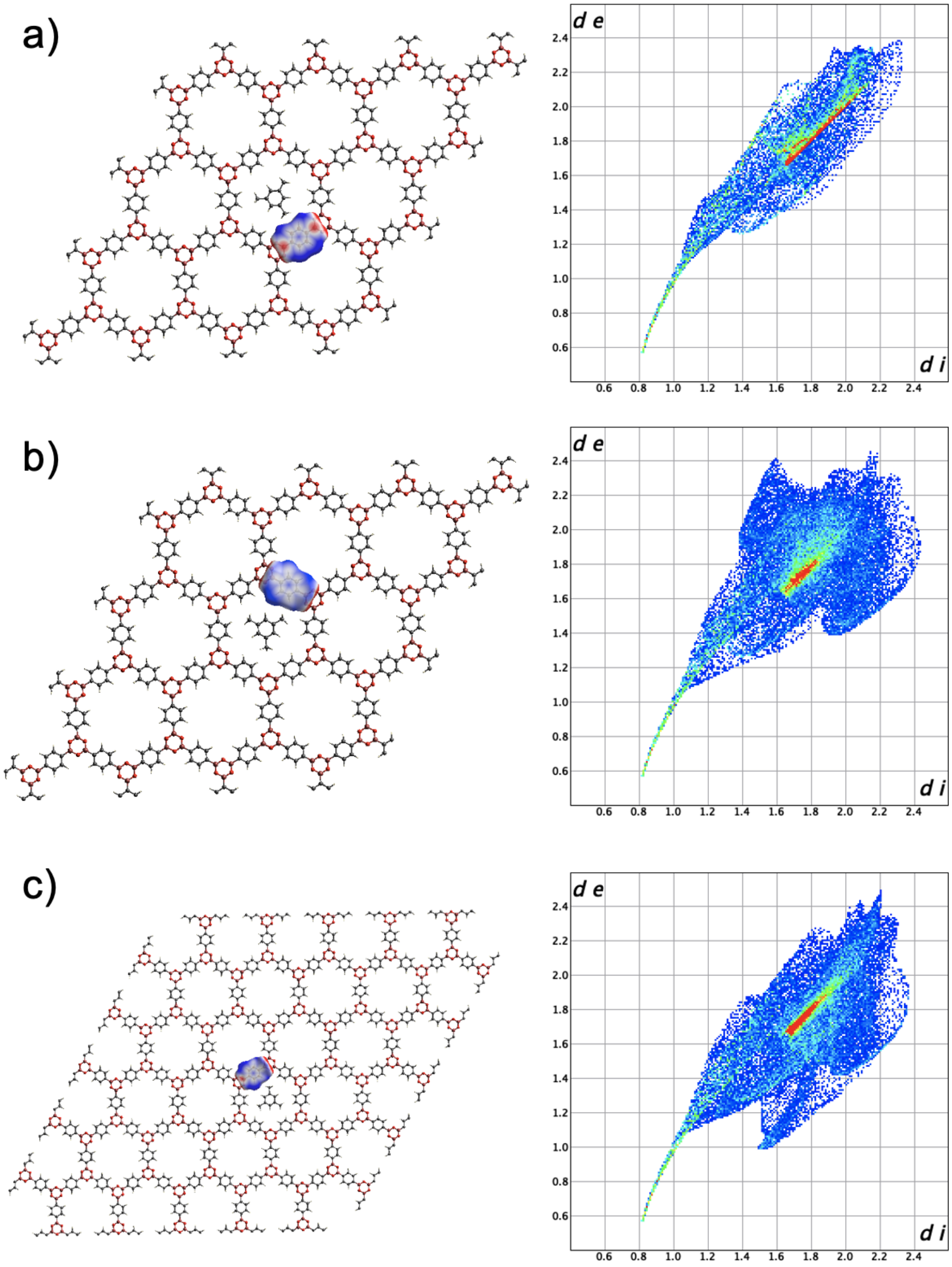

Figure 5.41. Calculated Hirshfeld surfaces and 2D fingerprint plots of COF-AA (a), COF-AB_1 (b), and COF-AB_2 (c). The quantitative analysis of interactions in the crystals is summarized in Figure 5.42.

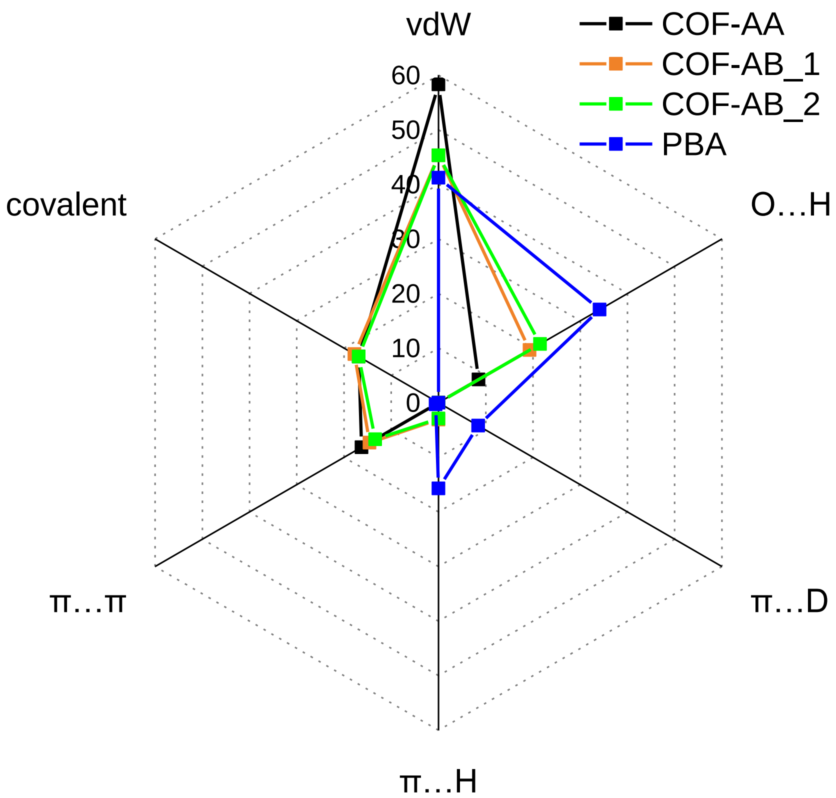

Figure 5.42. The radar chart of HSF analysis of COF-AA (black), COF-AB_1 (orange), COF-AB_2 (green), and PBA (blue) showing the percentage of different intermolecular interactions.

5.8.15. References of Supplementary information

1. Frisch, M. J.; Trucks, G. W.; Schlegel, H. B.; Scuseria, G. E.; Robb, M. A.; Cheeseman, J. R.; Scalmani, G.; Barone, V.; Petersson, G. A.; Nakatsuji, H.; Li, X.; Caricato, M.; Marenich, A. V.; Bloino, J.; Janesko, B. G.; Gomperts, R.; Mennucci, B.; Hratchian, H. P.; Ortiz, J. V.; Izmaylov, A. F.; Sonnenberg, J. L.; Williams; Ding, F.; Lipparini, F.; Egidi, F.; Goings, J.; Peng, B.; Petrone, A.; Henderson, T.; Ranasinghe, D.; Zakrzewski, V. G.; Gao, J.; Rega, N.; Zheng, G.; Liang, W.; Hada, M.; Ehara, M.; Toyota, K.; Fukuda, R.; Hasegawa, J.; Ishida, M.; Nakajima, T.; Honda, Y.; Kitao, O.; Nakai, H.; Vreven, T.; Throssell, K.; Montgomery Jr., J. A.; Peralta, J. E.; Ogliaro, F.; Bearpark, M. J.; Heyd, J. J.; Brothers, E. N.; Kudin, K. N.; Staroverov, V. N.; Keith, T. A.; Kobayashi, R.; Normand, J.; Raghavachari, K.; Rendell, A. P.; Burant, J. C.; Iyengar, S. S.; Tomasi, J.; Cossi, M.; Millam, J. M.; Klene, M.; Adamo, C.; Cammi, R.; Ochterski, J. W.; Martin, R. L.; Morokuma, K.; Farkas, O.; Foresman, J. B.; Fox, D. J. Gaussian 16 Rev. B.01, Wallingford, CT, 2016.

2. DataBase, C. C. C. a. B. Precomputed vibrational scaling factors. https://cccbdb.nist.gov/vibscalejust.asp (accessed 20 Aug. 2021).

3. Mamlouk, H.; Suriboot, J.; Manyam, P. K.; AlYazidi, A.; Bergbreiter, D. E.; Madrahimov, S. T.; Highly active, separable and recyclable bipyridine iridium catalysts for C–H borylation reactions. *Catal. Sci. Technol* **2018,** 8, 124-127.

4. Akita, M.; Saito, M.; Osaka, I.; Koganezawa, T.; Takimiya; K., Amide-bridged terphenyl and dithienylbenzene units for semiconducting polymers. *RSC Adv.* **2016,** 6, 16437-16447.

5. Gao, J.; Jiang, D., Covalent organic frameworks with spatially confined guest molecules in nanochannels and their impacts on crystalline structures. *Chem. Commun.* **2016,** 52, 1498-1500.

6. Leitonas, K.; Tomkeviciene, A.; Baratte, G.; Dabuliene, A.; Punniyakoti, S. M.; Volyniuk, D.; Grazulevicius, J. V., Oxygen sensing properties of thianthrene and phenothiazine derivatives exhibiting room temperature phosphorescence: Effect of substitution of phenothiazine moieties. *Sensors Actuators B: Chem.* **2021,** 345, 130369.

7. Zhou, Y.; Qin, W.; Du, C.; Gao, H.; Zhu, F.; Liang, G., Long-lived room-temperature phosphorescence for visual and quantitative detection of oxygen. *Angew. Chem. Int. Ed.* **2019,** 58, 12102-12106.

8. Nagl, S.; Baleizao, C.; Borisov, S. M.; Schäferling, M.; Berberan-Santos, M. N.; Wolfbeis, O. S., Optical sensing and imaging of trace oxygen with record response. *Angew. Chem. Int. Ed.* **2007,** 46, 2317-2319.

9. Dong, X.-Y.; Si, Y.; Yang, J.-S.; Zhang, C.; Han, Z.; Luo, P.; Wang, Z.-Y.; Zang, S.-Q.; Mak, T. C., Ligand engineering to achieve enhanced ratiometric oxygen sensing in a silver cluster-based metal-organic framework. *Nat. Commun.* **2020,** 11, 1-9.

10. Bruker, S., V8. 32A, Bruker AXS. Inc., Madison, Wisconsin, USA **2013**.

11. Krause, L.; Herbst-Irmer, R.; Sheldrick, G. M.; Stalke, D., Comparison of silver and molybdenum microfocus X-ray sources for single-crystal structure determination. J. *Appl. Crystallogr.* **2015,** 48, 3-10.

12. Scheldrick, G. M., SHELXT-Integrated space-group and crystals-structure determination. *Acta Crystallogr., Sect. A: Found. Adv.* **2015,** 71, 3-8.

13. Sheldrick, G. M., SHELXS-97, Program for Crystal Structure Determination, University of Göttingen, Germany, 1997;(b) Sheldrick, G. M., SHELXL-97-2, Program for Crystal Structure Refinement, University of Gottingen, 1997.

14. Sheldrick, G. M., SHELXTL V6. 1 Software Reference Manual, Bruker AXS Inc., Madison, WI, 2000 Search PubMed;(b) Dolomanov, O. V.; Bourhis, L. J.; Gildea, R. J.; Howard, J. A. K.; Puschmann H., OLEX2: a complete structure solution, refinement and analysis program, *J. Appl. Crystallogr.* **2009,** 42, 339-341.

15. Kratzert, D. FinalCIF, V84. https://dkratzert.de/finalcif.html (accessed 01/23/2021).

16. Sheldrick, G. M., Crystal structure refinement with SHELXL. *Acta Crystallogr. C* **2015,** 71, 3-8.

17. Spackman, M. A.; Jayatilaka, D., Hirshfeld surface analysis. *CrystEngComm* **2009,** 11, 19-32.

18. Spackman, M. A.; McKinnon, J. J., Fingerprinting intermolecular interactions in molecular crystals. *CrystEngComm* **2002,** 4, 378-392.

19. Wang, R.; Dols, T. S.; Lehmann, C. W.; Englert, U., The halogen bond made visible: experimental charge density of a very short intermolecular Cl··· Cl donor–acceptor contact. *Chem. Commun.* **2012,** 48, 6830-6832.

20. McKinnon, J. J.; Jayatilaka, D.; Spackman, M. A., Towards quantitative analysis of intermolecular interactions with Hirshfeld surfaces. *Chem. Commun.* **2007**, 3814-3816.

21. McKinnon, J.; Jayatilaka, D.; Spackman, M., Crystal Explorer 2.1. University of Western Australia (http://hirshfeldsurface. net/CrystalExplorer), Perth **2007**.

Chapter 6

Azatriangulene-based Near Infrared Emissive Covalent Organic Frameworks

Preface

In the previous chapters, we focused on ORTP materials and concluded that COFs are a promising platform for understanding the structure-photophysical properties relationships and the future crystal engineering of luminescent solids. TANGO (reported in Chapter2) and its oxygen-bridged trioxaazatriangulene counterpart (TANG) have attracted a great deal of attention as a building block for π-conjugated 2D-polymers and COFs (refs. 77-80 in this chapter). Replacing the electron-withdrawing carbonyl bridges (C=O) in TANGO with electron-donating ether bridges (–O–) in TANG makes the latter an attractive electron-rich candidate to explore donor-acceptor interactions in 2D materials. In collaboration with the surface physics group, we used brominated TANG and TANGO monomers to synthesize the first mesoscale-ordered monolayer of 2D π-conjugated polymers via surface-confined polymerization (ref. 79). Soon after, in collaboration with Dr. Lakshmi Vellanki, we reported the first crystalline TANG-based 2D-COF with small band-gap (1 eV) and electrical conductivity using a Schiff-base condensation (ref. 76). These results motivated us to investigate TANG COFs (particularly π-conjugated C=C linked ones) as optoelectronic materials. However, the extreme air sensitivity of the previously used triamino-TANG results in many defects (even when working in the glove-box) that trap the excitons, rendering the resulting COFs non-emissive. Also, the lengthy synthetic procedure for TANG with widely varied yields was a major hurdle for the further development of TANG materials in our group.

In this chapter, we report an improved synthetic route affording TANG with a 40% yield in 3 steps (compared to <20% over 6 steps in the previous works). We functionalized TANG with an aldehyde group preparing the bench-stable monomer TATANG for 2D polymerization. We used TATANG for the synthesis of cyanovinylene-linked COFs via Knovenagel condensation of TATANG with arenediacetonitriles. The C=C covalent links between the monomers provide π-conjugation and bring high chemical stability to the framework. Donor-acceptor interaction between the TANG nodes and the linker leads to band gaps of *ca.* 1.5 eV and corresponding NIR emission extending up to 1100 nm with ~1.0% PLQY (which is still high for organic solids in this spectral range). We explored the role of thermal vibrations and environmental quenching (by water) on the luminescent properties of the COF. We also found that the macroscopic morphology of the COFs can be tuned by the shape of the precursor crystals.

NMR spectra of all synthesized compounds are reported in Appendix 7 of the thesis.

Author contribution

Dmytro F. Perepichka and I conceived the project. Yuze Tao and I synthesized, purified, and characterized all reported COFs and their monomers. I performed all photophysical characterization (steady-state spectroscopy, lifetime analysis, and quantum yield measurements). M. Ghufran Rafique (co-supervised by Dmytro F. Perepichka and Hanadi F. Sleiman) performed the TEM and SAED analysis, Mahdi Salehi (supervised by Ali Seifitokaldani) performed SEM imaging, Jorge Ramos Sanchez (supervised by Gonzalo Cosa) performed the fluorescence microscopy, and Zhenzhe Zhang (co-supervised by Dmytro F. Perepichka and Rustam Z. Khaliullin) performed the density functional theory calculations. I analyzed all the reported experiments and wrote the chapter, and Dmytro F. Perepichka edited and revised it.

6.1. Abstract

We explored π-conjugated (cyanovinylene-linked) covalent organic frameworks based on trioxaazatriangulene (TANG) building blocks as the first example of near-infrared (NIR) emissive covalent organic frameworks (COFs). An improved synthetic route was developed for TANG which doubled the yield and halved the number of steps compared to the previous report. We have synthesized a new bench-stable triformyl-TANG derivative and performed its Knoevenagel condensation with arenediacetonitriles to prepare 2D π-conjugated COFs. The strong electron-rich character of TANG leads to intramolecular charge transfer (from TANG to the cyanated linker), resulting in small band gaps (as low as ~1.54 eV) and NIR emission (λ_{max} = 789 nm) with luminescence quantum yield 1.0% in the solid-state. We studied the impact of acceptor strength, rotational degree of freedom of the linker, temperature, and humidity on their NIR emission. Furthermore, we found that the morphology of the precursor crystals can readily determine the macroscopic morphology of the COFs.

6.2. Introduction

Covalent organic frameworks (COFs) are an emerging class of crystalline solids in which the organic building blocks are assembled via covalent bonds into two-dimensional (2D) or three-dimensional (3D) porous structures. The precise control over composition, topology, and porosity through the choice of the building blocks in COFs, have gained substantial attention for applications such as sensing, gas separation, gas storage, and catalysis.[1-3] In 2D COFs, the functional aromatic building blocks can be predictably assembled into cofacial π-stacking topology, facilitating transporting excitons or charge carriers in various optoelectronic applications. [3-5] In 2008, Jiang and co-workers reported strong blue luminescence ($\lambda_{max} = 472$ nm) and photoconductivity in a dioxaborole COF prepared by condensation of pyrene-2,7-boronic acid with 2,3,6,7,10,11-hexahydroxytriphenylene (HHTP). [6] During the next 10 years, different luminescent COFs with more stable linkages, such as β-ketoenamine-[7] and olefin-linked COFs,[8] have been reported[9, 10] for various applications, e.g. white-light emitting materials, [11-13] bioimaging/sensing, [7, 14, 15] and luminescent thermometry. [16] However, the design space of luminescent COFs is still very limited, especially compared to that of other explored aspects, such as porosity design for gas storage/separation. [17] This is because similar to most organic solids, COFs are typically non-emissive due to aggregation-caused quenching (ACQ) phenomena, in which the strong π-π interactions enable exciton delocalization/trapping and bimolecular exciton annihilations (such as singlet fission). [18-20]

Several strategies have been explored to improve the luminescence of COFs, such as incorporating aggregation-induced emission (AIE) chromophores in the framework, [23-2521-23] deuteration of the framework, [24] restrictions of intramolecular bond-rotation via interlayer H-bonding, [12] and dilution of emissive phosphorescent linkers in COF framework via covalent-doping. [25] Fluorescent (and recently, phosphorescent[25]) COFs with emission in the visible range (400-650 nm) and photoluminescent quantum yields (PLQYs) as high as 52% (at $\lambda_{max} = 508$ nm) [8] have been reported in the last decade. [9, 26, 27]

Nonetheless, the realization of near-infrared (>700 nm) emissive COFs remains a challenge because of the energy gap law, which predicts a dramatic increase in the internal conversion as the exciton energy decreases. [28] Dilute solutions of NIR-emissive organic small molecules and 1D π-conjugated polymers have been explored in biological imaging/sensing, [29-37] photodynamic therapy, [38, 39] NIR-emissive transistors, [40-42] diodes, [43-48] and telecommunication. [49] However, most of these dyes and polymers are non-emissive in the solid state, which hampers their application in optoelectronic devices. [50-53]

Two molecular design strategies are commonly employed to narrow the optical band gap and achieve NIR emission. The first strategy to obtain red-shifted chromophores is by extending the π-conjugation. [54] However, achieving NIR emission using this strategy alone is challenging due to limited air stability of the corresponding π-extended structures (*e.g.*, long acenes and oligoenes) and complex synthesis. [55-57] Alternatively, the donor-acceptor (D-A) strategy can reduce the optical bandgap and, in fact, is used in most NIR emissive organic dyes (Scheme 6.1). [58] Using both of these strategies, efficient NIR emissive organic molecules and 1D conjugated polymers[54, 59-61] have been reported, [37, 58, 61-72] some of which show AIE with quantum yields up to ~20% (λ_{max} = 725 nm in aggregated particles in water). [68]

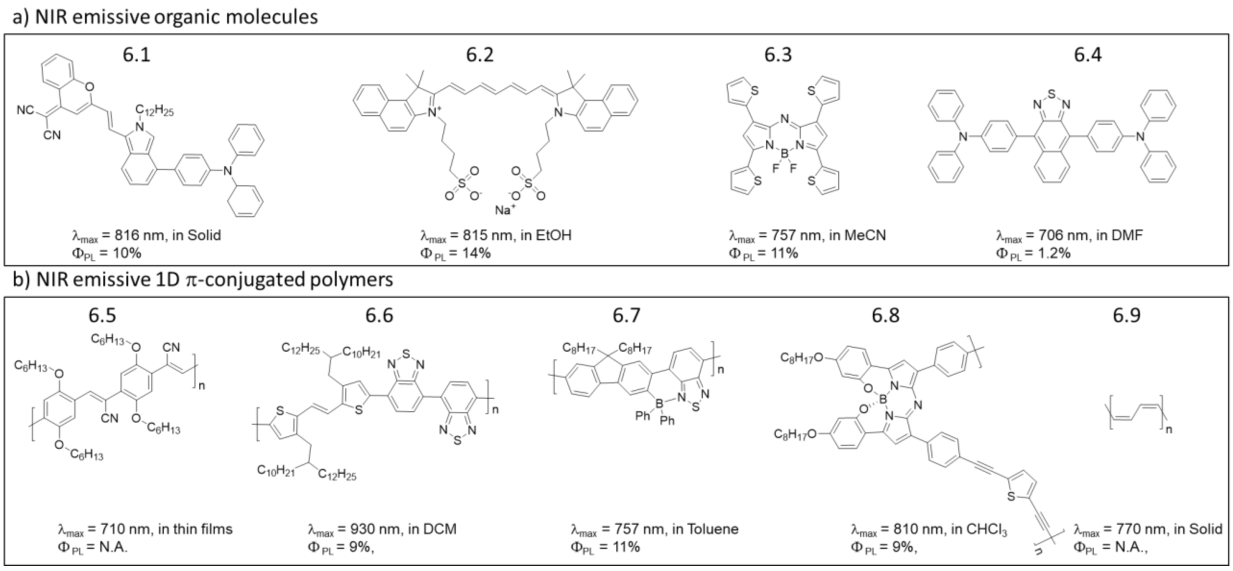

Scheme 6.1. Examples of NIR emissive a) molecule dyes and b) 1D-π conjugated polymers reported in ref. [70] (6.1), ref. [52] (6.2), ref. [71] (6.3), ref. [72] (6.4), ref. [59] (6.5), ref. [66] (6.6), ref. [60] (6.7.), ref. [61] (6.8.), ref. [54] (6.9).

D-A character is present in many, if not most, COFs to some extent due to different HOMO/LUMO energies of the constituent monomers and polar linkages (imine, cyno-vinylene). Most reported designs of D-A COFs have been utilized in low-bandgap NIR-*absorptive* materials for applications such as photodetection and photocatalysis.[73] Jiang and co-workers reported a series of hydrazone-linked COFs in which tuning the electronics of the linker dramatically perturbed the luminescent properties, mainly due to better conjugation and, in some substituents, tautomerization effects.[74] However, D-A strategy has not yet been explored to alter COFs' emission, nor have any COFs with NIR luminescence been reported to date (Table 6.1).

Trioxaazatriangulene (TANG) is a stable heteroanalogue of the triangulene biradical (Clar's hydrocarbon[75]). It is highly electron-rich (HOMO = -4.87 eV)[76] with a planar geometry, recently studied as a building block for π-electron functional oligomers[77] and polymers.[78-81] Our group has previously shown the use of tribromo-TANG for on-surface synthesis of a mesoscale ordered 2D polymer (P^2TANG)[81] and triamino-TANG for solvothermal condensation with 2,5-dihydroxyterephthaldehyde preparing imine-linked COF with paramagnetic and semiconducting properties. [78]

Here, we report π-conjugated cyanovinylnene-linked trioxaazatriangulene-based NIR-emissive COFs using D-A strategy (TANG as the donor) with ~1% quantum yield and λ_{max} = 789 nm extending up to 1100 nm. We show the effect of the linker, temperature, and humidity on the photophysical behavior of these COFs opening possibilities for future exploration of other NIR emissive COFs.

6.3. Synthesis and structural characterization

The lengthy synthesis and low yield of TANG have been a major hurdle toward the exploitation of this building block for 2D-polymers and COFs. In 2005, Okada reported the first synthetic methodology for TANG as a 6-step synthesis starting from 2,6-difluoronitrobenzene, reaching a final yield of 19%.[82] In 2019, we reported another methodology for the synthesis of TANG, using sequential Ullmann coupling of 1,6-dimethoxyaniline, with a similar (but widely varied) yield of up to ~20% over six steps. Here we developed a new synthetic route and improved the synthesis of TANG to achieve a 40% yield in 3 steps (Scheme 6.2) compared to previous reports of ~20%

over six steps.[78, 83] Bromination of TANG followed by lithiation-formylation afforded triformyl-TANG (TATANG). TATANG, as a poorly soluble solid (only slightly soluble in $C_2H_2Cl_4$) was then subjected to acetal protection to enhance the solubility and, after purification and deprotection, resulted in light orange compound. The electron-withdrawing aldehyde groups of TATANG increase its oxidation potential and significantly stabilize this monomer compared to TANG (Figure 6.5) and particularly to the previously used triamino-TANG. [78]

The donor-acceptor behavior in TATANG results in red-shifted fluorescence emission (λ^{FL}_{TANG} = 431 nm vs. λ^{FL}_{TATANG} = 585 nm) (Figure 6.6a, b). We envisaged that embedding TANG in a π-conjugated framework linked via electron-withdrawing groups would shift its emission further in the NIR range of the spectrum. Accordingly, 2D COFs were synthesized using cyano-vinylene linkages through base-catalyzed Knoevenagel condensation of TATANG with 1,4-phenylenediacetonitrile or 2,2'-biphenyl-4,4'-diacetonitrile resulting in cyanovinylene-linked pTANG1 and pTANG2, respectively (Scheme 6.1). The reactions were performed under solvothermal conditions catalyzed by aq. KOH at 90 °C. The precipitated black powders were purified by extensive washing with organic solvents (DMF, acetone), giving the COFs with ~ 85-88% yield. The model compound (CNTANG) was synthesized by a Knoevenagel condensation of TATANG with phenylacetonitrile.

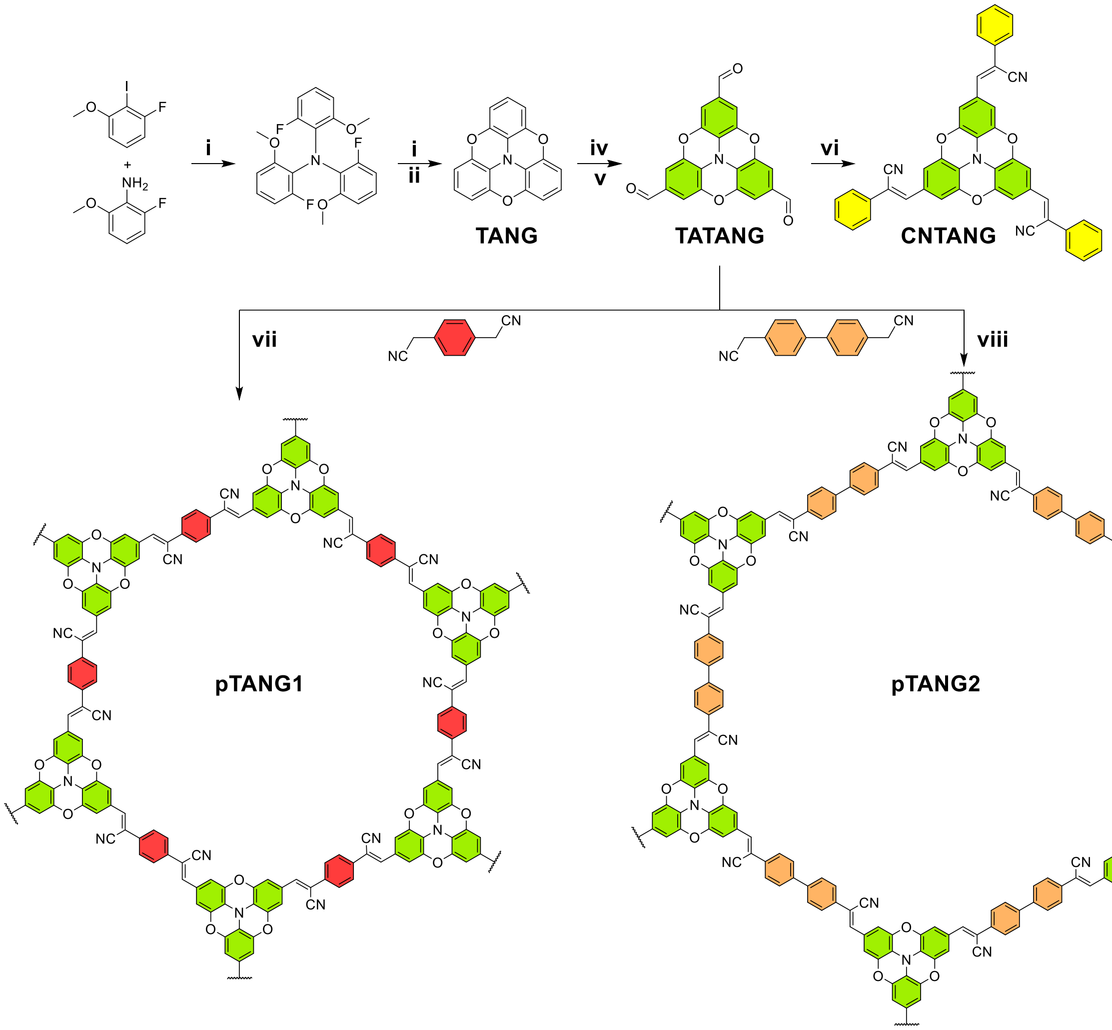

Scheme 6.2. Synthesis of TATANG, CNTANG, and pTANG1 and pTANG2 COFs: (i) Cu, CuI, K_2CO_3, Neat, 230 °C; (ii) BBr_3, DCM, -70°C → RT, 12 h; Aqueous work-up; (iii) K_2CO_3, DMF, overnight, 160°C; (iv) $PyH^+Br_3^-$, EtOH/benzene, 3 h, reflux; (v) n-BuLi, THF, -70°C followed by addition of DMF; (vi, vii, viii) corresponding phenylacetonitrile derivative, KOH (4M, aq.), dioxane, 90°C, 18h.

The FTIR of the obtained powders shows the disappearance of the TATANG carbonyl stretch at 1685 cm^{-1} and the emergence of C≡N stretch at 2212 cm^{-1}, indicative of the successful transformation of the aldehyde group into cyanovinylene linkers (Figure 6.1a). ^{13}C cross-polarization magic angle spinning (CP-MAS) NMR spectroscopy of the COF solids shows the disappearance of carbonyl groups (i.e., TATANG aldehyde signal at 191.9 ppm) and the emergence of new, compared to TATANG, peaks from ~110-140 ppm arising from the cyanovinylene and phenyl/biphenyl moieties (Figure 6.1b).

Powder X-ray diffraction (PXRD, Figure 6.1c, d) and small angle X-ray scattering (SAXS, Figure 6.8 in Supporting Information) measurements reveal the crystalline nature of both COFs, with characteristic diffraction peaks at 2θ = 3.35°(100), 5.7°(110), and 8.7°(210) for pTANG1 and 2.75° (100) and 4.75°(110) for pTANG2. Scherrer analysis of the *(100)* peak width (FWHM= 0.8° and 0.3° for pTANG1 and pTANG2, respectively) suggests an average crystallite size of at least ~10 nm for pTANG1 and ~30 nm for pTANG2. The (001) peak at 2θ ~26° in both COFs corresponds to an interlayer stacking of ~3.5 Å, and its broad appearance is an expected result of the turbostratic disorder in 2D COFs.[84] The experimental pattern is in agreement with the simulated XRD patterns of the eclipsed (AA) stacking arrangement of the COFs, but we cannot exclude significant (up to 10 Å) interlayer slippage (Figures 6.9, 6.10 in Supporting Information). Full-profile Pawley refinement (Figure 6.1 c,d) confirmed that the diffraction patterns are in agreement with the DFT-calculated (HSE06) unit cell for AA stacking arrangement of COFs ($a = b = 32.9$ Å, $c = 3.7$ Å, $\alpha = \beta = 90°$, $\gamma = 120°$ for pTANG1 and $a = b = 39.8$ Å, $c = 3.7$ Å, $\alpha = \beta = 90°$, $\gamma = 120°$ for pTANG2; ≤ 0.1 Å difference for DFT-calculated and Pawley refined unit cells).

On the other hand, the Brunauer-Emmett-Teller (BET) analysis of the N_2 isotherm at 77 K shows a rather low surface area of 132 m^2/g for pTANG1 (Figures 6.1, 6.11), possibly a result of the pore blockade due to the large interlayer slippage suggested above. Nevertheless, the average pore diameter of pTANG1 extracted for the absorption isotherms is 23 Å (Figure 6.1e), in line with the simulated pore diameter of 24 Å (the shortest distance between the opposite CN groups). High-resolution transmission electron microscopy (HR-TEM) of dispersed COFs in *N*-methylpyrrolidone shows that the individual COF particles are made of smaller (≤ 1 μm) needles (Figures 6.1g, 6.12). The observed lattice in the HR-TEM images illustrates the π-stacked layers with an inter-planar distance of ~3.6-3.7 Å of (Figures 6.12, 6.13).

The selected-area electron diffraction (SAED, Figure 6.1h) pattern of pTANG1 shows the highly ordered nature of the particles, and the diffraction pattern is in good agreement with that simulated from the Pawley-refined lattice (Figure 6.14, in supporting information). Both COFs show high thermal stability up to 400 °C (Figure 6.15).

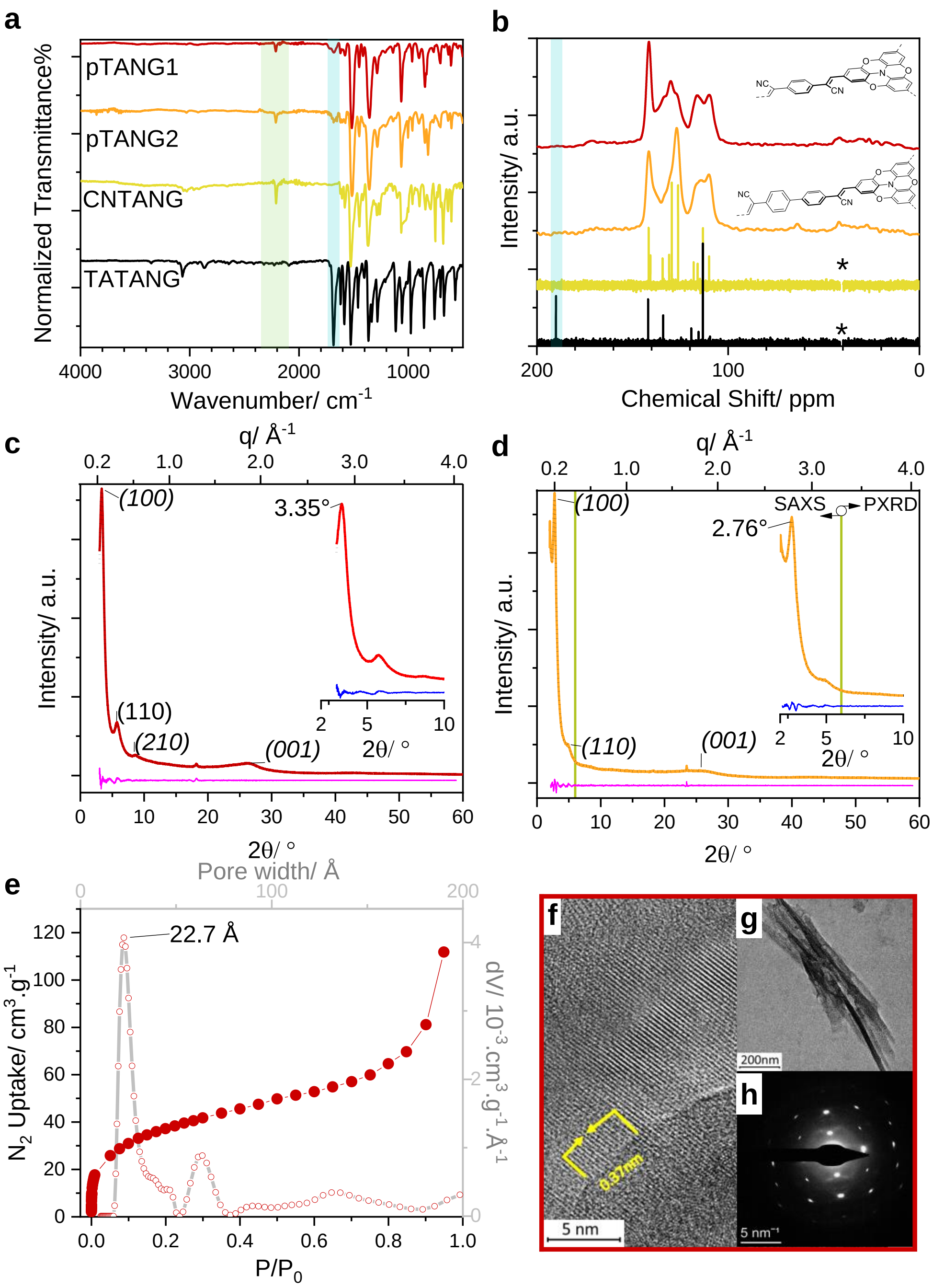

Figure 6.1. a) FTIR, b) CP-MAS ^{13}C-NMR spectroscopy of the pTANG1 (red) and pTANG2 (orange), and solution ^{13}C-NMR of CNTANG (yellow), and TATANG (black; the * at 40 ppm corresponds to omitted DMSO-*d6*). c, d) PXRD with full-profile Pawley refinement (R_p = 1.78%, R_{wp} = 2.55% for pTANG1, and R_p = 1.85%, R_{wp} = 2.65%) for pTANG2 (dashed; magenta is the residual of experimental and refined data) e) N_2 adsorption isotherm at 77 K and the corresponding non-linear density functional theory (NLDFT) pore size analysis. f, g) HR-TEM images of the dispersed pTANG2 sample in N-methylpyrrolidone and h) the SAED pattern of the pTANG1. The insets in figures c, and d are the zoomed-in graphs of the PXRD pattern. The data in figure c are from SAXS for 1-6° and PXRD for 6-60° as indicated by the green line.

Scanning electron microscopy (SEM) images of both COFs depict particles consisting of aggregated petal-like crystallites of COF (~1 μm) (Figure 6.2b, 6.16, 6.17, 6.18). XRD of a single needle-like COF particle shows their highly crystalline nature (Figure 6.19, in supporting information). The resemblance of the COF particles to the crystals of the TATANG monomer (Figure 6.2a, c) and the occassional observation of the hollow tube-shaped COF morphology (Figure 6.18, in supporting information) led us to the hypothesis that the COF is growing directly on the surface of (poorly soluble) crystals of the monomer. We tested this hypothesis by comparing the morphology of the pTANG1 COF synthesized from large TATANG crystals (prepared by recrystallization) and from TATANG powder (prepared by grinding the same crystals). The SEM shows that the size/morphology of TATANG precursor is maintained in the resulting COF (Figure 6.2). We note that the morphology modulation of COFs has drawn significant attention in the recent years, in the context of understanding the effect of morphology on physical properties (e.g., charge transport, guest absorption rates, etc.) of COFs towards their future applications. [62, 85]

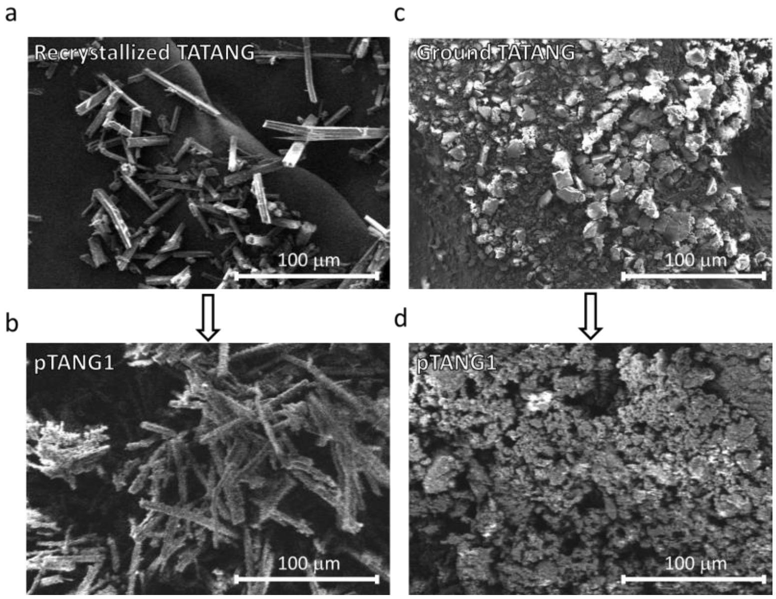

Figure 6.2. SEM images of TATANG crystals prepared by recrystallization (top left) and fine TATANG powder prepared by subsequent grinding (top right). The images on the bottom show the different morphologies of pTANG1 COF prepared from the above monomer samples (dioxane/EtOH, KOH (4M, aq.), 90 ˚C, 18 h).

6.4. Spectroscopic characterization

Both pTANG1 and pTANG2 are black solids with a broad absorption across the UV-Vis-NIR range, and the red edge at 788 nm (1.53 eV) for pTANG1 and 748 nm (1.64 eV) for pTANG2 (Figures 6.3c, 6.7). This absorption is significantly red-shifted compared to the model compound CNTANG (Figure 6.6) due to the extended π-conjugation and the π-π stacking interactions in the COFs. DFT calculation (HSE06) of free-standing layers of COFs suggests a direct bandgap energy (E_g) of 1.60 eV and 1.71 eV for pTANG1 and pTANG2, respectively, at the Γ point (Figure 6.20, in supporting information), very similar to the optical gaps measured from their diffuse-reflectance spectra. The band structure of the COFs is characteristic of the hexagonal/Kagome lattice which has been previously predicted in other triangulene-based 2D polymers.[78, 81] The partial density of states (DOS) analysis shows that both HOMO and LUMO are delocalized, but as expected, the HOMO has the highest density on the TANG building block, whereas the LUMO has the highest density on the arene(dicyanovinylene) linker (Figure 6.20, in supporting information). Interestingly, the LUMO band of pTANG1 (-2.85 eV) is significantly lower than that of pTANG2 (-2.52 eV), despite the smaller size of its linker. This behavior is attributed to the stronger electron-withdrawing effect of phenylene(dicyanovinylene) compared to biphenylene(dicyanovinylene) linkers. Natural transition orbital analysis (NTO) for the first excited state of the CNTANG, as a small representative molecule for the pTANG COFs, shows a similar D-A characteristic upon photoexcitation with a change of electron density from TANG to phenyldicyanovinylene for the S_1 excited state (charge transfer of 0.43 electrons for S_1; Figure 6.21).

Photoexcitation of the COF powders anywhere in the UV or Vis part of the spectrum (Figure 6.23b) results in a strong NIR emission: λ_{max} = 789 nm, PLQY 1.0 ± 0.2% for pTANG1; λ_{max} = 730 nm, PLQY, 1.0 ± 0.2% for pTANG2 (Figure 6.3a). Fluorescence microscopy shows a homogeneous emission from all COF particles revealing the same morphology as observed in SEM (Figure 6.3c,d). The radiative lifetimes of 4.2 ns (for pTANG1) and 2.4 ns (for pTANG2) confirm the fluorescence nature of the emission (Figure 6.3b).

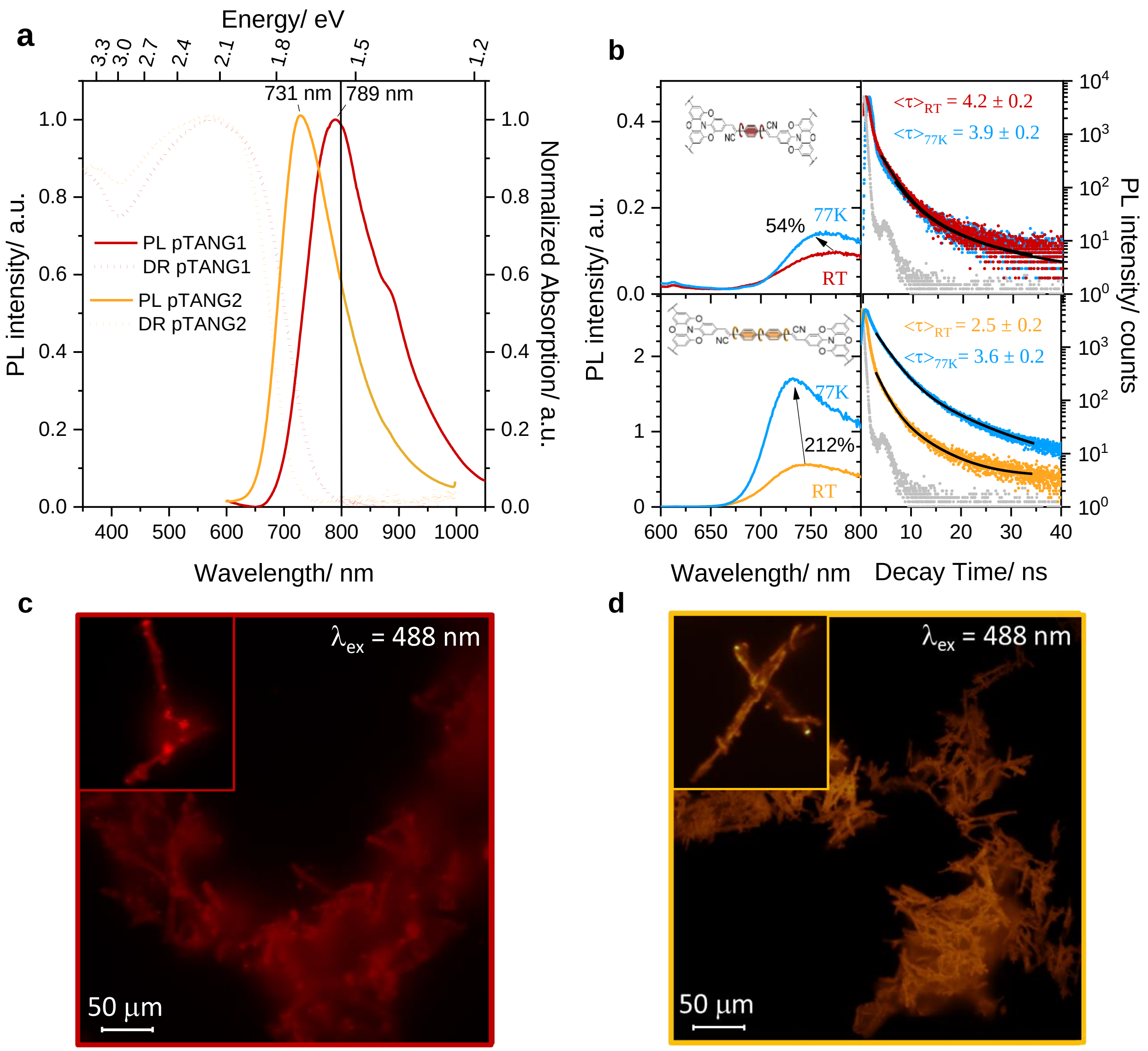

Figure 6.3. a) Diffuse reflectance (dashed lines) and steady-state fluorescence spectroscopy (solid lines) of the pTANG1 (red) and pTANG2 (orange). b) Fluorescence enhancement of the pTANG1 (top-left) and pTANG2 (bottom-left) and their corresponding lifetimes (top-right for pTANG1 and bottom-right for pTANG2, respectively) upon cooling the solid to liquid N_2 temperatures; c,d) Fluorescence microscopy imaging of pTANG1 c) and pTANG2 d) (inset: enlargement of individual needles). Panels c, d have been post-modified from their greyscale images for better visibility.

The fluorescence emission intensity of pTANG1 slightly increases (50%) with almost no change in the lifetime upon cooling to 77 K (Figure 6.3b). This lack of temperature effect suggests that intersystem crossing or exciton quenching (*e.g.*, charge separation and bimolecular annihilation[86]), not the vibrational relaxation is the primary pathway for the non-radiative deactivation in pTANG1. In contrast, cooling pTANG2 to 77 K results in a >2-fold increase of fluorescence intensity and ~50% longer emission lifetime (Figure 6.3d), suggesting a more significant role of vibrational relaxation in this COF. We attribute this behavior difference to higher flexibility of the biphenylene linker in pTANG2 compared to phenylene linker in pTANG1.

To investigate the rigidity of the COFs, we used variable temperature ^1H ss-NMR relaxometry and studied the spin-lattice relaxation times T_1 for both COFs in a 9.4 T (400 MHz) magnet. [87, 88] T_1 is dominated by molecular motions in the MHz regime and a longer decay time indicates less motion as compared to the Larmor frequency (minimum T_1 value). [87, 89] Both COFs show a monoexponential decay of the integrated ^1H-NMR intensity at all studied temperatures (Figure 6.24), indicative of uniform environment throughout the COF powder. The monotonous decrease of T_1 up to 100 °C points to the rigid matrix of both COFs with motions slower than 400 MHz. Furthermore, the shorter relaxation times in pTANG2 than pTANG1 at all temperatures and its more significant temperature dependency (Figure 6.25c) indicate more motions in pTANG2, in line with our observed trend of luminescence at different temperatures. DFT calculations further confirm that the phenyl in pTANG1 has an approximately two-fold higher rotation barrier as compared to the rotation of pTANG2 (7.0 kcal mol^{-1} versus 3.7 kcal mol^{-1}, Figure 6.22).

6.5. Effect of humidity on the luminescence of pTANG1

We found that when the vacuum-dried COF is exposed to humid air, it absorbs a noticeable amount of H_2O (Figure 6.4a). Deconvolution of ^1H solid-state NMR spectra of the dry pTANG1 exposed to air suggests an average of ~9.2 H_2O molecules per unit cell (Figures 6.4a, 6.26, in supporting information). Dynamic vapor sorption isotherm (DVS) measurements with H_2O showed a reversible adsorption/desorption (Figure 6.4b), with water uptake up to 19.5 wt% at 100% relative humidity, which corresponds to approximately 12 H_2O molecules per unit cell. The Brunauer–Emmett–Teller (BET) analysis of the DVS data reveals a surface area of 137 m^2.g^{-1}, which is consistent with the results of N_2 isotherm at 77 K (Figure 6.11, in supporting information).

Unlike oxygen, the absorbed water significantly affects the emission properties of the COFs (Figures 6.4c, 6.26, in supporting information). Exposing a vacuum-dried COF sample to high humidity (saturated vapor of H_2O at room temperature, estimated partial vapor pressure of ~24 torr) quenches the NIR emission to nearly half the original intensity (Figure 6.4c). Several imine-linked COFs have been reported to undergo quenching in the presence of water and used in water-sensing applications. [90-94] However, none of them can operate in the NIR part of the spectrum (which may be important for distant sensing applications due to better penetration of NIR light).

The maximum luminescent quenching happens in about ~20 min after exposure of pTANG1 to water vapor (~24 torr of partial water pressure in vacuum), consistent with the timescale of the DVS equilibration; Figure 6.3d inset) and shows reversibility over several cycles (Figure 6.3d). Luminescence lifetime analysis of the water-absorbed COF shows a decrease in the proportion of shorter-lived components compared to dry COF, while longer lifetimes remain almost intact (Figure 6.27). This observation suggests the presence of two different emissive sites: (i) the shorter-lived species exposed to interaction with the guest molecules and (ii) the longer-lived species, presumably in the blocked pores, inaccessible to the guest molecules, preserve the exciton from quenching. We have observed a similar phenomenon in halogen-doped phosphorescent COFs, in which the presence of mesitylene guest inside the pores substantially perturbs the access of oxygen quenchers, allowing for 14-fold increase in lifetime compared to the activated COF. [25]

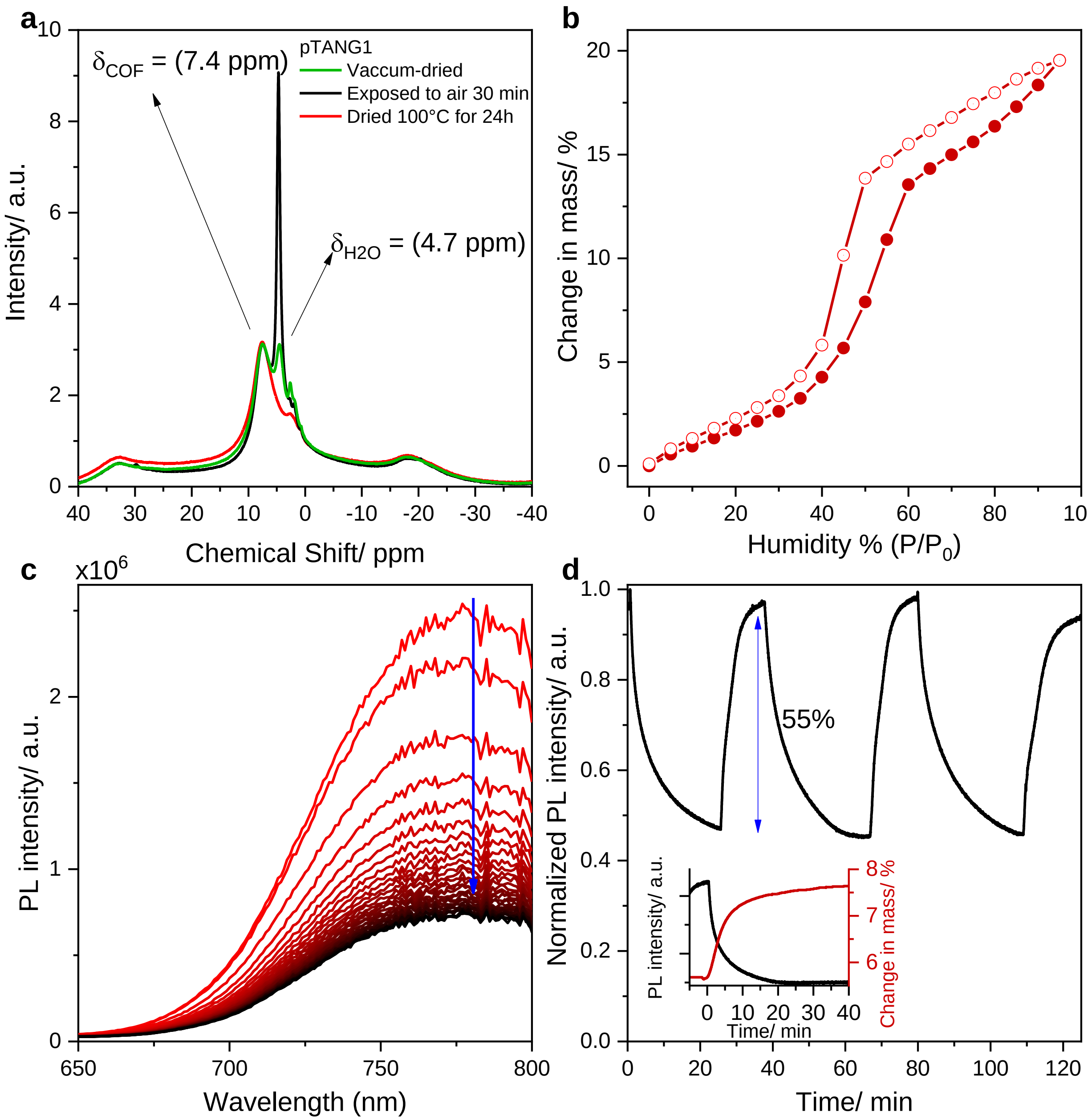

Figure 6.4. a) MAS-^{1}H NMR of the vacuum-dried pTANG1 (green) exposed to air for 30 min (black) and dried in the NMR instrument under nitrogen at 100 ˚C for 24 h (red). b) Dynamic vapor sorption analysis of pTANG1 showing water uptakes up to 20 w% in 100% humidity. c) Luminescent spectra of dry pTANG1 and its quenching in the presence of pure water vapor (RT, 24 torr). d) Reversible quenching and restoration of the luminescent of pTANG1 upon sequential exposure to humidity and vacuum (λ_{em} = 780 nm). Inset: luminescence quenching (black) vs. the DVS equilibration steps showing that the observed response over 20 min is in line with the water absorption kinetics of the COF.

6.6. Conclusion

Here, we report a new synthetic route to highly electron-rich heterotriangulene TANG in 3 steps with a 40% yield, almost 2-fold higher than the previously reported six-step procedure. [78, 82, 83] This compound was used to synthesize the triformyl-TANG (TATANG), a versatile monomer capable of forming conjugated COFs via Schiff-base condensation, [95, a] Michael addition-elimination, [7] aldol condensation, [96] and Knoevenagel condensation. [5] Exploiting Knoevenagel condensation of TATANG with 1,4-phenylenediacetonitrile or 2,2'-biphenyl-4,4'-diyldiacetonitrile resulted in obtaining the first examples of crystalline COFs with permanent open porosity.

The resulting crystalline COFs have low band-gap (~1.5 eV) and show bright NIR emission at 700-1000 nm range with moderate (for this spectral range) quantum yield of ~1% and characteristic fluorescence decay time of 2-4 ns. We explored the role of thermal vibrations and environmental quenching (by water) on the luminescent properties of the COFs.

Scanning electron microscopy results suggested that the macroscopic morphology of the COFs is determined by that of monomer, leading to the hypothesis that the COF is growing directly on the surface of (poorly soluble) crystals of the monomer. This observation may shed light on the previously reported COFs with multiple distinct morphologies that were obtained in a single reaction for precursors with limited solubility. [97]

Further in-depth analysis of the effect of morphology on the physical and photophysical properties of the COFs (e.g., interlayer stacking, porosity, crystallinity, photoluminescence) is required to understand the role of morphology in their function. For instance, the stacking difference of the two distinct morphologies reported in Figure 6.2 is currently under investigation using polarized vibrational microscopy in Prof. Pellerin's group at the University of Montreal.

Future studies may involve the electrochemical characterization of the COFs, and exploration of their electrical conductivity and photoconductivity. The calculated HOMO of -4.4 eV implies that

---

[a] We have also synthesized and characterized a series of Sciff-based linked TANG-based COFs, with varying linkage sizes, and the study of their luminescence, conductivity and paramagnetism upon I_2 doping is underway.

p-doping using F_4TCNQ or I_2 can generate polarons (radical-cations) in the framework, which may enhance the electrical conductivity of the COF for device application. [78, 95]

The current data showed that experimental surface area of pTANG1 (130 m^2g^{-1}) is ca. 10% of the theoretical surface area for AA-stacked arrangement pTANG1. Thus, the porosity of the COF requires future optimization. Respectively, methods such as Soxhlet extraction might be employed to remove the oligomers and unwanted guests from the pore. [78] CO_2 drying can be also used to prevent the pore-collapse upon activation and provide high porosity. [98] The optimization with the goal of higher porosity is likely to result in better accessibility of the pores and, thus, more pronounced environment quenching of luminescence (e.g., by humidity).

As the first example of NIR-emissive COFs, we envision this work to pave the way toward emissive low-bandgap COFs for further applications in two-photon absorption-emission materials[15], bioimaging/sensing, [99] and NIR light emitting diodes. [100]

6.7. Acknowledgments

We thank Hatem M. Titi for the help with N_2 isotherm analysis and DVS, and Alexander Wahba and Nadim Saade for mass spectrometry. We thank Lakshmi Vellanki for the constructive discussion on the synthesis of TANG and Kirill Levin for the discussion on the NMR relaxometry.

6.8. References:

1. Geng, K.; He, T.; Liu, R.; Dalapati, S.; Tan, K. T.; Li, Z.; Tao, S.; Gong, Y.; Jiang, Q.; Jiang, D., Covalent organic frameworks: design, synthesis, and functions. *Chem. Rev.* **2020,** *120*, 8814-8933.

2. Meng, Z.; Mirica, K. A., Covalent organic frameworks as multifunctional materials for chemical detection. *Chem. Soc. Rev.* **2021,** *50*, 13498-13558.

3. Liu, R.; Tan, K. T.; Gong, Y.; Chen, Y.; Li, Z.; Xie, S.; He, T.; Lu, Z.; Yang, H.; Jiang, D., Covalent organic frameworks: an ideal platform for designing ordered materials and advanced applications. *Chem. Soc. Rev.* **2021,** *50*, 120-242.

4. Gutzler, R.; Perepichka, D. F., π-Electron conjugation in two dimensions. *J. Am. Chem. Soc.* **2013,** *135*, 16585-16594.

5. Jin, E.; Asada, M.; Xu, Q.; Dalapati, S.; Addicoat, M. A.; Brady, M. A.; Xu, H.; Nakamura, T.; Heine, T.; Chen, Q., Two-dimensional sp^2 carbon–conjugated covalent organic frameworks. *Science* **2017,** *357*, 673-676.

6. Wan, S.; Guo, J.; Kim, J.; Ihee, H.; Jiang, D., A Belt-Shaped, Blue Luminescent, and Semiconducting Covalent Organic Framework. *Angew. Chem. Int. Ed.* **2008,** *47*, 8826-8830.

7. Rao, M. R.; Fang, Y.; De Feyter, S.; Perepichka, D. F., Conjugated covalent organic frameworks via michael addition-elimination. *J. Am. Chem. Soc.* **2017,** *139*, 2421-2427.

8. Jadhav, T.; Fang, Y.; Patterson, W.; Liu, C.-H.; Hamzehpoor, E.; Perepichka, D. F., 2D Poly(arylene vinylene) covalent organic frameworks via aldol condensation of trimethyltriazine. *Angew. Chem. Int. Ed.* **2019,** *58*, 13753-13757.

9. Haug, W. K.; Moscarello, E. M.; Wolfson, E. R.; McGrier, P. L., The luminescent and photophysical properties of covalent organic frameworks. *Chem. Soc. Rev.* **2020,** *49*, 839-864.

10. Zhang, L.; Yi, L.; Sun, Z. J.; Deng, H., Covalent organic frameworks for optical applications. *Aggregate* **2021,** *2*, e24.

11. Ding, H.; Li, J.; Xie, G.; Lin, G.; Chen, R.; Peng, Z.; Yang, C.; Wang, B.; Sun, J.; Wang, C., An AIEgen-based 3D covalent organic framework for white light-emitting diodes. *Nat. Commun.* **2018,** *9*, 5234.

12. Li, X.; Gao, Q.; Wang, J.; Chen, Y.; Chen, Z.-H.; Xu, H.-S.; Tang, W.; Leng, K.; Ning, G.-H.; Wu, J., Tuneable near white-emissive two-dimensional covalent organic frameworks. *Nat. Commun.* **2018,** *9*, 2335.

13. Yang, S.; Streater, D.; Fiankor, C.; Zhang, J.; Huang, J., Conjugation-and aggregation-directed design of covalent organic frameworks as white-light-emitting diodes. *J. Am. Chem. Soc.* **2021,** *143*, 1061-1068.

14. Dong, J.; Li, X.; Peh, S. B.; Yuan, Y. D.; Wang, Y.; Ji, D.; Peng, S.; Liu, G.; Ying, S.; Yuan, D., Restriction of molecular rotors in ultrathin two-dimensional covalent organic framework nanosheets for sensing signal amplification. *Chem. Mater.* **2018,** *31*, 146-160.

15. Zeng, J. Y.; Wang, X. S.; Xie, B. R.; Li, M. J.; Zhang, X. Z., Covalent organic framework for improving near-Infrared light induced fluorescence imaging through two-photon induction. *Angew. Chem. Int. Ed.* **2020,** *59*, 10087-10094.

16. Kaczmarek, A. M.; Liu, Y.-Y.; Kaczmarek, M. K.; Liu, H.; Artizzu, F.; Carlos, L. D.; Van Der Voort, P., Developing luminescent ratiometric thermometers based on a covalent organic framework (COF). *Angew. Chem. Int. Ed.* **2020,** *59*, 1932-1940.

17. Wang, Z.; Zhang, S.; Chen, Y.; Zhang, Z.; Ma, S., Covalent organic frameworks for separation applications. *Chem. Soc. Rev.* **2020,** *49*, 708-735.

18. Albacete, P.; Martinez, J. I.; Li, X.; Lopez-Moreno, A.; Mena-Hernando, S. a.; Platero-Prats, A. E.; Montoro, C.; Loh, K. P.; Perez, E. M.; Zamora, F., Layer-stacking-driven fluorescence in a two-dimensional imine-linked covalent organic framework. *J. Am. Chem. Soc.* **2018,** *140*, 12922-12929.

19. Martínez ‐ Abadía, M.; Mateo ‐ Alonso, A., Structural approaches to control interlayer interactions in 2D covalent organic frameworks. *Adv. Mater.* **2020,** *32*, 2002366.

20. Dadvand, A.; Moiseev, A. G.; Sawabe, K.; Sun, W.-H.; Djukic, B.; Chung, I.; Takenobu, T.; Rosei, F.; Perepichka, D. F., Maximizing field-effect mobility and solid-state luminescence in organic semiconductors. *Angew. Chem. Int. Ed.* **2012,** *51*, 3837-3841.

21. Ding, H.; Li, J.; Xie, G.; Lin, G.; Chen, R.; Peng, Z.; Yang, C.; Wang, B.; Sun, J.; Wang, C., An AIEgen-based 3D covalent organic framework for white light-emitting diodes. *Nat. Commun.* **2018,** *9*, 5234.

22. Dalapati, S.; Jin, E.; Addicoat, M.; Heine, T.; Jiang, D., Highly emissive covalent organic frameworks. *J. Am. Chem. Soc.* **2016,** *138*, 5797-5800.

23. Ma, L.; Feng, X.; Wang, S.; Wang, B., Recent advances in AIEgen-based luminescent metal–organic frameworks and covalent organic frameworks. *Mater. Chem. Front.* **2017,** *1*, 2474-2486.

24. Yuan, M.; Ma, F.; Dai, X.; Chen, L.; Zhai, F.; He, L.; Zhang, M.; Chen, J.; Shu, J.; Wang, X., Deuterated covalent organic frameworks with significantly enhanced luminescence. *Angew. Chem. Int. Ed.* **2021,** *60*, 21250-21255.

25. Hamzehpoor, E.; Ruchlin, C.; Tao, Y. Z.; Liu, C. H.; Titi, H. M.; Perepichka, D. F., Efficient room-temperature phosphorescence of covalent organic frameworks through covalent halogen doping. *Nat. Chem.* **2023**, 15, 83-90.

26. Xu, S.; Zhang, Q., Recent progress in covalent organic frameworks as light-emitting materials. *Mater. Today Energy* **2021,** *20*, 100635.

27. Ma, J.; Shu, T.; Sun, Y.; Zhou, X.; Ren, C.; Su, L.; Zhang, X., Luminescent covalent organic frameworks for biosensing and bioimaging applications. *Small* **2022,** *18*, 2103516.

28. Englman, R.; Jortner, J., The energy gap law for radiationless transitions in large molecules. *Mol. Phys.* **1970,** *18*, 145-164.

29. Frangioni, J. V., In vivo near-infrared fluorescence imaging. *Curr. Opin. Chem. Biol.* **2003,** *7*, 626-634.

30. Qian, C.; Chen, Y..; Feng, P..; Xiao, X.; Dong, M.; Yu, J.; Hu, Q.; Shen, Q.; Gu, Z., Conjugated polymer nanomaterials for theranostics. *Acta Pharmacol. Sin.* **2017,** *38*, 764-781.

31. Braeken, Y.; Cheruku, S.; Ethirajan, A.; Maes, W., Conjugated polymer nanoparticles for bioimaging. *Materials* **2017,** *10*, 1420.

32. Ding, D.; Liu, J.; Feng, G.; Li, K.; Hu, Y.; Liu, B., Bright far-red/near-infrared conjugated polymer nanoparticles for in vivo bioimaging. *Small* **2013,** *9*, 3093-3102.

33. Liu, J.; Geng, J.; Liu, B., A bright far-red and near-infrared fluorescent conjugated polyelectrolyte with quantum yield reaching 25%. *Chem. Commun.* **2013,** *49*, 1491-1493.

34. Yang, C.; Huang, S.; Wang, X.; Wang, M., Theranostic unimolecular micelles of highly fluorescent conjugated polymer bottlebrushes for far red/near infrared bioimaging and efficient anticancer drug delivery. *Polym. Chem.* **2016,** *7*, 7455-7468.

35. Rohatgi, C. V.; Harada, T.; Need, E. F.; Krasowska, M.; Beattie, D. A.; Dickenson, G. D.; Smith, T. A.; Kee, T. W., Low-bandgap conjugated polymer dots for near-infrared fluorescence imaging. *ACS Appl. Nano Mater.* **2018,** *1*, 4801-4808.

36. Yu, J.-C.; Chen, Y.-L.; Zhang, Y.-Q.; Yao, X.-K.; Qian, C.-G.; Huang, J.; Zhu, S.; Jiang, X.-Q.; Shen, Q.-D.; Gu, Z., pH-Responsive and near-infrared-emissive polymer nanoparticles for simultaneous delivery, release, and fluorescence tracking of doxorubicin in vivo. *Chem. Commun.* **2014,** *50*, 4699-4702.

37. Nawimanage, R. R.; Prasai, B.; Hettiarachchi, S. U.; McCarley, R. L., Cascade reaction-based, near-infrared multiphoton fluorescent probe for the selective detection of cysteine. *Anal. Chem.* **2017,** *89*, 6886-6892.

38. Wu, W.; Feng, G.; Xu, S.; Liu, B., A photostable far-red/near-infrared conjugated polymer photosensitizer with aggregation-induced emission for image-guided cancer cell ablation. *Macromolecules* **2016,** *49*, 5017-5025.

39. Sun, T.; Dou, J.-H.; Liu, S.; Wang, X.; Zheng, X.; Wang, Y.; Pei, J.; Xie, Z., Second near-infrared conjugated polymer nanoparticles for photoacoustic imaging and photothermal therapy. *ACS Appl. Mater. Interfaces* **2018,** *10*, 7919-7926.

40. Bürgi, L.; Turbiez, M.; Pfeiffer, R.; Bienewald, F.; Kirner, H. J.; Winnewisser, C., High‐mobility ambipolar near‐infrared light‐emitting polymer field-effect transistors. *Adv. Mater.* **2008,** *20*, 2217-2224.

41. Held, M.; Zakharko, Y.; Wang, M.; Jakubka, F.; Gannott, F.; Rumer, J. W.; Ashraf, R. S.; McCulloch, I.; Zaumseil, J., Photo-and electroluminescence of ambipolar, high-mobility, donor-acceptor polymers. *Org. Electron.* **2016,** *32*, 220-227.

42. Steckler, T.; Lee, M.; Chen, Z.; Fenwick, O.; Andersson, M. R.; Cacialli, F.; Sirringhaus, H., Multifunctional materials for OFETs, LEFETs and NIR PLEDs. *J. Mater. Chem. C* **2014,** *2*, 5133-5141.

43. Brabec, C. J.; Winder, C.; Sariciftci, N. S.; Hummelen, J. C.; Dhanabalan, A.; van Hal, P. A.; Janssen, R. A., A low‐bandgap semiconducting polymer for photovoltaic devices and infrared emitting diodes. *Adv. Funct. Mater.* **2002,** *12*, 709-712.

44. Tessler, N.; Medvedev, V.; Kazes, M.; Kan, S.; Banin, U., Efficient near-infrared polymer nanocrystal light-emitting diodes. *Science* **2002,** *295*, 1506-1508.

45. Xu, J.; Peng, F.; Sun, Z.; Yu, L.; Yang, W.; Cao, Y., Near-infrared polymer light-emitting diodes based on an inverted device structure. *J. Mater. Chem. C* **2019,** *7*, 12114-12120.

46. Steckler, T. T.; Fenwick, O.; Lockwood, T.; Andersson, M. R.; Cacialli, F., Near-infrared polymer light-emitting diodes based on low‐energy gap oligomers copolymerized into a High‐gap polymer host. *Macromol. Rapid Commun.* **2013,** *34*, 990-996.

47. Tregnago, G.; Steckler, T. T.; Fenwick, O.; Andersson, M. R.; Cacialli, F., Thia-and selena-diazole containing polymers for near-infrared light-emitting diodes. *J. Mater. Chem. C* **2015,** *3*, 2792-2797.

48. Thompson, B. C.; Madrigal, L. G.; Pinto, M. R.; Kang, T. S.; Schanze, K. S.; Reynolds, J. R., Donor–acceptor copolymers for red- and near-infrared-emitting polymer light-emitting diodes. *J. Polym. Sci., Part A: Polym. Chem.* **2005,** *43*, 1417-1431.

49. Haigh, P. A.; Bausi, F.; Ghassemlooy, Z.; Papakonstantinou, I.; Le Minh, H.; Fléchon, C.; Cacialli, F., Visible light communications: real time 10 Mb/s link with a low bandwidth polymer light-emitting diode. *Opt. Express* **2014,** *22*, 2830-2838.

50. Cosco, E. D.; Spearman, A. L.; Ramakrishnan, S.; Lingg, J. G.; Saccomano, M.; Pengshung, M.; Arús, B. A.; Wong, K. C.; Glasl, S.; Ntziachristos, V., Shortwave infrared polymethine fluorophores matched to excitation lasers enable non-invasive, multicolour in vivo imaging in real time. *Nat. Chem.* **2020,** *12*, 1123-1130.

51. Luo, S.; Zhang, E.; Su, Y.; Cheng, T.; Shi, C., A review of NIR dyes in cancer targeting and imaging. *Biomaterials* **2011,** *32*, 7127-7138.

52. Cosco, E. D.; Lim, I.; Sletten, E. M., Photophysical properties of indocyanine green in the shortwave infrared region. *ChemPhotoChem* **2021,** *5*, 727-734.

53. Jenekhe, S. A.; Osaheni, J. A., Excimers and exciplexes of conjugated polymers. *Science* **1994,** *265*, 765-768.

54. Carter, P. W.; Porter, J. D., Probing of π conjugation in trans-polyacetylene using near-infrared photoluminescence spectroscopy. *Phys. Rev. B* **1991,** *43*, 14478.

55. Yoshino, K.; Hayashi, S.; Inuishi, Y.; Hattori, K.; Watanabe, Y., Photoluminescence of cis- and trans-polyacetylene. *Solid State Commun.* **1983,** *46*, 583-585.

56. Sun, Z.; Ye, Q.; Chi, C.; Wu, J., Low band gap polycyclic hydrocarbons: from closed-shell near infrared dyes and semiconductors to open-shell radicals. *Chem. Soc. Rev.* **2012,** *41*, 7857-7889.

57. Qian, G.; Wang, Z. Y., Near-infrared organic compounds and emerging applications. *Chem. Asian J.* **2010,** *5*, 1006-1029.

58. Karton-Lifshin, N.; Albertazzi, L.; Bendikov, M.; Baran, P. S.; Shabat, D., "Donor–two-acceptor" dye design: a distinct gateway to NIR fluorescence. *J. Am. Chem. Soc.* **2012,** *134*, 20412-20420.

59. Greenham, N.; Moratti, S.; Bradley, D.; Friend, R.; Holmes, A., Efficient light-emitting diodes based on polymers with high electron affinities. *Nature* **1993,** *365*, 628-630.

60. Crossley, D. L.; Urbano, L.; Neumann, R.; Bourke, S.; Jones, J.; Dailey, L. A.; Green, M.; Humphries, M. J.; King, S. M.; Turner, M. L., Post-polymerization C–H borylation of donor–acceptor materials gives highly efficient solid state near-infrared emitters for near-IR-OLEDs and effective biological imaging. *ACS Appl. Mater. Interfaces* **2017,** *9*, 28243-28249.

61. Ma, X.; Jiang, X.; Zhang, S.; Huang, X.; Cheng, Y.; Zhu, C., Near-infrared emission of novel bent-core V-shaped conjugated polymers based on the B, O-chelated azadipyrromethene structure. *Polym. Chem.* **2013,** *4*, 4396-4404.

62. Sasmal, H. S.; Kumar Mahato, A.; Majumder, P.; Banerjee, R., Landscaping covalent organic framework nanomorphologies. *J. Am. Chem. Soc.* **2022,** *144*, 11482-11498.

63. Liu, H.-Y.; Wu, P.-J.; Kuo, S.-Y.; Chen, C.-P.; Chang, E.-H.; Wu, C.-Y.; Chan, Y.-H., Quinoxaline-based polymer dots with ultrabright red to near-infrared fluorescence for in vivo biological imaging. *J. Am. Chem. Soc.* **2015,** *137*, 10420-10429.

64. Chen, L.; Chen, D.; Jiang, Y.; Zhang, J.; Yu, J.; DuFort, C. C.; Hingorani, S. R.; Zhang, X.; Wu, C.; Chiu, D. T., A BODIPY-based donor/donor-acceptor system: towards highly efficient long-wavelength-excitable near-IR polymer dots with narrow and strong absorption features. *Angew. Chem. Int. Ed.* **2019,** *58*, 7008-7012.

65. Qian, G.; Dai, B.; Luo, M.; Yu, D.; Zhan, J.; Zhang, Z.; Ma, D.; Wang, Z. Y., Band Gap Tunable, Donor−Acceptor−Donor charge-transfer heteroquinoid-based chromophores: near Infrared photoluminescence and electroluminescence. *Chem. Mater.* **2008,** *20*, 6208-6216.

66. Deng, G.; Peng, X.; Sun, Z.; Zheng, W.; Yu, J.; Du, L.; Chen, H.; Gong, P.; Zhang, P.; Cai, L., Natural-killer-cell-inspired nanorobots with aggregation-induced emission characteristics for near-infrared-II fluorescence-guided glioma theranostics. *ACS Nano* **2020,** *14*, 11452-11462.

67. Neumann, P. R.; Crossley, D. L.; Turner, M.; Ingleson, M.; Green, M.; Rao, J.; Dailey, L. A., In vivo optical performance of a new class of near-infrared-emitting conjugated polymers: borylated PF8-BT. *ACS Appl. Mater. Interfaces* **2019,** *11*, 46525-46535.

68. Wang, S.; Liu, J.; Feng, G.; Ng, L. G.; Liu, B., NIR-II excitable conjugated polymer dots with bright NIR-I emission for deep iIn vivo two-photon brain imaging through intact skull. *Adv. Funct. Mater.* **2019,** *29*, 1808365.

69. Ni, Y.; Wu, J., Far-red and near infrared BODIPY dyes: synthesis and applications for fluorescent pH probes and bio-imaging. *Org. Biomol. Chem.* **2014,** *12*, 3774-3791.

70. Yu, C.; Fang, X.; Wu, Q.; Guo, X.; Chen, N.; Cheng, C.; Hao, E.; Jiao, L., Synthesis and spectral properties of agregation-induced emission-active push–pull chromophores based on isoindole scaffolds. *Org. Lett.* **2022,** *24*, 4557-4562.

71. Zhang, X.; Yu, H.; Xiao, Y., Replacing phenyl ring with thiophene: an approach to longer wavelength aza-dipyrromethene boron difluoride (Aza-BODIPY) dyes. *J. Org. Chem.* **2012,** *77*, 669-673.

72. Liu, T.; Zhu, L.; Zhong, C.; Xie, G.; Gong, S.; Fang, J.; Ma, D.; Yang, C., Naphthothiadiazole‐based near-infrared emitter with a photoluminescence quantum yield of 60% in neat film and external quantum efficiencies of up to 3.9% in nondoped OLEDs. *Adv. Funct. Mater.* **2017,** *27*, 1606384.

73. Zhao, J.; Ren, J.; Zhang, G.; Zhao, Z.; Liu, S.; Zhang, W.; Chen, L., Donor-acceptor type covalent organic frameworks. *Chem. Eur. J.* **2021,** *27*, 10781-10797.

74. Li, Z.; Geng, K.; He, T.; Tan, K. T.; Huang, N.; Jiang, Q.; Nagao, Y.; Jiang, D., Editing Light Emission with Stable Crystalline Covalent Organic Frameworks via Wall Surface Perturbation. *Angew. Chem. Int. Ed.* **2021,** *60*, 19419-19427.

75. Clar, E.; Stewart, D. G., Aromatic Hydrocarbons. LXV. Triangulene Derivatives. *J. Am. Chem. Soc.* **1953,** *75*, 2667-2672.

76. Livant, P. D.; Northcott, D. J. D.; Shen, Y.; Webb, T. R., Bonding along a Linear B···N···B Triad. *J. Org. Chem.* **2004,** *69*, 6564-6571.

77. Suzuki, S.; Tanaka, N.; Kozaki, M.; Shiomi, D.; Sato, K.; Takui, T.; Okada, K., Synthesis and magnetic properties of trioxytriphenylamine dimers in their di(radical cationic) states. *Chem. Eur. J.* **2017,** *23*, 16014-16025.

78. Lakshmi, V.; Liu, C.-H.; Rajeswara Rao, M.; Chen, Y.; Fang, Y.; Dadvand, A.; Hamzehpoor, E.; Sakai-Otsuka, Y.; Stein, R. S.; Perepichka, D. F., A Two-Dimensional poly(azatriangulene) covalent organic framework with semiconducting and paramagnetic states. *J. Am. Chem. Soc.* **2020,** *142*, 2155-2160.

79. Ni, X.; Huang, H.; Brédas, J.-L., Organic higher-order topological insulators: Heterotriangulene-based covalent organic frameworks. *J. Am. Chem. Soc.* **2022**, In Press, DOI: 10.1021/jacs.1022c11229.

80. Jing, Y.; Heine, T., Two-dimensional kagome lattices made of hetero triangulenes are Dirac semimetals or single-band semiconductors. *J. Am. Chem. Soc.* **2018,** *141*, 743-747.

81. Galeotti, G.; De Marchi, F.; Hamzehpoor, E.; MacLean, O.; Rajeswara Rao, M.; Chen, Y.; Besteiro, L. V.; Dettmann, D.; Ferrari, L.; Frezza, F.; Sheverdyaeva, P. M.; Liu, R.; Kundu, A. K.; Moras, P.; Ebrahimi, M.; Gallagher, M. C.; Rosei, F.; Perepichka, D. F.; Contini, G., Synthesis of mesoscale ordered two-dimensional pi-conjugated polymers with semiconducting properties. *Nat. Mater.* **2020,** *19*, 874-880.

82. Kuratsu, M.; Kozaki, M.; Okada, K., 2,2':6',2'':6'',6-trioxytriphenylamine: Synthesis and properties of the radical cation and neutral species. *Angew. Chem., Int. Ed.* **2005,** *44*, 4056-4058.

83. Kuratsu, M.; Kozaki, M.; Okada, K., 2, 2’: 6’, 2’’: 6’’, 6-Trioxytriphenylamine: synthesis and properties of the radical cation and neutral species. *Angew. Chem. Int. Ed.* **2005,** *44*, 4056-4058.

84. Zhang, Y. Y.; Polozij, M.; Heine, T., Statistical representation of stacking disorder in layered covalent organic frameworks. *Chem. Mater.* **2022,** *34*, 2376-2381.

85. Karak, S.; Dey, K.; Banerjee, R., Maneuvering applications of covalent Organic frameworks via framework-morphology modulation. *Adv. Mater.***2022***, 34*, 2202751.

86. Zhang, X.; Geng, K.; Jiang, D.; Scholes, G. D., Exciton diffusion and annihilation in an sp^2 carbon-conjugated covalent organic framework. *J. Am. Chem. Soc.* **2022,** *144*, 16423-16432.

87. Schmidt-Rohr, K.; Spiess, H. W., Multidimensional solid-state NMR and polymers. *Elsevier*: 2012.

88. Bloise Júnior, A. C.; Azevêdo, E. R. d.; Cossiello, R.; Bianchi, R. F.; Balogh, D. T.; Faria, R. M.; Atvars, T.; Bonagamba, T. J., Solid-state nuclear magnetic resonance study of relaxation processes in MEH-PPV. *Phys. Rev. B* **2005,** *71*, 174202-174201.

89. Devisscher, D.; Reekmans, G.; Kesters, J.; Verstappen, P.; Benduhn, J.; Van den Brande, N.; Lutsen, L.; Manca, J.; Vanderzande, D.; Vandewal, K., Analysis of bulk heterojunction organic solar cell blends by solid-state NMR relaxometry and sensitive external quantum efficiency–Impact of polymer side chain variation on nanoscale morphology. *Org. Electron.* **2019,** *74*, 309-314.

90. Deng, L.; Kang, X.; Quan, T.; Yang, L.; Liu, S.; Zhang, K.; Gao, M.; Xia, Z.; Gao, D., Highly crystalline covalent organic frameworks act as a dual-functional fluorescent-sensing platform for myricetin and water, and adsorbents for myricetin. *ACS Appl. Mater. Interfaces* **2021,** *13*, 33449-33463.

91. Qian, H.-L.; Dai, C.; Yang, C.-X.; Yan, X.-P., High-crystallinity covalent organic framework with dual fluorescence emissions and its ratiometric sensing application. *ACS Appl. Mater. Interfaces* **2017,** *9*, 24999-25005.

92. Jiang, S.; Meng, L.; Ma, W.; Pan, G.; Zhang, W.; Zou, Y.; Liu, L.; Xu, B.; Tian, W., Dual-functional two-dimensional covalent organic frameworks for water sensing and harvesting. *Mater. Chem. Front.* **2021,** *5*, 4193-4201.

93. Chen, Y.; Zhang, C.; Xie, J.; Li, H.; Dai, W.; Deng, Q.; Wang, S., Covalent organic frameworks as a sensing platform for water in organic solvent over a broad concentration range. *Anal. Chim. Acta* **2020,** *1109*, 114-121.

94. Gilmanova, L.; Bon, V.; Shupletsov, L.; Pohl, D.; Rauche, M.; Brunner, E.; Kaskel, S., Chemically stable carbazole-based imine covalent organic frameworks with acidochromic response for humidity control applications. *J. Am. Chem. Soc.* **2021,** *143*, 18368-18373.

95. Segura, J. L.; Mancheño, M. J.; Zamora, F., Covalent organic frameworks based on Schiff-base chemistry: synthesis, properties and potential applications. *Chem. Soc. Rev.* **2016,** *45*, 5635-5671.

96. Jadhav, T.; Fang, Y.; Patterson, W.; Liu, C. H.; Hamzehpoor, E.; Perepichka, D. F., 2D poly (arylene vinylene) covalent organic frameworks via aldol condensation of trimethyltriazine. *Angew. Chem. Int. Ed.* **2019,** *58*, 13753-13757.

97. Spitler, E. L.; Dichtel, W. R., Lewis acid-catalysed formation of two-dimensional phthalocyanine covalent organic frameworks. *Nat. Chem.* **2010,** *2*, 672-677.

98. Feriante, C. H.; Jhulki, S.; Evans, A. M.; Dasari, R. R.; Slicker, K.; Dichtel, W. R.; Marder, S. R., Rapid Synthesis of High Surface Area Imine-linked 2D covalent organic frameworks by avoiding pore collapse during isolation. *Adv. Mater.* **2020,** *32*, 1905776.

99. Cosco, E. D.; Spearman, A. L.; Ramakrishnan, S.; Lingg, J. G. P.; Saccomano, M.; Pengshung, M.; Arús, B. A.; Wong, K. C. Y.; Glasl, S.; Ntziachristos, V.; Warmer, M.; McLaughlin, R. R.; Bruns, O. T.; Sletten, E. M., Shortwave infrared polymethine fluorophores matched to excitation lasers enable non-invasive, multicolour in vivo imaging in real time. *Nat. Chem.* **2020,** *12*, 1123-1130.

100. Minotto, A.; Bulut, I.; Rapidis, A. G.; Carnicella, G.; Patrini, M.; Lunedei, E.; Anderson, H. L.; Cacialli, F., Towards efficient near-infrared fluorescent organic light-emitting diodes. *Light Sci. Appl.* **2021,** *10*, 18.

6.9. Supplementary Information

6.9.1. Synthesis

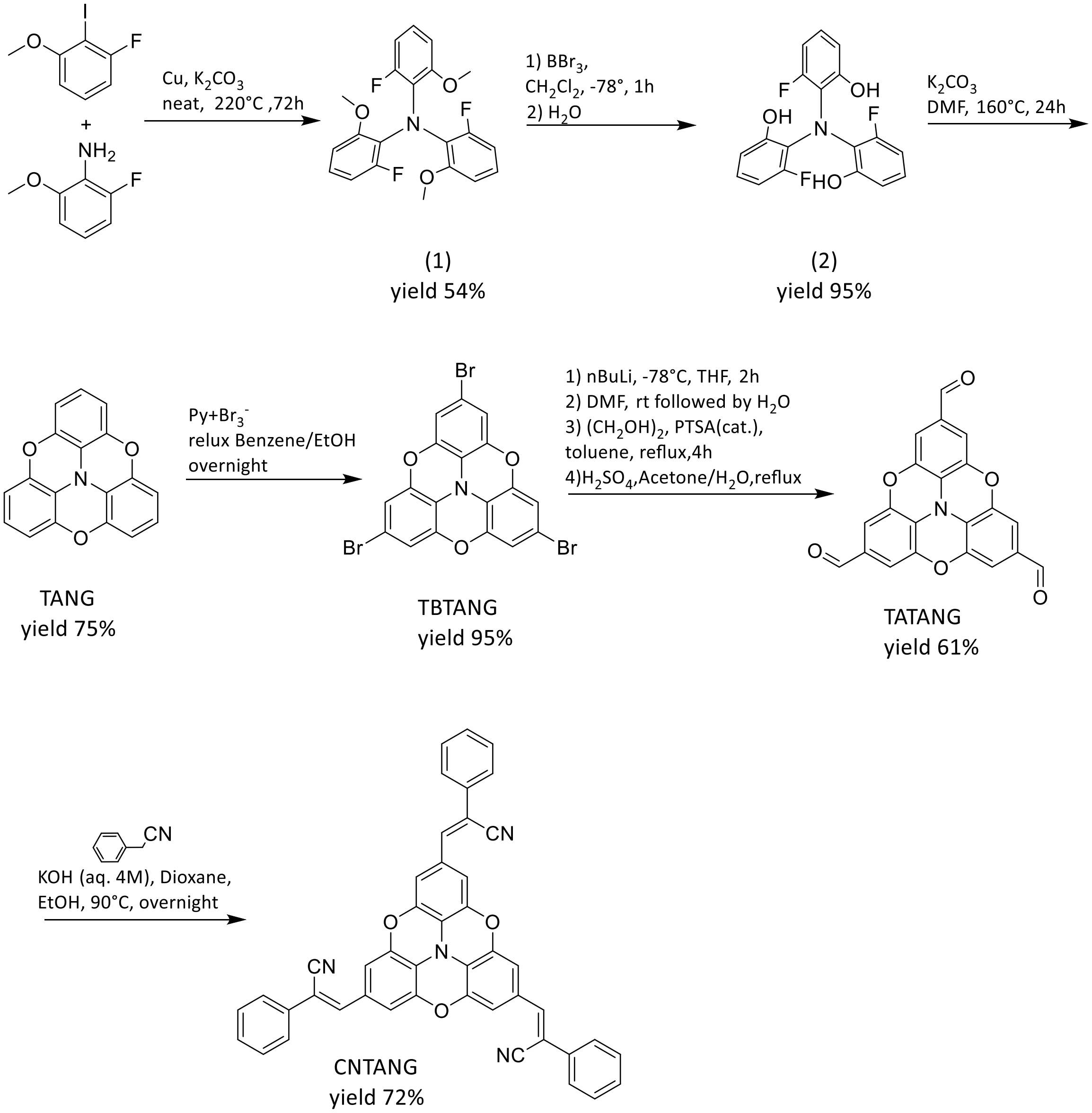

Scheme 6.2. The synthesis scheme of TANG, TATANG, and CNTANG.

Tris(2-fluoro-6-methoxyphenyl)amine (1). A mixture of 2-fluoro-6-methoxyaniline (2.00 g, 14.2 mmol), 3-fluoro-2-iodoanisole (10.71 g, 42.51 mmol), copper powder (1.80 g, 28.3 mmol) and K_2CO_3 (5.87 g, 42.5 mmol) was added into a 15 ml Pyrex high-pressure tube from ChemGlass. The mixture was further degassed and purged with N_2 for 5 min. The reaction mixture was then stirred up to 220 °C for 72 h. The resulting crude mixture (solid at room temperature) was slowly dissolved in 100 ml of aqueous HCl (1 M) and 100 ml CH_2Cl_2. The obtained crude mixture was extracted with CH_2Cl_2 (3 x 100 ml), washed with brine, dried over anhydrous Mg_2SO_4, and concentrated under vacuum. The residue was purified by column chromatography (SiO_2, hexanes/CH_2Cl_2 6:4) to afford the desired **1** (2.98 g, 54%) as a white solid. ^1H NMR (500 MHz, $CDCl_3$) δ 6.98 (td, J = 8.3, 6.0 Hz, 3H), 6.69-6.62 (m, 6H), 3.59 (s, 9H). ^{13}C NMR (126 MHz, $CDCl_3$) δ 159.82, 157.86, 156.39, 125.81 (d, J = 10.8 Hz), 123.95 (d, J = 10.8 Hz), 108.78 (d, J = 21.6 Hz), 56.84. ^{19}F NMR (376 MHz, $CDCl_3$) δ -122.91.

Tris(2-fluoro-6-hydroxyphenyl)amine (2) To a solution of **1** (1.00 g, 2.57 mmol) dissolved in dry CH_2Cl_2 (30 mL) was added dropwise of BBr_3 (3.20 g, 12.8 mmol) at -78 °C and stirred for 1h. The reaction mixture was then left to slowly warm up to room temperature and stirred for 12 h. After the reaction completion (checked by TLC), the reaction was quenched with H_2O. The crude mixture was extracted with chloroform, washed with brine, and dried under vacuum to give the compound **2** as a white solid (0.85 g, 95%), used without further purification for the next step. ^1H NMR (500 MHz, $CDCl_3$) δ 7.08 (td, *J* = 8.3, 5.8 Hz, 1H), 6.72 (t, *J* = 9.0 Hz, 2H), 6.40 (s, 1H). ^{13}C NMR (126 MHz, $CDCl_3$) δ 161.71, 159.76, 154.86, 127.68 (d, *J* = 10.8 Hz), 121.20 (d, *J* = 13.9 Hz), 108.44 (d, *J* = 21.0 Hz). ^{19}F NMR (376 MHz, $CDCl_3$) δ -120.79.

2,2':6',2'':6'',6-trioxytriphenylamine (TANG): **2** (0.80 g , 2.30 mmol) was dissolved in dry DMF (30 mL) and added to a 50ml round bottom flask along with K_2CO_3 (1.60 g, 11.5 mmol). The reaction mixture was slowly brought up to 150 °C for 24 h. The solvent was then evaporated by vacuum distillation. The obtained crude was purified on a silica gel column using a gradient (0-15%) ethyl acetate/hexane to afford the desired compound **TANG** (0.50 g, 75%) as a pale-yellow solid. ^1H

NMR (500 MHz, C_6D_6) δ 6.25 (m, 9H). ^{13}C NMR (126 MHz, C_6D_6) δ 142.36, 127.89, 116.81, 111.13. The ^{1}H and ^{13}C NMR spectra matched those reported previously. [1]

4,4',4'''-Tribromo-2,2':6',2'':6'',6-trioxytriphenylamine (TBTANG) (3). TANG (0.500 g, 1.74 mmol) and pyridinium tribromide (8.35 g, 26.1 mmol) were dissolved in 100 mL 3:2 (v:v) solution of Benzene: EtOH. The mixture was then refluxed at 90 °C overnight, during which a yellow precipitate was formed. After cooling to room temperature, the crude mixture was filtered out and washed with EtOH, affording **TBTANG** as a yellow solid (0.87 g, 95%) which was used without further purification for the next step. The extremely low solubility of the product in organic solvents precluded NMR characterization.

4,4',4'''-Triformyl-2,2':6',2'':6'',6-trioxytriphenylamine (TATANG). To a solution of TBTANG (0.10 g, 0.19 mmol) dispersed in dry THF (2 mL) was added n-butyllithium (0.25 mL, 2.5 M in hexanes, 0.63 mmol) at -78 °C (acetone/dry ice bath). After two hours, dry DMF (85.0 mg, 1.16 mmol) was added into the reaction mixture and the reaction was brought up to room temperature over 1 h and continued stirring at room temperature for an extra 1 h. The reaction mixture was then quenched with water and the resulting orange crude was filtrated out and washed with excess water, acetone, successively, to give **TATANG** as a red solid (65 mg, crude yield of 92%). The crude was then redispersed in toluene in which excess ethylene glycol (0.3 mL, 5.43 mmol), followed by a catalytic amount of 4-toluenesulfonic acid monohydrate (6 mg, 0.035 mmol) was added. Then the reaction was brought to reflux and stirred until all the crude solids disappeared (ca. 4 h). The reaction mixture was cooled down to room temperature, quenched with 10 ml of with 5% w/w aq. sodium hydroxide, and extracted with toluene. The organic phase was dried over anhydrous potassium carbonate and the solvent was evaporated under vacuum. The residue was then purified using flash column chromatography using 1% triethylamine in 15% EtOAc/toluene. The **acetal** (60 mg, 69%) was unstable and partially converted back to insoluble TATANG after column chromatography. Then solvent of this acetal fraction was evaporated under vacuum and to the acetal/TATANG mixture was then added concentrated hydrochloric acid (1 mL), acetone

(15 mL), and water (1 mL). The reaction mixture was brought to reflux for 1 h, during which light orange crystals of TATANG percipitated out of the solution. The reaction mixture was then cooled down to room temperature and was filtered out to afford a final yield with (43 mg, 97%). The final yield of TATANG was 61%. ^{1}H NMR (500 MHz, DMSO-d_6, 100°C) δ 9.71 (s, 1H), 7.06 (s, 2H). ^{13}C NMR (101 MHz, DMSO-d_6,100°C) δ 190.03, 141.88, 133.97, 119.29, 113.22.

4,4',4'''-Tris(cyanomethyl)-2,2':6',2'':6'',6-trioxytriphenylamine (CNTANG): TATANG (50 mg, 0.13 mmol) and aryl cyanide (0.42 mmol) were dissolved in dioxane (2 mL), followed by adding KOH (0.1 mL) and EtOH (0.25 mL). The reaction mixture was brought up to 90 °C (under Ar, 1 atm) overnight. The reaction was then cooled down to room temperature and quenched with 10 ml of EtOH:water 1:1. The resulting burgundy precipitates were then filtered and recrystallized in DMSO (twice) to afford CNTANG (71 mg, 81%). ^{1}H NMR (400 MHz, DMSO-d_6) δ 7.64 – 7.55 (m, 9H), 7.49 – 7.32 (m, 9H), 7.17 (s, 6H).^{13}C NMR (101 MHz, DMSO-d_6) δ 141.59, 140.65, 134.28, 130.85, 129.50, 129.44, 126.15, 118.07, 115.94, 113.13, 109.92.

General procedure for model compounds and COFs. TATANG (10 mg, 0.03 mmol) and aryl cyanide (0.045 mmol) were dispersed in dioxane (2 mL), followed by addition of EtOH (0.2 mL) and KOH (aq. 4M, 0.2 mL). The reaction mixture was brought up to 90 °C (under argon 1 atm) and stirred overnight. The resulting solids were collected by Teflon filtration and washed extensively with boiling DMF, water, and acetone, until no luminescence color was observed upon washing.

6.9.2. Survey of the reported red and far-red emissive COFs

Table 6.1. A survey of far-red emissive covalent organic frameworks

	λ_{max} (nm)	Lifetime (ns)	PLQY	λ_{edge} (nm)	Ref.
COF-JLU3	601	1.5	10%	700	Z. Li et al., Chem. Commun. **2016**, 52, 6613-6616.[2]
Sp2c-COF	622	1.9	14%	750	E. Jin, et al., Nat. Commun. **2018**, 9, 4143.[3]
Sp2c-COF-2	606	2.9	10%	720	E. Jin, et al., Nat. Commun. **2018**, 9, 4143.[3]
Sp2c-COF-3	609	3.4	6%	700	E. Jin, et al., Nat. Commun. **2018**, 9, 4143.[3]
DPP2-HHTP-COF	620,680	0.19	N.A.	870	S. Rager, et al., Chem. Mater. **2019**, 31, 2707-2712.[4]
SCU-COF-9d	645	1.39	8%	890	M. Yuan, et al., Angew. Chem. Int. Ed. **2021,** 60, 21250-21255.[5]
MHzcB-DHTA-COF	635	0.21	3.1%	690	Z. Li, *Angew. Chem. Int. Ed.* **2021**, 60, 19419.[6]
pTANG1	789	4.2 ±0.2	1%	1050	**This Work**
pTANG2	730	2.5 ±0.2	1%	980	**This Work**

6.9.3. Air stability test of TANG vs. TATANG

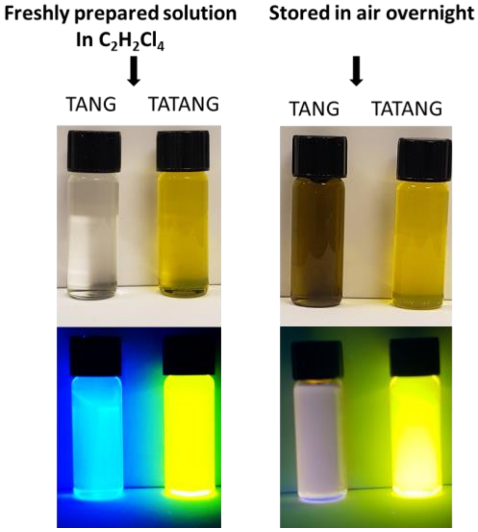

Figure 6.5. Photographs of TANG and TATANG in room light (top) and under UV (λ_{ex} = 360 nm, bottom) for freshly prepared solutions (left) as compared with the solution stored in air overnight (right).

6.9.4. Photophysical comparison of TANG, TATANG, CNTANG solutions *vs.* pTANG1 and pTANG2 COFs

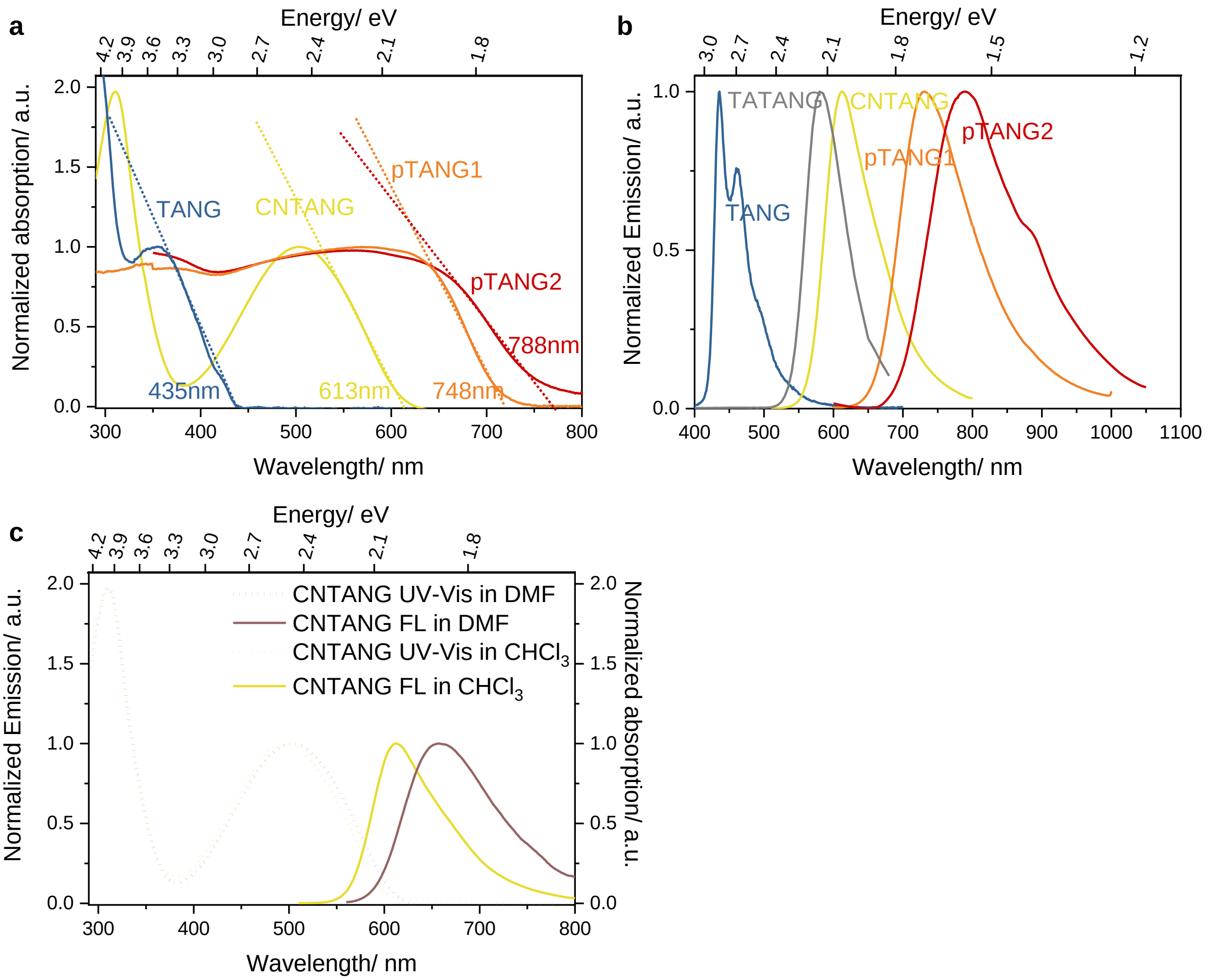

Figure 6.6. Comparison of a) UV-Vis absorption and diffuse reflectance and b) photoluminescence of the TANG, TATANG, CNTANG, pTANG1 and pTANG2 COFs. c) the solvatochromism of CNTANG, suggesting the CT character of its excited state.

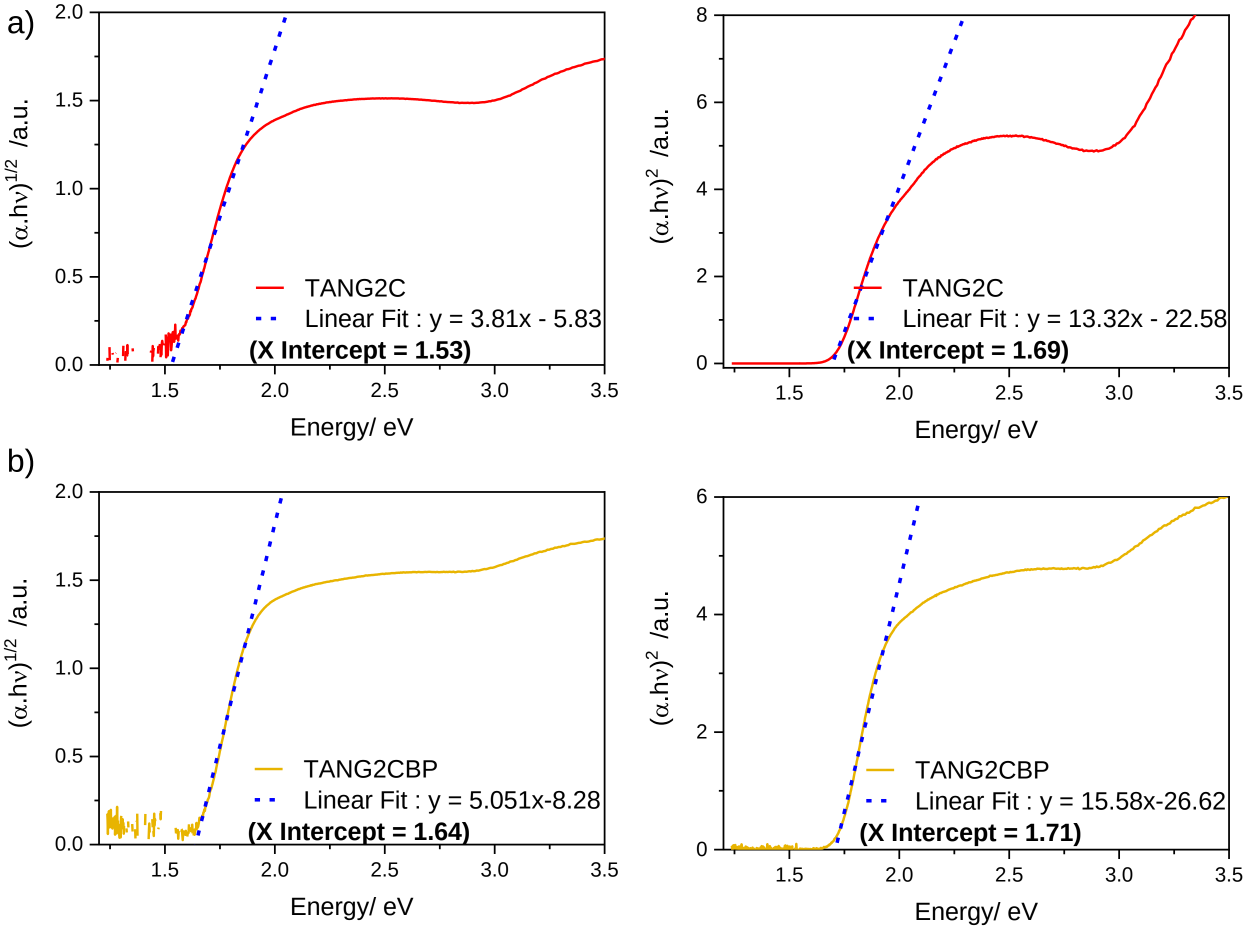

Figure 6.7. Tauc plot of diffuse reflectance data of a) pTANG1 and b) pTANG2.

6.9.5. Comparison of small angle X-ray diffraction and powder X-ray diffraction for pTANG2.

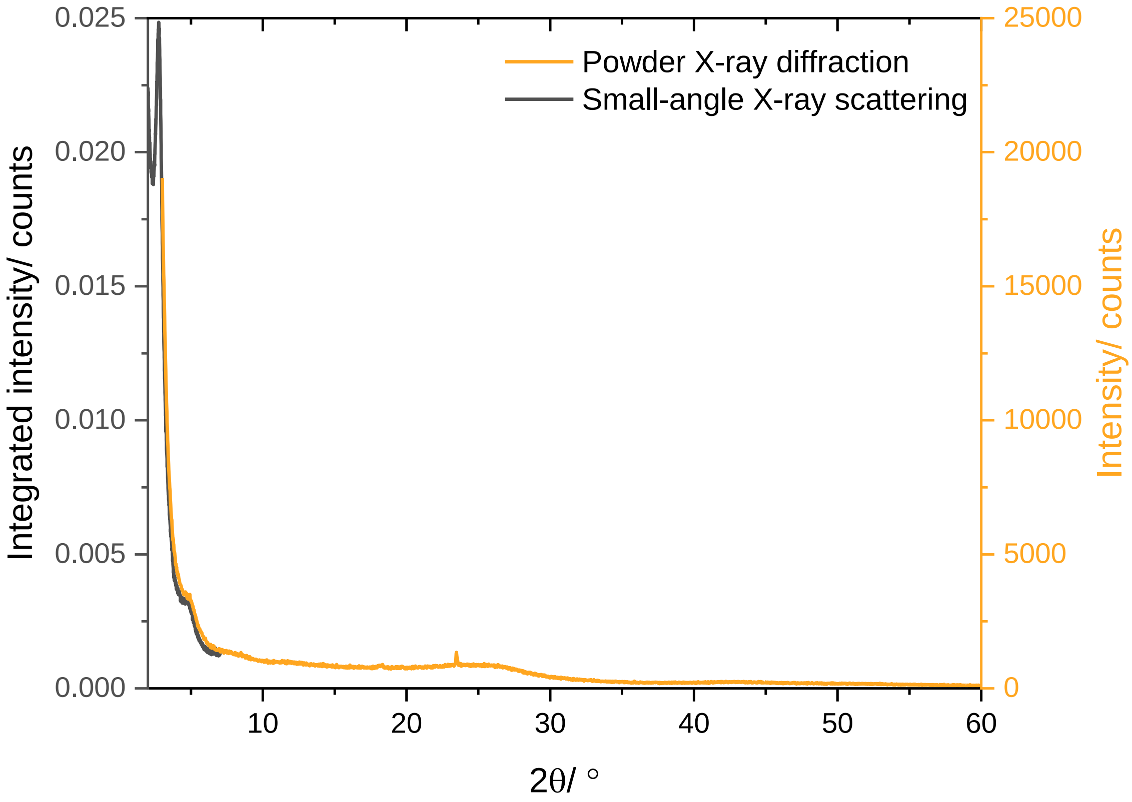

Figure 6.8. Small-angle X-ray scattering (SAXS) and powder X-ray diffraction (PXRD) data of pTANG2, superimposed on each other. The data in Figure 6.1d is a combination of SAXS (2-6°) and PXRD (6-60°), in which the SAXS data is normalized to the PXRD data at 2θ=6°.

6.9.6. Structural modeling of pTANG1 COF for AA, slipped stacks and AB

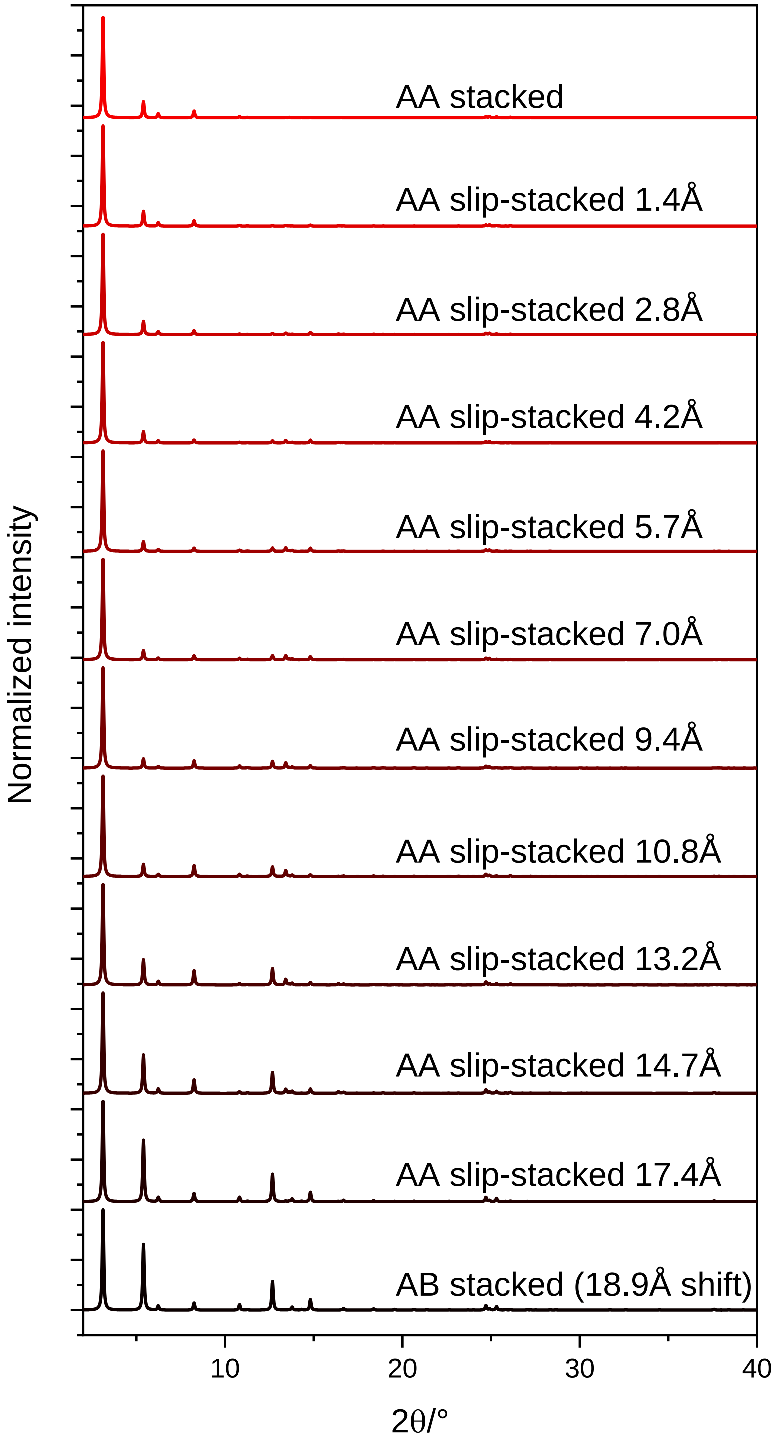

Figure 6.9. XRD simulation of the pTANG1 bilayer unit-cell upon shifting of the layers from pure AA to a zigzag AB form.

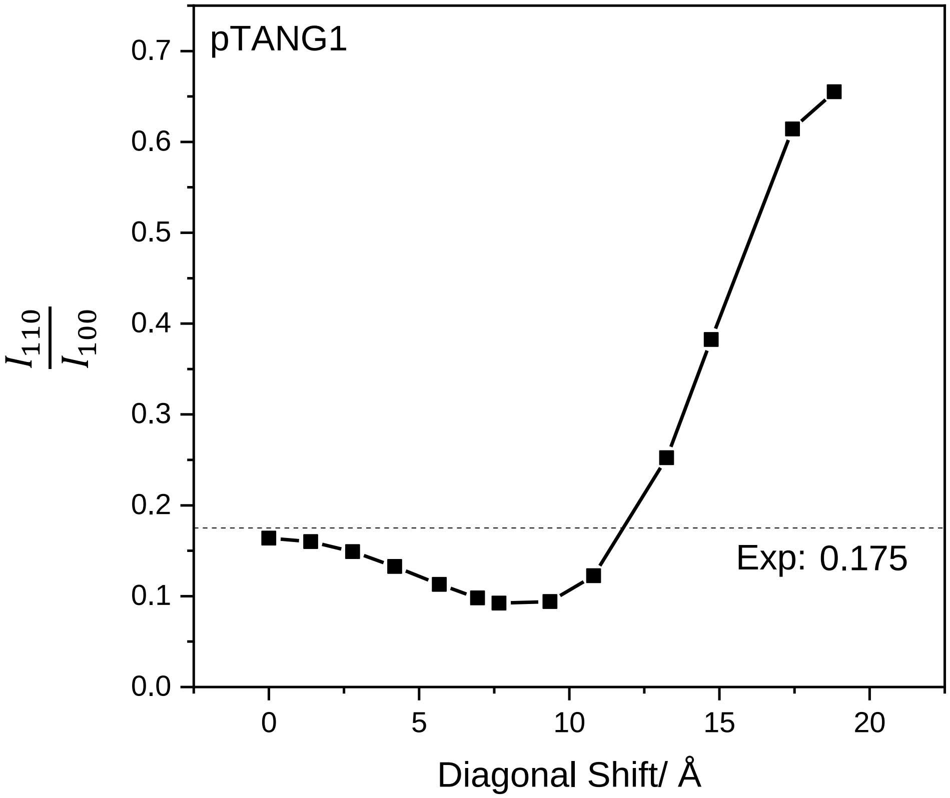

Figure 6.10. The relative intensity of the different stacking modes of the pTANG1 upon slipping the layer from AA to AB was obtained from Figure 6.9.

6.9.7. BET analysis of pTANG1

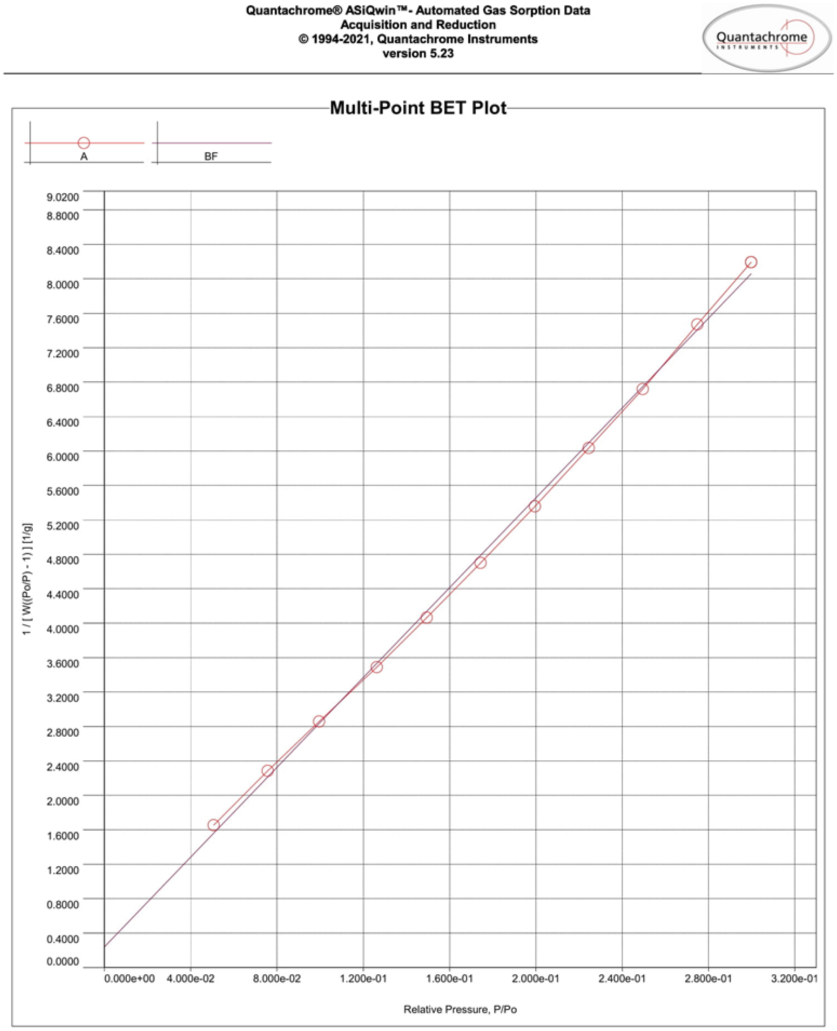

Figure 6.11. BET analysis of pTANG1 N_2 isotherm at 77 K. *R^2=0.998.*

6.9.8. Transmission electron microscopy (TEM) and selected area electron diffraction (SAED)

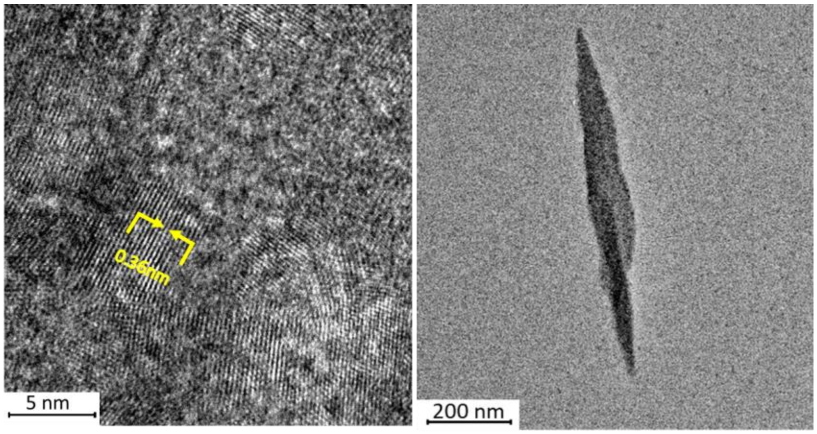

Figure 6.12. HR-TEM images of the dispersed pTANG2 sample in N-methylpyrrolidone.

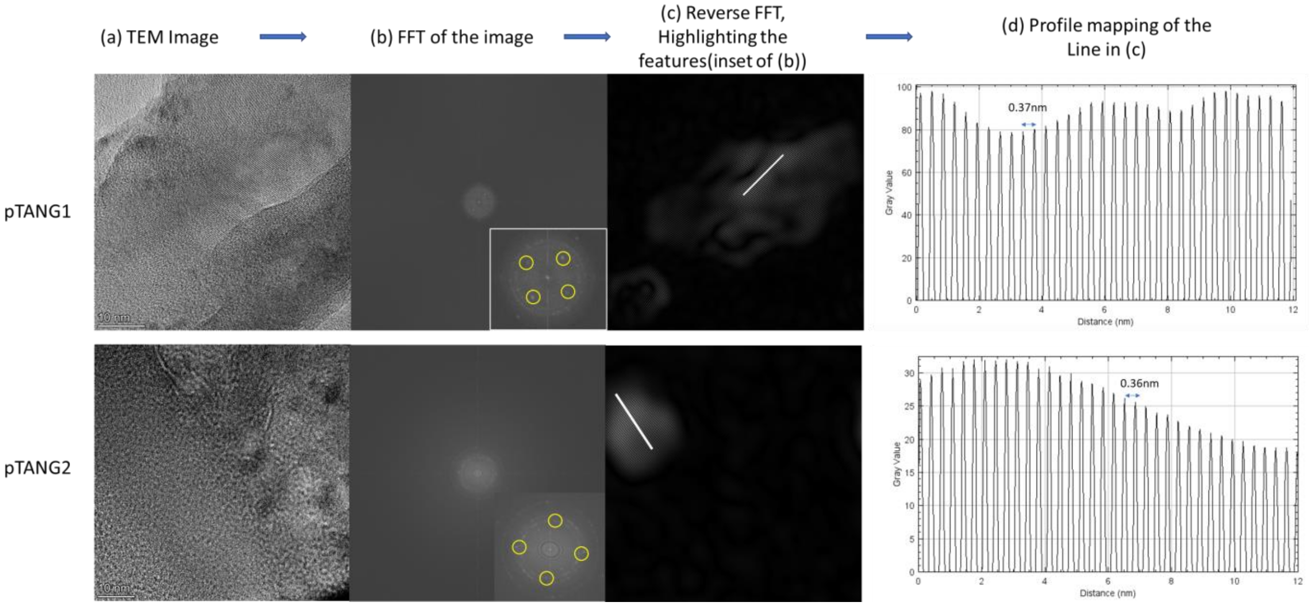

Figure 6.13. HR-TEM images of the dispersed pTANG2 sample in N-methylpyrrolidone. FFT-enhanced TEM images and the intensity profile showing a repeatable pattern of 0.36 nm in line with the expected value for the π-π stacked layers of COFs.

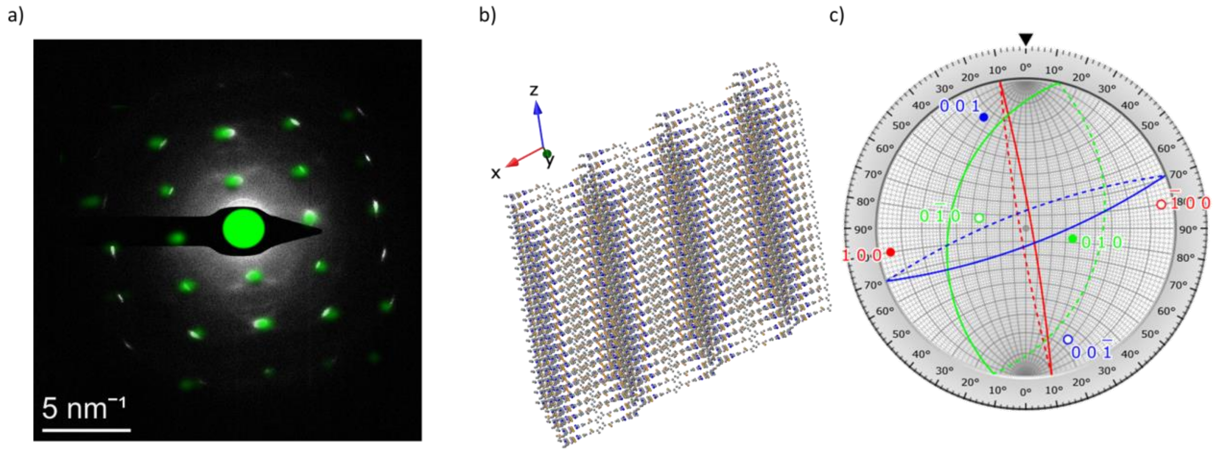

Figure 6.14. a) SAED of pTANG1 petal-like crystals and its simulated pattern based on the Pawley-refined unit cell (the green SAED), b) the unit cell direction of simulated SAED and c) its corresponding stereograph. Simulations were performed using Single Crystal 4.1. software.

6.9.9.Thermogravimetric analysis (TGA) of pTANG1 and pTANG2

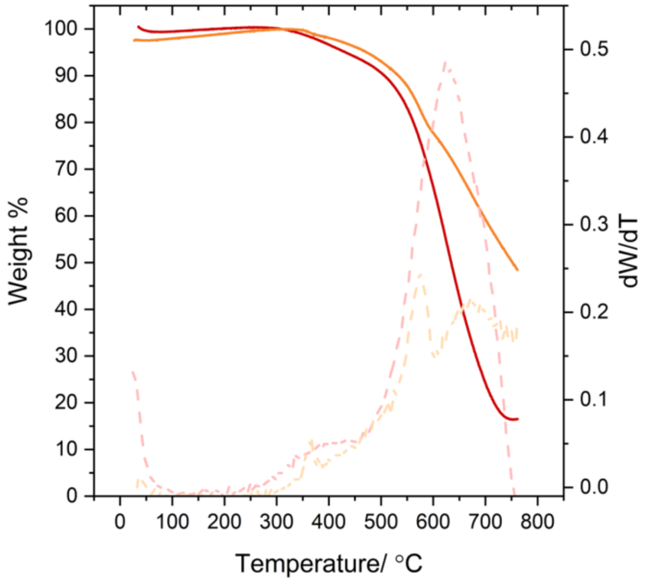

Figure 6.15. Thermal gravimetric analysis of pTANG1 (solid red line) and pTANG2 (solid orange line) and their corresponding first derivate curves (dashed lines) showing high thermal stabilities up to 400 ˚C under nitrogen.

6.9.10. Scanning electron microscopy (SEM) of pTANG1 and pTANG2

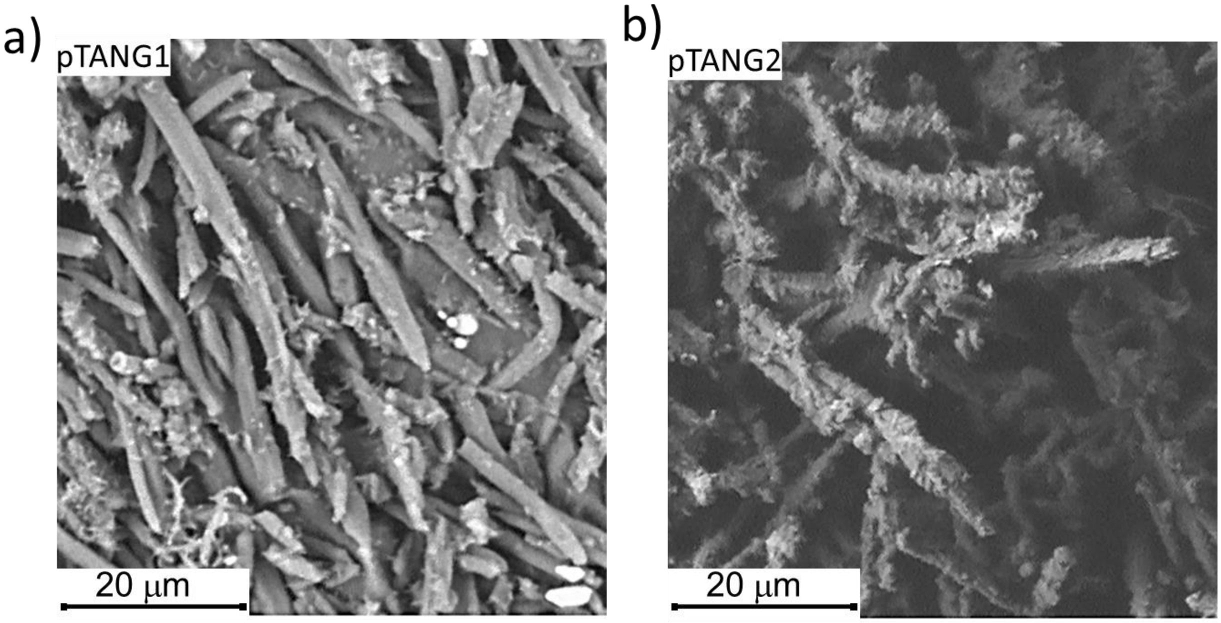

Figure 6.16. Scanning electron microscopy images of a) pTANG1 and b) pTANG2 synthesized from recrystallized TATANG precursors. Both COFs show similar morphology to that TATANG precursor (Figure 6.2a).

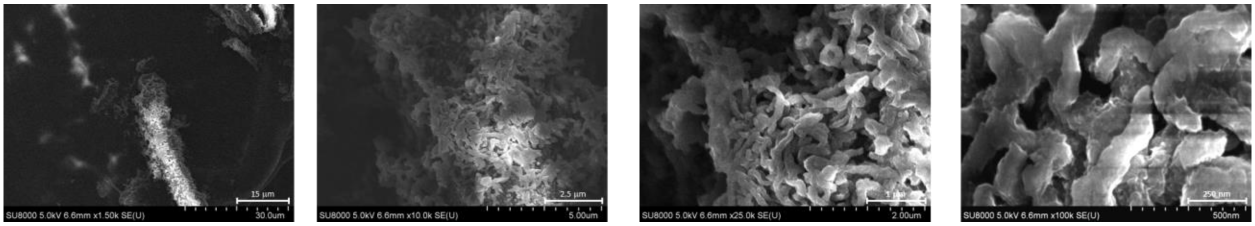

Figure 6.17. SEM images of pTANG1 with the subsequent zooming show that the large needle-like COF particles comprise ~1 μm COF plates.

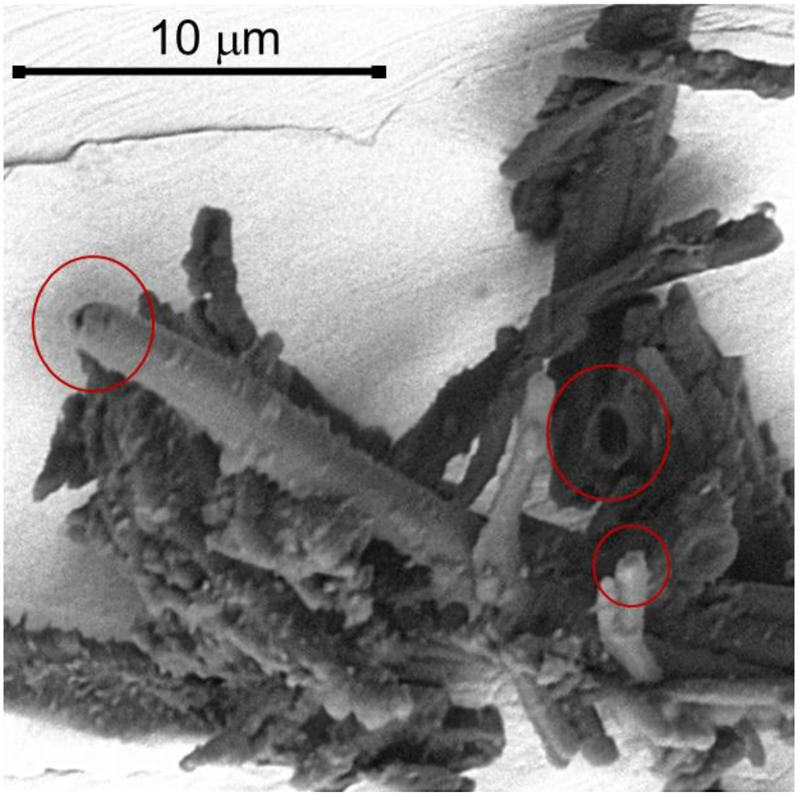

Figure 6.18. SEM images of pTANG1 particles showing hollow tube-shaped structures, corroborating formation of the COF on the surface of the TATANG monomer crystals and the dissolution of the monomer from the interior throughout the reaction.

6.9.11. X-ray diffraction (XRD) of the pTANG1 COF needles

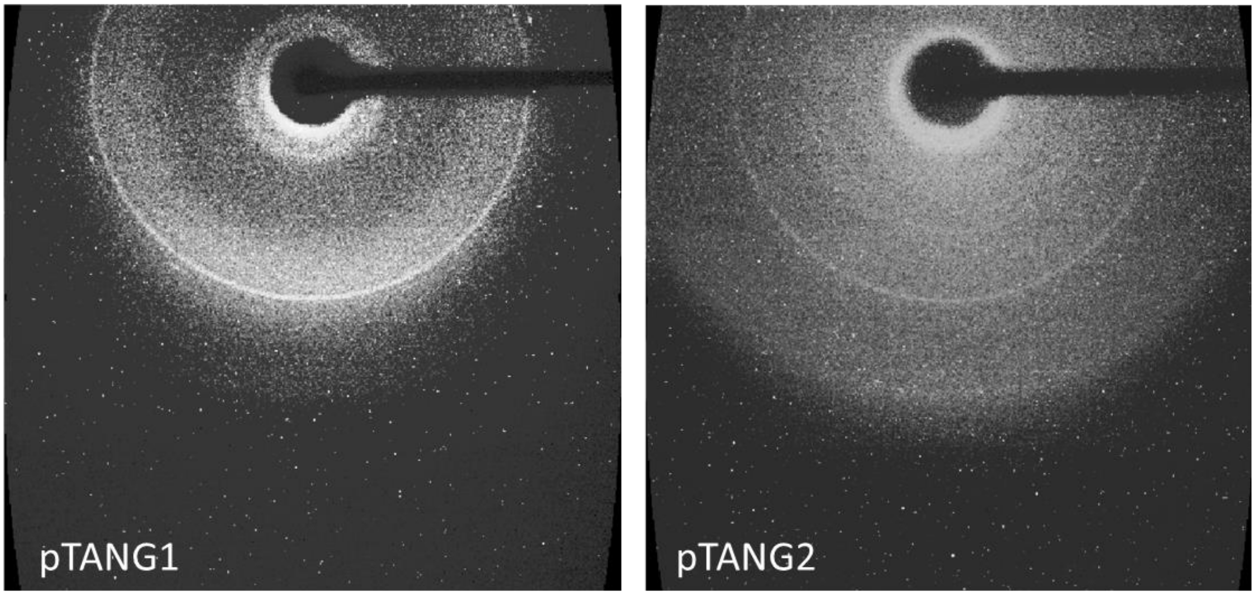

Figure 6.19. XRD of the needle-shaped particles of COFs, showing the polycrystalline nature of the particles.

6.9.12. Density functional theory calculations

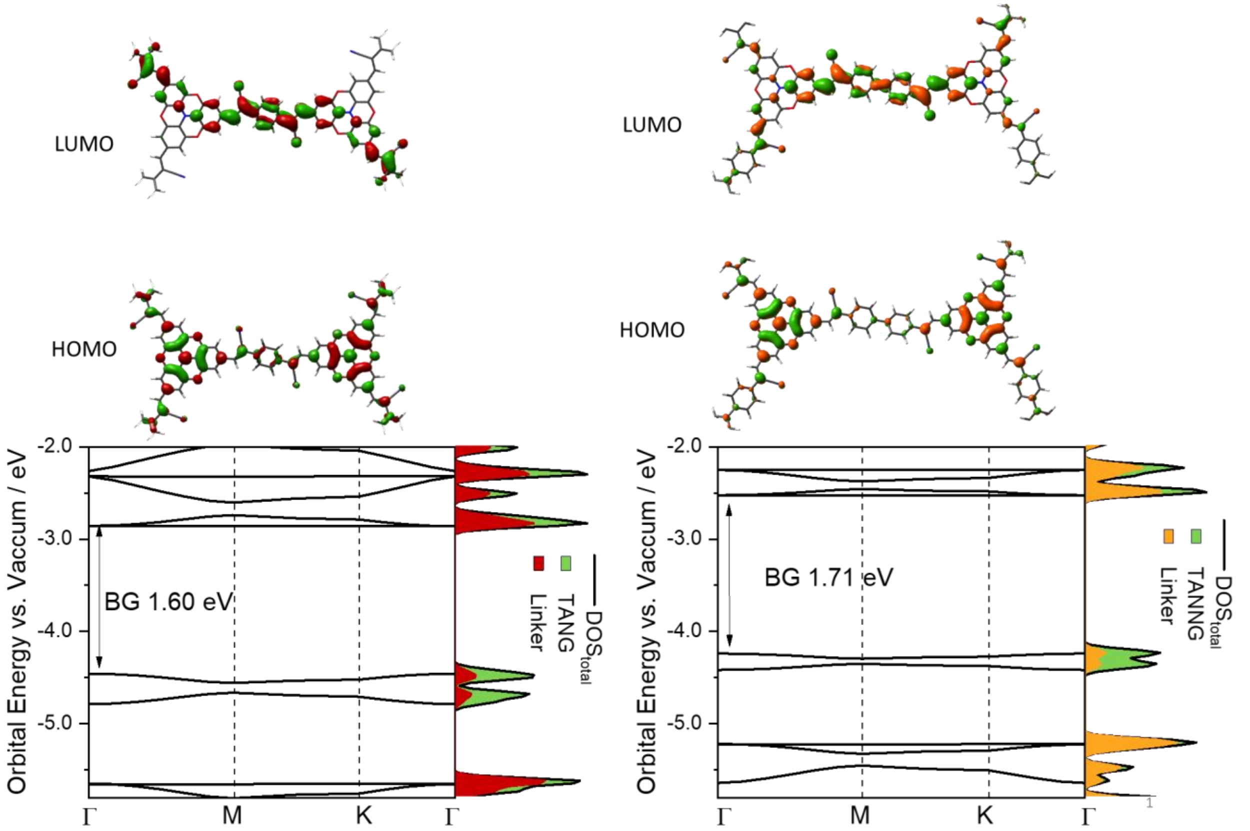

Figure 6.20. The orbital density of HOMO and LUMO of the pTANG1 (top left) and pTANG2 (top right) with HSE06 functional, showing that HOMO is mainly focused on TANG whereas the linker cyanovinylene groups dominate LUMO. The bottom graphs are the band structure and density of states (on the right Y-axis) for pTANG1 and pTANG2.

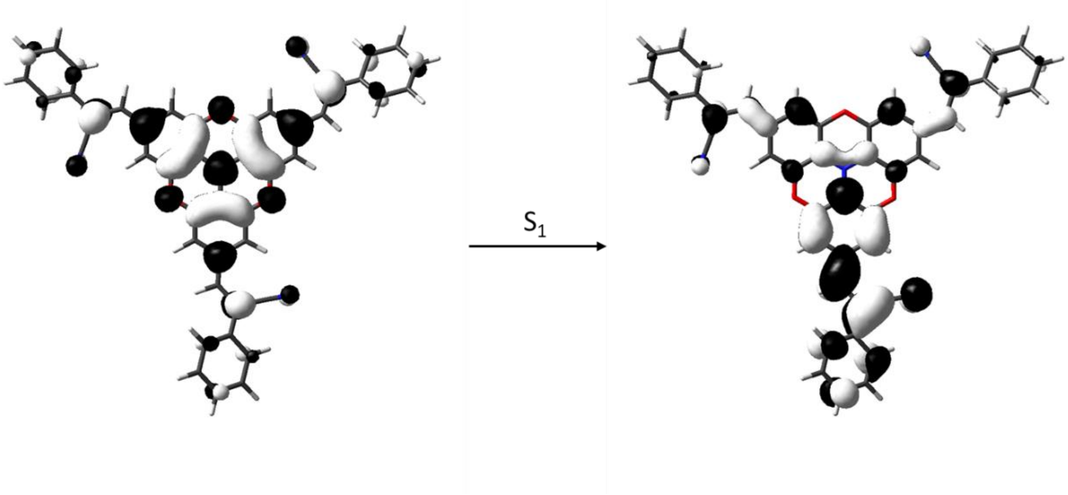

Figure 6.21. Natural transition orbitals (NTOs) for the first singlet excited state (S$_1$) of CNTANG, obtained using TD-DFT B3LYP 6-31G(d).

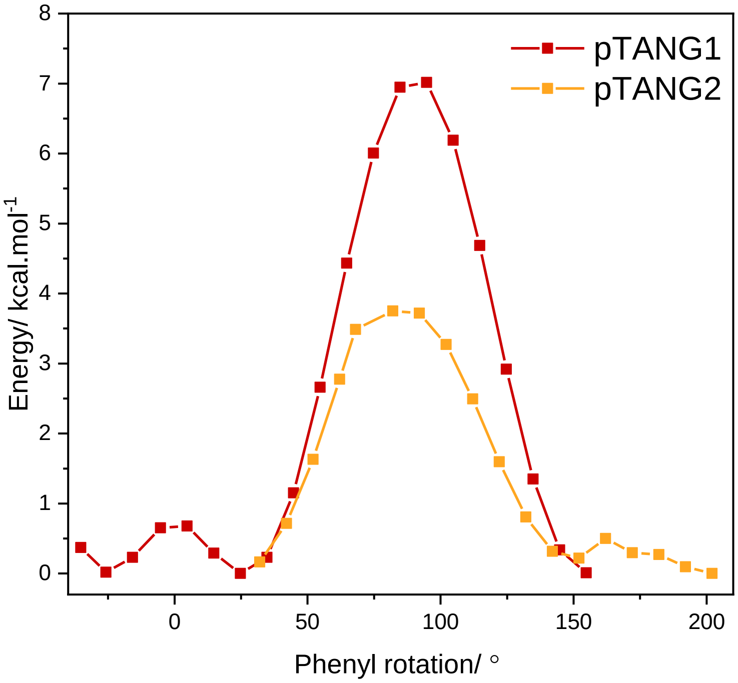

Figure 6.22. The energy of pTANG1 and pTANG2 unit-cell upon rotation of phenyl linkers (only 1 phenyl rotating while the dihedral of the other phenyl was fixed) using relaxed, periodic boundary condition DFT calculation (PBC-B3LYP 6-31g(d) using Gaussian 16 software).

6.9.13. Effect of dilution on photoluminescence of pTANG1

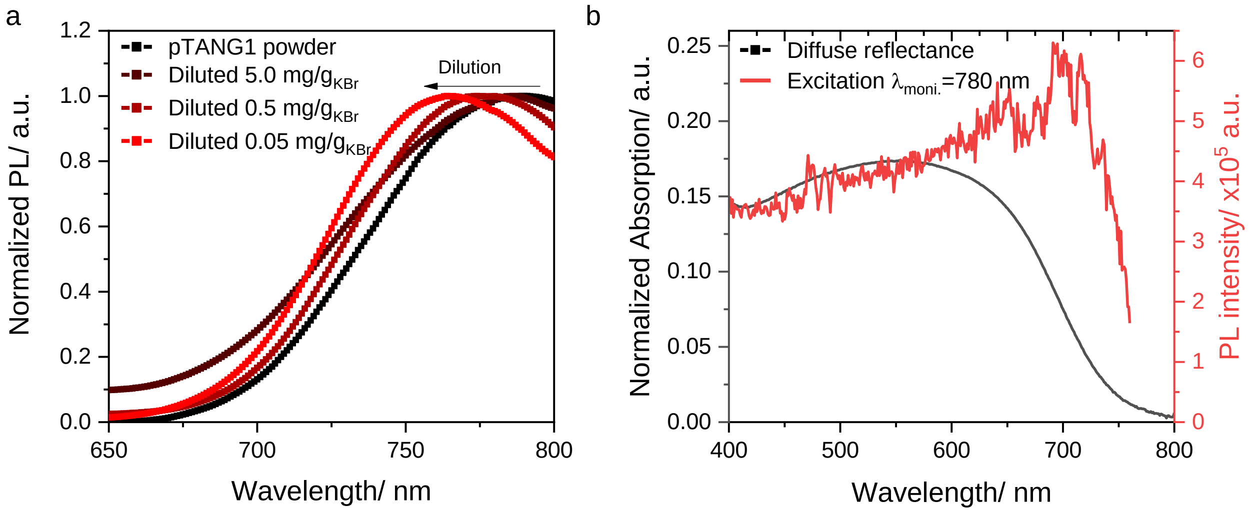

Figure 6.23. a) The effect of pTANG1 dilution, grounded in KBr, on the luminescence maxima of the emission. b) Diffuse reflectance spectra (black) vs. the excitation spectrum of the pTANG1 (monitored at 780 nm) showing a more efficient excitation at the band-edge energies ~730 nm despite its lower absorption cross-section.

6.9.14. NMR relaxometry

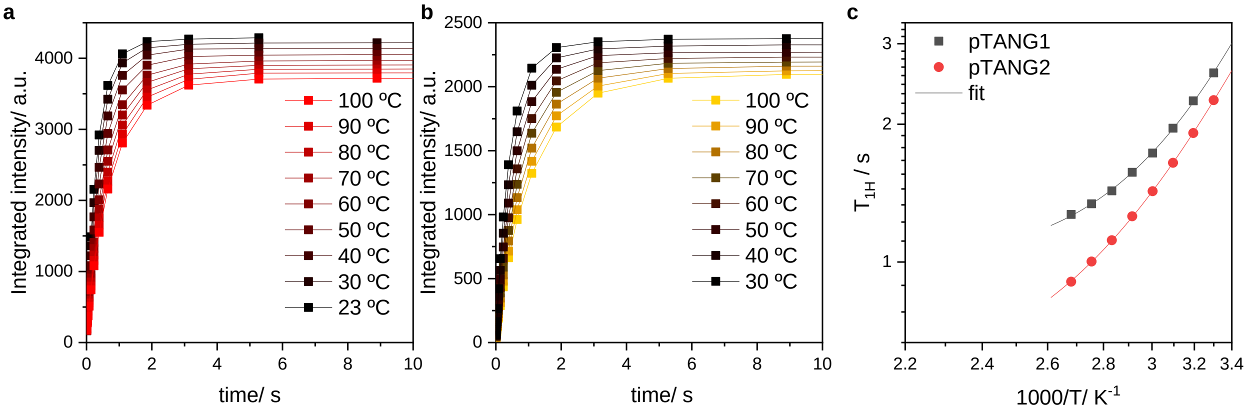

Figure 6.24. a,b) T1 relaxation time measurement at different temperatures and their corresponding exponential fitting for pTANG1 (a) and pTANG2 (b). c) the *T1* values of COFs vs. temperature show that atomic motions in pTANG1 are closer to the Larmor frequency with a faster decay over time, compared to pTANG2.

6.9.15. Characterizations of water absorption effects

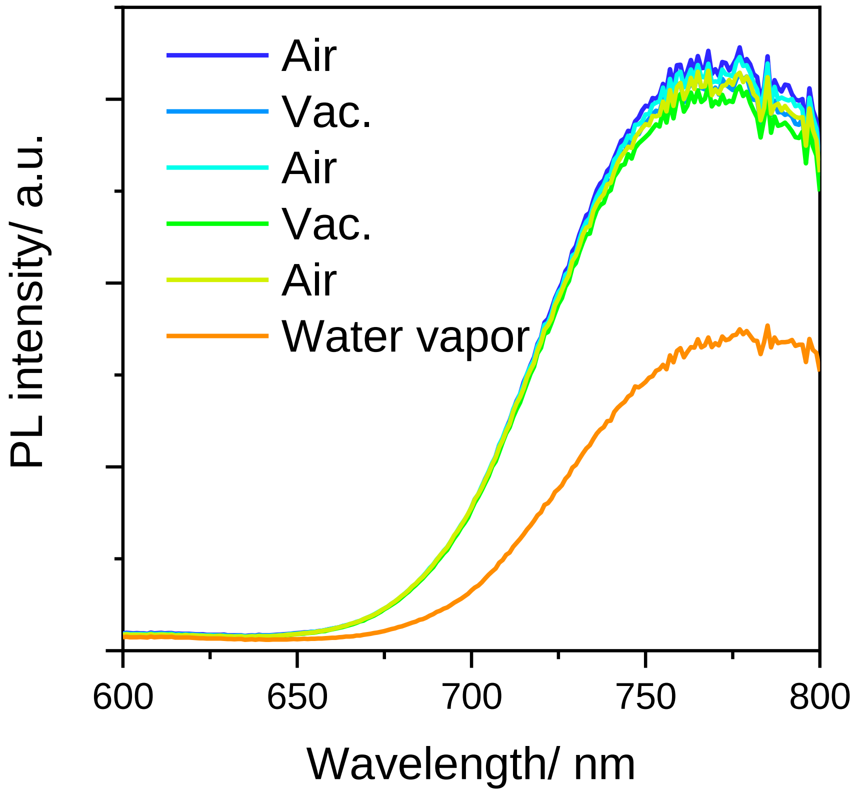

Figure 6.25. Effect of dry air, vacuum, and water vapor on the emission intensity of pTANG1.

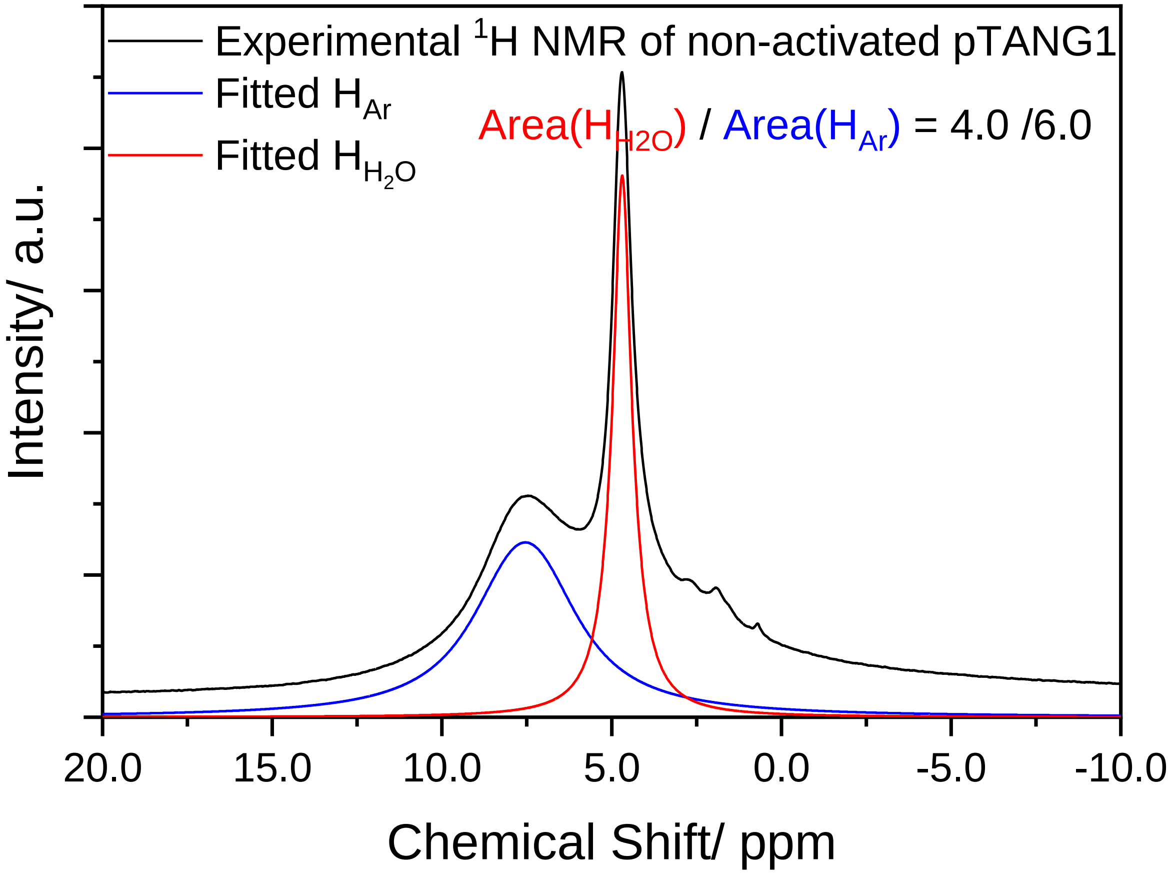

Figure 6.26. The deconvolution of the MAS-^{1}H NMR spectra of as-synthesized COF. Number of water per symmetric COF unit cell was then calculated according to $30H_{Ar}$:2n H_{water}.

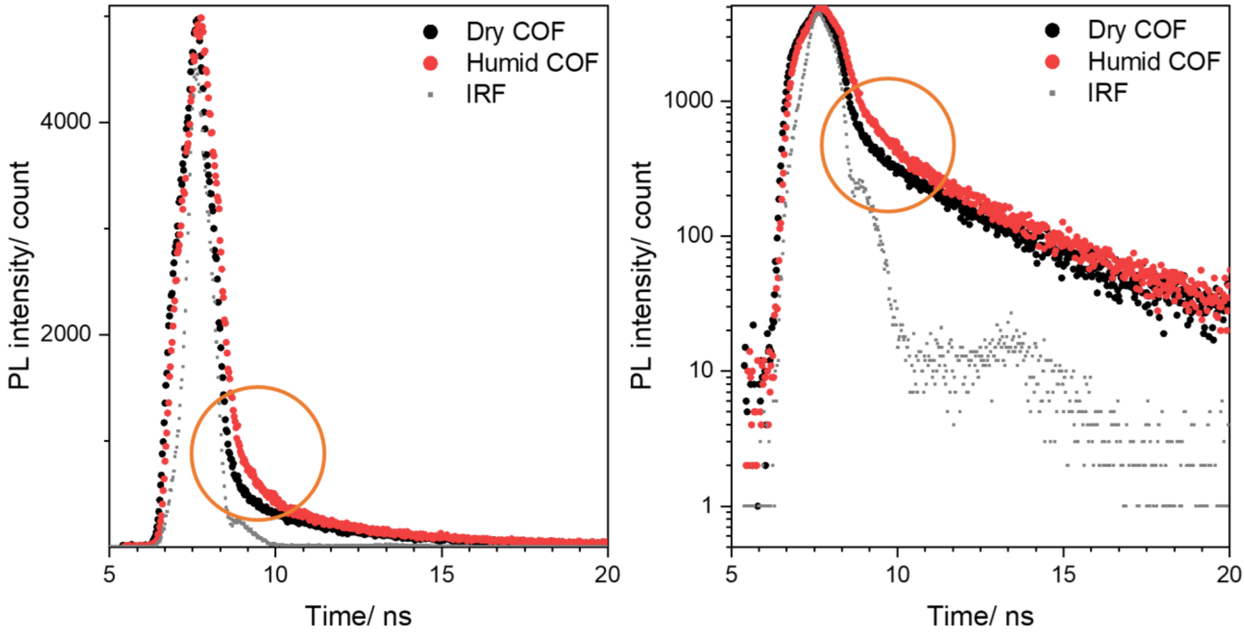

Figure 6.27. TCSPC lifetime analysis of the dry pTANG1 powders and the COF after humidity absorption (left is the linear intensity and right is logarithmic intensity) showing that only the short-lifetime species are affected by the water absorption.

6.9.16. References of Supplementary information

1. Kuratsu, M.; Kozaki, M.; Okada, K., 2, 2′: 6′, 2′′: 6′′, 6 ‐ Trioxytriphenylamine: Synthesis and Properties of the Radical Cation and Neutral Species. *Angew. Chem. Int. Ed.* **2005,** *44*, 4056-4058.

2. Li, Z.; Zhang, Y.; Xia, H.; Mu, Y.; Liu, X., A robust and luminescent covalent organic framework as a highly sensitive and selective sensor for the detection of Cu 2+ ions. *Chem. Commun.* **2016,** *52*, 6613-6616.

3. Jin, E.; Li, J.; Geng, K.; Jiang, Q.; Xu, H.; Xu, Q.; Jiang, D., Designed synthesis of stable light-emitting two-dimensional sp2 carbon-conjugated covalent organic frameworks. *Nat. Commun.* **2018,** *9*, 1-10.

4. Rager, S.; Jakowetz, A. C.; Gole, B.; Beuerle, F.; Medina, D. D.; Bein, T., Scaffold-induced diketopyrrolopyrrole molecular stacks in a covalent organic framework. *Chem. Mater.* **2019,** *31*, 2707-2712.

5. Yuan, M.; Ma, F.; Dai, X.; Chen, L.; Zhai, F.; He, L.; Zhang, M.; Chen, J.; Shu, J.; Wang, X., Deuterated covalent organic frameworks with significantly enhanced luminescence. *Angew. Chem. Int. Ed.* **2021,** *60*, 21250-21255.

6. Li, Z.; Geng, K.; He, T.; Tan, K. T.; Huang, N.; Jiang, Q.; Nagao, Y.; Jiang, D., Editing light emission with stable crystalline covalent organic frameworks via wall surface perturbation. *Angew. Chem. Int. Ed.* **2021,** *60*, 19419-19427.

Chapter 7

Discussion and Future Remarks

7.1. Discussion and outlook for future studies

7.1.1. On the room-temperature phosphorescence in molecular solids

Room temperature phosphorescence (RTP) has attracted increasing attention due to its peculiar photophysical process and potential applications, such as time-gated biological imaging/sensing,[1, 2] anti-counterfeiting, and data encryption,[3, 4] light-emitting,[5-9] and photovoltaic diodes,[10] nanowire lasing,[11] amplified photon up-conversion[12] and 3D displays.[13] Nearly all efficient phosphors are inorganic and organometallic complexes, and pure organic molecules capable of emitting efficient RTP (ORTP) are scarce. The quest to design ORTPs is for the promising advantages over their metal-containing counterparts, including reduced toxicity and environmental footprint, longer emission lifetimes, lower cost, and inexhaustible tunability of photophysical properties.

The scarcity of ORTPs arises from organic compounds' weak spin-orbit coupling to allow the spin-forbidden processes for both the generation of T_1 from an excited singlet state (usually S_1) and its radiative emission (transition from T_1 to S_0). Thus, most organics fail to populate the excited triplet state, and even if T_1 is formed, phosphorescence is most frequently outcompeted by non-radiative pathways, such as vibrational deactivation or quenching. Nevertheless, over the past several years, pure organic luminophores have been gradually developed to reach long-lived, efficient RTP through meticulous molecular and supramolecular designs.[14, 15] Intra-molecular designs such as incorporating heavy atoms (e.g., Br, I, Te, etc.)[16-21] and moieties capable of n-π* and π-π* transitions (for example, carbonyl, carboxyl, or triazine derivatives; El Sayed's rule)[3, 22-25] have been the prime design choices for ORTP scaffolds.

In turn, to inhibit competitive non-radiative deactivation pathways, ORTPs typically have to be embedded in rigid matrices such as polymers[26-28] and molecular crystalline[23, 29-31] solids. Triplet-triplet annihilation, where two T_1 states encounter one another and annihilate, has also been shown to play a prominent role in quenching the phosphorescence emission in pure crystals. As such, dilution of the precursors in rigid matrices, e.g., doping host crystals[4, 32-36] or isolation of the phosphorescent centers in the crystal structure,[28] have been used for efficient ORTPs. To this end, despite all the advances in molecular design and strategies to enhance the efficiency of

ORTPs, the field is still in its early stages, and the optimization of luminescent properties in ORTPs is still an empirical exercise.

Our acquaintance with the ORTPs was based on a serendipitous discovery of highly phosphorescence trioxoazatrangulenes (TANGOs). Initially, we designed and synthesized TANGOs and exploited them to achieve highly ordered 2D polymers showcasing semiconducting behavior with Dirac cones and high charge mobility.[37] Meanwhile, the unexpected solid-state luminescence of HTANGO and TBTANGO caught our attention since planar organic molecules tend to undergo aggregation-caused quenching, especially in the presence of halogen and carbonyl groups.[32, 38] Thus, we sought to determine the nature of TANGO's emission properties and found that it is indeed phosphorescent. By exploring other derivatives of TANGO, we discovered that the phosphorescence/fluorescence emission could be easily tuned in these molecular crystals through the rotational alignment of their molecules in the π-stacked crystals as a result of the steric bulkiness of the substituents.[39]

Since ORTPs are scarce, extending the scope of organic molecules capable of RTP is the key to uncovering practical design principles for these materials. In this thesis, we have addressed aspects concerning this challenge. In Chapters 2 and 3, we developed materials without heavy atoms and achieved highly efficient phosphorescence in these solids, starring HTANGO with a 42% phosphorescent quantum yield.

It is noteworthy to mention the role of impurities in the photophysics of these crystalline materials. The first discovered pure crystalline ORTPs probably originated from a small amount of impurities, as noted in the 1930s.[40] These impurities, mainly introduced during the synthesis, are not typically emissive in the pure form; however, when doped in a host, they dramatically affect the luminescence of organic crystals.[34] Several works in recent years have used doping as a deliberate introduction of impurities to achieve highly phosphorescent solids,[30, 41, 42]. In this context, the fundamental question of "what is a spectroscopically pure crystalline material?" is still open to debate.

For example, carbazole moieties have been one of the most common components of ORTPs, and several derivatives of it have been studied in the hope of extracting structure-property relationships behind ORTP solids.[43-50] However, a recent work by Bin Liu and coworkers showed that <0.5 mol% carbazole isomeric impurities present in commercial sources are responsible for the majority of the observed ultra-long phosphorescence in these materials, whereas a highly pure lab-synthesized carbazole failed to show any observable phosphorescence.[34]

During our investigations, we also found that ultra-low levels of impurities, undetectable by NMR, which are structurally similar compounds introduced during synthesis, profoundly influence the luminescent properties of organic crystals. For example, TANGO solids washed with organic solvents (excessive washing with $CHCl_3$, acetone, and ethanol) after the reaction showed a dual fluorescence/phosphorescence emission with only 8% photoluminescence quantum yield (PLQY). Sequential purifications reduced the fluorescence portion of the spectra, and the quantum yield of the crystals surged to 42% with only pure phosphorescence emission (Figure 7.1).

For future explorations of pure organic crystals, we recommend a rigorous examination of impurities and acquiring photophysical characteristics (for example, spectra, lifetimes) at each level of successive purification until these properties converge and remain unchanged upon further subsequent purifications.

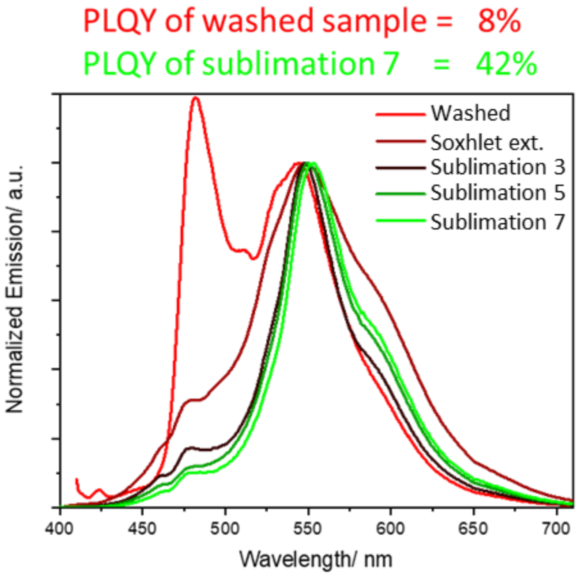

Figure 7.1. Steady-state spectra of the subsequently purified HTANGO after synthesis, showing the emergence of luminescent properties after five times sublimations, upon which the

fluorescence emission arising from impurities (~475 nm) is removed and the quantum yield dramatically enhanced.

Following the finding of Chapters 2 and 3, our group began exploring other possible structural designs based on acridone to expand the scope of organic phosphors and push the boundaries of ORTPs into other photophysical domains (e.g., near-Infrared NIR emission, thermally activated delayed fluorescence TADF, semiconductivity, etc.) in the hope of understanding principles underlying these materials.

Quinacridones (QAc) have received significant attention for their stability and promising optical and semiconducting properties, featuring some commercial pigments used to date.[51-53] The extended π-conjugation of QAcs significantly reduces the band-gap and potentially allows for synthesizing NIR-emissive ORTPs and/or those with semiconductive behavior.

N,N'-Dimethylquinacridone (compound 7.1) was synthesized as a potential semiconducting phosphor (Figure 7.2). The proposed compound 7.1 showed phosphorescence at room temperature. However, studying the photophysics of QAc derivatives proved difficult due to their low solubility and polymorphic nature, which requires additional scrutiny to establish the photophysics-structure relations. [52, 53]

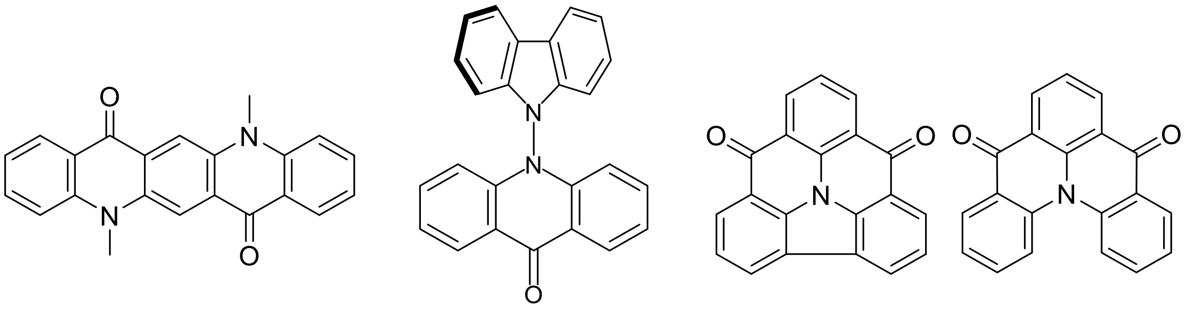

7.1 7.2 7.3 7.4

Figure 7.2. Acridone-based ORTP molecules currently under investigation in the Perepichka group.

We further designed non-symmetrical Ar_1N-NAr_2 carbazole-coupled acridones (compound 7.2). The N-N bond provides almost 90˚ alignment of the coupled moieties. Using this scaffold, twisted donor-acceptor structures could also be designed to study the effect of electronics and crystal packing on the ORTP of these compounds. The highly twisted structure also allows for the potential emergence of TADF. TADF, by which the singlet and triplet states can easily interconvert (through intersystem crossing ↔ reversed-intersystem crossing) due to small singlet-triplet energy gaps (ΔE_{ST}), has become a hot research topic in recent years.[54] A particular interest for these materials is their ability to utilize the non-emissive triplet states produced upon 75% of charge recombination events in light-emitting diodes and partially convert them into an emissive singlet state. This strategy allows for theoretical electroluminescent internal quantum yields of 100% compared to the 25% limit of fluorescent LEDs. A common strategy to achieve TADF is the design of twisted donor-acceptor moieties which separate the HOMO and LUMO orbitals, resulting in very small ΔE_{ST}. We synthesized compound 7.2, showing highly phosphorescent crystalline solids, and we are currently investigating its photoluminescent behavior as well as different permutations on the carbazole (donor) and acridone (acceptor).

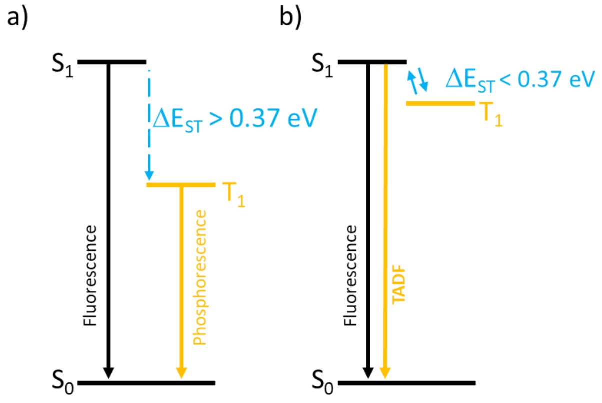

Figure 7.3. Energy level diagram depicting the a) phosphorescence emission and b) TADF emission depending on the energy gap between singlet and triplet excited states ΔE_{ST}.

Another relevant strategy toward TADF materials is the separation of HOMO-LUMO by the multi-resonance effect (MRE).[55] Having multiple influences on the resonance structure from different functional groups or heteroatoms present in the molecule induces the localization of the HOMO and LUMO on different atoms. This minimizes the exchange energy between the electrons separated by excitation, resulting in very small ΔE_{ST}.[56] We have designed TANGO mimics, with open bridges or direct C-C bridges (carbazolyl moiety) instead of carbonyls of TANGO (7.3 and 7.4), and their photophysics is currently under investigation in the Perepichka group.

There still exist several knots to be untangled in the field of ORTPs. Efficient NIR-emissive RTP solids are also very rare,[57] mainly because ultralong triplet lifetimes of organic materials (μs-s) make vibrational decays (ca. ps) highly effective non-radiative relaxation pathways for the triplet exciton. A possible solution to this challenge can be using low-bandgap π-conjugated polymers with enhanced ISC to result in NIR-RTP. The narrow band gap might also result in charge transport and semiconducting possibilities for further use as phosphorescence LEDs.[5]

Up to here, we mainly discussed the intrinsic nature of the triplet and singlet excitons in a solid; nonetheless, their dynamics play a significant role in determining the luminescent outcomes of the materials as well as the performance of optoelectronic devices.[58] Although the effect of triplet dynamics in molecular solids has been acknowledged, the nature of exciton dynamics is not well understood. Exciton dynamics is naturally a highly complex phenomenon, and its detection methods typically require complex characterization techniques,[59] thus making the engineering of delocalized excitons in organic solids a far-reaching goal.

In 2015, Hildner and coworkers reported that singlet excitons in carbonyl-bridged triphenylamine derivatives (having TANGO, termed CBT in the article, as the core) could propagate on several micron distances at room temperature, limited by the size of their aggregated fibers. Their designed dye molecules form an H-aggregate system (cofacial alignment of monomers).[60] Two years later, Aspuru-Guzik et al. provided a detailed theoretical analysis of exciton transport in 1D chains of TANGO-based dyes and suggested that the singlet exciton transport should be about 5-10 times shorter than the reported experiments by Hildner et al. unless other processes such as triplet exciton transport are involved.[61] Our discovery of the bright phosphorescence emission of TANGOs with co-facial alignment (described in Chapter 2) further strengthened the possibility of triplet exciton transport in Hildner's report.

We further discovered that when the tip of a large crystal of HTANGO is excited via a focused UV spot, the whole crystal will glow, with the emission exhibiting a monotonic redshift as one moves away from the excitation source (Figure 7.4.). Conversely, the crystals of *t*BuTANGO, which did not exhibit RTP in the solid state, did not show such behavior and only emitted at or near the excited spot. This observation also eliminates the waveguide effect as an explanation for HTANGO's spatially resolved emission based on the similar size and morphology of tBuTANGO and HTANGO crystals. This observation led us to believe that the triplet states in HTANGO undergo the migrations over ultra-long ranges responsible for these observations. In this context, V. Padzorov and coworkers have shown that triplet exciton diffusion in rubrene (a bench-mark organic semiconductor) occurs over micrometer distances (2-8 µm), whereas singlet excitons can only diffuse over nanometer distances (10-50 nm).[59]

Such long exciton diffusion could be revolutionary to organic photophysics and optoelectronics,[62] since exciton transport in organic materials is one of the key parameters in photovoltaics and quantum entanglement devices.[63] To investigate our described observation of the TANGO crystals in detail, we have established a collaboration with the molecular photophysical research group of Prof. A. Monkman at Durham University.

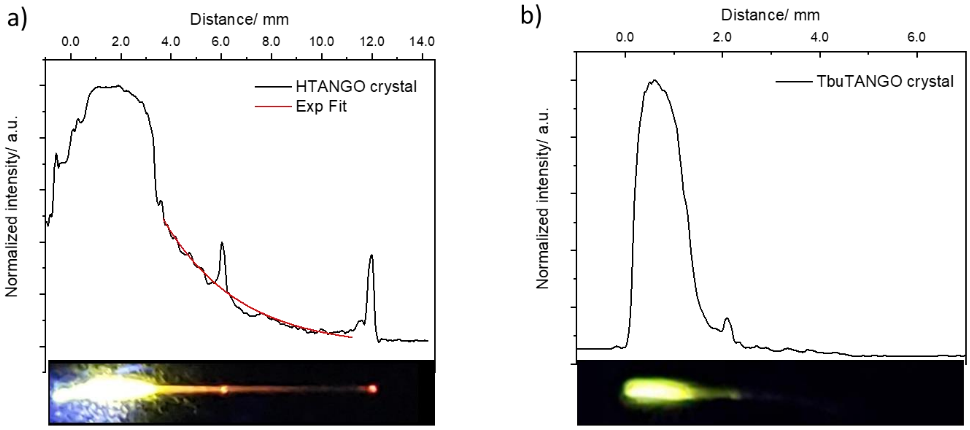

Figure 7.4. The gray scale intensity of the captured photographs (bottom) graphed vs. length of the a) HTANGO single crystal b) *t*BuTANGO single crystal.

7.1.2. On exploiting Covalent Organic Framework as predictable RTP solids

A general challenge we faced while exploring organic solids to establish structure-photoluminescent relationships was the ever-lasting formidable problem of crystal structure predictability (CSP).[64, 65] Although significant research has been done on CSP, the complexity of molecular interactions has kept the field nearly at a similar pace, as it was in the 1980s when John Maddox, editor of the journal "Nature" – a chemist and physicist by training – stated that "*One of the continuing scandals in the physical sciences is that it remains in general impossible to predict the structure of even the simplest crystalline solids from a knowledge of their chemical composition.*"[66]

A possible solution to this problem is to instead exploit self-assembled materials, such as covalent organic frameworks (COFs), as structurally predictable solids for our purposes.[67, 68] Since Yaghi's pioneering work, COFs have attracted a great deal of interest in materials chemistry.[69] Their ordered 2D/3D structures enable the design of new topologies previously unexplored in molecular solids, and the final topology of the COF can be readily predicted using an understanding of the rules of reticular chemistry (knowledge of the symmetry of the precursor and linkers).[65] At the same time, strong covalent bonding between the units provides remarkable stability and potentially strong electron coupling. Nevertheless, in this thesis, our interest in 2D-covalent organic frameworks is mainly due to the reticular aspect of COF design.

There has been significant progress and interest in the design and synthesis of fluorescent COFs.[70-74] However, RTP COFs remained unexplored until our recent work on covalently doped phosphorescent COFs (in Chapter 5). We showed that in-situ doping of the COF backbone with heavy atom-containing isostructural building blocks does not significantly perturb the COF topology but substantially increases the intersystem crossing. The COF's rigidity minimizes the triplet states' vibrational relaxation, while the separation of excitons suppresses triplet-triplet annihilation. Using this approach, we successfully synthesized and characterized 12 highly emissive COFs with different dopants and doping concentrations. The well-defined porous nature of the doped COFs provides a unique opportunity for rapid access/utilization of the triplet excitons and results in ratiometric oxygen sensing with an ultra-wide dynamic detection range and fast response time.

In the future, one might expand the covalent-doping strategy into other more stable and robust COFs, such as the Schiff-base[75] and olefin-linked COFs,[71, 76] that will also lead to narrower band gaps and potential electrical conductivity. In Chapter 5, we show that phosphorescent COFs show a strong TTA-induced delayed fluorescence that can be tuned via dilution of the phosphor. Further investigations are required to understand the nature of the triplet exciton transport and their inter/intra-layer energy transport contributions. Furthermore, one might utilize the open porosity of the COFs to externally dope and achieve phosphorescence emission of the guests embedded in the porous and rigid COF matrix.

7.1.3. On advances in the synthesis of functional COFs

Our interest in COFs started even before the discovery of phosphorescence in TANGOs. As a symmetric and planar building block, TANGO is deemed an ideal precursor for 2D-polymer formation. In collaboration with the surface scientists and physicists in the Rosei group, we made the first mesoscale monolayer 2D- conjugated polymers on Au surface.[37] We explored their exotic electronic behaviour, including high charge mobility and Dirac cone, which has remained state-of-the-art in the field. In 2019, we reported highly emissive (up to 52% PLQY) vinylene-linked COFs using aldol condensation of 1,3,5-trimethyltriazine and later discovered their 2D/3D inter-layer [2+2] reversible cycloaddition.[77, 78] Concurrently, we reported crystalline 2D-trioxaazatriangulene (TANG)-linked COFs using Schiff-base condensation of triamino TANG with 2,5-dihydroxyterephthaldehyde, resulting in semiconducting and paramagnetic property.[79]

Boroxine and dioxaborole linkages are two of the most widely used synthons in COF formation and have been exploited in the design of fluorescent COFs for over a decade.[72, 80, 81] Our attempts to realize boroxine- and dioxaborole-linked TANGO COFs (Figure 7.5), however, proved challenging due to the insolubility of the multifunctional tri-boronic acid TANGO (TBOTANGO) and its subsequent protodeborylation in the presence of water, the byproduct of condensation.[82] Additionally, most formed COFs suffer from optical impurity due to the partial oxidation of the catechol linkers, which drastically perturbs the luminescence of the resulting COF.[83] Thus, we called for a novel reaction route to make the TANGO-based COFs from more stable and soluble precursors, for example, tris(pinacolyl boronate ester)TANGO (TBpinTANGO) instead of TBOTANGO as in conventional synthesis.

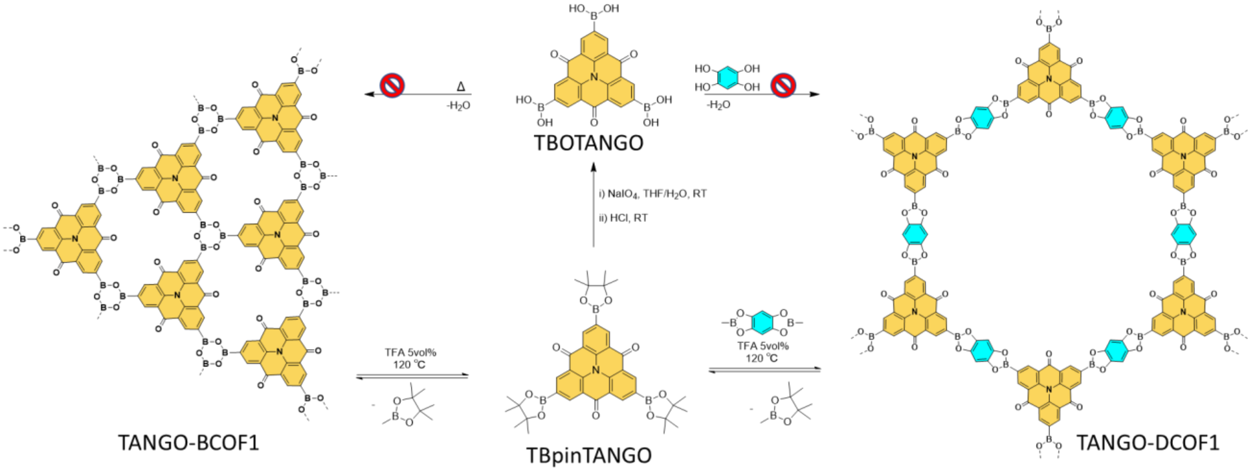

Figure 7.5. Proposed reaction routes toward boroxine (TANGO-BCOF1) and dioxaborole (TANGO-DCOF1) -based COFs from TANGO. The conventional route (top route) is challenging for the insolubility of the TBOTANGO and its proto-deborylation in reaction conditions. The bottom route using our reported metathesis (right) and transesterification (left), however, overcomes those challenges by using the highly soluble TBpinTANGO without the production of water.

In chapter 4, we have provided a solution to boroxine and dioxaborole synthesis challenges. We were able to solve the solubility and stability issue of the multifunctional arylboronic acids and catechols, using Bpin-protected arylboronic acids and methylboronic acid-protected catechols instead, with superior stability and solubilities compared to the free counterparts. The altered equilibrium conditions (reaching K_{eq}~1) allowed for a more efficient error-correction mechanism, in some cases leading to highly crystalline COFs. Furthermore, in the metathesis reaction, the byproduct is methylboronic pinacolate ester, which allows the use of hydrolytically unstable precursors (as showcased in the synthesis of B2HHTP). Using our developed metathesis and transesterification reactions, we have synthesized TANGO-DCOF1 and TANGO-BCOF1 (Figure 7.5). Their photophysics and structural characterizations are currently under investigation in Perepichka group.

This work has opened endless possibilities to explore functional building blocks of the COFs, for example, the exploration of large π-conjugated structures of multivalent boronic acids with more than four substitutions such as hexakisBpin hexabenzocoronene (Figure 7.4).

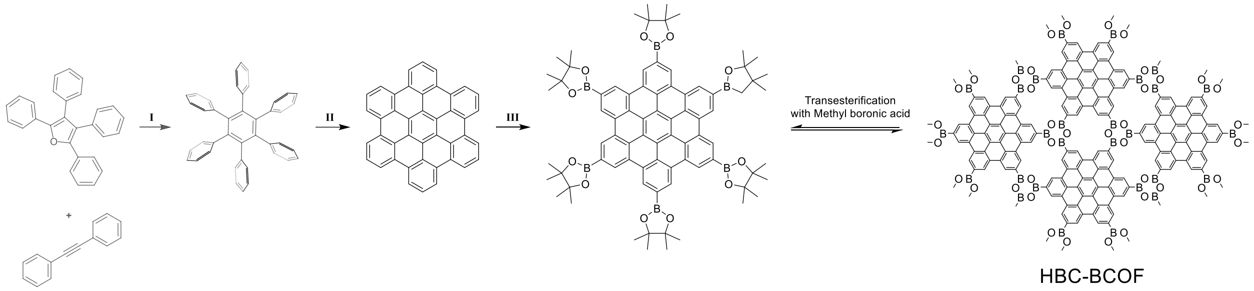

Figure 7.6. Synthesis of hexakisBpin hexabenzocoronene and its proposed boroxine-linked COF using transesterification. The reported reaction conditions are I) PhOPh, 250 °C, 24 h; II) $FeCl_3$ (in $MeNO_2$), DCM, RT. III) HBpin, $[Ir(OMe)cod]_2$, cyclopentyl methyl ether, 80 °C, 48 h.[84]

Furthermore, the faster equilibrium conditions in transesterification inspired us to use mechanochemical force to drive the reaction. Mechanochemistry provides green synthesis aspects to COF synthesis and opens future possibilities for large-scale production and exploitation of new materials that cannot be synthesized in conventional solvothermal synthesis.[85] To date, only Schiff-base linked covalent organic frameworks have been prepared by mechanochemistry, mainly due to the spontaneous imine condensation reaction at room temperature and its subsequent favor of equilibrium toward the products (COF).[86-88] In this context, boroxine and dioxaborole-based COF formation, as highly reversible reactions, have not been realized using mechanochemistry.

In collaboration with the Friščić group, we used trimethylboroxine, a condensed form of methylboronic acid, as the mediator of the COF formation reaction to synthesize crystalline 3D and 2D COFs at room temperature in 30 min. Our mechanochemically synthesized COFs require only 50 µL of solvent/100 mg of COF using ball-milling or resonance acoustic mixing techniques, incomparably more efficient and greener than the conventional reaction, which requires 72 h of reaction time at 120 °C, and >6 mL/100 mg of COF.[73, 83]

Chapter 6 reports the first NIR-emissive covalent organic framework as a similarly scarce class of emissive solid-state materials to ORTPs. Aggregation-caused quenching and effective vibrational relaxation at room temperature has made synthesizing organic NIR-emissive solids a formidable challenge.[89] In this chapter, we show the effects of linker electronics, temperature, structural flexibility, and humidity on the NIR emission of the COFs, hoping to pave the way toward the rational design of these materials for optoelectronic applications. In the future, exploring other donor-acceptor emissive building blocks could be the initial step toward expanding the scope of NIR emissive solids. Furthermore, photocleavable and bioactive molecules could be implemented in these COFs for targeted drug release and imaging.

7.2 Contributions to original knowledge

In Chapter 2, we explored the relationship between crystal structure and luminescent properties in azatriangulenetrione (TANGO) derivatives. Following our serendipitous discovery of highly-efficient ORTP in HTANGO crystal (PLQY up to 42%), we synthesized and investigated a series of new TANGO derivatives with different halogen and *t*-Bu substituents (TCTANGO, TBTANGO, TITANGO, and *t*BuTANGO). Despite similar photophysical properties in solution, these derivatives show either pure fluorescence or almost pure phosphorescence in the solid state, depending on their packing. Using X-ray crystallography and DFT calculations, we showed that the rotation of the molecules within the columnar π-stacks, controlled by the steric bulkiness of the substituent, is responsible for the different luminescent properties. The findings of this chapter are published as an article: E. Hamzehpoor, D. F. Perepichka, "Crystal Engineering of Room Temperature Phosphorescence in Organic Solids." *Angew. Chem. Int. Ed.* **2020**, 59, 9977-9981.

In Chapter 3, we have synthesized a series of six N-substituted acridone dyes, a structurally similar class of molecules to TANGOs, to further understand the effect of crystal structure on their luminescent behaviour. We designed a group of substituents with varying electronic and steric effects: N-methyl, N-phenyl(Ph), 4-CNPh, 4-OMePh, 4-tBuPh, and 4-SF_5Ph. According to solution photophysics and DFT-analysis, we showed that the N-substitution has not perturbed the electronic level of the acridone core. However, varying RTP emission and, in some cases, triplet-triplet annihilation (TTA)-induced delayed fluorescence was observed in the derivatives crystalline solids. This data led us to find a strong correlation between the acridone crystal packing and their TTA efficiency; TTA appeared strong in N-aryl acridones with small substituents, i.e., Ph, OMePh, and CNPh with antiparallel π-stacks; however, it was measurably weaker in MetAc with co-parallel π-stacks (despite shorter π-distances) and non-existent in the other derivatives with isolated π-dimers.

The findings of this chapter are published as an article: E. Hamzehpoor, C. Ruchlin, Y. Tao, J. E. Ramos-Sanchez; H. M.Titi, G. Cosa, D. F. Perepichka, "Room Temperature Phosphorescence vs. Triplet–Triplet Annihilation in N-Substituted Acridone Solids." *J. Phys. Chem. Lett.* **2021**, 12, 6431-6438.

In Chapter 4, we addressed the insolubility and instability of the arylboronic acids and polyfunctional catechols challenges in the synthesis of boroxine and dioxaborole-linked covalent organic framework (COF). We designed a versatile synthetic approach using transesterification (or metathesis) of pinacol arylboronates with methylboronic acid-protected catechols (MBA; or corresponding MBA-protected catechols) which are highly soluble, easy to purify, and bench-stable compared to free arylboronic acids and catechols used in conventional COF synthesis. Furthermore, the designed metathesis reaction does not form water as a byproduct, nor does it rely on it for the reversibility and error-correction mechanism (critical for achieving crystallinity). This opens the possibility of exploiting hydrolytically unstable building blocks. We confirmed the generality of this synthetic strategy by comparing it with seven known COFs, earlier prepared by the classical boronic acid/catechol condensation. To further showcase the applicability of this synthetic method, we obtained two novel COFs, Py4THB and B2HHTP, which synthesis was previously precluded by the insolubility/instability of the boronic acid precursors. The dioxaborole COFs synthesized using a metathesis polymerization have higher optical purity and low density of defects vs. those synthesized by conventional polycondensation due to the elimination of unprotected, chemically sensitive catechols. In addition to being a valuable new tool for the design/synthesis of new COFs, our approach introduced the use of liquid NMR to study the mechanistic studies of COF formation, for the first time. The findings of this chapter are published as: E. Hamzehpoor; A. Jonderian; E. McCalla; D. F. Perepichka; "Synthesis of Boroxine and Dioxaborole Covalent Organic Frameworks via Transesterification and Metathesis of Pinacol Boronates." *J. Am. Chem. Soc.* **2021**, 143, 13274-13280.

In Chapter 5, we reported a novel strategy for the design of phosphorescent COFs via *in-situ* doping of halogen-containing precursor molecules in the non-substituted COF building block for the first time. Such covalent doping allowed the optimization of RTP efficiency (phosphorescence quantum yields ≤ 29%, total photoluminescence quantum yields ≤ 40%) in COFs and the control of the phosphorescence/fluorescence ratio using different dopants and doping concentrations. We found that the solvent (mesitylene) guest molecules partially suppress oxygen permeation through the COF pores, allowing us to achieve RTP in air. The permanent porosity endows the

COFs with highly dynamic O_2-sensing capabilities of more than eight orders of magnitude (from 762 to 10^{-5} torr). Cumulatively, in this work, we established the principles for the rational design of phosphorescent COFs. The findings of this chapter are published as: E. Hamzehpoor, C. Ruchlin, Y. Tao, C.-H. Liu, H. M. Titi, D. F. Perepichka, Efficient room temperature phosphorescence of covalent organic frameworks through covalent halogen doping. *Nat. Chem.* **2023**, 18, 83-90.

In Chapter 6, we explored p-conjugated (cyanovinylene-linked) covalent organic frameworks based on trioxaazatriangulene (TANG) building blocks as the first example of near-infrared (NIR) emissive covalent organic frameworks (COFs). Previous challenges regarding the TANG molecule synthesis (<20% in 6 steps) were overcome in this work by developing a new synthetic strategy to improve the yield to 40% in 3 steps. Knovenagel condensation of aryldiacetonitriles resulted in crystalline and porous (cyano-vinylene-linked)-COFs with robust C=C covalent links between the monomers that bring outstanding stability to the framework and enhance the π-conjugation. We found that the partial charge transfer between the TANG nodes and the linker allows for small band gaps as low as 1.54 eV and results in NIR emission with λ_{max} = 789 nm extending up to 1100 nm with ~1.0% efficiency in the solid-state. The NIR emission could be easily tuned via the strength of electron-withdrawing cyano-vinylene linkers, as well as the flexibility of the linker in the solid framework. Furthermore, we found that COFs absorb ~20 wt.% water despite the lack of strong H-bonding motifs in the pores, resulting in quenching their emission (almost half of the intensity of dried samples). We further discovered that the macroscopic morphology of the COF matches the initial morphology of the reactants which could be used as a means to synthesize needle-shaped or small dispersed particles.

7.3. Conclusion

Overall, in this thesis, we present three new families of phosphorescent materials: substituted trioxoazatriangulenes (in Chapter 2), N-alkyl and N-arylacridones (in Chapter 3), and covalently doped Halogen-containing boroxine-linked COFs (in Chapter 5), furthering our understanding of the effect of molecular interactions on the ORTP of organic solids.

While exploring RTP solids, we developed a new reaction route toward optically pure boroxine- and dioxaborole-linked COFs (in Chapter 4) and synthesized the first NIR-emissive COF using trioxaazatriangulene (Chapter 6). Thus far, our achievements in this thesis to understand the luminescent nature of organic solids can be accounted as pebbles and shells on the shore "*whilst the great ocean of truth with myriads of charms and intrigues lay all undiscovered before [us]*" (referring to the quote by I. Newton).[90]

7.4. References

1. Yang, J.; Zhen, X.; Wang, B.; Gao, X.; Ren, Z.; Wang, J.; Xie, Y.; Li, J.; Peng, Q.; Pu, K.; Li, Z., The influence of the molecular packing on the room temperature phosphorescence of purely organic luminogens. *Nat. Commun.* **2018,** *9*, 840.

2. Fateminia, S. M. A.; Mao, Z.; Xu, S.; Yang, Z.; Chi, Z.; Liu, B., Organic nanocrystals with bright red persistent room-temperature phosphorescence for biological applications. *Angew. Chem. Int. Ed.* **2017,** *56*, 12160-12164.

3. Gu, M.; Shi, H.; Ling, K.; Lv, A.; Huang, K.; Singh, M.; Wang, H.; Gu, L.; Yao, W.; An, Z.; Ma, H.; Huang, W., Polymorphism-dependent dynamic ultralong organic phosphorescence. *Research* **2020,** *2020*, 8183450.

4. Su, Y.; Phua, S. Z. F.; Li, Y.; Zhou, X.; Jana, D.; Liu, G.; Lim, W. Q.; Ong, W. K.; Yang, C.; Zhao, Y., Ultralong room temperature phosphorescence from amorphous organic materials toward confidential information encryption and decryption. *Sci. Adv.* **2018,** *4*, eaas9732.

5. Zhan, G.; Liu, Z.; Bian, Z.; Huang, C., Recent advances in organic light-emitting diodes based on pure organic room temperature phosphorescence materials. *Front. Chem.* **2019,** *7*, 305.

6. Kang, S. W.; Baek, D.-H.; Ju, B.-K.; Park, Y. W., Green phosphorescent organic light-emitting diode exhibiting highest external quantum efficiency with ultra-thin undoped emission layer. *Sci. Rep.* **2021,** *11*, 8436.

7. Sun, J.; Ahn, H.; Kang, S.; Ko, S.-B.; Song, D.; Um, H. A.; Kim, S.; Lee, Y.; Jeon, P.; Hwang, S.-H., Exceptionally stable blue phosphorescent organic light-emitting diodes. *Nat. Photon.* **2022,** *16*, 212-218.

8. Lee, J.; Chen, H.-F.; Batagoda, T.; Coburn, C.; Djurovich, P. I.; Thompson, M. E.; Forrest, S. R., Deep blue phosphorescent organic light-emitting diodes with very high brightness and efficiency. *Nat. Mater.* **2016,** *15*, 92-98.

9. Zhan, G.; Liu, Z.; Bian, Z.; Huang, C., Recent advances in organic light-emitting diodes based on pure organic room temperature phosphorescence materials. *Front. Chem.* **2019,** *7*, 305.

10. Yum, J.-H.; Baranoff, E.; Hardin, B. E.; Hoke, E. T.; McGehee, M. D.; Nüesch, F.; Grätzel, M.; Nazeeruddin, M. K., Phosphorescent energy relay dye for improved light harvesting response in liquid dye-sensitized solar cells. *Energy Environ. Sci.* **2010,** *3*, 434-437.

11. Yu, Z.; Wu, Y.; Xiao, L.; Chen, J.; Liao, Q.; Yao, J.; Fu, H., Organic Phosphorescence Nanowire Lasers. *J. Am. Chem. Soc.* **2017,** *139*, 6376-6381.

12. Ieuji, R.; Goushi, K.; Adachi, C., Triplet–triplet upconversion enhanced by spin–orbit coupling in organic light-emitting diodes. *Nat. Commun* **2019,** *10*, 5283.

13. Wan, S.; Zhou, H.; Lin, J.; Lu, W., A Prototype of a Volumetric Three-Dimensional Display Based on Programmable Photo-Activated Phosphorescence. *Angew. Chem. Int. Ed.* **2020,** *59*, 8416-8420.

14. Zhao, W. J.; He, Z. K.; Tang, B. Z., Room-temperature phosphorescence from organic aggregates. *Nat. Rev. Mater.* **2020,** *5*, 869-885.

15. Chen, C.; Liu, B., Enhancing the performance of pure organic room-temperature phosphorescent luminophores. *Nat. Commun.* **2019,** *10*, 2111.

16. Wen, Y.; Liu, H.; Zhang, S.; Gao, Y.; Yan, Y.; Yang, B., One-dimensional π–π stacking induces highly efficient pure organic room-temperature phosphorescence and ternary-emission single-molecule white light. *J. Mater. Chem. C* **2019,** *7*, 12502-12508.

17. Yuan, W. Z.; Shen, X. Y.; Zhao, H.; Lam, J. W.; Tang, L.; Lu, P.; Wang, C.; Liu, Y.; Wang, Z.; Zheng, Q., Crystallization-induced phosphorescence of pure organic luminogens at room temperature. *J. Phys. Chem. C* **2010,** *114*, 6090-6099.

18. Bolton, O.; Lee, K.; Kim, H.-J.; Lin, K. Y.; Kim, J., Activating efficient phosphorescence from purely organic materials by crystal design. *Nat. Chem.* **2011,** *3*, 205.

19. Wang, J.; Gu, X.; Ma, H.; Peng, Q.; Huang, X.; Zheng, X.; Sung, S. H.; Shan, G.; Lam, J. W.; Shuai, Z., A facile strategy for realizing room temperature phosphorescence and single molecule white light emission. *Nat. Commun.* **2018,** *9*, 2963.

20. He, G.; Wiltshire, B. D.; Choi, P.; Savin, A.; Sun, S.; Mohammadpour, A.; Ferguson, M. J.; McDonald, R.; Farsinezhad, S.; Brown, A., Phosphorescence within benzotellurophenes and color tunable tellurophenes under ambient conditions. *Chem. Commun.* **2015,** *51*, 5444-5447.

21. He, G.; Torres Delgado, W.; Schatz, D. J.; Merten, C.; Mohammadpour, A.; Mayr, L.; Ferguson, M. J.; McDonald, R.; Brown, A.; Shankar, K.; Rivard, E., Coaxing solid-state phosphorescence from tellurophenes. *Angew. Chem.Int. Ed.,* **2014,** *53*, 4587-4591.

22. Gong, Y.; Zhao, L.; Peng, Q.; Fan, D.; Yuan, W. Z.; Zhang, Y.; Tang, B. Z., Crystallization-induced dual emission from metal-and heavy atom-free aromatic acids and esters. *Chem. Sci.* **2015,** *6*, 4438-4444.

23. Yuan, W. Z.; Shen, X. Y.; Zhao, H.; Lam, J. W. Y.; Tang, L.; Lu, P.; Wang, C. L.; Liu, Y.; Wang, Z. M.; Zheng, Q.; Sun, J. Z.; Ma, Y. G.; Tang, B. Z., Crystallization-induced phosphorescence of pure organic luminogens at room temperature. *J. Phys. Chem. C* **2010,** *114*, 6090-6099.

24. Zhao, W.; He, Z.; Lam, J. W.; Peng, Q.; Ma, H.; Shuai, Z.; Bai, G.; Hao, J.; Tang, B. Z., Rational molecular design for achieving persistent and efficient pure organic room-temperature phosphorescence. *Chem* **2016,** *1*, 592-602.

25. An, Z.; Zheng, C.; Tao, Y.; Chen, R.; Shi, H.; Chen, T.; Wang, Z.; Li, H.; Deng, R.; Liu, X.; Huang, W., Stabilizing triplet excited states for ultralong organic phosphorescence. *Nat. Mater.* **2015,** *14*, 685-690.

26. Chen, X.; He, Z.; Kausar, F.; Chen, G.; Zhang, Y.; Yuan, W. Z., Aggregation-induced dual emission and unusual luminescence beyond excimer emission of poly (ethylene terephthalate). *Macromolecules* **2018,** *51*, 9035-9042.

27. Zhang, G.; Chen, J.; Payne, S. J.; Kooi, S. E.; Demas, J.; Fraser, C. L., Multi-emissive difluoroboron dibenzoylmethane polylactide exhibiting intense fluorescence and oxygen-sensitive room-temperature phosphorescence. *J. Am. Chem. Soc.* **2007,** *129*, 8942-8943.

28. Cai, S.; Ma, H.; Shi, H.; Wang, H.; Wang, X.; Xiao, L.; Ye, W.; Huang, K.; Cao, X.; Gan, N., Enabling long-lived organic room temperature phosphorescence in polymers by subunit interlocking. *Nat. Commun.* **2019,** *10*, 1-8.

29. Xiong, Y.; Zhao, Z.; Zhao, W.; Ma, H.; Peng, Q.; He, Z.; Zhang, X.; Chen, Y.; He, X.; Lam, J. W. Y.; Tang, B. Z., Designing efficient and ultralong pure organic room-temperature phosphorescent materials by structural isomerism. *Angew. Chem. Int. Ed.* **2018,** *57*, 7997-8001.

30. Bilen, C.; Harrison, N.; Morantz, D., Unusual room temperature afterglow in some crystalline organic compounds. *Nature* **1978,** *271*, 235-237.

31. Shen, Q. J.; Wei, H. Q.; Zou, W. S.; Sun, H. L.; Jin, W. J., Cocrystals assembled by pyrene and 1, 2-or 1, 4-diiodotetrafluorobenzenes and their phosphorescent behaviors modulated by local molecular environment. *CrystEngComm* **2012,** *14*, 1010-1015.

32. Bolton, O.; Lee, K.; Kim, H. J.; Lin, K. Y.; Kim, J., Activating efficient phosphorescence from purely organic materials by crystal design. *Nat. Chem.* **2011,** *3*, 205-210.

33. Yan, X.; Peng, H.; Xiang, Y.; Wang, J.; Yu, L.; Tao, Y.; Li, H.; Huang, W.; Chen, R., Recent advances on host–guest material systems toward organic room temperature phosphorescence. *Small* **2022,** *18*, 2104073.

34. Chen, C.; Chi, Z.; Chong, K. C.; Batsanov, A. S.; Yang, Z.; Mao, Z.; Yang, Z.; Liu, B., Carbazole isomers induce ultralong organic phosphorescence. *Nat. Mater.* **2021,** *20*, 175-180.

35. Kabe, R.; Adachi, C., Organic long persistent luminescence. *Nature* **2017,** *550*, 384-387.

36. Hamzehpoor, E.; Ruchlin, C.; Tao, Y.; Liu, C.-H.; Titi, H. M.; Perepichka, D. F., Efficient room-temperature phosphorescence of covalent organic frameworks through covalent halogen doping. *Nat. Chem.* **2023**, 15, 83-90.

37. Galeotti, G.; De Marchi, F.; Hamzehpoor, E.; MacLean, O.; Rajeswara Rao, M.; Chen, Y.; Besteiro, L. V.; Dettmann, D.; Ferrari, L.; Frezza, F.; Sheverdyaeva, P. M.; Liu, R.; Kundu, A. K.; Moras, P.; Ebrahimi, M.; Gallagher, M. C.; Rosei, F.; Perepichka, D. F.; Contini, G., Synthesis of mesoscale ordered two-dimensional pi-conjugated polymers with semiconducting properties. *Nat. Mater.* **2020,** *19*, 874-880.

38. Mei, J.; Leung, N. L.; Kwok, R. T.; Lam, J. W.; Tang, B. Z., Aggregation-induced emission: together we shine, united we soar! *Chem. Rev.* **2015,** *115*, 11718-11940.

39. Hamzehpoor, E.; Perepichka, D. F., Crystal engineering of room temperature phosphorescence in organic solids. *Angew. Chem. Int. Ed.* **2020,** *59*, 9977-9981.

40. Clapp, D. B., The phosphorescence of tetraphenylmethane and certain related substances. *J. Am. Chem. Soc.* **1939,** *61*, 523-524.

41. Bolton, O.; Lee, K.; Kim, H.-J.; Lin, K. Y.; Kim, J., Activating efficient phosphorescence from purely organic materials by crystal design. *Nat. Chem.* **2011,** *3*, 205-210.

42. Ding, B.; Ma, L.; Huang, Z.; Ma, X.; Tian, H., Engendering persistent organic room temperature phosphorescence by trace ingredient incorporation. *Sci. Adv.* **2021,** *7*, eabf9668.

43. An, Z.; Zheng, C.; Tao, Y.; Chen, R.; Shi, H.; Chen, T.; Wang, Z.; Li, H.; Deng, R.; Liu, X., Stabilizing triplet excited states for ultralong organic phosphorescence. *Nat. Mater.* **2015,** *14*, 685-690.

44. Cai, S.; Shi, H.; Li, J.; Gu, L.; Ni, Y.; Cheng, Z.; Wang, S.; Xiong, W. w.; Li, L.; An, Z., Visible-light-excited ultralong organic phosphorescence by manipulating intermolecular interactions. *Adv. Mater.* **2017,** *29*, 1701244.

45. Xie, Y.; Ge, Y.; Peng, Q.; Li, C.; Li, Q.; Li, Z., How the molecular packing affects the room temperature phosphorescence in pure organic compounds: ingenious molecular design, detailed crystal analysis, and rational theoretical calculations. *Adv. Mater.* **2017,** *29*, 1606829.

46. Fateminia, S. A.; Mao, Z.; Xu, S.; Yang, Z.; Chi, Z.; Liu, B., Organic nanocrystals with bright red persistent room-temperature phosphorescence for biological applications. *Angew. Chem. Int. Ed.* **2017,** *56*, 12160-12164.

47. Sasabe, H.; Kato, Y.; Watanabe, Y.; Ohsawa, T.; Aizawa, N.; Fujiwara, W.; Pu, Y. J.; Katagiri, H.; Kido, J., Room-Temperature Phosphorescence from a Series of 3-Pyridylcarbazole Derivatives. *Chem. Eur. J.* **2019,** *25*, 16294-16300.

48. Zhang, Z.; Tang, L.; Fan, X.; Wang, Y.; Zhang, K.; Sun, Q.; Zhang, H.; Xue, S.; Yang, W., N -Alkylcarbazoles: Homolog manipulating long-lived room-temperature phosphorescence. *J. Mater. Chem. C* **2018,** *6*, 8984-8989.

49. Mao, Z.; Yang, Z.; Fan, Z.; Ubba, E.; Li, W.; Li, Y.; Zhao, J.; Yang, Z.; Aldred, M. P.; Chi, Z., The methylation effect in prolonging the pure organic room temperature phosphorescence lifetime. *Chem. Sci.* **2019,** *10*, 179-184.

50. Yuan, J.; Wang, S.; Ji, Y.; Chen, R.; Zhu, Q.; Wang, Y.; Zheng, C.; Tao, Y.; Fan, Q.; Huang, W., Invoking ultralong room temperature phosphorescence of purely organic compounds through H-aggregation engineering. *Mater. Horiz.* **2019,** *6*, 1259-1264.

51. Wang, C.; Zhang, Z.; Wang, Y., Quinacridone-based π-conjugated electronic materials. *J. Mater. Chem. C* **2016,** *4*, 9918-9936.

52. Lincke, G., A review of thirty years of research on quinacridones. X-ray crystallography and crystal engineering. *Dyes Pigm.* **2000,** *44*, 101-122.

53. Lincke, G., On quinacridones and their supramolecular mesomerism within the crystal lattice. *Dyes Pigm.* **2002,** *52*, 169-181.

54. Liu, Y.; Li, C.; Ren, Z.; Yan, S.; Bryce, M. R., All-organic thermally activated delayed fluorescence materials for organic light-emitting diodes. *Nat. Rev. Mater.* **2018,** *3*, 18020.

55. Hatakeyama, T.; Shiren, K.; Nakajima, K.; Nomura, S.; Nakatsuka, S.; Kinoshita, K.; Ni, J.; Ono, Y.; Ikuta, T., Ultrapure blue thermally activated delayed fluorescence molecules: efficient HOMO–LUMO separation by the multiple resonance effect. *Adv. Mater.* **2016,** *28*, 2777-2781.

56. Kondo, Y.; Yoshiura, K.; Kitera, S.; Nishi, H.; Oda, S.; Gotoh, H.; Sasada, Y.; Yanai, M.; Hatakeyama, T., Narrowband deep-blue organic light-emitting diode featuring an organoboron-based emitter. *Nat. Photon.* **2019,** *13*, 678-682.

57. Zhang, T.; Ma, X.; Tian, H., A facile way to obtain near-infrared room-temperature phosphorescent soft materials based on Bodipy dyes. *Chem. Sci.* **2020,** *11*, 482-487.

58. Mikhnenko, O. V.; Blom, P. W. M.; Nguyen, T.-Q., Exciton diffusion in organic semiconductors. *Energy Environ. Sci* **2015,** *8*, 1867-1888.

59. Najafov, H.; Lee, B.; Zhou, Q.; Feldman, L. C.; Podzorov, V., Observation of long-range exciton diffusion in highly ordered organic semiconductors. *Nat. Mater.* **2010,** *9*, 938-943.

60. Haedler, A. T.; Kreger, K.; Issac, A.; Wittmann, B.; Kivala, M.; Hammer, N.; Koehler, J.; Schmidt, H.-W.; Hildner, R., Long-range energy transport in single supramolecular nanofibres at room temperature. *Nature* **2015,** *523*, 196-199.

61. Saikin, S. K.; Shakirov, M. A.; Kreisbeck, C.; Peskin, U.; Proshin, Y. N.; Aspuru-Guzik, A., On the Long-Range Exciton Transport in Molecular Systems: The Application to H-Aggregated Heterotriangulene Chains. *J. Phys. Chem. C* **2017,** *121*, 24994-25002.

62. Mikhnenko, O. V.; Blom, P. W.; Nguyen, T.-Q., Exciton diffusion in organic semiconductors. *Energy Environ. Sci* **2015,** *8*, 1867-1888.

63. Glazov, M. M., Quantum Interference Effect on Exciton Transport in Monolayer Semiconductors. *Phys. Rev. Lett.* **2020,** *124*, 166802.

64. Thakur, T. S.; Dubey, R.; Desiraju, G. R., Crystal structure and prediction. *Annu. Rev. Phys. Chem.* **2015,** *66*, 21-42.

65. Oganov, A. R.; Pickard, C. J.; Zhu, Q.; Needs, R. J., Structure prediction drives materials discovery. *Nat. Rev. Mater.* **2019,** *4*, 331-348.

66. Maddox, J., Crystals from first principles. *Nature* **1988,** *335*, 201-201.

67. Nguyen, H. L., Reticular design and crystal structure determination of covalent organic frameworks. *Chem. Sci.* **2021,** *12*, 8632-8647.

68. Yaghi, O. M.; Kalmutzki, M. J.; Diercks, C. S., *Introduction to reticular chemistry: metal-organic frameworks and covalent organic frameworks*. John Wiley & Sons: 2019.

69. Côté, A. P.; Benin, A. I.; Ockwig, N. W.; O'Keeffe, M.; Matzger, A. J.; Yaghi, O. M., Porous, Crystalline, Covalent Organic Frameworks. *Science* **2005,** *310*, 1166-1170.

70. Keller, N.; Bein, T., Optoelectronic processes in covalent organic frameworks. *Chem. Soc. Rev.* **2021,** *50*, 1813-1845.

71. Jadhav, T.; Fang, Y.; Patterson, W.; Liu, C. H.; Hamzehpoor, E.; Perepichka, D. F., 2D poly (arylene vinylene) covalent organic frameworks via aldol condensation of trimethyltriazine. *Angew. Chem. Int. Ed.* **2019,** *58*, 13753-13757.

72. Dalapati, S.; Jin, E.; Addicoat, M.; Heine, T.; Jiang, D., Highly Emissive Covalent Organic Frameworks. *J. Am. Chem. Soc.* **2016,** *138*, 5797-5800.

73. Evans, A. M.; Castano, I.; Brumberg, A.; Parent, L. R.; Corcos, A. R.; Li, R. L.; Flanders, N. C.; Gosztola, D. J.; Gianneschi, N. C.; Schaller, R. D.; Dichtel, W. R., Emissive Single-Crystalline Boroxine-Linked Colloidal Covalent Organic Frameworks. *J. Am. Chem. Soc.* **2019,** *141*, 19728-19735.

74. Ding, S.-Y.; Dong, M.; Wang, Y.-W.; Chen, Y.-T.; Wang, H.-Z.; Su, C.-Y.; Wang, W., Thioether-based fluorescent covalent organic framework for selective detection and facile removal of mercury (II). *J. Am. Chem. Soc.* **2016,** *138*, 3031-3037.

75. Segura, J. L.; Mancheño, M. J.; Zamora, F., Covalent organic frameworks based on Schiff-base chemistry: synthesis, properties and potential applications. *Chem. Soc. Rev.* **2016,** *45*, 5635-5671.

76. Li, X.; Cai, S.; Sun, B.; Yang, C.; Zhang, J.; Liu, Y., Chemically robust covalent organic frameworks: progress and perspective. *Matter* **2020,** *3*, 1507-1540.

77. Jadhav, T.; Fang, Y.; Patterson, W.; Liu, C.-H.; Hamzehpoor, E.; Perepichka, D. F., 2D Poly(arylene vinylene) Covalent Organic Frameworks via Aldol Condensation of Trimethyltriazine. *Angew. Chem. Int. Ed.* **2019,** *58*, 13753-13757.

78. Jadhav, T.; Fang, Y.; Liu, C. H.; Dadvand, A.; Hamzehpoor, E.; Patterson, W.; Jonderian, A.; Stein, R. S.; Perepichka, D. F., Transformation between 2D and 3D Covalent Organic Frameworks via Reversible [2 + 2] Cycloaddition. *J. Am. Chem. Soc.* **2020,** *142*, 8862-8870.

79. Lakshmi, V.; Liu, C.-H.; Rajeswara Rao, M.; Chen, Y.; Fang, Y.; Dadvand, A.; Hamzehpoor, E.; Sakai-Otsuka, Y.; Stein, R. S.; Perepichka, D. F., A Two-Dimensional Poly(azatriangulene) Covalent Organic Framework with Semiconducting and Paramagnetic States. *J. Am. Chem. Soc.* **2020,** *142*, 2155-2160.

80. Evans, A. M.; Castano, I.; Brumberg, A.; Parent, L. R.; Corcos, A. R.; Li, R. L.; Flanders, N. C.; Gosztola, D. J.; Gianneschi, N. C.; Schaller, R. D., Emissive single-crystalline boroxine-linked colloidal covalent organic frameworks. *J. Am. Chem. Soc.* **2019,** *141*, 19728-19735.

81. Crowe, J. W.; Baldwin, L. A.; McGrier, P. L., Luminescent covalent organic frameworks containing a homogeneous and heterogeneous distribution of dehydrobenzoannulene vertex units. *J. Am. Chem. Soc.* **2016,** *138*, 10120-10123.

82. Cox, P. A.; Leach, A. G.; Campbell, A. D.; Lloyd-Jones, G. C., Protodeboronation of heteroaromatic, vinyl, and cyclopropyl boronic acids: pH–rate profiles, autocatalysis, and disproportionation. *J. Am. Chem. Soc.* **2016,** *138*, 9145-9157.

83. Hamzehpoor, E.; Jonderian, A.; McCalla, E.; Perepichka, D. F., Synthesis of Boroxine and Dioxaborole Covalent Organic Frameworks via Transesterification and Metathesis of Pinacol Boronates. *J. Am. Chem. Soc.* **2021,** *143*, 13274-13280.

84. Nagase, M.; Kato, K.; Yagi, A.; Segawa, Y.; Itami, K., Six-fold C–H borylation of hexa-peri-hexabenzocoronene. *Beilstein J. Org. Chem.* **2020,** *16*, 391-397.

85. Do, J.-L.; Friščić, T., Mechanochemistry: a force of synthesis. *ACS Cent. Sci.* **2017,** *3*, 13-19.

86. Das, G.; Shinde, D. B.; Kandambeth, S.; Biswal, B. P.; Banerjee, R., Mechanosynthesis of imine, β-ketoenamine, and hydrogen-bonded imine-linked covalent organic frameworks using liquid-assisted grinding. *Chem. Commun.* **2014,** *50*, 12615-12618.

87. Biswal, B. P.; Chandra, S.; Kandambeth, S.; Lukose, B.; Heine, T.; Banerjee, R., Mechanochemical synthesis of chemically stable isoreticular covalent organic frameworks. *J. Am. Chem. Soc.* **2013,** *135*, 5328-5331.

88. Emmerling, S. T.; Germann, L. S.; Julien, P. A.; Moudrakovski, I.; Etter, M.; Friščić, T.; Dinnebier, R. E.; Lotsch, B. V., In situ monitoring of mechanochemical covalent organic framework formation reveals templating effect of liquid additive. *Chem* **2021,** *7*, 1639-1652.

89. Du, X.; Qi, J.; Zhang, Z.; Ma, D.; Wang, Z. Y., Efficient non-doped near infrared organic light-emitting devices based on fluorophores with aggregation-induced emission enhancement. *Chem. Mater.* **2012,** *24*, 2178-2185.

90. More, L. T., *Isaac Newton: a biography*. Dover publications: 1962.

Appendix

Appendix 1. NMR and HRMS data from Chapter 2

HRMS of HTANGO

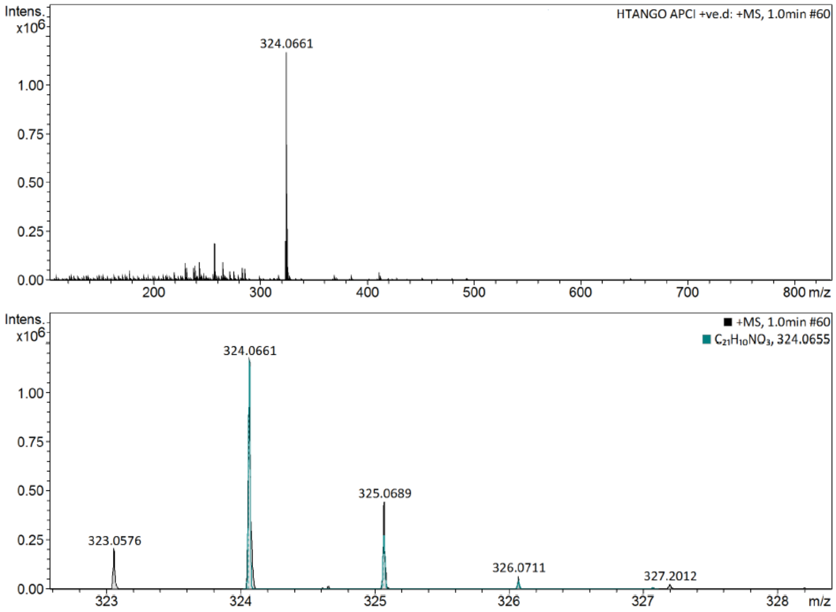

HRMS of TCTANGO

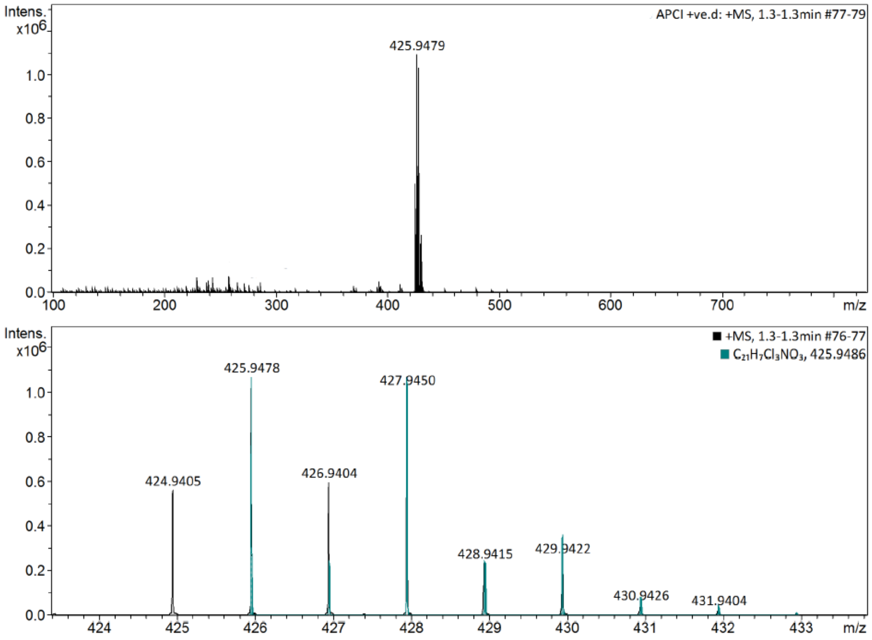

HRMS of TBTANGO

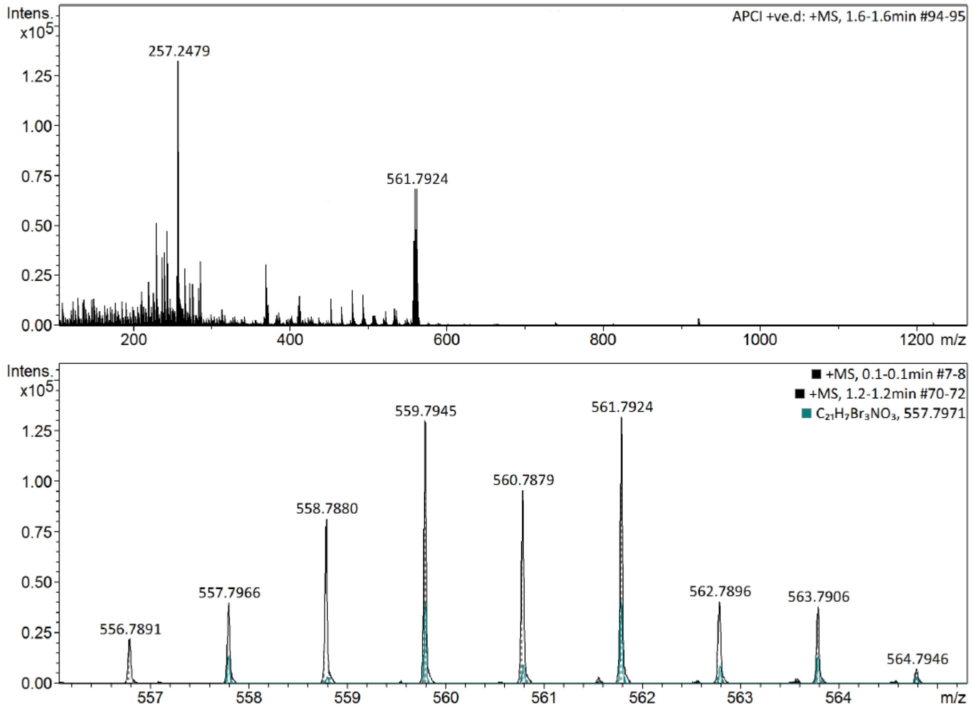

HRMS of TITANGO

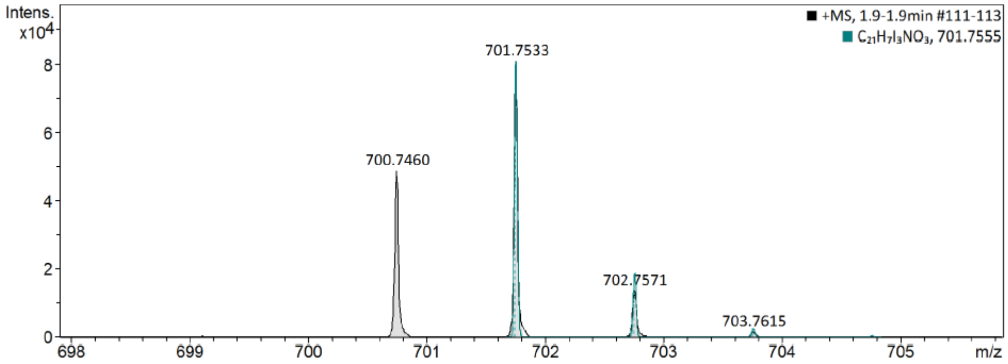

^1H NMR (500 MHz, $CDCl_3$) of trimethyl 6,6',6''-nitrilotris(3-(*tert*-butyl)benzoate).

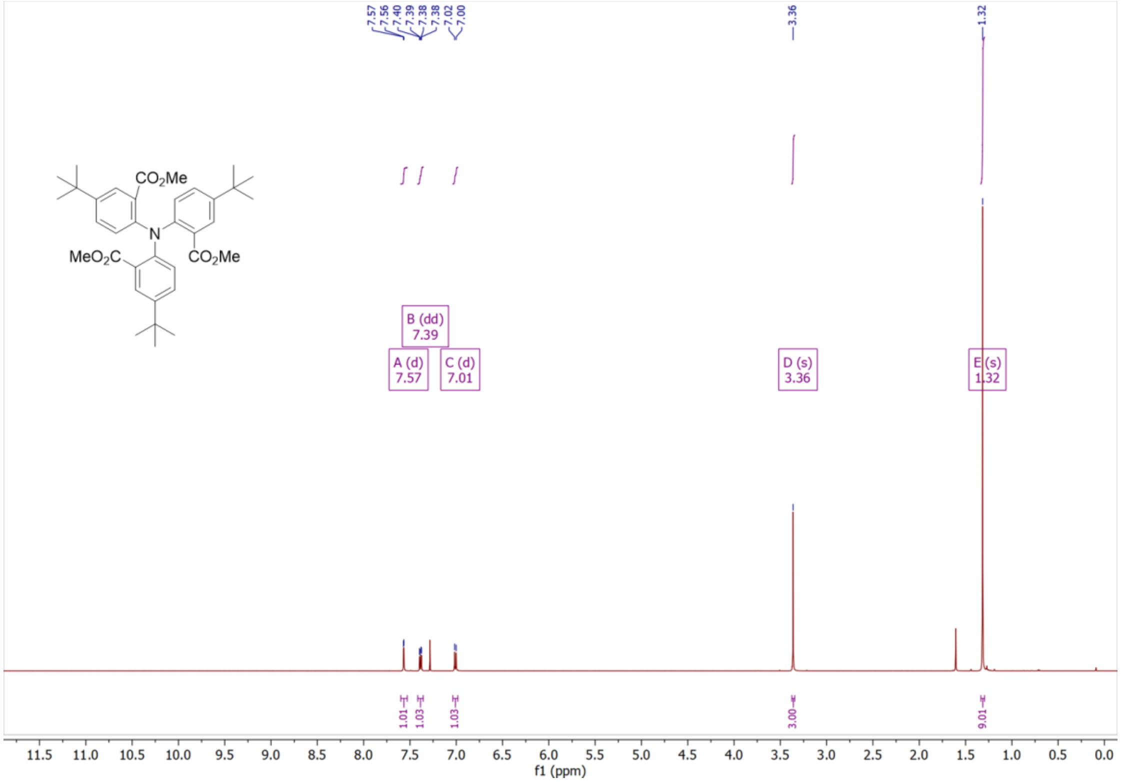

^{13}C NMR (126 MHz, $CDCl_3$) of trimethyl 6,6',6''-nitrilotris(3-(*tert*-butyl)benzoate).

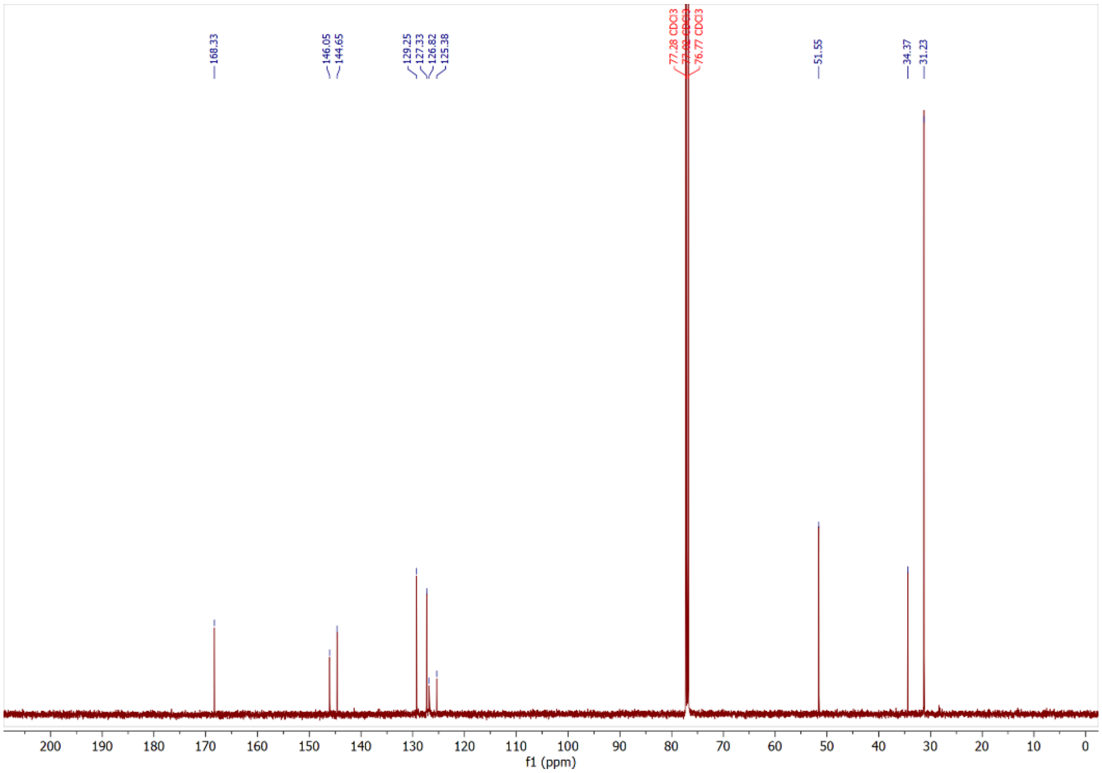

^{1}H NMR (500 MHz, CDCl$_3$) of *t*BuTANGO

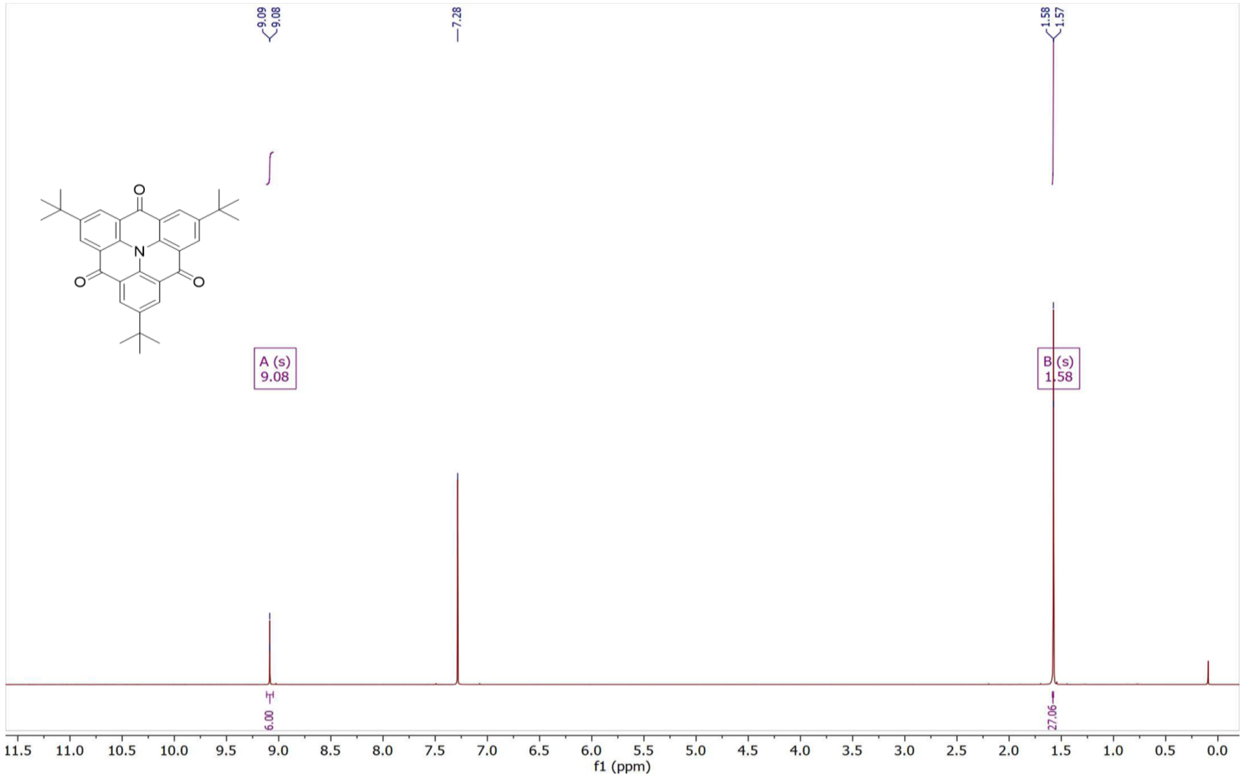

^{13}C NMR (126 MHz, CDCl$_3$) tBuTANGO

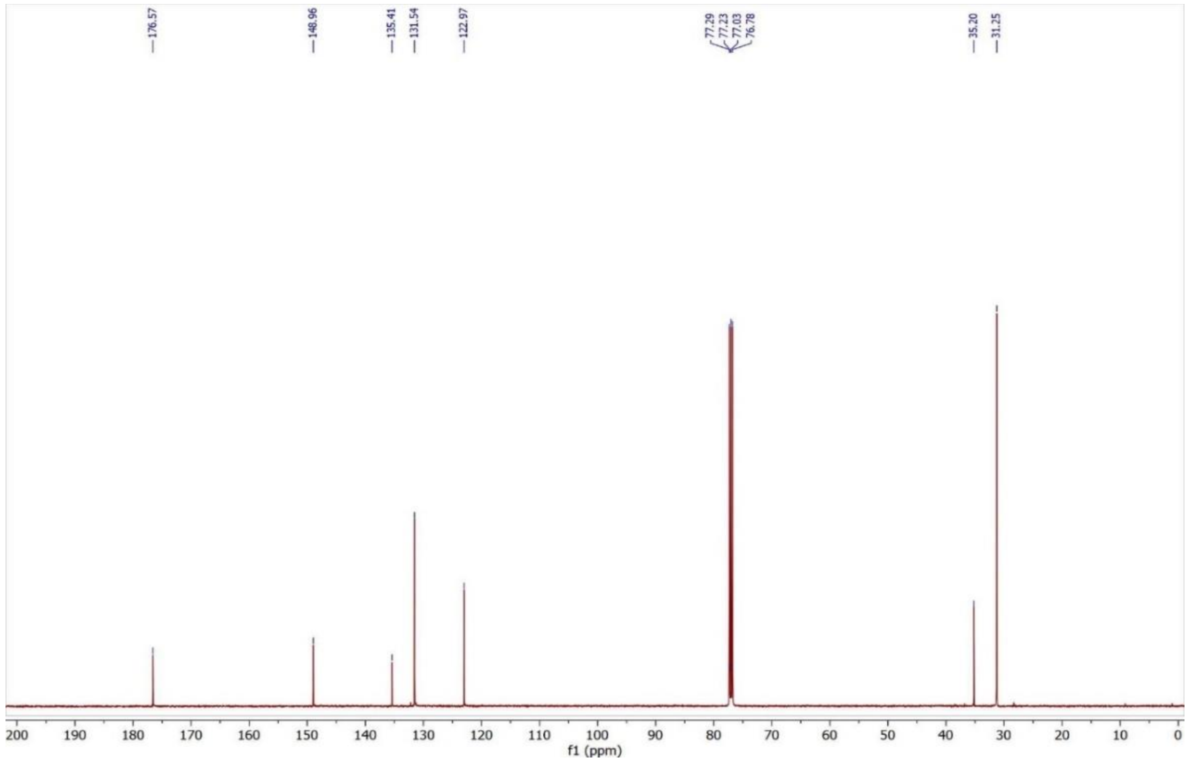

^{1}H NMR (500 MHz, CDCl$_3$) of trimethyl 6,6',6''-nitrilotris(3-chlorobenzoate)

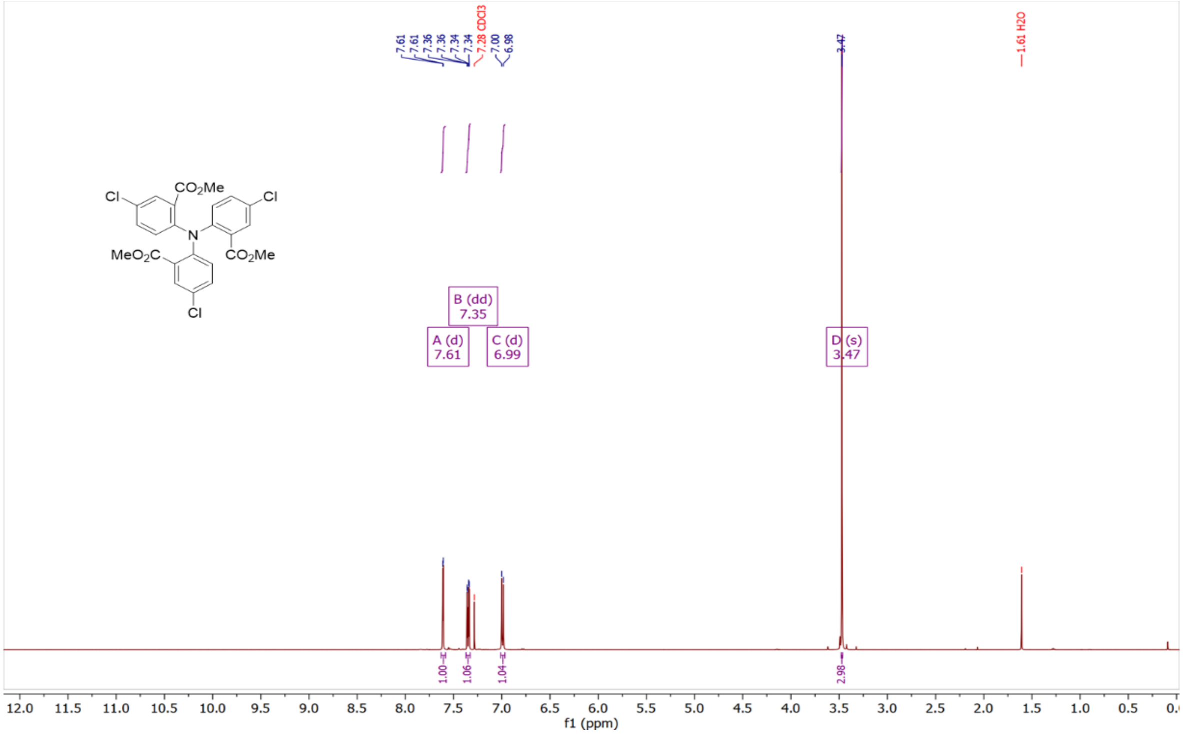

^{13}C NMR (126 MHz, CDCl$_3$) of trimethyl 6,6',6''-nitrilotris(3-chlorobenzoate)

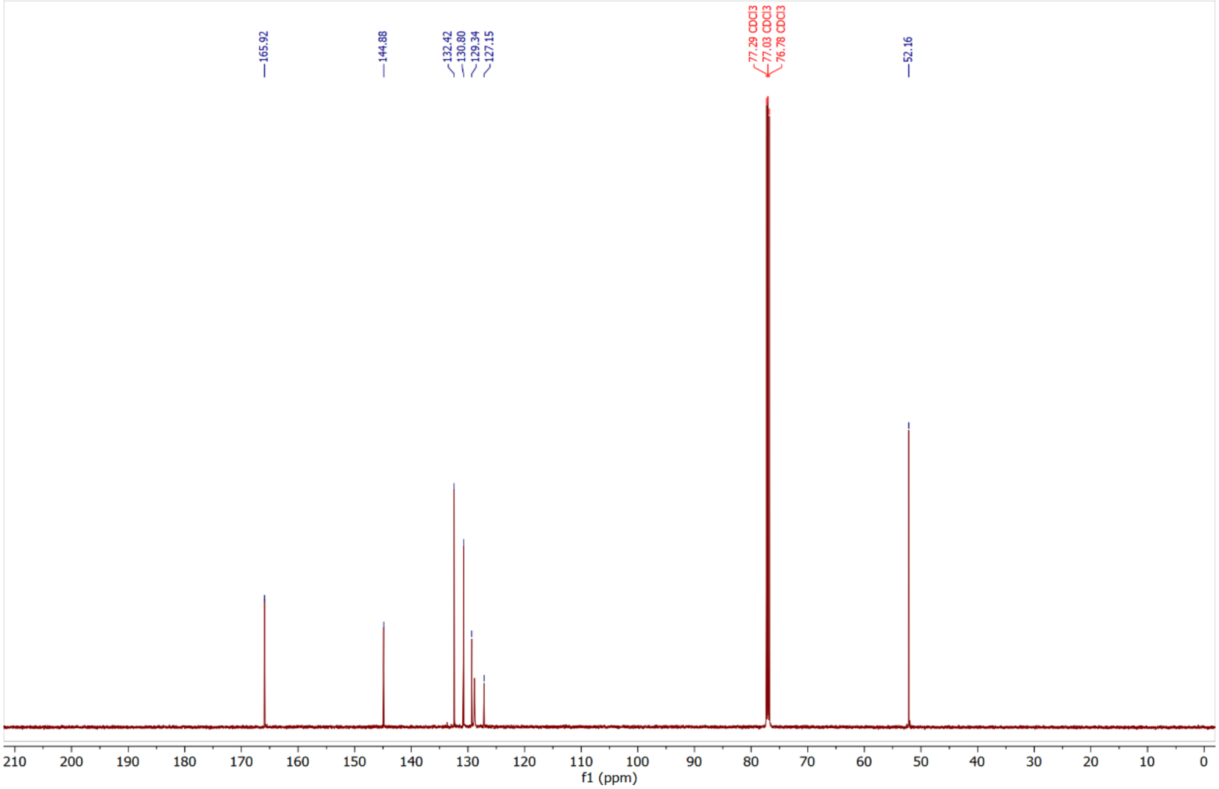

^{1}H NMR (500 MHz, CDCl$_3$) of trimethyl 6,6',6''-nitrilotris(3-bromobenzoate)

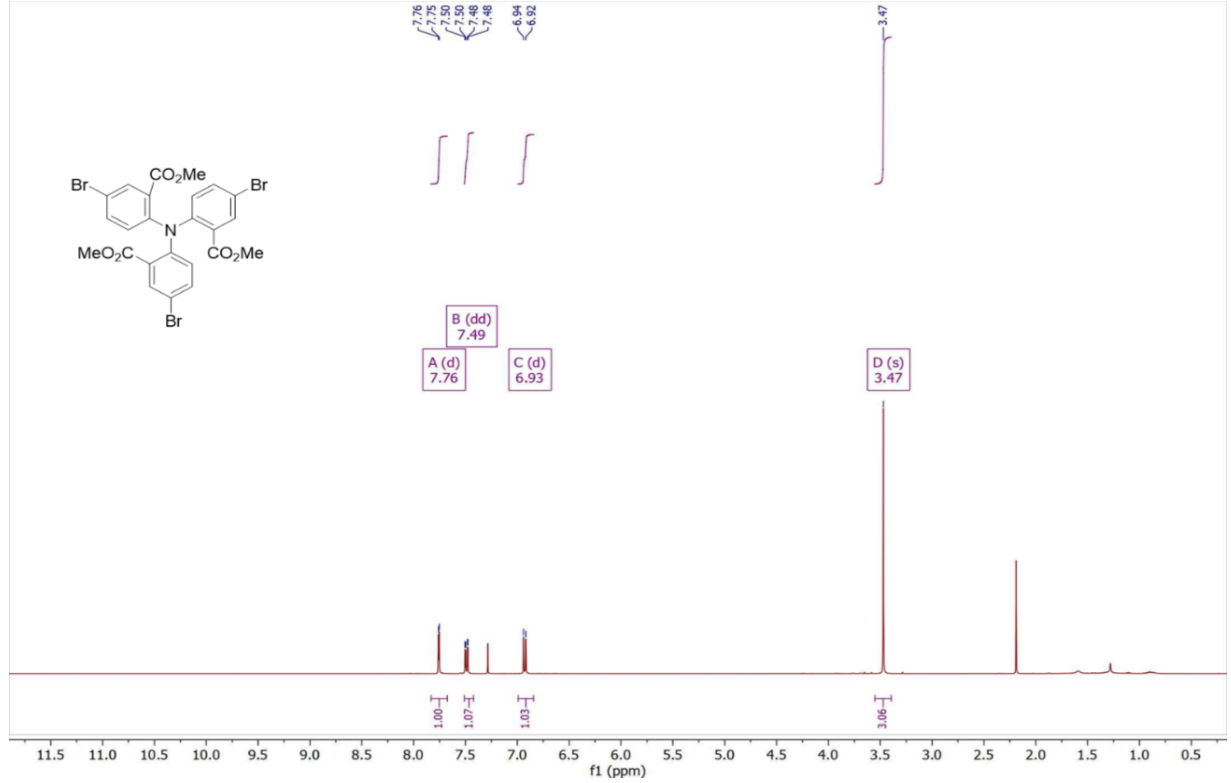

^{13}C NMR (126 MHz, CDCl$_3$) of trimethyl 6,6',6''-nitrilotris(3-bromobenzoate)

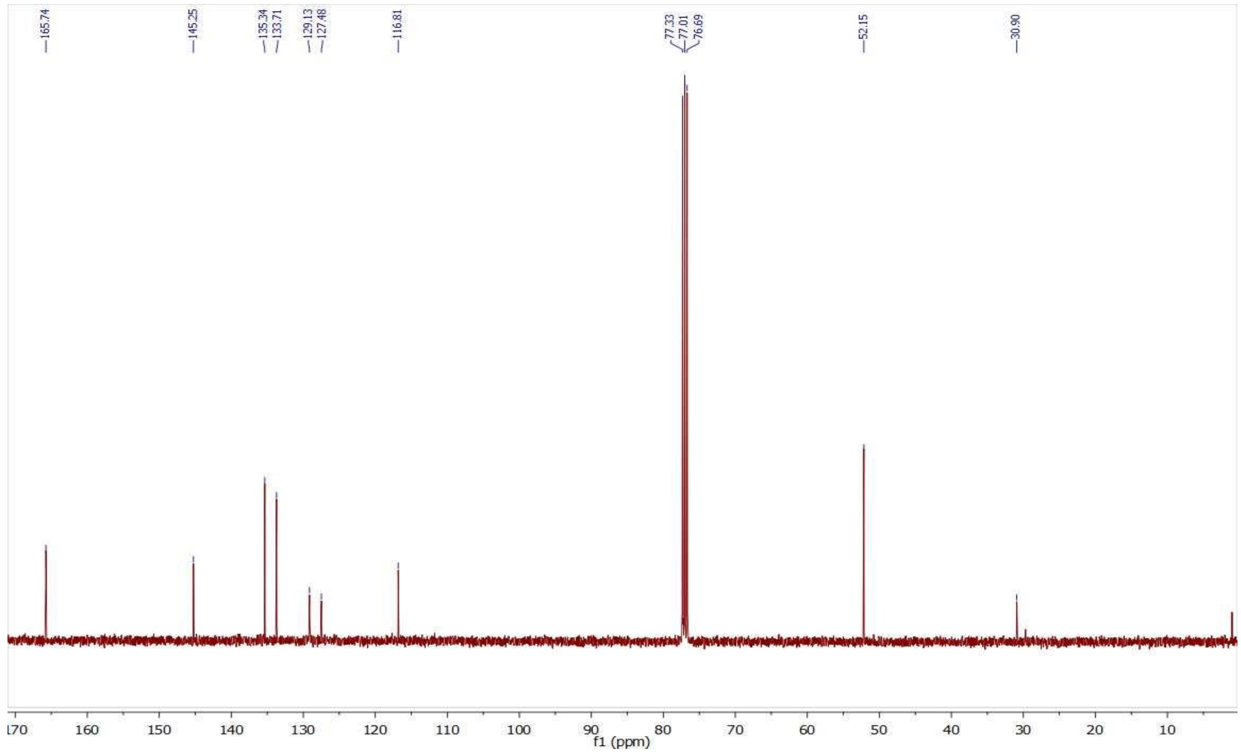

^{1}H NMR (500 MHz, $CDCl_3$) of trimethyl 6,6',6''-nitrilotris(3-iodobenzoate)

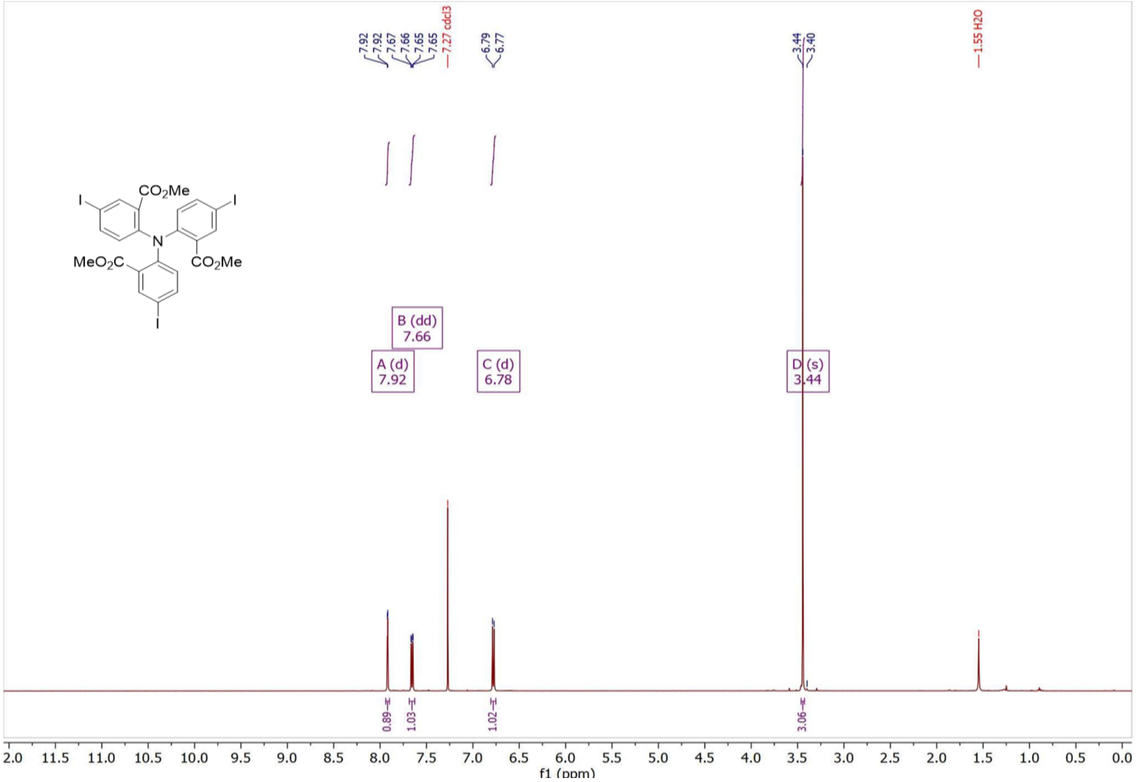

^{13}C NMR (126 MHz, $CDCl_3$) of trimethyl 6,6',6''-nitrilotris(3-iodobenzoate)

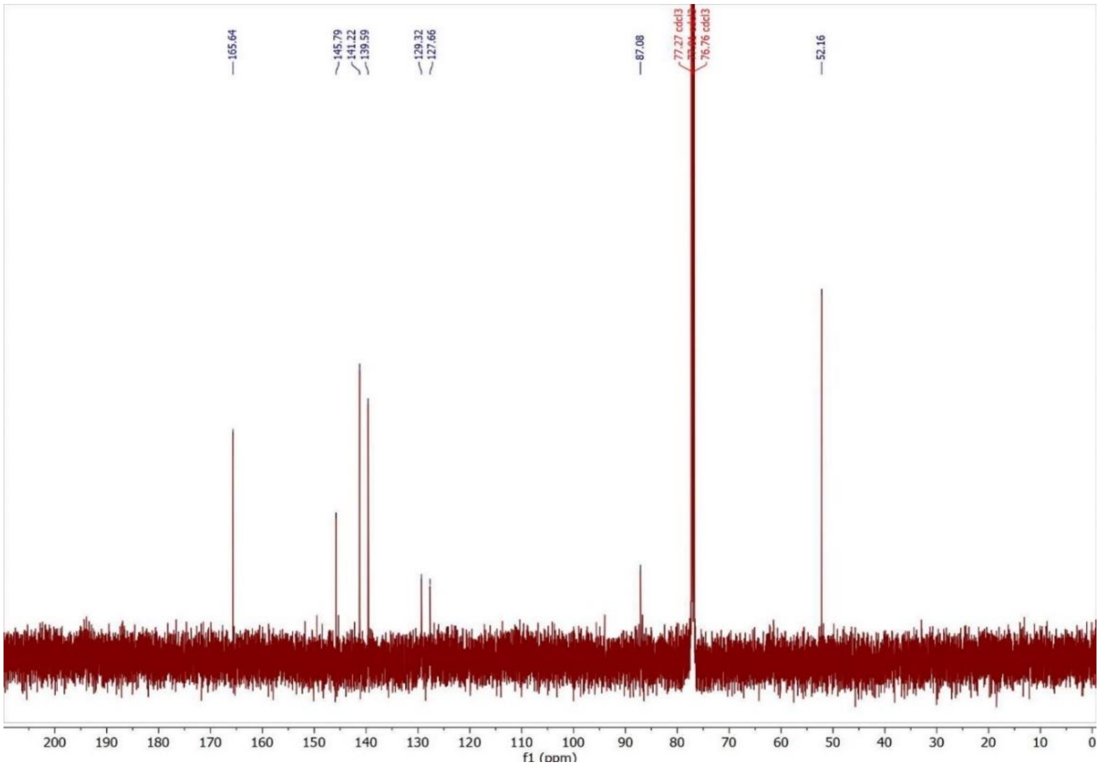

Appendix 2. NMR Spectra and HRMS data from Chapter 3

HRMS of SF5Ac

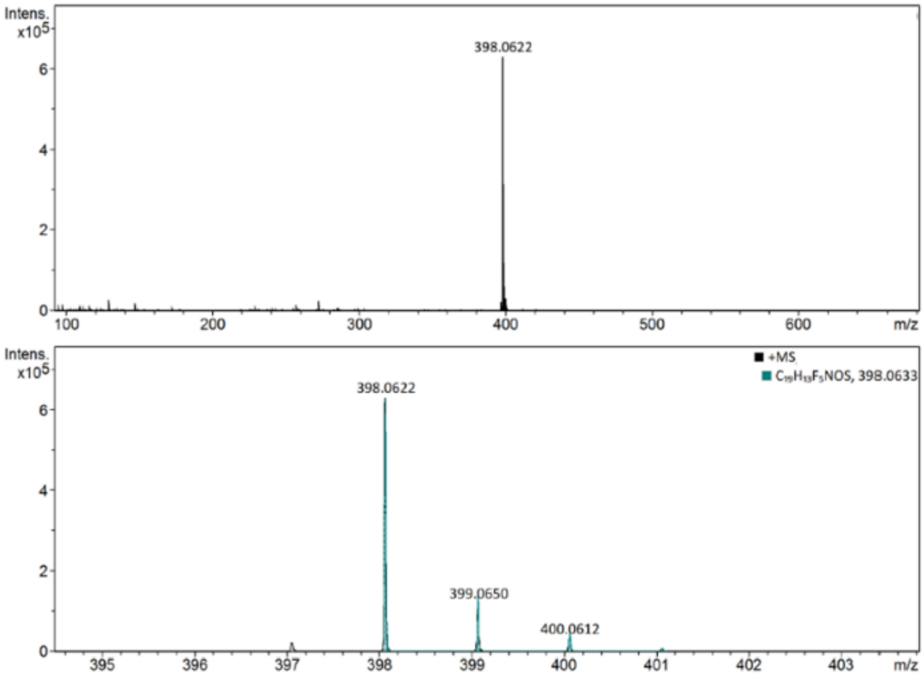

^{1}H NMR (500 MHz, $CDCl_3$) of SF5Ac

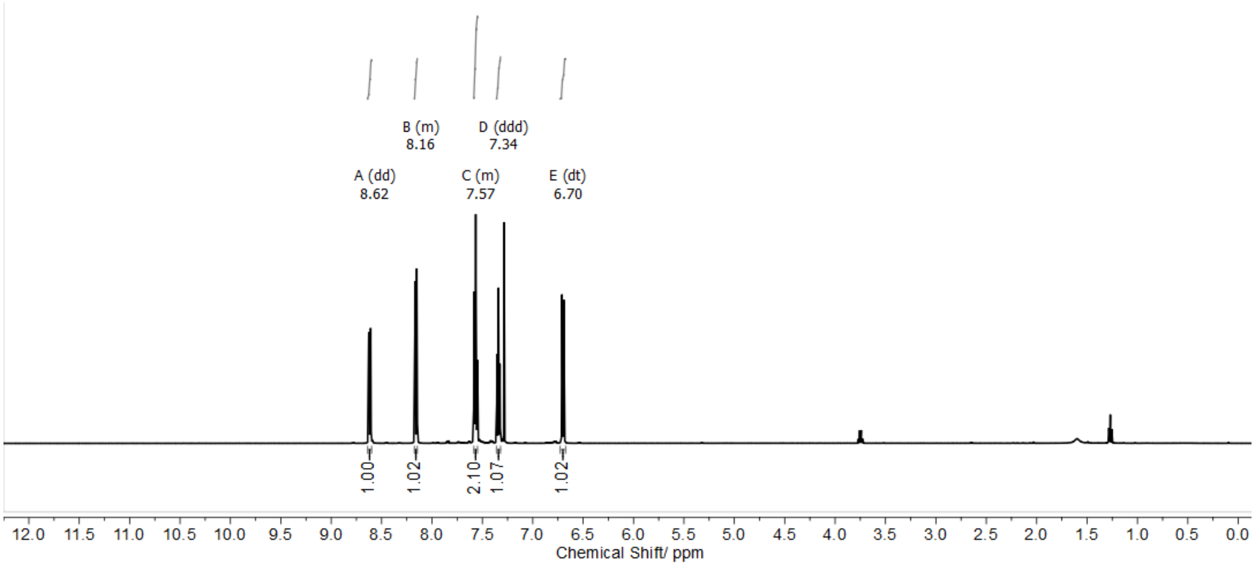

^{1}H NMR (500 MHz, $CDCl_3$) of SF5Ac zoomed in the aromatic region.

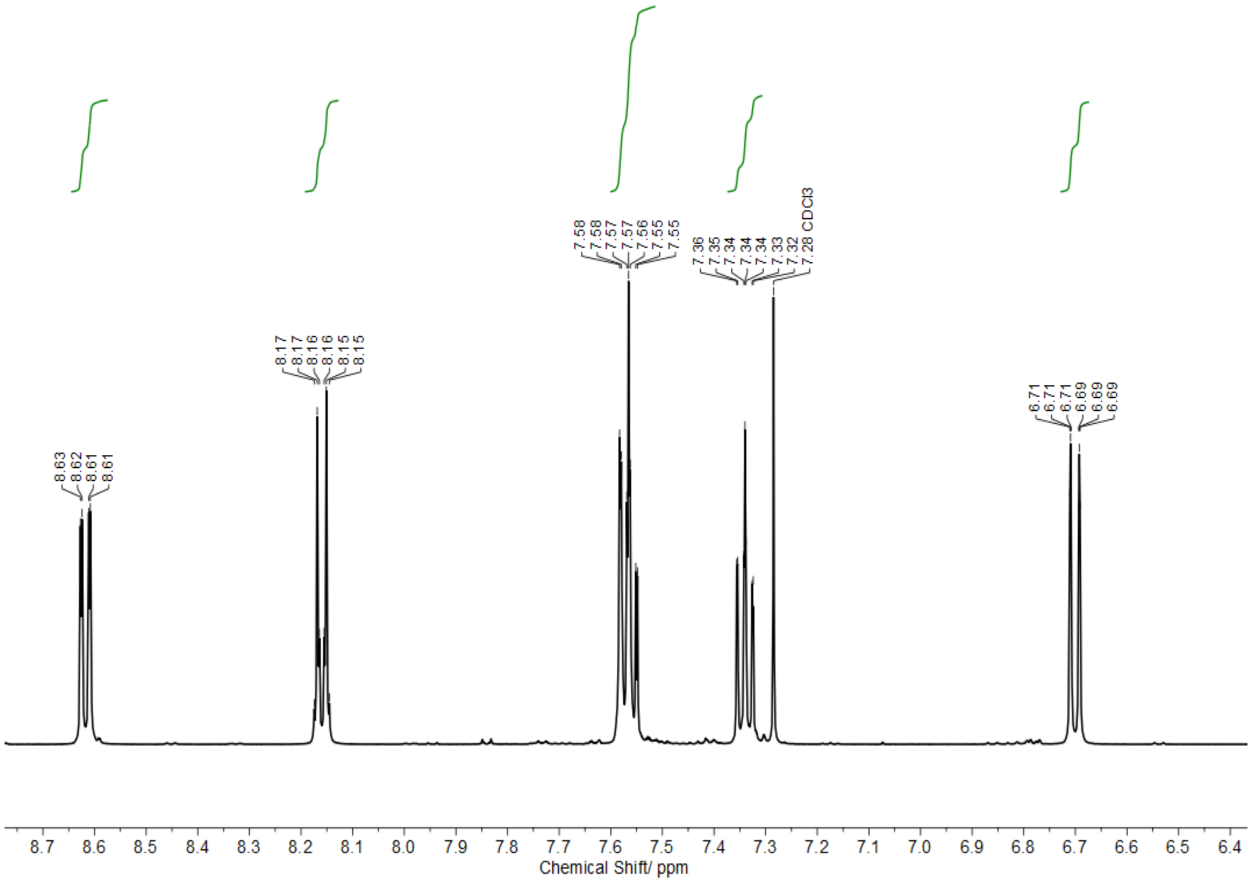

^{13}C NMR (126 MHz, $CDCl_3$) of SF5Ac

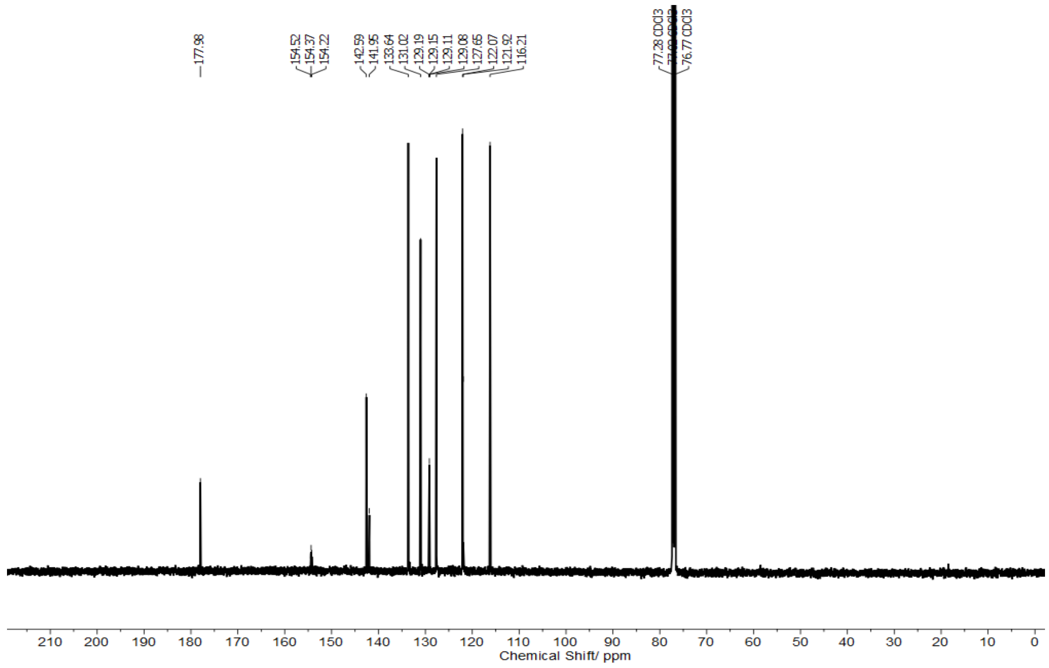

^{13}C NMR (126 MHz, $CDCl_3$) of SF5Ac zoomed in the aromatic region.

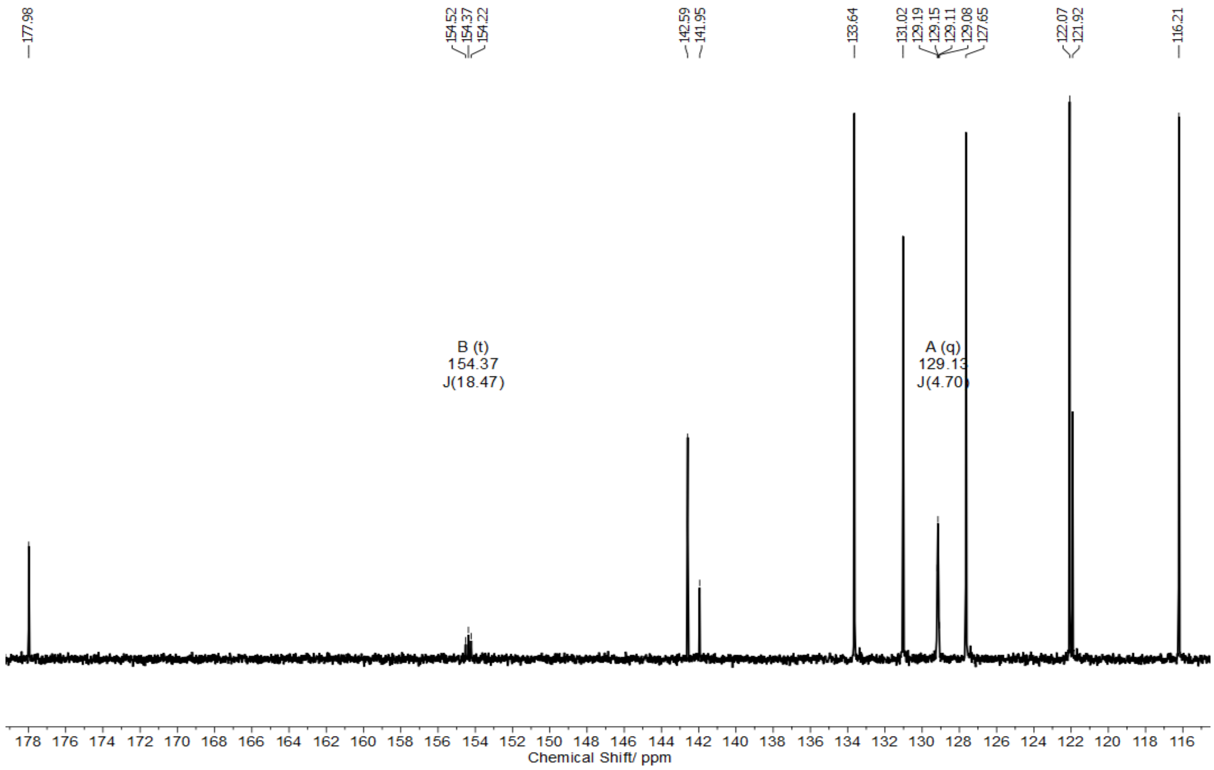

^{19}F NMR (376 MHz, CDCl$_3$) of SF5Ac

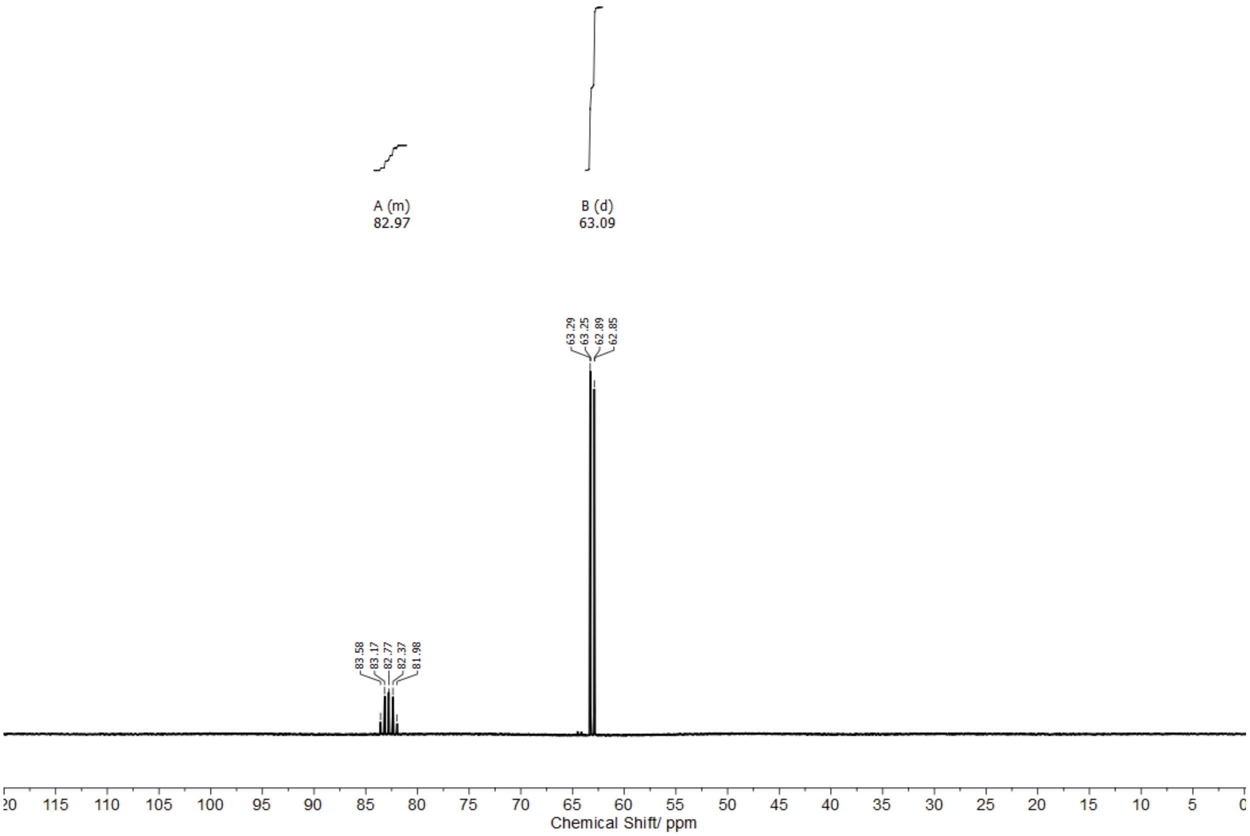

Appendix 3. TD-DFT data from Chapter 3

1.MetAC:

1.1. Gas-phase:

<u>Orbital Topology:</u>
60*(L+4): π* (Ac)
59*(L+3): σπ* (MetAc)
58*(L+2): π* (Ac)
57* (L+1): π* (Ac)
56* (L): π* (Ac)
55 (H): π (Ac)
54 (H-1): n (C=O)
53 (H-2): π (Ac)
52 (H-3): π (Ac)
51 (H-4): π (Ac)

- Singlet:

Excitation energies and oscillator strengths:

```
 Excited State   1:      Singlet-A      2.8651 eV  432.73 nm  f=0.0001  <S**2>=0.000
      54 -> 56         0.70092
 Excited State   2:      Singlet-A      3.4223 eV  362.28 nm  f=0.0863  <S**2>=0.000
      53 -> 56        -0.14121
      55 -> 56         0.67996
```

- Triplet:

Excitation energies and oscillator strengths:

```
 Excited State   1:      Triplet-A      2.2501 eV  551.02 nm  f=0.0000  <S**2>=2.000
      53 -> 56         0.22840
      55 -> 56         0.66002
 Excited State   2:      Triplet-A      2.5465 eV  486.89 nm  f=0.0000  <S**2>=2.000
      54 -> 56         0.69425
      54 -> 60        -0.11950
Excited State   3:      Triplet-A      3.1182 eV  397.62 nm  f=0.0000  <S**2>=2.000
      51 -> 58         0.18022
      52 -> 57        -0.12517
      53 -> 56         0.60753
      55 -> 56        -0.23717
      55 -> 59        -0.10702
 Excited State   4:      Triplet-A      3.2650 eV  379.74 nm  f=0.0000  <S**2>=2.000
      51 -> 56         0.15847
      51 -> 59         0.14301
      52 -> 56         0.46000
```

```
     53 -> 58        0.21234
     55 -> 57       -0.40984
     55 -> 58       -0.11316
Excited State   5:      Triplet-A      3.7774 eV  328.23 nm  f=0.0000  <S**2>=2.000
     51 -> 56        0.46478
     53 -> 58        0.15524
     55 -> 57        0.43535
     55 -> 58       -0.23386
```

1.2. CHCl$_3$ solvated:

Orbital Topology:
60*(L+4): π* (Ac)
59*(L+3): σπ* (MetAc)
58*(L+2): π* (Ac)
57* (L+1): π* (Ac)
56* (L): π* (Ac)
55 (H): π (Ac)
54 (H-1): n (C=O)
53 (H-2): π (Ac)
52 (H-3): π (Ac)
51

- Singlet:

```
Excitation energies and oscillator strengths:
 Excited State   1:      Singlet-?Sym    3.0128 eV  411.52 nm  f=0.0002  <S**2>=0.000
     54 -> 56        0.70116
Excited State   2:      Singlet-?Sym    3.2891 eV  376.95 nm  f=0.1527  <S**2>=0.000
     53 -> 56       -0.10171
     55 -> 56        0.69212
```

- Triplet:

```
Excitation energies and oscillator strengths:
 Excited State   1:      Triplet-?Sym    2.3688 eV  523.40 nm  f=0.0000  <S**2>=2.000
     53 -> 56        0.14023
     55 -> 56        0.68715
Excited State   2:      Triplet-?Sym    2.9037 eV  426.98 nm  f=0.0000  <S**2>=2.000
     54 -> 56        0.69417
     54 -> 60        0.11913
 Excited State   3:      Triplet-?Sym    3.1863 eV  389.11 nm  f=0.0000  <S**2>=2.000
     51 -> 58       -0.19434
     52 -> 57       -0.14659
     52 -> 58       -0.10195
```

```
     53 -> 56         0.61888
     55 -> 56        -0.13785
     55 -> 59        -0.14757
Excited State   4:      Triplet-?Sym    3.2974 eV  376.01 nm  f=0.0000  <S**2>=2.000
     51 -> 56         0.22982
     51 -> 59         0.15014
     52 -> 56         0.42374
     53 -> 58        -0.21189
     55 -> 57        -0.39397
     55 -> 58         0.16976
Excited State   5:      Triplet-?Sym    3.7527 eV  330.39 nm  f=0.0000  <S**2>=2.000
     51 -> 56        -0.47953
     53 -> 58         0.11508
     55 -> 57        -0.40091
     55 -> 58        -0.29391
```

2. PhenAC:

2.1. Gas Phase:

Orbital Topology:
78* (L+6): π* (Ac)
77* (L+5): π* (Ac)
76* (L+4): π* (PhenAc)
75* (L+3): π* (PhenAc)
73* (L+1): π* (PhenAc)
72* (L): π* (Ac)
71 (H): π (Ac)
70 (H-1): n (C=O)
69 (H-2): π (Ac)
68 (H-3): π (Ac)
67 (H-4): π (PhenAc)
65 (H-6): π (PhenAc)

- Singlet:

```
Excitation energies and oscillator strengths:
Excited State   1:      Singlet-A      2.8963 eV  428.08 nm  f=0.0000  <S**2>=0.000
     70 -> 72         0.70087
Excited State   2:      Singlet-A      3.4658 eV  357.74 nm  f=0.1034  <S**2>=0.000
     69 -> 72        -0.14150
     71 -> 72         0.67926
```

- Triplet:

```
Excitation energies and oscillator strengths:
```

```
 Excited State   1:      Triplet-A      2.3250 eV  533.27 nm  f=0.0000  <S**2>=2.000
      69 -> 72         0.22250
      71 -> 72         0.66183
 Excited State   2:      Triplet-A      2.6091 eV  475.20 nm  f=0.0000  <S**2>=2.000
      70 -> 72         0.69367
      70 -> 78         0.12130
 Excited State   3:      Triplet-A      3.1127 eV  398.31 nm  f=0.0000  <S**2>=2.000
      67 -> 76        -0.15103
      68 -> 76        -0.11798
      69 -> 72         0.60571
      71 -> 72        -0.22839
      71 -> 77        -0.12272
 Excited State   4:      Triplet-A      3.2797 eV  378.03 nm  f=0.0000  <S**2>=2.000
      67 -> 72         0.13014
      67 -> 77         0.14144
      68 -> 72         0.43547
      69 -> 76        -0.20566
      71 -> 73        -0.21551
      71 -> 75        -0.38861
 Excited State   5:      Triplet-A      3.7273 eV  332.64 nm  f=0.0000  <S**2>=2.000
      65 -> 72         0.10558
      67 -> 72        -0.37150
      68 -> 72        -0.14889
      69 -> 76         0.13507
      71 -> 73        -0.45672
      71 -> 75        -0.20250
      71 -> 76        -0.22567
```

2.2. $CHCl_3$ solvated:

Orbital Topology:
78* (L+6): π* (Ac)
77* (L+5): π* (Ac)
76* (L+4): π* (PhenAc)
75* (L+3): π* (PhenAc)
73* (L+1): π* (PhenAc)
72* (L): π* (Ac)
71 (H): π (Ac)
70 (H-1): n (C=O)
69 (H-2): π (Ac)
68 (H-3): π (PhenAc)
67 (H-4): π (PhenAc)
65 (H-6): π (PhenAc)

- Singlet:

```
Excitation energies and oscillator strengths:
  Excited State   1:      Singlet-?Sym    3.2979 eV  375.94 nm  f=0.1601  <S**2>=0.000
      71 -> 72         0.69814
 Excited State   2:      Singlet-?Sym    3.5250 eV  351.73 nm  f=0.0000  <S**2>=0.000
      70 -> 72         0.69967
```

- Triplet:

```
Excitation energies and oscillator strengths:
  Excited State   1:      Triplet-?Sym    2.4296 eV  510.30 nm  f=0.0000  <S**2>=2.000
      69 -> 72         0.12396
      71 -> 72         0.69008
Excited State   2:      Triplet-?Sym    2.9616 eV  418.64 nm  f=0.0000  <S**2>=2.000
      70 -> 72         0.69360
      70 -> 78         0.11864
 Excited State   3:      Triplet-?Sym    3.1942 eV  388.15 nm  f=0.0000  <S**2>=2.000
      67 -> 76        -0.11945
      68 -> 73         0.14397
      68 -> 76         0.12367
      69 -> 72         0.61795
      71 -> 72        -0.11594
      71 -> 77        -0.16382
 Excited State   4:      Triplet-?Sym    3.3039 eV  375.26 nm  f=0.0000  <S**2>=2.000
      65 -> 72        -0.12012
      67 -> 72         0.17018
      67 -> 77         0.12928
      68 -> 72        -0.40878
      69 -> 73        -0.11259
      69 -> 76        -0.18862
      71 -> 73        -0.26090
      71 -> 75         0.34655
      71 -> 76         0.12926
Excited State   5:      Triplet-?Sym    3.7270 eV  332.66 nm  f=0.0000  <S**2>=2.000
      65 -> 72        -0.21807
      67 -> 72         0.36757
      71 -> 73         0.48534
      71  -> 76        0.24451
```

3. OMeAc:

3.1. Gas Phase:

Orbital Topology:

86* (L+6): π* (Ac)
85* (L+5) π* (Ac)
84* (L+4): π* (PhAc)
83* (L+3): π* (OMePhAc)
82* (L+2): π* (OMePhAc)
81* (L+1): π* (PhAc)
80* (L): π* (Ac)
79 (H): π (Ac)
78 (H-1): n (C=O) **<- inversion w.r.t. $CHCl_3$**
77 (H-2): π (OMePh) <-
76 (H-3): π (Ac)
75 (H-4): π (Ac)
74 (H-5): π (PhAc)
73 (H-6): π (PhAc)

- Singlet:

```
Excitation energies and oscillator strengths:
Excited State   1:     Singlet-?Sym    2.8982 eV  427.80 nm  f=0.0000  <S**2>=0.000
     78 -> 80        0.70088
Excited State   2:     Singlet-?Sym    3.4612 eV  358.21 nm  f=0.1106  <S**2>=0.000
     77 -> 80       -0.14021
     79 -> 80        0.67957
```

- Triplet:

```
Excitation energies and oscillator strengths:
Excited State   1:     Triplet-?Sym    2.3352 eV  530.94 nm  f=0.0000  <S**2>=2.000
     76 -> 80        0.21589
     79 -> 80        0.66420
Excited State   2:     Triplet-?Sym    2.6293 eV  471.56 nm  f=0.0000  <S**2>=2.000
     78 -> 80        0.69357
     78 -> 86        0.12137
Excited State   3:     Triplet-?Sym    3.1178 eV  397.66 nm  f=0.0000  <S**2>=2.000
     74 -> 84       -0.15487
     75 -> 84        0.11807
     76 -> 80        0.60680
     79 -> 80       -0.22118
     79 -> 85       -0.12555
Excited State   4:     Triplet-?Sym    3.2826 eV  377.70 nm  f=0.0000  <S**2>=2.000
     74 -> 80        0.13661
     74 -> 85        0.14341
     75 -> 80       -0.43193
```

```
     76 -> 84       -0.20572
     79 -> 81        0.20376
     79 -> 82       -0.34249
     79 -> 83       -0.19820
     79 -> 84        0.10191
Excited State   5:      Triplet-?Sym    3.6906 eV  335.94 nm  f=0.0000  <S**2>=2.000
     73 -> 81        0.32927
     73 -> 83        0.10052
     74 -> 81       -0.14277
     77 -> 81       -0.20361
     77 -> 82       -0.33257
     77 -> 83        0.42437
```

3.2. CHCl$_3$ solvated:

Orbital Topology:
86* (L+6): π* (PhAc)
80* (L): π* (Ac)
85* (L+5): π* (PhAc)
84* (L+4): π* (PhAc)
83* (L+3): π* (OMePh)
82* (L+2): π* (PhAc)
81* (L+1): π* (PhAc)
80* (L): π* (Ac)
79 (H): π (Ac)
78 (H-1): π (OMePh)   <- inversion w.r.t. GP
77 (H-2): n (C=O)   **<-**
76 (H-3): π (Ac)
75 (H-4): π (Ac)
74 (H-5): π (PhAc)
73 (H-6): π (PhAc)

- Singlet:

```
Excitation energies and oscillator strengths:
  Excited State   1:      Singlet-?Sym    3.1394 eV  394.92 nm  f=0.1668  <S**2>=0.000
     79 -> 80        0.69963
Excited State   2:      Singlet-?Sym    3.5148 eV  352.75 nm  f=0.0012  <S**2>=0.000
     77 -> 80        0.69594
```

- Triplet:

```
Excitation energies and oscillator strengths:
Excited State   1:      Triplet-?Sym    2.4259 eV  511.08 nm  f=0.0000  <S**2>=2.000
     76 -> 80        0.12043
     79 -> 80        0.69076
```

```
Excited State   2:      Triplet-?Sym    2.9670 eV  417.88 nm  f=0.0000  <S**2>=2.000
      77 -> 80         0.69070
      77 -> 86         0.11826
Excited State   3:      Triplet-?Sym    3.1949 eV  388.06 nm  f=0.0000  <S**2>=2.000
      74 -> 84        -0.12797
      75 -> 81         0.14023
      75 -> 84        -0.12209
      76 -> 80         0.61836
      79 -> 80        -0.11184
      79 -> 85        -0.16472
Excited State   4:      Triplet-?Sym    3.3047 eV  375.18 nm  f=0.0000  <S**2>=2.000
      73 -> 80         0.10861
      74 -> 80         0.18609
      74 -> 85         0.13566
      75 -> 80         0.40492
      76 -> 81         0.11251
      76 -> 84        -0.18889
      79 -> 81         0.24216
      79 -> 82        -0.35542
      79 -> 84         0.13403
Excited State   5:      Triplet-?Sym    3.6909 eV  335.91 nm  f=0.0000  <S**2>=2.000
      73 -> 81        -0.22686
      73 -> 82        -0.17528
      73 -> 84        -0.12174
      74 -> 81         0.18033
      74 -> 82         0.13235
      78 -> 81         0.15445
      78 -> 82         0.15333
      78   -> 83      -0.53464
```

4. CNAc:

4.1. Gas Phase:

Orbital Topology:
86* (L+8): σ* (CNPh)
83* (L+5): π* (CNPhAc)
82* (L+4): π* (PhAc)
81* (L+3): π* (PhAc)
80* (L+2): π* (PhAc)
79* (L+1): π* (Ac)
78* (L): π* (CNPh)
77 (H): π (Ac)

76 (H-1): n (C=O)
75 (H-2): π (Ac)
74 (H-3): π (Ac)
73 (H-4): π (PhAc)

- Singlet:

```
Excitation energies and oscillator strengths:
 Excited State   1:      Singlet-A      2.7073 eV  457.97 nm  f=0.0000  <S**2>=0.000
      77 -> 78         0.70505
Excited State   2:      Singlet-A      3.6042 eV  344.00 nm  f=0.0000  <S**2>=0.000
      76 -> 79         0.69864
Excited State   3:      Singlet-A      3.6539 eV  339.32 nm  f=0.1101  <S**2>=0.000
      75 -> 81        -0.10535
      77 -> 79         0.68892
```

- Triplet:

```
Excitation energies and oscillator strengths:
Excited State   1:      Triplet-A      2.2853 eV  542.53 nm  f=0.0000  <S**2>=2.000
      75 -> 79         0.25217
      77 -> 79         0.65009
Excited State   2:      Triplet-A      2.5237 eV  491.28 nm  f=0.0000  <S**2>=2.000
      76 -> 79         0.69395
      76 -> 86         0.12013
Excited State   3:      Triplet-A      3.0966 eV  400.38 nm  f=0.0000  <S**2>=2.000
      73 -> 82        -0.16109
      74 -> 82         0.11368
      75 -> 79         0.59902
      77 -> 79        -0.26059
      77 -> 83        -0.10949
Excited State   4:      Triplet-A      3.1066 eV  399.09 nm  f=0.0000  <S**2>=2.000
      77 -> 78         0.70363
Excited State   5:      Triplet-A      3.2692 eV  379.25 nm  f=0.0000  <S**2>=2.000
      73 -> 79         0.12014
      73 -> 83         0.14230
      74 -> 79        -0.45085
      75 -> 82        -0.21076
      77 -> 80        -0.17008
      77 -> 81        -0.40173
```

4.2. $CHCl_3$ solvated:

Orbital Topology:
86* (L+8): π* (Ac)
83* (L+5): π* (CNPhAc)

82* (L+4): π* (PhAc)
81* (L+3): π* (PhAc)
80* (L+2): π* (PhAc)
79* (L+1): π* (Ac)
78* (L): π* (CNPh)
77 (H): π (Ac)
76 (H-1): n (C=O)
75 (H-2): π (Ac)
74 (H-3): π (Ac)
73 (H-4): π (PhAc)

- Singlet:

```
Excitation energies and oscillator strengths:
  Excited state symmetry could not be determined.
 Excited State   1:      Singlet-?Sym    2.8768 eV  430.98 nm  f=0.0000  <S**2>=0.000
      77 -> 78         0.70498
 This state for optimization and/or second-order correction.
 Total Energy, E(TD-HF/TD-DFT) =  -953.992213129
 Copying the excited state density for this state as the 1-particle RhoCI density.
  Excited state symmetry could not be determined.
 Excited State   2:      Singlet-?Sym    3.5217 eV  352.06 nm  f=0.1916  <S**2>=0.000
      77 -> 79         0.69575
```

- Triplet:

```
Excitation energies and oscillator strengths:
Excited State   1:      Triplet-?Sym    2.4525 eV  505.55 nm  f=0.0000  <S**2>=2.000
      75 -> 78         0.14485
      77 -> 78         0.68559
Excited State   2:      Triplet-?Sym    2.9272 eV  423.56 nm  f=0.0000  <S**2>=2.000
      76 -> 78         0.69370
      76 -> 86         0.11856
Excited State   3:      Triplet-?Sym    3.1854 eV  389.22 nm  f=0.0000  <S**2>=2.000
      73 -> 82         0.16487
      74 -> 81         0.10731
      74 -> 82         0.12598
      75 -> 78         0.61529
      77 -> 78        -0.13979
      77 -> 83        -0.15687
 Excited State   4:      Triplet-?Sym    3.2666 eV  379.55 nm  f=0.0000  <S**2>=2.000
      77 -> 79         0.70428
 Excited State   5:      Triplet-?Sym    3.3055 eV  375.08 nm  f=0.0000  <S**2>=2.000
      73 -> 78         0.19212
      73 -> 83         0.15201
      74 -> 78         0.42225
      75 -> 82         0.20563
```

```
     77 -> 80       -0.13022
     77 -> 81        0.40013
     77  -> 82      -0.14426
```

5. tBuAc:

5.1. Gas Phase:

Orbital Topology:

95* (L+7): π* (Ac)
93* (L+5): π* (Ac)
92* (L+4): π* (PhAc)
91* (L+3): π* (PhAc)
90* (L+2): π* (*t*BuPhAc)
89* (L+1): π* (PhAc)
88* (L): π* (Ac)
87 (H): π (Ac)
86 (H-1): n (C=O)
85 (H-2): π (Ac)
84 (H-3): π (Ac)
83 (H-4): π (PhAc)
82 (H-5): π (*t*BuPhAc)
81 (H-6): π (PhAc)

- Singlet:

```
Excitation energies and oscillator strengths:
Excited State   1:      Singlet-A      2.8973 eV  427.93 nm  f=0.0000  <S**2>=0.000
     86 -> 88        0.70088
Excited State   2:      Singlet-A      3.4588 eV  358.46 nm  f=0.1141  <S**2>=0.000
     85 -> 88       -0.14008
     87 -> 88        0.67967
```

- Triplet:

```
Excitation energies and oscillator strengths:
Excited State   1:      Triplet-A      2.3310 eV  531.89 nm  f=0.0000  <S**2>=2.000
     85 -> 88        0.21645
     87 -> 88        0.66403
Excited State   2:      Triplet-A      2.6249 eV  472.34 nm  f=0.0000  <S**2>=2.000
     86 -> 88        0.69360
     86 -> 95        0.12153
Excited State   3:      Triplet-A      3.1164 eV  397.84 nm  f=0.0000  <S**2>=2.000
     83 -> 92        0.13759
     84 -> 92       -0.11846
     85 -> 88        0.60690
     87 -> 88       -0.22178
```

```
     87 -> 93       -0.12507
Excited State   4:      Triplet-A      3.2814 eV  377.84 nm  f=0.0000  <S**2>=2.000
     83 -> 88       -0.12118
     83 -> 93       -0.13054
     84 -> 88        0.43199
     85 -> 92       -0.20405
     87 -> 89        0.20807
     87 -> 90        0.10870
     87 -> 91        0.37987
Excited State   5:      Triplet-A      3.7151 eV  333.73 nm  f=0.0000  <S**2>=2.000
     81 -> 89       -0.31193
     81 -> 90       -0.12501
     81 -> 91        0.17284
     81 -> 92       -0.10277
     82 -> 89        0.18531
     82 -> 90       -0.47101
     83   -> 89     -0.26343
```

5.2. $CHCl_3$ solvated:

<u>Orbital Topology:</u>
95* (L+7): σ* (*t*BuPh)
93* (L+5): π* (Ac)
92* (L+4): π* (PhAc)
91* (L+3): π* (PhAc)
90* (L+2): π* (*t*BuPhAc)
89* (L+1): π* (PhAc)
88* (L): π* (Ac)
87 (H): π (Ac)
86 (H-1): n (C=O)
85 (H-2): π (Ac)
84 (H-3): π (*t*BuPh)
83 (H-4): π (Ac)
82 (H-5): π (PhAc)
81 (H-6): π (PhAc)

- Singlet:

```
Excitation energies and oscillator strengths:
Excited State   1:      Singlet-?Sym    3.2911 eV  376.73 nm  f=0.1696  <S**2>=0.000
     87 -> 88        0.69817
Excited State   2:      Singlet-?Sym    3.5286 eV  351.37 nm  f=0.0000  <S**2>=0.000
     86 -> 88        0.69820
```

- Triplet:

```
Excitation energies and oscillator strengths:
Excited State   1:      Triplet-?Sym    2.4249 eV  511.29 nm  f=0.0000  <S**2>=2.000
     85 -> 88        0.12088
```

```
     87 -> 88         0.69066
Excited State   2:      Triplet-?Sym    2.9656 eV  418.08 nm  f=0.0000  <S**2>=2.000
     86 -> 88         0.69345
     86 -> 94         0.11861
Excited State   3:      Triplet-?Sym    3.1949 eV  388.07 nm  f=0.0000  <S**2>=2.000
     81 -> 92        -0.10165
     82 -> 92        -0.10029
     83 -> 89         0.14614
     83 -> 92        -0.12336
     85 -> 88         0.61795
     87 -> 88        -0.11250
     87 -> 93        -0.16441
Excited State   4:      Triplet-?Sym    3.3035 eV  375.31 nm  f=0.0000  <S**2>=2.000
     81 -> 88         0.14203
     81 -> 93         0.10805
     82 -> 88         0.14521
     82 -> 93         0.11658
     83 -> 88         0.40930
     85 -> 89         0.11078
     85 -> 92        -0.18386
     87 -> 89         0.27392
     87 -> 90         0.14385
     87 -> 91         0.30665
     87 -> 92         0.12585
Excited State   5:      Triplet-?Sym    3.7194 eV  333.35 nm  f=0.0000  <S**2>=2.000
     81 -> 89         0.18799
     81 -> 91        -0.18303
     81 -> 92         0.12905
     82 -> 89        -0.20466
     82 -> 91         0.22686
     82 -> 92        -0.14390
     84 -> 89        -0.15918
     84  -> 90        0.51047
```

6. SF5Ac:

6.1. Gas Phase:

Orbital Topology:

109* (L+7): π* (SF_5-Ac)
106* (L+4): π* (PhAc)
105* (L+3): π* (PhAc)
104* (L+2): π* (SF_5Ac)

103* (L+1): σ* (SF_5Ac)
102* (L): π* (Ac)
101 (H): π (Ac)
100 (H-1): n (C=O)
99 (H-2): π (Ac)
98 (H-3): π (Ac)
97 (H-4): π (PhAc)
96 (H-5): π (SF_5Ph)
95 (H-6): π (Ph)

- Singlet:

```
Excitation energies and oscillator strengths:
Excited State   1:      Singlet-A      2.8903 eV  428.97 nm  f=0.0000  <S**2>=0.000
    100 ->102        0.70081
 Excited State   2:      Singlet-A      3.3929 eV  365.43 nm  f=0.0000  <S**2>=0.000
    101 ->104        0.70350
Excited State   3:      Singlet-A      3.4956 eV  354.68 nm  f=0.1098  <S**2>=0.000
     98 ->106       -0.10044
     99 ->102       -0.14989
    101 ->102        0.67696
```

- Triplet:

```
Excitation energies and oscillator strengths:
Excited State   1:      Triplet-A      2.2858 eV  542.40 nm  f=0.0000  <S**2>=2.000
     99 ->102        0.25291
    101 ->102        0.64977
Excited State   2:      Triplet-A      2.5234 eV  491.34 nm  f=0.0000  <S**2>=2.000
    100 ->102        0.69396
    100 ->109        0.11958
Excited State   3:      Triplet-A      3.0964 eV  400.42 nm  f=0.0000  <S**2>=2.000
     97 ->107        0.16113
     98 ->107        0.11382
     99 ->102        0.59879
    101 ->102       -0.26137
    101 ->108       -0.11044
Excited State   4:      Triplet-A      3.2691 eV  379.26 nm  f=0.0000  <S**2>=2.000
     97 ->102        0.11959
     97 ->108        0.14442
     98 ->102        0.45196
     99 ->107        0.21105
    101 ->105        0.16853
    101 ->106        0.40113
Excited State   5:      Triplet-A      3.3828 eV  366.51 nm  f=0.0000  <S**2>=2.000
    101 ->104        0.70353
```

6.2. $CHCl_3$ solvated:

Orbital Topology:
109* (L+7): π* (Ac)
106* (L+4): π* (PhAc)
105* (L+3): π* (PhAc)
104* (L+2): π* (SF_5Ph)
103* (L+1): σ* (SF_5Ph)
102* (L): π* (Ac)
101 (H): π (Ac)
100 (H-1): n (C=O)
99 (H-2): π (Ac)
98 (H-3): π (Ac)
97 (H-4): π (PhAc)
96 (H-5): π (PhAc)
95 (H-6): π (SF_5Ph)

- Singlet:

```
Excitation energies and oscillator strengths:
Excited State   1:      Singlet-?Sym    3.0343 eV  408.61 nm  f=0.0000  <S**2>=0.000
    100 ->102        0.70117
Excited State   2:      Singlet-?Sym    3.3722 eV  367.66 nm  f=0.1862  <S**2>=0.000
     99 ->102       -0.10867
    101 ->102        0.68996
Excited State   3:      Singlet-?Sym    3.6004 eV  344.36 nm  f=0.0000  <S**2>=0.000
    101 ->104        0.70392
```

- Triplet:

```
Excitation energies and oscillator strengths:
Excited State   1:      Triplet-?Sym    2.4528 eV  505.48 nm  f=0.0000  <S**2>=2.000
     99 ->102        0.14702
    101 ->102        0.68509
Excited State   2:      Triplet-?Sym    2.9225 eV  424.24 nm  f=0.0000  <S**2>=2.000
    100 ->102        0.69373
    100 ->109        0.11810
Excited State   3:      Triplet-?Sym    3.1830 eV  389.52 nm  f=0.0000  <S**2>=2.000
     97 ->107        0.16635
     98 ->106        0.11067
     98 ->107        0.12593
     99 ->102        0.61526
    101 ->102       -0.14222
    101 ->108       -0.15802
Excited State   4:      Triplet-?Sym    3.3054 eV  375.10 nm  f=0.0000  <S**2>=2.000
     97 ->102        0.19117
```

```
     97 ->108         0.15463
     98 ->102         0.42439
     99 ->107         0.20656
    101 ->105        -0.12297
    101 ->106         0.40041
    101 ->107        -0.14544
 Excited State   5:      Triplet-?Sym    3.5620 eV  348.08 nm  f=0.0000  <S**2>=2.000
    101 ->104         0.70431
```

Appendix 4. NMR spectroscopy and HRMS data from Chapter 4

a) ^{1}H NMR (500 MHz, $CDCl_3$), b) ^{13}C NMR (126 MHz, $CDCl_3$) c) ^{11}B NMR (128 MHz, $CDCl_3$) of the **MBA-CAT**.

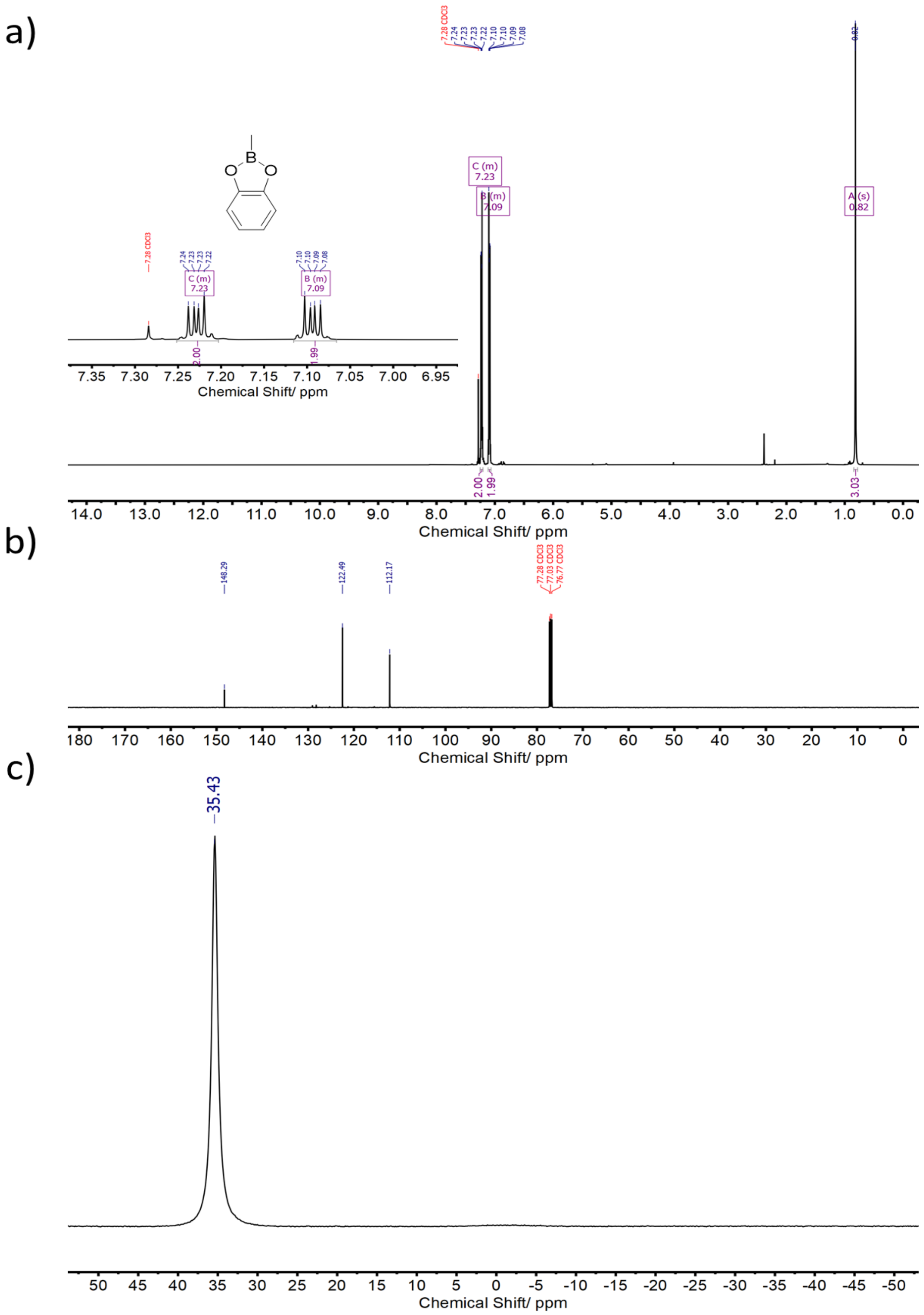

a) ^{1}H NMR (500 MHz, DMSO-d_6), b) ^{13}C NMR (126 MHz, DMSO-d_6) of **THB**.

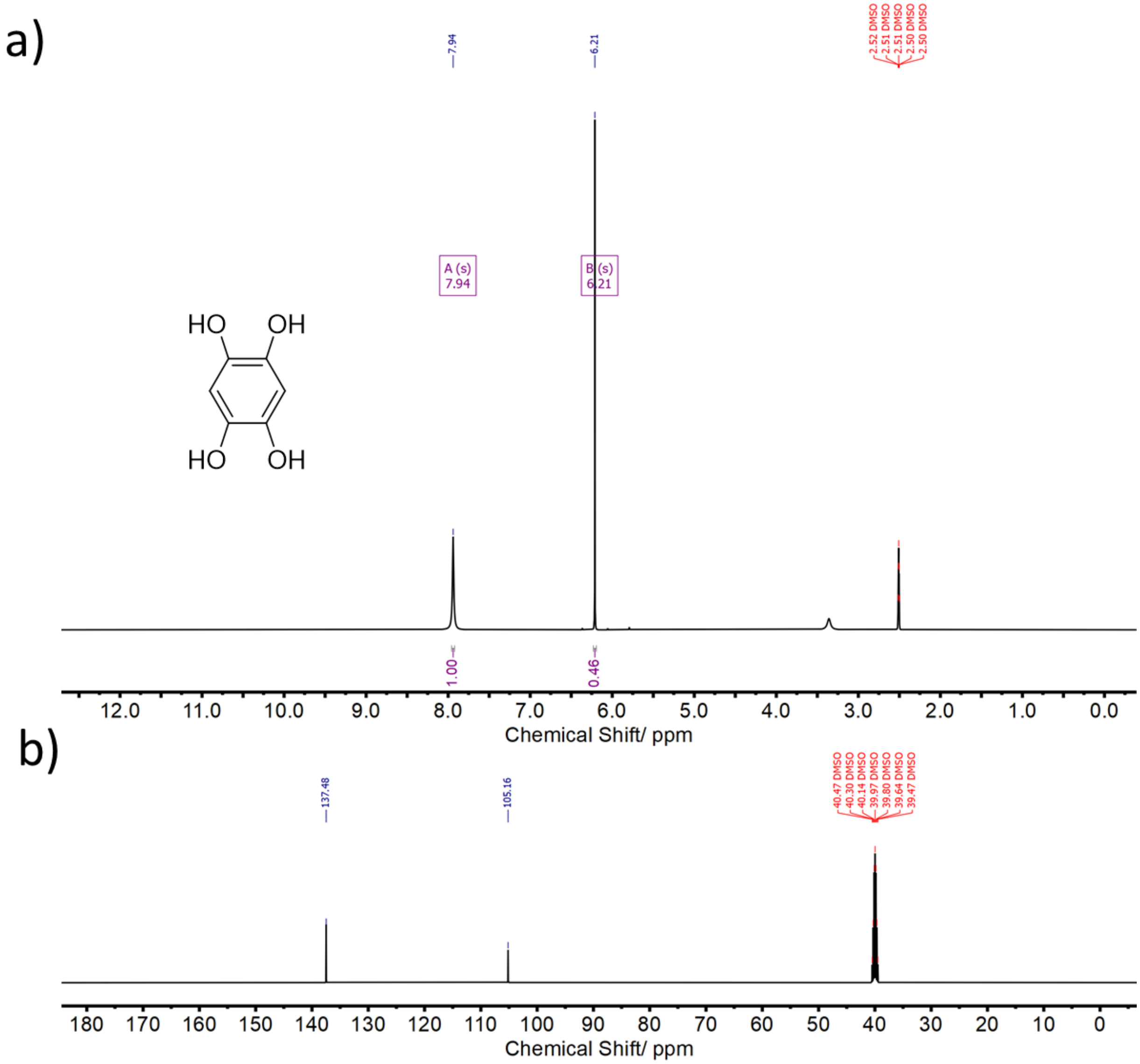

a) ^{1}H NMR (500 MHz, CDCl$_3$), b) ^{13}C NMR (126 MHz, CDCl$_3$) c) ^{11}B NMR (128 MHz, CDCl$_3$) and d) HRMS of **MBA-THB**.

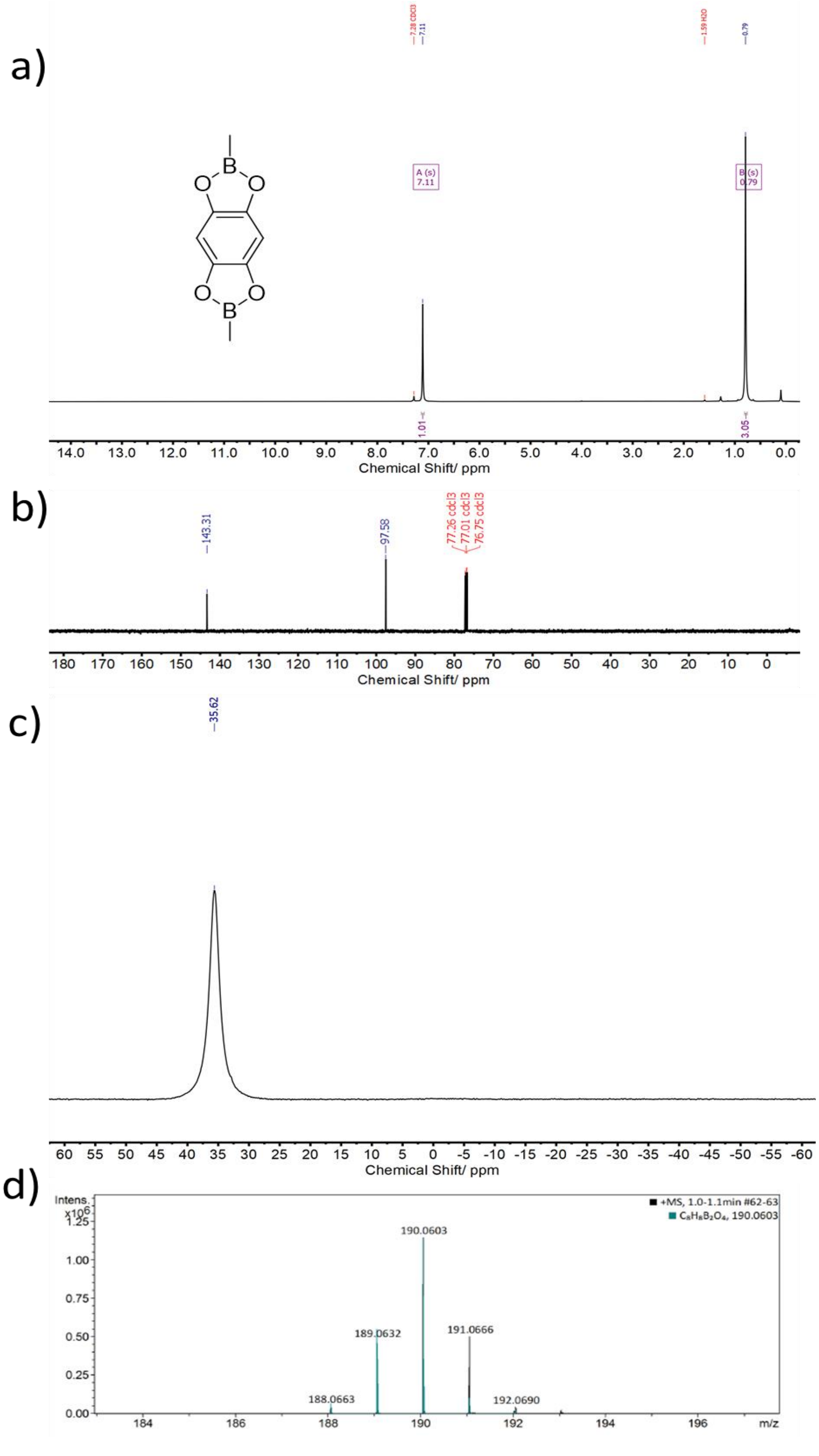

a) ^{1}H NMR (500 MHz, $CDCl_3$), b) ^{13}C NMR (126 MHz, $CDCl_3$) **HMTP**.

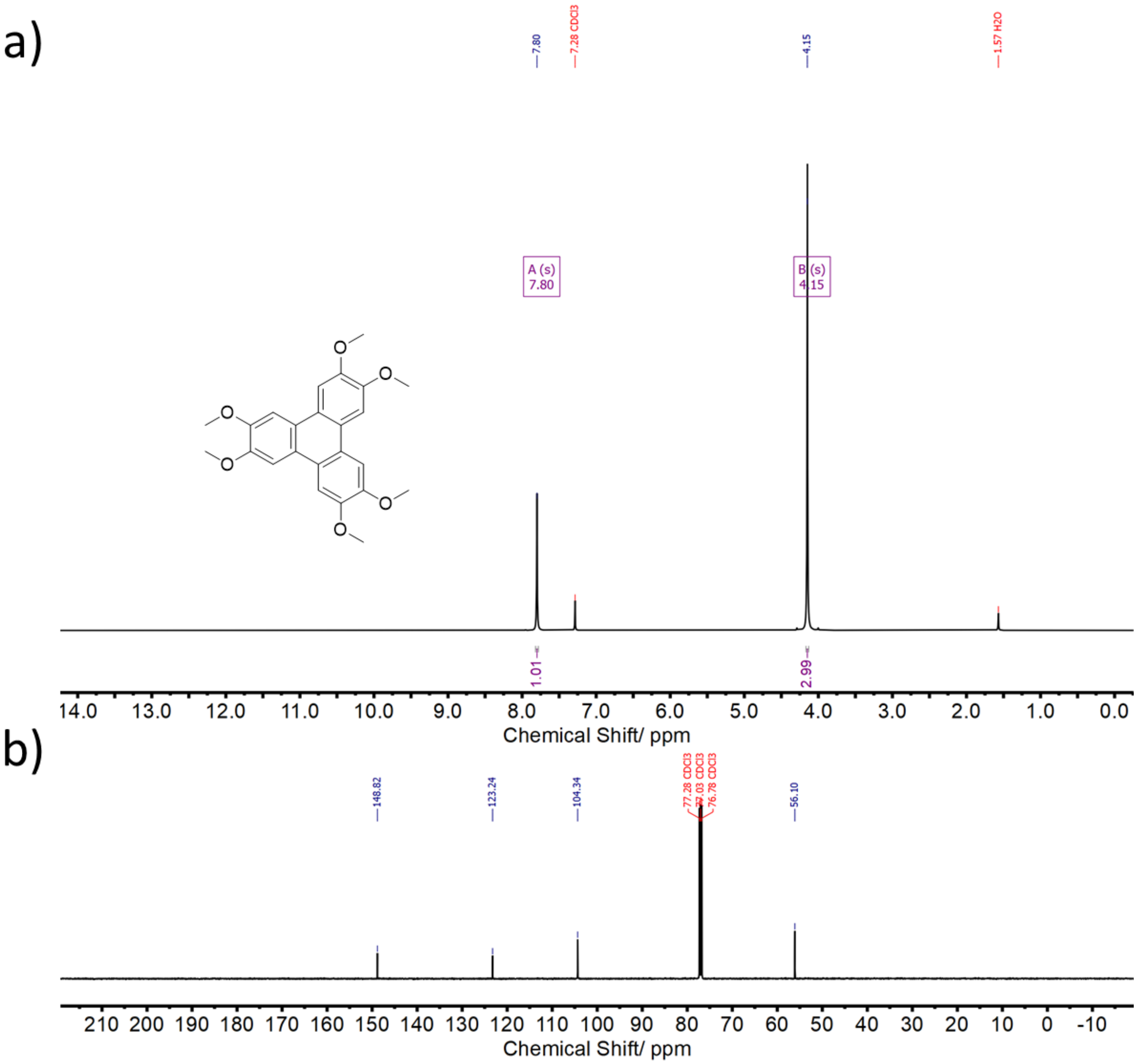

a) ^{1}H NMR (500 MHz, DMSO-d_6), b) ^{13}C NMR (126 MHz, DMSO-d_6) of **HHTP** (the peaks labeled in the gray area due to residual acetic acid).

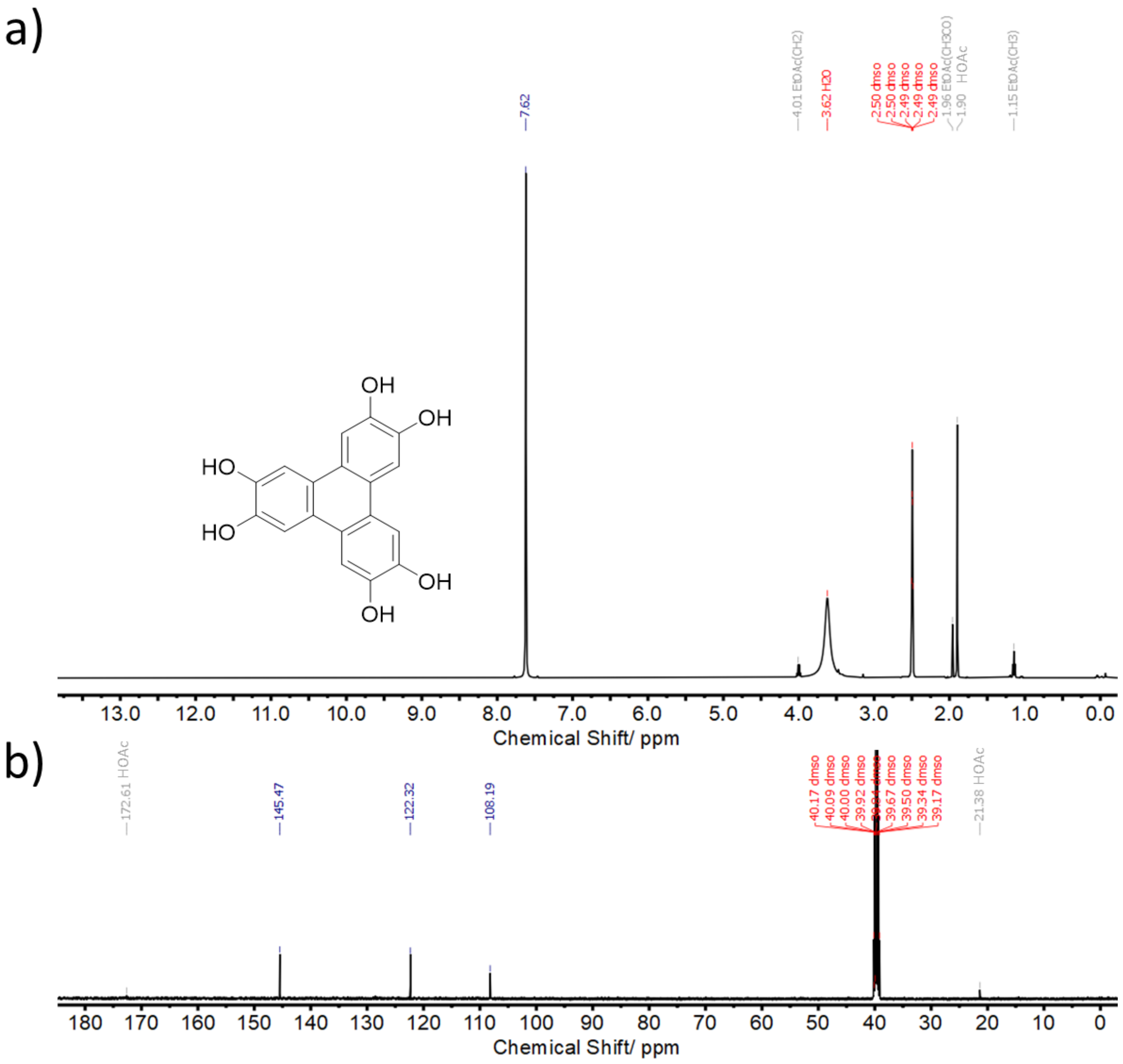

a) ^{1}H NMR (500 MHz, CDCl$_3$), b) ^{13}C NMR (126 MHz, CDCl$_3$) c) ^{11}B NMR (128 MHz, CDCl$_3$) and d) HRMS of **MBA-HHTP**. The small peak in ^{11}B NMR at ~-2 ppm is due to the B-impurities of the NMR tube glass.

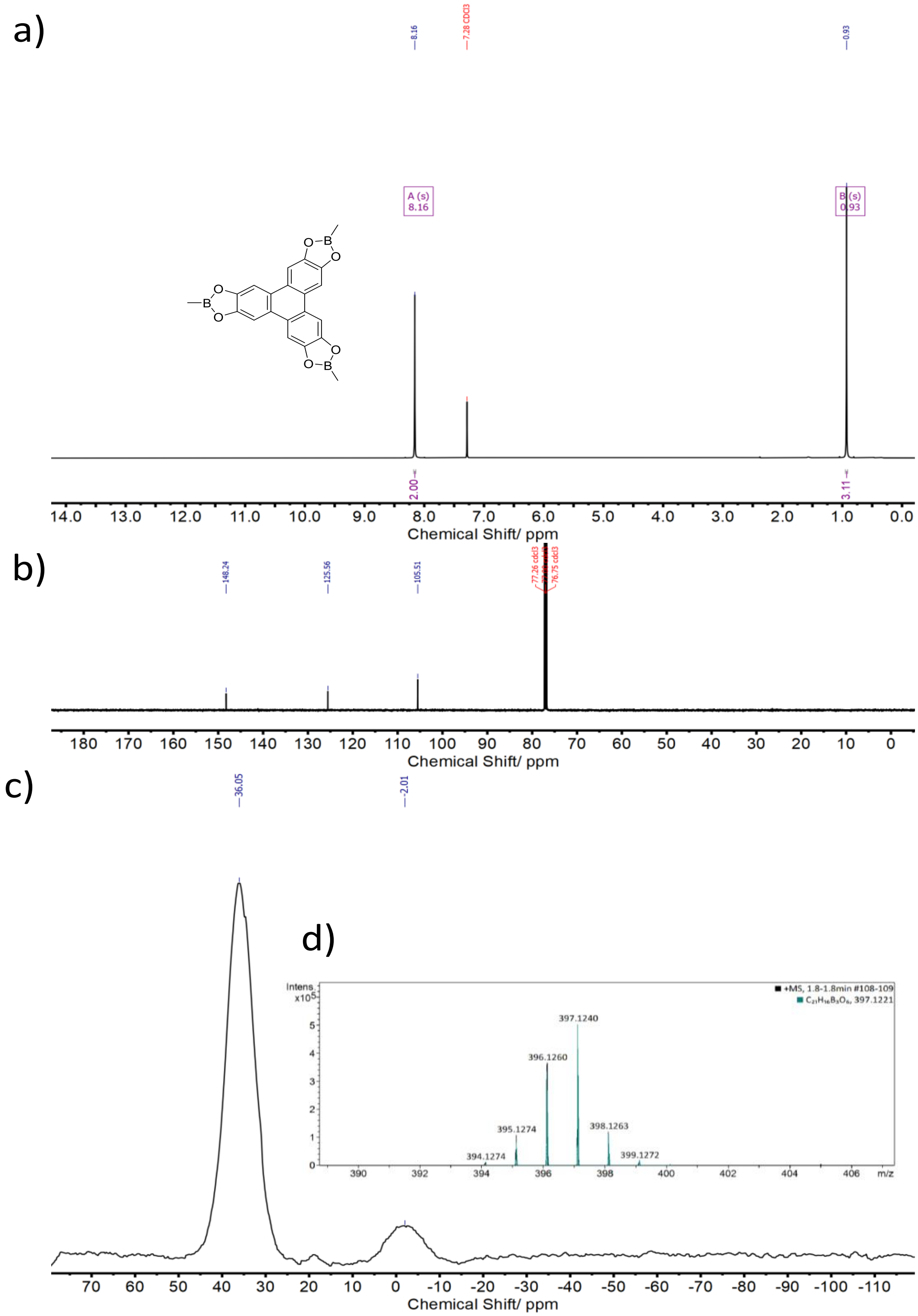

a) ^{1}H NMR (500 MHz, CDCl$_3$), b) ^{13}C NMR (126 MHz, CDCl$_3$) c) ^{11}B NMR (128 MHz, CDCl$_3$) of **Py4Bpin**.

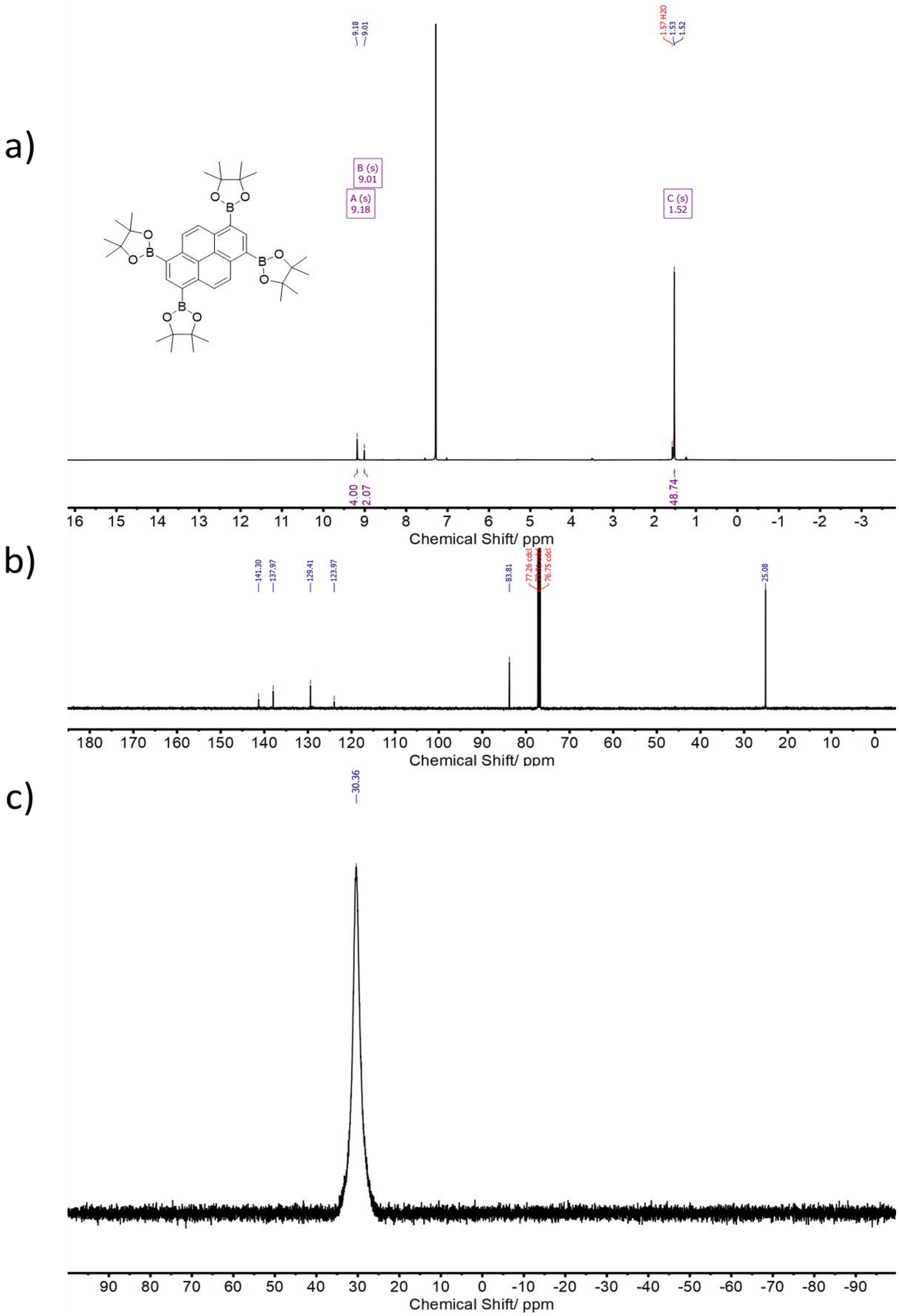

Appendix 5. NMR Spectra of precursors in Chapter 5

a) ^{1}H NMR (500 MHz, CDCl$_3$), b,c) ^{13}C NMR (126 MHz, CDCl$_3$) of ClBpin; the broad ^{13}C signal is for the C-B carbon.

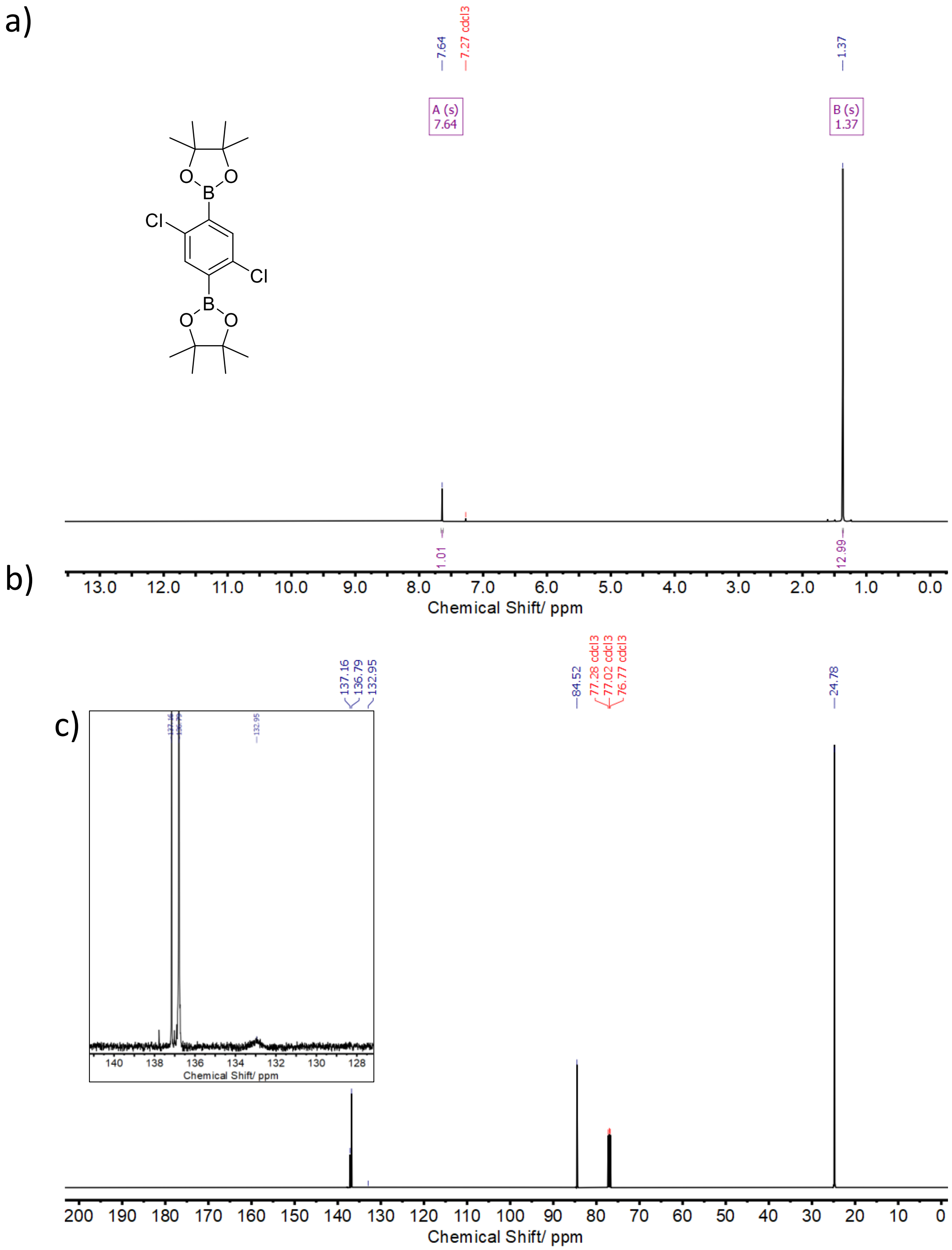

a) ^{1}H NMR (500 MHz, DMSO-d_6 / D_2O), b,c) ^{13}C NMR (126 MHz, DMSO-d_6 / D_2O) of ClPBA; the broad ^{13}C signal is for the C-B carbon.

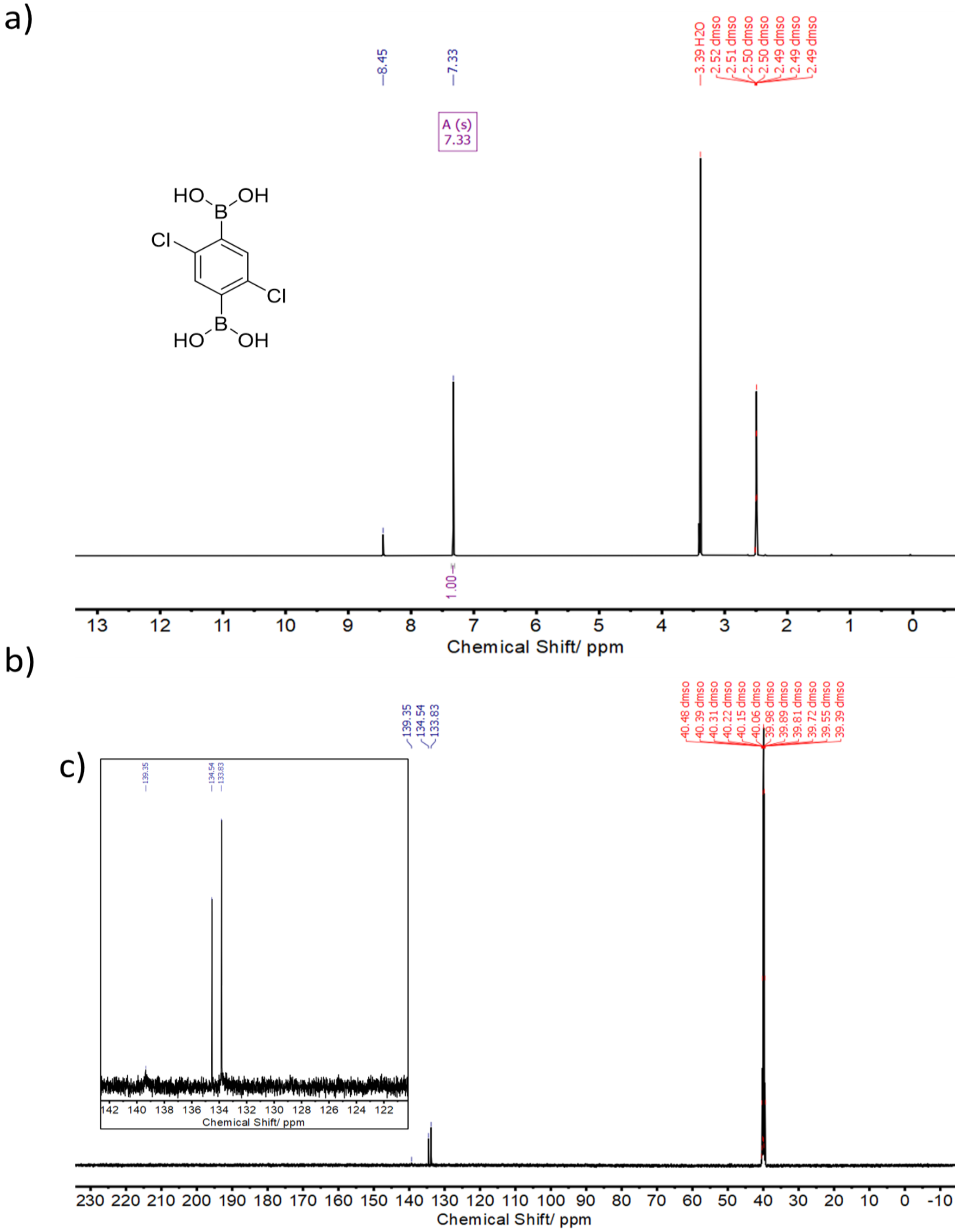

a) ^{1}H NMR (500 MHz, $CDCl_3$), b,c) ^{13}C NMR (126 MHz, $CDCl_3$) of BrBpin in $CDCl_3$; the broad ^{13}C signal is for the C-B carbon.

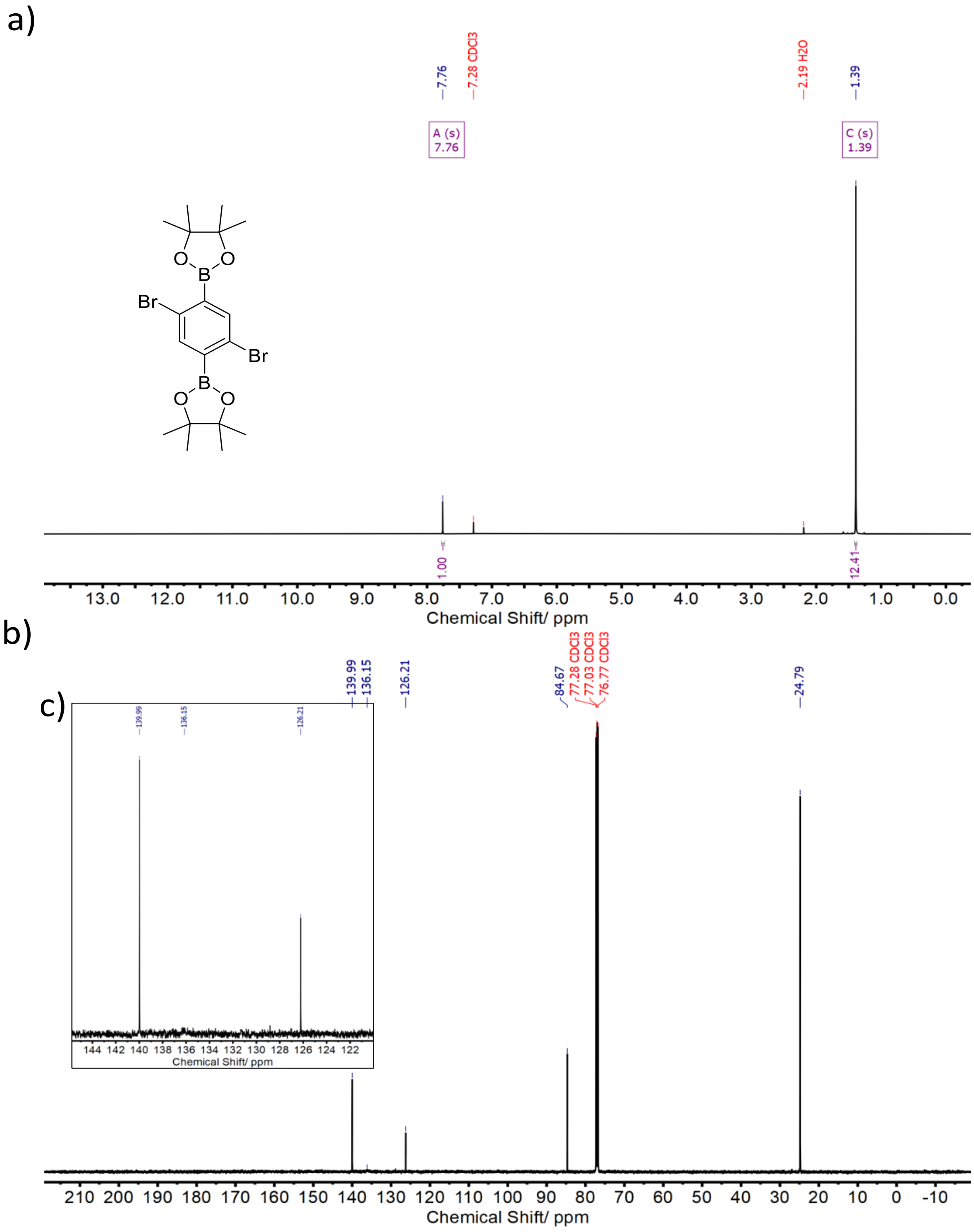

a) ^{1}H NMR (500 MHz, DMSO-d_6 / D_2O), b,c) ^{13}C NMR (126 MHz, DMSO-d_6 / D_2O)of BrPBA; the broad ^{13}C signal is for the C-B carbon.

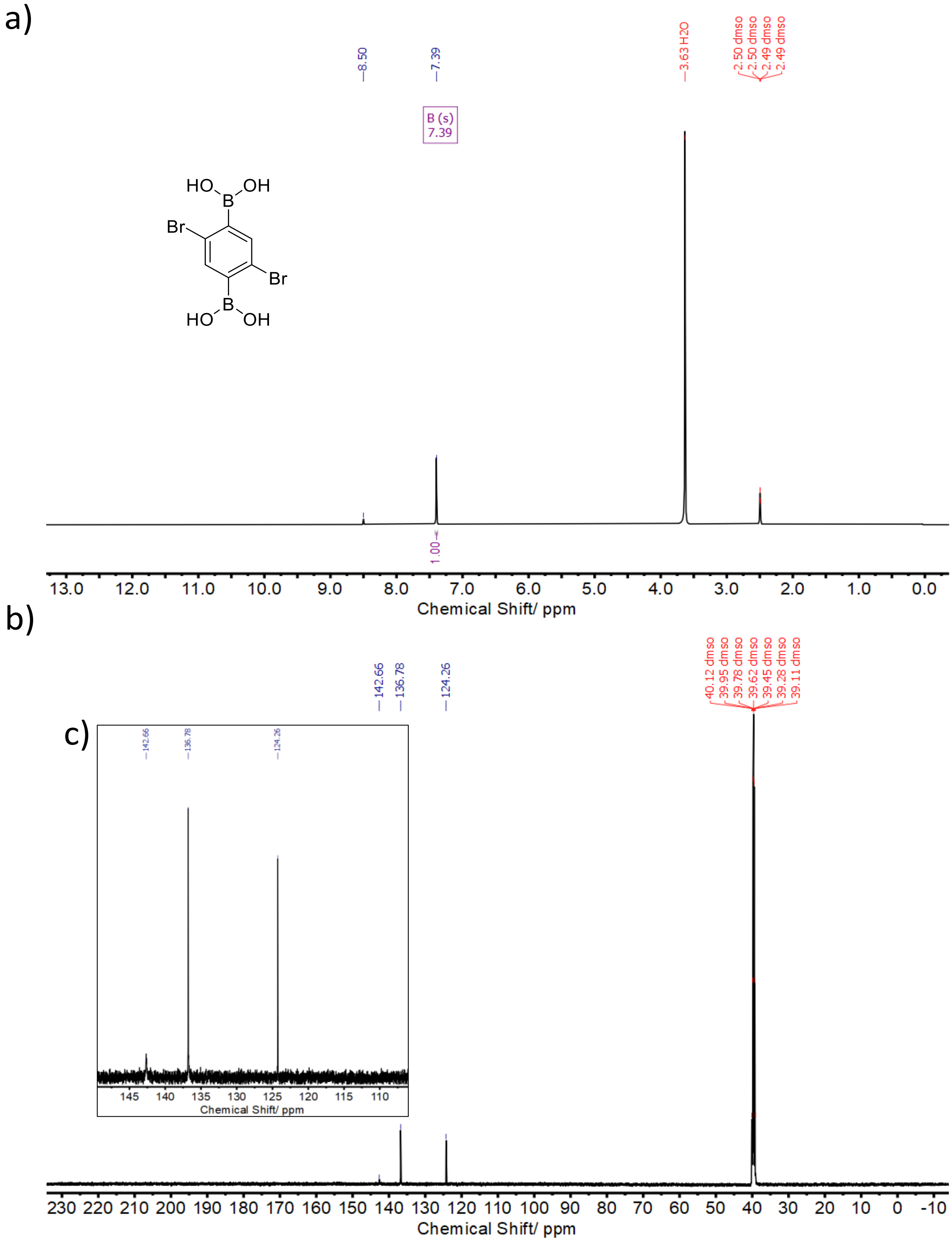

^{1}H NMR (500 MHz, $CDCl_3$) of mesitylene

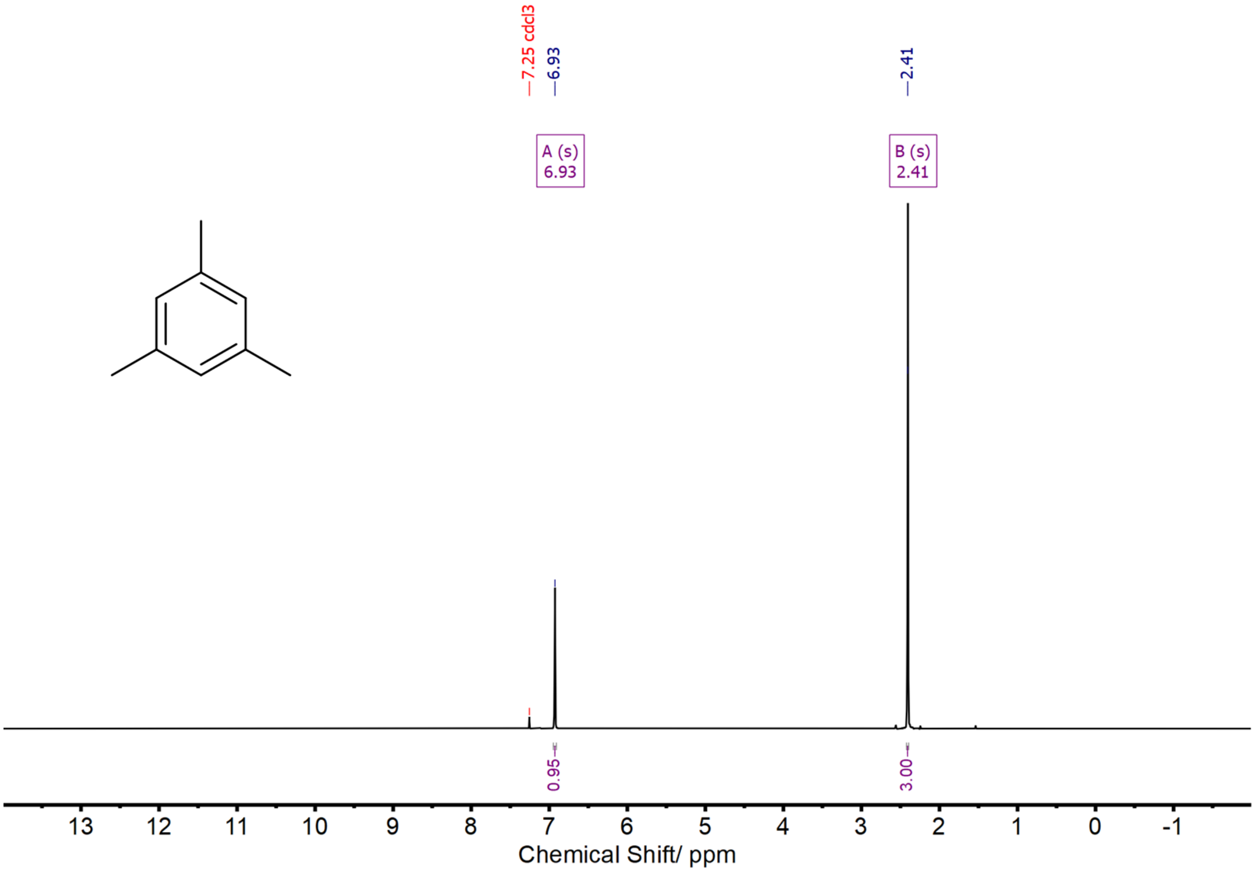

Appendix 6: The experimental and DFT-calculated vibrational modes of ClPBA and BrPBA from Chapter 5

Peak assignments for IR spectrum of ClPBA.

Exp. (cm^{-1})	Calc. (cm^{-1})	Vibration (Displacement vector scale in 5)	Notes
3301 (B)	3640	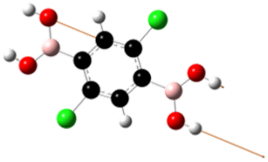	O-H stretch from -B(OH)$_2$ groups
1473(S)	1453	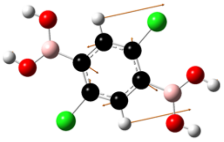	C-H vibration (overtone band) of substituted benzene and overlapped with phenyl ring C=C vibration
1388 (M)	1381	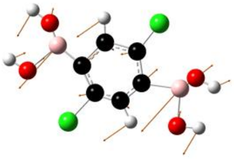	B-O stretch from -B(OH)$_2$ groups
1366 (M)	1321	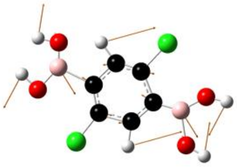	B-O stretch from -B(OH)$_2$ groups
1282 (S)	1260	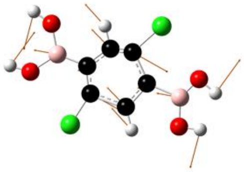	C-B stretch and overlapped with C-C and C-H stretch
1155 (M)	1245	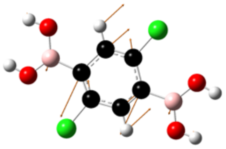	C-H in-plane deformation band for substituted benzene
1126 (M)	1118	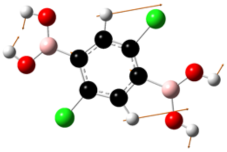	C-H in-plane deformation band for substituted benzene

1080 (M)	1039	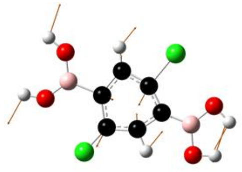	B-C stretch and overlapped with C-H vibration
1017 (S)	969	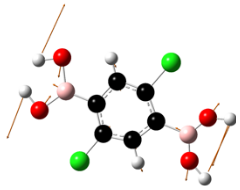	B-C stretch and overlapped with C-H vibration
907 (S)	902	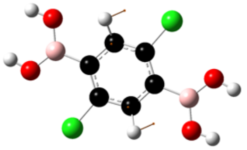	C-H out of plane deformation band for substituted benzene
806 (B)	903	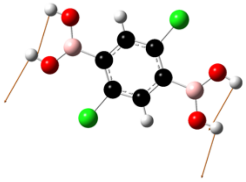	O-H bend vibration from -B(OH)$_2$ groups
683 (M)	632	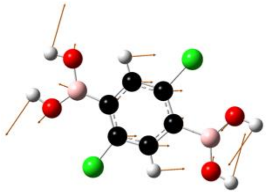	Out-of-plane deformation for -B(OH)$_2$ and overlapped with C-H vibration
592 (S)	561	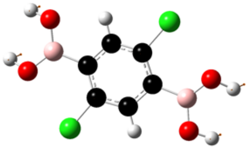	The vibration of -B(OH)$_2$ groups
519 (S)	544	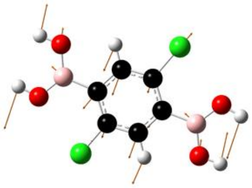	C-Cl stretch (characteristic band for ClPBA)

Peak assignments for IR spectrum of BrPBA

Exp. (cm^{-1})	Calc. (cm^{-1})	Vibration (Displacement vector scale in 5)	Notes
3299 (B)	3674	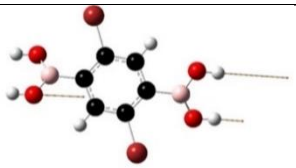	O-H stretch from $-B(OH)_2$ groups
1471(S)	1453	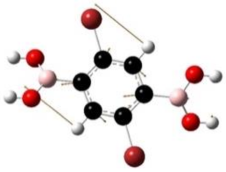	C-H vibration (overtone band) of substituted benzene and overlapped with phenyl ring C=C vibration
1384 (M)	1373	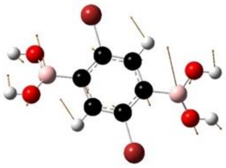	B-O stretch (compressing) from $-B(OH)_2$ groups
1361 (M)	1359	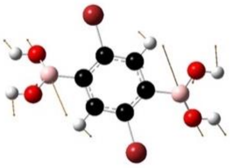	B-O stretch (stretching) from $-B(OH)_2$ groups
1276 (S)	1323	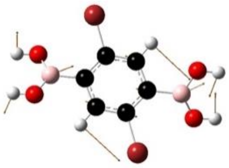	C-B stretch and overlapped with C-C and C-H stretch
1159 (M)	1260	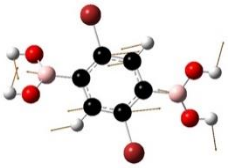	C-H in-plane deformation band for substituted benzene
1124 (M)	1239	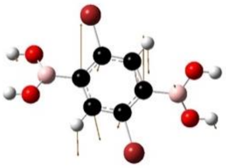	C-H in-plane deformation band for substituted benzene

1065 (M)	1119	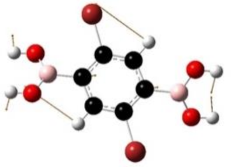	B-C stretch and overlapped with C-H vibration
1008 (S)	1021	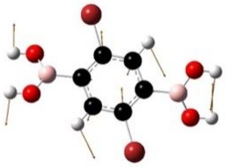	B-C stretch and overlapped with C-H vibration
903 (S)	966	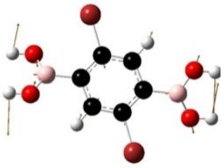	C-H out of plane deformation band for substituted benzene
805 (B)	906	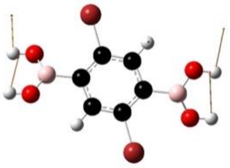	O-H bend vibration from $-B(OH)_2$ groups
676 (M)	589	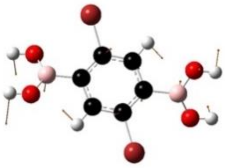	Out-of-plane deformation for $-B(OH)_2$ and overlapped with C-H vibration
557 (S)	536	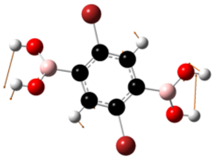	The vibration of $-B(OH)_2$ groups
476 (S)	467	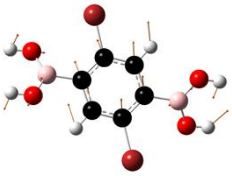	C-Br stretch (characteristic band for BrPBA)

Appendix 7. NMR Spectra of precursors in Chapter 6

^{1}H NMR (500 MHz, $CDCl_3$) Tris(2-fluoro-6-methoxyphenyl)amine (1).

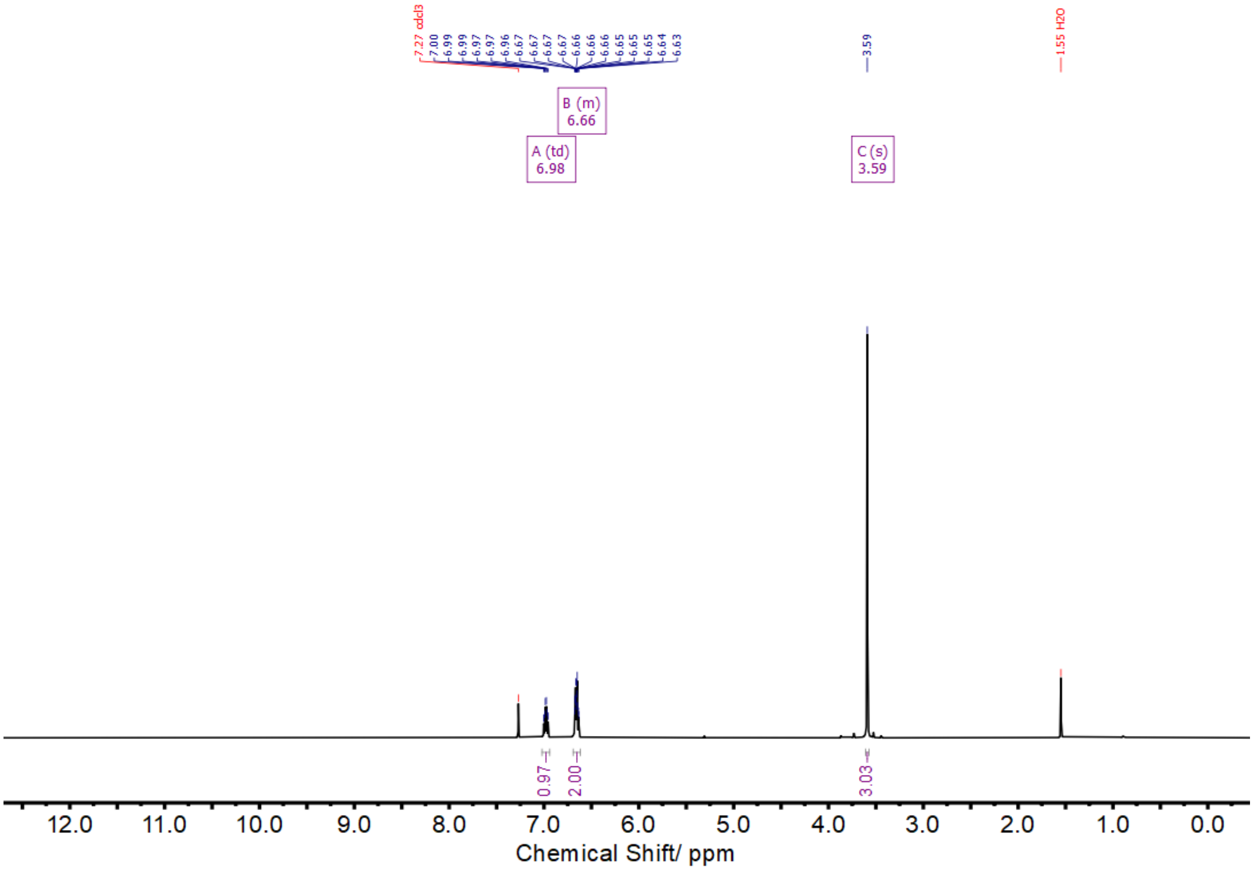

^{13}C NMR (126 MHz, $CDCl_3$) of Tris(2-fluoro-6-methoxyphenyl)amine (1)

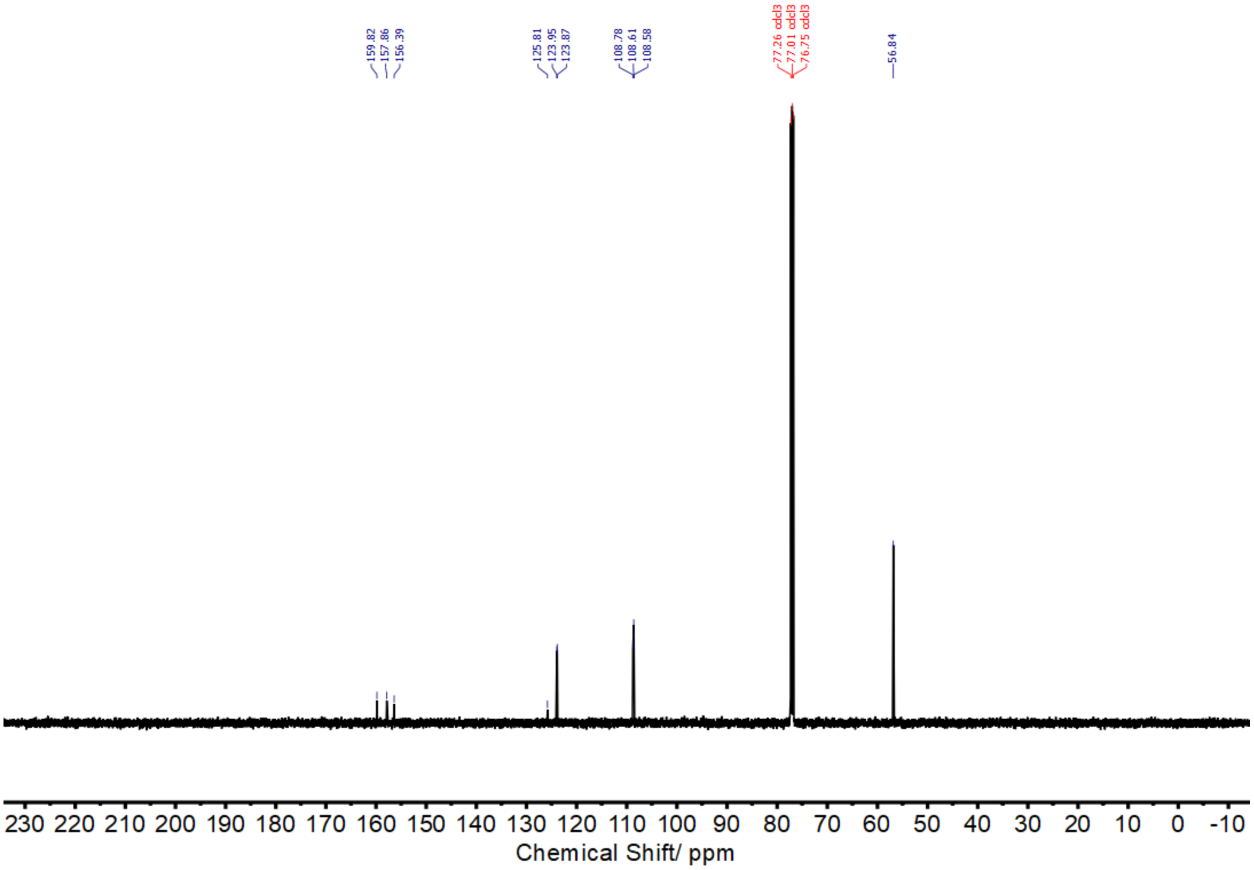

^{19}F NMR(376 MHz, $CDCl_3$) of Tris(2-fluoro-6-methoxyphenyl)amine (1).

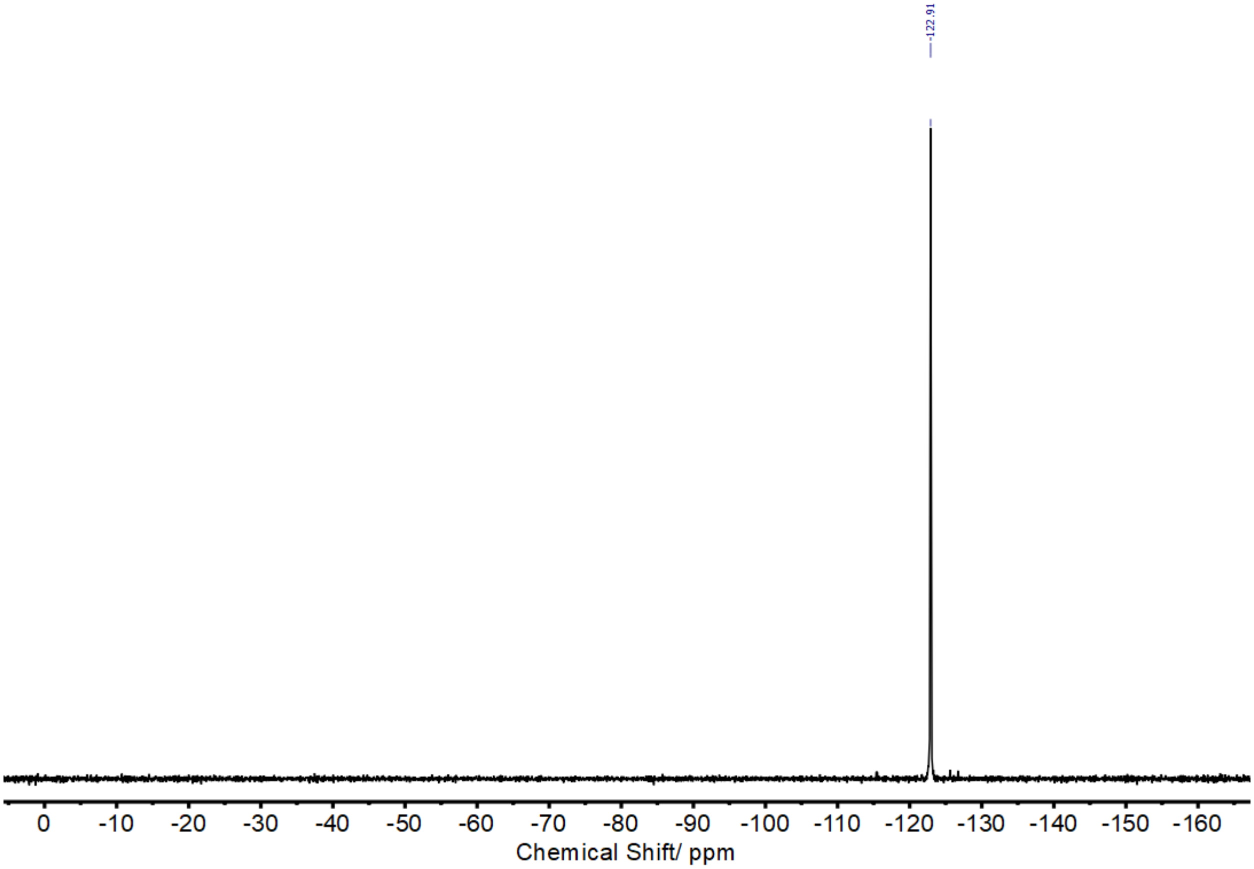

^{1}H NMR (500 MHz, CDCl$_3$) of Tris(2-fluoro-6-hydroxyphenyl)amine (2).

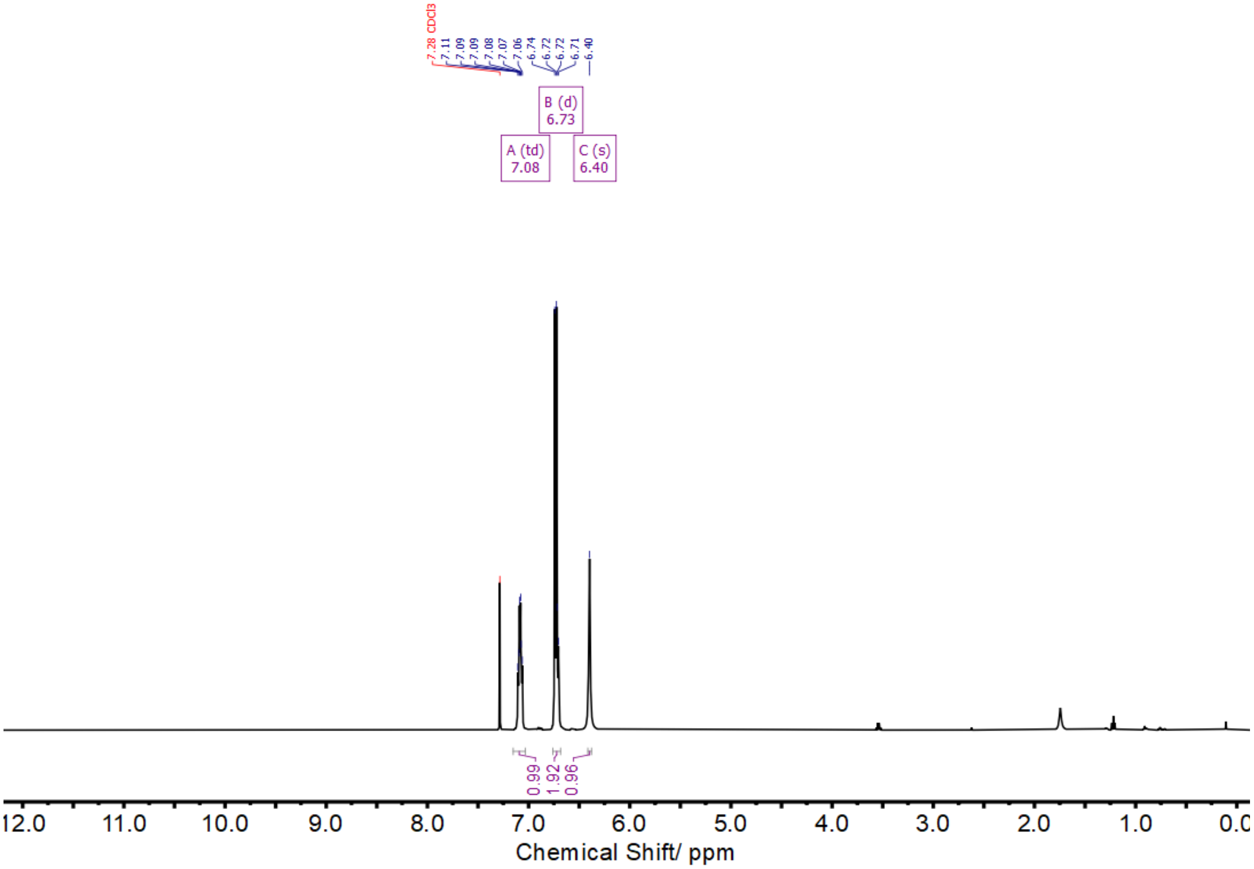

^{13}C NMR (126 MHz, $CDCl_3$) spectra Tris(2-fluoro-6-hydroxyphenyl)amine (2).

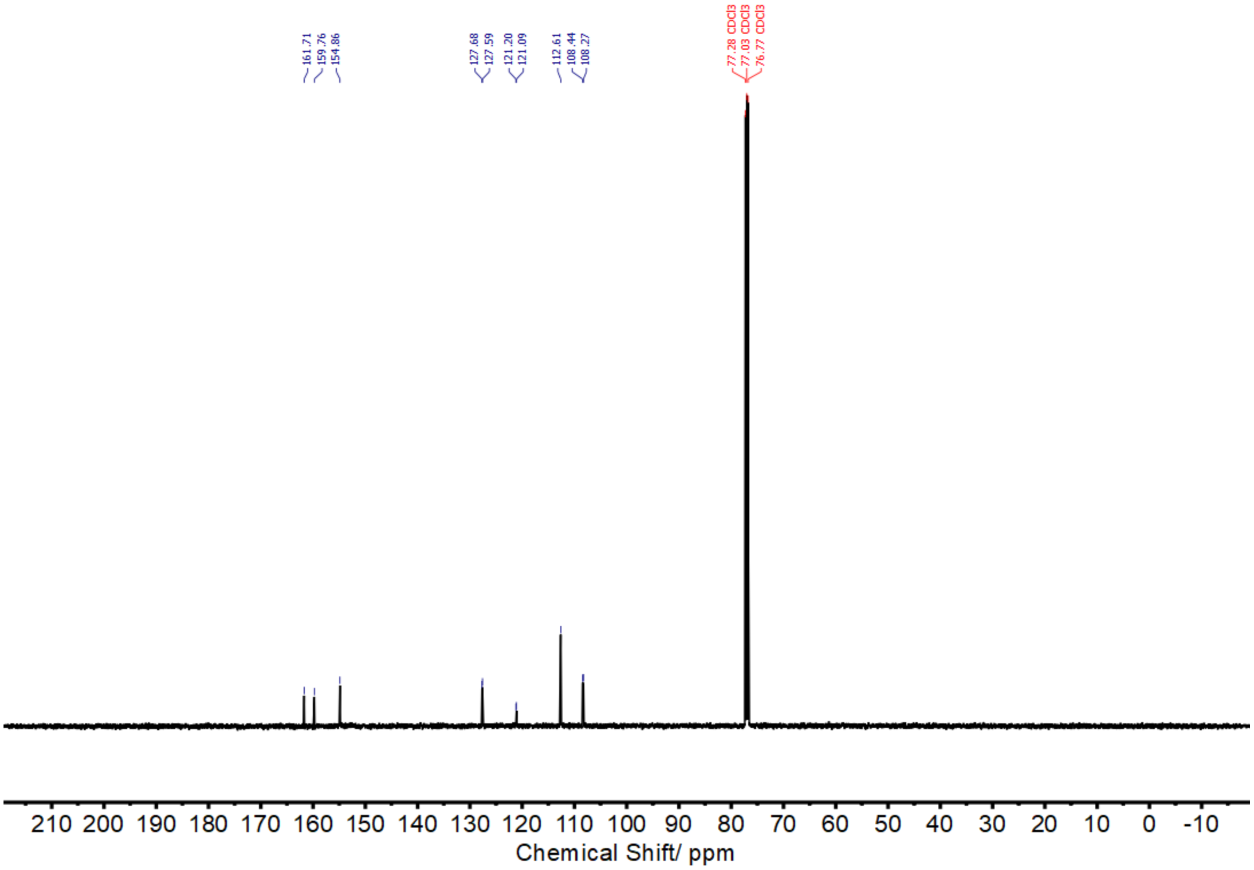

^{19}F NMR(376 MHz, $CDCl_3$) Tris(2-fluoro-6-hydroxyphenyl)amine (2).

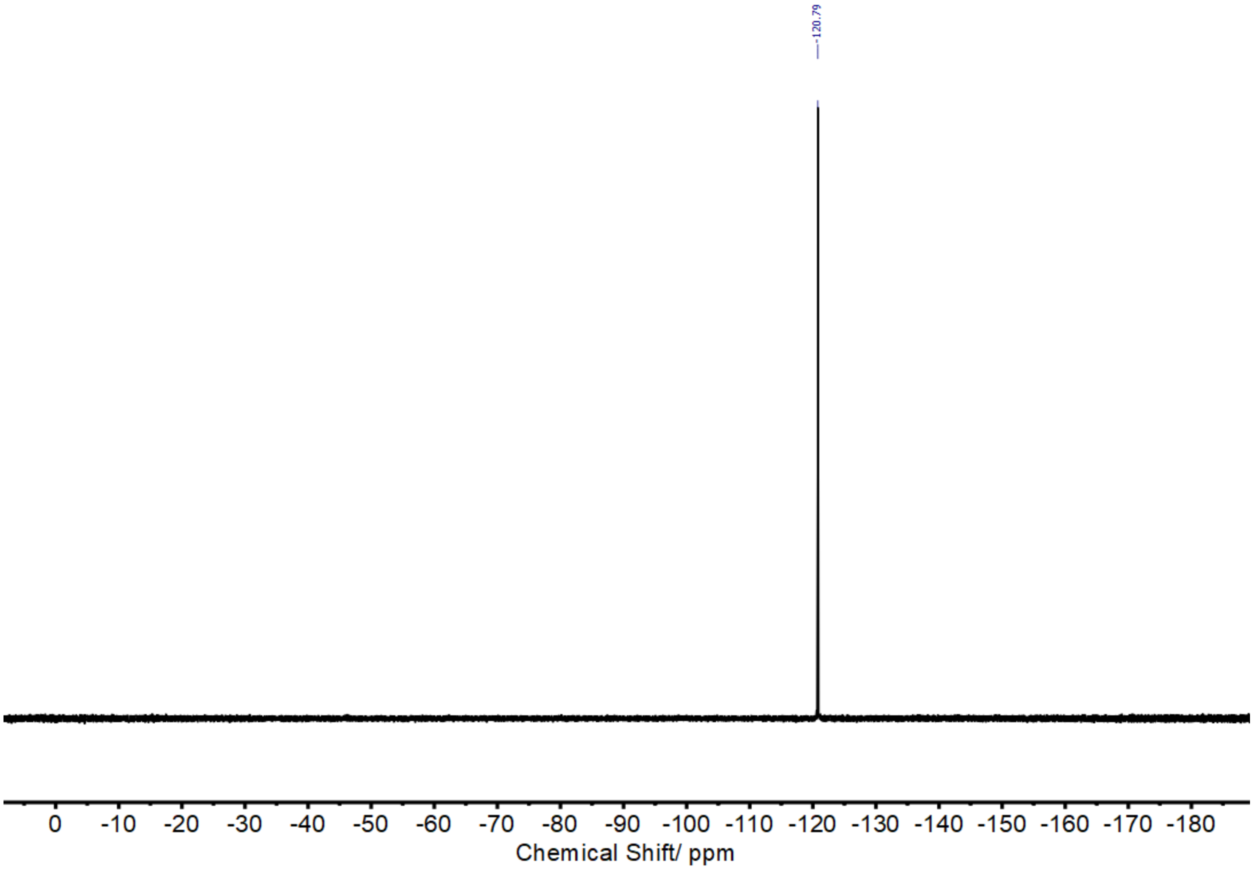

^{1}H NMR (500 MHz, C_6D_6) of 2,2':6',2'':6'',6-trioxytriphenylamine (TANG).

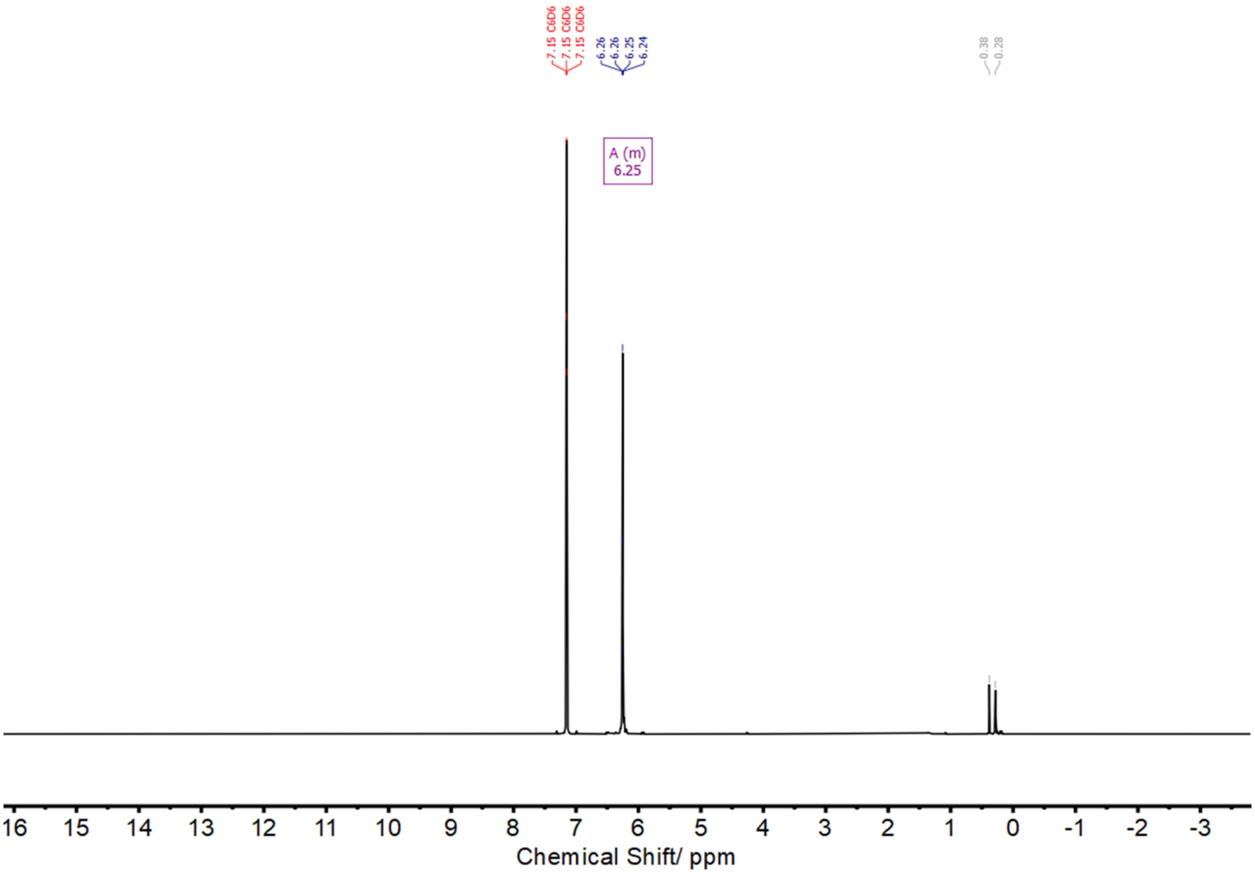

^{113}C NMR (126 MHz, C_6D_6) NMR spectra 2,2':6',2'':6'',6-trioxytriphenylamine (TANG).

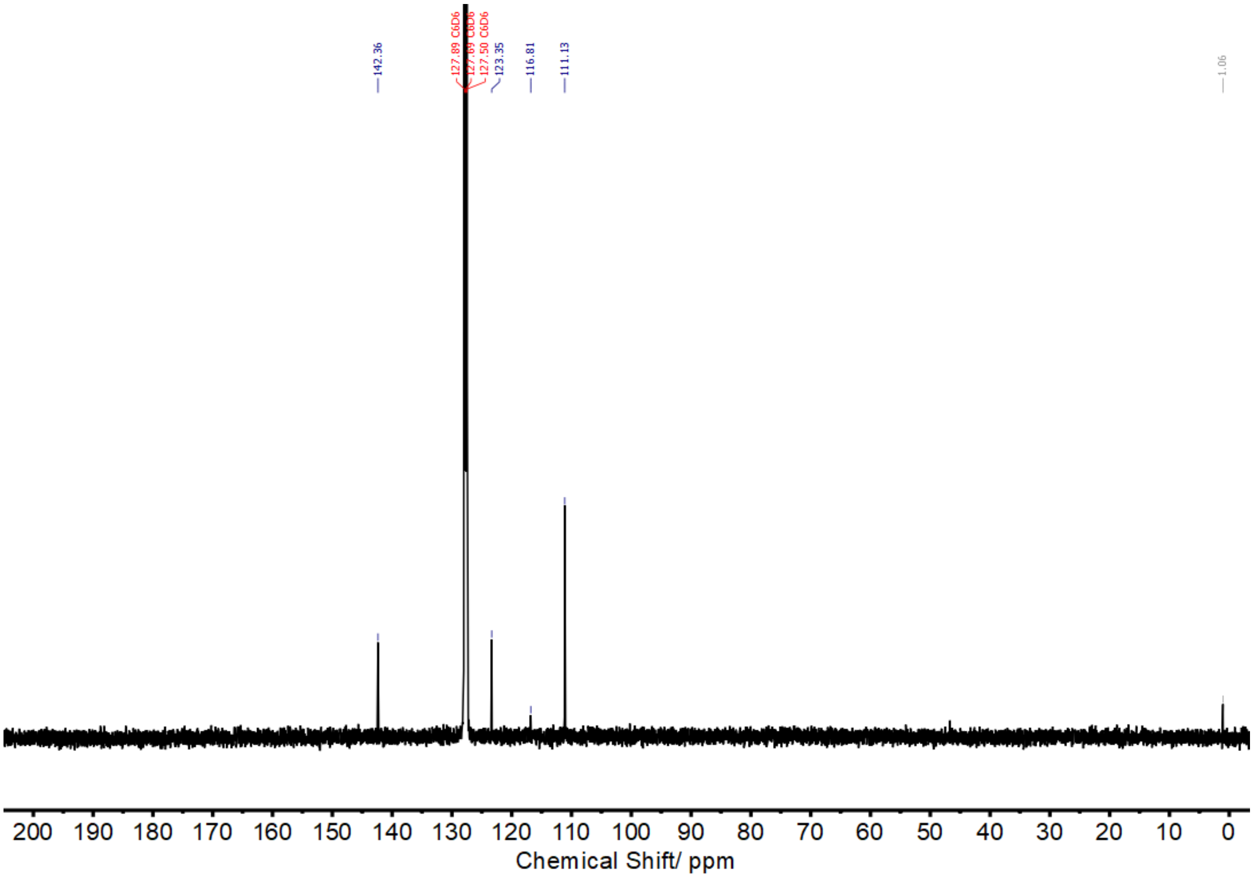

^{1}H NMR (500 MHz, DMSO-d_6) of 4,4',4'''-Triformyl-2,2':6',2'':6'',6-trioxytriphenylamine (TATANG) at 90 °C

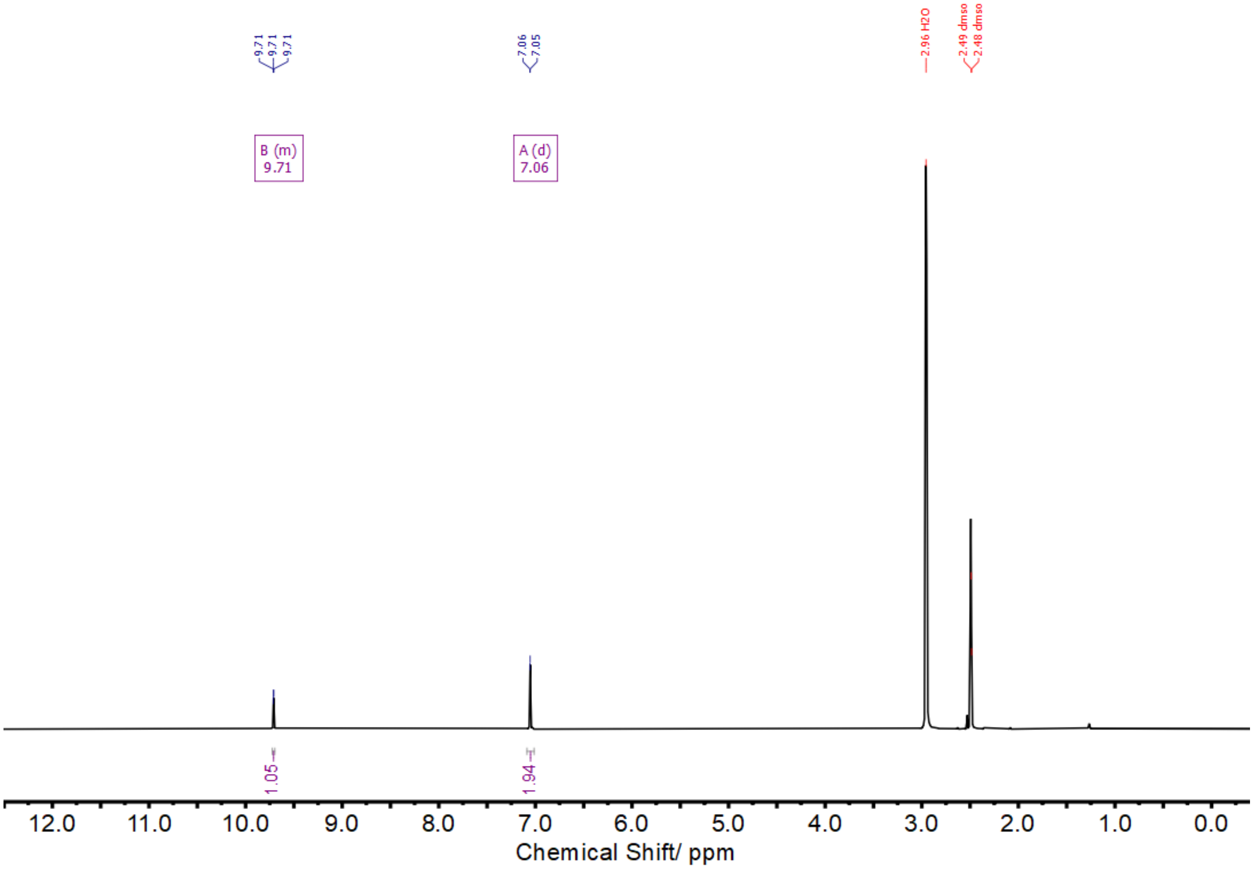

^{13}C NMR (126 MHz, DMSO-d_6) of 4,4',4'''-Triformyl-2,2':6',2'':6'',6-trioxytriphenylamine (TATANG) at 90 °C.

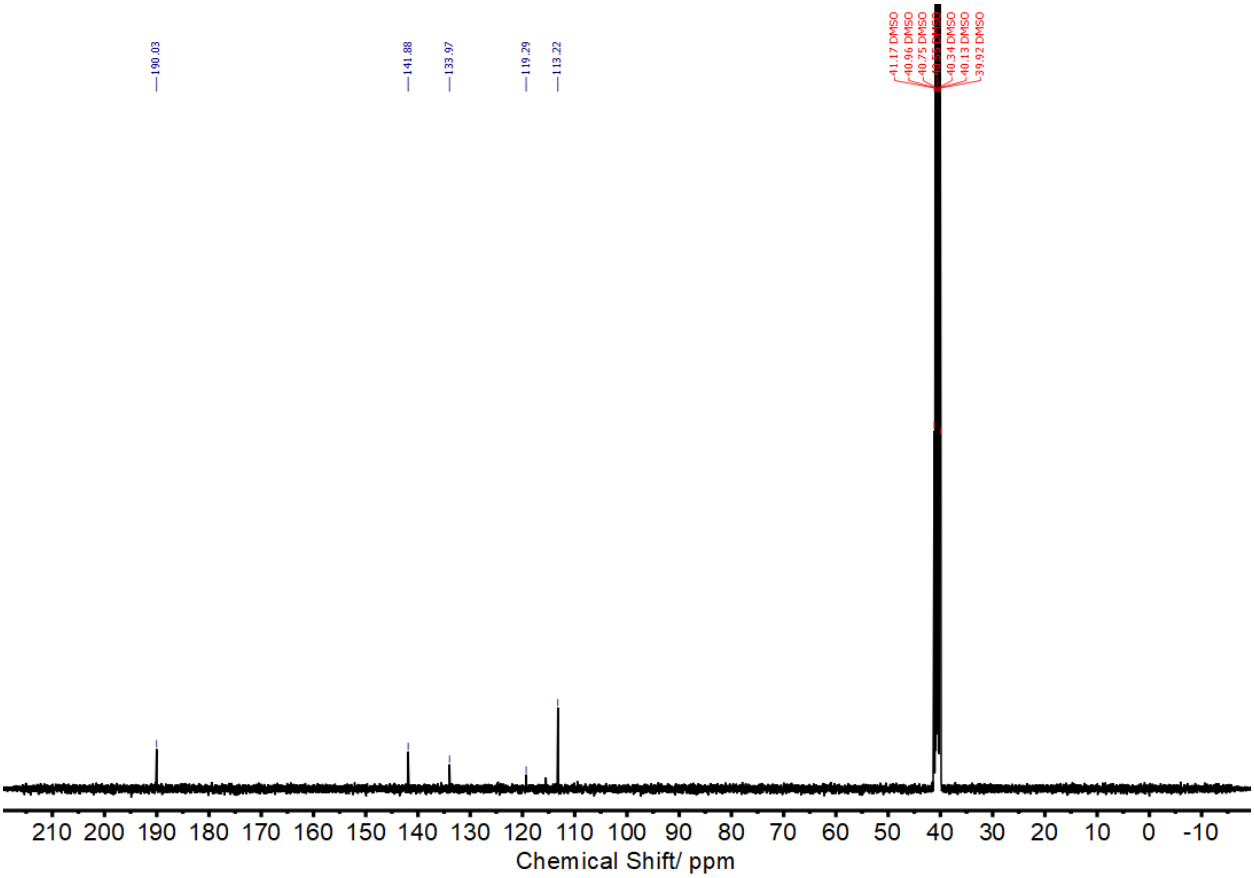

^{1}H NMR (500 MHz, DMSO-d_6) of 4,4',4'''-Tris(cyanomethyl)-2,2':6',2'':6'',6-trioxytriphenylamine (CNTANG) at 90 °C

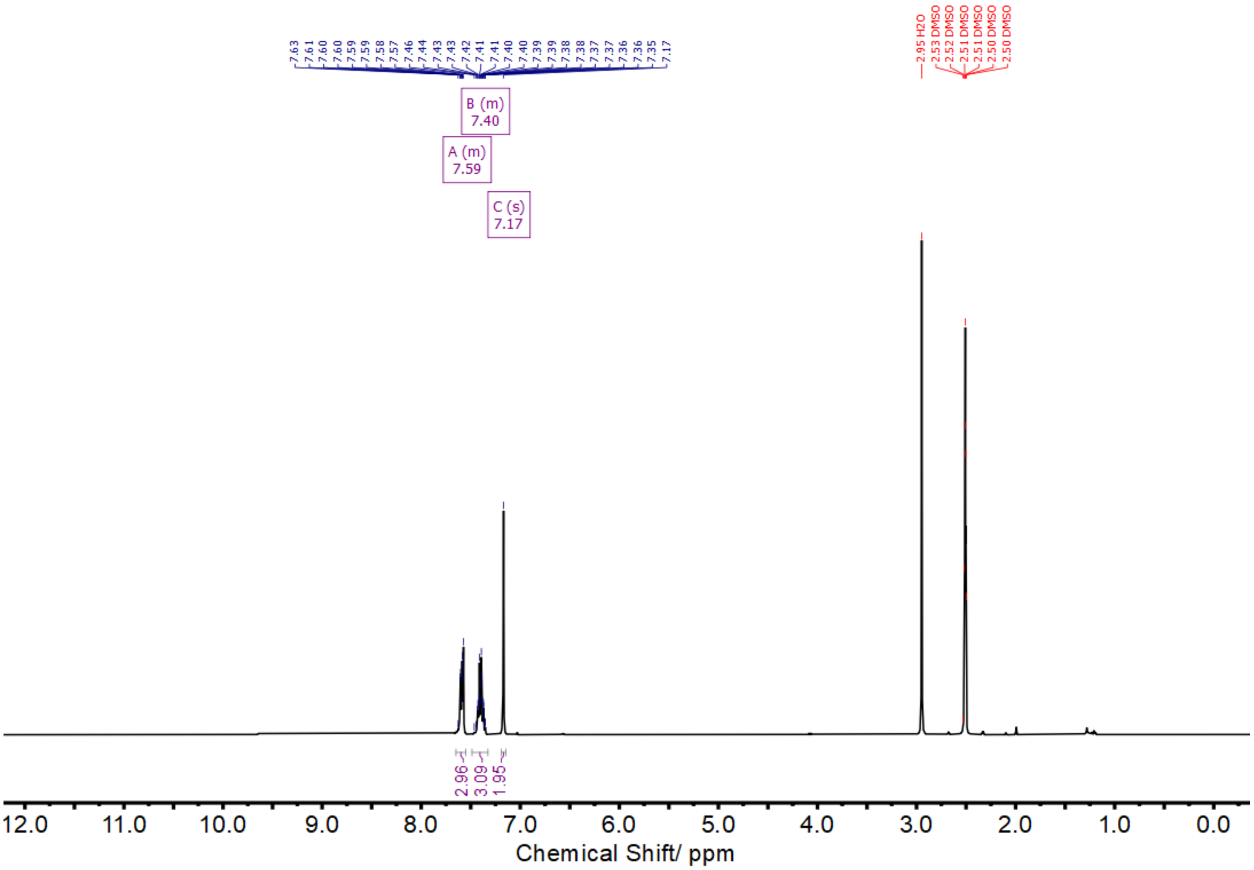

^{13}C NMR (126 MHz, DMSO-d_6) of 4,4',4'''-Tris(cyanomethyl)-2,2':6',2'':6'',6-trioxytriphenylamine (CNTANG) at 90 °C.

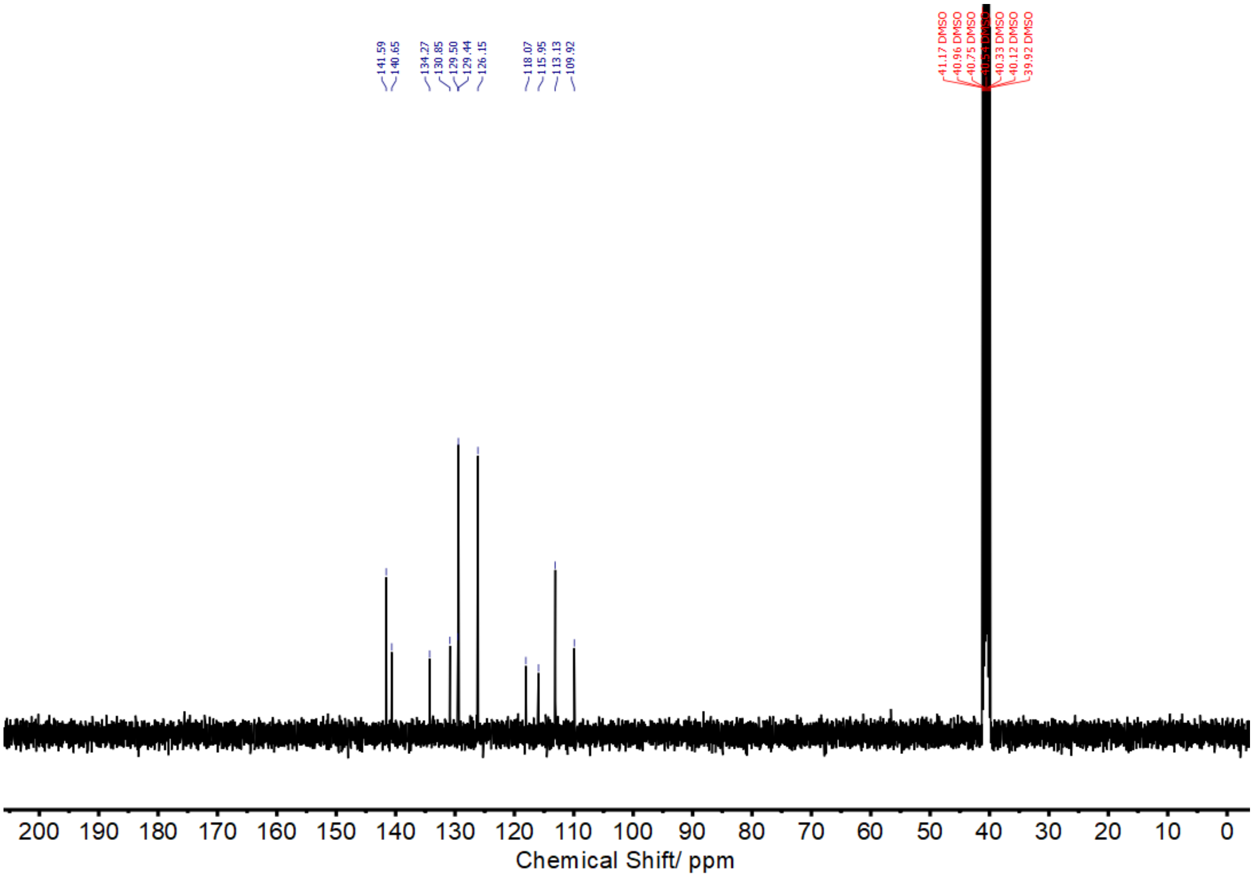

Appendix 8: Copyright authorizations from publishers

Copyright clearance from John Wiley and Sons (Chapter 2)

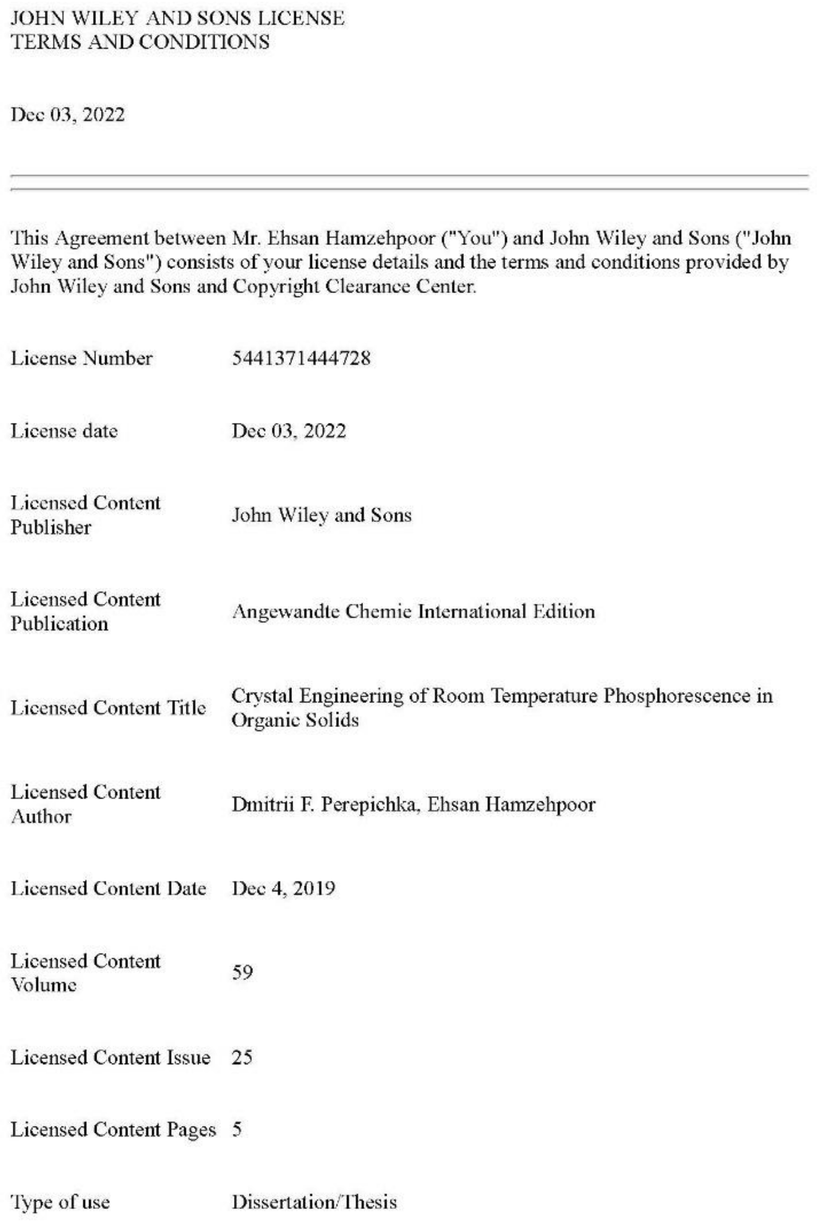

JOHN WILEY AND SONS LICENSE
TERMS AND CONDITIONS

Dec 03, 2022

This Agreement between Mr. Ehsan Hamzehpoor ("You") and John Wiley and Sons ("John Wiley and Sons") consists of your license details and the terms and conditions provided by John Wiley and Sons and Copyright Clearance Center.

License Number	5441371444728
License date	Dec 03, 2022
Licensed Content Publisher	John Wiley and Sons
Licensed Content Publication	Angewandte Chemie International Edition
Licensed Content Title	Crystal Engineering of Room Temperature Phosphorescence in Organic Solids
Licensed Content Author	Dmitrii F. Perepichka, Ehsan Hamzehpoor
Licensed Content Date	Dec 4, 2019
Licensed Content Volume	59
Licensed Content Issue	25
Licensed Content Pages	5
Type of use	Dissertation/Thesis

Requestor type	Author of this Wiley article
Format	Print and electronic
Portion	Full article
Will you be translating?	No
Title	Crystal Engineering of Room Temperature Phosphorescence in Organic Solids
Institution name	McGill University
Expected presentation date	Jan 2023
Order reference number	42361211
Requestor Location	Mr. Ehsan Hamzehpoor Department of Chemistry, McGill University, Otto Maass Chemistry 801 Sherbrooke Street West, Montreal, QC H3A0B8 Canada Attn: Mr. Ehsan Hamzehpoor
Publisher Tax ID	EU826007151
Total	0.00 USD
Terms and Conditions	

TERMS AND CONDITIONS

This copyrighted material is owned by or exclusively licensed to John Wiley & Sons, Inc. or one of its group companies (each a"Wiley Company") or handled on behalf of a society with which a Wiley Company has exclusive publishing rights in relation to a particular work (collectively "WILEY"). By clicking "accept" in connection with completing this licensing transaction, you agree that the following terms and conditions apply to this transaction (along with the billing and payment terms and conditions established by the Copyright Clearance Center Inc., ("CCC's Billing and Payment terms and conditions"), at the time that

Copyright clearance from American Chemical Society (Chapter 3)

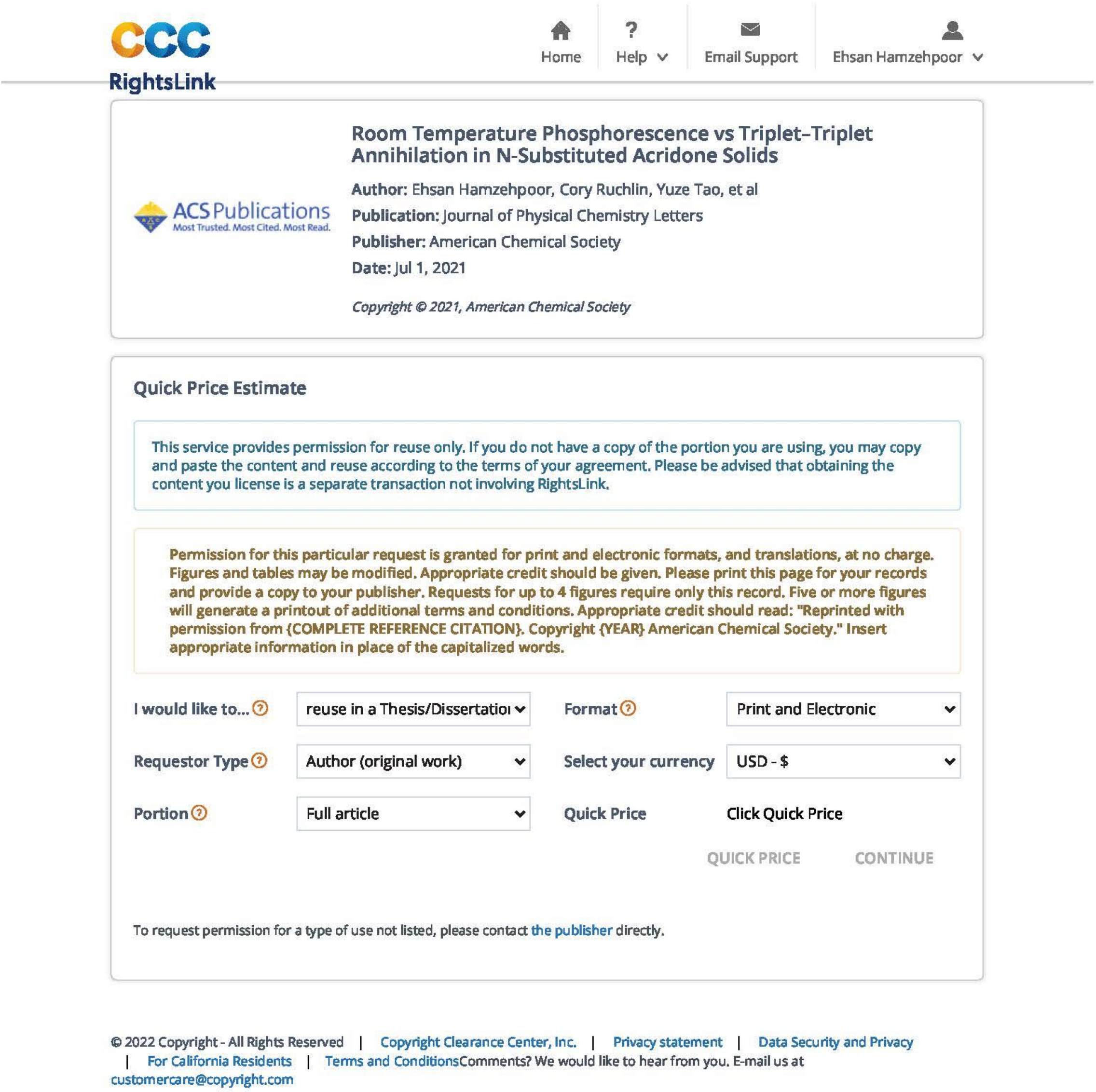

Room Temperature Phosphorescence vs Triplet–Triplet Annihilation in N-Substituted Acridone Solids

Author: Ehsan Hamzehpoor, Cory Ruchlin, Yuze Tao, et al
Publication: Journal of Physical Chemistry Letters
Publisher: American Chemical Society
Date: Jul 1, 2021

Copyright © 2021, American Chemical Society

Quick Price Estimate

This service provides permission for reuse only. If you do not have a copy of the portion you are using, you may copy and paste the content and reuse according to the terms of your agreement. Please be advised that obtaining the content you license is a separate transaction not involving RightsLink.

Permission for this particular request is granted for print and electronic formats, and translations, at no charge. Figures and tables may be modified. Appropriate credit should be given. Please print this page for your records and provide a copy to your publisher. Requests for up to 4 figures require only this record. Five or more figures will generate a printout of additional terms and conditions. Appropriate credit should read: "Reprinted with permission from {COMPLETE REFERENCE CITATION}. Copyright {YEAR} American Chemical Society." Insert appropriate information in place of the capitalized words.

I would like to...	reuse in a Thesis/Dissertatioı	Format	Print and Electronic
Requestor Type	Author (original work)	Select your currency	USD - $
Portion	Full article	Quick Price	Click Quick Price

To request permission for a type of use not listed, please contact the publisher directly.

Copyright clearance from American Chemical Society (Chapter 3)

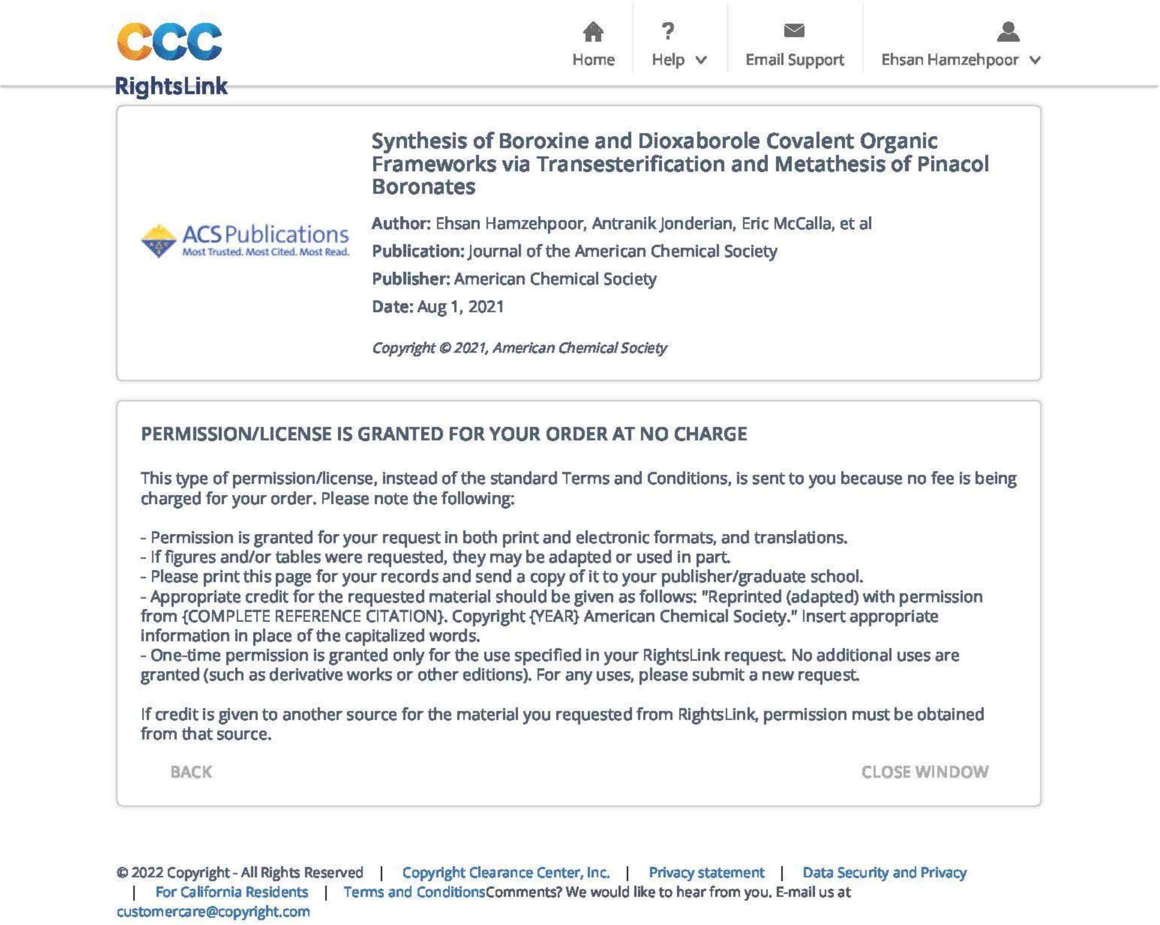

Synthesis of Boroxine and Dioxaborole Covalent Organic Frameworks via Transesterification and Metathesis of Pinacol Boronates

Author: Ehsan Hamzehpoor, Antranik Jonderian, Eric McCalla, et al
Publication: Journal of the American Chemical Society
Publisher: American Chemical Society
Date: Aug 1, 2021

Copyright © 2021, American Chemical Society

PERMISSION/LICENSE IS GRANTED FOR YOUR ORDER AT NO CHARGE

This type of permission/license, instead of the standard Terms and Conditions, is sent to you because no fee is being charged for your order. Please note the following:

- Permission is granted for your request in both print and electronic formats, and translations.
- If figures and/or tables were requested, they may be adapted or used in part.
- Please print this page for your records and send a copy of it to your publisher/graduate school.
- Appropriate credit for the requested material should be given as follows: "Reprinted (adapted) with permission from {COMPLETE REFERENCE CITATION}. Copyright {YEAR} American Chemical Society." Insert appropriate information in place of the capitalized words.
- One-time permission is granted only for the use specified in your RightsLink request. No additional uses are granted (such as derivative works or other editions). For any uses, please submit a new request.

If credit is given to another source for the material you requested from RightsLink, permission must be obtained from that source.

Copyright clearance from Springer Nature Limited (Chapter 3)

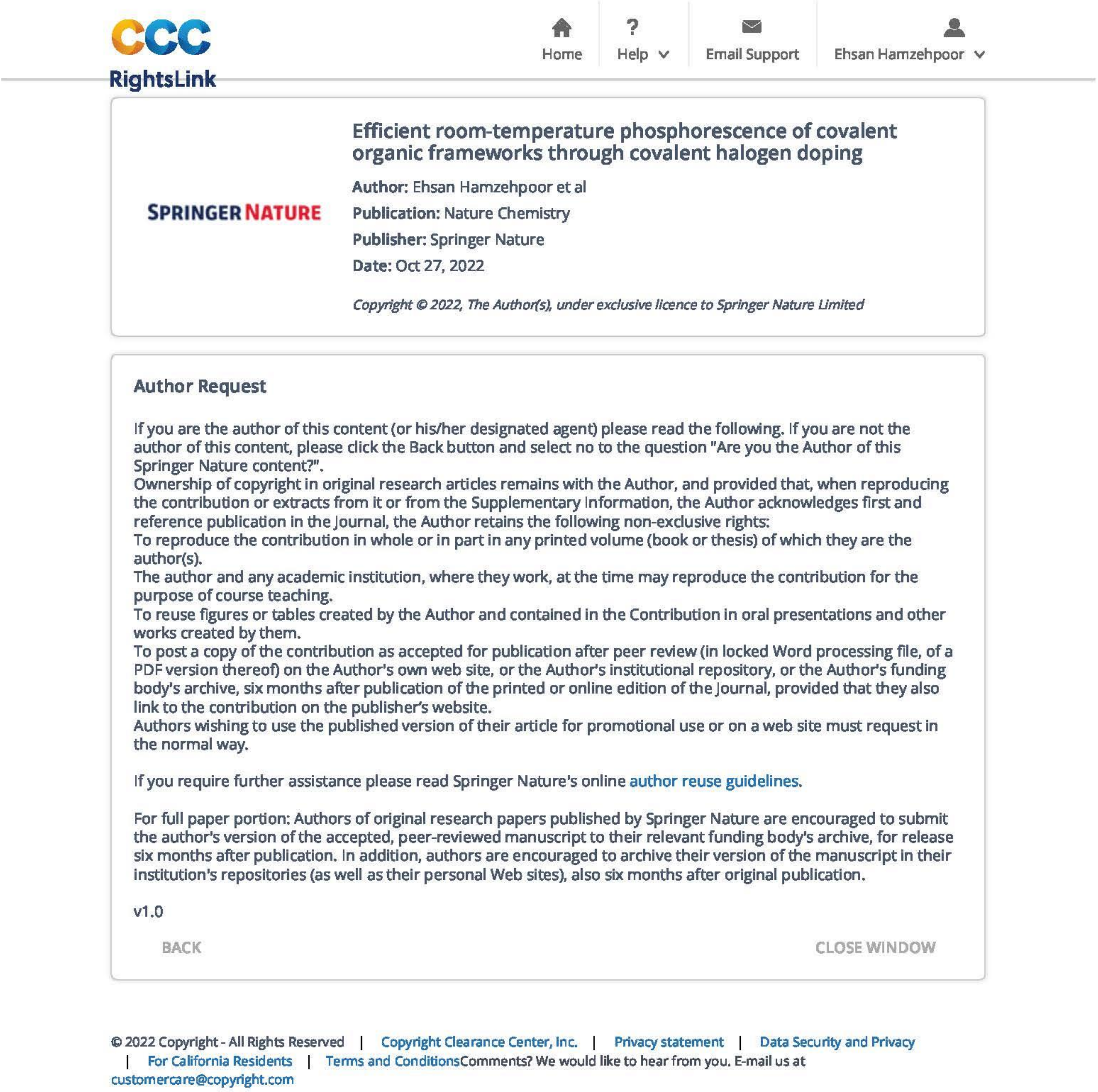

Efficient room-temperature phosphorescence of covalent organic frameworks through covalent halogen doping

Author: Ehsan Hamzehpoor et al
Publication: Nature Chemistry
Publisher: Springer Nature
Date: Oct 27, 2022

Copyright © 2022, The Author(s), under exclusive licence to Springer Nature Limited

Author Request

If you are the author of this content (or his/her designated agent) please read the following. If you are not the author of this content, please click the Back button and select no to the question "Are you the Author of this Springer Nature content?".
Ownership of copyright in original research articles remains with the Author, and provided that, when reproducing the contribution or extracts from it or from the Supplementary Information, the Author acknowledges first and reference publication in the Journal, the Author retains the following non-exclusive rights:
To reproduce the contribution in whole or in part in any printed volume (book or thesis) of which they are the author(s).
The author and any academic institution, where they work, at the time may reproduce the contribution for the purpose of course teaching.
To reuse figures or tables created by the Author and contained in the Contribution in oral presentations and other works created by them.
To post a copy of the contribution as accepted for publication after peer review (in locked Word processing file, of a PDF version thereof) on the Author's own web site, or the Author's institutional repository, or the Author's funding body's archive, six months after publication of the printed or online edition of the Journal, provided that they also link to the contribution on the publisher's website.
Authors wishing to use the published version of their article for promotional use or on a web site must request in the normal way.

If you require further assistance please read Springer Nature's online author reuse guidelines.

For full paper portion: Authors of original research papers published by Springer Nature are encouraged to submit the author's version of the accepted, peer-reviewed manuscript to their relevant funding body's archive, for release six months after publication. In addition, authors are encouraged to archive their version of the manuscript in their institution's repositories (as well as their personal Web sites), also six months after original publication.

v1.0